DEVELOPMENT OF NEW ANALYTICAL PROCEDURES OF ISOTOPE GEOCHEMISTRY BY MASS SPECTROMETRY

APPLICATION TO THE STUDY OF HIGH-PRESSURE METAMORPHIC ROCKS FROM THE IBERIAN MASSIF

eman ta zabal zazu

Universidad del País Vasco

Euskal Herriko Unibertsitatea

Aratz Beranoaguirre de Miguel

ZTF-FCT

Zientzia eta Teknologia Fakultatea

Facultad de Ciencia y Tecnología

PhD Thesis

Leioa, 2016

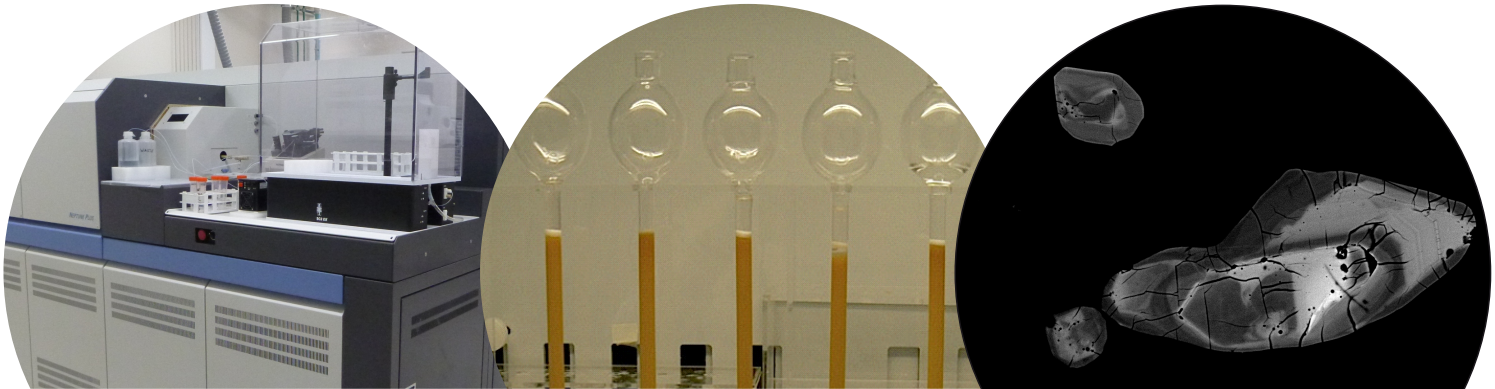

MASA-ESPEKTROMETRIA BIDEZKO PROZEDURA ANALITIKO BERRIEN GARAPENA GEOKIMIKA ISOTOPIKOAN

IBERIAR MAZIZOKO PRESIO-ALTUKO ARROKA METAMORFIKOEN AZTERKETARAKO APLIKAZIOA

Geologia Zientzetan doktore graduarako
Aratz Beranoaguirre de Miguel-ek
aurkezten duen memoria

Zuzendariak:
José Ignacio Gil Ibarguchi
Pablo Puelles Olarte

2016 Otsaila

Universidad del País Vasco Euskal Herriko Unibertsitatea

NAZIOARTEKO BIKAINTASUN CAMPUSA
CAMPUS DE EXCELENCIA INTERNACIONAL

ZTF-FCT
Zientzia eta Teknologia Fakultatea
Facultad de Ciencia y Tecnología

DEVELOPMENT OF NEW ANALYTICAL PROCEDURES OF ISOTOPE GEOCHEMISTRY BY MASS SPECTROMETRY

APPLICATION TO THE STUDY OF HIGH-PRESSURE METAMORPHIC ROCKS FROM THE IBERIAN MASSIF

Dissertation submitted for the degree of
Doctor in Geological Sciences

Aratz Beranoaguirre de Miguel

Supervisors:
José Ignacio Gil Ibarguchi
Pablo Puelles Olarte

2016 February

"Poesiarik gabe hankamotz geratzen da zientzia"

Kirmen Uribe, 2012

ESKERRAK

Esaten dute, euskaldunak ez garela sentimenduak adierazten jaioak. Horrenbeste eskertzeko daukadanean baina, ahalegin berezia egiteko premian nago. Ea zer ateratzen den hurrengo lerroetatik...

En primer lugar, quisiera agradecer a los directores de esta tesis la oportunidad que me han dado. Cuando era niño, en casa siempre me decían: "estudia, para que cuando seas mayor puedas trabajar en lo que te gusta". Estudie Geología, pero desde luego que sin vuestra ayuda no hubiese llegado a trabajar en "lo que me gusta".

Millones de gracias, Iñaki, por poner a mi disposición todo tu conocimiento. Gracias también por poner todos los medios para que mi formación haya sido la más correcta posible.

Eskerrik asko Pablo, urduritasun momentuetan patxada jartzeagatik. Eskerrik asko baita ere, euskaraz idatzitako kapituluak zuzentzeko egindako esfortzuagatik.

Asimismo, me gustaría agradecer a Benito toda la ayuda prestada, tanto por el respaldo ofrecido por su proyecto como por las correcciones a cualquiera de los manuscritos hechos en estos años.

Maru y Sonia, Sonia y Maru. Nunca os podre agradecer lo suficiente todo lo que habéis hecho para que esta tesis haya salido adelante. Tengo la sensación de que por muchas líneas de agradecimiento que os escriba no voy a poder expresar todo lo que me habéis ofrecido. Muchísimas gracias por aconsejarme, apoyarme, ayudarme, ¿abroncarme?, ... Ha sido un placer trabajar a vuestro lado. Como no, muchísimas gracias también a ti Cris, por dibujar una sonrisa en la cara de la gente que te rodea!

Quisiera agradecer también la ayuda que me brindaron Antonio García-Casco e Idael Blanco-Quintero durante mi tiempo en Granada. Muchas gracias Antonio por guiar mis primeros pasos en el mundo de la ciencia y enseñarme como funciona todo esto. Idael, mil gracias por haberme ayudado en mis inicios, cuando tenía la sensación de no saber ni encender un ordenador... "*No hay en la vida nada como la pena de ser ciego en Granada*", ¡ya lo creo!

Cher Christian, sans ton aide c'est sur que les systèmes Rb-Sr et Lu-Hf jamais seraient arrivés à bon port. Je suis persuadé qu'aucun de nous deux est vraiment conscient de tout ce que j'a appris à partir de nos discussions. Un grand merci d'avoir partagé tes connaissances avec moi.

Danke sehr Axel, for your help on set up the Hf isotope analysis procedures and for sharing with us some tricks for working with the Neptune.

Muchas gracias a Pablo Valverde, por darme la oportunidad de continuar en este mundo, enseñándome además nuevas técnicas de análisis. Gracias por compartir conmigo tus conocimientos sobre el sistema U-Th-Pb.

Durante los años que he estado en Leioa, ha habido mucha más gente que me ha ayudado, ya sea por resolver cualquiera mis dudas "científicas", "burocráticas" e incluso "lingüísticas". Muchas gracias a Ainhoa, Ana, Cayo, Egoitz, Fernando, Javi, Jon, Jota, Lidia, Luis Ángel, Manu, Nestor, Ruth, Saioa, etc. Esker berezia eman nahiko nioke Miren Mendiari, zure klaseek sortu bait zidaten Petrologia Metamorfikoan murgiltzeko grina.

En esta acelerada vida que nos ha tocado vivir, es imprescindible también ocupar la mente con cosas menos importantes, a ser posible varias veces al día. En mi rutina diaria, han sido dos los momentos que me han proporcionado ese oxígeno; el café de la mañana y la hora de la comida. Muchísimas gracias a los y las que habéis formado parte de esos momentos, Aritz, Asier, Belén, Idoia, Javi, Jota, Leire, Maru, Pablo y Sonia.

Lehenago esan dut Geologia gustuagatik ikasi dudala. Hori egia da bai, baina zuen ondoan ikasteak liluragarriago egin zituen apunteen artean pasatako urteak! Eskerrik asko Ainhoa, Beñat, Irati, Maite, Nagore, Nagore, Naroa, Ondarru, Pablo, Salcedo, Uxue, etab., pasatako momentu onengatik!

Por suerte, en mi primer periplo por el extranjero también pude rodearme de grandes compañeros y compañeras. Gracias a la gente "granaína"; Chiara, Concha, Edu, Idaira, Juan, Juan Antonio, etc. ¡Tenemos una cerveza pendiente!

"Ez diren gauzak ere badira. Bizitza, ez diren gauzez ere osatzen delako". Horrela mintzo zaigu Joseba Sarrionandia. Esaldi hau neureganatuz, bizitzan Geologia ez diren gauzak ere badirela esan beharko dut. Askotan zer egiten dudan zehazki ez ulertu arren ondoan izan ditudan lagunak ere badira kontu honen parte. Nerbion tabernako familia, zenbat une on bizi izan ditugu azken urteotan!, Koadrilakoak, penak garagardotan itotzeko beti prest, Urtzi eta Iratxe, eta etorriko direnak!, Basauri, Galdakao eta Madrilgo bertso-eskoletako kideak, Euskarabila Basauriko Euskaldunon Elkarteko koadrila, Basaurin Be Bagara herri ekimeneko lagunak, Barandiaranen zein Bolintxun lan egiten duen jendea, etab. Oro har, zuen presentziarekin bizitza alaitzen didazuenoi.

Azkenik nola ez, FAMILIA, eta euren artean gurasoak. Eskerrik asko gaur naizena izateko erakutsitako bideagatik. Eskerrik asko garai hartako Basauri erdaldunean, gu euskaraz hezteko egin zenuten apustuagatik!

ESKERRIK ASKO!

IÑIGO CABACAS JUSTIZIA!!!

Laburpena

Geokimika Isotopikoak/Geokronologiak azken hamarkadatan izan duen bilakaerak hainbat teknika analitikoren hobekuntza eragin du, kate orogeniko metamorfikoen tektonikaren gaineko informazioan iraultza eraginez. Ondorioz, erabiltzen diren tekniketako zehaztasun, zuzentasun edo sentikortasun parametroak, orain dela urte batzuk pentsaezinak ziren mailetara heldu dira, lagin kopuru txikien datazioa ahalbidetuz arroka eta mineraletan. Aurrerapen hauek, ikerlarien kezkekin batera, aukera sorta zabala zabaldu dute datazioei dagokienez.

Azken urteotan, Euskal Herriko Unibertsitateak UPV/EHU berariazko tresneria analitikoa erosi eta gela zuriak eraiki ditu, doktorego tesi honen barruan munduan gehien erabiltzen diren metodo geokronologikoen inplementazioa eta hobekuntza ahalbidetuz. Gainera, metodo hauek arrakastarekin erabili dira lagin naturalen azterketan.

Lan honen helburuetako bat ID-MC-ICP-MS bidezko metodo analitikoen garapena izan da, Rb-Sr eta Lu-Hf sistemen erabilerarako. Rb-Sr sistemaren inplementazioa ^{86}Sr trazatzailea erabiliz egin da gainera, ikerketa geokronologikoetan lehen aldiz. Egiaztatu ahal izan denez, lagin geologikoen tratamendurako ezarritako fusio-disoluzio zein sistema bakoitzaren elementuak isolatzeko prozedurek ondo funtzionatzen dute; metodo biak ikerketa geokimiko/geokronologikoetan erabiltzeko erabat fidagarriak direla baieztatuz. Are gehiago, Rb-Sr eta Lu-Hf sistemen analisiei lotutako ziurgabetasun guztientzako irtenbideak topatu ahal izan dira, eta beraz, esan daiteke bi metodoak zuzen garatu direla eta komunitate zientifikoaren eskura geratzen direla.

Bestalde, laginaren lekuan bertako (*in situ*) analisiak egiteko teknikak ere martxan jarri dira, Geologian gero eta interes handiagoa daukatenak. Doktorego tesi honetan, U-Th-Pb eta Lu-

Hf sistemak zirkoietan analizatzeko metodoak arrakastarekin garatu ahal izan dira. Nazioarteko estandarretan lortutako emaitzak bat datoz erreferentziazko balioekin, prozedura analitikoei datxekien arazoak zuzen konpondu direla erakutsiz. Horrela, metodo biak euren erabilerarako prest geratzen dira.

Azkenik, teknika hauek Iberiar Mazizoaren Ipar-Mendebaldeko Malpica-Tui eta Cabo Ortegal Konplexu Aloktonoetako presio-altuko arroka metamorfikoen datazio eta trazaketarako erabili dira. Lortutako emaitzen arabera, arroka hauek Erdi eta Goi Devoniarrean gertatutako protolito Ordoviziarren subdukzio prozesu baten ondorioz sortutakoak dira. Behe Aloktonoaren subdukzioa geroago ematen da, presio-altuko goi aloktonoaren unitateena baino 15-20 mu geroago. Zirkoiek erakusten duten Hf-aren konposizio isotopikoan oinarrituz ondorioztatu daiteke Goi Aloktonoaren lurperatze maximoan sistema partzialki zabaldu egin zela. Rb-Sr adinak, bi aloktonoetan, berrabiarazitako adintzat hartzen dira, eta zirkoi berrien hazkuntzarekin batera, exhumazioan fluidoen aktibitate garrantzitsua iradokitzen dute.

Abstract

The development of Isotope Geochemistry/Geochronology has triggered many technical improvements in the past decades and has revolutionised the potential information available on the tectonics of metamorphic belts. As a consequence, parameters such as precision, accuracy and sensitivity of the used techniques have reached levels that were inconceivable years ago, thus permitting to date effectively minerals and rocks at small spatial scales. These advances, along with the concerns of researchers have opened a wide range of possibilities in the field of rock dating.

The University of the Basque Country UPV/EHU has acquired the specific analytical equipment and constructed clean laboratories in the last years which has allowed the implementation and improvement of several of the worldwide most used geochronological methods in the course of this PhD Thesis. Additionally, successful application of those methods on natural samples was also carried out.

One of the objectives of the present study was the development of ID-MC-ICP-MS analyses by applying the Rb-Sr and Lu-Hf systems. The Rb-Sr method has been implemented using a ^{86}Sr tracer for the first time in geochronological studies. The procedure of fussion-dissolution set up for the treatment of geological samples, as well as the chromatographic isolation of each isotope in both systems, have proven to work fine in all the cases considered and are regarded as fully reliable for geochemical/geochronological research. Furthermore, since it has been possible to find a solution for all the possible uncertainties associated with the measurements of the Rb-Sr and Lu-Hf systems, it can be stated with certainty that both methods have been implemented correctly being now available for the scientific community.

On the other hand, refined techniques for analysing samples in situ, an area of increasing interest in geology, have been also set up. In this PhD Thesis, the methods for measurements of the U-Th-Pb and Lu-Hf systems on zircons have been developed successfully. The results obtained on international standards are in agreement with the values of reference, which demonstrates that all the problems inherent to the analytical procedures are solved properly and therefore the methods are fully operational for their use.

Finally, these techniques have been employed to date and trace the origin of high-pressure rocks from the Malpica-Tui and Cabo Ortegal Allochthonous Complexes of the NW Iberian Massif. The results obtained for the Upper Allochthon suggest that those rocks were formed as a consequence of the subduction of Ordovician protoliths during middle to late Devonian times. The subduction of the regional Lower Allocthon took place subsequently, 15-20 Ma after. The Hf isotopic data on zircons suggest that the system was partially open during the maximum burial of the Upper Allochthon. Rb-Sr ages for both allochthons, interpreted as reset ages, along with new zircon growth, point to an important activity of fluids during the exhumation of these units.

Resumen

El desarrollo de la Geoquímica Isotópica/Geocronología ha experimentado numerosas mejoras técnicas durante las últimas décadas, revolucionando de este modo la información disponible para la solución de problemas relacionados con la tectónica de cinturones metamórficos. En consecuencia, parámetros como la precisión, la exactitud o la sensibilidad de las técnicas empleadas han alcanzado niveles que eran inconcebibles hace tan solo unos pocos años, permitiendo así la datación de rocas y minerales incluso a muy pequeña escala. Estos avances, junto con las inquietudes propias de los investigadores y las investigadoras, han abierto un amplio abanico de posibilidades en lo que a las dataciones se refiere.

En los últimos años, la Universidad del País Vasco UPV/EHU ha adquirido equipamiento analítico específico y ha construido salas blancas que han permitido la implementación y mejora durante el transcurso de esta tesis doctoral de varios de los métodos geocronológicos más utilizados. Asimismo, se ha llevado a cabo con éxito la aplicación de estos métodos en muestras naturales.

Uno de los objetivos del presente estudio ha sido el desarrollo de métodos analíticos mediante ID-MC-ICP-MS para la aplicación de los sistemas de Rb-Sr y Lu-Hf. La implementación del método Rb-Sr se ha hecho además utilizando por primera vez en lo que a estudios geocronológicos se refiere un trazador enriquecido en ^{86}Sr. Se ha demostrado que el procedimiento de fusión-disoluciónestablecido para el tratamiento de muestras geológicas, así como el aislamiento mediante cromatografía de cada uno de los elementos de interes en ambos sistemas, funciona bien en todos los casos considerados, y por lo tanto, se estima que ambos métodos son totalmente fiables para la investigación geoquímica/geocronológica. Es más, debido

a que se ha podido establecer una solución para todas las incertidumbres posibles asociadas a los análisis de los sistemas Rb-Sr y Lu-Hf, se puede afirmar que ambos métodos se han implementado correctamente y están disponibles para la comunidad científica..

Por otro lado, también se han puesto a punto técnicas para analizar muestras 'in situ', un ámbito de creciente interés en Geologia. En esta Tesis Doctoral, se han desarrollado con éxito los métodos de análisis para los sistemas U-Th-Pb y Lu-Hf en circones. Los resultados obtenidos en los análisis de patrones internacionales se ajustan a los valores de referencia, lo que demuestra que todos los problemas inherentes a los procedimientos analíticos se han solucionado con éxito y que, por lo tanto, los métodos quedan totalmente operativos para su posible uso.

Finalmente, todas estas técnicas se han empleado para datar y trazar el origen de las rocas metamórficas de alta presión de los Complejos Alóctonos de Malpica-Tui y Cabo Ortegal, en el NO del Macizo Ibérico.

Los resultados obtenidos sugieren que las rocas del Alóctono Superior (Ortegal) se formaron como consecuencia de la subducción de protolitos Ordovícicos durante el Devónico medio a superior. La subducción del Alóctono Inferior (Malpica-Tui) tuvo lugar 15-20 Ma despues. La signatura isotópica de Hf en los circones sugiere una apertura parcial del sistema durante el enterramiento máximo de los materiales del Alóctono Superior. Por otra parte, las edades Rb-Sr en ambos alóctonos se interpretan como edades de reajuste isotópico y, junto con el crecimiento de nuevos circones, apuntan a una importante actividad de fluidos durante la exhumación de estas unidades.

INDEX

Chapter 1: Introduction and objectives

1. Introduction and objectives

1.1. Introduction

How old is the Earth? The attempt to give an answer to this question has exerted an enormous influence on the human thought for centuries. The first approaches were made by priests and bishops based on the Old Testament. But undoubtedly this issue became much more objective with the birth of Geology, when the first geologists began to study rock formations. Nicolas Steno (1638-1686) was one of the pioneers. He is considered as the father of Stratigraphy and, actually, he was the first geologist who provided the basic chronological ordering of layers by layers, units by units, fossil assemblage by assemblage, growth zone by growth zone, etc. During the 1600s, 1700s and 1800s geologists developed a geologic time scale based on relative ages.

In this line, and as far as rock dating is concerned, the discovery of radioactivity by Henri Becquerel in 1896 was a major milestone. Some years after, Ernest Rutherford suggested that it might be used as a clock and later on, Bertram Boltwood (1907) published the first radiometric age. It is at this moment when Geochronology was born, the discipline of geosciences that measures the age of earth materials and provides the temporal framework in which other geoscience data can be interpreted.

In fact, thanks to Geochronology, the age of the Earth and the continents is known, and some light has been shed on rock crystallisation processes and rates in magmatic and metamorphic environments. Somehow, it can be assured that the scientific community have gained some perspective on the rate and manner of evolution of the Earth. Besides, the products of radioactive decay, 'radiogenic elements', can also be used as tracers to gain insight into the evolution of magma, the convection pattern of the mantle or the circulation of the oceans, for example.

The development of Isotope Geochemistry/Geochronology has triggered many technical improvements in the past decades and has revolutionised the potential information available on the tectonics of metamorphic belts. As a consequence, parameters such as precision, accuracy and sensitivity of the used techniques have reached levels that were inconceivable years ago permitting effectively to date minerals and rocks at small spatial scales. These advances, along with the concerns of researchers have opened a wide range of possibilities in the field of rock dating. Thus, besides the classically used geochronometers (U-Pb, Sm-Nd, Rb-Sr, Ar-Ar), new systems and routines have been designed (e.g., Lu-Hf or Re-Os) and are widely used within the scientific community.

The group of Petrology and Geochemistry at the Department of Mineralogy and Petrology of the University of the Basque Country UPV/EHU has progressively focussed on the study of geochemistry and geochronology of igneous and metamorphic rocks, mostly within subduction/collision environments, although other research fields, e.g. related to environmental geochemistry or archaemetry have been also tackled (Santos Zalduegui et al., 2004; Inza, 2011; Nocete et al., 2014). The development of new analytical methodologies has been one of the main aims of the group. This represents undoubtedly an advance in the knowledge on the characterization of materials and has led to a significant number of PhD Thesis since the mid 1990s (Ortega Cuesta, 1995; Santos Zalduegui, 1996; Menéndez, 2001, Rodríguez, 2003; García de Madinabeitia, 2004; Sánchez-Lorda, 2013) and concomitant publications. The purchase of specific analytical equipment and construction of clean laboratories in the last years has facilitated the design of new methods of mineral analysis and, with the opportune work and dedication, might promote this institution to a high level among the best laboratories in their class.

As far as high precision isotope measurements are concerned, the Thermal Ionization Mass Spectrometry (TIMS) technique has seen a great development during the 20th century. In fact, the IUPAC (International Union of Pure and Applied Chemistry) recommendations for the standard atomic weights are based on isotope abundance measurements done by TIMS (Coplen, 2001). During the 1980s, Inductively Coupled Plasma Mass Spectrometry (ICP-MS) also appeared as a new tool for analysis (Houk et al., 1980). However, there are some noteworthy differences between both techniques. Whereas TIMS allows to analyse isotope ratios with high precision and accuracy after a cumbersome and time-consuming sample preparation, the ICP-MS, originally designed for elemental analysis, allows the ionization of poorly ionizing elements such as Fe, Cu, Zr, Hf or W (Halliday et al., 1995; Blichert-Toft et al., 1997; Vance and Thirwall, 2002) with a simple and robust sample introduction interface allowing high sample throughput.

A dramatic change took place in the mid 1990s: the ICP-MS instruments were equipped with a magnetic mass filter and a multiple collection system and the high-resolution Multi-Collector Inductively Coupled Plasma Mass Spectrometry (MC-ICP-MS) was born. This allowed accurate and precise determination of isotope ratios, with a precision comparable in most cases to that achieved by TIMS (Albarède et al., 2004). In addition to this 'war' between thermal ionization and plasma source spectrometers, SIMS (Secondary Ion Mass Spectrometer) instruments were installed in several laboratories over the world. Although they are mainly focused on U-Pb analyses, currently they are also used for other studies, such as oxygen isotopes analysis (Ickert et al., 2008; Martin et al., 2014). Furthermore, the development of the laser ablation systems (LA) connected to the ICP-MS instruments allows direct sampling of solids with little or no sample preparation and provides high spatial resolution data. However, despite being

a powerful tool, there are some limitations associated with the technique that need to be taken into account, such as mass discrimination of isotopes, laser-induced elemental fractionation, precision and accuracy of the acquired data, inability to measure samples with low element concentration, etc.

Lately, there is an increasing amount of research works that include age data obtained by means of the U-Pb geochronometer, probably the best known and most used system. There are currently three methods or techniques for U-Pb age determination: (i) Isotope dilution (ID)-TIMS, (ii) SIMS and (iii) LA-ICP-MS. All of them have reached a technological and methodological maturity in data quality and quantity, and the method to use depends on: (i) the duration of the geological process to be dated, (ii) the size of the sample, (iii) the complexity of the sample, and (iv) the number of data needed to address the problem. A review of the strengths and weaknesses of each method can be found in Schaltegger et al. (2015, cf. Table 1).

The ID-TIMS method allows to determine the Pb and U isotopic compositions of separated zircon crystals (or other mineral suitable for U-Pb age determination). In order to do so, the sample needs to be pre-treated (Mattison, 2005), dissolved and spiked. During this process, U and Pb are separated using chromatographic separation techniques in a very clean environment (Schoene, 2014). This technique yields the most precise and accurate U-Pb dates and is mainly applied to magmatic zircons (or other accessory minerals). The accuracy of a U-Pb date determined by ID-TIMS depends on the accuracy of the tracer calibration and the U decay constant uncertainty. Nowadays, the use of specific tracer solutions (Bowring et al., 2005, www.earth-time.org) has improved reproducibility to better than 0.05 % on $^{206}Pb/^{238}U$ dates (McLean et al., 2015). The mass biass may be corrected by repeated measurements of an international reference material or (preferably) by using double-isotope tracers.

SIMS and LA-ICP-MS are two high spatial resolution techniques. The analyses are performed directly on the sample, both in mounted minerals or thin sections, and thus, it is crucial to know the sample. For that purpose, conventional cathodoluminescence (CL) imaging, back-scattered electron (BSE) imaging or electron probe elemental maps are needed.

The strength of the geochronological SIMS lies in its high spatial resolution. It is conditioned by the small diameter of the spot (10–40 µm), its very shallow pit depth (< 4 µm) and the high sensitivity of the technique, which makes it the least destructive of the three analytical methods. For bias correction, the unknowns are analysed between a mineral standard of known Pb/U and a correction is applied assuming that fractionation of Pb from U during sputtering is the same in both cases. However, this statement is not generally achievable (Hinthorne et al., 1979) due to matrix effects or compositional differences. In order to assume that they are the same, the conditions for both standard and unknown (flatness of the polished sample surface or spot size

and beam intensity) must be identical (Williams, 1998; Black et al., 2004). As of today, reported precision on SIMS U-Pb dates is on average ≈ 2-3 % (Schoene, 2014; Schaltegger et al., 2015).

Although in comparison to TIMS and SIMS, LA-ICP-MS is a relatively new technique, its rapid evolution has led to a growing number of review papers (Košler and Sylvester, 2003; Horstwood et al., 2003; Simonetti et al., 2005; Cocherie and Robert, 2008; Gehrels et al., 2008; Sylvester, 2008; Arevalo et al., 2010; Schoene, 2014; Schaltegger et al., 2015). The major strengths of this technique are the following: flexibility, capability of analysing any U-bearing mineral suitable for geochronology, speed of data acquisition (ideal for studies requiring large datasets), and its affordability relative to SIMS.

The laser ablation system can be connected to either multi-collector or single-collector instruments, whether magnetic sector or quadrupole. All those instruments report similar uncertainties, due to the main source of errors derived from: (i) the complicated nature of the ablation process and/or transport to and ionization in the plasma, such as the laser-induced fractionation or depth of the ablation spot (Horn et al., 2000; Košler et al., 2005; Hergenroder, 2006; Paton et al., 2010), (ii) the process by which the laser forms aerosols (Günther et al., 1997; Günther and Heinrich, 1999a; Guillong et al., 2003), and (iii) ionization problems introduced by the choice of the carrier gas (Günther and Heinrich, 1999b; Horn and Günther, 2003; Guillong and Heinrich, 2007). Strategies for managing these uncertainties are described in several reviews (e.g., Koch and Günther, 2011; Russo et al., 2013).

The implementation of these improvements has led to reproducibilities of ca. 2-4 % (Košler et al., 2013). As mentioned before for SIMS, LA-ICP-MS U-Th-Pb dating is a comparative method that depends on a suitable natural or artificial reference material. Therefore, the quality of a SIMS or LA-ICP-MS date is strongly conditioned by the homogeneity of the reference materials and, consequently, the results cannot be more accurate (i.e. including precision) than the level to which the reference materials are defined.

Accurate U-Pb analysis for any of the three techniques described above requires the correction of the initial lead, the so-called 'common Pb' (Pb_c). In ID-TIMS analysis, this correction may be done directly by measuring the ^{204}Pb. The Pb_c correction in SIMS is critical due to the small volume of the sample and in this case, anthropogenic surface derived Pb must be also corrected. The correction in LA-ICP-MS is trickier: since ^{204}Pb is always the least abundant Pb isotope ($^{206}Pb/^{204}Pb >> 1000$ is typical for zircon) it is difficult to measure and besides, it is also affected by isobaric interferences. In fact, in many analytical setups typical for LA-ICP-MS U-Pb dating, ^{204}Pb is not measured due to the unresolvable isobaric interference from ^{204}Hg, requiring different methods of Pb_c correction (Andersen, 2002; Horstwood et al., 2003). Most of them are similar and

assume an initial $^{207}Pb/^{206}Pb$ or $^{208}Pb/^{206}Pb$ value and concordance between the U-Th systems (Williams, 1998).

Unprecedented levels of precision, spatial resolution, flexibility of approach and range of application are now possible at increasingly higher analytical efficiency. Moreover, the possibility to discriminate between two similarly aged materials or data points within data sets, is greatly increased by combining these data with other information, such as trace element information (Rubatto and Hermann, 2007; Claiborne et al., 2010; Schoene et al., 2012) or Hf and O isotopic composition (Davis et al., 2005; Gerdes and Zeh, 2006, 2009).

The Rb-Sr clock was one of the first described geochronometers (Hahn eta al., 1943) and it has been widely used for decades. Traditionally, Rb-Sr ages have been obtained by TIMS analysis, resulting in excellent precision and accuracy for $^{87}Sr/^{86}Sr$ data (ca. 0.002% RSD, e.g. Waight et al., 2002) but less precise $^{87}Rb/^{86}Sr$ values (external reproducibility of ± 1 %, e.g. Waight et al., 2002). The limitation on obtaining the Rb contents is the major source of error in attaining accurate and reproducible ages from Rb-Sr geochronology. Rb has only two naturally occurring isotopes and this precludes correction for mass fractionation during conventional TIMS analysis. Therefore, the fractionation is usually corrected by the measurement of Rb standards, assuming that fractionation of standards and samples is similar. This assumption is not always valid and mass fractionation of Rb may be assessed by repeated analyses of standards.

The introduction of MC-ICP-MS has led to significant improvements in the precision of Rb-Sr isotope ratio measurements. As the ICP source provides the ionization of all elements, a stable isotope ratio of one element can be used to monitor the mass bias of different isotope ratios, and this mass bias can be approximated by using an exponential law (Albarède et al., 2004). The results obtained for $^{87}Sr/^{86}Sr$ after biass correction can be reproduced to 0.003 % (Nebel et al., 2005), comparable to reproducibilities typically given by TIMS analyses.

In the same way, using stable isotope ratios of a different element for mass bias correction is a useful tool for measuring the isotope ratio of elements that have only two isotopes by MC-ICP-MS (Maréchal et al., 1999; Wombacher et al., 2003). Although the assumption that two elements show identical mass bias effects is not necessarily absolutely correct (Albarède et al., 2004), these effects are considerably smaller than the external reproducibility required for a Rb isotope dilution analysis (< 0.1 %). Using Zr for mass bias correction during MC-ICP-MS measurement of $^{87}Rb/^{85}Rb$ has proven suitable for Rb isotope analyses and provides a reproducibility of ± 0.02 % (2 s.d.) and ± 0.2 % (2 s.d.) for unspiked and spiked Rb isotope compositions (Waight et al., 2002; Willigers et al., 2004; Nebel et al., 2005).

Attempts to measure $^{87}Rb/^{85}Rb$ for Rb-Sr chronology using a single collector ICP-MS achieved a reproducibility similar to that of TIMS analyses (Montero and Bea, 1998, Vanhaecke et al, 2001; Pin et al., 2003).

Much of the error involved in the Rb isotope dilution and Sr isotope ratio measurements by multiple collector inductively coupled plasma mass spectrometry (MC-ICP-MS) is derived from uncertainties as to which $^{87}Sr/^{86}Sr$ (and $^{87}Rb/^{85}Rb$) ratios to use when correcting for isobaric interferences due to the presence of spike Sr and Rb at mass 87. If isobaric interferences are minimised by efficient separation of Rb from Sr during cation exchange chemistry, the use of natural ratios for isobaric interference corrections yields the most reproducible data, indicating that the interferences are derived from environmental blank. Larger isobaric interferences at mass 87 are indicative of inefficient chemical separations. The geological community is aware of the importance of this step, and numerous methods for isolating Rb and Sr have been addressed (Pin et al., 2003; Nebel et al., 2005; Yang et al., 2010). It should be mentioned that this step is even more important in ICP-MS, since the burning off of Rb during TIMS Sr isotope analysis nullifies this isobaric interference.

Isotope dilution (ID) is the most accurate method for the determination of Rb and Sr contents of a sample. The spike usually used for Sr analysis is an ^{84}Sr-enriched solution, which allows a straightforward correction for its contribution. The new methodologies of the Zr-based biass correction could be also applied to Sr measurements (Yang et al., 2008), allowing the use of other tracers such as ^{86}Sr-enriched solutions. The main disadvantage of the ^{86}Sr tracer is that it is necessary to measure two aliquots for each analysis, one without spiking for isotopic composition measurement (IC), and the other one with added spike for the concentration. By contrast, it represents a cheaper alternative for Rb-Sr analysis, and it is less sensitive to the Kr correction (Kr comes together with the Ar used in ICP instruments). In this PhD, a new method based on the use of such tracer, so far only employed in trace element analysis but not in geochronology, is developed.

Despite the above-mentioned improvements, the accuracy of the Rb-Sr ages has still been limited by the uncertainty of $\lambda^{87}Rb$. Fortunately, some laboratories over the world are working in order to assess a value (as precise and accurate as possible) to the Rb decay constant (Kossert, 2003; Nebel et al., 2011; Rotenburg et al., 2012; Villa et al., 2015). All these considerations will improve the Rb-Sr dating due to the precision and accuracy that might be achieved in the $^{87}Rb/^{86}Sr$ ratio, which has been traditionally the major source of error.

As stated above, the Lu-Hf radiogenic isotope system was not generally adopted in solid earth sciences until the advent of Multi-Collector Inductively Coupled Plasma Mass Spectrometry (MC-ICP-MS) in the mid-1990s, mainly because of the poor ionization efficiency of hafnium by

TIMS (Halliday et al., 1995). However, the rapid development of the MC-ICP-MS has allowed the utilization of Hf isotopes as a tracer (Thirlwall and Walder, 1995; Blichert-Toft and Alvarède, 1997; Blichert-Toft et al., 1997) and as a geochronological tool (Duchêne et al., 1997; Scherer et al., 2000), either by laser ablation or by isotope dilution.

One potential problem of Lu-Hf dating by isotope dilution is the presence of Hf-rich inclusions, such as zircon or rutile, in the datable minerals, which can result in imprecise and inaccurate ages (Scherer et al., 2000; Blichert-Toft and Frei, 2001). Due to the difficulty of removing all zircon and rutile inclusions from the mineral separates using only standard physical techniques such as crushing, magnetic separation and hand picking, several strategies to get rid of them have been published over the last years (Blichert-Toft et al., 1997; Duchêne et al., 1997; Anczkiewicz and Thirlwall, 2003; Cheng et al., 2008; Herwartz et al., 2008; etc.)

As in the Rb-Sr system, the addition of tracers and the total separation of Lu and Hf is necessary to obtain precise and accurate analyses. The protocols that have been proposed for this purpose also allow the straightforward separation of Sm and Nd, and thus, permit to date the rock with both geochronometers (Pin and Joannon, 2002; Vry et al., 2004; Cheng et al., 2008; Seth et al., 2008; Kirchenbaur et al., 2012). The Sm-Nd system is sensitive to Nd-rich inclusions, such as apatite, zoisite or monazite, and a specific sample treatment is also required (Anczkiewicz and Thirlwall, 2003; 2004).

The main analytical challenge to produce precise and accurate Lu-Hf isotope data is to make accurate corrections for the isobaric interferences from ^{176}Yb and ^{176}Lu on ^{176}Hf as well as the mass bias correction for each element. In ID-MC-ICP-MS techniques, Yb, Lu and Hf are separated before the analysis and thus, those interferences are prevented. However, as Lu is a two-isotope element, it is necessary to correct for mass bias using a stable isotope ratio of a different element, either Yb (with correction for the isobaric interference from ^{176}Yb on ^{176}Lu, e.g., Vervoort et al., 2004) or Hf (with some correction factor to account for the difference between Hf and Yb mass bias, e.g., Chu et al., 2002). Those corrections are much more important in LA-MC-ICP-MS analyses since there is no element separation and all the mineral forming elements reach the detectors. The largest correction needed in zircon (the most analysed mineral) is from ^{176}Yb, because ^{176}Lu comprises only 2.6 % of Lu, and Lu/Hf is generally very low, and thus an accurate correction could be applied for the isobaric interference from ^{176}Lu. In contrast, ^{176}Yb presents a much more significant correction because Yb contents in zircon are approximately four times higher than those of Lu and also because ^{176}Yb comprises more of Yb (12.7 %) (Hoskin and Ireland, 2000). As discussed in detail by Woodhead et al. (2004), for laser ablation analysis it is strongly recommended to measure directly two interference-free Yb masses (^{171}Yb, ^{172}Yb or ^{173}Yb), which enables both mass bias and interference correction.

This approach requires the use of several isotope ratios, e.g. $^{173}Yb/^{171}Yb$, $^{171}Yb/^{176}Yb$ and $^{176}Lu/^{175}Lu$. Although the $^{176}Lu/^{175}Lu$ is well established (0.02656, e.g. Patchett and Tatsumoto, 1980), there is currently no consensus on which Yb isotope ratios to use for this correction (e.g., Chu et al., 2002; Segal et al., 2003; Amelin and Davis, 2005; Vervoort et al., 2004). Due to the uncertainties that these values can produce in the final result, it is essential that the authors of any LA-MC-ICP-MS study report the assumed Yb isotope ratios used in mass bias and interference corrections.

1.2. Objectives

Since the University of the Basque Country UPV/EHU had the instrumental required to carry out the implementation and improvement of the above-mentioned methods, the objetives intended with this PhD Thesis have been the following:

i). Set up of ID-MC-ICP-MS analytical techniques for Rb-Sr and Lu-Hf analysis.
ii). Implementation of LA-ICP-MS techniques for U-Pb and Lu-Hf 'in-situ' measurements directly on thin section.
iii). Application of the implemented methods to the study of high-pressure rocks from the Allochthonous Complexes of the NW Iberian Massif with the purpose of unraveling the geological evolution of specific units.

In order to achieve these objectives it was necessary to solve a series of basic and essential issues related to each one of the analytical routines to be implemented. Among them the following would necessarily to be taken into consideration:

- Calibration of the tracer solutions and establishment of a protocol for sample preparation and subsequent separation of elements, both for determining the elemental and isotopic composition of Rb-Sr and Lu-Hf.
- Optimization of the measurement parameters in the equipment to enable further analysis of unknown samples by isotope dilution technique with confidence.
- Optimization of the measurement parameters in the equipment for laser ablation analysis.
- Validation of the previous points by repeated analyses on samples of known composition.

Throughout the following pages it will be described the process followed to solve the analytical problems related to: (i) treatment of samples and instrumental parameters, and (ii) validation of results for the methods set up by the analysis of a series of international reference materials. Finally, the data obtained by the application of these new methods to the high-pressure rocks will be presented.

Thus, this PhD Thesis is structured into five chapters:

- Chapter 1: main approaches and issues.
- Chapter 2: description of the equipment used during this work.
- Chapter 3: description of the implemented analytical techniques for Rb-Sr and Lu-Hf by ID-MC-ICP-MS and U-Pb and Lu-Hf by LA-ICP-MS.
- Chapter 4: application of the implemented methods to high-pressure rocks from the Allochthonous Complexes of the NW Iberian Massif.
- Chapter 5: conclusions.

2. Kapitulua: Tresneria

2. Tresneria

Tesi honetan egindako lanik garrantzitsuena masa-espektrometroen bidezko analisiak izan dira. Bi espektrometro izan dira zehazki, lana aurrera eramateko erabili direnak. Alde batetik, detektagailu anitzeko, induktiboki akoplatutako plasma iturridun masa-espektrometroa (*Multicollector Inductively Coupled Plasma Mass Spectrometer*, MC-ICP-MS, Finnigan Neptune, Thermo Fisher Scientific, 2.1. Irudia), eta bestetik, induktiboki akoplatutako plasma iturridun masa-espektrometro kuadrupolarra (*Quadrupole Inductively Coupled Plasma Mass Spectrometer*, Q-ICP-MS, Xseries 2, Thermo Fisher Scientific, 2.2. Irudia). MC-ICP-MSaren bidez laginak solido-zein likido-egoeran analizatu dira, aurrerago azalduko diren beharrizanen arabera. Q-ICP-MSan berriz, solido-egoeran sartutako laginak neurtu dira soilik. Lagin solidoen analisirako, Nd:YAG solido-egoerako laser ablazio-sistema erabili da (UP213, New Wave Research).

Ekipo hauek Geokronologia eta Geokimika Isotopikoaren Zerbitzuari (IBERCRON) dagozkio, Universidad del País Vasco/Euskal Herriko Unibertsitatearen (UPV/EHU) Ikerkuntzarako Zerbitzu Orokorren (SGIker) barruan.

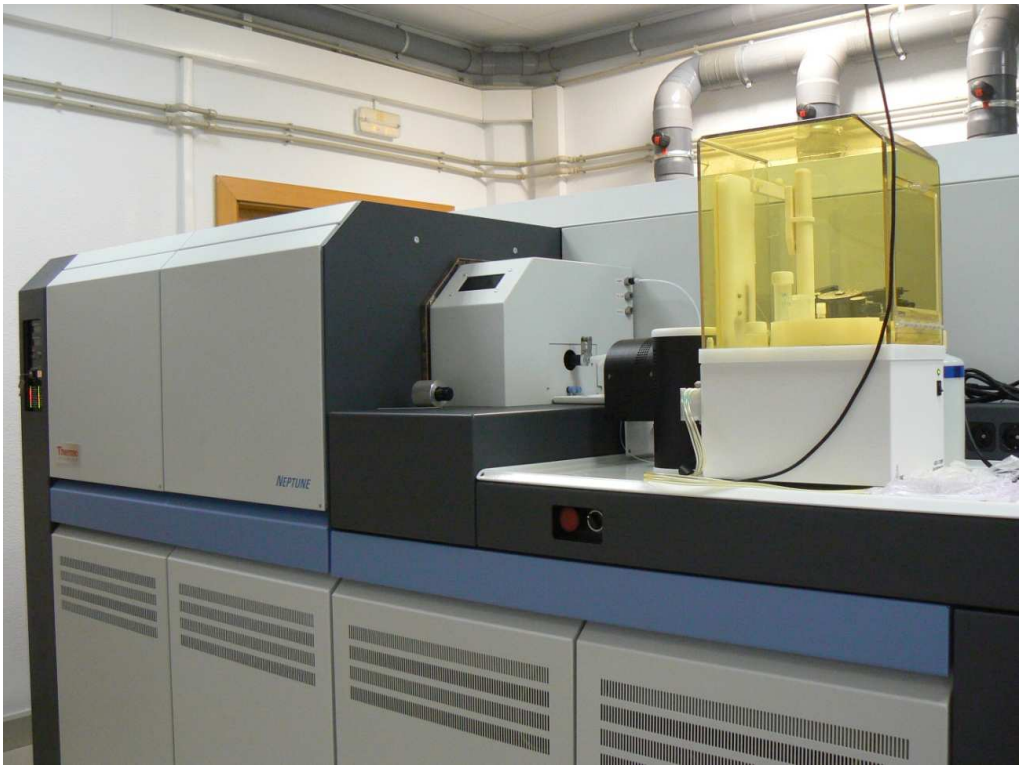

2.1. Irudia. UPV/EHUko Ikerkuntzarako Zerbitzu Orokorretako MC-ICP-MS Neptune espektrometroa.

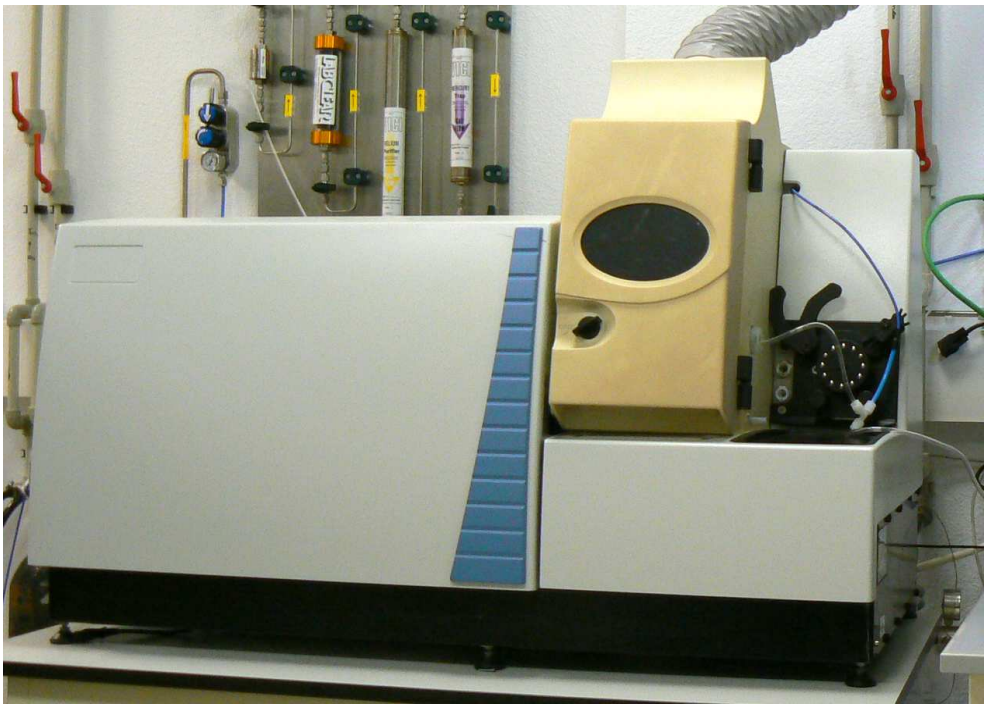

2.2. Irudia. UPV/EHUko Ikerkuntzarako Zerbitzu Orokorretako Q-ICP-MS XSeries2 espektrometroa.

Espektrometro biak, bai eta laser ablazio-sistema ere, klimatizazioa eta iragazitako airezko gainpresioa (HEPA iragazki terminalak eta aurre-iragazkiak) dauzkan laborategi batean daude instalatuak. Espektrometroek etengabeko elikadura elektrikoa bermatzen duen unitateak (*uninterruptible power supply*, UPS) dituzte.

Jarraian, ekipo hauen funtsezko ezaugarrien zehaztasunak deskribatuko dira, baina horren aurretik, espektrometroen oinarrizko fundamentuak gogoratuko dira era labur eta sinplifikatuan. Instrumentuen aukera analitikoen deskribapen zehatzetarako, literaturara jotzea gomendatzen zaio irakurleari (Taylor, 2001; Wieser eta Schwieters, 2005; Hoffmann eta Stroobant, 2007; Vanhaecke eta Degryse, 2012; Prohaska et al., 2014; etab.).

2.1. Masa-espektrometria

Masa-espektrometria (MS) analisi elemental, isotopiko zein molekularretan erabili daitekeen detekzio-teknika da, eta masa-espektrometroetatik lortutako informazioa kualitatiboa zein kuantitatiboa izan daiteke. Masa-espektrometria gas-egoeran dauden molekulen edo atomoen ionizazioan datza. Ioni zatutako atomo/molekulak eremu magnetikoaren bidez azkartzen dira eta euren masa/karga (m/z) erlazioaren arabera banatu egiten dira.

Masa-espektrometroen bidezko analisien fundamentua oso erraza, dagoen tresneria ikaragarri konplexua den arren. Era sinplifikatu batean, ondokoak dira masa-espektrometro bat

osatzen duten atalak: laginen sarrera-sistema, ionizazio-iturria, masa-analizatzailea eta detektagailua (2.3. Irudia).

1.- Laginen sarrera-sistema ez da berez masa-espektrometroen atala, laginak espektrometroetan sartu ahal izateko osagarri bat baizik. Lagina gas-egoeran sartzen da espektrometrora, eta atal honen helburua, solido- zein likido-egoeran dauden lagin kantitate txikiak aerosol bihurtzea da. Horretarako, sarrera-sistema ezberdinak daude (2.3. atala).

2.- Ionizazio-iturriaren helburua masa-espektrometrora heltzen den elementua edo molekula ionizatzea da. Ioinizazioa teknika ezberdinen bitartez lortu daiteke, hala nola, elektroi edo molekulen bonbardaketa, edota energia termiko edo elektrikoa erabiliz. Izan ere, ionizazio-sistemen aniztasuna oso handia da, masa-espektrometroaren aplikazioen faktore mugatzailea izan daitekeelarik. Ionizazioan erabilitako energia kopuruak sortutako ioi mota baldintzatzen du (ioi poliatomikoak, isolatutako isotopoak, molekula konplexuak, etab.), eta beraz, baita ekipoen aukera analitikoak ere.

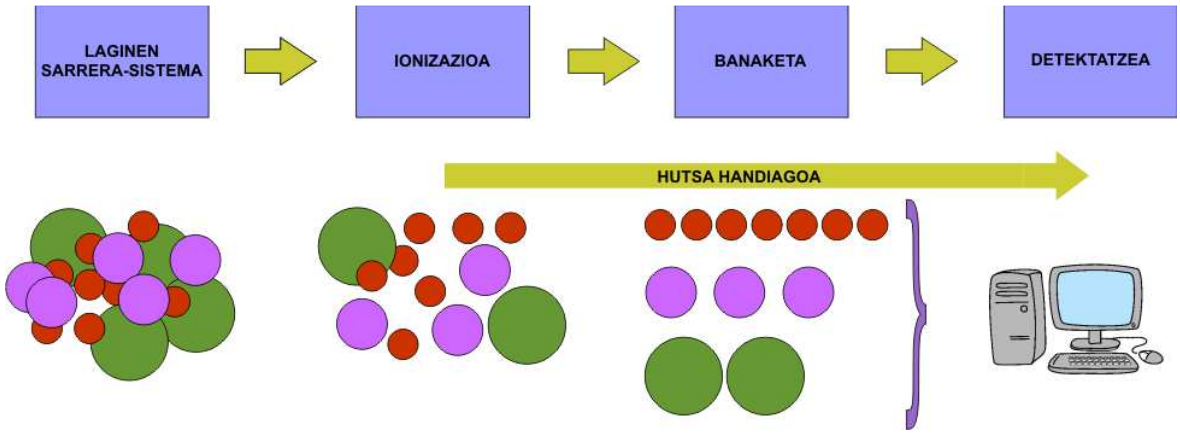

2.3. Irudia. Masa-espektrometro baten oinarrizko eskema.

3.- Masa-analizatzailea, sortutako ioien banaketaz arduratzen den gailua da, masa/karga (m/z) erlazioaren arabera bereiziz. Analizatzailerik arruntenak, kuadrupoloa, sektore magnetikoa, hegaldi-denbora (*time of flight*) eta ioi tranpa dira.

4.- Detektagailuaren funtzioa m/z balio bakoitzeko ioi kopurua zenbatzea da eta horretarako elektroi sorta prozesatu eta gorde daitekeen seinale elektriko bihurtzen du. Gehien erabiltzen den detektagailua, elektroi sekundarioen biderkagailua (*Secondary Ion Multiplier,* SEM) da.

Iturri ezberdinen eta banaketa-sistema ezberdinen arteko konbinazioek, ahalmen eta aplikazio anitzetarako konfigurazioak ahalbidetzen dituzte. Hori dela eta, masa-espektrometriaren tekniketan arrunta izan ohi da akronimo ezberdinen konbinazioa; ionizazio-sistema, analizatzailea eta, batzuetan, detektagailu mota adierazteko (GC-MS, Q-ICP-MS, TIMS, SIMS, SF-ICP-MS, VPD-ICP-MS, HPLC-ICP-MS, UHR-SEC-HPLC-ICP-MS, etab.).

2.1.a. Ionizazio-iturria: ICPa

Tesi honetan erabili den ionizazio-iturria induktiboki akoplatutako plasma (*Inductively Coupled Plasma*, ICP) izan da, masa-espektrometria ez-organikoan ionizazio-iturririk erabiliena. Plasmen ezaugarri nagusiena daukaten tenperatura altua da, 7.000 eta 10.000 K bitartekoa. Horri esker, laginen lotura guztiak apurtzen dira eta analisi elementalak edota isotopikoak ahalbidetzen dira. Plasma eratzeko, argona indukzio-haril batean kokatutako kuartzozko zuzi batetik pasarazten da, zeinari 750 eta 1700 W-ko irrati-frekuentzia energia ezartzen zaion, eremu elektromagnetiko handia sortuaz bere eraginpeko inguruan (2.4. Irudia).

Momentu horretan zuzitik pasatzen ari den argonari (Ar) txinparta bat eraginez gero, elektroi batzuk Ar atomoetatik bereiziko dira. Elektroi hauek eremu magnetikoan harrapatuta geratzen dira, eta ibilbide zirkular itxietan azeleratzen dira. Prozesu honi induktiboki akoplatua deritzo eta horregatik horrela sortutako plasma induktiboki akoplatutako plasma bezala ezagutzen da. Azkar mugitzen ari diren elektroiak argonaren atomo neutroekin talka egiten duten heinean, elektroi gehiago bereizten dira atomoetatik, kate-erreakzio bat emanez. Talka prozesu hau da plasmaren tenperatura altua sortarazten duena. Plasma-hodeia elektroi eta argonezko ioi positibo eta atomo neutroez osatua dago beraz. Plasma egoera bere horretan mantenduko da indukzio-harilaren bidez irrati-frekuentziak irauten duen bitartean. Tresna analitikoetan solido-zein likido-egoeran dagoen lagina ioietan eraldatzea da plasmaren betebeharra. Horrela, aerosol moduan sartutako lagina, desolbatatu, lurrundu eta atomizatu egiten da berehala, azkenik, partzialki ionizatua delarik.

Zuzia kuartzozko hiru hodi zentrokidez osatua dago, zeinetatik argon fluxu ezberdinak pasarazten diren. Barneko hoditik, edo hodi injektoretik, lagina sartzen da. Kanpoko hoditik, plasma bilakatuko den argona dator, 15 L/min-ko jarioarekin eta era tangentzialean, plasma zuzitik aldendu eta honen eta zuziaren kanpoko pareten kontaktua saihestuz, azken honen fusioa ekidinez beraz. Erdiko hoditik, gas laguntzailea pasatzen da 0,7 L/min-ko fluxuarekin Q-ICP-MS-an eta 0,45 L/min MC-ICP-MSaren kasuan. Gas hori argona da ere eta bere betebeharra sortutako plasma barneko hoditik aldentzea da, injektorea urtu ez dadin. Zuzia gainera zilarrezko kanpo-estalki zilindriko batez osatzen da, '*torch screen*' edo '*guard electrode*' izenekoa, (2.5. eta 2.6. Irudiak), zeinak ekipoak seinaleekiko duen erantzuna nabarmenki handitzen duen. Zuzia azkenik, 3 buelta dituen kobrezko haril-hodi batez inguratuta dago, zeinaren barnetik ura pasarazten den harila hoztu eta funtzionamendu egonkorra mantentzeko helburuarekin (2.6. Irudia). Kobrezko harila irrati-frekuentzia sorgailu bati konektatua dago, eremu magnetiko bat sortuz harilaren barnekaldean eta zuziaren amaieran.

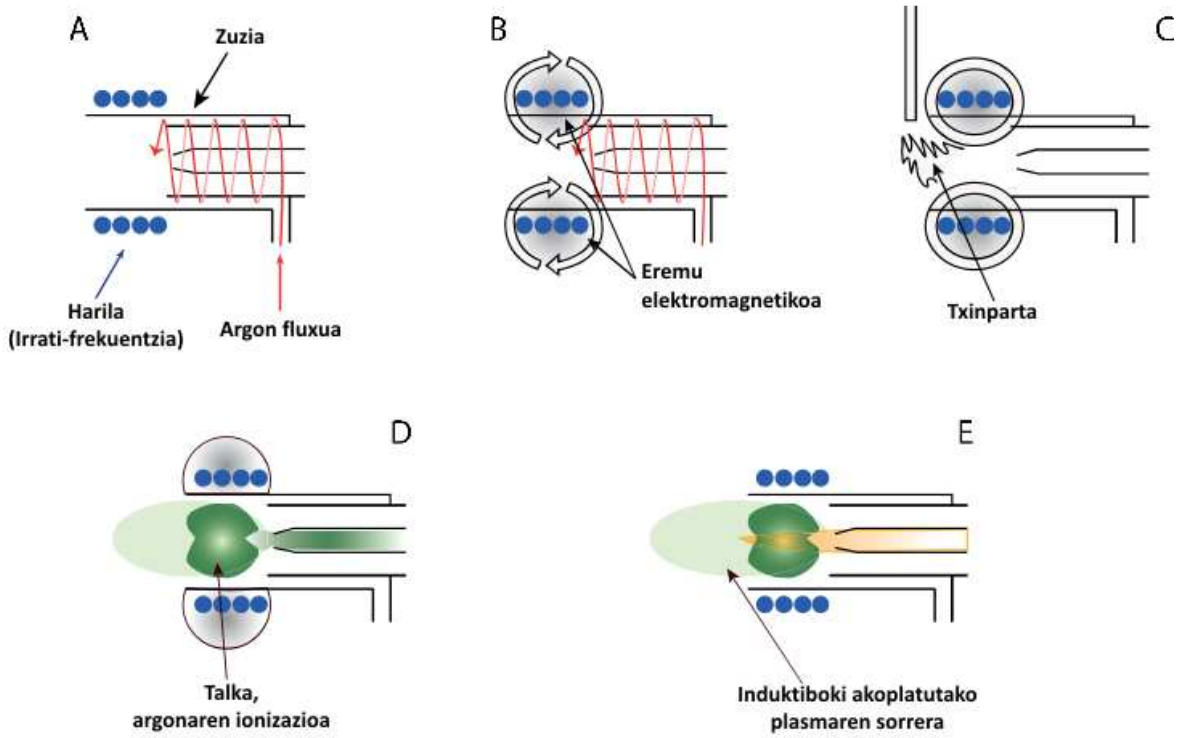

2.4. Irudia. Plasmaren sorrera ahalbidetzen duten prozesuen eskema.

Bi zuzien arteko ezberdintasunik nabarmenena zuziaren geometrian datza, izan ere, Q-ICP-MSaren zuzia kuartzozkoa eta pieza batekoa den bitartean, MC-ICP-MSarena desmuntagarria da, injektorea zafirozkoa delarik. Plasma sorreran ez dago ezberdintasunik.

2.1.b. Interfasea

Interfase edo fasearte izenez ezagutzen den eremuaren funtzioa plasma iturrian sortutako ioiak masa-analizatzailera bideratzea da, behar diren huts-baldintzak mantenduz. Izan ere, ionizazio-iturria presio atmosferikoan dago analizatzailea maila altuko hutsean dagoen bitartean.

Interfasea erdialdean oso zulo txikia duten bi kono metalikoz osatua dago (2.7. Irudia): laginketa konoa (*sampler cone*) eta edo bereizketa konoa (*skimmer cone*). Bi konoen arteko eremuan behar den huts-baldintzak lortzeko, huts-ponpak erabiltzen dira, plasma piztu aurretik egunero martxan jartzen direnak. Horrez gain, masa-analizatzailean behar diren huts-baldintzak mantentzeko '*slide valve*' edo '*skimmer valve*' izeneko balbula irristakor bat dago, interfaseko hutsa ona denean soilik irekitzen dena.

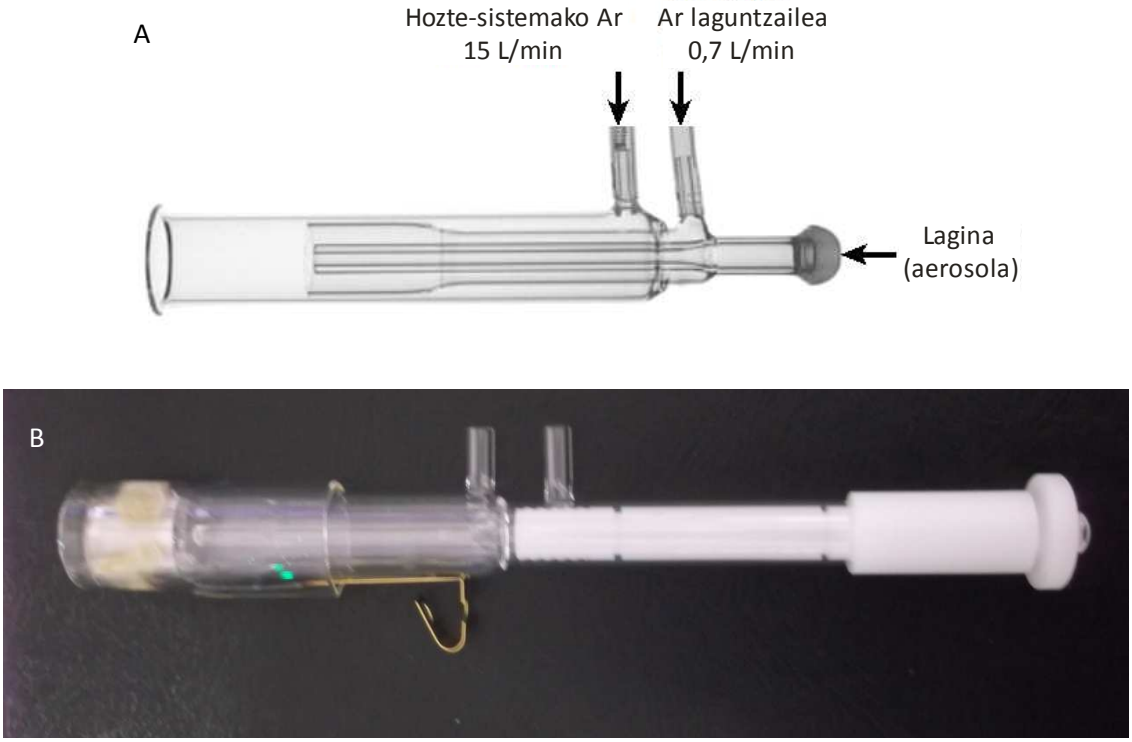

2.5. Irudia. Tesian erabilitako zuziak. A: Q-ICP-MSarekin erabiltzen dena. B: MC-ICP-MSarekin erabiltzen dena, kanpo-estalki zilindrikoarekin.

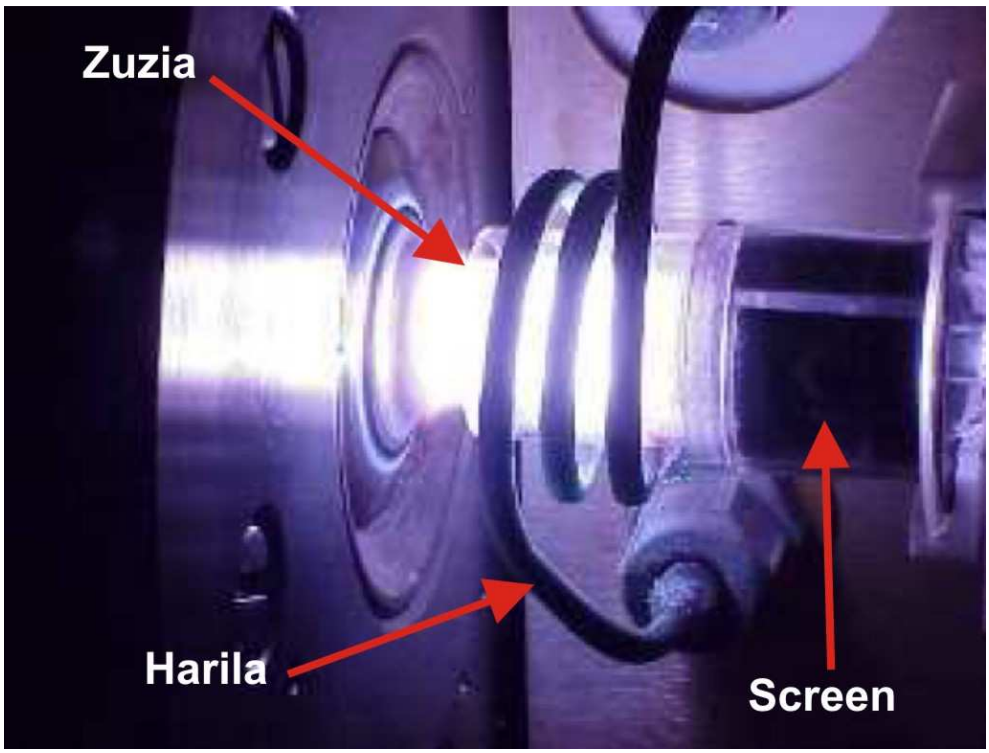

2.6. Irudia. Zuzia, harila eta '*torch screen*'-a (zuziaren estalkia).

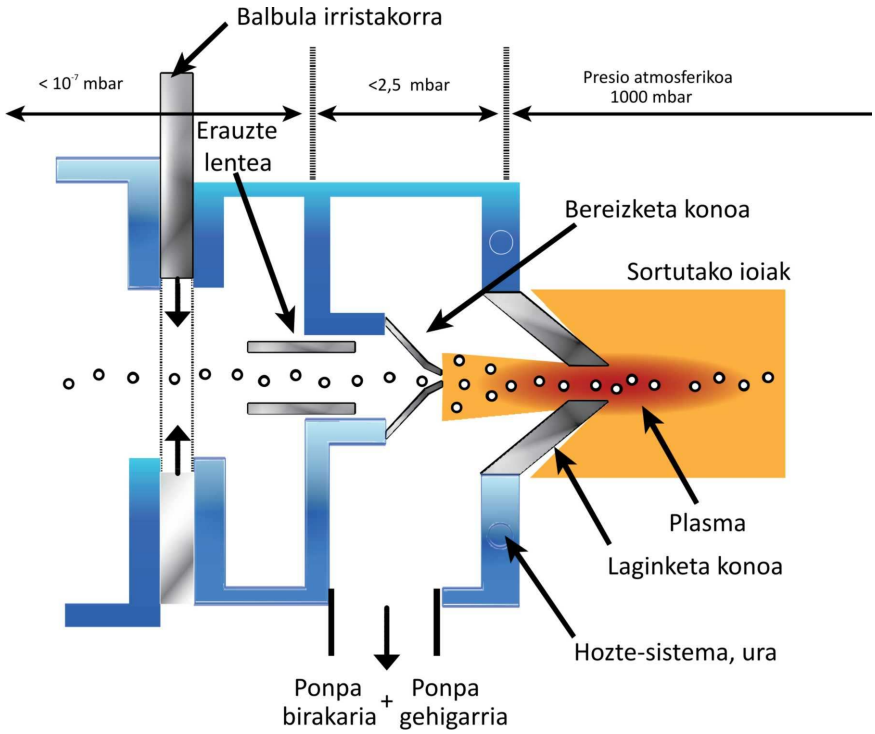

2.7 Irudia. ICP-MS arrunt baten interfaseko eskema (bereizketa konoa, laginketa konoa, hozte-sistema).

Horrelako ekipoetan erabiltzen diren konoak ezberdinak izaten dira laginen sarrera-sistemara egokitzeko. XSeries 2 ekipoan *Xt* izeneko interfasea erabiltzen da, non laginketa konoa eta bereizketa konoa nikelezkoak diren (2.8. Irudia).

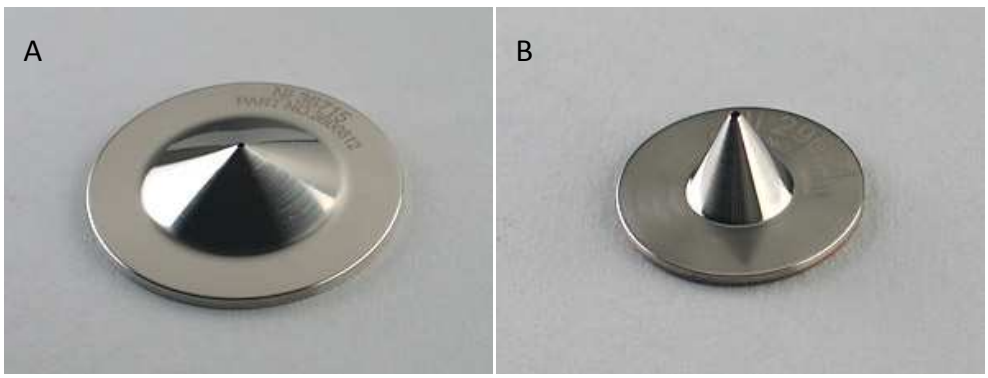

2.8. Irudia. Q-ICP-MSaren interfasean erabilitako konoak. A: Laginketa konoa. B: Bereizketa konoa.

MC-ICP-MS-an kono ezberdinak erabili dira. Lagina egoera likidoan sartzen bada konoak estandarrak dira, nikelez eginak (2.9A eta C Irudiak). Egoera solidoan sartzeko konoak ere nikelez eginak dira, baina laginketa konoak punta pikoagoa dauka (2.9B Irudia), plasma lehorren sentikortasuna areagotzeko.

2.9. Irudia. MC-ICP-MSaren interfaseko konoak. A: '*Skimmer*' edo bereizketa konoa (plasma heze zein lehorretarako baliogarria). B: Plasma lehorretarako (laser bidezko lagin sarrera) '*sampler*' edo laginketa konoa. C: Plasma hezeetarako (disoluzio bidezko lagin sarrera) '*sampler*' edo laginketa konoa.

Interfasearen huts-baldintzak guztiz erlazionaturik daude espektrometroak duen sentikortasunarekin. Hori dela eta, UPV/EHUn dauden ekipoek huts-ponpa sistema hobeturik dute, ponpa gehigarriaren bitartez kuadrupoloan eta turbo-ponparen bidez MC-ICP-MSan.

2.1.c. Ioien ardazte-sistema

Ioien ardazte-sistema garrantzi bereziko eremua da ICP-MSaren barruan, masa-analizatzailera sartuko diren ioi sortaren bideratzea bertan egiten baita. Bere betebeharra interfasetik analizatzailera analitoen ioi kopuru ahalik eta handiena eramatea da, aldi berean matrizean dauden osagairik gehienak baztertuz.

UPV/EHUn dauden ekipoen kasuan, sistema hau metalezko lente ioniko batzuen bidez osatzen da, zenei tentsio bat ezartzen zaien ioien ibilbidea aldatzeko helburuarekin. Hau da, lente ionikoek analitoaren ioiak elektrostatikoki gidatzen dituzte interfasetik masa-banaketa sistemaraino. Ekipoaren gune honetan erauzte-lentea ere topatu daiteke, zeina ioi positiboak eta espezie ez-ionikoak, hala nola, partikulak, espezie neutroak (atomoak eta molekulak) eta fotoiak banatzeaz arduratzen den, azken hauek masa-analizatzaile eta detektagailura heltzea ekidinez. Lente ionikoak aurkitzen diren bitarteko eremu honetan presio baxuak daude, huts-baldintzak handituz baitoaz detektagailurako bidean.

Q-ICP-MSko eta MC-ICP-MSko ioen ardazte-sistema eta huts-baldintzak oso ezberdinak dira. Kuadrupoloak lente ioniko-sistema simplea du, behar duen hutsa 10^{-7}- 10^{-6} mbar bitartekoa izanik.

Neptunearen kasuan sistema konplexuagoa da (2.10. Irudia), interfasetik analizatzailera dagoen eremuan, ioiak bideratzeaz gain, bereizi ere egiten direlako. Horretarako MC-ICP-MSen ardazte-sistemak zenbait lente ioniko ditu, ondoko atalez osatuak: analizatzaile elektrostatikoa (*Electrostatic Sector Analizer*, ESA), kuadrupolo bat eta erresoluzioa aldatzeko sarrera zirrikitua (*entrance slit*). Sistema honek maila altuko hutsean funtzionatzen du, 10^{-7} mbar inguru.

Analizatzaile elektrostatikoa okertutako bi plakek osatzen dute. Korronte zuzena ezartzen zaie eta honi esker, barruko plakak, polaritate negatiboarekin, karga positibodun ioiak erakartzen ditu, polaritate positibodun kanpoko plakak aldaratzen dituen bitartean. Ioi sorta bi plaken artean igarotzerakoan fokatu egiten da, 40^{o}-ko angelu okertua sortuz. Horrela, energia zinetiko jakin bateko ioiak bakarrik izango dira ESA zeharkatzeko kapazak, hau da, bi plaka hauek energia eraginkorreko iragazi moduan jokatzen dute, analizatzaile magnetikora interesgarriak diren masak pasatzen uzten dutelarik.

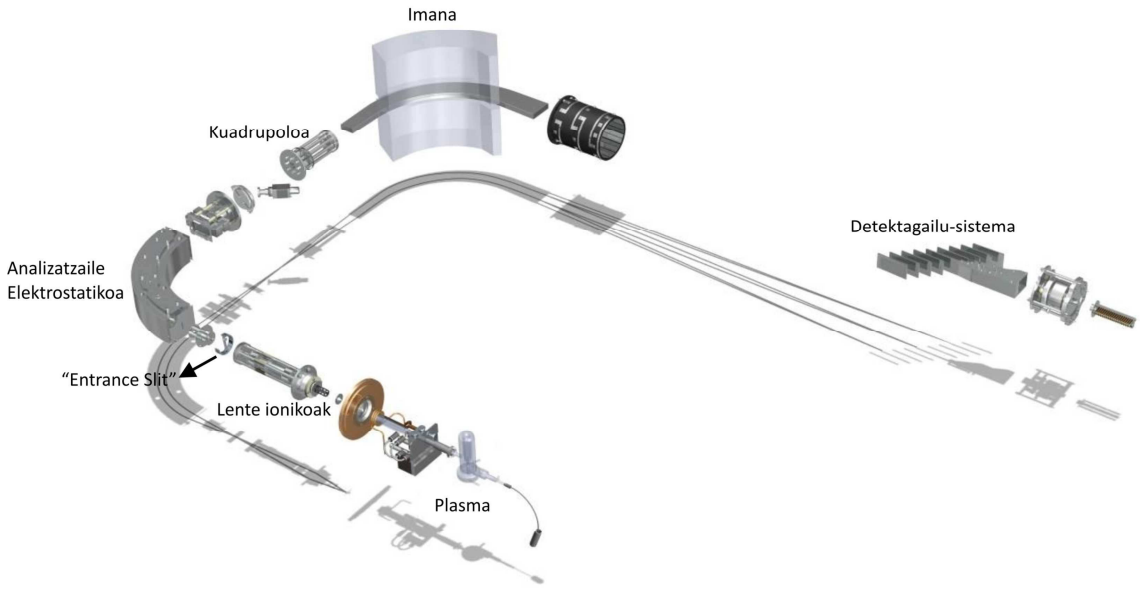

2.10. Irudia. MC-ICP-MSaren ioien ardazte-sistema. Testuan aurrerago azalduko diren atalak ere agertzen dira irudian, masa-analizatzailea eta detektagailu-sistema besteak beste.

2.1.d. Masa-analizatzailea

Masa-analizatzailea ardazte-sistema eta detektagailuaren artean kokatzen da. Ioiak lente-sistema igaro ostean, ioien bereizketa egiten da iragazki edo masa-analizatzailean masa/karga erlazioaren arabera. Behin analizatzailearen eremuaren barruan, gasa positiboki kargatutako ioietatik banatzen da eta ponpa turbomolekular baten bidez kanpora bideratzen da. Tesi honetan erabili diren bi ICPen arteko bereiztasun handiena masa-analizatzailean datza.

2.1.d.1. *Q-ICP-MS*

Thermo XSeries2-ak masa-iragazki kuadrupolarra dauka, paraleloki kokatutako eta ardatz zentral batekiko distantziakideak diren molibdenozko lau barra zilindrikoz osatua (2.11. Irudia). Kontrako posizioan dauden barra pareei korronte zuzen eta irrati-frekuentzian kontrako tentsioak ezarriz, barra pare batentzat korronte zuzen positiboa lortzen da, korronte zuzen negatiboa lortuz beste parearentzat. Era berean, pare bakoitzeko irrati-frekuentziako tentsioak 180^{o}-ko desfasea dauka, hau da, kontrako zeinua dute, anplitude ezberdinarekin.

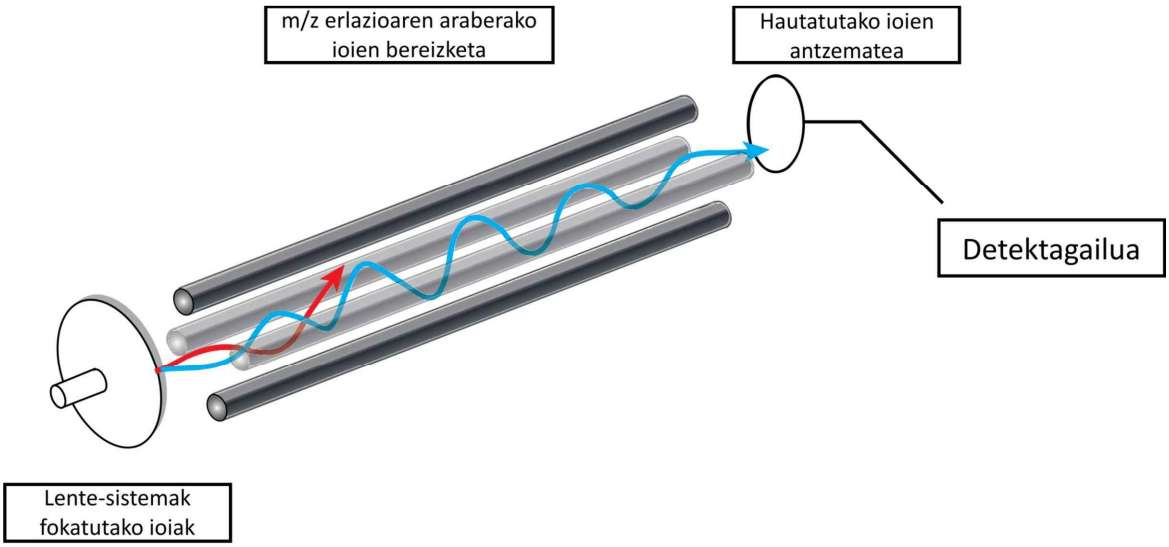

2.11. Irudia. Masa analizatzaile kuadrupolar baten eskema

Kuadrupoloan sartzen diren ioiek ibilbide oszilakorrak jasaten dituzte irrati-frekuentziaren tentsioa dela eta. Irrati-frekuentzia eta korronte zuzenaren tentsio balio egokiak aukeratuta, masa/karga erlazio jakin bateko ioiek baino ez dute lortuko kuadrupoloaren luzeera guztia zeharkatu eta beste muturretik ateratzea. Gainontzeko ioiak kuadrupoloaren barruan galtzen dira, euren ibilbide oszilakorrak oso handiak direlako eta barren kontra talka egiten dutelako, neutralizatuz.

2.1.d.2. *MC-ICP-MS*

Mota honetako masa-espektrometroetan ioiak sektore magnetikoak bereizten ditu (2.12. Irudia), elektroimanak induzitutako ibilbide zirkularrean.

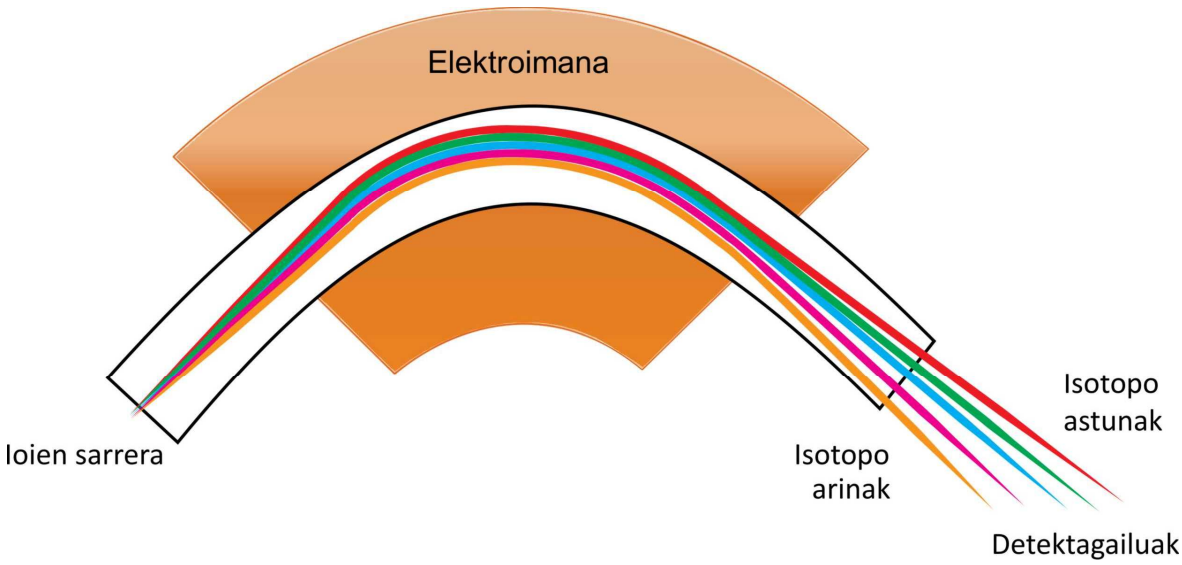

2.12. Irudia. Sektore magnetikodun espektrometro bateko analizatzailearen eskema.

Behin elektroimanaren energia-eremura heltzean, ioiak masa/karga erlazioaren arabera banatzen dira, masa ezberdinetako ioiek bide zirkular ezberdinak jarraitzen bait dituzte (18. Irudia). Modu honetan, imanaren eremu magnetikoa zuzen konfiguratuz, masa/karga erlazio jakin bateko ioiak aukeratzea posible da, detektagailu ezberdinetara bideratuz.

2.1.e. Detektagailu-sistema

Masa-espektrometroak banatutako masak, detektagailurainoko bidea egiten du azkenik, huts handiko baldintzapean baita ere. Ekipo bakoitzak detektagailu-sistema ezberdina du, ondoren azalduko den legez.

2.1.e.1. *Q-ICP-MS*

Q-ICP-MS-an erabilitako detektagailua dinodo diskretu motako elektroi-biderkagailua da (*Secondary Electron Multiplier, SEM*) (2.13. Irudia), zeinak aldi berean seinale analogiko zein zortzi magnitude-ordena baino gehiagoko tarte dinamiko lineala duen pultsu kontaketak neurtu ditzakeen. Horrek elementu nagusi, urri, aztarna eta ultra-aztarnak aldiberekotasunez neurtzeko ahalbidetzen du.

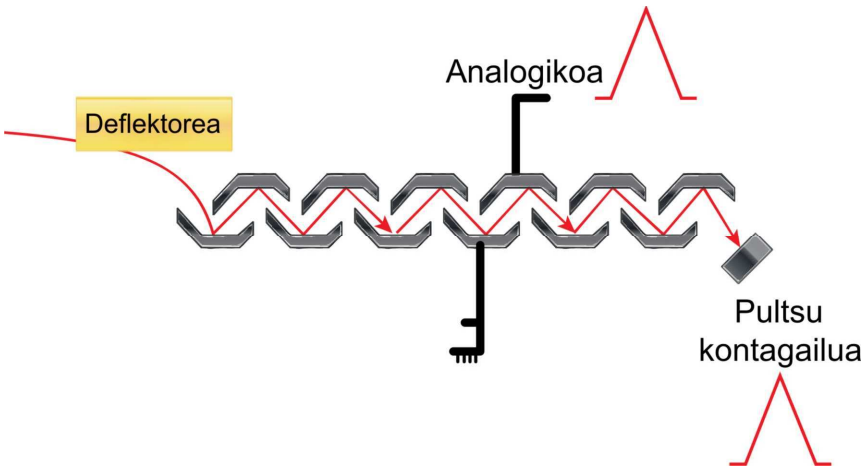

2.13. Irudia. Elektroi-biderkagailu baten diseinuaren eskema.

Elektroi-biderkagailu motako detektagailuak, plasma iturridun espektrometroetarako oso sentikortasun altukoak dira. Egunerokotasuneko aukera moduan, 10^7 cps (‘*counts per second*’ edo kontuak segunduko) baino altuagoak diren seinaleetarako erabiltzen dira.

2.1.e.2. *MC-ICP-MS*

MC-ICP-MSa detektagailu anitzeko ekipoa da, beraz, detektagailu-sistema konplexua du, 3 detektagailu mota ezberdinekin:

- Faraday kaxak: detektagailu honetara heltzen diren ioiak anplifikatu eta zenbatu egiten dira. Faraday kaxek dauzkaten onura garrantzitsuenak eskaintzen duten egonkortasuna eta masen desbiderazio eza dira, erlazio isotopikoen neurketak zehaztasun handiz egiteko aukera emanez. Seinaleak altuak direnean, detektagailu hauek erabiltzen dira.
- SEM: kuadrupoloaren kasuan azaldutako detektagailu bera da.
- MIC (*Multi Ion Counting*): bere funtzionamendua SEMaren antzekoa da, baina MICek ezin dituzte 10^6 cps baino altuagoak diren seinaleak jasan. Hori dela eta, oso seinale baxuekin erabiltzen dira.

Tesi honetan erabili den Thermo Scientific Neptune espektrometroak konfigurazio berezia dauka, UPV/EHUko laborategietako arazoetarako bereziki egina, bederatzi Faraday kaxa, zortzi MIC eta elektroi sekundarioen biderkagailu batekin, proportzio ezberdinetan dauden erlazio isotopiko asko neurtzeko aukera ugari ematen dituelarik (2.14. Irudia).

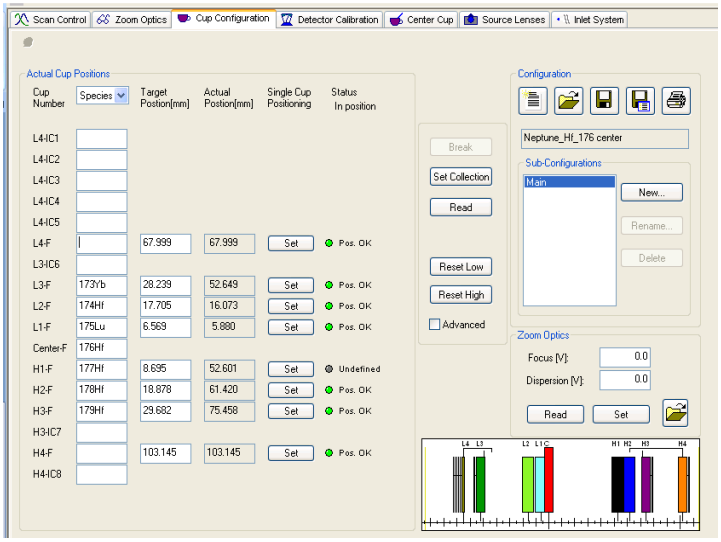

2.14. Irudia: Detektagailuen konfigurazioaren adibidea, 173 eta 179 masen arteko isotopoak aldi berean neurtzeko.

2.1.f. ICParekin lotutako arazoak

Era orokor batean, ICP-MSan eman daitezkeen arazorik arruntenak, elementu ezberdinek sortutako interferentziak (espektral eta ez-espektralak) eta zatikapen isotopikoa dira. Hala ere, badago bestelako arazorik.

Interferentzia espektralak analitoaren masak masa bera duen interferente batekin bat egiten dutenean ematen dira. Elementu ezberdinen edo plasmak berak sortutako molekulen masa atomikoaren gainjartzearen emaitza izan daitezke, hau da, interferentzia isobarikoak edo molekularrak izan daitezke. Azken hauek, plasmaren argona edo/eta laginaren prestaketan erabilitako erreaktiboen ondorio izan daitezke. Gainera, bitan kargatutako espezieak (masa/karga erlazioa neurtzen da), hidroxido eta oxidoen sorreraren ondorio ere izan daitezke.

Espezie hauen ondorioz sortutako arazoak ekiditeko hainbat aukera daude. Horietako bat interferentearen ezabatzea da, molekula apurtuz edo honen presentzia saihestuz teknika kromatografikoen bidez edo ekipoaren sintonizazio egokiaren bitartez.

Interferentzia ez-espektralak edo matrizearen interferentziak seinalearen txikitzea eragiten dute. Interferentzia hauek ekiditeko estrategiak oso diferenteak dira espektralak zuzentzeko erabiltzen direnekiko, besteak beste, diluzio faktoreen eta barne patroien erabilera gero zuzenketak egiteko, diluzio isotopikoa, laginaren xurgapen-sistemako aldaketak edota bereizketa kromatografia.

Plasma iturri bat erabiltzeak teknikari atxikitutako arazo batzuei irtenbidea ematea eskatzen du. Arazo gehienak laginaren sarrera-sistemarekin lotutakoak dira. Arazoak oso desberdinak dira lagina disoluzio moduan sartzen bada edo laser ablazio sistema batetik

eratorritako aerosola bada. Laginak disoluzio moduan sartuta hainbat arazo gerta daitezke, langargailuan buxadurak, matrizearekin arazoak, etab. Arazo gehienak material eta elementu egokiak erabilita gainditu daitezke, baita ere analisirako estrategia ezberdinak erabilita.

Laser bidezko lagin-sarreretan ere matrize arazoak sor daitezke, eta horretarako antzeko matrizea duten patroiak erabiltzea lagungarria izaten da. Beste arazo bat, espektrometroa eta laser-sistema kontrolatzen dituzten softwareen sinkronizazioa da, bi software ezberdin lanean jarri behar baitira aldi berean. Laser ablazio-sistemak argonaz gain helioa (eta batzuetan nitrogenoa) ere erabiltzen du. Gasak kontrolatzea ere ezinbestekoa da seinale egonkor bat lortzekotan.

Aipatutako tresneria eta interferentzia arazo edota laginak berak sortutako arazoez gain, detektagailu anitzeko ekipoek daukaten arazo nagusienetakoa masen arteko bereizketa da. Prozesu horretan isotopoen masen araberako neurketa diferentzialak sortzen dira, neurtutako masen ugaritasunean ematen diren ezberdintasun edo aldakuntza txikiak, alegia. Aldakuntza hauek zatikapen isotopikoa deritzon prozesuarekin erlazionatzen dira.

Elementu baten isotopoek ezaugarri kimiko berberak dituzten arren, ezaugarri fisiko ezberdinak dituzte, euren arteko masa ezberdintasuna dela eta. Horregatik ematen da zatikapen isotopikoa. Horrela, elementu jakin bateko isotopo astunenak dituen molekulak, pisu, bolumen, erreakzio abiadura, etab. ezberdinak izango ditu isotopo arinenak dituenekin alderatuta. Horrek, txirotze edo aberaste isotopikora gidatuko du lagina lurruntze edo prezipitazio moduko prozesu naturalen ondorioz.

Prozesu naturaletatik aparte, masa-espektrometria bidezko arrazoi isotopikoen analisietan, laginaren ionizazio prozesuan zehar, elementu arinak astunak baina azkarrago lurruntzen dira. Denborarekin, isotopo astun eta arinen arteko proportzioa aldatuz doa, eta horrek ezberdintasun bat sortzen du espektrometroak neurtutako eta laginaren benetako erlazio isotopikoaren artean. Sistema isotopiko batzuen kasuan, Sr edo Hf esaterako, fenomeno honen zuzenketa barne-era batean egiten da, egonkorra den erlazio isotopiko bat dagoelako. Beste kasuetan, arrazoi isotopiko ezagunak dituzten estandar edo materialak erabili beharko dira, zatikapen hau kontrolatu eta beharrezkoa balitz zuzentzeko.

2.1.g. Laginaren sarrera-sistema

Laginen sarrera-sistemak, lagin kantitate txikia espektrometroan sartzea du helburu. Masa-espektrometroan sartzeko gas-egoeran egon behar da eta, sistema honetan, lagina aerosol bihurtzen da, bai likido- zein solido-egoeratik. Lagina masa-espektrometrora sartzeko hainbat aukera dago. Lan honetan erabili direnak deskribatuko dira.

2.1.g.1. *Likido-egoeran*

Likido-egoeran dauden laginak espektrometrora sartzeko hainbat sistema daude. Guztiekin emaitza bera lortzea da helburua: laginetik aerosol fin bat sortzea, segidan tanta handien iragazketa azkarra eginez, hauek plasman sartu ez daitezen. Laginaren sarrera-mekanismoa beraz bi prozesuren emaitza da: (i) aerosolaren sorrera eta (ii) tanten hautaketa. Lehen prozesua egitearen arduraduna langargailua da, bigarren prozesua lainoztapen ganbaran egiten delarik.

Tesi honetan, bi sistema ezberdin erabili dira lagin likidoak analizatzeko. Funtsezko helburua berdina izan arren, badaude zenbait ezberdintasun eta kasu bakoitzerako sistema egokitzea komenigarria da.

a. Lagina sartzeko sistema arrunta: SIS

Laginen kontzentrazioa handia denean, SIS (*Standard Introduction Sistem*) izeneko sistema erabiltzen da (2.15. Irudia). Erabili den langargailua PFAz eginda dago, eta 100 µL/min-ko fluxuarekin lan egiten du. Langargailuaren barruan, gas-fluxuaren eragin pneumatikoaren ondorioz, likidoa tamaina ezberdinetako tantetan zatitzen da. Erabilitako lainoztapen ganbara bide-bikoitzekoa da eta, ponpa peristaltiko batek sortzen duen aire-korrontearen laguntzaz tanta handiak bereizten dira, masa-espektrometroan sar daitezen galaraziz.

b. Desolbatazio-sistema: Apex

Sistema hau konzentrazio txikiak dituzten laginekin erabiltzen da, sentikortasuna handitzeko. Hala ere, kontuan hartu behar da sentikortasun handitzeak kutsaduraren eragina handitzen duela eta beraz, garbiketa protokoloetan arreta handiagoa jarri behar dela.

Tesi honetan erabili den desolbatazio-sistema, Apex sentikortasun altuko lagin sarrera-sistema da, Elemental Scientific markakoa (Omaha, USA, 2.16A Irudia). Apex-a ondoko atalez osatzen da; kuartzoz egindako tenperatura altura dagoen ganbera, 50 µL/min-ko fluxua ematen duen PFAzko mikrolangargailu zentrokidearekin (2.16B Irudia), Peltier bidez hoztutako kondentsadorea eta kuartzoz egindako nahasketarako ganbera gehigarri bat, egonkortasun eta doitasun altuko neurketak egin ahal izateko. Sistema honek laginak duen ur-kopurua, txikiagotu edo deuseztatu egiten du. Horrela, oxido eta partikula poliatomikoek sortutako interferentziak ekiditen dira eta sentikortasuna hobetu daiteke.

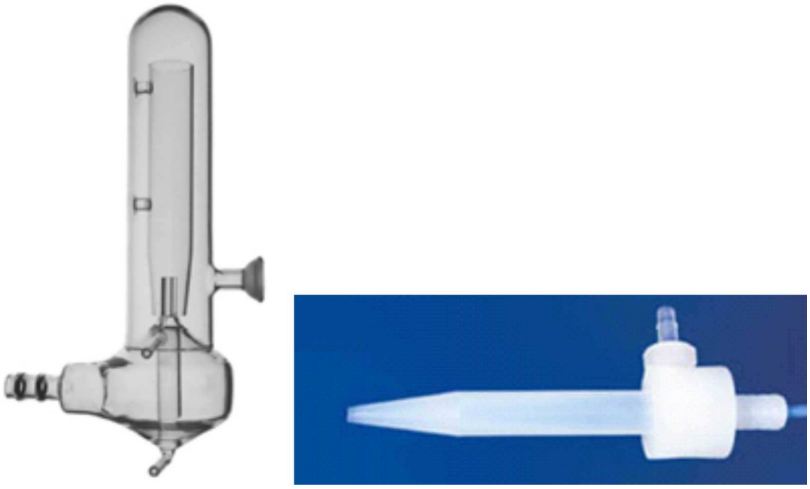

2.15. Irudia. Erabili diren bide-bikoitzeko lainoztapen ganbara eta langargailua, ezkerrean eta eskuman, hurrenez hurren.

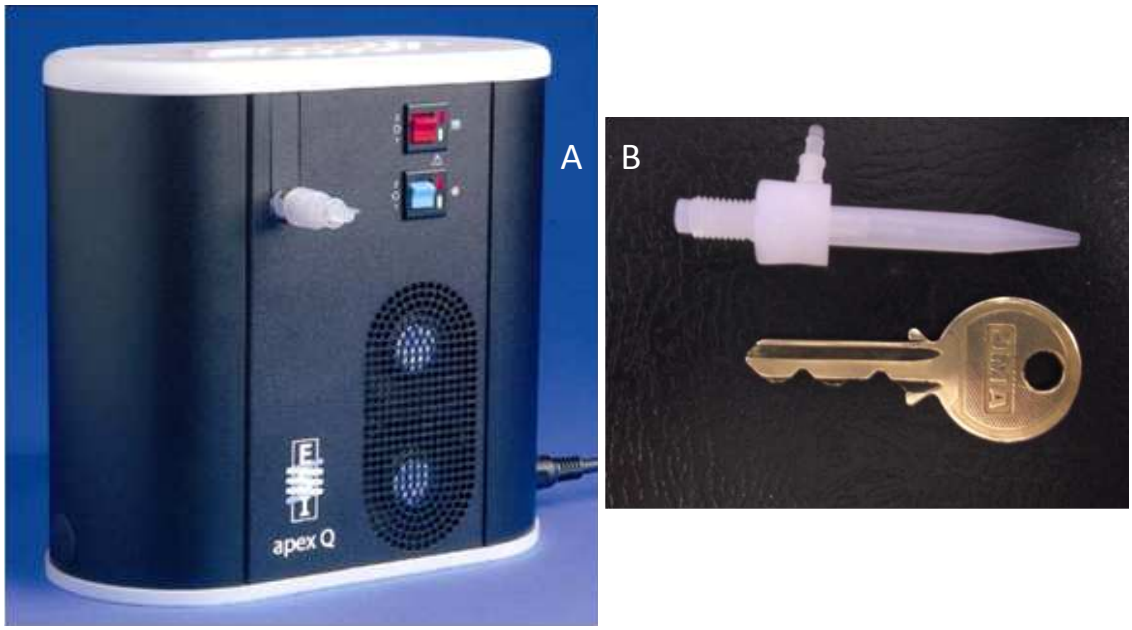

2.16. Irudia. A: Apex desolbatazio-sistemaren irudia. B: Fluxu baxuko mikrolangargailu zentrokidea.

Oxido-kopurua eta interferentzia poliatomikoak erabat deuseztatu eta analitoarekiko sentikortasuna handitu nahi badira, Elemental Scientific markako Spiro izeneko gailu bat gehitu dakioke Apex-ari. Spiro-a PTFE Teflon® materialez egindako desolbatazio-mintz makroporotsua da.

2.1.g.2. *Solido-egoeran: Laser ablazio-sistema*

Lagin solidoen zuzeneko analisietarako erabiltzen den teknika da. Laser hitza ingelerazko ***L**ight **A**mplification by **S**timulated **E**mission of **R**adiation* izenetik dator, estimulatutako erradiazio-

igorpen bidezko argi anplifikatua, hau da, gailu egokietan atomoen fotoiak askatzen diren prozesu kontrolatua.

Laser-sistematik eratorritako fotoiak laginaren gainean energia-kolpe izugarri moduan elkar eragiteko fokatu egiten dira, eta elkar eragin horren ondorioz, aerosol bat sortuko da laginaren gainazaletik askatutako ioi, atomo eta partikula txikiekin (2.17. Irudia). Gaur egun eskuragarri dauden laser-sistemek, bereizmen espazial handian (< 5 µm) zein txikian (> 100 µm) lan egiteko aukera ematen dute. Laserraren eraginez sortutako aerosolean lagin-kopuru txikiak lortzen direnez, sentikortasun analitiko altua daukaten sistemak ezinbestekoak dira, batez ere aztarna eta ultra-aztarna mailako elementuen analisirako.

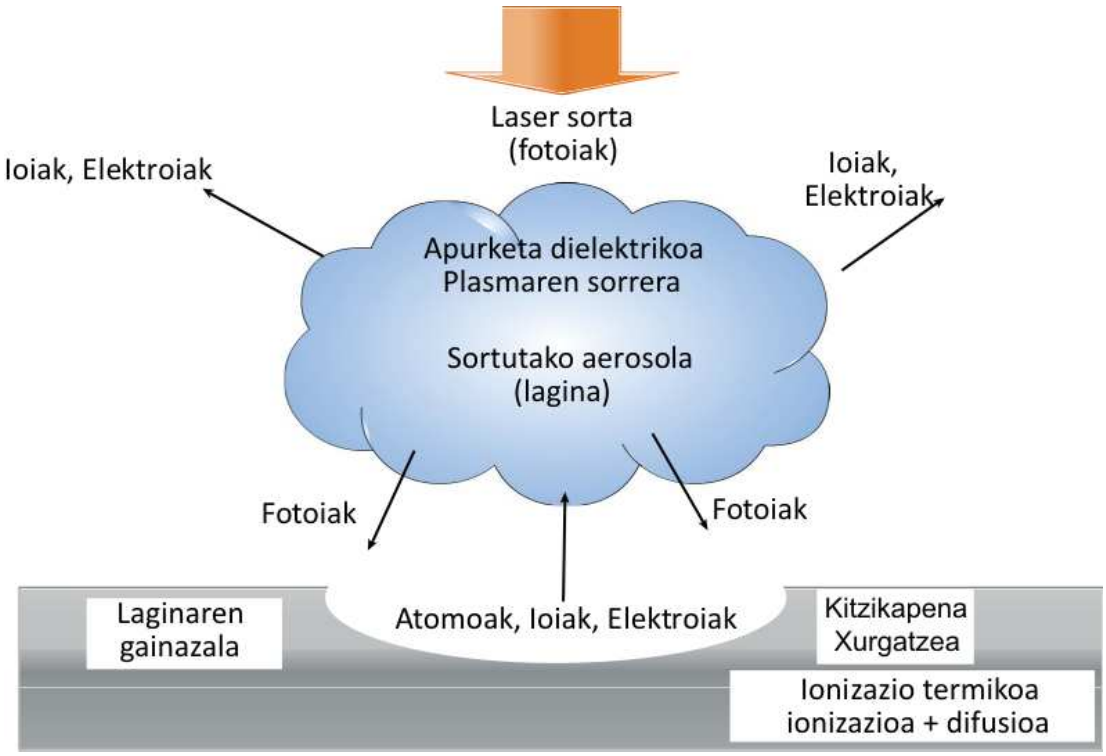

2.17. Irudia. Laginaren ablazio-prozesua.

Era orokorrean, laser ablazio-sistema ondoko atalez osatua dago; fotoi sorta sistema sortzaile bat, lagina bere barnean hartuko duen ablazio-gelaxka eta software bidezko kontrol- eta ikuste-sistema, zeinak sistema osoaren kontrola eta analizatu beharreko puntuaren aukeraketa ahalbidetzen duen.

Universidad del País Vasco/Euskal Herriko Unibertsitateko (UPV/EHU) Ikerkuntzarako Zerbitzu Orokorretako (SGIker) Geokronologia eta Geokimika Isotopikoaren Zerbitzuak (IBERCRON) daukan laser ablazio-sistema, New Wave Research enpresak fabrikatutako UP213-a da (2.18. Irudia). '*Solid state*' edo solido-egoerako laser mota da, laserraren iturria matrize solido bat delako. Normalean beira edo kristal gardenak izaten dira, Cr^{3+} edo Nd^{3+} moduko ioi metaliko tribalenteen kopuru txikiekin dopatuak. Materiala deskarga-lanpara baten bitartez kitzikatzen da.

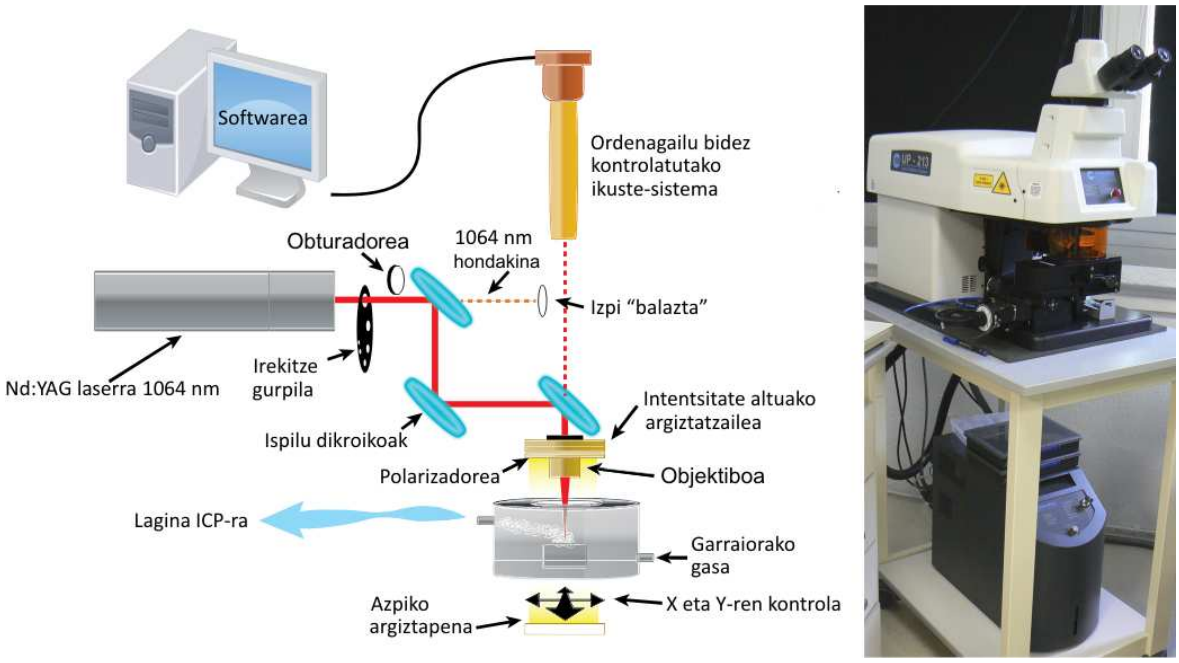

2.18. Irudia. Nd: YAG laser-sistema baten irudi eskematikoa ezkerrean eta tesi honetan erabilitako UP213 laserra eskuman.

UP213 laserra Nd:YAG motakoa da, eta ytriodun granatez dopatutako neodimioz eginda dago: Nd-$Y_3Al_5O_{15}$ (2.18. Irudia). Sistema hauek lau mailatako laserrak izateagatik ezberdintzen dira (2.19. Irudia). Laser sorta sortzeko, Nd ioiak energia maila nagusi bateraino kitzikatzen dira (ponpaketa maila), nondik maila metaegonkor batera azkar jaisten diren (laser maila). Maila metaegonkor hauen artean, gaineko eta azpiko laser mailak, populazio-alderantzikatze bat sortzen da, laser sorta sortarazteko oinarrizko pausua dena. Gaineko eta azpiko laser mailen arteko tarteak sortutako laser sortaren uhin-luzeera baldintzatzen du. Uhin-luzeerarik indartsuena 1064 nm-koa da. Ispilu dikroikoen erabileraren bidez, 213 nm-ko uhin-luzeera lortzen da sorkuntza armonikoz.

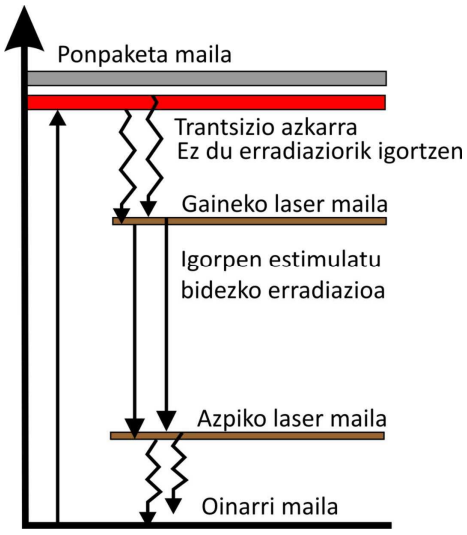

2.19. Irudia. Nd:YAG solido-egoerako laser-sistema bateko laser sortaren sorrera.

Aerosolaren garraiorako, seinalearen intentsitatea eta lortutako zarata-maila aldarazi dezaketen gas nahasketa ezberdin asko proposatu dira (Günther eta Heinrich, 1999b). Argon gasa erabiliena da sistema honetarako. Garraio-gas bezala dauka abantailarik handiena, ablazio-gelaxkatik ICPko zuzira zuzenean igaro ahal izatea da, bestelako gasik gehitu gabe, eta beraz, plasmaren baldintzetan inolako eraginik sortu gabe.

Garraio-gasari nitrogenoaren (N_2) gehitzeak masa altuetako elementuen intentsitatearen areagotzea ahalbidetzen du, baina aldi berean, interferentziak sortu ditzaketen ioi poliatomikoen ($^{14}N^{14}N^{1}H$ edo $^{14}N^{14}N^{14}N$) eraketa handiagotzen du.

Seinale/hondo-zarata erlazioa areagotu egin daiteke ablazio-gelaxkako garraio-gas moduan helioa erabili eta ablazio-gelaxkaren ondoren argonarekin nahasten bada (Eggins et al., 1998; Günther eta Heinrich, 1999b). Hainbat azalpen daude fenomeno honetarako, baina bistakoa da helioa erabilita ablazio-puntuaren inguruan partikulen metaketa gutxitzen dela. Gas biek eroankortasun termikoari dagokionez ezaugarri ezberdinak dituztenez laserrak induzitutako mikroplasma ezberdinak sortzen dira laginaren gainazalean (19. Irudia). Helioak partikula txikiagoak (< 200 nm) sortzen ditu argonak sortutako mikroplasmak baino, kondentsazioa txikituz eta partikula txikien garraioaren eraginkortasuna hobetuz.

Ablazio-gelaxka ondoko atalez osatua dago; gasaren sarrera eta irteera bana, laserrarekiko gardena den ablazio-leiho bat, lagina sartzeko tokia eta lagina argiztatzeko gailu optikoak, argi transmititu zein islatu bidez. Laginaren behaketa mikroskopio bati akoplatutako bideo-kamera digital baten bitartez egiten da.

Ablazio-gelaxkaren bolumena eta geometria, garraio-gas eta fluxuarekin estuki lotuak, kontuan hartu beharreko ezaugarri garrantzitsuak dira masa espektrometrora helduko den seinalerako. Garraio-prozesuan eginiko edozein onura, laserraren puntu-tamaina txikitu ahal izatea dakar, eta beraz, bereizmen espaziala handitzea, beti ere intereseko masa neurgarria baldin bada. Erabilera jakin batzuek beraz analizatu beharreko laginaren araberako moldaketak beharko dituzte ablazio-gelaxkan, bai tamainagatik dela, bai ezaugarri fisiko-kimikoengatik dela.

Tesi honetan, Super Cell™ motako ablazio-gelaxka erabili da (2.20. Irudia). Ablazio-gelaxka estandarrarekiko duen moldaketarik nagusiena gas fluxuen aldaketa zorrotza da, gelaxka barruan fluxu laminarra lortzen delarik. Horrela, garraiorako eraginkortasun txikia duten eremuak murrizten dira eta ondorioz, garbiketa-denbora ere txikitzen da. Hori lortzeko, gasaren sarrera eta irteeraren orientazioak moldatu egin dira eta sartzen den gasaren dispertsio-sistema bat erantsi zaio. Diseinu-aldaketa horiei esker, 33 cm^2-ko bolumena duen gelaxkaren garbiketa-denbora 2 segundu baino gutxiagokoa da, gelaxka estandarrarekin behar diren 8 segundu baino 4 aldiz txikiagoa.

Nahiz eta ablazio-gelaxka diseinu horrek garbiketa-denborak optimizatu, lagin bakarra sartzeko aukera ematen du soilik, eta horregatik, UPV/EHUko laborategietan, diseinu komertzial hau moldatua izan da aldi berean laginak eta patroiak sartzeko.

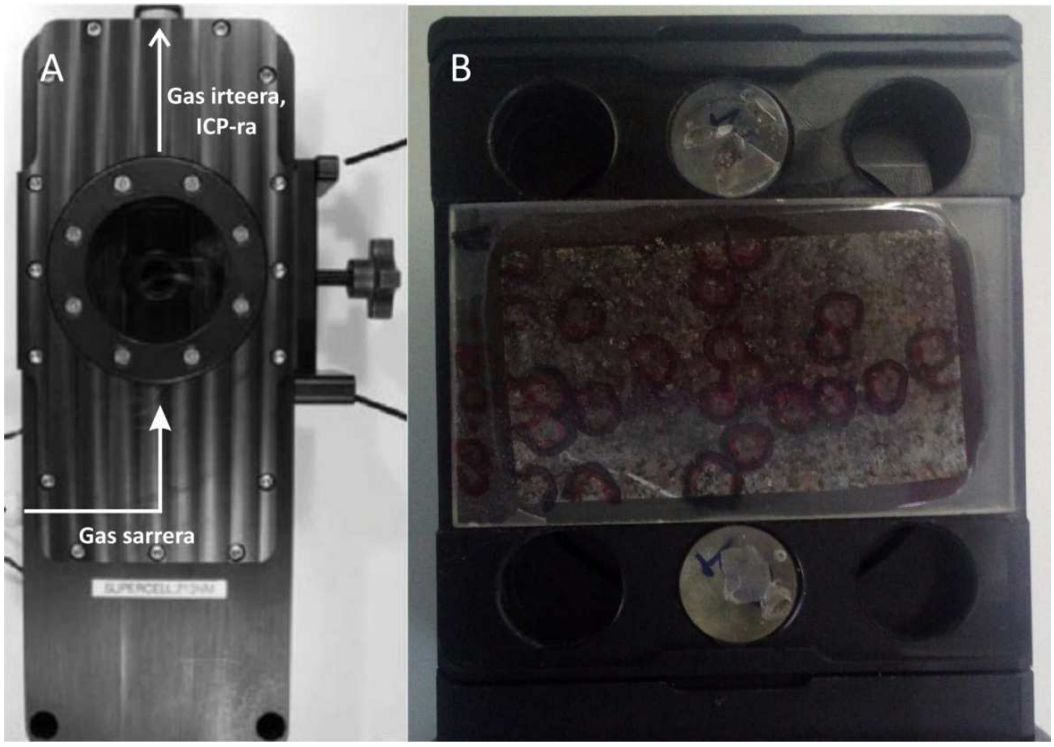

2.20. Irudia. Supercell^{TM} motako ablazio-gelaxka moldatua. A: Gaineko bista. B: Moldatutako gailua, lagin eta patroiak batera sartzea ahalbidetzen duena.

2.1.h. Laser ablazio-sistematik ICPra

Laser ablazio-sistematik ICPra lagina eramateko aukera ezberdinak daude, egin nahi diren analisien arabera. Laser ablazio-sistema eta masa-espektrometroa bi tresna independiente dira, eta era egoki batean akoplatu behar dira, funtzionamendu zuzenerako. Seguidan tesi hau egiteko erabili direnak aipatuko dira, bat kuadrupoloarekin eta beste bat detektagailu anitzen ekipoarekin egokitzeko.

2.1.h.1. *Q-ICP-MS*

Esan bezala, ablazio-gelaxka tresnak gas sarrera bat dauka eta laserrak sortutako aerosola ICP-MSaren zuziraino iristeko irteera bat. Ablazioan He erabiltzen da eta ICPrako bidean sortutako aerosola (He + lagin lainoztatua) argonarekin nahastuko duen gailu batetik pasatu behar du ICPra iritsi aurretik (2.21. Irudia).

Ablazioaren berariazko parametroetatik aparte, zeinak laser-sistemaren softwaretik kontrolatzen diren, beharrezkoa da ablazio-zeldatik igarotzen den He fluxuaren kontrola. Horretarako, masa-espektrometroak berak instalaturik daukan gas fluxu-kontrolagailua erabiltzen da. Horrela, laser-ablazioan erabiliko den He kopurua, ICP ekipotik pasarazten da, espektrometroaren softwaretik fluxua kontrolatzen delarik.

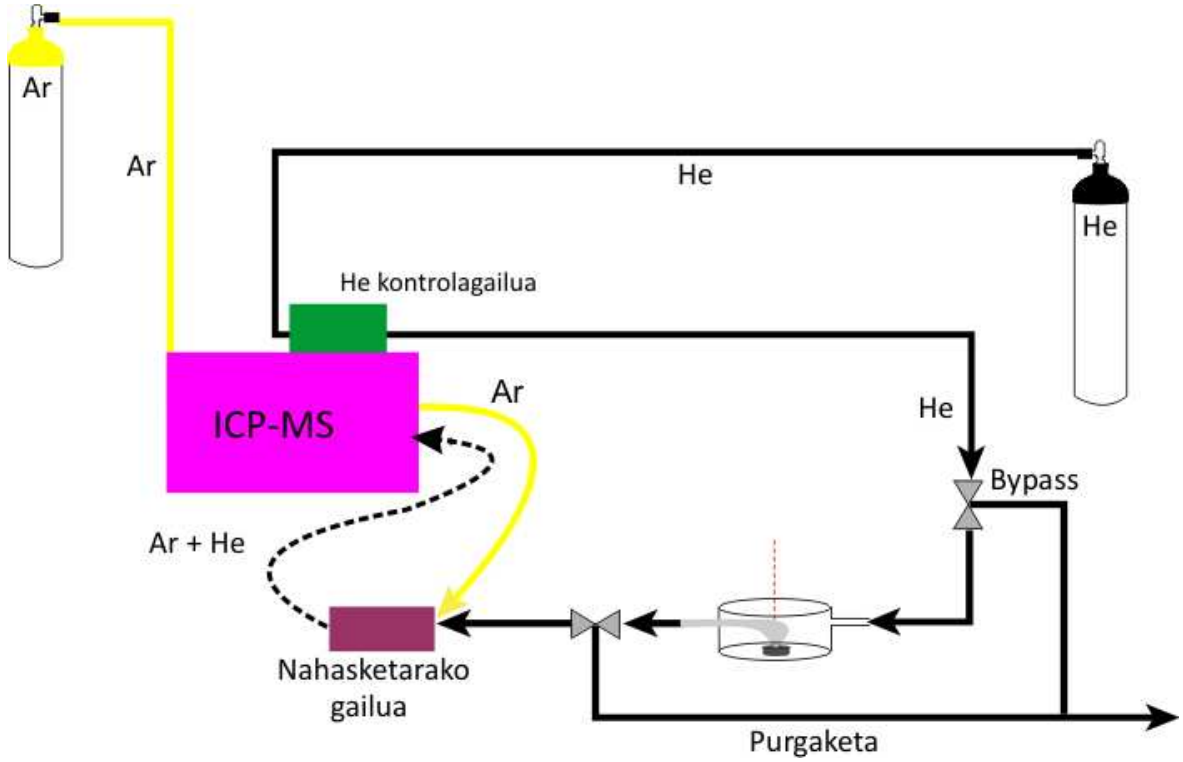

2.21. Irudia. Laser ablazio-sistema eta ICP baten akoplamendu bateko gasen banaketaren eskema.

2.1.h.2. *MC-ICP-MS*

MC-ICP-MSan sartzen diren laginek antzekotasun handiak dituzte Q-ICP-MSarentzat azaldutako sistemarekin. Tesi honetan neurtu diren analitoak direla eta, N_2-a sartzea ezinbestekotzat jo da. Garraio-gasei nitrogenoa gehitzeak masa altuko elementuen intentsitatearen areagotzea ahalbidetzen du. Nitrogenoa, ablazio-gelaxkatik datorren aerosolari (He + lagina) gehitzen zaio. Ondoren nahasketa hau argonarekin nahastuko da zuzira heldu aurretik. Espektrometrora sartuko den nitrogenoa ere gas fluxu-kontrolagailu batetik (2.22. Irudia) pasarazten da, berau kontrolatzeko, eta fluxurik ohikoena, 10 mL/min ingurukoa izaten da.

2.22 Irudia. Nitrogenoaren fluxua neurtzen duen fluxu-kontrolagailua.

2.2. Erreaktiboak eta materialak

Aztarna edo ultra-aztarna elementuen analisiak egiterakoan, kontuan hartu beharreko faktore garrantzitsu bat, purutasun handiko material eta erreaktiboen erabilera da, oso kontzentrazio baxuan dauden elementuen kuantifikazioan eragin dezaketen kutsadura arazoak (ikusi beherago) ekiditeko (adibidez, Robinson et al., 1998).

2.2.a. Erreaktiboak

Prozesu guztietan erabiltzen den H_2O, ultrapurua da eta 18 MΩ.cm^{-1} baino erresistibitate handiagoa dauka. Berau lortzeko, iturriko ura desionizatzen da lehendabizi Elix (Milipore) ekipo baten bidez, eta ondoren Easypure II (Barnstead) ekipoarekin purifikatu egiten da, alderantzizko osmosi bidez.

a. Azido nitrikoa, HNO_3 (% 69.8) eta azido klorhidrikoa, HCl (% 37) Pro Analysi (Merck) kalitatekoak dira. HCl eta HNO_3 garbitu egiten dira erabili aurretik, Berghof '*sub-boiling*' edo azpitakite bidezko azidoen purifikazio-sistemarekin.
b. Azido fluorhidrikoa (% 50.2) ere Pro Analysi (Merck) kalitatekoa da, eta azpirakite metodoaren bidez (Matison, 1972) destilatzen da Teflon® PFAzko (Savillex®) ontzietan (Menéndez, 2001; García de Madinabeitia, 2004).
c. Azido perklorikoa, $HClO_4$ (% 70-72), Pro Analysi (Merck) kalitatekoa da baita ere, baina berau, hornitzaileak eman bezala erabiltzen da.
d. Urtugarri moduan erabiltzen den $LiBO_2$-a purutasun altukoa da (Corporation Scientifique Claisse, For Analysis Grade Pure). Urtutako materiala arragoan ez itsasteko, H_2O ultrapuruan (18 MΩ.cm^{-1}) % 50era diluitutako LiBr (Merck Suprapur) soluzioa erabiltzen da.

2.2.b. Materialak

Lehenago esan den bezala, materiala kutsadura iturri garrantzitsua da. Arazo hau saihestu edo gutxienenez txikiagotzeko, laginen tratamendu kimikoan Teflon® PFAzko 15 mL-ko ontziak erabili dira (Savillex®). Hauen garbiketarako '*aqua regia*' beroa erabili da eta H_2O ultrapuru beroarekin garbitu dira gero. Ziklo hau bi aldiz errepikatu da.

Ahal den heinean, erabili eta botatzeko materiala erabili da, hala nola, 1 mL eta 5 mL-ko polipropilenozko mikropipeten puntak (Eppendorf), laginetarako polipropilenozko poteak (Gosselin), etab. Erabili aurretik, garbitu egin dira 24 orduz HNO_3 diluituan mantenduz eta gero H_2O ultrapurutik pasaz. Ziklo hau bi aldiz errepikatu da.

Intereseko elementuen isolamendurako erabiltzen diren materialak ondokoak dira: Sr-Spec (Eichrom) erauzte kromatografia erretxina sintetikoa (50-100 µm-ko partikula tamaina), Ln-Spec (Eichrom) erauzte kromatografia erretxina eta Dowex AG50-W8 (200-400 mesh) katio-truke erretxina (Fluka, Sigma Aldrich). Sr-Spec eta Ln-Spec erretxinak erabiliko diren zutabeetan bertan garbitzen dira HNO_3 kontzentratua eta diluituarekin eta HCl kontzentratuarekin hurrenez hurren. Dowex katio-truke erretxina, HCl-rekin lehenengo eta miliQ H_2O-rekin gero garbitzen da. Garbiketa-zikloa hainbat alditan errepikatzen da, erretxina suspentsioan jarriz irabiagailu magnetiko baten laguntzaz. Garbiketa hau, erretxina lehen aldiz erabili aurretik egiten da. Behin lehen kromatografia eginda, HNO_3 eta HCl kontzentratuak eta miliQ H_2O zutabeetatik pasaz, erretxina prest geratuko da hurrengo banaketa kromatografikorako.

2.2.c. Estandarrak eta trazatzaile isotopikoak

Laborategi batean metodo berri bat balioztatzeko, nazioarteko CRM (*Certified Reference Materials*) estandarren analisi ugari egin behar dira. Hauek, ezagunak diren instituzioetan erosi daitezke, besteak beste, CNRS (*Centre de Recherches et Géochimiques Pétrographiques*), USGS (*U.S. Geological Survey*) eta GSJ (*Geological Survey of Japan*). Tesi honetan erabili diren estandarrak honakoak dira: (i) AC-E, AGV-2, BHVO-2, FK-N, G-2 eta W-2 disoluzio bidezko analisietan eta (ii) 91500, GJ-1, Plešovice eta Temora Laser-ablazio bidezko analisietan. Material guzti hauen erreferentziazko balioak 3. Kapituluko eztabaidetan ematen dira.

Era berean, ekipoen funtzionamendua egokia dela eta denborarekin inolako jitorik ez dagoela egiaztatzeko ezagunak diren disoluzio komertzialak neurtzen dira epe luzera, prozedura analitikoak ezarri aurretik. Helburu horretarako erabili diren disoluzioak honakoak dira: SRM984 Rb-rako (*National Institute for Standards and Technology,* NIST), SRM987 Sr-rako (NIST), JMC 475

Johnson Matthey Hf-rako (P. Jonathan Patchett Irakasleak emandako disoluzioa) eta 'Standard for ICP Solution' (Fluka Analytical) disoluzioa Lu-rako.

Disoluzio bidezko analisietarako Diluzio Isotopikoa deritzon teknika erabili da (ikusi 3. Kapituluko sarrera). Lan honetan erabilitako trazatzaile guztiak (^{176}Lu: % 44,23, ^{179}Hf: % 89,87, ^{87}Rb: % 98, ^{86}Sr: % 97,02) Brieuc Le Fèvre dk.-ak eta Christian Pin dk.-ak emandakoak dira, eta ORNL (*Oak Ridge National Laboratory*) laborategiko produktuetatik prestatu dira. Alderantzizko Diluzio Isotopikoaren bidez trazatzaileen kontzentrazioak kalibratzeko elementu bakarreko dizoluzioak erabiltzen dira. Erabili diren disoluzioak honakoak dira: azido nitriko ingurunean dagoen eta 1000 ± 2 mg/L kontzentrazioa duen 'Rubidium Plasma Standard Specpure 13872' (Alpha Aesar) disoluzioa Rb-rako, azido nitriko ingurunean dagoen eta 1000 ± 2 mg/L kontzentrazioa duen 'Strontium standard for ICP 75267' (Fluka Analytical) disoluzioa Sr-rako, azido klorhidriko + azido fluorhidriko ingurunean dagoen eta 1000 mg/L kontzentrazioa duen 'CertiPUR ICP Standard 170322' (Merck) disoluzioa Hf-rako eta azido nitriko ingurunean dagoen eta 997 ± 5 mg/L kontzentrazioa duen 'Standard for ICP Solution' (Fluka Analytical) disoluzioa Lu-rako. Lu-aren eta Rb-Sr-aren analisietarako gainera 'Ytterbium ICP Standard 601902A' eta 'Zirconium dichloride oxide hydrate, Puratronic, 99.9985% (metal basis) 11135' (Alfa Aesar) erabili dira, hurrenez hurren.

2.3. Bestelako ekipoak

Tesi honetan, lagin eta estandarren kutsadura ekiditeko asmoarekin (ikusi beherago), tratamendu kimiko osoa (disoluzio, ebaporazio, kromatografia, etab.) lan-eremu babestuan egin dira, azidoekiko erresistenteak diren polipropilenozko fluxu laminardun kabinen barruan (LFE-1500BT, Salare Inc.). Kabinak era berean, iragazitako airezko gainpresioa duen gela egokituan aurkitzen dira, 1:10.000 klaseko gela zurian.

Lagin eta urtugarriaren pisaketarako Sartorius Handy H51 balantza analitikoa erabiltzen da, 30 ± 0.0001 g-ko gaitasuna duena.

Fusioak Katanax K1 (Canada) markako urtzaile baten bidez egin dira (2.23. Irudia). Fusioak elektrikoki egiten dira 'Joule efektuaren' bidez. Ekipoa mikro-prozesadore batekin kontrolatzen da eta horrek tenperaturaren kontrola eta arragoaren baitan dagoen galdatuaren lekuan bertako ('in situ') disoluzioa ahalbidetzen du. Laginen fusiorako platinozko arragoak erabiltzen dira, zeinak, ultrasoinuan jarritako HNO_3 diluituan garbitzen diren erabili ondoren.

MC-ICP-MSan laginen sarrerarako Cetac ASX-110FR (Cetac, Omaha, NE, USA) lagin-hargailu automatikoa erabili da, 56 laginen edo patroientzako edukiera duena.

2.23. Irudia. Tesi honetan erabilitako Katanax K1 urtzailea.

2.4. Mineral banaketa

Masa espektrometrora era likidoan, disoluzio moduan, sartu diren laginak mineral jakin baten kontzentratuak izan dira batzuetan. Mineral hauen banaketarako Euskal Herriko Unibertsitateko UPV/EHU Zientzia eta Teknologia Fakultateko Mineralogia eta Petrologia Sailak duen tresneria erabili da.

Lehendabizi, aztertu beharreko arroka geologo mailuaren laguntzarekin 5 zentimetro inguruko zatietan txikitzen da, eta ondoren baraila-birrintzaile baten bidez (Retsch bb200 Wolframcarbid) 1 cm-ko zatietara zehatzen da. Bertan lortutako materiala bitan banatzen da, lehena mineralen banaketan erabiltzeko eta bigarrena arroka osoaren analisiak egiteko.

Arrokaren analisia egiteko bideratzen den frakzioa, eraztun-errota (Retsch RS1 motakoa) baten bitartez ehotu egiten da, widiazko eraztunen bidez, elementu nagusien analisirako bada edo agatazko eraztunen bidez aztarna eta lur arraroen analisirako. Mineralen banaketarako utzi den frakzioa, Reuland markako disko-errota batetatik pasatzen da, arroka nahi dugun pikor tamainaraino txikituz. Pikor tamaina banatu nahi den mineralen araberakoa izango da. Behar

izanez gero, baheak erabiltzeko aukera dago pauso honetan. Arroken birrintze-prozesuak hauts asko harrotzen du, eta horregatik aire erauzgailuak dituen laborategi batean egiten da.

Behin lan hau eginda, mineralak magnetikoki banatzen dira, Frantz banagailu magnetiko isodinamiko (Frantz Company Inc., 13. modeloa) baten laguntzarekin. Banagailua erabili aurretik, berau ez buxatzeko, mineral magnetiko eta printz metalikoak kendu egiten dira iman indartsu batekin. Frantz-ean, eremu magnetikoaren intentsitate baldintzetan eta berau sortzen duen imanaren okerduran aldaketak eginez, mineralak banatu egiten dira, bakoitzaren propietate magnetikoen arabera.

Frantz-etik ateratako mineral frakzioak nahiko garbiak izaten dira. Hala ere, mineral bakoitzaren frakzioa garbitzeko, hau da, gainontzeko mineralak kentzeko, Olympus markako lupa binokular bat erabili da.

2.5. Kutsadura

Geokimika isotopikoan, analisiak egiteko metodo berri bat martxan jarri aurretik hainbat gauza eduki behar dira gogoan, besteak beste, zein den egokitzat jotzen den kutsadura maila. Rb-Sr sistemarako adibidez, maila horietara heltzea erraza den bitartean, U-Pb sistemaren kasuan material eta erreaktiboak etengabe eta era neketsuan garbitu behar dira, kutsadura maila onak mantendu eta laginen kutsadura ekiditeko.

Kutsadura kontrolatu eta saihesteko, kutsadura-iturri ezberdinen identifikazioa eta ezagupena beharrezkoa da:

Arroken xehatze eta ehotze prozesuan edota mineralen banaketan emandako kutsadura: kutsadura gurutzatua ekiditeko, erabiliko diren materialen garbiketa ezinbestekoa da, hauek erabili aurretik zein ondoren. Hau bereziki garrantzitsua da birrintzaile eta galbaheetan, non mineralak isolaturik geratzeko arriskua dagoen, lagin batetik bestera igaroz.

Kutsadura zuzena atmosferatik: aire kutsatua duten hiri handietan gertatu daitekeena eta iragazitako airezko gainpresioa duen gela egokituetan (gela zuriak) lan eginda gutxiagotu daitekeena.

Ikerlariak berak sartutako kutsadura: gorputzari atxikitutako partikulak, ilea, etab., direla medio. Lanerako ohitura zuzenekin (zabalik dauden ontzien gainetik objetu edo materialik ez pasatzea adibidez) eta jantzi, txano edo eskularruen erabilerekin ekidin daiteke.

Laborategiko materialen eta erreaktiboen bidezko kutsadura: erabilitako erreaktiboek, aztarna elementuak (Sr, Pb,…) eduki ditzakete, eta beharrezkoa da hauen garbiketa azpirakite baldintzetan (Mattison, 1972) edo kuartzozko destilagailuen bidez. Zenbait kasutan, erreaktiboen edukiontziek arazoak sortu ditzakete, edukiontziaren ikuzketak kutsadura sortu baitezake.

Bestetik, laginen disoluziorako erabiltzen diren ontziek, ‘memoria-efektua’ jasan dezakete, erabileraren ostean zuzen garbitzen ez badira.

Espektrometroekin arazoak: aerosolaren sortze-prozesuan zein laginaren ionizazioan ioi kopuru handia jalki daiteke espektrometroaren atal ezberdinetan. Metaketa hauek emisio sekundario bat eragin dezakete denborarekin, analisietan interferentziak sortuz. Horiek eragozteko, ezinbestekoa da atal hauen aldizkako garbiketa (azido nitriko diluituarekin, % 0,05).

3. Kapitulua: Geokronologia-Geokimika – Metodologia

3. Geokronologia-Geokimika - Metodologia

Tesi honetan, munduan zeharreko laborategietan erabilera handienetarikoa duten hiru sistema geokronologikoetarako metodo analitikoak inplementatu dira Universidad del País Vasco/Euskal Herriko Unibertsitatearen (UPV/EHU) Ikerkuntzarako Zerbitzu Orokorren (SGIker) laborategietan. Rb-Sr sistema disoluzio bezala analizatu da MC-ICP-MSaren bitartez, U-Th-Pb sistema Q-ICP-MSari egokitutako laser ablazio-sistemaren (LA) bidez analizatu delarik. Lu-Hf sistemarako, disoluzio zein laser bidezko analisiak egin dira, biak ere MC-ICP-MSaren bitartez. Hala ere, azalpen sakonetan hasi aurretik, oinarrizko printzipio batzuk birpasatuko dira.

3.1. Sarrera

3.1.a. Isotopo erradioaktiboen desintegrazioa/hazkuntza

Naturan, 300 isotopo inguru aurkitu daitezke (Henderson eta Scott McIndoe, 2005). Batzuk egonkorrak dira eta beste batzuk ez. Mineral eta arrokak datatzeko erabiltzen direnak erradioaktiboak edo ez-egonkorrak dira.

Desintegrazio-erradiaktiboaren abiadura, nukleido-gurasotik isotopo-kume egonkorrera, *t* denboran presente dauden atomo kopuruarekiko, *n*, proportzionala da (Rutherford eta Soddy, 1902):

$$-\frac{dn}{dt} = \lambda n \quad [1]$$

non λ proportzionaltasunaren konstantea den, erradionukleido jakinaren ezaugarri dena eta desintegrazio-konstante izena duena (denbora unitateetan adierazia). Desintegrazio-konstanteak, erradionukleido jakin bateko atomoak denbora jakin batean desintegratzeko duen probabilitatea adierazten du. $\frac{dn}{dt}$ terminoa atomo-guraso kopuruaren aldaketa-tasa da. Tasa hori denborarekin txikituz doanez negatiboa da . [1] ekuazioa berrantolatuz, honakoa lortzen da:

$$\frac{dn}{dt} = -\lambda n \quad [2]$$

Ekuazio hau *t=0*-tik *t*-ra integratuta dago, *t=0* denboran dauden atomo kopurua n_0 delarik:

$$\int_{n_0}^{n} \frac{dn}{n} = -\lambda \int_{t=0}^{t} dt \quad [3]$$

Horregatik,

$$\ln\left(\frac{n}{n_0}\right) = -\lambda t \quad [4]$$

beste era honetan ere idatzi daitekeena:

$$n = n_0 e^{-\lambda t} \quad [5]$$

[5] ekuazioak, edozein *t* denboran*, t=0* denboran presente zegoen jatorrizko atomoaren kopurutik (n_0) gelditzen den guraso erradioaktiboaren atomo kopurua adierazten du. Prozesu erradioaktiboen desintegrazioa deskribatzeko oinarrizko ekuazioa da.

Sortutako atomo-kume erradiogenikoaren kopurua, D^*, kontsumitutako guraso-atomo kopuruaren berbera da:

$$D^* = n_0 - n \quad [6]$$

eta $n_0=ne^{\lambda t}$ denez ([5] ekuaziotik); n_0 [6] ekuazioan ordezkatuta hau lortzen da,

$$D^* = ne^{\lambda t} - n \quad [7]$$

Hau da,

$$D^* = n\left(e^{\lambda t} - 1\right) \quad [8]$$

t=0 denboran dagoen atomo-kumeen kopurua D_0 bada, denbora jakin baten ondoren dagoen atomo-kume kopurua honela adieraziko da,

$$D = D_0 + n\left(e^{\lambda t} - 1\right) \quad [9]$$

Azken ekuazio hau datazio geokronologikoen oinarria da. [9] ekuazioko *D* eta *n* neurtzea posiblea da gailu egokiak erabilita, eta *t* denborarako modu honetan ebatzi daiteke ekuazioa:

$$t = \frac{1}{\lambda} ln\left(\frac{D - D_0}{n} + 1\right) \quad [10]$$

[10] ekuazioan lortutako *t*-aren zenbakizko balioa iraganeko data bat da. Data horren interpretaziorako suposizio batzuk onartzea ezinbestekoa da, bai datatzen ari den arroka edo mineralaren historia geologikoari dagokionean bai eta erabiliko diren D_0 eta λ zenbakizko balioei dagokienean ere. Supozisioak honakoak dira:

1.- Datatuko den arrokak edo mineralak ez du irabazitako edo galdutako isotopo-kumerik, isotopo-gurasoaren desintegraziotik sortutakoak salbu.

2.- Nukleido-gurasoaren desintegrazio-konstantea denborarekiko independientea da, nukleidoak jasan izan dituen baldintza fisikoek ez dute inolako eraginik izan bere baitan eta bere balioa zehaztasunez ezagutzen da.

3.- Kalkuluetarako D_0-ren balio egokia erabiltzen da, elementu-alabaren propietate kimikoen ezagutzan edota arrokaren edo mineralaren jatorrizko erreserborioaren konposizio isotopikoan oinarrituta.

4.- Neurtutako *D* eta *n* balioak zehatzak dira eta datatzen ari den arroka edo mineralaren adierazgarri dira.

3.1.b. Diluzio isotopikoa (isotopic dilution, ID)

Tesi honetan neurtutako sistema isotopikoetan, diluzio isotopikoaren teknika erabili da emaitza zehatz eta zuzenak lortzeko asmotan.

Diluzio isotopikoa kontzentrazioak ahalik eta zehatzen determinatzeko teknika analitikorik onena da. Faure eta Mensing-ek (1986) teknika honen onurak zerrendatzeaz gain, bere erabilerak dituen zailtasunak ere aipatu zituzten. Diluzio isotopikoaren bidez, konposizio isotopiko naturala duen lagina, isotopoetako batean artifizialki aberastuta dagoen eta kontzentrazio ezaguna duen trazatzaile batekin nahasten da. Bi disoluzio ezberdinen kopuru ezagunak nahasten direnean, lortutako konposizio isotopikoa (masa-espektrometroaren bidez neurtua), laginaren parte den elementu baten kontzentrazioa kalkulatzeko erabili daiteke, ondoko eran:

Demagun R_m, *A* eta *B* isotopoen arteko arrazoia dela eta *A* eta *B* isotopoak atomo kopuruan adierazten direla, *m*, *t* eta *s* azpiindizeak nahasteari (*mixture*), trazatzaileari eta eta analizatutako laginari (*sample*) dagozkielarik. Beraz,

$$R_m = \left(\frac{A}{B}\right)_m = \frac{A_t + A_s}{B_t + B_s} \quad [11]$$

Eskumaldeko izendatzaile eta zatitzaileak B_t-gatik zatituz ezaguna den $\frac{A_t}{B_t}$ arrazoia agerian uzteko (hau da, trazatzailearen arrazoia R_t), hau lortzen da:

$$R_m = \frac{R_t + \frac{A_s}{B_t}}{1 + \frac{B_s}{B_t}} \quad [12]$$

non $\frac{B_s}{B_t}$ determinatu beharreko ezezaguna den.

Horrela, gehitutako trazatzaile kopurua eta honen konposizio isotopikoa ezagututa, B_t ondorioztatu daiteke eta beraz, B_s kalkulatu daiteke.

[12]-a horrela ordenatuz:

$$R_m = \frac{R_t + \frac{A_s B_s}{B_s B_t}}{1 + \frac{B_s}{B_t}} \quad [13]$$

beraz,

$$R_m \left[1 + \frac{B_s}{B_t}\right] = R_t + R_s \frac{B_s}{B_t} \quad [14]$$

eta,

$$R_m + R_m \frac{B_s}{B_t} = R_t + R_s \frac{B_s}{B_t} \quad [15]$$

$\frac{B_s}{B_t}$ terminoak elkartuz,

$$\frac{B_s}{B_t}(R_m - R_s) = R_t - R_m \quad [16]$$

Eta azkenik,

$\frac{B_s}{B_t} = \left(\frac{R_t - R_m}{R_m - R_s}\right)$ [17]

Hortaz: $B_s = \frac{R_t B_t - R_m B_t}{R_m - R_s}$ [18]

$A_t = [A]_t M(t)$ denez, non *M(t)* laginari gehitutako trazatzailearen masa (g) eta $[A]_t$ trazatzaileko *A* isotopoaren kontzentrazioa (µmol.g^{-1}) diren, $B_s = \frac{\left[1 - R_m\left(\frac{B}{A}\right)_t\right][A]_t M(t)}{R_m - R_s}$ atomo kopuruan neurtzen da (µmol).

Elementuaren konposizio isotopikoa $\frac{K}{B}$ ugaritasun-arrazoi bezala adierazteko, *B* isotopoa erreferentzia-isotopo aukeratuta, ugaritasun-arrazoi bakoitza (naturan konstantea edo aldakorra) B_s-gatik eta ondoren, isotopo bakoitzaren pisu atomikoagatik *P(K)* biderkatu beharko da analizatutako laginean presente dauden isotopo bakoitzaren masa k_s lortzeko:

$$k_s = \left(\frac{K}{B}\right)_s B_s \ (\mu\text{mol})\ \mathrm{P(K)}\ (\mathrm{g.mol^{-1}}) \quad [19]$$

Isotopo bakoitzaren pisuaren batuketa aztertzen ari den elementuaren masari dagokio eta kontzentrazioa (µg.g^{-1}) lortzeko analizatutako laginaren masagatik (g) zatitu behar da:

$$kontzentrazioa(\mu\mathrm{g.g^{-1}}) = \sum_{k=1}^{k=n} k\ (\mu g)\frac{1}{M_s(g)} \quad [20]$$

3.1.b.1. *Erroreen hedatzea diluzio isotopikoan*

Alde batetik, diluzio isotopiko masa-espektrometria (ID-MS) bidez kalkulatutako kontzentrazioaren errore totala, neurketak bere baitan izan litzakeen ausazko erroreei dagokio. Diluzio isotopikoa isotopo egonkorretan egiten denean, hedatutako errorea R_m-aren errorearekiko proportzionala da. Neurtutako elementuaren konposizio isotopikoa aldakorra denean, baita bere pisu molekularra ere, ausazko errorea handitu egiten da konposizio isotopiko bakoitzaren neurketen eta birkalkulatutako masa molekularren erroreekin (ikusi García Alonso, 1995, kasuan kasuko kalkulatutako erroren tratamentu zehatzetarako).

Bestetik, faktore sistematikoei dagozkien erroreak ere badaude, hala nola, masa-zatikapenaren zuzenketan ziurgabetasunak, detektagailuaren denbora-hilaren (*dead time*) gaineko zuzenketa eta trazatzailearen kontzentrazioaren baitako ziurgabetasunak edota interferentzia isobarikoen presentzia. Azken hori teknika ezberdinen bidez txikiagotu egin daiteke, besteak beste, banaketa kimikoa, desolbatazioa edota plasmaren baldintzen aldaketa. Azkenik, laginaren prestaketan egindako pisaketak ere erroreen iturria izan daitezke, baina balantzek normalean izaten duten zehaztasuna dela eta, errore hauek arbuiagarriak dira beste errore iturriekin alderatuta.

Erroreen formulazioen azalpen zehatzak bestelako erreferentzietan aurkitu daitezke (Pin et al., 2000), eta horregatik hemen ez da gehiagorik sakonduko. k_s-an hedatutako errore totala ondoko eran idatzi daiteke:

$$\left(\frac{\sigma\,[\mathrm{k_s}]}{[\mathrm{k_s}]}\right)^2 = \left(\frac{\sigma\,[A]_t}{[A]_t}\right)^2 + \left(\frac{\sigma(R_{corr})}{(R_{corr})}\right)^2 M \quad [21]$$

non *M* errorearen anplifikazio-faktorea den, Webster-ek (1960) definitua:

$$M = (R_t - R_s)\left[\frac{R_m}{(R_m - R_s)(R_t - R_{m)}}\right] \quad [22]$$

3.2. Rb-Sr sistema, ID-MC-ICP-MS bidez

3.2.a. Sarrera

Rb-Sr bikotea prozesu geokimikoetako isotopo trazatzaile bezala erabili daiteke, baita geokronometro bezala ere, ^{87}Rb-a ^{87}Sr-a emateko desintegrazio-erradioaktiboa dela eta, β partikula baten eta anti-neutrino ($^{-}\nu$) baten emisioz;

$^{87}Rb \rightarrow {}^{87}Sr + \beta^{-} + {}^{-}\nu + Q$

non *Q* desintegrazio-energia den.

Rubidioa, alkalinoen taldeko elementua da, eta bere erradio atomikoa (1,48 Å) K^+-aren antzekoa izanik (1,33 Å), potasiodun mineraletan, halaber, miketan, feldespato potasikoan, buztin mineral jakin batzuetan eta mineral ebaporitikoetan K^+ ordezkatzeko ahalmena dauka. Bien bitartean, lurralkalinoen taldekoa den Sr^{2+}-aren erradio ionikoa (1,13 Å) da, Ca^{2+}-arena (0,99 Å) baino apur bat handiagoa, honen ordezkapena ahalbidetuz. Ezaugarrien ezberdintasuna dela eta, elementu biak frakzionatu egiten dira arroka eta mineral ezberdinetan, Rb/Sr erlazio ezberdinak eraginez eta ondorioz isokrona metodoaren bidez datazio erradiometrikoak kalkulatzeko aukera emanez.

Datazio erradiometrikoetarako sistema baten lehen baldintza, isotopo-gurasoaren desintegrazio-konstantea ezartzea da. Hala ere, ^{87}Rb-aren erdibizitzaren determinazioa zaila da, emititzen dituen partikulen energia txikia delako (0,275 MeV) eta desintegrazio-tasa geldoa delako. Azken berrogeita hamar urteotan, desintegrazio-konstantearen balioak aldakorrak izan dira, 1,47 × 10^{-11} (fisikoki neurtua) eta 1,39 × 10^{-11} u^{-1} (geologikoki ondorioztatua) bitartean. Urteetan erabili izan den balioa, 1,42 × 10^{-11} u^{-1} ($t_{1/2}$ = 48,8 Ga), IUGS (*International Union of Geological Sciences*) elkarteak onartua izan zen, eztabaida luzen baten ondorioz (Steiger eta Jäger, 1977). Azken urteotan publikatutako balioak, U-Pb sistemarekiko alderaketan oinarrituak,

gertuago daude 1.395×10^{-11} u^{-1} baliotik (Kossert, 2003; Nebel et al., 2011; Rotenburg et al., 2012; Villa et al., 2015).

Rb-aren eta Sr-aren espektroskopian zerikusia duten isotopoak eta pisu atomikoak ondoko tauletan aurkezten dira (3.1., 3.2. eta 3.3. Taulak).

3.1. **Taula.** Rubidio eta estrontzio isotopo ezberdinen ugaritasuna (%). Interferentziak sor ditzakeen Kr-aren ^{83}Kr, ^{84}Kr eta ^{86}Kr isotopoak eta ICP-MS ekipoen berezko zatikapen instrumentala zuzentzeko erabiltzen diren ^{90}Zr eta ^{91}Zr isotopoak ere azaltzen dira. IUPAC (*International Union of Pure and Applied Chemistry*) erakundeak gomendatutako balioak (De Laeter et al., 2003).

	83	84	85	86	87	88	90	91
Kr	11,50	57,00		17,27				
Rb			72,17		27,83			
Sr		0,56		9,87	7,04	82,53		
Zr							51,45	11,22

3.2. Taula. Rubidioaren masa atomikoak, IUPAC (*International Union of Pure and Applied Chemistry*) erakundearen arabera (De Laeter et al., 2003)

Isotopoa	85	87
Masa	84,9117924	86,9091858

Table 3.3. Estrontzioaren masa atomikoak, IUPAC (*International Union of Pure and Applied Chemistry*) erakundearen arabera (De Laeter et al., 2003)

Isotopoa	84	86	87	88
Masa	83,913426	85,9092647	86,9088816	87,9056167

3.2.b. Laginaren disoluzioa, diluzio isotopikoa eta banaketa kimikoa

Isotopoen arrazoien neurketa egin aurretik, intereseko elementuak gainontzeko elemetuetatik isolatzea beharrezkoa da. Nahiz eta normalean ICP-MSak TIMSak besteko purutasunik eskatu ez, Rb-Sr sistemaren kasuan kontrakoa gertatzen da. Izan ere, TIMSean ez bezala, ezinezkoa da elementu hauen ionizazio potentzial edo irakite tenperaturan oinarritutako Rb-aren edo Sr-aren ionizazio hautakorra. Are gehiago, induktiboki akoplatutako plasmak sortzen duen tenperatura altua dela eta, elementu biak erabat ionizatzen dira. Ondorioz, m/z = 87-an gerta daitekeen Rb-aren eta Sr-aren intereferentzia isobarikoa arazo-iturri handiena da, bi elementuen arteko banaketa-maila altua eskatzen duena. Hurrengo lerroetan, gure laborategiak Rb-Sr sistemarako garatu duen laginen tratamentuaren deskribapena egingo da. Metodoa optimizatzeko asmoz egindako saiakuntza errepikakorren emaitza da eta Pin eta Santos Zalduegui-k (1997) azaldutako prozeduran oinarritzen da.

1.- Lagin-hauts kopuru egokia (100 mg inguru) pisatzen da, 15 mL-ko Teflon® PFAzko (Savillex®) ontzian.

2.- Lehen eraso azidoan, 14 mol/L den HNO_3 1mL eta 29 mol/L den HF 2 mL gehitzen dira; ontzia itxi egiten da eta 70 °C-ra berotzen da lagina disolbatzeko. Pauso honek 12 ordu behar ditu gutxienez (gau bat).

3.- Sortutako disoluzioa ebaporatu egiten da 100 °C-ko tenperaturan, silizio fluoruroak lurruntzeko. Erabateko ebaporazioa lortu aurretik 11 mol/L den $HClO_4$ 0,1 mL gehitzen dira, azidoan disolbaezinak diren eta beste elementu batzuk estali ditzaketen fluoruroak sortu ez daitezen (Sulcek eta Povondra, 1989). Azido perklorikoa ebaporatzeko tenperatura altuak beharrezkoak dira, eta lagina erabat ebaporatzeko, siliziozko beiraz egindako berogailu infragorri baten beroa erabiltzen da, 100 °C-ra dagoen plaka beroarekin batera.

4.- Behin azido denak (HF, HNO_3 eta $HClO_4$) ebaporatuta, 6 mol/L den HCl 5 mL erabiltzen dira lagina birdisolbatzeko eta beste gau batez 70 °C-an uzten da, nitrato guztiak kloruro bihurtuz. Ondoren, lagina erabat ebaporatzen da berriro ere.

5.- Hondarra 14 mol/L den HNO_3 1 mL -tan disolbatzen da eta beste gau batez uzten da 70 °C-ko tenperaturan, fluorurorik geratuz gero erabat suntsitzeko. Hurrengo egunean azidoa erabat ebaporatzen da.

6.- Lagina 1,25 mol/L den HCl 2 mL-tan disolbatu egiten da eta 50 °C-an uzten da 2-3 orduz.

^{84}Sr-an aberastutako trazatzailearen kasuan, berau eraso azidoaren lehen pausoarekin batera gehituko litzateke, trazatzaile honek beharrezkoak diren arrazoiak aldibereko neurketa ahalbidetzen baitu, $^{84}Sr/^{86}Sr$ (diluzio isotopikorako) eta $^{87}Sr/^{86}Sr$ (zuzenketa bat eginda, ^{84}Sr-a ez baita % 100 purua eta beraz $^{87}Sr/^{86}Sr$ eta $^{88}Sr/^{86}Sr$ arrazoiak -azken hau normalizaziorako erabiltzen dena- trazatzaileagatik eraldatuta bait daude). Hala ere, ^{86}Sr-an aberastutako trazatzailea erabiltzen denean, ezinezkoa da aldibereko neurketa egitea, eta lagina bi alikuotatan banatzea ezinbestekoa da, bata laginaren $^{87}Sr/^{86}Sr$ arrazoia neurtzeko eta bestea trazatzailedun $^{88}Sr/^{86}Sr$ arrazoia analizatzeko. Rb trazatzaileak ez du inolako arazorik ematen, diluzio isotopikoa erabiltzen delako soilik.

Tesi honetan erabilitako trazatzaileak ^{86}Sr (% 97,02ra aberastua, *Oak Ridge National Laboratory*, AEB) eta ^{87}Rb (% 98ra aberastua, *Oak Ridge National Laboratory*, AEB) dira. Banakako disoluzioak prestatu ziren eta euren kontzentrazioak alderantzizko diluzio isotopikoen bidez kalibratu ziren, konposizio isotopiko naturala duten disoluzioak erabiliz. Azken horiek, Sigma-Aldrich (Sr) eta Alfa Aesar (Rb) enpresetan erositako 1000 ± 2 mg/L-ko kontzentrazioa duten elementu bakarreko disoluzietatik egindako diluzio grabimetriko zuzenen bidez prestatu dira. Tesian erabili diren trazatzaileen konposizio isotopikoak MC-ICP-MS bidez analizatu dira. Hauen ezaugarriak 3.4. Taulan aurkezten dira.

Esan bezala, ^{86}Sr-an aberastutako trazatzailea erabiltzeko disoluzioaren bi alikuota egin behar dira. Pauso hau pisaketen bidez egin da. Lehendabizi, egokia den trazatzaile kopurua (analitoaren kontzentrazioaren araberakoa) pisatu egiten da 15 mL-ko Teflon® PFAzko (Savillex®) ontzian eta ebaporatu egiten da. Ondoren, laginaren alikuota (disoluzio sekuentziako 6. pausotik), normalean laginaren bosten bat dena, hau da 15-20 mg, trazatzailea duen ontzira gehitu eta ebaporatu egiten da. Lagin eta trazatzailearen artean oreka isotopikoa lortzeko asmoz, ebaporatuta dagoen hondarra 6 mol/L den HCl 1mL-tan disolbatzen da, jarraian ebaporatzeko. Disoluzio-ebaporazio pausoa errepikatu egiten da 7 mol/L den HNO_3 1 mL rekin. Une honetan, lagina banaketa kimikorako prest dago.

3.4 Taula. ^{87}Rb eta ^{86}Sr trazatzaileen ezaugarriak.

Isotopo trazatzailea	Isotopo trazatzailearen ugaritasuna	Kontzentrazio elemental (ppm)	Isotopo trazatzailearen kontzentrazioa (µmol/g)
^{87}Rb	% 98,00	0,978 ± 0,008 (2σ)	% $1{,}13.10^{-2}$ ± 0,05 (RSD)
^{86}Sr	% 89,87	1,210 ± 0,014 (2σ)	% $1{,}41.10^{-2}$ ± 0,05 (RSD)

3.2.c. Banaketa kimikoa

^{87}Sr-ak eta ^{87}Rb-ak masa bera dutenez, MC-ICP-MSaren bidez neurtu ahal izateko, Sr-a eta Rb-a kimikoki erabat banatu behar dira. Horrez gain, frakzio biek Zr gabeak izan behar dute, izan ere, analisietako zatikapen instrumentala zuzentzeko Zr (Alfa Aesar) gehitzen bait zaio (Waight et al., 2002; Nebel et al., 2005; Yang et al., 2008). Banaketa hau aurrera eramateko, laginek bi banaketa prozesu jasaten dituzte, erauzte eta katio-truke kromatografian oinarritutako erretxina ezberdinekin.

3.2.c.1. *Lehen zutabea: Sr-aren banaketa*

Helburu honetarako, Sr-Spec (Eichrom Europe, Paris, France) erauzte kromatografia materiala (50-100 µm-ko partikula tamaina) erabiltzen da. Sr-aren banaketa prozedura Pin et al. (2003) lanetik moldatua dago, erabiltzen diren zutabe eta azidoen doiketaz. Doiketa prozesu honetan, zutabeak erreferentziazko material geologikoen disoluzioekin kalibratu dira, zutabeetatik ateratzen diren frakzioak batuz Sr-a non ateratzen den zehazteko.

Prozedura ondokoa da (3.1. Irudia):

Sr-Spec erretxina pisatu egiten da (83 mg gutxi gorabehera) eta HNO_3 0,05 mol/L azidoaren laguntzarekin 0,5 mm-ko barne-diametroa duen kuartzozko beiraz egindako zutabe batera eramaten da. Erabiltzen hasi aurretik, erretxina sakonki garbitzen da 6 mol/L den HCl eta 0,05 mol/L den HNO_3 azidoekin eta ondoren 2 mol/L den HNO_3 2 mL-rekin zutabea egokitzen da.

Lagina, nitrato hondar bezala dagoena, 2 mol/L den HNO_3 1,5 mL –tan disolbatzen da eta zutabean 0,5 mL-ko frakzioetan kargatzen da. Ba-a eta Sr-a (baita Pb ere) Sr-Spec erretxinak harrapatuta geratzen dira. Gainontzeko elementuak, Rb barne, azpian kokatuta dagoen beste zutabe batera igarotzen dira, non Rb frakzioa purifikatu egingo den (irakurri beherago). Zutabea 2 mol/L den HNO_3 1 mL–rekin garbitu egiten da, Rb-aren frakzioa erabat garbitzen delarik. Jarraian, Ba-aren eluzioa ematen da zutabetik 7 mol/L den HNO_3 2 mL pasaraziz. Gero, 2 mol/L den HNO_3 1 mL sartzen da azidoen nahasketa ekiditeko eta azkenik Sr-a ateratzen da, 0,05 mol/L den HNO_3 2 mL-rekin.

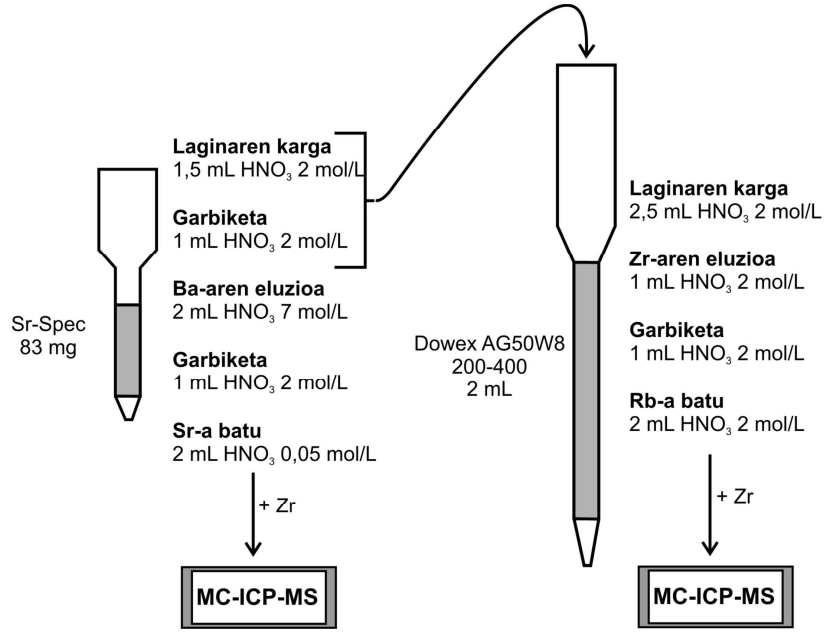

3.1. Irudia. Intereseko analitoen banaketarako prozedura kimikoaren diagrama, Sr-rako Sr-Spec erretxina eta Rb-rako AG50W8 katio-truke erretxina erabiliz. Azalpen gehigarrietarako irakurri testua

3.2.c.2. *Bigarren zutabea: Rb frakzioaren garbiketa*

Hurrengo pausoan, Rb-aren eta Zr-aren erabateko banaketa lortu behar da. Purifikazioa Dowex AG50-W8 (200-400 mesh) katioi-truke erretxinarekin lortzen da, 0,7 mm-ko barne diametroa duen kuartzozko zutabe batean erretxinaren 2 mL kargatuz. Bi elementuen arteko banaketa errez lortzen da 2 mol/L den HNO_3 (0,5 mL-ko kargetan) zutabean zehar pasaraziz. Zr-a lehen pausuetan (2 mL) eluitzen den bitartean, Rb frakzioa beranduago batzen da beste 2 mL-an (3.1. Irudia). Dowex erretxinak matrizea ere garbitzen du. Izan ere, Q-ICP-MS bidez egindako analisi erdikuantitatiboak erakusten du Rb frakzioak elementu nagusien parte bat baino ez daukala, batez ere K, Na, Mg eta Ca. Hala ere, plasmak elementu guztiak ionizatzen ditu, eta ez du inolako arazo analitikorik sortzen (Nebel et al., 2005).

Prozedura honen bitartez berreskuratutako analitoen kopurua % 95 baino handiagoa da. Prozeduraren garbitasuna, laginaren disoluzio eta banaketa kimikoa eta gero, 1 ng baino txikiagoa da Rb-an eta 4 ng baino txikiagoa Sr-an.

3.2.d. Rb-aren espektrometria

Rb-aren analisi isotopikoak detektagailu anitzeko, induktiboki akoplatutako plasma iturridun masa-espektrometroan (MC-ICP-MS, Finnigan Neptune) burutu dira, Euskal Herriko Unibertsitatearen (UPV/EHU) Ikerkuntzarako Zerbitzu Orokorren (SGIker) barruan. Ekipoari buruzko informazio osagarrirako, 2. Kapitulura jo. Analisiak era estatikoan egin dira, 3.5. Taulan azaltzen den Faraday Kaxen konfigurazioarekin.

3.5 Taula. Rb analisietan erabili den detektagailuen konfigurazioa.

L3	L2	L1	Erdia	H1	H2	H3	H4
83	84	85	86	87	88	90	91
Kr	Sr/Kr	Rb	Sr/Kr	Rb/Sr	Sr	Zr	Zr

Rb-aren analisirako erabili diren masak 85 (Rb) eta 87 (Rb/Sr) dira. Rb-aren gaineko interferentzia isotopiko bakarra ^{87}Sr-rena da. Gorago deskribatu den moduan, interferentzia hau Rb-aren eta Sr-aren arteko banaketa kimikoa erabilita ekidin daiteke. Geratu daitekeen Sr-ak sortutako interferentzia zuzendu egin daiteke ^{88}Sr neurtuz. Lagin naturaletan, ^{87}Sr/^{88}Sr arrazoia aldakorra da, ^{87}Rb-aren desintegrazioak eraginda. Waight et al.-ek (2002) azaltzen duten moduan, interferentzia zuzentzeko ^{87}Sr/^{88}Sr konposizio 'naturala' erabiltzeak, teorian, lehen hurbilketa bezala baino ez du balio. Zuzenketa sendo baterako, benetako ^{87}Sr/^{88}Sr balioa neurtu beharko litzateke Sr-aren analisi bereizi baten bidez. Praktikan, zuzenketa hauek oso txikiak dira, Sr-Spec erretxinaren erabilerak Rb frakziotik ia Sr dena kentzen baitu. Horrela, interferentzien zuzenketarako, Sr-aren konposizio isotopiko bezala 0,085 balioa hartu daiteke ^{87}Sr/^{88}Sr arrazoirako (^{87}Sr/^{86}Sr arrazoirako $\sim$ 0,71 balioarekin konpatiblea dena).

Rb isotopoen zatikapen instrumentalaren zuzenketa linean egiten da (*online*), Rb frakzioari gehitzen zaion Zr disoluzio estandarraren Zr-aren konposizio isotopikoarekiko (Waight et al., 2002). Zr-aren konposizio isotopikoa ziurtatzeko, lehendabizi disoluzio hau neurtu egin da, frakzionazioa ^{88}Sr/^{86}Sr-rekiko zuzenduz. ^{90}Zr/^{91}Zr arrazoirako lortutako balioa 4,5880 da, Sahoo eta Masuda-k (1997) aurkeztutako balioen baitan (^{90}Zr/^{91}Zr = 4,5874 ± 74; 2 s.d.) eta beste autore batzuen baloreekin bat etorriz (Minster eta Ricard, 1981; Sanloup et al., 2000).

Behin ^{87}Sr-ren interferentzia isobarikoa zuzenduta, ^{87}Rb/^{85}Rb arrazoia ondoko adierazpen esponentziala erabiliz zuzentzen da:

$$\left(\frac{^{87}Rb}{^{85}Rb}\right)_{egia} = \left(\frac{^{87}Rb}{^{85}Rb}\right)_{neurt} / \left(\frac{^{90}Zr/^{91}Zr}{4.5880}\right)^{\frac{\ln(^{87}Rb\ masa/^{85}Rb\ masa)}{\ln(^{90}Zr\ masa/^{91}Zr\ masa)}} \quad [23]$$

Neurketen kalibrazioa erreferentziazko Rb estandar batekiko egin da (SRM 984, 3.2. Irudia). Hori laginen artean aldizka neurtu da ekipoan inolako jitorik ez dagoela ziurtatzeko. $^{85}Rb/^{87}Rb$ arrazoirako lortutako balioa 2,5905 ± 0,0005 da (2 s.d, 3.2. Irudia), TIMSarekin lortutako balioak baino baxuagoa (2,5976, Edmunson et al., 2009; eta 2,612, Borg et al., 2009), baina hauen erroreen baitan. Hala ere, NIST (*National Institute of Standards and Technology*) institutuaren ziurtagiriaren araberako balioa 2,593 ± 0,002 da (% 95 CL; Cali, 1970), gure laborategian lortutako baloretik hurbilago dagoena. Nebel et al.-ek (2005) 2,5937 balioa lortu zuten ($^{87}Rb/^{85}Rb$ = 0,38554± 30, 2 s.d.) MC-ICP-MS teknikak erabiliz, ikerketa honetan lortutakoa baino altuagoa. Euren emaitza eta gurearen arteko diferentzia zatikapena zuzentzeko eragatik sortu daiteke. Izan ere, Nebel et al.-ek (2005) $^{92}Zr/^{90}Zr$ arrazoia erabiliz zuzenketa egiten duten bitartean lan honetan $^{90}Zr/^{91}Zr$-a erabili da. Nebel et al.-en (2005) arabera $^{90}Zr/^{91}Zr$-arekin zuzendutako Rb arrazoiak sistematikoki altuagoak dira $^{92}Zr/^{90}Zr$-zuzendutakoak baino (nahiz eta zuzenketa biak gainjarri egiten diren).

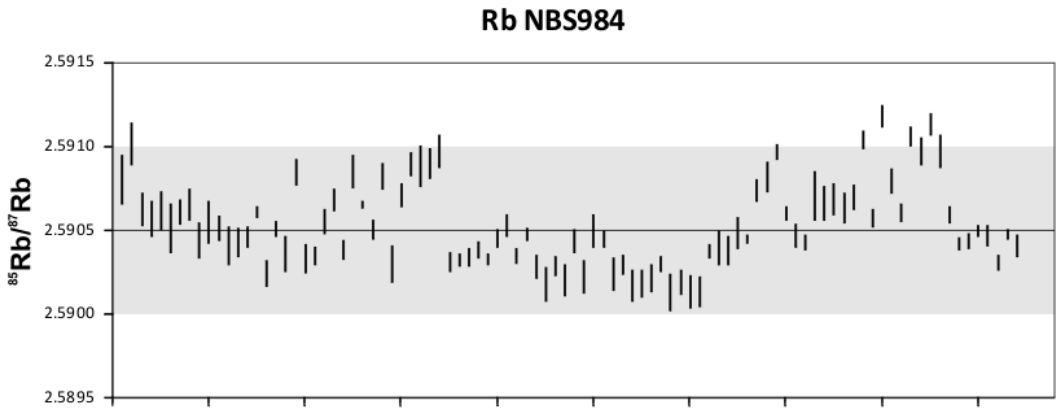

3.2. Irudia. Tesi honetan burututako NBS984 estandarraren analisiak.

3.2.e. Sr-aren espektrometria

Sr-aren analisi isotopikoak detektagailu anitzeko, induktiboki akoplatutako plasma iturridun masa-espektrometroan (MC-ICP-MS, Finnigan Neptune) burutu dira, Euskal Herriko Unibertsitatearen (UPV/EHU) Ikerkuntzarako Zerbitzu Orokorren (SGIker) barruan. Ekipoari buruzko informazio osagarrirako, 2. Kapitulura jo. Analisiak era estatikoan egin dira, 3.6. Taulan azaltzen den Faraday Kaxen konfigurazioarekin.

Sr-aren analisietan erabiltzen diren masak 86 (Sr/Kr), 87 (Rb/Sr) eta 88 (Sr) dira. ^{86}Kr-ak ^{86}Sr-ren gaineko eta ^{87}Rb-ak ^{87}Sr-ren gaineko interferentzia isobariko txikiak automatikoki

zuzentzen dira, ^{83}Kr eta ^{85}Rb kaxetan aldiberean neurtutako intentsitateetan oinarrituta (IUPAC erakundeak gomendatutako balioak erabiltzen dira $^{83}Kr/^{86}Kr$ eta $^{85}Rb/^{87}Rb$ arrazoietarako).

3.6. Taula. Sr analisietan erabili den detektagailuen konfigurazioa.

L3	L2	L1	Erdia	H1	H2	H3	H4
83	84	85	86	87	88	90	91
Kr	Sr/Kr	Rb	Sr/Kr	Rb/Sr	Sr	Zr	Zr

Gorago azaldu den moduan, Sr-aren kontzentrazioa eta konposizio isotopikoa neurtzeko bi alikuota beharrezkoak dira. Trazatzailerik gabeko alikuotan $^{87}Sr/^{86}Sr$ konposizioa neurtzen da. Arrazoi horren masa-zatikapena zuzentzeko lege esponentziala erabiltzen da $^{88}Sr/^{86}Sr$-ren 0,1194 balio konstantea erabiliz. Trazatzailea duen alikuotari, zeina kontzentrazioa kalkulatzeko erabiliko den, Zr estandarra gehitzen zaio Rb-arekin egin den modu berean. Sr isotopoen zatikapen instrumentalaren zuzenketa linean egiten da, Zr disoluzio estandarraren Zr-aren konposizio isotopikoarekiko (Yang et al., 2008). Kasu honetan ezinezkoa da ohikoa den $^{86}Sr/^{88}Sr$-rekiko frakzionazioaren zuzenketa egitea, trazatzailea gehitu baita eta beraz $^{86}Sr/^{88}Sr$ arrazoia ezezaguna delako. Zatikapenaren zuzenketa era honetan egiten da:

$$\left(\frac{^{88}Sr}{^{86}Sr}\right)_{egia} = \left(\frac{^{88}Sr}{^{86}Sr}\right)_{neurt} / \left(\frac{^{90}Zr/^{91}Zr}{4{,}5880}\right)^{\frac{\ln(^{88}Sr\ masa/^{86}Sr\ masa)}{\ln(^{90}Zr\ masa/^{91}Zr\ masa)}} \qquad [24]$$

Neurketen kalibrazioa erreferentziazko Sr estandar batekiko egin da (SRM 987, 3.3. Irudia). Hori laginen artean aldizka neurtu da ekipoan inolako jitorik ez dagoela ziurtatzeko. SRM987-aren $^{87}Sr/^{86}Sr$ arrazoirako 100 erreferentziazko balio baino gehiago daude (http://georem.mpch-mainz.gwdg.de/) MC-ICP-MS bidez neurtuta. Baloreak 0,7101 eta 0,71065 artean daude, gehienak 0,71025 inguruan daudelarik. Tesi honetan lortutako balioa 0,710251 ± 0,000026 da (2 s.d.), erreferentziako balioekin bat etorriz.

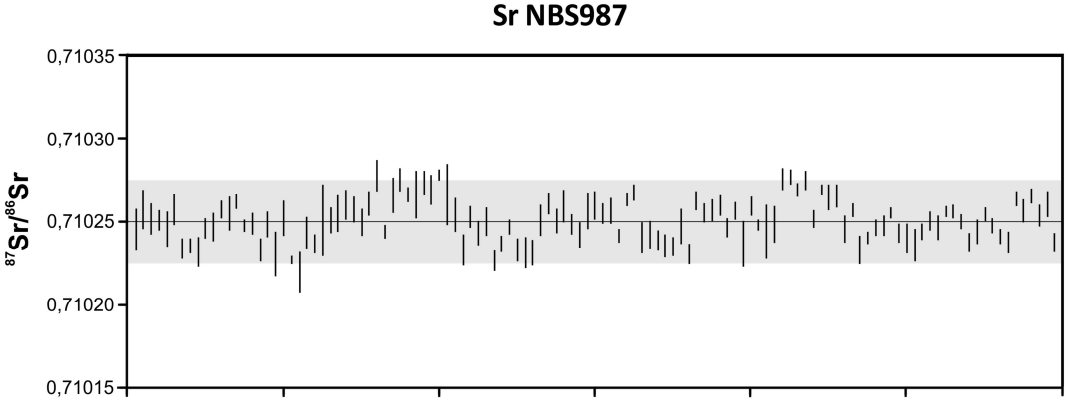

3.3. Irudia. Tesi honetan burututako NBS987 estandarraren analisiak eta erreferentziazko balioa ($^{87}Sr/^{86}Sr$ = 0,71025).

3.2.f. Neurketa parametroak

Espektrometroaren erabileran kontsideraturiko parametroak 3.7. Taulan laburbiltzen dira. Neurketa-sekuentzia hasi aurretik, komenigarria da plasma eta Apex desolbatazio-gailua egonkortu arte itxarotea, 45 minutuz. Denbora honen ostean, lente ionikoen doiketa eta optimizazioa burutzen da, ^{86}Sr-aren tontorraren forma ondu eta sentsibilitatea maximizatzeko. Helburu honetarako, Thermo Scientific-ek saltzen duen 'Neptune Multi Element Standard Solution (8 element)' disoluzioa erabiltzen da (Tune-Up Solution, ref. 1149340). Disoluzioak 200 ng.g^{-1}-ko kontzentrazioa dauka, eta Apex-a erabiltzekotan, 25 ng.g^{-1}-ra diluitzen da. Disoluzio estandar honetan, ^{86}Sr isotopoaren seinalearen intentsitatea 3 V ingurukoa da. Rb analisietarako ere optimizazio-eredu bera erabiltzen da, Sr-a monitorizatuz.

Behin parametro guztiak doituta daudela, esperimentu analitikoa prestatzen da. Datuen bereganatzea era estatikoan burutzen da eta 10 neurketa-ziklotako 7 bloke egiten dira, 6 minutu inguruko analisian.

Laginak MC-ICP-MS bidez analizatzen direnean, intrumentuaren zatikapena kontrolatu behar da. Horretarako, Sr eta Rb analisietan NBS987 eta NBS984 laginen artean tartekatu egiten dira, hurrenez hurren. Nahiz eta esperimentu luzeetan seinalearen intentsitatea aldakorra izan, % 10eraino ere iritsiz, ez da inolako desplazamendurik aurkitu ^{87}Sr/^{86}Sr edo ^{85}Rb/^{87}Rb arrazoietan. Hori dela eta, laginei ez zaie inolako kanpo-zuzenketarik aplikatu.

3.7. Taula. Sr eta Rb analisi isotopikoetarako MC-ICP-MSaren parametroak.

ICP-aren baldintzak	
Irrati-frekuentzia	1200 W
Laginaren gas jarioa	0,75-0,8 L/min
Gas hoztailearen jarioa	15 L/min
Gas laguntzailearen jarioa	0,45 L/min
Gas gehigarriaren jarioa (N_2)	0,28-0,35 L/min
Laginaren xurgatzea	60 s
Garbiketa denbora	60 s
Xurgatze denbora (garbiketa)	120 s
Laginketa denbora	6 min (10 ziklotako 7 bloke)
Integrazio denbora	4,194 s/ziklo
Denbora geldia	3 sec
Apex	
T Apex 1	140 ^{o}C
T Apex 2	2 ^{o}C

3.2.g. Metodoaren balioztatzea nazioarteko estandarretan

Metodoa balioztatzeko, sei nazioarteko CRM (*Certified Reference Materials*) estandarretan lortutako balioak eta haien gomendatutako baloreak alderatu egin dira, bai kontzentrazioari dagokionez baita konposizio isotopikoari ere. Estandarrak konposizio sorta zabala

aztertzeko aukeratu dira. Posible izan denean, plasma bidezko ekipoetan neurtutako balioak hartu dira gomendagarri moduan. ICP baliorik egon ezean, ID-TIMS bidez analizatutako balioak hartu dira haintzat. Lortutako emaitzak 3.8. Taulan ikus daitezke. Aipatu beharra dago balio bakoitza disoluzio berberaren bi neurketen batezbestekoa dela.

Laginaren prestaketa eta banaketa kimikoaren ostean neurtutako $^{87}Sr/^{86}Sr$ arrazoiak espero zitezkeen balioetan daude, hirugarren analisiak kenduta (kasuan kasuko C lagina). Emaitzak oso dispertsio gutxirekin ageri dira, prozedura analitikoak erreproduzigarriak diren emaitzak ematen dituela baieztatuz. Lortutako balioak zehaztasun eta zuzentasun handikoak dira, eta beraz, metodoa ikerketa geologikoetan erabiltzeko baliagarria dela ondorioztatu daiteke. Literaturan AC-E eta FK-N estandarren arrazoi isotopikorik ez dago. Zehazgabetasun handiagoa ikusi da Rb-an aberatsagoak diren lagin hauetan, baina azalpen argirik ez dago momentuz. Rb-aren eta Sr-aren arteko banaketa erabatekoa dela onartuta, laginaren heterogeneotasun batekin espekulatu daiteke, baina momentuz ez dago hori babestuko duen daturik.

Lehenago esan bezala, estandar bakoitzaren hirugarren errepikanerako ez da balio koherenterik lortu. Elementuen banaketa kimikoaren prozedura arruntean, trazatzailerik ez duen alikuota banatzen da lehendabizi eta erretxina garbitu ondoren, trazatzaileadun alikuota banatzen da. Bi banaketen ostean, erretxina aldatu egiten da. 'C' izeneko errepikapenetan, prozedura atzekoz aurrera egin da, lehengo trazatzailedun alikouta banatuz eta gero, trazatzailerik gabekoa. Laginak neurtu eta gero, garbi egon behar luketen laginak trazatzaileaz kutsatuta daudela ikusi da, eta beraz, ordena hau ez da inondik inora erabili behar.

Rb eta Sr kontzentrazioetarako lortutako emaitzak ere erreproduzigarriak dira, AGV-2 D analisietan salbu, zeinean bi elementuetan balio altuagoak lortu diren. Lortutako kontzentrazioak gainera, espero zitezkeen balioetatik gertu daude. Rb eta Sr frakzioak bi ontzi ezberdinetan mantendu eta diluitu direnez banaketaren ostean, AGV-2 D-arekin izandako arazoa laginaren prestaketan jazotakoa dela ondorioztatu da. Horrela, lagin horretako $^{87}Rb/^{86}Sr$ arrazoia gainontzeko errepikapenen balioetan dagoela ikusita, errorea pisatutako laginaren balorea idazterakoan izandako akats bati dagokio seguruenik.

AGV-2 A-ren Sr kontzentrazioa gainontzeko laginetan baino altuagoa da, eta Rb-an ikusitako antzeko kontzentrazioak eta $^{87}Rb/^{86}Sr$ arrazoi baxuagoak direla kontuan hartuta, banaketatik analisira doan denbora tartean izandako kutsadura txiki bat gertatu dela proposatu daiteke. Esan beharra dago AGV-2 alikuotak, oso Sr kontzentrazio altua dutenak, asko diluitu behar direla, eta posiblea dela pauso horretan kutsadura eman izana. Hala ere, AGV-2 A-ren balioa AGV-2-aren gainontzeko errepikapenen erroren baitan dago. Bost errepikapenak egun berean neurtu ziren, eta beraz, zehazgabetasun analitikoak baztergarriak dira.

3.8 Taula. Testuan deskribatzen den konposizio isotopiko eta diluzio isotopiko prozedurarekin nazioarteko estandarretan lortutako emaitzak. Gomendatutako balioekin alderatuta. (a) Yang et al. (2012); (b) Balcaen et al. (2006); (c) Yang et al. (2010); (d) Zhang et al. (2012); (e) Georem Preferred Value (Jochum eta Nehring, 2006); (f) Yu et al. (2001); (g) Govindaraju (1995).

Estandarra	$^{87}Sr/^{86}Sr$			Sr kontzentrazioa			Rb kontzentrazioa			$^{87}Rb/^{86}Sr$	± 2σ
	Erreferentzia	Neurtua	± 2 S.E.	Erreferentzia	Neurtua	± 2σ	Erreferentzia	Neurtua	± 2σ		
AGV-2-A		0,703974	2E-05		675	8		65,3	0,5	0,2802	0,0014
AGV-2-B	0,703994 ± 15 (2σ) (a)	0,703993	1E-05	654 ± 3 (1σ) (d)	649	7	67,7 ± 0,7 (1σ) (d)	65,2	0,5	0,2910	0,0015
AGV-2-C					664	8		66,2	0,5	0,2888	0,0014
AGV-2-D		0,704004	2E-05		723	8		72,8	0,6	0,2912	0,0015
AGV-2-E		0,703994	1E-05		664	8		66,2	0,5	0,2886	0,0014
BHVO-2-A		0,703477	2E-05		397	5		8,84	0,07	0,0645	0,0003
BHVO-2-B	0,703479 ± 20 (2σ) (a)	0,703476	3E-05	396 ± 1 (1σ) (e)	399	5	9,11 ± 0,04 (1σ) (e)	8,92	0,07	0,0648	0,0003
BHVO-2-C					396	5		8,83	0,07	0,0645	0,0003
BHVO-2-D		0,703509	2E-05		397	5		8,83	0,07	0,0644	0,0003
BHVO-2-E		0,703485	2E-05		397	5		8,91	0,07	0,0650	0,0003
G-2-A		0,709774	2E-05		483	6		164	1	0,9816	0,005
G-2-B	0,70977 ± 16 (2σ) (TIMS) (b)	0,709744	2E-05	483 ± 2 (1σ) (d)	485	6	166 ± 4 (1σ) (d)	164	1	0,9774	0,005
G-2-C					485	6		164	1	0,9782	0,005
G-2-D		0,709729	2E-05		481	5		164	1	0,9895	0,005
G-2-E		0,709766	3E-05		481	5		164	1	0,9897	0,005
W-2-A		0,706983	2E-05		195	2		19,24	0,15	0,2861	0,0014
W-2-B	0,706966 ± 31 (2σ) (TIMS) (c)	0,706973	2E-05	202 ± 3 (1σ) (d)	195	2	19,5 ± 0,1 (1σ) (d)	19,39	0,16	0,2875	0,0014
W-2-C					198	2		19,29	0,15	0,2823	0,0014
W-2-D		0,706999	2E-05		196	2		19,14	0,15	0,2825	0,0014
W-2-E		0,706995	2E-05		198	2		19,33	0,15	0,2835	0,0014
AC-E-A		0,86623	1E-04	No tracer added				145	1		
AC-E-B		0,85935	5E-05					145	1		
AC-E-C				2,6 ± 8,14 RSD(%) (f)	2,61	0,03	148 ± 5 RSD(%) (f)	144	1	162,24	0,81
AC-E-D		0,85342	7E-05		2,60	0,03		145	1	163,23	0,82
AC-E-E		0,86356	7E-05		2,60	0,03		145	1	163,35	0,82
FK-N-A		1,2080	3E-05	No tracer added				849	7		
FK-N-B		1,2063	1E-04					856	7		
FK-N-C				39 (g)	38,7	0,4	860 (g)	850	7	66,701	0,33
FK-N-D		1,2075	2E-05		38,4	0,4		853	7	67,446	0,34
FK-N-E		1,2080	4E-05		38,4	0,4		853	7	67,524	0,34

Rb-aren kontzentrazioak gomendatutako balioak baino baxuagoak dira sistematikoki, nahiz eta erroreen baitan egon. Neurtutako balioen eta gomentatutako balioen diferentzia azaltzeko alderantzizko diluzio isotopikoan emandako zehazgabetasun edo eraso azidoan galdutako materialaren inguruan eztabaidatu genezake. Hala ere, ID-TIMS bidez AGV-2 eta BHVO-2 estandarretan lortutako balioak (Raczek et al., 2001; Willbold eta Jochum, 2005) bat datoz hemen aurkezten diren emaitzekin. Horrela, ikusitako ezberdintasunak era errazago batean azaldu daitezke, espektrometro eta teknika analitikoen ezberditasunak eragindakoak

liratekeelarik. Alde batetik, detektagailu bakarreko ICP-MSak kanpo-doiketa (*standard bracketing correction*) bidez eta konposizio isotopiko naturalarekiko zatikapen lege linear batekin zuzentzen dira, eta beste aldetik, ID-MC-ICP-MSan barne-zuzenketa egiten da zatikapen lege esponentziala jarraiki.

Dakigun arte, nazioarteko materialen $^{87}Rb/^{86}Sr$ arrazoiak ez dira literaturan aurkitzen. Aipatzea merezi du beraz, metodo honen bidez lortutako emaitzak erabat erreproduzigarriak direla. Kanpoko erreproduzigarritasuna lagin guztien barne-zehaztazunaren berbera da, sistematikoki % 3 RSD baino baxuagoa.

Sei nazioarteko estandarretan lortutako emaitzek, bai $^{87}Sr/^{86}Sr$ arrazoian bai Rb eta Sr kontzentrazioan, martxan jarritako prozedura baliozkoa dela ondorioztatzen dute. Hortaz, Rb-Sr sistemaren baitako azterketa geokronologikoak egiteko erabilgarria dela baieztatu daiteke.

3.3. Lu-Hf sistema, ID-MC-ICP-MS bidez

3.3.a. Sarrera

Lu-Hf bikotea ere isotopo trazatzaile eta geokronometro bezala erabiltzen da. ^{176}Lu-ak adarkatutako desintegrazio isobarikoa erakusten du, ^{176}Hf-ra β -emisioz eta ^{176}Yb-ra elektroi bat harrapatuz. Azken hori, hala ere, aktibitate osoaren ehuneko txikiari dagokio eta baztergarria da (Dixon et al., 1954).

$$^{176}Lu \rightarrow {}^{176}Hf + \beta^{-} + Q$$

Lutezioa lantanidoen serieko azken elementua da, lur arraroen (*Rare Earth Elements, REE*) elementurik astunena izanik. Hafnioa aldiz, Potentzial Ioniko Handiko Elementuen taldeko elementua da (*High Field Strength Element, HFSE*). Horrela, prozesu geokimiko askok bi elementu hauen banaketa handia eragiten dute, gorputz geologiko berdinaren barnean ezaugarri erradiogeniko ezberdinak dituzten erreserborio bereizgarriak ahalbidetuz. Zehazki, Lu-a errez sartzen da granate, apatito edo lawsonitaren kristal egituraren barruan, Hf-a mineral osagarri jakin batzuekin soilik (zirkoia, rutiloa, baddeleyita) konpatiblea den bitartean.

^{176}Lu-aren desintegrazio-konstanterako ez dago adostasunik (Scherer et al., 2000; Blichert-Toft, 2001). Azken urteetan balio ugari publikatu dira, kontaketa zuzenaren bidez (Dalmasso et al., 1992; Nir-El et Lavi, 1998) edo bai U-Pb sistemarekin alderatuz (Scherer et al., 2001). Tesi honetako Lu-Hf adinak $1{,}867\times10^{-11}$ u^{-1} desintegrazio-konstantearekin kalkulatu dira (Scherer et al., 2001; Söderlund et al., 2004), gehien erabiltzen den konstantea baita (Anczkiewicz et al., 2007; Kylander-Clark et al., 2007; Schmidt et al., 2008; Kirchenbaur et al., 2012).

Lu-aren eta Hf-aren espektroskopian zerikusia duten isotopoak eta pisu atomikoak ondoko tauletan aurkezten dira (3.9., 3.10., 3.11. eta 3.12. Taulak).

3.9. Taula. Iterbio, lutezio eta hafnio isotopoen ugaritasuna (%), IUPAC (*International Union of Pure and Applied Chemistry*) erakundearen arabera (De Laeter et al., 2003)

	168	170	171	172	173	174	175	176	177	178	179	180
Yb	0,13	3,04	14,28	21,83	16,13	31,83		12,76				
Lu							97,41	2,59				
Hf						0,16		5,26	18,60	27,28	13,62	35,08

3.10. Taula. Iterbioaren masa atomikoak, IUPAC (*International Union of Pure and Applied Chemistry*) erakundearen arabera (De Laeter et al., 2003)

Isotopoa	168	170	171	172	173	174	176
Masa	167,933895	169,934759	170,936322	171,936378	172,938207	173,938858	175,94256

3.11. Taula. Lutezioaren masa atomikoak, IUPAC (*International Union of Pure and Applied Chemistry*) erakundearen arabera (De Laeter et al., 2003)

Isotopoa	175	176
Masa	174,940768	175,942682

3.12. Taula. Hafnioaren masa atomikoak, IUPAC (*International Union of Pure and Applied Chemistry*) erakundearen arabera (De Laeter et al., 2003)

Isotopoa	174	176	177	178	179	180
Masa	173,940042	175,941403	176,9432204	177,9436981	178,9458154	179,9465488

3.3.b. Laginaren disoluzioa eta diluzio isotopikoa

Laginaren disoluzio-prozesua ezberdina izan daiteke helburuaren arabera. Zirkoia eta rutiloa bezalako mineral osagarriak Hf-aren erreserborio nagusienak dira eta beraz, disolbatuta ala ez, lortuko diren emaitzetan eragin handia izan dezakete. Mineral osagarri hauek beste arazo batzuk ere sor ditzakete, euren izaera erregogorra dela eta, oso zaila baita hauek disolbatzea. Gure kasuan, mineral hauek disoluzioaren parte izateko fusioaren bidezko erasoa egin da, laginean dagoen Hf osoa disoluziora pasa dela ziurtatuz. Helburua arrokaren parte jakin baten Hf konposizioa aztertzea bada (banatutako mineralena adibidez), azidoaren bidezko erasoa egokiagotzat jo da, erregogorrak diren mineral hauek disolbatu gabe uztea ahalbidetzen baitu.

Tesi honetan erabilitako trazatzaileak ^{176}Lu (% 44,23ra aberastua, *Oak Ridge National Laboratory*, AEBAEB) eta ^{179}Hf (% 89,87ra aberastua, *Oak Ridge National Laboratory*, AEB) izan dira. Banakako disoluzioak prestatu dira eta euren kontzentrazioak alderantzizko diluzio isotopiko bidez kalibratu dira, konposizio isotopiko naturala duten disoluzioak erabiliz. Azken horiek, Fluka Analytica (Lu) eta Merck (Hf) enpresetan erositako 1000 ± 2 mg/l-ko kontzentrazioa duten elementu bakarreko disoluzietatik diluzio grabimetriko zuzenen bidez prestatu dira. Tesian erabili diren trazatzaileen konposizio isotopikoak MC-ICP-MS bidez analizatu dira, eta zatikapen

instrumentala zuzentzeko kanpo-zuzenketa erabili da (*standard bracketing*). ^{176}Lu eta ^{179}Hf puruen nahasteak kontzentrazio egokia duen Lu-Hf trazatzaile mistoa egitea ahalbidetzen du, fusio bidezko erasoan ahalik eta trazatzaile kopuru txikiena erabiltzeko. Trazatzailearen Lu/Hf erlazioa (6 inguru) egokia da konposizio-eremu zabal bateko laginak aztertzeko, arroka subkondritikoen arrazoietatik (Lu/Hf ≈ 0,23) granatea duten laginen arrazoietara (30-era heldu daitekeen Lu/Hf erlazioa).

Arrokek eta granateek elementu hauetan dituzten kontzentrazio arruntak kontuan hartuta eta trazatzailearen kopurua ahalik eta txikiena gehitzea interesatzen zaigula aintzat harturik, Hf-aren kontzentrazio aproposena 0,25 µg.g^{-1} dela erabaki da. Horrela, trazatzailearen Lu kopurua Hf-arena baino 6 aldiz handiagoa izan arte doitu da, 1,5 µg.g^{-1} inguru.

Kontzentrazio honek onura garrantzitsuak dakartza. Alde batetik, ^{176}Hf/^{177}Hf arrazoia neurtu behar da, eta Hf-a trazatzaile/lagin erlazioarekiko elementu sentikorrena da. Horregatik, trazatzailea gehitu eta gero ^{176}Hf/^{177}Hf ahalik eta hoberen babestu beharko da, geroko zuzenketen magnitudea txikiagoa izan dadin. Bestetik, honek ^{179}Hf/^{177}Hf arrazoia 1-etik gertu neurtzea ahalbidetzen du, eta beraz, diluzio isotopikoen kalkuluetako erroreen handipena (Webster, 1960) minimoan mantentzen da.

^{176}Lu-^{179}Hf trazatzaile mistoaren ezaugarriak 3.13. Taulan ematen dira.

3.13. Taula. ^{176}Lu-^{179}Hf trazatzaile-mistoaren ezaugarriak.

Isotopo trazatzailea	Isotopo trazatzailearen ugaritasuna	Kontzentrazio elemental (ppm)	Isotopo trazatzailearen kontzentrazioa (µmol/g)
^{176}Lu	% 44,23	1,629 ± 0,024 (2σ)	% 9,29.10^{-3} ± 0,05 (RSD)
^{179}Hf	% 97,02	0,2132 ± 0,0016 (2σ)	% 1,191.10^{-3} ± 0,05 (RSD)

3.3.b.1. *Fusio bidezko erasoaren prozedura*

Fusio bidezko laginaren deskonposiziorako 'Joule efektuaren' bidezko fusioa egiten duen urtzailea erabiltzen da (Katanax K1), Le Fèvre eta Pin-en (2002) prozedura jarraituz. Laginarekin kontaktua izan dezaketen urtzailearen atal guztiak garbitu egiten dira lagin bakoitza urtu baino lehen.

Gehituko den trazatzaile kopurua ahalik eta hoberen doitzeko, laginak duen analito kopurua ezagutzea lagungarria da. Horregatik, aurretiazko Q-ICP-MS bidezko analisi erdikuantitatiboak egiten dira, Lu eta batez ere Hf kopuruak ezagutzeko.

Lagin-hautsa (50-100 mg) platinozko arrago batean pisatzen da. Pisatzen den lagin kopurua duen Hf kopuruaren araberakoa da, eta gutxienez 40 ng Hf ateratzeko beste pisatzen da (arroketan ez da arazorik egoten normalean). Ondoren urtugarria ($LiBO_2$) gehitzen da, urtugarri eta laginaren proportzioa 5:1 izan arte. Arragoen eta urtzailearen ezaugarriek urtugarri kopuru

handia eskatzen dute, horren ezean urtutako materiala ez baita arragotik ateratzeko kapaza. Nazioarteko estandarretan lortutako emaitzek eta garbitasun-mailak (begiratu beherago) adierazten dute horrenbesteko urtugarrik ez duela inolako eraginik.

Trazatzaile mistoa egoera likidoan bezala gehitu eta pisatzen da. Gero arragoari eskuarekin eragiten zaio lagin-hautsa, urtugarria eta trazatzailea nahasteko eta ondoren, sikatu egiten da denbora tarte batez urtzailearen ondoan jarrita. Homogeneizazioa eta gero, nahasketa urtzailean jartzen da 10 minutuz 1200 °C-ra (hori da arragoaren tenperatura fabrikatzailearen arabera).

Lortutako lagin galdatua 30 mL-ko erabilera bakarreko ontzietara isurtzen da non hozte-lasterra jasaten duen. Ontzi horiek poliestirenozkoak dira, 2 mol/L den HCl - % 0.15 den $H_2O_2$10 mL nahasketa dute barnean eta irabiagailu magnetiko batekin etengabe irabiatzen dira. HFSEen hidrolisia saihesteko gehitzen da hidrogeno peroxidoa (Dahmer eta Fritz, 1965). 10-15 minututan erabateko disoluzioa eta hoztea ematen dira.

3.3.b.2. *Azido bidezko erasoaren prozedura*

Lehen esan bezala, kasu batzuetan azido bidezko erasoa hobesten da. Prozedura hau beharrizan zehatz batzuk betetzeko erabiltzen da, batez ere, Hf-an aberatsak diren eta lagina kutsatu dezaketen inklusioak saihestea, adibidez, granatean egon daitezkeen zirkoi edo rutiloak.

Aurrerago azalduko den legez, Lu-aren banaketa kimikoan zehar, interesgarriak diren beste REE batzuk (Sm-a eta Nd-a) banatzeko aukera dago, gerora TIMS edo MC-ICP-MS bidez neurtu daitezkeenak. Sm-Nd sistema beste geokronometro bat da, eta kasu honetan REEtan aberatsak diren inklusioak saihestu behar dira (apatito edo monazita bezalako fosfatoak adibidez). Arazo hauei aurre egiteko lan honetan Anczkiewicz eta Thirwall-ek (2004) aurkeztutako azido sulfuriko bidezko disoluzio partziala edo '*sulphuric acid (H_2SO_4) leaching*' teknika erabili da.

Tesi honetan Sm eta Nd frakzioak lagin errealetan batu dira soilik (4. Kapitulua). Elementu hauen banaketarako eta analisietarako prozedurak aspaldi balioztatu ziren gure laborategietan (Menéndez, 2001 edo Sanchez-Lorda et al., 2013), eta horregatik analisietarako egokitzat hartu dira.

Hf-ak eman dezakeen beste arazo bat, hidrolisirako sentikortasun handia da. Gainera, azido fluorhidrikoa bezalako agente egoki bat erabili ezean, zaila da berau disoluzioan mantentzea. Hori gutxi balitz, fluoruroak ez dira Hf-a banatzeko erabiltzen den erretxinan (Dowex AG50-W8) harrapaturik geratzen. Fluoruroen presentzia ahalik eta gehien gutxitzeko, disoluzioak azido perklorikoko ($HClO_4$) lurrun indartsuen bitartez tratatzen dira (Pin eta Joannon, 2003).

Hidrolisi arazoak ekiditeko, hidrogeno peroxidoa erabili da eta soluzioak ahal bezain azkar erabili dira.

Azido bidezko erasoaren prozedura honako da:

Egokia den lagin-hauts kopurua (40 ng Hf banatzeko beste) agatazko morteiru baten ehotzen da, eta azetona eta H_2O-rekin garbitu. Lagina lehortu ondoren, PFA Teflonezko (Savillex®) ontzi batera pasatzen da. Anczkiewicz eta Thirlwall-ek (2004) esan bezala azido sulfurikoa gehitzen zaio laginari, 0,5 eta 1 mL artean (laginaren tamainaren araberakoa) eta fosfatoak disolbatzeko ontzia 180 °C-ra berotzen da 24 orduz. Disoluzioa baztertu egiten da, eta lagin solidoa H_2O-rekin garbitzen da hainbat bider azido sulfuriko guztia kendu arte (azido sulfurikoaren lurruntze tenperatura, tefloiaren urtze tenperatura baino handiagoa da). Garbiketa-pauso hau bereziki garrantzitsua da. Prozedurak daukan beste arazoetako bat H_2SO_4-aren likatasun handia da. Tamaina txikieneko pikorrak azidoan esekituta geratu daitezke eta garbiketa-prozesu honetan azidoarekin batera kentzeko arriskua dago, lagina zati baten galera eraginez. H_2O-rekin garbiketa errepikakorra egiteak azidoaren kontzentrazioa (eta likatasuna) jaisten du eta ondorioz, lagin galera saihesten laguntzen du.

Behin garbituta, lagina ontzi berri batera aldatzen da ur tanta baten laguntzaz, tanta hori lehortuz eta berriro ere lagina pisatuz. Lurrunketa hau abiadura eta tenperatura baxuan egin behar da, bestela, indar elektrostatikoak direla eta, laginak ontzitik kanpora ‘salto’ egiteko arriskua dago. Lurrunketa geldoak gainera, H_2O-ren erabateko lurrunketa ziurtatzen du, laginaren pisuaren gainestimazioak ekidinez. Azido bidezko erasoarekin hasi aurretik, Lu-Hf eta Sm-Nd trazatzaileak gehitzen dira, pisaketa bidez.

Azido bidezko erasoa ondoko azidoen adizioz hasten da; 14 mol/L den HNO_3 2 mL, 29 mol/L den HF 1 mL eta 11,8 mol/L den $HClO_4$ 0,5 mL.Ontzia itxi egiten da eta 75 °C-an uzten da lagina disolbatu arte (gau bat). Ontzia irekitzerakoan azido nitriko eta fluorhidrikoaren soberakinak lurrundu egingo dira, SiF_4 lurrunkorrarekin batera. Lurrunketa gertatzen den bitartean, 11,8 mol/L den $HClO_4$ 4 mL gehitzen dira eta disoluzioa azido perkorikoko lurrun indartsuen pausora pasatzen da berogailu infragorri baten azpian, beti ere lagina erabat ez lurruntzeko kontuz ibiliz. Ontziaren paretetan kondentsazioz sortzen diren tantak urarekin garbitu behar dira noizean behin. Lurrunketa indartsu hau 0,5-1 mL likido geratzen denean gelditzen da. 6 mol/L den HCl 5 mL gehitzen dira eta lagina zentrifugagailu tutu batera aldatzen da, disolbatu gabeko mineralak (zirkoia eta rutiloa batez ere) isolatzeko. Likido-egoeran dagoen lagina lehengo ontzira bueltatu eta 1 mL geratu arte ebaporatzen da.

Banaketa kimikoaren lana hasi aurretik, 1 mL dituen laginari 1,5 mol/L den HCl - % 0,15 H_2O_2 dun 9 ml gehitzen zaizkio. Horrela, fusio bidezko erasoan prestatutako bolumen eta medio

berean dago lagina (2 mol/L den HCl - % 0,15 H_2O_2 10 mL). Horrek, eraso prozedura bientzako banaketa eskema bera erabiltzea ahalbidetzen du.

3.3.c. Banaketa kimikoa

^{176}Yb, ^{176}Lu eta ^{176}Hf isotopoek bata bestearengan interferentziak sortzen dituztenez, behar-beharrezkoa da Yb-a eta Lu-a Hf-tik banatzea MC-ICP-MSan analisiak egin aurretik. Banaketa hau aurrera eramateko, laginek bi banaketa prozesu jasaten dituzte, katio-truke eta erauzte-kromatografian oinarritutako erretxina ezberdinekin (3.4. Irudia).

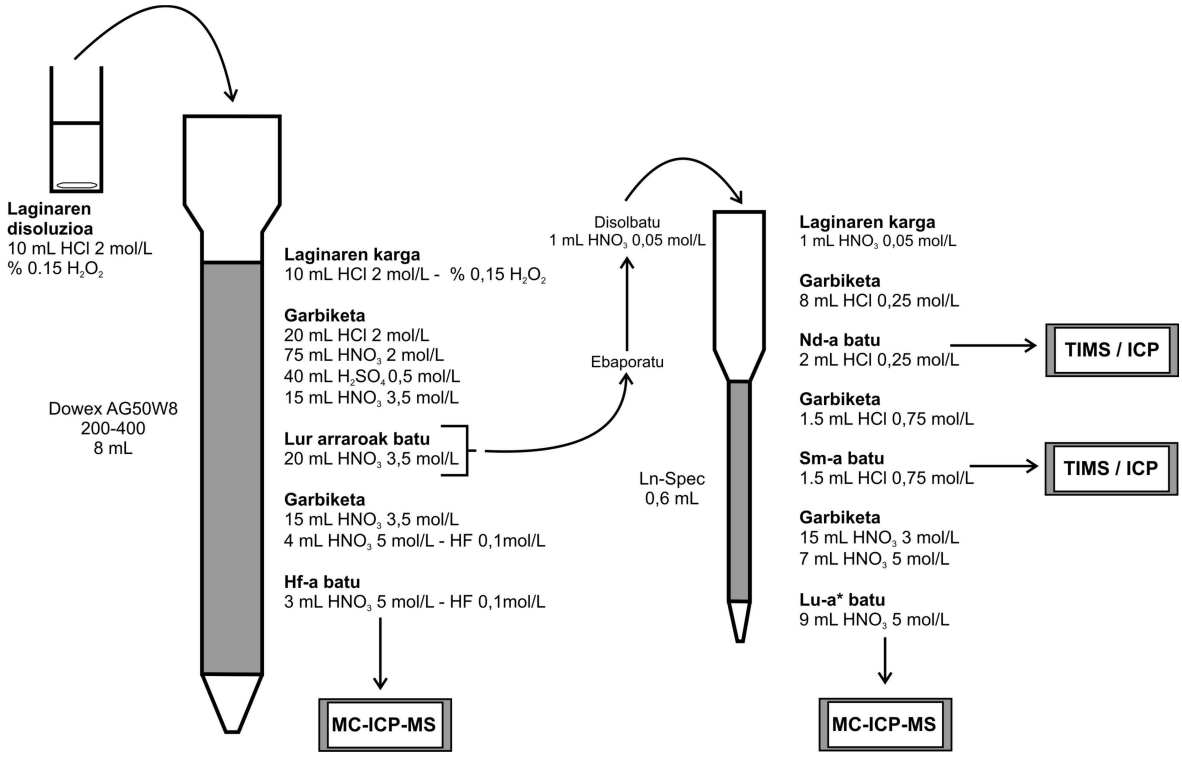

3.4. Irudia. Intereseko analitoen banaketarako prozedura kimikoaren diagrama, Hf-rako AG50W8 katio-truke erretxina erabiliz eta Sm-rako, Nd-rako eta Lu*-rako Ln-Spec erauzte komatografiarako materiala. Lu*: frakzio honek Yb parte bat dauka. Azalpen gehigarrietarako irakurri testua.

3.3.c.1. *Lehen zutabea: katio-truke bidezko Hf-aren eta REEn banaketa*

Hf-aren banaketa Dowex AG50-W8 (200-400 mesh) katioi-truke erretxinarekin lortzen da, 1 cm-ko barne-diametroa duen kuartzozko zutabe batean 8 mL erretxina kargatuz. Zutabea erabili aurretik (aurreko egunean), erretxina sakonki garbitzen da 6 mol/L den HCl eta 5 mol/L den HNO_3–0,1 mol/L den HF azidoak pasaraziz. Azkenik, H_2O pasarazten uzten da gauean zehar. Zutabeak daukan erreserborioak 100 mL edukiera dauka, eta horrek gauean pasaraziko den H_2O nahikoa uzteko aukera ematen du. Lagina kargatu aurretik erretxina 2 mol/L den HCl 10 mL-rekin

egokitzen da. Ondoren lagina kargatzen da. Esan beharra dago prozedura honen bitartez beste elementu batzuk ere banatzen direla, eta kasu honetarako interesgarriak ez diren arren, aipatu egingo dira.

Lehen pausoan, zutabea 2 mol/L den HCl 20 mL -rekin garbitzen da. Ondoren 2 mol/L den HNO_3 20 mL sartzen dira. 20 mL hauetan U eta Rb frakzioak daude, nahi izanez gero batu egin daitezkeenak. Azido bereko 30 mL gehiagorekin Sr-a batu daiteke eta beste 25 mL kargatuta Ba-a ere agertzen da. Honen ostean, 0,5 mol/L den H_2SO_4 40 mL-rekin Zr-a garbitzen da. Hurrengo pausoan azido nitrikora egingo da buelta, baina oraingoan 3,5 mol/L kontzentrazioarekin. Azido honen lehen 15 mL-ak baztertu egiten dira, eta hurrengo 20 mL-etan REEak batzen dira. Beste 15 mL baztertu egiten dira. Hf-aren banaketarako 5 mol/L den HNO_3 – 0,1 mol/L dun HF nahasketa bat beharrezkoa da. Lehendabizi, 4 mL kargatu eta baztertzen dira eta azkenik, Hf frakzioa batzen da hurrengo 3 mL-ekin. Hf-aren frakzioa MC-ICP-MS bidez neurtzeko prest egongo litzateke dagoeneko. Normalean banaketa kimikoa hemen uzten da, baina Th-a batu nahi izanez gero, azken azidoaren beste 13 mL zutabera botata elementu honen frakzioa lortuko litzateke.

3.3.c.2. *Bigarren zutabea: REE-n aldibereko banaketa erauzte kromatografia bidez*

Sm-aren, Nd-aren eta Lu-aren banaketa Le Fèvre eta Pin-en (2005) prozedura jarraituz egiten da, Ln-Spec erauzte komatografiarako materiala erabiliz, 0,5 mm-ko barne-diametroa duen kuartzozko zutabe batean 0,6 mL erretxina kargatuz. Lagina kargatu aurretik zutabea 6 mol/L den HCl azidoarekin garbitzen da eta erretxinaren egokitzea 0,05 mol/L den HNO_3 azidoarekin egiten da.

REEak dituen 20 mL-ko disoluzioa, lehen zutabetik banatutakoa, erabat lurruntzen da. Hondarra 0,05 mol/L den HNO_3 1 mL -rekin berreskuratu eta zutabean kargatzen da. Ln-Spec materialak REE guztiak banatzeko aukera ematen du, eta gure kasuan erabilitako sekuentzia honakoa da: 0,25 mol/L den HCl 8 mL (La-Ce-Pr zati bat), 0,25 mol/L den HCl 2 mL (Nd gehi Pr zati bat), 0,75 mol/L den HCl 1,5 mL, 0,75 mol/L den HCl 1,5 mL (Sm gehi < % 5 Eu), 3 mol/L den HNO_3 15 mL (Gd-Tb-Dy-Ho-Er-Tm) eta 5 mol/L den HNO_3 7 mL (% 90 Yb). Azkenik, Lu frakzioa (gehi ≈ % 10 Yb) beste 5 mol/L den HNO_3 8 mL-rekin batzen da. Lu-arekin batera Yb-aren % 10a batzeko arrazoia Lu-aren espektrometria atalean azalduko da (ikusi beherago).

Sm eta Nd frakzioak neurtu egin behar badira, bietako bakoitza erabilera bakarreko poliestirenozko poteetan batu eta erabat sikatzen da TIMS zein MC-ICP-MS bidezko analisiak egin aurretik. Neurketa hauek egiteko prozedurak bibliografian aurki daitezke (Menéndez, 2001 edo Sánchez-Lorda et al., 2013).

Prozedura honen bitartez berreskuratutako analitoen kopurua % 95 baino handiagoa da. Prozeduraren garbitasuna, laginaren disoluzio eta banaketa kimikoa eta gero, 35 pg ingurukoa da Hf-an eta 20 pg ingurukoa Lu-an.

3.3.d.Lu-aren espektrometria

Lu-aren analisi isotopikoak detektagailu anitzeko, induktiboki akoplatutako plasma iturridun masa-espektrometroan (MC-ICP-MS, Finnigan Neptune) burutu dira, Euskal Herriko Unibertsitatearen (UPV/EHU) Ikerkuntzarako Zerbitzu Orokorren (SGIker) barruan. Ekipoari buruzko informazio osagarrirako, 2. Kapitulura jo. Analisiak era estatikoan egin dira, 3.14. Taulan azaltzen den Faraday Kaxen konfigurazioarekin.

Lu-aren analisietarako erabilitako masak 175 (Lu) eta 176 (Yb, Lu, Hf). Lu-ak bi isotopo baino ez ditu eta ondorioz ezinezkoa da arrazoi egonkor batekiko zuzenketak egitea. Zatikapen instrumentala zuzentzeko, antzeko masa eta propietate kimikoak dituen dituen aldameneko elementu bat erabiltzen da: Yb, nahiz eta elementu honek interferentzia zuzena egiten duen m/z = 176-an. Hau da arestian aipatutako Lu-aren frakzioan Yb-aren % 10 batzearen arrazoia. $^{171}Yb/^{173}Yb$ = 0,88296 arrazoia (Amelin eta Davis, 2005) erabiltzen da Lu-aren frakzionazioa zuzentzeko, bi elementuen portaera alderagarria dela onartuz. ^{176}Yb-aren ^{176}Lu-aren gaineko interferentzia zuzentzeko naturan konstantea den $^{176}Yb/^{173}Yb$ = 0,7964 arrazoia (Amelin eta Davis, 2005) erabiltzen da, espektrometroaren zatikapena kontuan hartuta beti ere. Hf-aren gabezia m/z = 178 (edo 177 edo 179) monitorizatuz baieztatzen da. Dena dela, Hf-aren seinalea hondo-zarataren parekoa izaten da eta eragiten duen interferentzia, beraz, baztergarria da.

3.14. Taula. Lu analisietan erabili den detektagailuen konfigurazioa.

L4	L3	L2	L1	Erdia	H1	H2
171	173	175	176	177	178	179
Yb	Yb	Lu	Lu/Yb/Hf	Hf	Hf	Hf

Neurketen kalibrazioa laborategian erositako elementu bakarreko disoluzio estandarrarekiko (alderantzizko diluzio isotopikorako erabilitako bera) egin da. Hori laginen artean aldizka neurtu da ekipoan inolako jitorik ez dagoela ziurtatzeko. $^{176}Lu/^{175}Lu$ arrazoi naturalarentzako lortutako balioa 0,02656 ± 0,00001 da (2 s.d., 3.5. Irudia), hainbat ikerketatan jazotako balioen antzekoa (Patchett eta Tatsumoto, 1980; Blichert-Toft eta Albarède, 1997; Scherer et al., 2001; Vervoort et al., 2004). Balio hauen zehaztapenerako, Yb elementu bakarreko disoluzio estandarra gehitu da zatikapenaren zuzenketak egitekoburuzko informazio osagarrirako, 2. Kapitulura jo. Analisiak era estatikoan egin dira, 3.14. Taulan azaltzen den Faraday Kaxen konfigurazioarekin.

3.3.d.1. *Yb-aren parte hartzearen zuzenketa 176 masan*

Lu-aren frakzio berean Yb-a batzeak interferentzia arazo handia sortzen du 176 masan. Interferentzia hau aldez aurretik zuzendu behar da, ondorengo lerroetan deskribatzen den metodoarekin.

$\left(\frac{176}{175}\right)_{neurt}=\frac{^{176}Lu+\ ^{176}Yb}{^{175}Lu}$ arrazoiaren neurketatik $\frac{^{176}Lu}{^{175}Lu}$ kalkulatu dezakegu. Hau ere idatzi daiteke:

$$\frac{^{176}Lu}{^{175}Lu}=\frac{^{176}Lu+\ ^{176}Yb}{^{175}Lu}\cdot\frac{^{176}Lu}{^{176}Lu+\ ^{176}Yb}=\left(\frac{176}{175}\right)_{neurt}\cdot\frac{^{176}Lu}{^{176}Lu+\ ^{176}Yb} \quad [25]$$

non ^{176}totala = ^{176}Yb + ^{176}Lu den, beraz:

$$\frac{^{176}Lu}{^{176}Lu+\ ^{176}Yb}=1-\frac{^{176}Yb}{^{176}Lu+\ ^{176}Yb} \quad [26]$$

[26] ekuazioaren bigarren atala $\frac{^{173}Yb}{^{173}Yb}$-gatik biderkatuz gero, ezagunak edo neurgarriak diren balioak topatuko ditugu:

$$1-\frac{^{176}Yb}{^{173}Yb}\cdot\frac{^{173}Yb}{^{176}Lu+\ ^{176}Yb}=1-\left(\frac{\left(\frac{173}{176}\right)Yb}{\left(\frac{176}{173}\right)_{neurt}}\right) \quad [27]$$

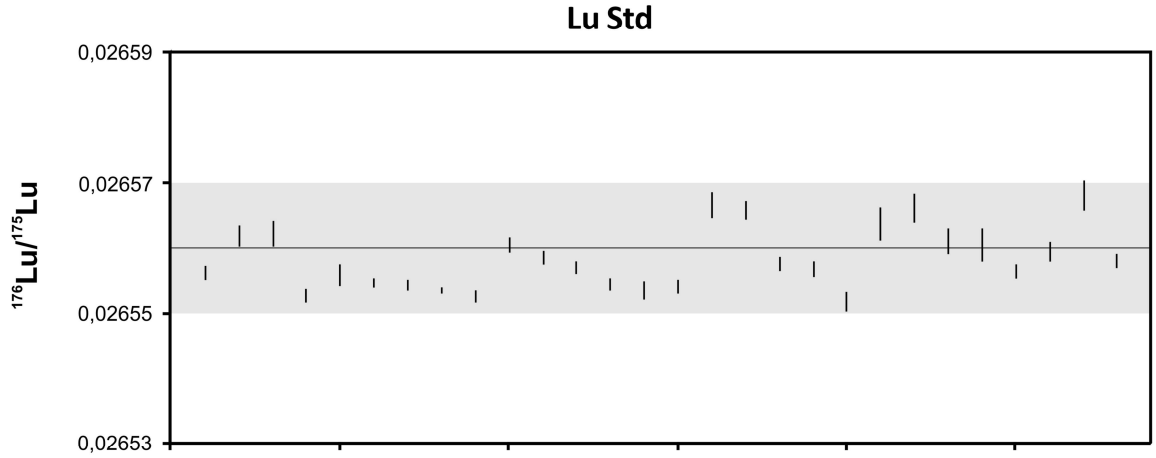

3.5. Irudia. Tesi honetan burututako Lutezio estandarraren (Fluka Analytica) analisiak.

Hau [25] ekuazioan sartuz,:

$$\frac{^{176}Lu}{^{175}Lu}=\left(\frac{176}{175}\right)_{neurt}-\left[1-\left(\frac{\left(\frac{173}{176}\right)\mathrm{Yb}}{\left(\frac{176}{173}\right)_{neurt}}\right)\right] \quad [28]$$

Kasu honetan, ^{176}Yb/^{173}Yb arrazoian eragiten duen zatikapen instrumentala zehaztu behar da, neurtutako $\left(\frac{^{176}Lu+\ ^{176}Yb}{^{173}Yb}\right)_{neurt}$ arrazoiarekin alderagarria dela onartuz. Zehaztutako balioa,

$^{176}Yb/^{173}Yb$ arrazoi natural eta egonkorrean eta erabilitako zatikapen legearen alderantzizkoan oinarritua dago. Hau, lege esponentziala erabiliz egiten da, ondoko eran:

$$\left(\frac{I_1}{I_2}\right)_{egia} = \left(\frac{I_1}{I_2}\right)_{neurt} \cdot \left(\frac{MM\,(I_1)}{MM\,(I_2)}\right)^{f} \quad [29]$$

non I_1 eta I_2 analizatutako elementuaren bi isotopo diren, atomo kopuru bezala adieraziak, *MM* parentesi artean dagoen isotopoaren masa molekularra den eta *f* zatikapenaren zuzenketa-faktorea den. Lege esponentziala erabiltzen da, enpirikoki, plasma iturridun gailuen zatikapena zuzentzeko egokiena dela ematen duelako (Taylor et al., 1995; Halliday et al., 1995).

Legea era erraz batean alderantzikatu daiteke balio naturaletik (edo egiazkoa) 'neurtutako' balioa lortzeko:

$$\left(\frac{I_1}{I_2}\right)_{neurt} = \left(\frac{I_1}{I_2}\right)_{egia} \cdot \left(\frac{MM\,(I_1)}{MM\,(I_2)}\right)^{-f} \quad [30]$$

Yb-aren kasuan, gure esperimentuan analizatutako masen arabera, interferentziarik gabeko isotopoena da *f* faktorea kalkulatzeko aukera bakarra (^{171}Yb eta ^{173}Yb).

Kalkulatu egingo da [29] eta [30] ekuazioetatik:

$$f_{173} = \frac{\ln\left(\frac{\left(\frac{171}{173}\right)_{nat}}{\left(\frac{171}{173}\right)_{neurt}}\right)}{\ln\left(\frac{MM(171)}{MM(173)}\right)}, \quad [31] \qquad \text{beraz,}$$

$$\left(\frac{^{176}Yb}{^{173}Yb}\right)_{neurt} = \left(\frac{^{176}Yb}{^{173}Yb}\right)_{nat} \cdot \left(\frac{MM\,(176)}{MM\,(175)}\right)^{-f_{173}} \quad [32]$$

[28] ekuaziotik $^{176}Lu/^{175}Lu$ arrazoia kalkulatu daiteke. Arrazoi hau zatikapenerako zuzendu gabe dago momentu horretan, eta lege esponentzialaren bidez zuzendu behar da, $^{176}Yb/^{173}Yb$ arrazoia zuzentzeko erabili den *f* berbera erabilita.

3.3.d.2. *Kontzentrazioaren kalkulua*

Lu-aren kontzentrazioa kalkulatzeko diluzio isotopikoaren ekuazio bera erabiltzen da, kapituluaren hasieran azaldu dena. Gogoratzeko, azken ekuazioa honako hau da:

$$^{175}Lu_s = \frac{\left(\frac{^{176}Lu}{^{175}Lu}\right)_m \left(\frac{^{175}Lu}{^{176}Lu}\right)_t - 1}{\left(\frac{^{176}Lu}{^{175}Lu}\right)_s - \left(\frac{^{176}Lu}{^{175}Lu}\right)_m} \cdot \left[^{176}Lu\right]_t \cdot Pds(t) \quad [33]$$

3.3.d.3. *Erroreen hedatzea eta amaierako ziurgabetasuna*

Lu-aren kontzentrazioan erroreen hedatzerako kalkuluetarako, irakurlea diluzio isotopikoaren teoriara bidaltzen da berriz ere. Hemen soilik ziurgabetasunaren formula da adieraziko da:

$$\left(\frac{\sigma\,[Lu]}{[Lu]}\right)^2 = \left(\frac{\sigma\left[^{176}Lu\right]_t}{\left[^{176}Lu\right]_t}\right)^2 + \left(\frac{\sigma\left(\frac{^{176}Lu}{^{175}Lu}\right)_m}{\left(\frac{^{176}Lu}{^{175}Lu}\right)_m}\right)^2 M \quad [34]$$

non kortxeteen arteko balioek kontzentrazioak adierazten dituzten (masa Lu-aren kasuan eta molarra 176_t-ren kasuan), eta non *M* errorearen anplifikazio-faktorea den (Webster, 1960).

3.3.e. Hf-aren espektrometria

Hf-aren analisi isotopikoak detektagailu anitzeko, induktiboki akoplatutako plasma iturridun masa-espektrometroan (MC-ICP-MS, Finnigan Neptune) burutu dira, Euskal Herriko Unibertsitatearen (UPV/EHU) Ikerkuntzarako Zerbitzu Orokorren (SGIker) barruan. Ekipoari buruzko informazio osagarrirako, 2. Kapitulura jo. Analisiak era estatikoan egin dira, 3.15. Taulan azaltzen den Faraday Kaxen konfigurazioarekin.

3.15. Taula. Hf analisietan erabili den detektagailuen konfigurazioa.

L4	L3	L2	L1	Erdia	H1	H2
171	173	175	176	177	178	179
Yb	Yb	Lu	Lu/Yb/Hf	Hf	Hf	Hf

Hf isotopoen analisietan, ^{176}Hf-ren gaineko ^{176}Yb-aren eta ^{176}Lu-aren interferentzia isobarikoak 173 eta 175 masak neurtuz monitorizatzen dira, eta baita zuzendu ere behar izanez gero. Interferentzia isobarikoak zuzentzeko erabiltzen diren isotopo egonkorren arrazoiak ondokoak dira: ^{176}Yb/^{173}Yb = 0,7964 (Amelin eta David, 2005), eta ^{176}Lu/^{175}Lu= 0,02656 (Patchett eta Tatsumoto, 1980), hurrenez hurren. Hala ere, ^{176}Lu/^{175}Lu arrazoia naturan aurkitzen denarekiko ezberdina da Lu-Hf trazatzailea erabili delako. Lu ez-naturalak 176 masan eragin dezakeen desplazamendua ekiditeko, posiblea da diluzio isotopikoaren bitartez lehenago neurtutako ^{176}Lu/^{175}Lu arrazoia erabiltzea. Dena dela, Lapen et al.-ek (2004) erakutsi bezala, zuzentzeko prozedura honek desadostasunak sor ditzake trazatzailedun eta trazatzailerik gabeko laginen artean. Autore hauen gomendioak jarraituta, interferentzia zuzentzeko Lu-aren arrazoi naturala erabiltzea erabaki da, Hf-aren frakzioan dagoen Lu kopurua txikia edo hutsala delako.

Neurketen kalibrazioa erreferentziazko Hf estandar batekiko egiten da (JMC 475 Johnson Matthey). Hori laginen artean aldizka neurtu da ekipoan inolako jitorik ez dagoela ziurtatzeko.

Gure ekipoan lortutako $^{176}Hf/^{177}Hf$ arrazoiaren balioa 0,282151 ± 6 izan da (2 s.d., 3.6. Irudia), MC-ICP-MS mota bera duten beste laborategi batzuetan lortutako balioen antzekoa (adibidez, Schmidt et al., 2011; Cheng et al., 2012; 0,282152).

Zatikapen instrumentala lege esponentziala eta $^{179}Hf/^{177}Hf$ = 0,7325 (Patchett eta Tatsumoto, 1980) erreferentziazko balioa erabiliz zuzentzen da, eta arrazoi guztiak 177 masarekiko erreferentzian ematen dira. Lan honetan aurkezten diren Hf-aren konposizio isotopikoen analisiak eta berauen erroreak linean kalkulatutakoak dira.

Trazatzailedun laginetarako, konposizio isotopiko eta diluzio isotopikoen aldibereko analisiak prozedura berbera erabiliz egin dira, baina kasu honetan 176 masaren gaineko interferentziak baino ez dira linean zuzendu. Landugabeko datuak espektrometrotik kanpo (*offline*) tratatzen dira, zatikapen intrumentala eta trazatzailearen parte hartzea zuzendu eta egiazko emaitzak lortzeko. Kalkuluetarako prozedura datozen orrialdeetan deskribatuko da.

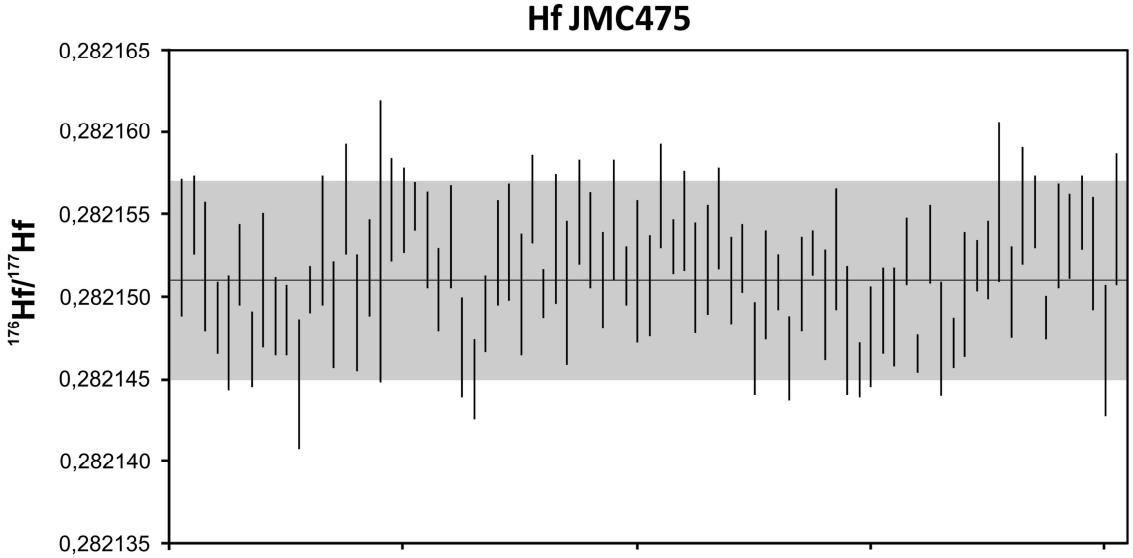

3.6. Irudia. Tesi honetan burututako JMC475 estandarraren analisiak.

3.3.e.1. *Zatikapenaren zuzenketa*

Arazo horri aurre egiteko hainbat metodo proposatu dira, konstanteak diren terminoekin egindako konbinazioetan ezberdintzen direlarik, adibidez: Kostitsyn eta Zhuravlev (1987). Lan honetan erabili den prozedura Brieuc LeFèvre-k (2002) erabilitakoan oinarrituta dago.

Kalkuluak, elementu bereko hiru isotopoetan *A*, *B* eta *C* oinarritzen dira, bi arrazoi independiente lortu daitezkeelarik, $\frac{A}{B}$ eta $\frac{C}{B}$. *A* isotopo trazatzailea da, *B* erreferentzia-isotopoa eta *C* zuzenketak egiteko erabiliko den isotopoa. Diluzio isotopikoaren ekuazioak (kapituluaren

hasieran) trazatzailea (*t*) eta laginaren (*s*) arteko nahasketaren (*m*) ekuazio bi hauek idazteko aukera ematen digu:

$$\frac{B_S}{B_t} = \frac{\left(\frac{A}{B}\right)_m - \left(\frac{A}{B}\right)_t}{\left(\frac{A}{B}\right)_S - \left(\frac{A}{B}\right)_m} \text{ eta } \frac{B_S}{B_t} = \frac{\left(\frac{C}{B}\right)_m - \left(\frac{C}{B}\right)_t}{\left(\frac{C}{B}\right)_s - \left(\frac{C}{B}\right)_m} \quad [35]$$

berrantolatu ondoren;

$$\overbrace{\left(\frac{A}{B}\right)_t\left(\frac{C}{B}\right)_s - \left(\frac{A}{B}\right)_s\left(\frac{C}{B}\right)_t}^{\alpha} = \left(\frac{A}{B}\right)_m \overbrace{\cdot\left(\left(\frac{C}{B}\right)_s - \left(\frac{C}{B}\right)_t\right)}^{\beta} + \left(\frac{C}{B}\right)_m \overbrace{\cdot\left(\left(\frac{A}{B}\right)_s - \left(\frac{A}{B}\right)_t\right)}^{\gamma} \quad [36]$$

eta azkenik ,

$$\left(\frac{C}{B}\right)_m = \frac{\alpha - \left(\frac{A}{B}\right)_m \cdot \beta}{\gamma} \quad [37]$$

Zatikapenaren zuzenketa egiteko erabiltzen den lege esponentziala gogora ekarriz,

$$\left(\frac{I_1}{I_2}\right)_{egia} = \left(\frac{I_1}{I_2}\right)_{neurt} \cdot \left(\frac{MM\,(I_1)}{MM\,(I_2)}\right)^f \quad [38]$$

egia eta *neurt* atzizkiak egiazko eta neurtutako arrazoiei dagozkielarik, hurrenez hurren.

Beraz:

$$\left(\frac{C}{B}\right)_m = \left(\frac{C}{B}\right)_{neurt} \cdot \left(\frac{MM(C)}{MM(B)}\right)^f = \frac{\alpha - \left(\frac{A}{B}\right)_m \cdot \beta}{\gamma} \quad [39]$$

Eta $a^b = e^{b \ln a}$ jakina denez, hau idaztea posiblea da:

$$\left(\frac{C}{B}\right)_{neurt} \cdot e^{f \ln\left(\frac{MM(C)}{MM(B)}\right)} = \frac{\alpha - \left(\frac{A}{B}\right)_m \cdot \beta}{\gamma} \quad [40]$$

Aurreko ekuazioa berrantolatu ondoren:

$$f = \ln\left(\frac{\alpha - \left(\frac{A}{B}\right)_m \cdot \beta}{\gamma \cdot \left(\frac{C}{B}\right)_{neurt}}\right) \cdot \frac{1}{\ln\left(\frac{MM(C)}{MM(B)}\right)} \quad [41]$$

Eta azkenik:

$$f = \ln\left(\frac{\alpha - \left(\frac{A}{B}\right)_{neurt}\left(\frac{MM(A)}{MM(B)}\right)^f \cdot \beta}{\gamma \cdot \left(\frac{C}{B}\right)_{neurt}}\right) \cdot \frac{1}{\ln\left(\frac{MM(C)}{MM(B)}\right)} \quad [42]$$

Ekuazio honek ez dauka *f*-rako emaitza analitiko posiblerik, eta beraz hurbilketa iteratiboa beharrezkoa da. Horretan f_0 balioa sartzen da ondoko prozesu iteratiboetan emaitzak bat datozen arte:

$$f_{n+1} = \ln\left(\frac{\alpha - \left(\frac{A}{B}\right)_{neurt}\left(\frac{MM(A)}{MM(B)}\right)^{f_n}\cdot\beta}{\gamma\cdot\left(\frac{C}{B}\right)_{neurt}}\right)\cdot\frac{1}{\ln\left(\frac{MM(C)}{MM(B)}\right)} \quad [43]$$

Hf-aren kasuan, ekuazio hau ondoko eran erabiltzen da.

Hf-ak sei isotopo ditu (174, 176, 177, 178, 179 eta 180), horietariko hiru beste elementuen isotopoekin inolako interferentziarik gabeak (177, 178 eta 179). Gainera, Neptunean erabiltzen den normalizazio-arrazoia $^{179}Hf/^{177}Hf$ da eta landugabeko arrazoi guztiak ^{177}Hf-rekiko erreferentzian ematen dira, konposizio isotopikorako eta diluzio isotopikorako prozedura bera erabiltzen baita. Kasu horretan erabiliko den normalizazio arrazoia $^{178}Hf/^{177}Hf$ izango da, eta erreferentziazko balioa 1,46711 ($^{179}Hf/^{177}Hf$ = 0,7325-rekin bat datorrena). Azkenik, gure trazatzailea ^{179}Hf-an aberastua dago. Horregatik aukeraketa hau egin da, azalduko diren kalkuluak erabili ahal izateko:

A (isotopo trazatzailea):^{179}Hf

B (erreferentziazko isotopoa):^{177}Hf

C (zuzenketetarako isotopoa):^{178}Hf

Aukera honek *f* faktorearen kalkulurako interferentziarik ez duten bi arrazoi erabiltzeko aukera ematen digu, interferentziak zuzentzeko beharra saihestuz. Goian azaldutako iterazioa f_0 = -2 balioarekin hasten da, benetako faktoretik urrun egongo ez den balioa. Konbergentzia azkar lortzen da, $|f_4 - f_3| < 10^{-5}$. Laginaren $^{176}Hf/^{177}Hf$ arrazoiaren kalkulua

Behin *f* zehaztuta dagoela neurtutako arrazoiak zatikapenerako zuzendu daitezke. Horrela laginaren $^{176}Hf/^{177}Hf$ arrazoia kalkulatuko dugu, zeina aldakorra den naturan, ^{176}Hf-a sortzen baita ^{176}Lu-aren desintegrazioaren ondorioz. Diluzio isotopikoaren ekuazioak berrantolatuz $^{176}Hf/^{177}Hf$ eta $^{179}Hf/^{177}Hf$ arrazoietarako, hau idatzi genezake:

$$\left(\frac{^{176}Hf}{^{177}Hf}\right)_s = \frac{\left(\frac{^{176}Hf}{^{177}Hf}\right)_m\cdot\left(\left(\frac{^{179}Hf}{^{177}Hf}\right)_s - \left(\frac{^{179}Hf}{^{177}Hf}\right)_t\right) + \left(\frac{^{176}Hf}{^{177}Hf}\right)_t\cdot\left(\left(\frac{^{179}Hf}{^{177}Hf}\right)_m - \left(\frac{^{179}Hf}{^{177}Hf}\right)_s\right)}{\left(\frac{^{179}Hf}{^{177}Hf}\right)_m - \left(\frac{^{179}Hf}{^{177}Hf}\right)_t} \quad [44]$$

3.3.e.2. *Hf kontzentrazioaren kalkulua*

Hf-aren kontzentrazioa kalkulatzeko diluzio isotopikoaren ekuazio bera erabiltzen da, kapituluaren hasieran azaldu dena:

$$^{177}Hf_s = \frac{\left(\frac{^{179}Hf}{^{177}Hf}\right)_m \left(\frac{^{177}Hf}{^{179}Hf}\right)_t - 1}{\left(\frac{^{179}Hf}{^{177}Hf}\right)_s - \left(\frac{^{179}Hf}{^{177}Hf}\right)_m} \cdot \left[^{179}Hf\right]_t \cdot Pds(t) \quad [45]$$

3.3.e.3. *Erroreen hedatzea eta amaierako ziurgabetasuna*

Erroreen hedatzeen formulen garapena oso luzea eta konplexua da, eta ez da bertan azalduko. Irakurleak honen inguruko azalpen zehatza nahi izanez gero Le Fèvre-ren (2002) tesira jotzeko gomentatzen zaio. Tesi honetan, hainbat erroreren eta ziurgabetasunen azken formulak emango dira.

3.3.e.4. *f-ren gaineko ziurgabetasuna*

[41] ekuazioan ikusi denez, *f* faktorea diluzio isotopikoko trazatzailearen arrazoiaren eta normalizazio-arrazoiaren araberakoa da (gure kasuan, ^{179}Hf/^{177}Hf eta ^{178}Hf/^{177}Hf, hurrenez hurren). Ziurgabetasunaren azken ekuazioa honakoa da:

$$\left(\frac{\sigma f}{f}\right)^2 \approx \left(\frac{-\beta}{\left(\alpha - \left(\frac{^{179}Hf}{^{177}Hf}\right)_m \cdot \beta\right) \cdot ln\left(\frac{MM(^{178}Hf)}{MM(^{177}Hf)}\right)}\right)^2 \cdot \left(\frac{\sigma\left(\frac{^{179}Hf}{^{177}Hf}\right)_{neurt}}{\left(\frac{^{179}Hf}{^{177}Hf}\right)_{neurt}}\right)^2 + \left(\frac{-1}{\left(\frac{^{178}Hf}{^{177}Hf}\right)_{neurt} \cdot ln\left(\frac{MM(^{178}Hf)}{MM(^{177}Hf)}\right)}\right)^2 \cdot \left(\frac{\sigma\left(\frac{^{178}Hf}{^{177}Hf}\right)_{neurt}}{\left(\frac{^{178}Hf}{^{177}Hf}\right)_{neurt}}\right)^2 \quad [46]$$

3.3.e.5. *Zatikapenerako zuzenketa eginda duten arraoiek hedatutako ziurgabetasuna*

Neurtutako arrazoi guztiak lege esponentzial bati jarraiki zuzentzen dira ([14] ekuazioa). $R = \left(\frac{I_1}{I_2}\right)$ trazatzaile/lagin nahasketako bi isotoporen arrazoia bada, erroreen hedatze-legeak hona garamatza:

$$\left(\frac{\sigma R_m}{R_m}\right)^2 = \left(\frac{MM(I_1)}{MM(I_2)}\right)^{2f} \cdot \left(\frac{\sigma R_{neurt}}{R_{neurt}}\right)^2 + \left(\ln\left(\frac{MM(I_1)}{MM(I_2)}\right) \cdot R_{neurt} \cdot e^{f \ln\left(\frac{MM(I_1)}{MM(I_2)}\right)}\right)^2 \cdot \left(\frac{\sigma f}{f}\right)^2 \quad [47]$$

3.3.e.6. *$^{176}Hf/^{177}Hf$ arrazoian hedatutako ziurgabetasuna*

[37] ekuazioak erakusten du ziurgabetaunei lotutako aldagaiak $\left(\frac{^{176}Hf}{^{177}Hf}\right)_m$ eta $\left(\frac{^{179}Hf}{^{177}Hf}\right)_m$ direla. [40] ekuazioa erabilita, amaierako ekuazioa lortzen da:

$$\left(\frac{\sigma\left(\frac{^{176}Hf}{^{177}Hf}\right)_s}{\left(\frac{^{176}Hf}{^{177}Hf}\right)_s}\right)^2$$

$$= \left(\frac{\left(\frac{^{179}Hf}{^{177}Hf}\right)_s - \left(\frac{^{179}Hf}{^{177}Hf}\right)_t}{\left(\frac{^{179}Hf}{^{177}Hf}\right)_m - \left(\frac{^{179}Hf}{^{177}Hf}\right)_t}\right)^2 \cdot \left(\frac{\sigma\left(\frac{^{176}Hf}{^{177}Hf}\right)_m}{\left(\frac{^{176}Hf}{^{177}Hf}\right)_m}\right)^2$$

$$+ \left(\frac{\left(\frac{^{176}Hf}{^{177}Hf}\right)_m \cdot \left(\left(\frac{^{179}Hf}{^{177}Hf}\right)_t - \left(\frac{^{179}Hf}{^{177}Hf}\right)_s\right) + \left(\frac{^{176}Hf}{^{177}Hf}\right)_t \cdot \left(\left(\frac{^{179}Hf}{^{177}Hf}\right)_s - \left(\frac{^{179}Hf}{^{177}Hf}\right)_t\right)}{\left(\frac{^{179}Hf}{^{177}Hf}\right)_m - \left(\frac{^{179}Hf}{^{177}Hf}\right)_t}\right) \cdot \left(\frac{\sigma\left(\frac{^{176}Hf}{^{177}Hf}\right)_m}{\left(\frac{^{176}Hf}{^{177}Hf}\right)_m}\right)^2 \quad [48]$$

3.3.e.7. *Hf-aren kontzentrazioaren gaineko ziurgabetasuna*

Hf-aren kontzentrazioan erroreen hedatzerako kalkuluak diluzio isotopikoaren teorian jorratu dira. Era laburrean, ziurgabetasunaren formula ondokoa da:

$$\left(\frac{\sigma\,[Hf]}{[Hf]}\right)^2 = \left(\frac{\sigma\left[^{179}Hf\right]_t}{\left[^{179}Hf\right]_t}\right)^2 + \left(\frac{\sigma\left(\frac{^{179}Hf}{^{177}Hf}\right)_m}{\left(\frac{^{179}Hf}{^{177}Hf}\right)_m}\right)^2 M \quad [49]$$

non kortxeteen arteko balioek kontzentrazioak adierazten dituzten (masa Hf-aren kasuan eta molarra $^{179}Hf_t$ -ren kasuan), eta non *M* errorearen anplifikazio-faktorea den (Webster, 1960).

Hala ere, praktikan, Neptune MC-ICP-MSarekin egindako neurketek zehaztasun nahikoa dute eta trazatzailearen gaineko ziurgabetasuna da esanguratsua den bakarra. Beraz, Hf-aren kontzentrazioaren ziurgabetasuna, trazatzailearen kontzentrazioaren ziurgabetasunaren berdina da.

3.3.f. Neurketa parametroak

Espektrometroaren erabilera-parametroak 3.7. Taulan laburbiltzen dira. Neurketa-sekuentzia hasi aurretik, komenigarria da plasma eta Apex desolbatazio-gailua egonkortu arte itxarotea, 45 minutuz. Denbora honen ostean, lente ionikoen doiketa eta optimizazioa burutzen

da, ^{176}Hf -aren tontorraren forma ondu eta sentsibilitatea maximizatzeko. Helburu honetarako, Thermo Scientific-ek saltzen duen Neptune Multi Element Standard Solution (8 element) disoluzioa erabiltzen da (Tune-Up Solution, ref. 1149340). Disoluzioak 200 $ng.g^{-1}$ kontzentrazioa dauka, eta Apex-a erabiltzekotan, 25 $ng.g^{-1}$-ra diluitzen da. Disoluzio estandar honetan, ^{176}Hf isotopoaren seinalearen intentsitatea 1,5 V ingurukoa da. Lu analisietarako ere optimizazio eredu bera erabiltzen da, Hf-a monitorizatuz.

Behin parametro guztiak doituta daudela, esperimentu analitikoa prestatzen da. Datuen eskuratzea era estatikoan burutzen da eta 10 neurketa-ziklotako 8 bloke egiten dira, 7 minutu inguruko analisian.

Laginak MC-ICP-MS bidez analizatzen direnean, instrumentuaren zatikapena kontrolatu behar da. Horretarako, JMC475 eta Lu disoluzio estandarra, laginen artean tartekatu egiten dira Hf eta Lu analisietan, hurrenez hurren. Nahiz eta esperimentu luzeetan seinalearen intentsitatea aldakorra izan, % 10eraino ere iritsiz, ez da inolako desplazamendurik aurkitu $^{176}Hf/^{177}Hf$ edo $^{176}Lu/^{175}Lu$ arrazoietan. Hori dela eta, laginei ez zaie inolako kanpo-zuzenketarik aplikatu.

3.3.g. Metodoaren balioztatzea nazioarteko estandarretan

Metodoa balioztatzeko, lau nazioarteko CRM (*Certified Reference Materials*) estandarretan lortutako balioak eta haien gomendatutako baloreak alderatu egin dira, bai kontzentrazioari dagokionez baita konposizio isotopikoari dagokionez ere. Estandarrak konposizio sorta zabala aztertzeko aukeratu dira. Posible izan denean, MC-ICP-MS ekipoetan neurtutako balioak hartu dira gomendagarri moduan. MC-ICP-MS baliorik egon ezean, TIMS bidez analizatutako balioak hartu dira aintzat.

Lortutako emaitzak 3.16. Taulan aurkezten dira. Esan beharra dago balioen bikote bakoitza (A-B, C-D eta E-F) disoluzio berean egindako bi analisi direla.

Laginaren prestaketa eta banaketa kimikoaren ondoren neurtutako $^{176}Hf/^{177}Hf$ arrazoiak eta euren erroreak espero zitezkeen balioetan daude. Emaitzak oso dispertsio gutxirekin ageri dira, prozedura analitikoak erreproduzigarriak diren emaitzak ematen dituela baieztatuz. BHVO-2 estandarrerako lortutako arrazoiak gomendatutako balioak baino baxuagoak dira (datu ezberdinen batezbestekoa). Hala ere, antzeko balioak lortu dira bai TIMS bidez (Yang et al., 2009) bai MC-ICP-MS bidez (Todd et al., 2010; McCoy-West et a., 2010).

Lu-aren eta Hf-aren kontzentrazioetarako lortutako emaitzak erreproduzigarriak dira, AGV-2 A eta AGV-2 B analisietan salbu. Lortutako kontzentrazioak gainera, espero zitezkeen balioetatik gertu daude. AGV-2 A eta AGV-2 B analisiek balio nabarmen baxuagoak erakusten dituzte bi elementuentzako. Lehenago azaldu den moduan, $^{176}Hf/^{177}Hf$ eta Hf kontzentrazio-

kalkuluak analisi berdinetik abiatuta egiten dira. Hala ere, nahiz eta ustekabeko eta isolatutako kutsadura gertatzea posiblea izan, analisi horietako arrazoiak gainontzekoak baino apur bat altuagoak dira. Ziur asko errorea kontzentrazioen kalkuluan egin da, agian lagina pisatzerakoan egindako akats baten ondorioz.

3.16. Taula. Testuan deskribatzen den konposizio isotopiko eta diluzio isotopiko prozedurarekin nazioarteko estandarretan lortutako emaitzak. Gomendatutako balioekin alderatuta. (a) Pourmand eta Dauphas (2010); (b) Georem Preferred Value (Jochum eta Nehring, 2006); (c) Weis et al. (2007); (d) Le Fèvre eta Pin (2001); (e) Zhang et al. (2012).

Estandarra	$^{176}Hf/^{177}Hf$			Hf concentration			Lu concentration			$^{176}Lu/^{177}Hf$	± 2σ
	Erreferentzia	Neurtua	± 2 S.E.	Erreferentzia	Neurtua	± 2σ	Erreferentzia	Neurtua	± 2σ		
AGV-2-A		0 ,282996	4E-06		4 ,95	0 ,04		0 ,225	0 ,001	0 ,00646	0,001
AGV-2-B		0 ,283000	8E-06		4 ,95	0 ,04		0 ,225	0 ,001	0 ,00646	0,001
AGV-2-C	0 ,282981 ± 9 (2σ) (a)	0 ,282987	1E-05	5 ,23 ± 0 ,1 (1σ) (e)	5 ,20	0 ,04	0 ,25 ± 0 ,01 (1σ) (e)	0 ,262	0 ,002	0,00715	0,001
AGV-2-D		0 ,282973	1E-05		5 ,22	0 ,04		0 ,263	0 ,002	0,00715	0,001
AGV-2-E		0 ,282977	1E-05		5 ,19	0 ,04		0 ,266	0 ,002	0,00728	0,001
AGV-2-F		0 ,282972	5E-06		5 ,19	0 ,04		0 ,266	0 ,002	0,00728	0,001
BHVO-2-A		0 ,283095	4E-06		4 ,32	0 ,03		0 ,294	0 ,002	0 ,00965	0,002
BHVO-2-B		0 ,283094	7E-06		4 ,32	0 ,03		0 ,294	0 ,002	0 ,00965	0,002
BHVO-2-C	0 ,283104 ± 12 (2σ) (b)	0 ,283093	9E-06	4 ,36 ± 0 ,1 (1σ) (b)	4 ,33	0 ,03	0,274 ± 0 ,1 (1σ) (b)	0 ,287	0 ,002	0 ,00947	0,002
BHVO-2-D		0 ,283085	7E-06		4 ,33	0 ,03		0 ,291	0 ,002	0 ,00954	0,002
BHVO-2-E		0 ,283099	9E-06		4 ,34	0 ,03		0 ,289	0 ,002	0 ,00947	0,002
BHVO-2-F		0 ,283097	8E-06		4 ,33	0 ,03		0 ,290	0 ,002	0 ,00953	0,002
G-2-A		0 ,282527	4E-06		7 ,75	0 ,06		0 ,110	0 ,001	0 ,00202	0,0004
G-2-B		0 ,282533	4E-06		7 ,75	0 ,06		0 ,110	0 ,001	0 ,00202	0,0004
G-2-C	0 ,282529 ± 26 (2σ) (c)	0 ,282528	1E-05	7 ,88 ± 0 ,26 (1σ) (e)	7 ,68	0 ,06	0 ,11 ± 0 ,01 (1σ) (e)	0 ,107	0 ,001	0 ,00197	0,0004
G-2-D		0 ,282518	9E-06		7 ,68	0 ,06		0 ,107	0 ,001	0 ,00199	0,0004
G-2-E		0 ,282515	1E-05		7 ,78	0 ,06		0 ,108	0 ,001	0 ,00198	0,0004
G-2-F		0 ,282527	1E-05		7 ,78	0 ,06		0 ,108	0 ,001	0 ,00198	0,0004
W-2-A		0 ,282711	9E-06		2 ,48	0 ,02		0 ,314	0 ,002	0 ,01799	0,004
W-2-B		0 ,282724	9E-06		2 ,48	0 ,02		0 ,314	0 ,002	0 ,01799	0,004
W-2-C	0 ,282715 ± 30 (2σ) (d)	0 ,282732	8E-06	2 ,45 ± 0 ,18 (1σ) (b)	2 ,47	0 ,02	0 ,31 ± 0 ,01 (1σ) (b)	0 ,318	0 ,002	0 ,01809	0,004
W-2-D		0 ,282728	9E-06		2 ,47	0 ,02		0 ,318	0 ,002	0 ,01804	0,004
W-2-E		0 ,282722	1E-05		2 ,46	0 ,02		0 ,313	0 ,002	0 ,01809	0,004
W-2-F		0 ,282702	1E-05		2 ,46	0 ,02		0 ,313	0 ,002	0 ,01809	0,004

G-2-aren Hf kontzentrazioen emaitzek gainontzeko estandarrek baino balio sorta zabalagoa erakusten dute, eta gainera, nahiz eta erroreen baitan egon, gomendatutako balioetatik urrunen kokatzen diren baloreak ditu. G-2 arroka granitikoa da eta beraz zirkoietan aberatsa da, zeintzuk era berean Hf-an aberatsak diren. Nahiz eta estandarrak homogeneoak diren definizioz, G-2-a heterogeneoa dela ondorioztatu daiteke, Hf-ari dagokionean behintzat. Horrela, bibliografian 1,9 $\mu g.g^{-1}$-tik 8,7 $\mu g.g^{-1}$-ra doazen balioak topatu daitezke (Mana et al., 2012 eta Shellnutt eta Zhou, 2007, hurrenez hurren). Berez, ikerketa honetan lortutako balioak bat

datoz García de Madinabeitia et al.-ek (2008) argitaratutako balioekin. Azken horiek ICP-MS bidez eta laginaren fusio-disoluzio trataera bidez lortu dira SGIker laborategi berean, hau da, G-2 estandarraren ontzi berberetik. Lu-a zirkoien kristal egituran harrapatuta geratzen ez denez, Lu-aren kontzentrazioek ez dute dispertsiorik erakusten.

Lu-aren kontzentrazioak erreproduzigarriak dira, eta G-2 eta W-2 estandarretan gomendatutako balioekin bat datozen bitartean, AGV-2 eta BHVO-2 estandarretan lortutako balioak gomendatutakoak baino altuagoak dira. Lu-aren kontzentrazio balore altuago horiek azaltzeko hainbat hipotesi plazaratu daitezke, besteak beste, TIMS, ICP-MS eta ID-MC-ICP-MS tekniken arteko ezberdintasunak, trazatzailearekin lotutako arazoak, fusioan emandako arazoak, kutsadura, etab. Dena den, ez dugu balio altuago hoiek azaltuko dituen ezer antzeman. BHVO-2 estandarrean lortutako balioak adibidez Raczek et al.-ek (2001) ID-TIMS bidez neurtutako balioak baino altuagoak dira, baina literaturan aurkitu daitezkeen beste balio batzuekin alderagarriak dira (adibidez, García de Madinabeitia et al., 2008 -SGIker laborategi berean- edo Deegan et al., 2013). Beraz, prozedura egokia dela ondorioztatzen da. AGV-2-aren kasua antzekoa da baina gure datuekin bat datozen argitalpen gutxiago daude (e.g. Yang eta Li, 2008; Huang et al., 2013).

Dakigun arte, nazioarteko materialen $^{176}Lu/^{177}Hf$ arrazoiak ez dira literaturan aurkitzen. Le Fèvre-k (2002) BHVO-2 estandarraren $^{176}Lu/^{177}Hf$ arrazoia kalkulatu du, gutxi gorabehera 0,0108 balioak lortuz, tesi honetan lortutakoak baino altuagoa. Hala ere, bai $^{176}Hf/^{177}Hf$ arrazoia baita Hf eta Lu kontzentrazioak gomendatutako balioetatik urrun daude. Aipatzea merezi du beraz, metodo honen bidez lortutako emaitzak erabat erreproduzigarriak direla. Kanpoko erreproduzigarritasuna lagin guztien barne-zehaztazunaren berbera da, sistematikoki % 3 RSD baino baxuagoa.

Sei nazioarteko estandarretan lortutako emaitzek, bai $^{176}Hf/^{177}Hf$ arrazoian bai Hf eta Lu-en kontzentrazioan, martxan jarritako prozedura baliozkoa dela adierazten dute. Beraz, Lu-Hf sistemaren baitako azterketa geokronologikoak egiteko erabilgarria dela ondorioztatu daiteke.

3.4. U-Th-Pb sistema, LA-Q-ICP-MS bidez

3.4.a. Sarrera

Geologian, gehien erabiltzen den geokronometroa U-Th-Pb da, batez ere zirkoien datazioarako. Sistema honetan 3 desintegrazio-sistema bereizten dira, uraniotik berunerako desintegrazio bi eta toriotik berunera doan beste desintegrazio bat (balioak Steiger eta Jäger-enak, 1977, dira):

$^{238}U \rightarrow {}^{206}Pb$ ($\lambda = 1{,}55125 \times 10^{-10}$ u^{-1} edo 4,468 Ga-ko erdibizitza)

$^{235}U \rightarrow {}^{205}Pb$ ($\lambda = 9{,}8485 \times 10^{-10}$ u^{-1} edo 0,704 Ga-ko erdibizitza)

$^{232}U \rightarrow {}^{206}Pb$ ($\lambda = 4{,}9475 \times 10^{-11}$ u^{-1} edo 14,01 Ga-ko erdibizitza)

Uranio eta torioa antzeko ezaugarri kimikoak dituzten bi HFSE dira. Elementu oso ez-konpatibleak dira eta horregatik, zirkoia edo monazita bezalako mineral osagarrietan kontzetratzeko joera dute. Beruna berriz, Ioi Handi Litofiloak taldeko (*Large Ion Lithophile Elements*, LILE) elementua da eta ezaugarri kimiko erabat ezberdinak ditu. Duen afinitate kalkofilo indartsua dela eta beruna sulfuroei elkartuta agertzen da normalean, bereziki galenarekin (PbS ≈ % 85 Pb). Ezaugarri kimikoen ezberdintasun honek elementu hauen banaketa dakar arroka eta mineral ezberdinetan, U/Pb eta Th/Pb erlazio ezberdinak emanez eta adin erradiometrikoen kalkuluak ahalbidetuz.

U-Pb emaitzak Concordia izeneko diagrama batean irudikatu daitezke (3.7. Irudia; Wetherill, 1956), $^{238}U/^{235}U$ konstantea delako lurrazaleko arroketan (137,88; Steiger eta Jäger, 1977). Diagrama binarioa da ($^{207}Pb/^{235}U$ vs $^{206}Pb/^{238}U$), eta Concordia kurbak $^{207}Pb/^{235}U$ adina eta $^{206}Pb/^{238}U$ adina berbera duten puntuak lotzen ditu. $^{238}U/^{235}U$ naturan konstantea denez, $^{206}Pb^*$ eta $^{207}Pb^*$ isotopo erradiogenikoen analisien bidez adina kalkulatzea ere posiblea da, jatorria eta Concordia puntua lotzen dituen zuzenaren malda baita. Adina ekuazio honen bitartez kalkulatu daiteke (*t*-a kalkulu iteratiboen bidez askatuz):

$$^{206}Pb/^{207}Pb = 137{,}88\left[\left(e^{\lambda_1 t}-1\right)/\left(e^{\lambda_2 t}-1\right)\right] \quad [50]$$

Grafiko hau lagungarria da sistema itxita mantendu den ezagutzeko. Horrela bada, analisiak Concordia kurbarekin bat datoz. Kontrakoa gertatuz gero, hau da, arrokaren eboluzioan zehar sistema zabaldu bada, analisiak ez dira Concordia kurbarekin bat etorriko, kurbaren gainean edo azpian kokatzen direlarik. Hala ere, datuen interpretazioa ez da beti erraza izaten.

U-aren, Th-aren eta Pb-aren espektroskopian zerikusia duten isotopoak eta pisu atomikoak ondoko tauletan aurkezten dira (3.17., 3.18., 3.19. eta 3.20. Taulak).

3.17. Taula. Uranio, torio eta beruna isotopoen ugaritasuna (%). IUPAC (*International Union of Pure and Applied Chemistry*) erakundearen arabera (De Laeter et al., 2003)

	204	206	207	208	232	234	235	238
Pb	1,4	24,1	22,1	52,4				
Th					100			
U						0,005	0,72	99,27

3.18. Taula. Berunaren masa atomikoak, IUPAC (*International Union of Pure and Applied Chemistry*) erakundearen arabera (De Laeter et al., 2003)

Isotope	204	206	207	208
Mass	203,973028	205,974449	206,975880	207,976636

3.19. Taula. Torioaren masa atomikoa, IUPAC (*International Union of Pure and Applied Chemistry*) erakundearen arabera (De Laeter et al., 2003)

Isotope	232
Mass	232,0380495

3.20. Taula. Uranioaren masa atomikoak, IUPAC (*International Union of Pure and Applied Chemistry*) erakundearen arabera (De Laeter et al., 2003)

Isotope	234	235	238
Mass	234,0409447	235,0439222	238,0507835

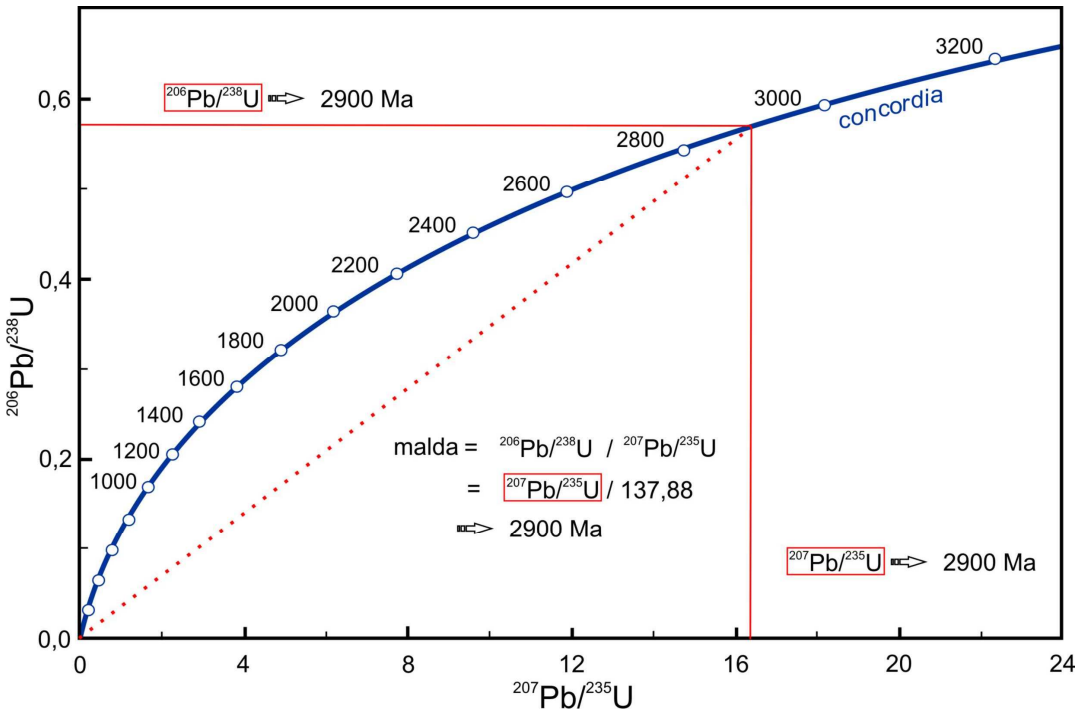

3.7. Irudia. Kurbarekin bat datorren analisi bateko $^{207}Pb/^{235}U$, $^{206}Pb/^{238}U$ eta $^{206}Pb/^{207}Pb$ adinak erakusten dituen Concordia diagrama.

3.4.b. Laginen prestaketa

Lehenago aipatu den moduan, *SuperCell*^{TM} ablazio-gelaxkaren moldaketak laginak eta estandarrak batera sartzeko aukera ematen du (2.20. Irudia, 2. Kapitulua). Lagina gelaxkaren erdian sartzen da, xafla petrografiko lodi moduan, xafla mehe arrunt bat baino lodiagoa dena (50-80 µm). Estandarrak 10 mm-ko diametroa duen epoxy erretxinan muntatzen dira eta xaflaren alde banatan kokatzen dira gelaxkaren barruan. Ohiko lan moduan, muntaketetako batek GJ-1 eta 91500 zirkoi estandarrak izaten ditu eta besteak NIST SRM 612 beira izaten du. Azkena analisien aurretik espektrometroaren parametroak doitzeko erabiltzen da.

Laser-ablazio bidezko analisiek ez dute laginaren lehunketa sakonik eskatzen, nahiz eta ablazio-sistemaren barruan mineralak identifikatzeko aholkugarria den. Gogoratu behar da, laserrak mikroskopio optiko arrunt bat baino argiztapen eta irudi-kalitate baxuagoak dauzkala.

Hortaz, mineral ezberdinen ertzak ikusi ahal izateko laginaren lehunketa erabat gomendagarria da.

Analisiak egin aurretik, beharrezkoa da zirkoiaren egiturari buruzko ahalik eta informazio gehien eskuratzea, besteak beste, konposizioan zonaziorik dagoen, hazkunde-eredurik daukan edota inklusio edo heredatutako nukleorik daukan. Honek, emaitza okerrak eragin ditzakeen Pb konposizio ezberdinak dauzkaten aldeen analisiak ekiditen lagundutzen du. Zirkoien barne-egituraren irudiak eskuratzeko metodorik arruntenak Katodoluminiszentzia (*Cathodoluminescence, CL*) eta Atzera Sakabanatutako Elektroiak (*Back Scattered Electrons, BSE*) teknikak dira. Tesi honetan BSE teknika erabili da eta mikroargazkiak Euskal Herriko Unibertsitateako UPV/EHU Ikerkuntzarako Zerbitzu Orokorren (SGIker) barruan dagoen JEOL JSM-6400 ekorketazko mikroskopio elektronikoarekin (*Scanning Electronic Microscopy, SEM*) egin dira.

3.4.c. Datuen bereganatzea eta murrizketa

U-Pb analisiak induktiboki akoplatutako plasma iturridun masa-espektrometro kuadrupolarrari elkartutako Nd:YAG 213 nm New Wave laser ablazio-sistemaren bidez burutu dira, Geokronologia eta Geokimika Isotopikoaren Zerbitzuan (SGIker, UPV/EHU). Ekipoari buruzko informazio osagarrirako, 2. Kapitulura jo.

Masen arteko kalibrazio eta instrumentuaren doiketa saio analitiko hasi aurretik burutzen da erreferentziazko NIST SRM 612 beirarekiko, ^{238}U seinalea optimizatuz (^{238}U-an 400.000 cps - '*counts per second*' edo kontuak segunduko- izateko gutxienez) eta ThO^+/Th^+ erlazioak txikituz (<< % 1). Espektrometroaren ohiko erabilera-parametroak 3.21. Taulan laburbiltzen dira.

Behin instrumentuaren parametroak egokitu direla, eta plasma egonkortzeko 30 minutu igaro ondoren, sekuentzia analitikoarekin hastea posiblea da. Lehen lau analisiak GJ-1 zirkoi estandarrean egiten dira, ondoren laginaren 10 analisi eta gero, estandarraren beste 2 analisi, sekuentzian inolako jitorik ez dagoela ziurtatzeko. 10 lagin – 2 estandarreko sekuentzia behar beste errepikatzen da nahi den analisi kopurua egiteko. Sekuentziaren amaieran GJ-1 estandarraren beste 4 analisi egiten dira. 91500 estandarraren analisiak laginen artean sartzen dira ezezagunak balira moduan, zuzenketa guztiak ondo egiten direla eta lortutako adinak zuzenak direla balioztatzeko. Datuen eskurapena 90 segunduko analisien bidez egiten da, zeinean lehen 30 segunduak gasen hondo-zarata neurtzeko erabiltzen diren eta hurrengo 60 segunduak ablazioa diren. Datuak isotopo ezberdinen arteko etengabeko ekorketa bidez bereganatzen dira, ^{202}Hg, ^{204}Pb, ^{206}Pb, ^{208}Pb, ^{232}Th eta ^{238}U isotopoetan 10 ms eta ^{207}Pb isotopoan 20 ms egonez. Berun arruntaren (Pb_c) presentzia $^{204}(Pb+Hg)$ seinalearekin monitorizatu daiteke, baina hala ere, ez da

Pb_c zuzenketarik egiten Hg-ren interferentzia isobariko handia dela eta. ^{235}U seinalea ^{238}U seinaletik kalkulatzen da $^{238}U/^{235}U$= 137,88 balioan oinarrituta.

Analisi bakoitzeko datuak gordinean aztertu dira, analisiak asaldatu ditzakeen zerbait dagoen ikusteko, besteak beste inklusioak, hausturak, adin diferenteetako domeinuen nahasketa edota Pb_c-ren presentzia. Oro har, seinaleak homogeneoak direla onartzen da isotopo bakoitzaren espektroa besteekiko paralelo denean, hau da, isotopoen arteko erlazioak konstanteak direnean. Tesi honetan, datuen murrizketa GLITTER® softwarearekin egin da (Macquarie Research Ltd, 2001; van Achterbergh et al., 2001; Jackson et al., 2004). GJ-1-aren analisiak zatikapen eta jito instrumentalak zuzentzeko erabili dira. % 10eko baino diskordantzia altuagoa daukaten analisiak ([($^{206}Pb/^{238}U$ adina)/($^{207}Pb/^{206}Pb$ adina)]×100 bezala kalkulatuta, Meinhold et al., 2011) ez dira kontuan hartu. Seinale aldakorrak edo denboran murritzak diren analisiak ere baztertu egin dira.

Kalkulatutako arrazoiak esportatu egiten dira eta Isoplot/Ex v.2.49 softwarearekin (Ludwig, 2001) Concordia adinak eta diagramak sortzen dira. U-Th-Pb kontzentrazioak erreferentziazko GJ-1 zirkoi estandarrarekiko (Jackson et al., 2004) kalkutatzen dira.

Erroreen hedatzea eztabaida handiko gaia da zientzialarien artean, eta tesi honen helburuetatik kanpo dago. Hala ere, LA-ICP-MS bidezko datuen murrizketa aurrera eramateko programek ondoko zuzenketa eta ziurgabetasunak izaten dituzte:

a. Kontaketaren estatistika isotopo bakoitza neurtzen ari den bitartean
b. Laser sortaren ezegonkotasuna
c. Zatikapen elementala (U eta Pb artean), ablazioan eta ionizazioan zehar
d. Masa-zatikapena (elementu bereko bi isotopoen artean) ablazioan eta ionizazioan
e. Matrizeak sortutako jitoa
f. Detektagailuaren kalibrazioa
g. Aldakortasun espaziala
h. Hg-aren zuzenketa (zuzenketaren magnitudea eta Hg-aren konposizio isotopikoa)
i. Pb arruntaren zuzenketa (magnitudea eta konposizioa)
j. Hondo-zarataren zuzenketa, gasaren garbitasunari dagokionean
k. Estandar primarioen arrazoien zehaztapena
l. Estandarren adinaren gaineko ziurgabetasunak
m. Desintegrazio-konstantearen ziurgabetasunak

3.21 Taula. U-Th-Pb analisi isotopikoetarako erabilera parametroak.

Laborategiaren informazioa	
Laborategiaren izena	SGIker, Euskal Herriko Unibertsitatea UPV/EHU
Laginaren prestaketa	Xafla petrografiko 'lodiak' laginetarako, epoxy-erretxinan eginiko 10 mm-ko diametroko muntaketak estandarretarako
Irudiak	BSE, JEOL JSM-6400
Laser ablazio-sistema	
Enpresa, modeloa eta mota	New Wave Research, UP213, Nd:YAG
Ablazio-gelaxka eta bolumena	Moldatutako SuperCell^{TM}, 33 cm^3
Laserraren uhin-luzeera	213 nm
Pultsu zabalera	3-5 ns
Dentsitate energetikoa	5 $J.cm^{-2}$
Errepikapen tasa	10 Hz
Ablazioaren iraupena	90 s (30 s gasaren garbitasuna neurtzeko eta 60 s laginerako)
Analisiaren tamaina	25-30 µm
ThO^+/Th^+	< % 0,05
Garraio-gasa	% 100 He gelaxkaren barruan, Ar gas gehigarria Y-pieza batekin nahastua espektrometroaren zuzira iritsi aurretik
Gelaxkaren barneko garraio-gasaren jarioa	0,9-1 L/min
ICP-MS	
Enpresa, modeloa eta mota	Thermo Fisher Scientific, X-Series 2, Q-ICP-MS
Laginaren sarrera	Ablazio-aerosola
Irrati-frekuentzia	1350 W
Gas gehigarriaren jarioa	0,90 L/min (egunero doitua)
Plasma gasaren jarioa	14,9 L/min
Gas hoztailearen jarioa	0,9 L/min
Ekorketa modua	Tontoren arteko saltoak, puntu 1 tontorreko
Detektagailu modua	Pultsu kontaketa, denbora-hilen zuzenketa eginda, eta modu analogikoa seinalearen intentsitatea 1.000.000 cps baino handiagoa bada
Neurtutako masak	202, 204, 206, 207, 208, 232, 238
Tontor bakoitzeko egonaldia	10 ms isotopo bakoitzeko, 207-an salbu, 20 ms

3.4.d. Metodoaren balioztatzea nazioarteko estandarretan

Lagina hartzen duen gailuaren ezaugarriak direla eta, xafla mehearen gaineko LA-Q-ICP-MS bidezko analisiak egiteko, teknika analitiko arruntetan (Wilfley taula, dentsitate handiko likido edota Frantz banagailu magnetikoen bidez banatutako zirkoien muntaketak) moldaketak egin behar dira. Horrela, nahi den mineralaren lodiera eza edo azpian dagoen mineralaren ezaugarriak, baten bat egonez gero, kontuan hartu behar dira. Beste faktore batzuk edozein teknikari lotutakoak dira, zirkoiaren finkapen-maila edo sakonerarekin duen homogeneotasuna adibidez. Laser-ablazioaren parametroak kontrolatu eta egokitu egin behar dira espektrometroak kuantifikaziorako beharrezkoa duen sentikortasun baldintzak lortzeko.

Azken horri dagokionez, erabilera-parametroak zehazterako garaian bereziki garrantzitsua da analisiaren (puntuaren) tamaina erabakitzea. Lehen esan bezala, GJ-1 zirkoia erabili da

erreferentziazko estandar modura, eta horregatik, parametro ezberdinekin hainbat analisi egin dira, baldintzarik onenak zehazteko asmoz. Analisien tamainarako aukera ezberdinak aztertu ondoren, 25 µm eta 30 µm-ko diametroko analisisiak arazo geologikoak aztertzeko egokiak direla ondorioztatu da. Gainontzeko parametroak, laserraren uhin-zabalera edo indarra adibidez, honen arabera egokitu dira.

GJ-1 zirkoi estandarraren analisiak, 3.8. Irudian ikus daitezkeenak, baldintza horiekin burutu dira, eta lortutako U-Pb adinak erreferentziazko balioekin alderagarriak dira (Jackson et al., 2004). Balioztapenerako erabiltzen diren zirkoien emaitzak ere bat datoz argitaratutako datuekin (91500: Wiedenbeck et al., 1995 eta Plešovice: Sláma et al., 2008; Figure 3.8). Lortutako emaitzekin, 1.059,9 ± 4,2 Ma-ko adina kalkulatzen da zaharragoa den 91500 zirkoi estandarrean, gazteagoa den Plešovice zirkoian 338,0 ±1,9 Ma adina estimatzen den bitartean. 91500 estandarraren gaineko errore handiagoak U, Th eta Pb kontzentrazio baxuagoak dituzten zirkoien analisirako, teknikak dituen mugak agerian uzten ditu.

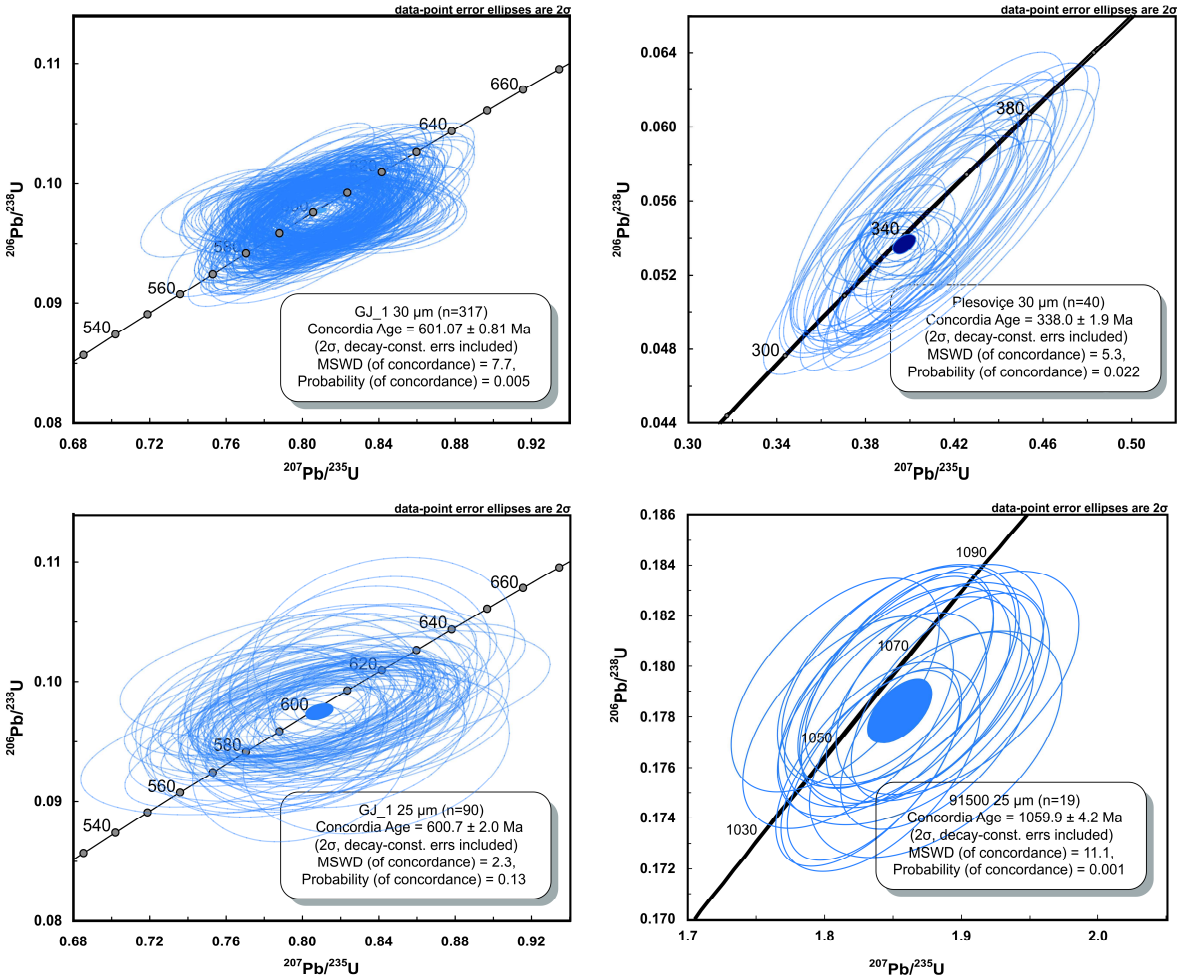

3.8. Irudia. Zirkoi estandarretan egindako U-Pb analisien Concordia diagramak.

Laginen $^{232}Th/^{208}Pb$ arrazoien eta adinen zehaztapena egitea ezinezkoa izan da neurketa baldintza horiekin, GJ-1 estandarrak dituen Th kontzentrazio (11 $\mu g.g^{-1}$) eta ondoriozko ^{208}Pb-ren balio baxuak direla eta (Elhlou et al., 2007).

3.5. Hf isotopoak, LA-MC-ICP-MS bidez

3.5.a. Sarrera

Lu-Hf sistemaren ezaugarriak direla eta, Hf-aren konposizio isotopikoa mineral jakin batzuen trazatzaile gisa erabiltzeko aukera dago, zirkoia horien artean garrantzitsuena delarik (beste batzuk; rutiloa, baddeleyita, wadeita,…). Zirkonioaren jokaera geokimiko antzekoa daukanez, Hf-a zirkoia bezalako mineraletarako konpatibilitate askoz handiagoa dauka REEak baino. Horrela, Hf-a zirkoien kristal egituran harrapatuta geratzen da, Lu-a ez bezala, eta % 3a baino kontzentrazio altuagoak ere topa daitezke. Hori dela eta, $^{176}Lu/^{177}Hf$ arrazoi baxuak (< 0,001) zirkoien berezko ezaugarriak dira, eta ondorioz, ^{176}Hf erradiogenikoagatik Hf-aren konposizio isotopikoan gerta daitezkeen aldaketak baztergarriak dira. Hau da, zirkoiak kristalizatu ziren magmako $^{176}Hf/^{177}Hf$ arrazoiak mantentzen ditu denboran zehar. Ezaugarri horri esker, zirkoiak duen Hf kontzentrazio altu eta difusio baxuarekin batera, baldintza eta Hf konposizio isotopiko ezberdinetan hazitako kristal baten domeinu ezberdinen mantentzea ahalbidetzen du.

3.5.a.1. *Hf-aren eboluzioa Lurraren lurrazal eta mantuan*

Lu-Hf sistema, lurrazal-mantu sistemaren eraketa ekarri zuen Lur Silikatatu Osoaren (*Bulk Silicate Earth*) diferentziazioaren historia ikertzeko erabiltzen da. Lu-a eta Hf-a REE eta HFSE elementuak dira, hurrenez hurren. Horrek, Lu-aren eta Hf-aren portaera fisiko-kimiko ezberdina iradokitzen du lurrazal-mantu sistemaren eboluzioan. Hf-a Lu-a baino ez-konpatibleagoa da mantuaren fusio partzial prozesuetan, eta beraz, Arkear garaiko lehen lurrazalen sorkuntzan, lurrazala Hf-an aberastu egingo zen eta Lu-an txirotu, Lu-an aberastutako eta Hf-an txirotutako mantua utziz. Horrela, Hf eta Lu kondrita-konposizioak zituen jatorrizko mantu bakarretik, CHUR konposizio (*Chondritic Uniform Reservoir*) bezala ezagutzen dena, Lu/Hf erlazio ezberdinak dituzten bi erreserborio sortu ziren, lurrazala ($Lu/Hf_{lurrazal} < Lu/Hf_{CHUR}$) eta mantu txirotua ($Lu/Hf_{mantua} > Lu/Hf_{CHUR}$).

Beste sistema isotopiko batzuetarako legez, $^{176}Hf/^{177}Hf$ arrazoiak kondrita balioetatik daukan desbiderapena Epsilon (ε) notazioaren bidez adierazten da:

$$\varepsilon_{Hf} = \left[\frac{\left(^{176}Hf/^{177}Hf\right)_{lagina}}{\left(^{176}Hf/^{177}Hf\right)_{CHUR}} - 1\right] x\ 10^4 \quad [51]$$

'*model age*' edo adin-eredua (T_{DM}) Mantu Txirotuarekiko (*Depleted Mantle, DM*) erreferentziaz kalkulatzen delarik, ondoko formularen bidez:

$$\text{Hf } T_{DM} = \frac{1}{\lambda} x\ \ln\left\{\frac{\left(^{176}Hf/^{177}Hf\right)_{CHUR} - \left(^{176}Hf/^{177}Hf\right)_{DM}}{\left(^{176}Lu/^{177}Hf\right)_{CHUR} - \left(^{176}Lu/^{177}Hf\right)_{DM}} + 1\right\} \quad [52]$$

Arroken analisietarako etapa bakarreko T_{DM} adina kalkulatzen den bitartean, zirkoien ikerketetarako bi etapatako T_{DM} adina behar izaten da (Nebel et al., 2007).

Zirkoien T_{DM} adina zirkoiaren Hf-aren hasierako konposizio isotopikoa erabiliz kalkulatzen da, lurrazalaren batezbesteko Lu/Hf erlazioa erabiliz. Zirkoiaren Hf-aren hasierako konposizio isotopikoak zirkoia kristalizatu zeneko garaiko $^{176}Hf/^{177}Hf$ balioaren adierazgarria da, kristal berean lortutako U-Pb adinarena. Adin-eredu honek zirkoia gordetzen duen arroka lurrazalean izan duen erresidentzia denbora adierazten du.

3.5.b. Laginen prestaketa

Laginak U-Pb analisietarako era berean prestatzen dira. Hala ere, aipatu beharra dago Hf isotopoen analisirako BSE irudiak lagungarriagoak direla katodoluminiszentzia irudiak baino, irudiaren disdira masa atomikoaren araberakoa baita. Horregatik, kristal berean Hf kopuru ezberdina duten domeinuak ezberdintzea errazagoa da. Disdira handiagoko eremuak Hf kopuru handiagoa duten guneei dagozkie (Hanchar eta Miller, 1993; Corfu et al. 2003a).

3.5.c. Hf-aren espektrometria

Hf-aren analisi isotopikoak detektagailu anitzeko, induktiboki akoplatutako plasma iturridun masa-espektrometroari elkartutako Nd:YAG 213 nm New Wave laser ablazio-sistemaren bidez burutu dira, Geokronologia eta Geokimika Isotopikoaren Zerbitzuan (SGIker, UPV/EHU). Ekipoari buruzko informazio osagarrirako, 2. Kapitulura jo. Analisiak era estatikoan egin dira, 3.15. Taulan azaltzen den Faraday Kaxen konfigurazioarekin.

3.5.d. Interferentzia eta zatikapenen zuzenketa

Disoluzioetan ez bezala, non elementuak kimikoki banatzen diren,, laser bidezko analisietan matrize dena plasmara igarotzen da. $^{176}Hf/^{177}Hf$ arrazoi zuzenen zehaztea erronka handia da, Hf, Yb eta Lu ionizazioan emandako zatikapenak eta 176 masan elkarri eragiten dioten

interferentzia dela eta. Azken hori bereziki garrantzitsua da, izan ere ^{176}Yb-ak eta ^{176}Lu-ak presente dagoen ^{176}Hf-aren % 10-30 (nekez > % 70) osatu dezakete eta.

Hf-aren frakzionazio isotopikoa zehaztu eta zuzentzeko ^{179}Hf/^{177}Hf erabiltzen da, biak interferentzia gabeko isotopoak direlako eta ^{179}Hf/^{177}Hf arrazoia konstantea delako naturan, bere balioa 0,7325 delarik (Patchett eta Tatsumoto, 1980). Zatikapena, β_{Hf}, ondoko legea jarraituz kalkulatzen da (Russell et al., 1978):

$$\beta = \frac{\ln\left(\frac{\left(^{179}Hf/^{177}Hf\right)_{neurt}}{\left(^{179}Hf/^{177}Hf\right)_{egia}}\right)}{\ln\left(\frac{m_{179}}{m_{177}}\right)} \quad [53]$$

Yb-aren zatikapena ez da Hf-arenaren berdina (Chu et al., 2002; Woodhead et al., 2004), eta horregatik β_{Yb}, ^{173}Yb/^{171}Yb arrazoiaren (biak interferentziarik gabeak) neurketaren bidez zehazten da. ^{173}Yb/^{171}Yb konstantea da naturan, eta bere balioa 1,13255 da (Amelin eta Davis, 2005).

Lu-ak bi isotopo dituenez, ^{176}Lu eta ^{175}Lu, zatikapenaren zuzenketak zuzenean egitea ezinezkoa da. Hori dela eta, Lu-ak eta Yb-ak antzeko portaera fisiko-kimikoa dutela onartzen da, eta beraz β_{Yb} erabiltzen da β_{Lu} ordez. Onarpen honen eragina baztergarria da, normalean ^{176}Lu gutxi dagoelako ^{176}Yb-arekin edo ^{176}Hf-arekin alderatuta.

^{176}Yb-aren interferentziaren zuzenketa ^{173}Yb-a monitorizatuz zehazten da, ^{176}Yb/^{173}Yb balioa 0,7964 dela onartuz (Amelin eta Davis, 2005). ^{176}Lu-aren interferentziaren zuzenketa ^{175}Lu-a monitorizatuz zehazten da, β_{Yb} erabiliz eta ^{176}Lu/^{175}Lu=0,02656 dela onartuz (Patchett eta Tatsumoto, 1980).

Aipatu bezala, Yb-aren interferentziaren zuzenketa bereziki garrantzitsua da ^{176}Hf/^{177}Hf arrazoi zuzen eta zehatzak lortzeko (Woodhead et al., 2004; Hawkesworth eta Kemp, 2006). Literaturan hainbat balio topa daitezke Yb-aren arrazoietarako (e.g., Chu et al., 2002; Segal et al., 2003; Vervoort et al., 2004; Amelin eta Davis, 2005). 0,06 moduko Yb/Hf arrazoi moderatuetan, Yb konposizio ezberdinek ^{176}Hf/^{177}Hf-an eragin dezaketen dezplazamendua ziurgabetasun analitikoaren barnean daude (Gerdes eta Zeh, 2009; Kemp et al., 2009). Hala ere, Yb/Hf arrazoien balio handiagoetarako, konposizio ezberdin hauek zuzenketa-akats garrantzitsuak eragin ditzakete. Interferentzien zuzenketetarako balio egokienak aldakorrak izan daitezke instrumentutik instrumentura.

Aipatu beharra dago ^{176}Hf/^{177}Hf arrazoiaren zuzentasuna oso sentikorra dela erabiltzen den Yb konposizioarekiko. Apur bat ezberdina den konposizioa erabilita (Segal et al., 2003), % 0,03 baxuagoak diren ^{176}Hf/^{177}Hf arrazoiak neurtzen dira (0,282110, JMC475).

$^{176}Hf/^{177}Hf$ arrazoi sinesgarriak lortzeko interferentzien zuzenketa sendoak egin behar dira, eta erabiltzen diren zuzenketa eta onarpen guztiak kontu handiz egiaztatu behar dira. Gure kasuan, Yb-arekin eta Lu-arekin dopatutako JMC475 Hf estandarra neurtuz egin dira egiaztapen hauek. Behin ekipoaren parametroak finkatuta daudela (3.7. Taula), Yb eta Lu kopuru ezberdinekin dopatutako JMC475 disoluzioa neurtu da, $^{176}Hf/^{177}Hf$-ren gaineko zuzenketak zuzenak direla egiaztatzeko.

Lortutako emaitza 3.9. Irudian ikus daiteke. Antzeman daitekeen moduan, Yb eta Lu kopuruaren eta $^{176}Hf/^{177}Hf$ arrazoiaren artean ez dago inolako korrelaziorik, interferentzien zuzenketa sendoa dela erakutsiz.

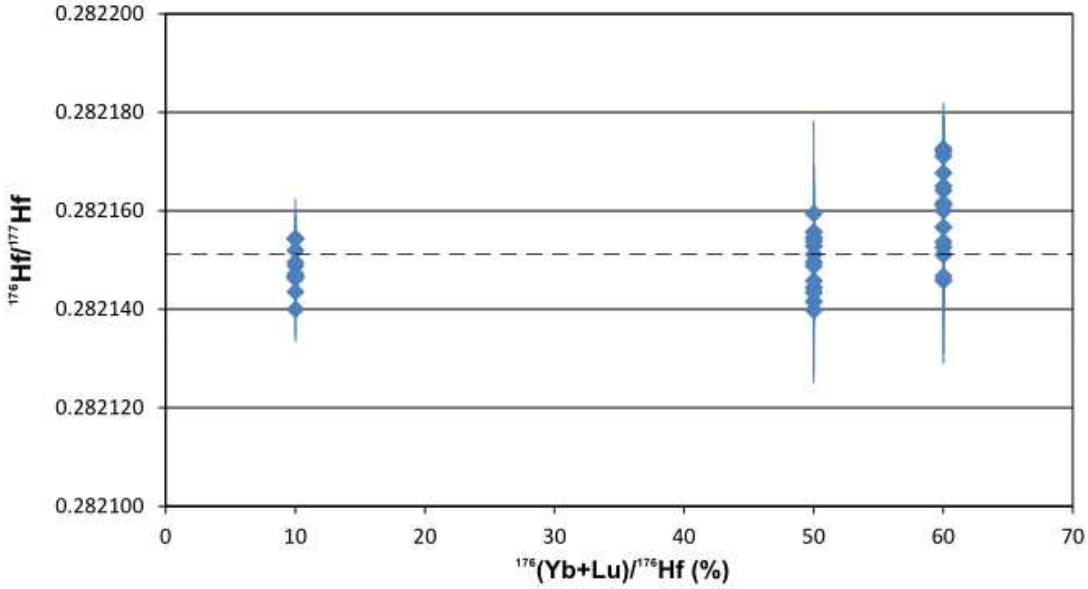

3.9. Irudia. $^{176}Hf/^{177}Hf$ vs. $^{176}(Yb+Lu)/^{176}Hf$ diagrama, analizatutako disoluzio guztientzat. Marra etenak JMC475 disoluzioan ezaguna den $^{176}Hf/^{177}Hf$ arrazoia da (0,282151, gorago ikusi).

3.5.e. Datuen bereganatzea eta murrizketa

Disoluzioen analisietatik zatikapen eta interferentzia zuzenketak sendoak direla baieztatu ondoren, zirkoi estandarrak LA-MC-ICP-MS bidez analizatzen dira. Estandarren muntaketa U-Pb sistemarako azaldutakoa da, are gehiago, erabiltzen diren estandarretako batzuk berberak dira.

Hf isotopen datuak 40 µm-ko puntu-tamaina erabiliz eskuratzen da (beherago ikusi), eta gainontzeko parametro analitikoak 3.22. Taulan laburbiltzen dira. Kasu honetan, argonarekin batera nitrogenoa ere erabiltzen da gas gehigarri moduan. Horrek, plasman oxidoen formazioa saihesten du eta seinalearen sentikortasuna % 30 inguru areagotzen du.

Datuen bereganatzeko prozedura U-Th-Pb sistemaren analisietarako azaldutakoaren antzekoa da. Erreferentziazko zirkoiak saio analitikoaren hasieran eta amaieran neurtzen dira, eta baita ere 10 laginero. Kasu honetan, GJ-1 estandarra (Jackson et al., 2004) ekipoan inolako jitorik

ez dagoela baieztatzeko erabiltzen da soilik, eta ez zatikapena zuzentzeko. Datuen murrizketa Iolite® softwarearekin egin da (Paton et al., 2011).

3.5.f. Analisiaren tamaina

Laser-ablazio analisiak egiterakoan, zientzialariek materialaren bolumena ahalik eta txikiena analizatzeko aukerak aztertzen dituzte etengabe. LA-ICP-MS motako teknikek duten bereizmen espaziala ahal den gehiena aprobetxatzea dute xedea, beti ere zuzentasun eta zehaztasun nahikoa duten arrazoi isotopikoak neurtuz.

3.22. Taula. LA-MC-ICP-MS bidezko Hf-aren analisi isotopikoetarako erabilera parametroak.

Laborategiaren informazioa	
Laborategiaren izena	SGIker, Euskal Herriko Unibertsitatea UPV/EHU
Laginaren prestaketa	Xafla petrografiko 'lodiak' laginetarako, epoxy-erretxinan eginiko 10 mm-ko diametroko muntaketak estandarretarako
Irudiak	BSE, JEOL JSM-6400
Laser ablazio-sistema	
Enpresa, modeloa eta mota	New Wave Research, UP213, Nd:YAG
Ablazio-gelaxka eta bolumena	Moldatutako SuperCell^{TM}, 33 cm^3
Laserraren uhin-luzeera	213 nm
Pultsu zabalera	3-5 ns
Dentsitate energetikoa	5 $J.cm^{-2}$
Errepikapen tasa	10 Hz
Ablazioaren iraupena	90 s (30 s gasaren garbitasuna neurtzeko eta 60 s laginerako)
Analisiaren tamaina	40 µm
Garraio-gasa	% 100 He gelaxkaren barruan, N_2 (lehenengo) eta Ar (gero) gas gehigarriak Y-pieza birekin nahastuak, zuzira iritsi aurretik
Gelaxkaren barneko garraio-gasaren jarioa	0,35 L/min
ICP-MS	
Enpresa, modeloa eta mota	Thermo Finnigan Neptune, MC-ICP-MS
Laginaren sarrera	Ablazio aerosola
Irrati-frekuentzia	1300 W
Gas gehigarriaren jarioa (N_2)	0,01 L/min
Gas gehigarriaren jarioa (Ar)	0,75 L/min (egunero doitua)
Plasma gasaren jarioa	15 L/min
Gas hoztailearen jarioa	0,4 L/min
Ekorketa modua	Estatikoa
Detektagailu modua	Faraday kaxak
Neurtutako masak	171, 173, 175, 176, 177, 178, 179

Hf isotopoen laser bidezko analisien erronka handienetakoa laginketa-puntuaren tamaina da, U-Pb analisiena baino handiagoa dena. Prozeduraren egokitasunak puntuaren tamaina txikiagotzea ahalbidetzen du, baina beti ere seinale onargarri bat mantenduz.

Lu-Hf prozeduraren ezarpenerako 15 µm, 25 µm, 30 µm eta 40 µm-ko analisiak egin dira, azken tamaina honetan, 5 Hz eta 10 Hz errepikapen-tasekin. 3.10. Irudian analisi tamaina ezberdinekin

lortutako emaitzak erakusten dira. Ikus daitekeen moduan, 15 µm eta 25 µm-ko tamaina duten analisiak zehaztasun eta zuzentasunik gabeak dira erabat. 30 µm-ko puntuekin lortutako emaitzak ez dira erabat txarrak, arrazoiak erreferentziazko materialaren balioetatik gertu daudelako, baina agertzen diren errorea oso handia da. 40 µm-ko laginketa-puntuarekin egindako analisiek, bai 5 Hz-tan zein 10 Hz-tan, balio eta errore onargarriak dituzte. Hamar Hz-ko errepikapen-tasarekin errore txikiagoak lortzen dira, aerosolak lagin kopuru handiagoa baitauka eta beraz, detektagailura heltzen den seinalea handiagoa da.

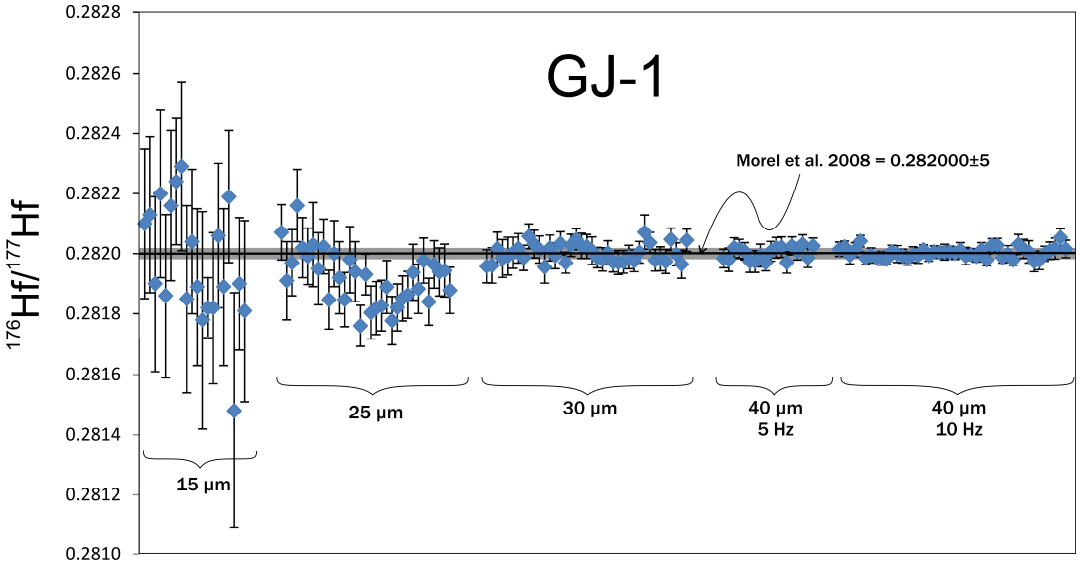

3.10. Irudia. Puntu-tamaina eta frekuentzia ezberdinekin egindako analisien grafikoa.

3.5.g. Metodoaren balioztatzea nazioarteko estandarretan

Prozeduraren optimizazio eta balioztapenerako gehien erabiltzen diren lau zirkoi estandarrak analizatu dira: GJ-1, 91500, Mudtank eta Plešovice (3.11. Irudia). Zirkoi horiek $^{176}Hf/^{177}Hf$ arrazoi- eta Yb kontzentrazio sorta zabala baitan hartzen dute, azkena zuzenketak era egokian egiten direla baieztatzeko.

Prozeduraren ezarpenean analizatutako zirkoien emaitzak 3.11. Irudian eta 3.23. Taulan erakusten dira, erreferentziazko balioekin batera. Gogoratu beharra dago disoluzioan egindako analisiek errore txikiagoak dituztela beti, seinalea egonkorragoa delako eta matrizerik ez dagoelako.

Erreferentziazko materialen analisiak behar duten balioetan daude, eta Yb-rik eta Lu-rik gabeko Hf disoluzioen analisiak baino 2-3 aldiz zehaztasun txarragoa erakusten dute soilik. Ohiko saioetarako, estandarretako bakoitzaren $^{176}Hf/^{177}Hf$ arrazoiaren batezbestekoa erreferentziazko balioaren epsilon unitate baten barruan dago, hau da, analisiek epsilon unitate baten barruko zehaztasuna dute.

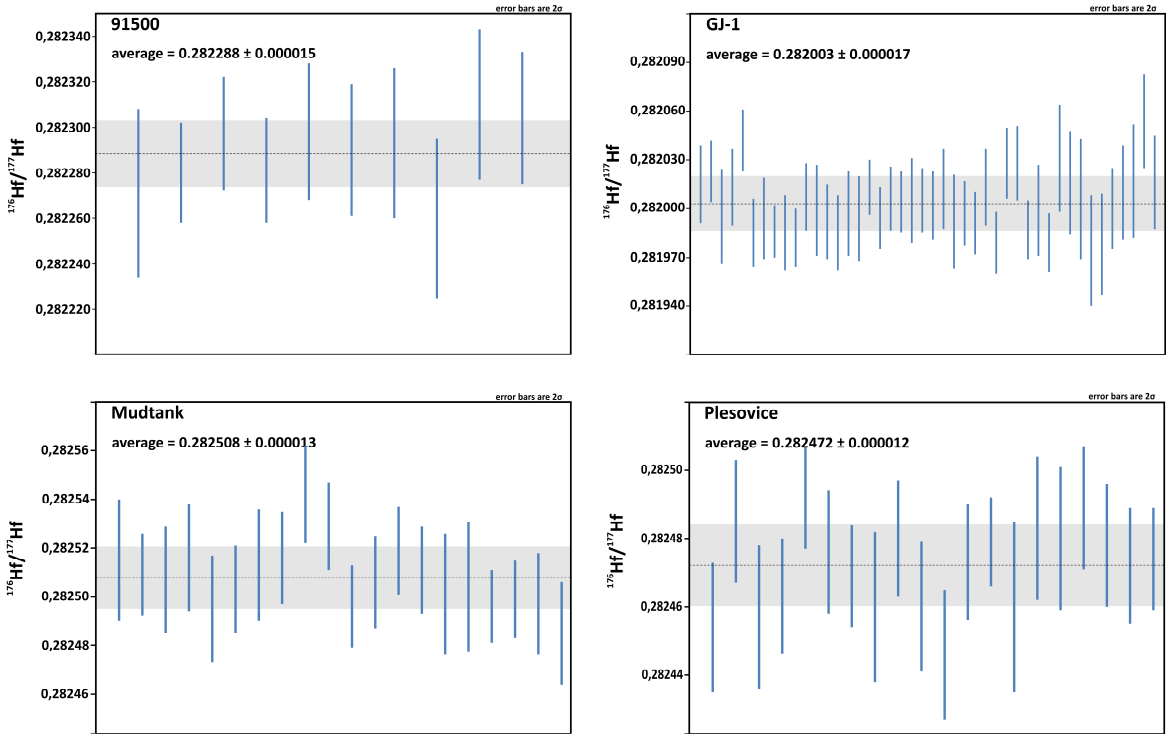

3.11. Irudia. LA-MC-ICP-MS bidezko Hf isotopoen emaitzak zirkoi estandarretan.

3.23.Taula. Zirkoi estandarren erreferentziazko balioak, disoluzio eta laser ablazio bidezko analisietarako, eta lortutako emaitzak. Erroreak 2σ-koak dira. 1: Morel et al. (2008); 2: Woodhead eta Hergt (2005); 3: Slama et al. (2008); 4: Schwieters et al. (2009).

	Disoluzioa	Laser Ablazioa[4]	Tesi honetan	n
GJ-1	0,282000±5[1]	0,282015±29	0,282003±17	44
91500	0,282306±8[2]	0,282299±26	0,282288±15	10
Mudtank	0,282507±6[2]	0,282522±19	0,282508±13	20
Plešovice	0,282484±8[3]	0,282486±28	0,282472±12	20

Chapter 4: Application of the implemented methods

4. Application of the implemented methods

In order to check the usefulness of the methods implemented several high-pressure and high-temperature metamorphic rocks from the Cabo Ortegal and Malpica-Tui (also written Tuy) complexes (NW Iberian Massif) have been dated during this PhD thesis.

4.1. Geological background

The studied samples are located in the northwestern section of the Iberian Massif and correspond to the westernmost outcrops of the European Variscan Belt (Figure 4.1). The Variscan Orogen resulted from the collision of the continental margins of Laurussia and Gondwana during the Late Paleozoic (Devonian-Permian), prior to the formation of the last Pangea supercontinent. This collision involved Gondwana-derived intermediate continental blocks (the so-called peri-Gondwanan terranes) that were amalgamated upon Gondwana forming a large orogenic wedge through the Devonian-Carboniferous before its final accretion to Laurussia (Martínez Catalán et al., 2007, 2009; von Raumer and Stampfli, 2008). In central and western Europe, rocks affected by the Hercynian or Variscan orogeny crop out within a number of pre-Mesozoic massifs separated by large Mesozoic basins (Figure 4.1). The presence of a Hercynian basement underlying these basins has been revealed by drill cores (Lefort, 1989). The extent of this sector of the Hercynian fold-belt in Europe is close to 3,000 km long and 700-800 km wide (Matte, 1991).

On the basis of available stratigraphic, tectonic and petrologic criteria, the Variscan terranes of the Iberian Peninsula have been divided into different zones (Lotze, 1945; Julivert et al, 1972; Quesada, 1991). Julivert et al. (1972) proposed 5 different zones for the Iberian Massif (Figure 4.1). The samples studied in the current work belong to the Central Iberian Zone.

Two different areas can be differentiated within the Central Iberian Zone: (i) autochthon sequences making up most of the zone and (ii) allochthon/para-autochthon sequences located in the most internal parts of the Central Iberian Zone. The latter can be further divided into two domains (Arenas et al., 1986; Farias et al., 1987):

- Galicia-Trás-os-Montes Schistose Domain, formed by pelitic metasediments with minor intercalations of metavolcanites. This is interpreted as a section of the most distal margin of Gondwana, tectonically transported towards the Central Iberian Zone.
- Allochthonous Complexes, including mafic and ultramafic rocks affected by high-pressure metamorphism.

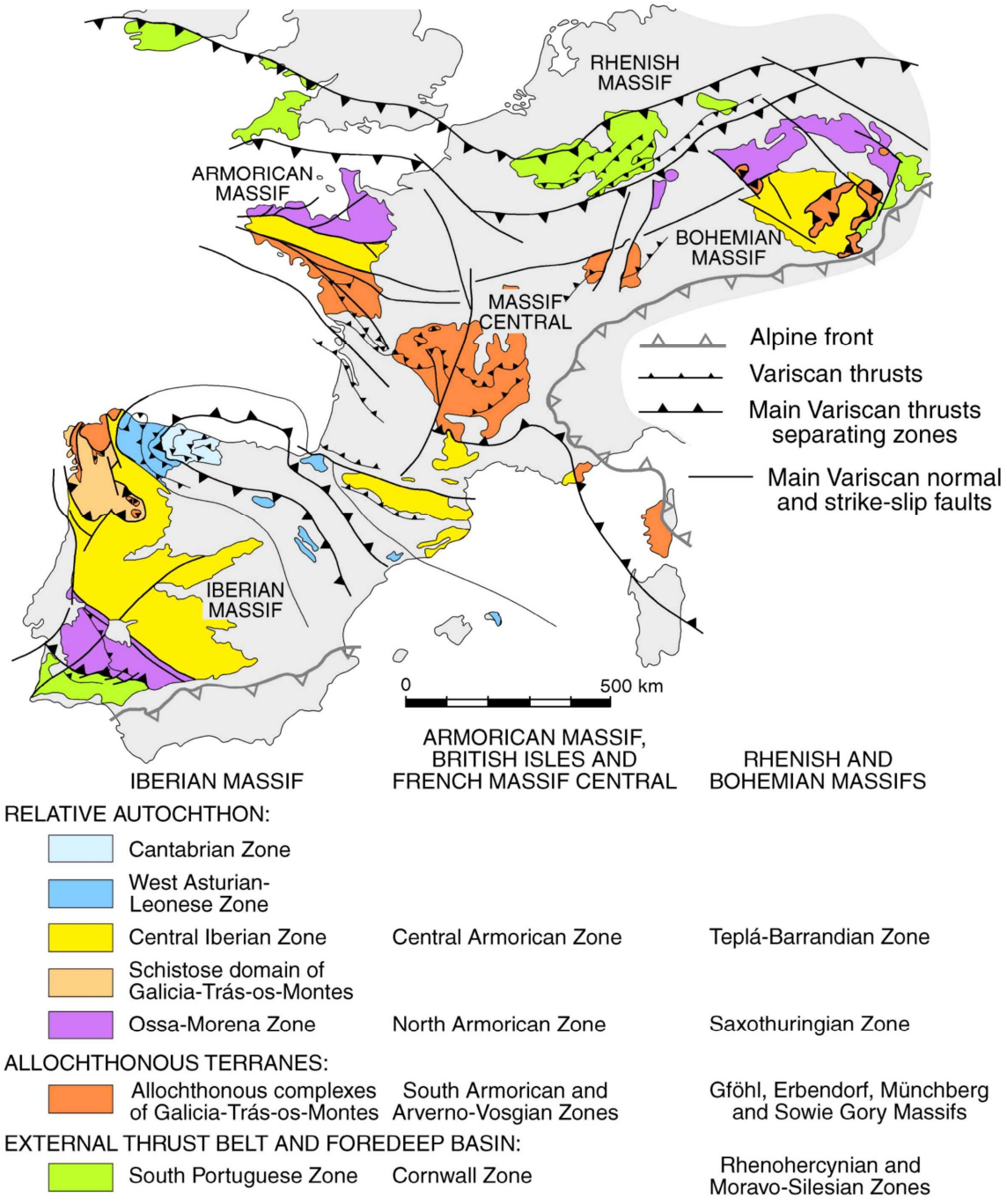

Figure 4.1. Generalized geological map of the European Variscan orogen. Modified after Martínez Catalán (1990).

4.1.a. Allochthonous complexes

Five metamorphic complexes, including a significant component of mafic-ultramafic rocks, are exposed in the northwestern part of the Iberian Peninsula. Three of the complexes (Órdenes, Cabo Ortegal and Malpica-Tui) are located in Galicia whereas the other two (Bragança and Morais) occur in the area of Trás-os-Montes in northeast Portugal (Figure 4.2).

Early theories on the origin of these complexes suggested that they represented either the relics of an old Proterozoic basement, or were related to an early Paleozoic rift (Matte and Ribeiro, 1967; Vogel, 1967; Van Calsteren, 1977; Van Calsteren and Den Tex, 1978). The interpretation of gravimetric surveying by Van Overmeeren (1975) and Keasberry (1979) supported these theories. Alternatively, Ries and Shackleton (1971) suggested that the complexes might be the remnants or klippen from a large metamorphic nappe dismembered and amalgamated to the Hercynian fold-belt. Bayer and Matte (1979) reinterpreted from this allochthonist point of view the geophysical data cited above and built a coherent geological model. According to this perspective, the root zone of the nappes would be located to the west of the current western Iberian coast, and its emplacement would have required west-to-east tectonic translation of at least 100 km during the Siluro-Devonian collision between Gondwana and Laurentia (Lefort and Ribeiro, 1980; Burg et al., 1981, 1987).

Nowadays, it is well accepted that these complexes represent fragments of variably subducted continental and oceanic s.l. lithosphere that were subsequently obducted onto the Gondwana edge during the Hercynian orogeny (Ries and Shackleton, 1971; Bard et al., 1980; Iglesias et al., 1983; Bastida et al., 1984; Vogel, 1984; Arenas et al., 1986; Matte, 1991; etc.). The complexes structurally overlay low-grade, Early-Middle Paleozoic, mainly metasedimentary rocks interpreted as para-autochthonous units (Schistose Domain of Galicia-Trás-os-Montes) of the Central Iberian Zone.

Three main structural elements may be recognized within the complexes: a low-to intermediate-temperature/high-pressure Basal Unit or Lower Allochthon at the bottom, a sandwiched Ophiolitic Complex and an Upper Allochthon comprising rock units metamorphosed under high-pressure and high-temperature conditions at the top. These may be correlated at a regional scale, although not all the units are always present.

The lowermost Basal and Ophiolitic units correspond to the passive margin of Gondwana and outboard oceanic sequences related to this continent, and record evidence of Hercynian compressive events and continental accretion (Van Calsteren et al., 1979; Peucat et al., 1990; Dallmeyer and Gil Ibarguchi, 1990; Dallmeyer et al., 1991). The high-grade/high-pressure units of the Upper Allochthon are the most distinctive element of the complexes and the ones that first allowed for an interpretation in terms of an allochthonous origin. Previous petrological, structural and geochronological studies have led to two main hypotheses on the origin and tectonothermal evolution of this Upper Allochthon. On the one hand, a Precambrian age of the high-pressure events was postulated by Vogel and Abdel Monem (1971), Engels et al. (1974), Marques et al. (1992, 1996) and Santos et al. (1995, 1997), among others. On the other hand, Paleozoic

extension followed by subduction events were proposed by Bernard-Griffiths et al. (1985), Peucat et al. (1990), Santos Zalduegui et al. (1997) and Martínez Catalán et al. (1997) among others.

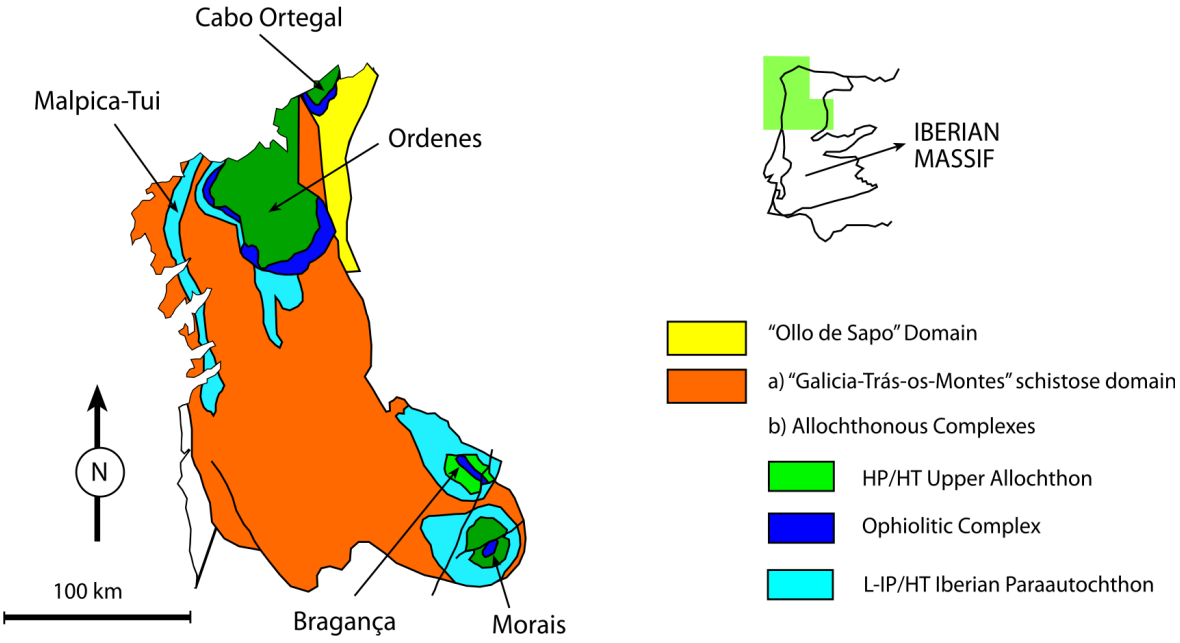

Figure 4.2. Geological map of the NW Iberia, showing the different Allochthonous Complexes. Modified after Arenas et al. (1986) and Ribeiro et al. (1990).

4.1.b. The Cabo Ortegal Complex

The Cabo Ortegal Complex is the easternmost of the Allochthonous Complexes of Galicia, forming a ca. 450 km^2 N-plunging semi-elliptic synformal basin (Bastida et al., 1984). Despite its smaller size, this complex includes a rather complete collection of the allochthonous terranes described in NW Iberia, with excellent outcrops on the Atlantic coast (Figure 4.3). The eastern and southern margins of the complex are in tectonic (thrust) contact with lower-grade Silurian metasediments and acidic metavolcanic rocks exposed along the western flank of a regional Hercynian antiformal structure (the so-called Ollo de Sapo antiform). The western margin of the complex is delineated by a sheared Hercynian granitoid pluton, a thin layer of metasediments, and the Valdoviño fault, that separates the Órdenes Complex to the west.

The Cabo Ortegal Complex has attracted much attention due to its size and good outcrop conditions. Its geological setting is well known from previous studies beginning in the XIX century (e.g., Schulz, 1835; Macpherson, 1881, 1883). However, much of the present knowledge of the complex is due to geological surveying carried out during the second half of the 20th century (Carlé, 1945; Parga Pondal, 1956), mostly to that resulting from the collaboration from 1952 to 1980 between the Laboratorio Geológico de Laxe and the University of Leiden (e.g., Vogel, 1967; Maaskant, 1970; Engels, 1972; Van Calsteren, 1977, 1978; Van Calsteren et al., 1979; Kuijper,

1979). Fernández Pompa and Monteserín (1976), and Fernández Martínez and Fernández Pompa (1977) mapped the complex on a scale 1:50,000 following basically the lithostratigraphical background previously established. Bastida et al. (1984) synthesized and interpreted the structure and constitution of the complex based upon a map on a scale of 1:200,000 that contained the most relevant tectonostratigraphic units of the northern branch of the Iberian Massif. Since then, a wealth of studies, too large to be cited here, has been completed by members of different institutions.

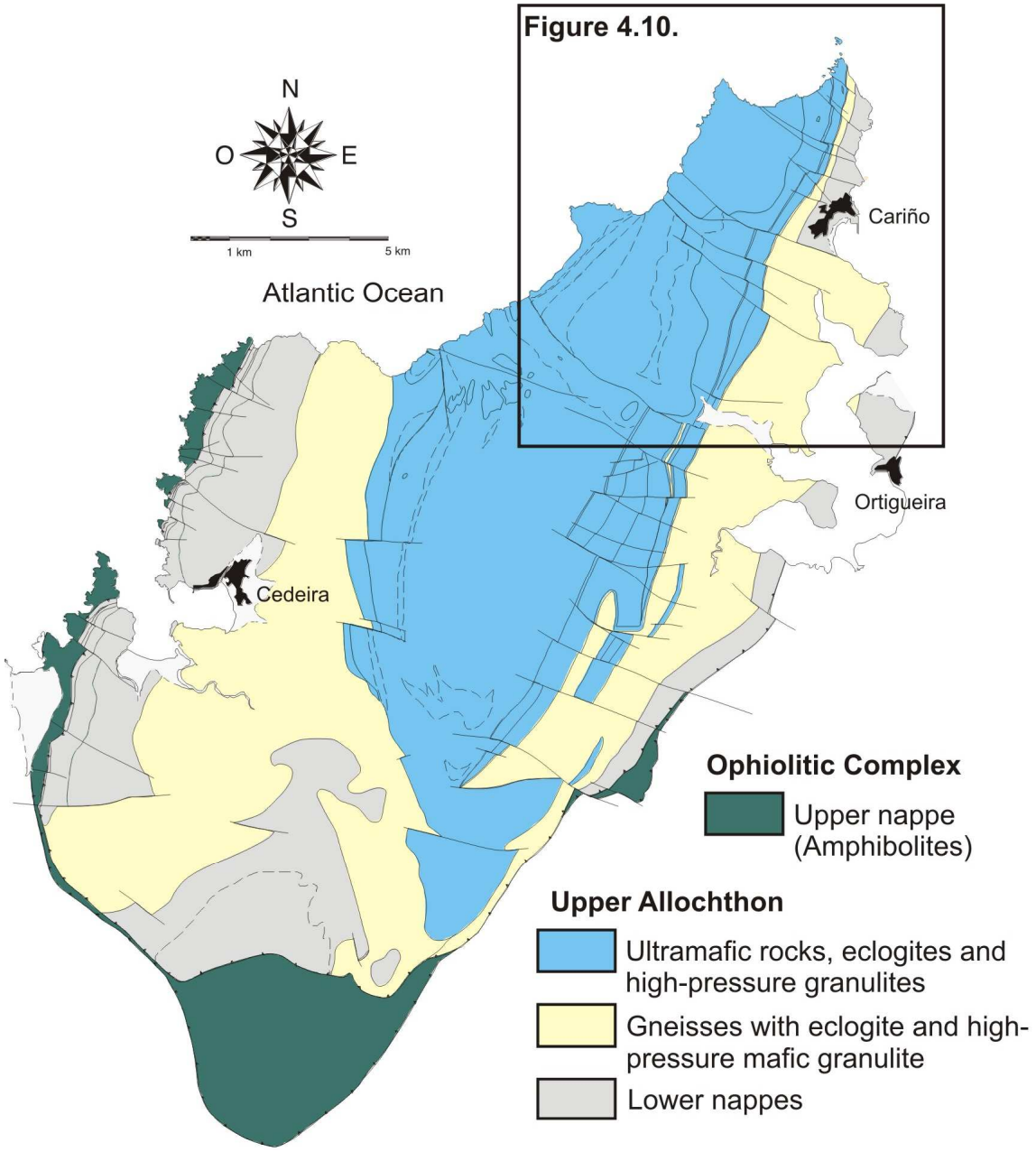

Figure 4.3. Simplified geological map of the Cabo Ortegal complex after Ábalos et al. (2003) and Gil Ibarguchi et al. (2000) showing the high-grade/high-pressure metamorphic nappe units (Upper Allochthon).

The Cabo Ortegal Complex is composed of internally imbricated nappe units that mainly belong to the regional Ophiolitic Unit to the bottom and the Upper Allochthon on the top. A lower nappe member (Moeche unit), not dealt with in the present dissertation, comprises tectonic slices of strongly retrogressed eclogites and slightly metamorphosed remnants of an ophiolitic suite (metabasalts, serpentinites), together with various types of low-grade metasediments (limestones, metapelites) and acid metavolcanites. Although the lithostratigraphical units recognised in the complex have been grouped and subdivided by researchers several times with the aim of emphasising particular geodynamic aspects or interpretations, the labelling of the units most often used today has seen minor changes since it was first established by Vogel (1967).

As stated before, the Upper Allochthon is the most characteristic structural unit of the complex. In the Cabo Ortegal area it is represented by high-pressure rocks including high-pressure granulites, eclogites, metaperidotites, ortho- and paragneisses, metagabbros and metaserpentinites (cf. Vogel, 1967, Gil Ibarguchi et al., 2000, and references therein). High-pressure garnet-clinopyroxene granulites were formed from basic and even ultrabasic to acid protoliths of calc-alkaline affinity (Peucat et al., 1990) and currently conform the largest outcrops in the complex. Eclogites, in turn, are derived from the high-pressure metamorphism of basic rocks with N-MORB compositions, while ultramafic rocks are mostly spinel-bearing harzburgites with abundant dunite and pyroxenite. This association has been interpreted as a portion of moderately depleted mantle wedge and associated mantle partial melting products.

Associated high-pressure gneiss units like the migmatitic Chimparra and Banded Gneiss formations contain boudins of garnet and omphacite-bearing rocks, with or without plagioclase. The basic protoliths of these rocks are similar to LREE-enriched basalts with alkaline affinity. The high-pressure gneisses bear inherited zircon components older than c. 2 Ga (Albert et al. 2015a), have semi-pelitic compositions (mainly arkosic but also rich in mafic components at places) and may represent a volcano-sedimentary complex formed in a thinned-crust environment.

Other rock units within this Upper Allochthon correspond to the metagabbros and amphibolites of broadly oceanic affinity (N-type to T-type MORB) from the Candelaria formation, and the non-migmatitic Cariño gneisses. These gneisses, which were apparently affected by a younger metamorphic episode, contain amphibolites and metagabbros and have typical features of a greywacko-pelitic sequence.

4.1.c. Malpica-Tui Complex

The Malpica-Tui Complex occupies the core of a narrow synform which extends ca. 150 km in N-S direction (Figure 4.4). This synform is located on the western flank of the Padrón

Antiform, a migmatitic dome originated during the extensional collapse of the Variscan orogen (Martínez Catalán et al., 2009; Díez Fernández and Martínez Catalán, 2009). To the east it is bounded by a basal shear zone overlying the para-authocthon (i.e. the Schistose Domain of Galicia-Trás-os-Montes; Gil Ibarguchi and Ortega Gironés, 1985; Llana-Fúnez and Marcos, 2002) and to the west by a subvertical dextral shear zone (Coke and Ribeiro, 2000; Llana-Fúnez, 2001).

The Malpica-Tui Complex was first identified as an 'amphibolite-gneiss band between Malpica and Vigo' (Carlé, 1945). It was not recognised as a tectonic domain until 1953, when Isidro Parga Pondal (1953a, b and c, 1956) defined it as the 'Complejo Antiguo' (Old Complex). Years later, den Tex and Floor (1967) recognized that it was a polymetamorphic unit that would be originally located at higher cortical levels. These authors proposed that after an initial metamorphic process it collapsed by extension and was sunken with respect to the adjacent migmatitic materials, being named as the 'Blastomylonitic Graben' (den Tex and Floor, 1967; den Tex, 1981a, b). Other authors pointed to the allochthonous character of the unit (Ries and Shackleton, 1971; Anthonioz and Ferragne, 1978; Lefort and Ribeiro, 1980) while Van der Wegen (1978) definitely demonstrated the LT-HP (eclogitic) nature of the metamorphism in metabasites of this area. All in all, Malpica-Tui Unit or zone is an accepted term used by the geologists working in this area. It was established in the early 80´s by Ortega Gironés and Gil Ibarguchi (1983) and has no genetic connotations, as it refers strictly to its geographical boundaries.

Rodríguez (2005) noted however the existence of two distinct lithological domains within this unit comprising a sequence of oceanic affinity (N-MORB) overlaying a set of continental materials. This led to the consideration of a new nomenclature for the Malpica-Tui Unit, which according to the guidelines used for the rest of the Allochthonous Complexes of NW Iberia, would adopt the name of 'Malpica-Tui Complex'. Since the oceanic sequence does not represent an ophiolitic sequence comparable to those described in the rest of the Allochthonous Complexes (e.g., Sánchez Martínez, 2009), many studies continue using the 'old' term. However, in order to unify the terminology, the denomination of Malpica-Tui Complex will be used from now on.

This complex includes essentially lithologies of the Basal Units, which show here a large variety in terms of composition and tectonic fabrics. The Upper Sequence (or oceanic unit) crops out in a small area (Ceán-Razo) in the northern sector. The rest of the complex is constituted by lithologies of the Lower Sequence or continental unit of Rodríguez et al. (2003). The contact between both sequences is marked by a several meter-thick layer of mylonites related to an extensional deformation (López-Carmona, 2014).

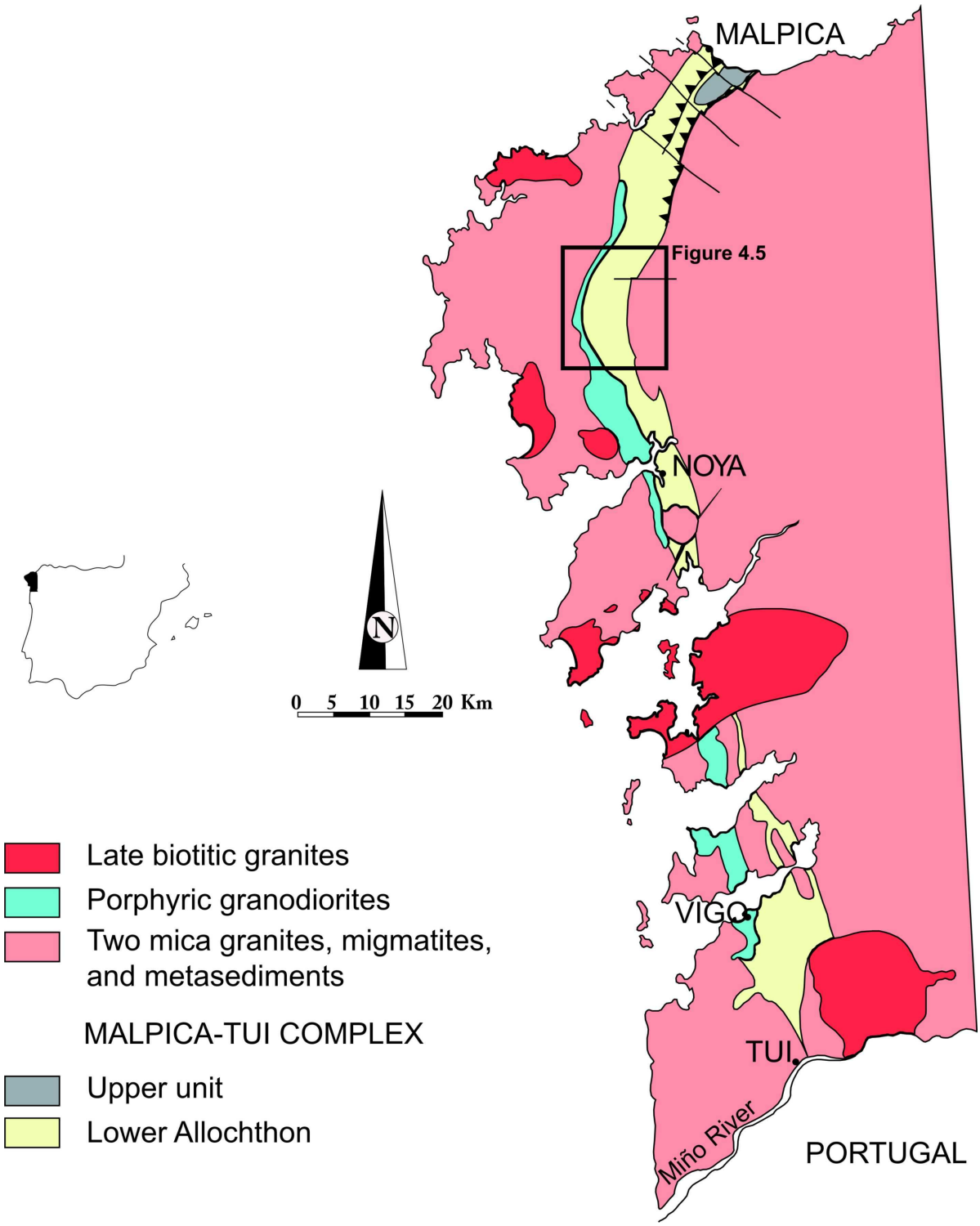

Figure 4.4. Simplified geological map of the Malpica-Tui complex after Ortega Gironés and Gil Ibarguchi (1983) and Rodríguez (2005).

The Lower Allochthon in the Malpica-Tui Complex consists of a heterogeneously deformed monotonous pile of terrigenous sediments and igneous rocks (Díez Fernández, 2011). On the one hand, the sedimentary sequence comprises sandstones (greywakes) alternating with minor layers or lenses of pelites, graphite-bearing schists, calc-silicate rocks and quartzites.

On the other hand, orthogneisses include: (i) a calc-alkaline suite formed by high-K granites, granodiorites and tonalites and (ii) an alkaline to peralkaline suite including metaluminous alkali-feldspar quartz-syenites and granites, peraluminous alkali-feldspar granites, and peralkaline granites (Montero, 1993; Rodríguez, 2005; Montero et al., 2009). The alkaline to peralkaline rock series has an A-type granite affinity (Whalen et al. 1987) and is associated with metabasites of alkali basalt compositions, all related to an extensional event interpreted to reflect Ordovician rifting (Pin et al., 1992). Additionally, there is a second type of basic rocks with tholeiitic to calc-alkaline compositions (Rodríguez, 2005). During the Variscan orogeny the non-alkaline acid to basic rocks were certainly metamorphosed under eclogite-facies conditions while the evolution for the alkaline types is less well constrained.

Metabasites, represented by greenschists, garnet-bearing amphibolites, amphibolites without garnet, amphibolites with plagioclase porphyroblasts or eclogites, are enclosed in both orthogneisses and in metasedimentary rocks (e.g., Arps 1970, 1981)**.**

4.1.d. Geochronological background

The interest in deciphering the geologic evolution of Allochthonous Complexes has made this region one of the European areas where more geochronological studies have been conducted. Due to the large amount of available data and for the sake of simplicity, only those ages calculated for the Upper and Lower Allochthons of the Complexes are included in Table 4.1. Recent data related to provenance studies in metasedimentary rocks (Albert et al., 2015a, 2015b) or radiometric analysis concerning the Ophiolitic Units (e.g., Dallmeyer and Gil Ibarguchi, 1990; Dallmeyer et al., 1997; Díaz García et al., 1999; Sánchez-Martínez et al., 2011) are not included. Since the knowledge and interpretation of the geological history undergone by these complexes has changed so much from the first geochronological studies of for instance Priem et al. (1970) and Vogel and Abdel-Monem (1971) until recent times, Table 4.1 lists the data obtained by different authors without addressing its geological meaning.

As a brief summary, available geochronological data for the rocks comprising the Upper and Lower Allochthons are interpreted by most of the scientific community as follows:

(i) Lower Paleozoic age of ca. 480-500 Ma for the mafic and acid igneous protoliths and a single episode of high-pressure metamorphism, dated at 385-400 Ma for the Upper Allochthon and a bit younger, ca. 370 Ma, for the Lower Allocthon. There is also local evidence for thermal overprint related to the emplacement of the lower Paleozoic intrusives.

Table 4.1. Compilation of published ages for the Allochthonous Complexes of the Iberian Massif. Abbreviations of the minerals are after Kretz (1983): Bt-biotite, Cpx-clinopyroxene, Grt-garnet, Hbl-hornblende, Mnz-monazite, Ms-muscovite, Pg-paragonite, Phe-phengite, Phl-phlogopite, Pl-plagioclase, Rt-rutile, Ttn-titanite, Zrn-zircon. Other abbreviations: WR-whole rock, u.i.- upper intercept, l.i.- lower intercept, t.g.- total gas age. In case of $^{40}Ar/^{39}Ar$ dating, preferred ages are considered. * Recalculated by Kuijper et al. (1982).

Cabo Ortegal Upper Allochthon				
Rocks	***Age (Ma)***	***Comment***	***Method***	***Author***
Banded gneiss	417 + 3/-2 (l.i.)		U/Pb Zrn	(1)
	376 ± 1		Ar/Ar Ms	(1)
	472 ± 27 (l.i.)		U/Pb Zrn	(2)
Cariño gneiss	355 ± 8		Rb/Sr WR-Bt	(1)
Chimparra gneiss	422 ± 41 (l.i.)		U/Pb Zrn	(1)
	371 ± 8		Rb/Sr WR-Ms	(1)
	349 ± 7		Rb/Sr WR-Bt	(1)
	382 ± 3		U/Pb Rt	(3)
	394 ± 11		U/Pb Zrn	(4)
	385 ± 25 (l.i.) /486 ± 22 (u.i)		U/Pb Mnz	(2)
	≈ 400		U/Pb Zrn	(5)
Eclogite	480-420 (l.i.)		U/Pb Zrn	(6)
	480 ± 5 (u.i.)		U/Pb Zrn	(1)
	898 ± 32		K/Ar Am	(7)
	495 ± 11		U/Pb Zrn	(4)
	386 ± 41		U/Pb Zrn	(4)
	510-550		U/Pb Zrn	(5)
Ky-bearing eclogite	469 ± 9		U/Pb Zrn	(4)
	380 ± 14		U/Pb Zrn	(4)
Basic granulite	354 ± 17	347 ± 17 *	Rb/Sr WR-Bt	(8)
	482 ± 7(u.i.) 497 + 11/-13 (u.i)	2 samples	U/Pb Zrn	(1)
	387 ± 4		Ar/Ar Am	(4)
	383 ± 8		U/Pb Zrn	(9)
	430-440	Different ages	U/Pb Zrn	(9)
	387 ± 5		U/Pb Ttn	(5)
	474 ± 16		U/Pb Zrn	(1)
Leucosome in basic granulite	486 ± 4		U/Pb Zrn	(2)
	387		U/Pb Ttn	(2)
	372		U/Pb Rt	(2)
	397 ± 3 / 391 ± 4	Cores / rims	U/Pb Zrn	(9)
Carbonate-rich Grt-Cpx rock	406 ± 4		U/Pb Zrn	(10)
	383 ± 3		U/Pb pale Ttn	(10)
Carbonate-rich Grt-Cpx layer	388 ± 3		U/Pb Zrn	(10)
	389 ± 2		U/Pb Brown Ttn	(10)
	388 ± 2		U/Pb pale Ttn	(10)
	390 ± 11		U/Pb Ep	(10)
Plagiogranite	470 + 2/-3 (l.i.)		U/Pb Zrn	(10)
Spinel Harzburgite (Uzal)	391 ± 8		U/Pb Zrn	(4)
Lherzolite	390 ± 16	Spinel lherzolite	U/Pb Zrn	(5)
	??	Complex age	Rb/Sr WR	(8)
	??	386 ± 10	Rb/Sr Am	(8)
	??	337 ± 10	Rb/Sr Phl	(8)
Pegmatite cutting peridotites (Uzal)	388 ± 2		U/Pb Mnz	(10)
	387 ± 1		U/Pb Zrn	(10)
Garnet pyroxenite	392 ± 4 (u.i.)		U/Pb Zrn	(1)
	392 ± 16		U/Pb Zrn	(5)
	383 ± 1	Herbeira	U/Pb Rt	(10)
	383 ± 8	Uzal	U/Pb Zrn	(4)
Amphibolite (Peña Escrita)	389 ± 6		Ar/Ar Am	(1)
Felsic gneiss (Candelaria)	380 ± 4		Ar/Ar Am	(1)
Low grade metapelitic phyllonite	365		Ar/Ar WR	(11)

Table 4.1. Continue…

Órdenes Complex Upper Allochthon				
Rocks	***Age (Ma)***	***Comment***	***Method***	***Author***
Orthogneiss (Melide)	481		U/Pb Zrn	(12)
	459	Border zone	U/Pb Zrn	(12)
	409 ± 26	400 ± 20 *	Rb/Sr WR	(8)
Paragneiss (Melide)	386	Average age	U/Pb Mnz	(2)
Pre-Hercynian rocks (incl. Corredoiras)	460-430		Rb/Sr WR	(13)
Orthogneiss (Curtis)	283 (l.i.) / 761 (u.i.)		U/Pb Zrn	(12)
	450 ± 25		Rb/Sr WR	(12)
Orthogneiss (Corredoiras)	500 ± 2		U/Pb Zrn	(14)
Muscovite-chlorite gneiss (Sobrado)	475 (l.i.)		U/Pb Zrn, Mnz	(12)
Paragneiss (Sobrado)	488 ± 3 (u.i.)		U/Pb Mnz	(2)
Basic granulite (Sobrado)	489 + 17/-19 (l.i.)		U/Pb Zrn	(1)
Mylonitic amphibolite	432	376 (t.g.)	Ar/Ar Am	(11)
	discordant spectra.	318 (t.g.)	Ar/Ar Ms	(11)
Phyllite	333 ± 0.3	Chl zone	Ar/Ar WR	(15)
	295 ± 0.2	Bt zone	Ar/Ar WR	(15)
	330 ± 2 (p.a)		Ar/Ar WR	(16)
Micaschist	371 ± 4		Ar/Ar Ms	(16)
Amphibolite	≈ 375		Ar/Ar Am	(15)
	425 ± 1		Ar/Ar Am	(15)
	423 ± 12 / 382 ± 13 / 382± 4 (p.a.)	Plateau age	Ar/Ar Am	(16)
Garnet amphibolite	410 ± 14 / 384 ± 5 / 376 ± 4 (p.a.)	3 samples	Ar/Ar Am	(16)
	396.6 ± 12		Ar/Ar Am	(16)
Paragneiss	≈ 325		Ar/Ar Ms	(15)
Diabase dyke	510 + 8/-2		U/Pb Zrn	(17)
Granodiorite (A Silva)	510 + 2/-1		U/Pb Zrn	(18)
Gabbro (Monte Castelo)	499 ± 2		U/Pb Zrn	(14)
	515 ± 7		U/Pb Zrn	(9)
Granodioritic orthogneiss	492 ± 3		U/Pb Zrn	(19)
Metapelitic enclave (M. Castelo)	498 ± 2		U/Pb Mnz	(14)
Metapelitic granulite (M. Castelo)	505 ± 2		U/Pb Zrn	(14)
Granulitic shear zone (M. Castelo)	483 ± 5		U/Pb Zrn	(21)
Garnet amphibolites (M. Castelo)	393.4 ± 35 (p.a.)		Ar/Ar Am	(21)
Paragneiss	493 ± 1 / 496 ± 3	2 samples	U/Pb Mnz	(16)
Migmatite	493 ± 2 / 484 ± 2	2 samples	U/Pb Mnz	(14)
Granulite	387 ± 5		U/Pb Zrn	(14)
Órdenes Complex Lower Allochthon				
Rocks	***Age (Ma)***	***Comment***	***Method***	***Author***
Paragneiss (Agualada)	346 ± 2		U/Pb Mnz	(22)
	341 ± 3		U/Pb Rt	(22)
Eclogite (Agualada)	351 ± 2		U/Pb Zrn	(23)
Felsic gneiss (Agualada)	493 ± 2		U/Pb Zrn	(23)
	372 ± 3		U/Pb Zrn	(23)
	352 ± 5		U/Pb Zrn	(23)

Bragança Complex Upper Allochthon				
Rocks	***Age (Ma)***	***Comment***	***Method***	***Author***
Eclogite like	509 to 430 (u.i.)		U/Pb Zrn	(1)
Eclogite	385 ± 1		U/Pb Zrn	(24)
	382 ± 2		U/Pb Rt	(24)

Table 4.1. Continue…

Malpica-Tui Complex Lower Allochthon				
Rocks	***Age (Ma)***	***Comment***	***Method***	***Author***
Orthogneiss (near Vigo)	466 ± 29	456 ± 25 *	Rb/Sr WR	(8)
	170 (l.i.) / 550 (u.i.)		U/Pb Zrn	(12)
Orthogneiss (Malpica/Noya)	462	452 *	Rb/Sr WR	(8)
Migmatitic augengneiss (Noya)	478 (l.i.)		U/Pb Zrn	(12)
Orthogneiss (Noya)	270 (l.i.) / 600 (u.i.)		U/Pb Zrn	(12)
Eclogite (La Pioza)	370 to 378	362 to 370 *	Rb/Sr Ms	(8)
	324 to 337	328 to 341 *	K/Ar Ms	(8)
	347 to 358	352 to 362 *	K/Ar Ms	(8)
	498 ± 6 / 494 ± 2 / 493 ± 3	3 samples	U/Pb Zrn	(23)
	437 / 398 /363 ± 10	3 samples	Ar/Ar Pg	(25)
	365 ± 1		Ar/Ar Phe	(25)
	357 ± 3 / 353 ± 2	2 samples	Ar/Ar Phe	(25)
	365		Rb/Sr Phe-Grt	(26)
Metagranodiorite	409		Ar/Ar Bt	(25)
Pg-Qtz-Ky vein	347 ± 12		Ar/Ar Pg	(25)
Amphibolite	358		Ar/Ar Am	(25)
Granodioritic orthogneiss	489 ± 4		U/Pb Zrn	(19)
Leucocratic gneiss	347 ± 6 / 341 ± 6 / 342 ± 6 / 303	4 samples (Syn-D2)	Ar/Ar Phe-Ms	(25)
	337 / 330 ± 8 / 330	3 samples (Syn-D3)	Ar/Ar Phe	(25)
Metasediment	304 ± 3 / 294	2 samples	Ar/Ar Ms	(25)
	371 ± 4 / 333 / 396 ± 12	3 samples		(25)
	384 ± 5			(25)
Micaschist (oceanic unit)	348 ± 8		Ar/Ar Phe	(25)
Metapelite (oceanic unit)	354 ± 1 / 354 ± 1 / 363 ± 2	3 samples	Ar/Ar Ms	(27)
Mylonite (oceanic unit)	337 ± 2		Ar/Ar Ms	(27)
Biotitic gneiss	469 ± 6		Rb/Sr WR	(28)
	457 ± 18		Rb/Sr WR	(7)
Alkaline orthogneiss	462±3		U/Pb Zrn	(19)
Peralkaline gneiss	466 ± 22		Pb/Pb Zrn	(29)
	370		U/Pb Zrn	(29)
	474 ± 4		U/Pb Zrn	(19)
Granodiorite	479 ± 2 (l.i.)		U/Pb Zrn	(26)
	352 ± 3		Rb/Sr WR-Pl-Bt	(26)
Alkali-granite orthogneiss	474±3		U/Pb Zrn	(19)
	490±3		U/Pb Zrn	(19)

(1) Peucat et al. (1990); (2) Fernández-Suárez et al., (2002); (3) Valverde Vaquero et al. (1996); (4) Ordóñez Casado et al. (2001); (5) Schäfer et al. (1993); (6) Bernard Griffiths et al. (1985); (7) Vogel et al. (1971); (8) Van Calsteren et al. (1979); (9) Fernández-Suárez et al. (2007); (10) Santos Zalduegui et al. (1996); (11) Dallmeyer and Tucker (1993); (12) Kuijper et al. (1982); (13) Priem et al. (1970); (14) Abati et al. (1999); (15) Dallmeyer et al. (1997); (16) Díaz García et al. (2010); (17) Castiñeiras et al. (2010); (18) Andonaegui et al. (2012); (19) Díez Fernández et al. (2012); (20) Abati et al. (2007); (21) Gómez Barreiro et al. (2006); (22) Abati and Dunning (2002); (23) Abati et al. (2010); (24) Roger and Matte (2005); (25) Rodríguez et al. (2003); (26) Santos Zalduegui (1996); (27) López-Carmona et al. (2014); (28) García Garzón et al. (1981); (29) Montero et al. (1998).

(ii) Occurrence of magmatic events nearly coeval with the HP/HT metamorphism that resulted in the formation of minor bodies of acid rocks through partial melting of acid/intermediate protoliths and metasediments.

(iii) Development of amphibolite- to greenschist-facies associations and localized intense shear deformations through a long time span 385-340 Ma ago, as recorded by dating on mica and amphibole in various lithotypes. These retrograde events are related to several episodes of uprising and tectonic emplacement of the complexes into its final position.

4.2. Sample description and results

Four samples from the Allochthonous Complexes have been dated. Two of them were collected from the Lower Allochthon of the Malpica-Tui Complex and the other two from the Upper Allocthon of the Cabo Ortegal Complex.

4.2.a. Lower Allochthon

Two types of eclogites from the Lower Allochton of the Malpica-Tui Complex have been investigated during the present research. Both rocks were collected from the same outcrop in the central part of the Malpica-Tui Complex (Figure 4.5).

Eclogites appear forming lenses or 'boudins' concordant to the regional foliation of the host rocks and, occasionally, they exhibit a distinct dyke-like tabular morphology. These rocks occur within the biotite orthogneisses, felsic gneisses and metasediments, but not in the (per)-alkaline orthogneisses. The foliation is parallel or subparallel to that in the enclosing rocks.

The geochemistry of those high-pressure rocks indicates that they derive from a calc-alkaline igneous suite (Rodríguez Aller, 2005). The common eclogite samples (MT-9619) might be related to a spinel-bearing coronitic gabbro as a tentative protolith whereas the other samples (Pioza-4) would be the result of the eclogitization of basic dykes crosscutting the previously mentioned gabbros. Both types of eclogitic rocks are spatially associated in the field, and their chemical composition is similar, suggesting that they may be products of the same magmatic evolution.

Both eclogitic types have been previously dated by Rodríguez et al. (2003) and Rodríguez (2005) using the $^{40}Ar/^{39}Ar$ technique on phengites and paragonites of those rocks, yielding age values of ca. 365-370 Ma for the high-pressure event, down to ca. 350 Ma on some samples that attest to retrograde overprinting. Calculated P-T conditions give maximum values of 26 kbar and 610 ^{o}C (Rodríguez, 2005). Although these rocks seem to have a homogeneous mineralogy at the outcrop scale, variations in the modal composition have been observed.

4.2.a.1. *MT-9619*

Common eclogites are medium- to fine-grained rocks that locally show a compositional layering and grain-size variations. These eclogites are mostly bimineralic and have a mineral assemblage in equilibrium composed basically of clinopyroxene (omphacite) and garnet with

minor amounts of quartz, rutile, white mica, zoisite and kyanite. Amphibole and albite occur as secondary minerals. These rocks show an oriented porphyroclastic microstructure (Figure 4.6a).

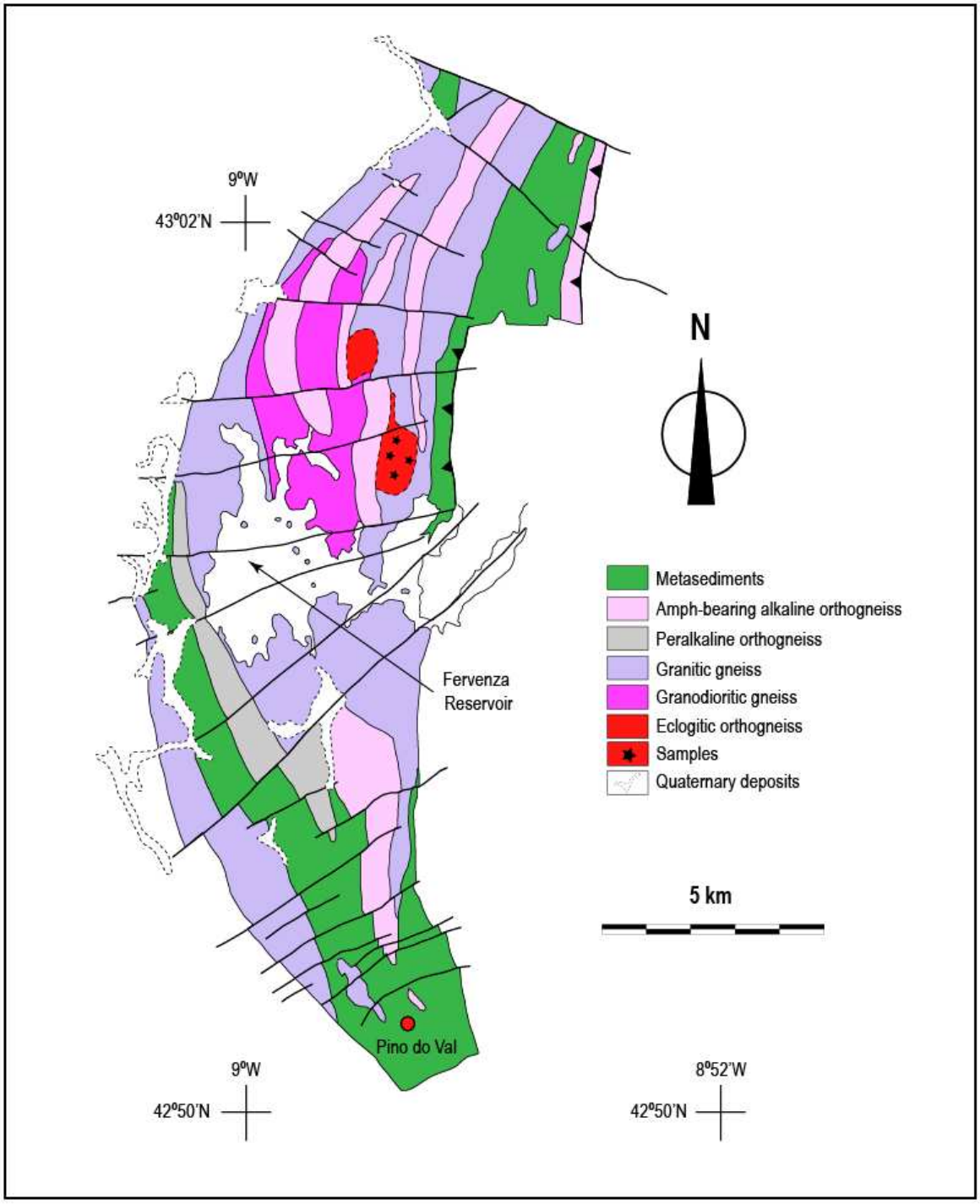

Figure 4.5. Detailed geological map of the northern sector of the Malpica-Tui Complex and sample locations. Modified after Gil Ibarguchi, 1995.

Clinopyroxene represents ca. 75 % of the rock. Two main clinopyroxene types may be differentiated: relict omphacite porphyroclasts with a grain size of ca. 1-5 mm and smaller grains (0.1-0.2 mm) that make up the matrix of the rock. The former is more or less equidimensional and

has xenomorphic morphologies (Figure 4.6a), whereas the latter is prismatic and shows a very clear shape-preferred orientation that contributes to define the macroscopic lineation recognised in the samples (Figure 4.6a-d). Omphacite porphyroclasts include numerous crystals of small prismatic rutile. The occurrence of irregular greenish areas with minute crystals of spinel within them is very common (Figure 4.6e and f). Omphacite exhibits deformational features such as undulose extinction and sigmoidal geometries in agreement with the shear sense criteria recognised in the area, indicating a top-to-the-N relative displacement of the hanging wall blocks. This type of clinopyroxene occurs only in certain domains of the rock, whereas in other parts they seem to have recrystallised to an oriented polycrystalline aggregate (Figure 4.6a-g). Some of these aggregates are surrounded by coronitic garnet (Figure 4.6b and c), which may indicate that this textural feature could be prior to the recrystallisation process affecting the rock. Both types of clinopyroxene show evidence of retrogression to amphibole, and along with garnet, occur as non-completely replaced inclusions within large amphibole crystals (Figure 4.6h).

Garnet shows a grain size ranging between 0.15-0.80 mm. This phase exhibits very well-developed faces and a clear shape-preferred orientation in accord with that marked by the rest of the constituent minerals of the high-pressure mineral assemblage (Figure 4.6b and c). Some of these crystals form part of coronitic microstructures around omphacite porphyroclasts or omphacite polycrystalline aggregates that, in turn, show elongated morphologies parallel to the orientation of the foliation (Figure 4.6b and c). Most of the garnets are polyphasic and show a concentric textural zoning marked by relatively clean cores surrounded by an intermediate zone rich in inclusions and an outer clear rim (Figure 4.6d). Zoisite modal proportions are very low in the MT samples (< 0.4 %). When they can be found it is clear the shape-preferred orientation marked by this phase parallel to that of the rest of the primary phases that make up the mineral assemblage in equilibrium. Rutile occurs in these samples as minute inclusions within garnet and clinopyroxene (Figure 4.6d) or as individual grains with a larger grain size up to 0.3 mm in the matrix of the rock (Figure 4.6g). Amphibole appears as large crystals up to 5 mm. It includes all the primary phases and shows a strong shape-preferred orientation parallel to that of the primary minerals of the high-pressure mineral assemblage (Figure 4.6h). Amphibole replaces clinopyroxene from rim to core. Scarce white mica crystals have also been observed with apparent stable textures in contact with garnet and pyroxene.

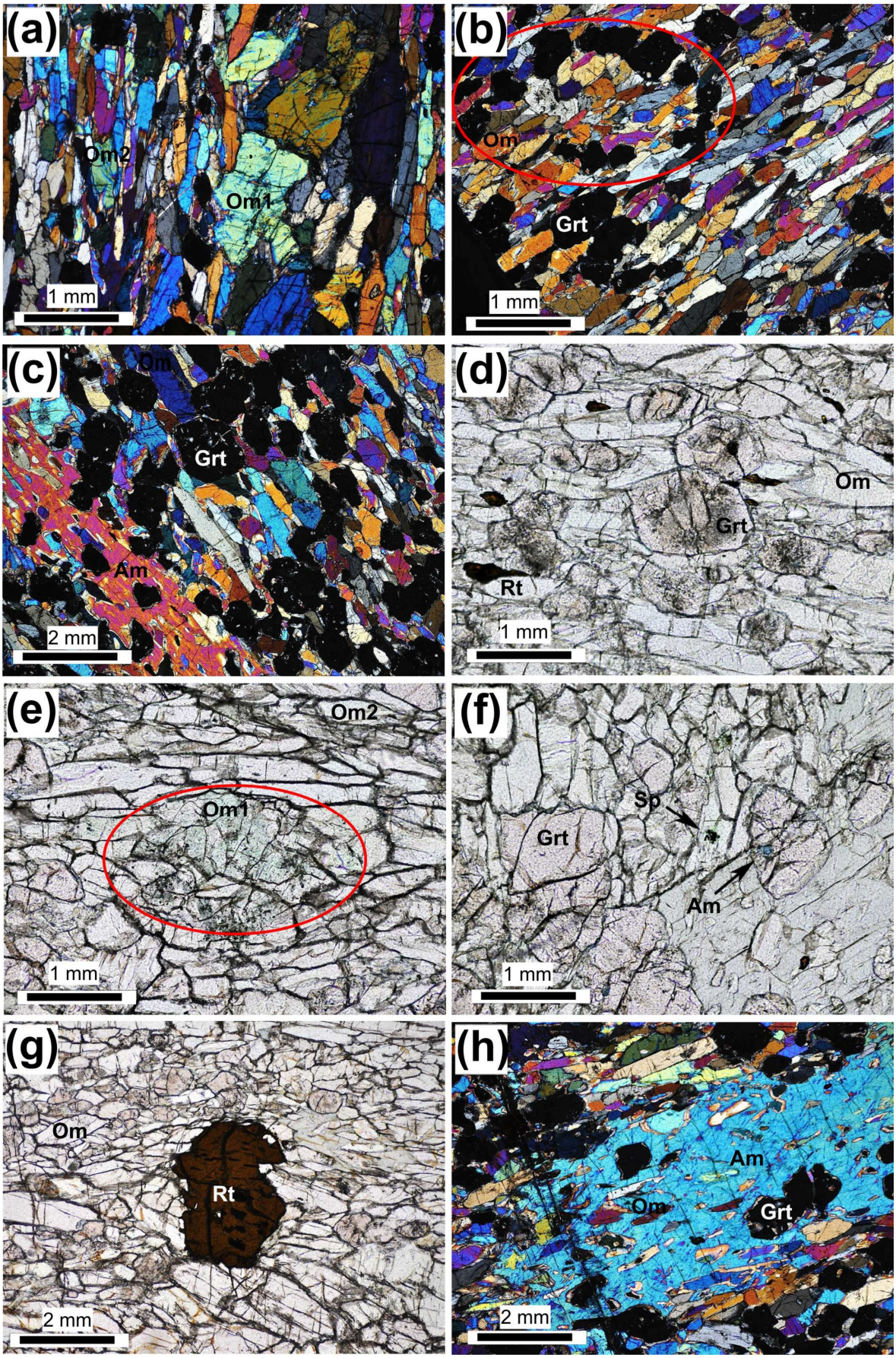
(a)
Om2
Om1
1 mm
(b)
Om
Grt
1 mm
(c)
Om
Grt
Am
2 mm
(d)
Om
Grt
Rt
1 mm
(e)
Om2
Om1
1 mm
(f)
Sp
Grt
Am
1 mm
(g)
Om
Rt
2 mm
(h)
Am
Om
Grt
2 mm

Figure 4.6. Photomicrographs of MT-9619 eclogites. All the sections correspond to the XZ structural plane. **(a)** Relict and xenomorphic Om1 omphacite (right sector of the photomicrograph) in contact with recrystallized prismatic Om2 clinopyroxene (left sector). Crossed nicols. **(b)** Red circle indicates the localization of a polycrystalline omphacite aggregate surrounded by coronitic garnet. This textural feature might be inherited from the protolith, prior to the recrystallisation process affecting the rock. In sections where garnet is not present the microstructure can be identified as nematoblastic. Crossed nicols **(c)** Porphyroclastic microstructure. Note the clear shape-preferred orientation shown by the prismatic omphacite (Om) parallel to the orientation of the secondary amphibole (Am) and how some of the garnet (Grt) crystals exhibit morphologies parallel to the orientation of the foliation trace. Crossed nicols. **(d)** Concentric textural zoning in garnet marked by relatively clean cores surrounded by an intermediate zone rich in minute rutile inclusions and an outer clear rim. Note the occurrence of oriented rutile (Rt) grains in the matrix parallel to the lineation. Parallel nicols. **(e)** Irregular greenish areas within relict Om1 omphacite porphyroclasts (red circle). These areas include minute crystals of spinel. Parallel nicols. **(f)** Spinel (Sp) within omphacite and blue amphibole included in garnet. Parallel nicols. **(g)** Sigmoidal geometry shown by the polycrystalline aggregate of omphacite around rutile. Parallel nicols. **(h)** Non-completely replaced inclusions of prismatic omphacite and garnet within large secondary amphibole crystals. Crossed nicols.

4.2.a.2. *Pioza-4*

These samples show a tabular morphology and sharp contacts with the host rocks in field outcrops. They are likely derived from basic dykes and are generally finer grained and less retrogressed than the previous common eclogite type. They exhibit a more heterogeneous mineralogy, with primary clinopyroxene, garnet, quartz, zoisite, phengite and minor rutile, apatite and zircon making up the high-pressure mineral assemblage in equilibrium. Amphibole also occurs as a secondary phase.

Clinopyroxene crystals display a grain size up to 0.6 mm, they are prismatic in shape and show a clear shape-preferred orientation, defining the lineation observed at the mesoscopic scale. Garnet shows a grain size up to 0.70 mm, well developed faces (Figure 4.7a-d) and in some cases a weak shape-preferred orientation parallel to that of the rest of the constituent minerals of the high-pressure mineral assemblage. As in the common eclogites, clear cores, intermediate zones rich in inclusions and relatively clean outer rims can be observed in garnet (Figure 4.7 a and c). In some cases the inclusions within the crystal tend to be aligned in accord with the preferred orientation marked by the rest of the minerals in the matrix (Figure 4.7a). Garnet also develops planar fractures subperpendicular to the elongation direction as well as interdigitating sutures between adjacent grains indicative of pressure-dissolution processes (Figure 4.7b and c). Quartz (up to 10 % in volume) appears as elongated crystal aggregates parallel to the rest of the high-pressure minerals that make up the mineral assemblage in equilibrium (Figure 4.7d and e) or as inclusions within secondary amphiboles. Undulose extinction and subgrains with rectangular morphologies and subgrain boundaries parallel and perpendicular to the lineation direction have also been recognised. Zoisite shows a very clear shape-preferred orientation parallel to that

depicted by clinopyroxene, garnet, quartz aggregates and white mica (Figure 4.7d and e). Most crystals show the development of planar fractures perpendicular to the elongation direction of the grains. Whica mica shows a shape-preferred orientation parallel to the foliation of the rock (Figure 4.7b, c, e and f), a grain size of around 0.4 mm and in some cases deformational features such as mica-fish and bookshelf microstructures (Figure 4.7f) that indicate a top-to-the-N tectonic displacement of the hanging wall blocks. It also appears as inclusions within secondary amphiboles showing a shape-preferred orientation parallel to that of the minerals in the matrix. Rutile occurs in the same fashion as that of MT samples. When it is enclosed within garnet it occurs as minute crystals and parallels the primary constituent minerals. Nevertheless, when it forms part of the matrix, occurs as aggregates that contribute to the development of the preferred orientation shown by these rocks (Figure 4.7c). Amphibole in these samples is a secondary phase formed as a consequence of the static replacement undergone by the primary clinopyroxene. It includes all the primary high-pressure phases exhibiting the same shape-preferred orientation as that marked by the outer phases. Among them, it is possible to recognise the presence of relict pyroxene with retrogressed borders as incomplete products of the amphibolitization process (Figure 4.7e).

4.2.a.3. *Results*

Mineral separates and whole-rock samples of eclogites were processed for Rb-Sr, Sm-Nd and Lu-Hf geochronology following the methods explained in the previous chapter. ^{176}Lu-^{179}Hf and ^{149}Sm-^{150}Nd mixed spikes, as well as independent ^{87}Rb and ^{86}Sr tracers were used.

Both eclogite samples have been analysed for their Lu-Hf and Sm-Nd isotope compositions, using one whole rock aliquot as well as garnet and pyroxene mineral separates. The results of the Lu-Hf and Sm-Nd measurements are given in Table 4.2 and are illustrated in Figure 4.8. Isochron regressions are calculated using ISOPLOT v.2.49 (Ludwig, 2001) and λ ^{176}Lu values of 1.867×10^{-11} y^{-1} (Scherer et al., 2001, Söderlund et al. 2004).

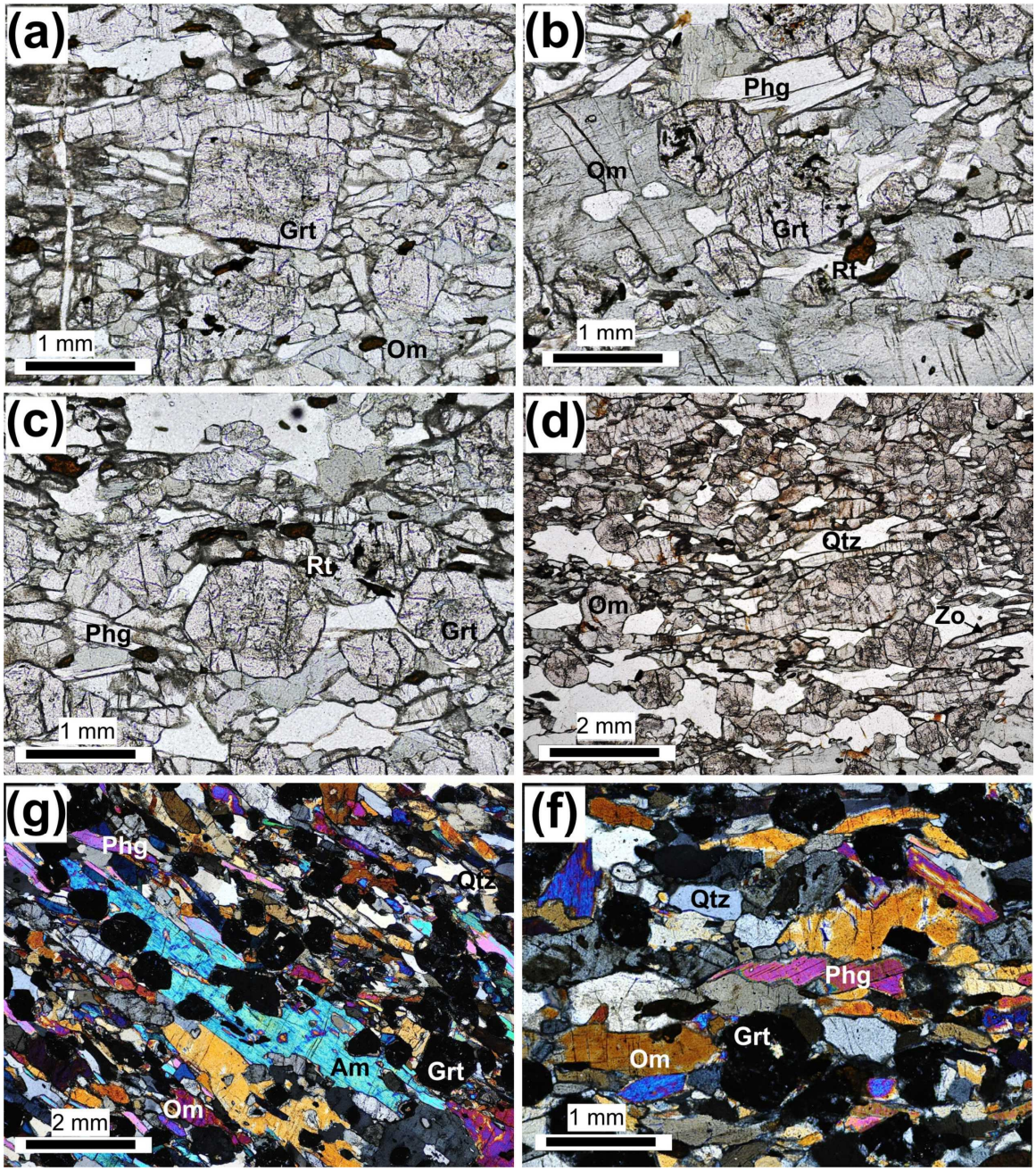

Figure 4.7. Photomicrographs of Pioza-4 eclogites. All the sections correspond to the XZ structural plane. **(a)** Garnet aligned parallel to the foliation trace. Note the textural zoning with clear cores, intermediate zones rich in inclusions and relatively clean outer rims. Parallel nicols. **(b)** Planar fractures in garnet perpendicular to the elongation direction and interdigitating sutures between adjacent grains. Parallel nicols. **(c)** Rutile aggregates running parallel to the shape-preferred orientation shown by the constituent minerals making up the mineral assemblage in equilibrium. Parallel nicols. **(d)**. Zoisite (Zo) grains depict a very clear shape-preferred orientation parallel to that exhibited by clinopyroxene, garnet, quartz (Qtz) aggregates and phengite (Phg). Note the elongated geometry of the quartz aggregates parallel to the foliation trace. Parallel nicols. **(e)**. Large secondary amphibole including the primary phases of the eclogitic mineral assemblage. Phengite shows a shape-preferred orientation parallel to the foliation of the rock. Crossed nicols. **(f)** Bookshelf microstructures in phengite coherent with a top-to-the-N tectonic displacement of the hanging wall blocks. Crossed nicols.

The Hf content of the whole-rock samples is almost the same in MT-9619 (2.24 $\mu g.g^{-1}$) and Pioza-4 (2.37 $\mu g.g^{-1}$). However, a significant difference has been found in the Lu concentration (0.188 and 1.074 $\mu g.g^{-1}$, respectively). As expected, garnets have a low content of Hf (0.151 and 0.177 $\mu g.g^{-1}$) and a higher concentration of Lu (1.295 and 1.081 $\mu g.g^{-1}$ in MT-9619 and Pioza-4). The $^{176}Lu/^{177}Hf$ value of the garnets is ca. 1, being higher for the sample MT-9619. Pyroxenes and whole-rock samples display a very low $^{176}Lu/^{177}Hf$ ratio, ranging from 0.012 to 0.064. The whole rock-garnet-omphacite isochron for sample MT-9619 yields an age of 377.4 ± 1.4 Ma, and the statistic (MSWD of 0.107) suggests full sample-spike equilibrium during digestion (especially critical in mineral separates). A three-point age for Pioza-4 has been considered meaningless because of the large differences in $^{176}Hf/^{177}Hf$ with similar $^{176}Lu/^{177}Hf$ (between whole-rock and omphacite). As it will be explained below, whole-rock was discarded, obtaining a Lu-Hf age of 373.9 ± 3.9 Ma from the garnet-omphacite isochron .

The Nd content of the whole-rock samples varies from 3.4 $\mu g.g^{-1}$ measured in MT-9619 to 11.8 $\mu g.g^{-1}$ in Pioza-4, though both rocks show similar $^{147}Sm/^{144}Nd$ ratios (0.1662 and 0.1692, respectively). The garnet fractions display similar Sm concentrations whereas the Nd content vary from 0.3 $\mu g.g^{-1}$ in MT-9619 to 0.8 $\mu g.g^{-1}$ in Pioza-4, resulting in a significant difference in $^{147}Sm/^{144}Nd$ values. In fact, the garnet separates from Pioza-4 show a very similar $^{147}Sm/^{144}Nd$ ratio to that obtained for the whole-rock. The three-point isochron for sample MT-9619 yields an age of 373.9 ± 5.9 Ma, very close to that obtained using the Lu-Hf system. The Sm-Nd age determined for Pioza-4 was 244 ± 31 Ma. In that case, due to a mistake during the sample preparations, no tracer was added to the clinopyroxene mineral separate, and thus, the isochron has been plotted considering the garnet and bulk rock analyses. The meaning of this younger age will be discussed below.

Rb-Sr isotope compositions have also been determined in both eclogites. Whole rock-amphibole and whole rock-muscovite pairs were chosen for MT-9619 and Pioza-4, respectively, due to the modal proportions of each mineral in each sample. The results obtained for Rb-Sr measurements are given in Table 4.3 and are illustrated in Figure 4.9. Isochron regressions were also calculated using ISOPLOT v.2.49 (Ludwig, 2001), considering the ^{87}Rb decay constant of Villa et al. (2015) (1.3972×10^{-11} y^{-1}). This constant is similar to recent values determined by Kossert (2003), Nebel et al. (2011) or Rotenburg et al. (2012), and in the case of samples with ages ranging between 350-400 Ma it produces ages ca. 6 to 10 Ma older than those calculated using the old decay constant of Steiger and Jäger (1977).

Table 4.2. Sm–Nd and Lu-Hf isotope compositions of the whole rocks and mineral separates.

Label	*Sample wt (mg)*	*Sm ($\mu g.g^{-1}$)*	*Nd ($\mu g.g^{-1}$)*	*$^{147}Sm/^{144}Nd$[a]*	*$^{143}Nd/^{144}Nd$[b]*	*Age (Ma)*	*Initial $^{143}Nd/^{144}Nd$*
Pioza-4							
Whole-rock	99.6	3.23	11.8	0.1662	0.512600 ± 05	244 ± 31	0.512335 ± 38
Garnet	188.9	0.25	0.8	0.2013	0.512656 ± 05		
Omphacite[d]	62.7	-	-	-	0.512607 ± 06		
MT-9619							
Whole-rock	98.2	0.95	3.4	0.1692	0.512599 ± 05	373.9 ± 5.9	0.512185 ± 10
Garnet	195.2	0.24	0.3	0.4357	0.513260 ± 15		
Omphacite	87.2	0.31	0.5	0.4079	0.513180 ± 08		

Label	*Lu ($\mu g.g^{-1}$)*	*Hf ($\mu g.g^{-1}$)*	*$^{176}Lu/^{177}Hf$[b]*	*$^{176}Hf/^{177}Hf$[b]*	*Age (Ma)*	*Initial $^{176}Hf/^{177}Hf$*
Pioza-4						
Whole-rock	1.07	2.37	0.064	0.282890 ± 06	373.9 ± 3.9	0.283517 ± 61
Garnet	1.08	0.18	0.869	0.291443 ± 25		
Omphacite	0.06	0.15	0.058	0.282981 ± 27		
MT-9619						
Whole-rock	0.19	2.25	0.012	0.282848 ± 13	377.4 ± 1.4	0.2828056 ±65
Garnet	1.30	0.15	1.221	0.289602 ± 10		
Omphacite	0.06	0.32	0.026	0.283920 ± 58		

a) Uncertainties for $^{147}Sm/^{144}Nd$ for the purpose of regressions and calculations is estimated to be 0.2 %.

b) Errors in Nd and Hf isotope ratios are expressed as 2SE from internal measurements and refer to least significant digits.

c) Uncertainties for $^{176}Lu/^{177}Hf$ for the purpose of regressions and calculations is estimated to be 0.2 %.

d) Sm-Nd tracer was not added, it was forgotten during sample manipulation.

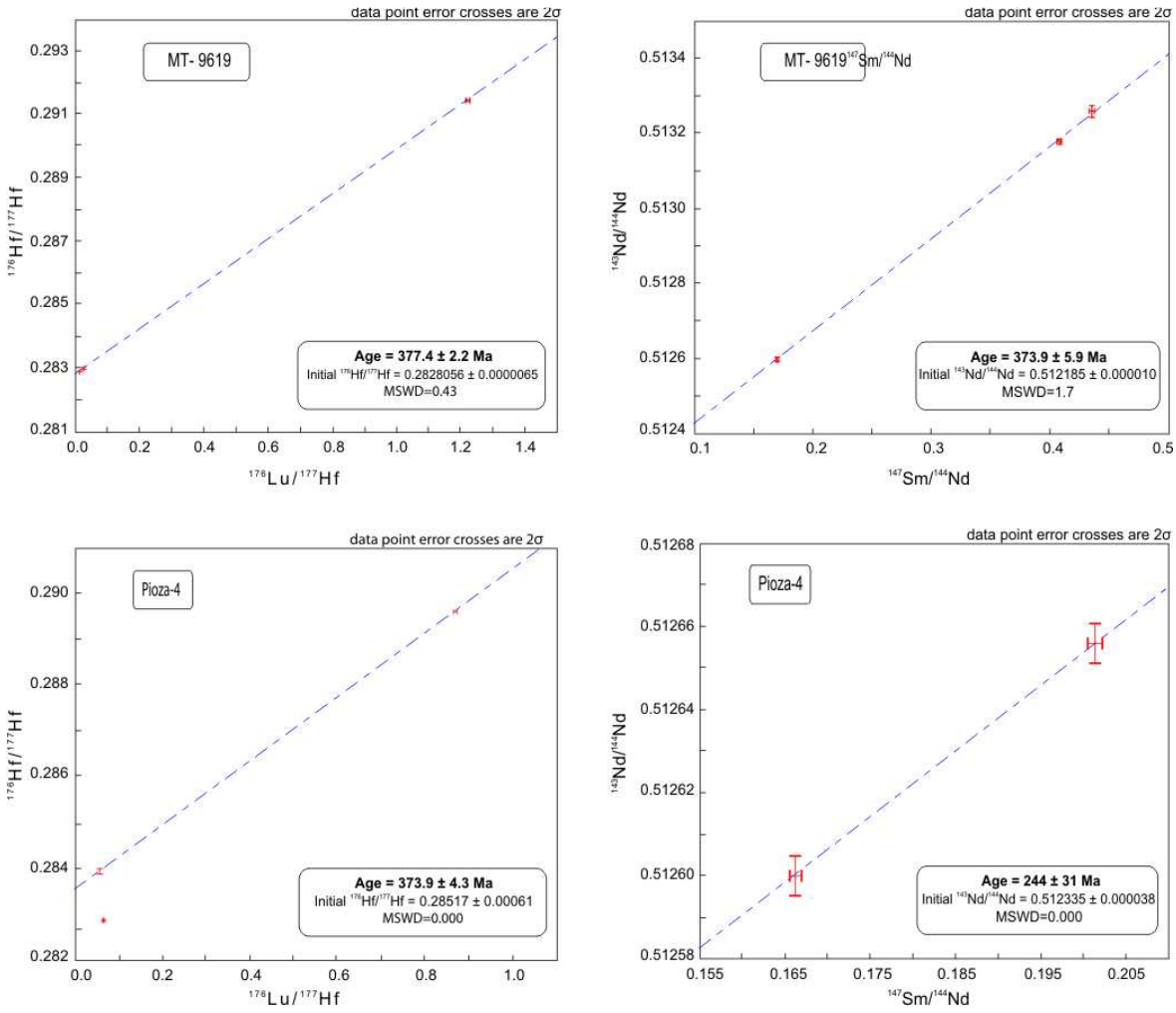

Figure 4.8. Lu-Hf and Sm-Nd isochrons from the studied eclogites.

The Rb content in MT-9619 whole-rock is very low, and consequently, since there is almost no Rb to capture/fractionate, the analysed amphibole fractions are also poor in Rb. The whole-rock gives values of 0.42 $\mu g.g^{-1}$ of Rb, whereas the concentration of both amphibole fractions is slightly above 1.5 $\mu g.g^{-1}$. The $^{87}Sr/^{86}Sr$ ratio in the amphibole-2 fraction is lower than the $^{87}Sr/^{86}Sr$ ratio in the whole-rock. As the $^{87}Rb/^{86}Sr$ is higher in amphibole, the isochron between these two fractions would result in negative ages and therefore, the amphibole-2 fraction was discarded. Thus, the whole rock-amphibole-1 pair was used, obtaining a Rb-Sr age of 360 ± 26 Ma for this sample. The high error is highly influenced by the close values of the $^{87}Sr/^{86}Sr$ ratios.

Table 4.3. Rb-Sr isotope compositions of the whole rocks and mineral separates.

Label	*Sample wt (mg)*	*Rb (µg.g^{-1})*	*Sr (µg.g^{-1})*	*^{87}Rb/^{86}Sr^{a}*	*^{87}Sr/^{86}Sr*	*2σ error (%)*	*Age (Ma)*	*Initial ^{87Sr}/^{86}Sr*
Pioza-4								
Whole-rock	50.1	15.5	166.1	0.2392	0.705908	0.005	349.1 ± 2.6	0.704739 ± 39
Muscovite-1	37.2	200.2	103.6	5.6450	0.732445	0.001		
Muscovite-2	40	232.3	125.1	5.4343	0.731185	0.003		
MT-9619								
Whole-rock	51.3	0.42	40.4	0.0300	0.706032	0.002	360 ± 26	0.705881 ± 19
Amphibole-1	53	1.78	51.4	0.1003	0.706386	0.003		
Amphibole-2	42	1.62	63.7	0.0736	0.705675	0.005		

a) Uncertainties for ^{87}Rb/^{86}Sr for the purpose of regressions and calculations is estimated to be 0.5 %.

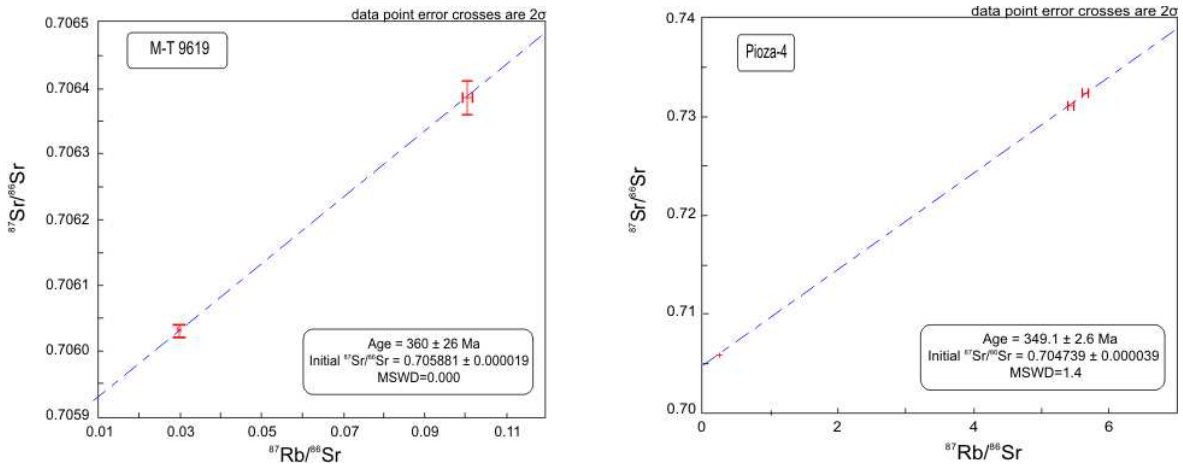

Figure 4.9. Rb-Sr isochrons from the studied eclogites.

Pioza-4 is richer in Rb, with concentrations of 15.5 µg.g^{-1}, and that is probably the reason of muscovite growth. Muscovite with Rb contents higher than 200 µg.g^{-1} strongly captures Rb and therefore, ^{87}Rb/^{86}Sr ratios are usually high (>5). The obtained three-point isochron yields a precise age of 349.1 ± 2.6 Ma.

Results obtained by Lu-Hf, Sm-Nd and Rb-Sr, as well as their geological significance will be discussed below.

4.2.b. Upper Allocthon

Four samples from two different rock types have been dated in the Upper Allochthon of the Cabo Ortegal Complex: kyanite-bearing eclogites (Mendia, 2000) and high-pressure migmatitic gneises (Puelles, 2004; Puelles et al., 2005).

4.2.b.1. *Ky-bearing eclogites*

The Cabo Ortegal eclogite unit forms a N-S striking band 0.1-2 km wide and over 15 km long. Tectonic contacts separate the eclogite band from the underlying Banded Gneisses formation and the overlying granulites (Figure 4.10). Three types of eclogites have been differentiated within this unit (Gil Ibarguchi et al., 1990; Mendia, 2000): (i) N-MORB type eclogites, constituting the central part of the unit, (ii) kyanite-bearing eclogites, occurring essentially within ductile shear zones bounding the main tectonic slices and developed under eclogite-facies conditions, and (iii) minor Fe- and Ti-rich eclogites. The three eclogite types are co-genetic, where the kyanite-rich eclogites would represent cumulates from the tholeitic series, rich in plagioclase contents and with positive Sr and Eu anomalies (Mendia, 2000). Since these kyanite-rich eclogites are richer in Mg and Al and have lower REE and trace element contents than the N-MORB types, their origin has been related to plagioclase-rich cumulates of troctolitic composition (Gil Ibarguchi et al., 1990).

The kyanite-bearing eclogite have been previously dated by Ordóñez Casado et al. (2001) using the SHRIMP technique on zircons. The results obtained in in five magmatic domains on five zircon grains yielded a mean age of 469 ± 9 Ma, whereas four spots from high luminescent rim domains of three zircon grains provided an average age of 380 ± 14 Ma. Similar data have been published in the literature for the N-MORB eclogites (Table 4.1), although in the first dating studies, the 470-480 Ma event was interpreted as the age of the HP–HT metamorphism (Bernard-Griffiths et al., 1985, Peucat et al., 1990). Mendia (2000) carried out the geothermobarometric study of these rocks, obtaining values of 780-800 ^{o}C and a minimum pressure of 22 kbar, although values as high as 25-28 kbar might have been achieved.

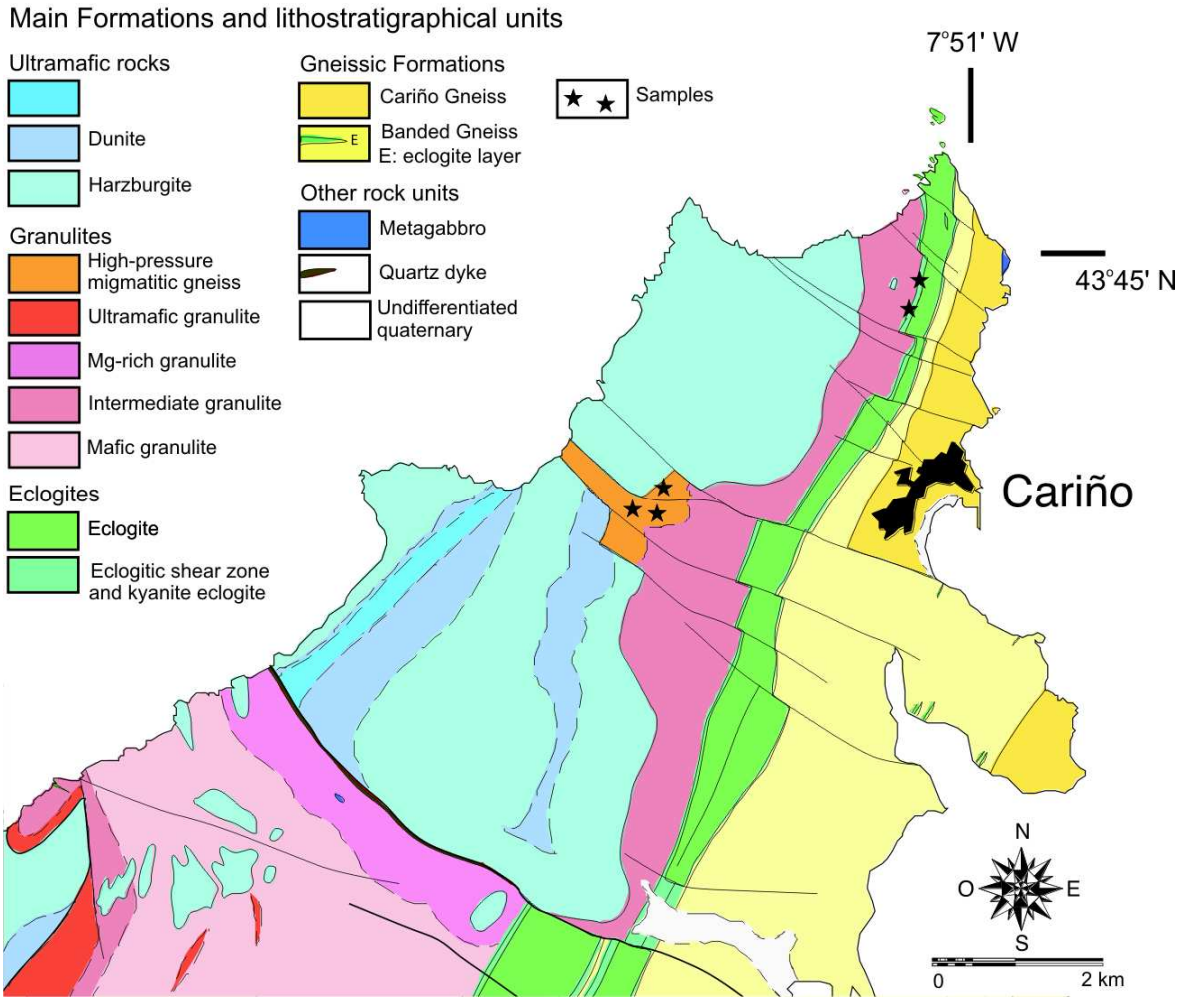

Figure 4.10. Detailed geological map of the northernmost area of the Cabo Ortegal Complex. The location of the collected samples is indicated by stars. Modified after Gil Ibarguchi et al. (2000) and Ábalos et al., (2000).

The samples studied in the present work were collected from the northern part of the eclogitic band (Figure 4.10). This type of eclogite shows a centimetric compositional banding parallel to the tectonic banding that can be observed at the outcrop scale. The compositional banding is determined by the different concentration of the constituent minerals, such as clinopyroxene, kyanite, amphibole, zoisite and quartz. Different degrees of deformation and retrogression can be detected. Both fresh (OAXZ-2) and deformed (CO-39) Ky-bearing eclogites have been considered in this study.

a. OAXZ-2

The fresh lithotype is lighter in colour than the surrounding rocks (N-MORB-type eclogites and granulites) due to the abundance of kyanite and the lighter green colour of the primary pyroxene. Pyroxene may appear forming elongated polycrystalline aggregates of over 3-5 cm,

interpreted as pseudomorphs after previous large pyroxenes (Mendia, 2000, Figure 4.11a). The sample is a medium- to coarse-grained rock with an oriented granonematoblastic microstructure. It is composed of garnet, clinopyroxene, amphibole and kyanite, with minor (and not always present) zoisite, quartz, rutile, zircon and apatite (Figure 4.11b). The occurrence of white mica has been also described in this rock (Mendia, 2000), though not observed in the studied samples.

Clinopyroxene (omphacite) is the most abundant mineral, representing ca. 50 % of the sample. It appears as idiomorphic elongated crystals, with a grain size up to 4 mm and also as primary inclusions within garnet or as poikiloblastic crystals including the matrix minerals. It shows undulose extinction reflecting the accommodation of intracrystalline deformation. Sometimes this phase shows a more intense green colour (Figure 4.11c and d), attributed to a higher content in chromium (even 6 % Cr_2O_3, Mendia, 2000). Garnet (up to 30 %) occurs mainly as subidiomorfic crystals with a variable grain size from 1 mm to near 1 cm (Figure 4.11b, e and h). In some cases it can be observed that several crystals coalesced to form larger grains. This mineral depicts a clear compositional zoning under the microscope and encloses all the matrix minerals, with zoisite and quartz as the most abundant inclusions (Figure 4.11e and h). The occasional occurrence of radial cracks around the quartz inclusions (Figure 4.11e) has been interpreted as coesite pseudomorphs (Schmadicke, 1991) or due to the partial melting of the eclogites. Similar fractures have been recognised in the pyroxenes. As stated above, the presence of kyanite is the most revealing feature of these rocks. This phase constitutes up to 10% of the rock and two kyanite types have been distinguished: (i) rounded grains with a grain size up to 0.4 mm that concentrate defining almost monomineralic layers in these rocks and (ii) poikiloblastic crystals that include the matrix minerals and may attain a grain size of 3 mm (Figure 4.11f). Some of the kyanites exhibit a blueish colour, indicating a high content in chromium. In the border of some of these crystals, zoisite rims are present. Amphibole is subidiomorphic and seems to be in equilibrium with the rest of the matrix minerals (Figure 4.11g). Low proportions of zoisite can be found with a clear shape-preferred orientation phase parallel to that of the rest of the primary phases that make up the mineral assemblage in equilibrium. Rutile occurs in these samples as minute inclusions within garnet and clinopyroxene (Figure 4.11h) showing the same orientation as the surrounding minerals.

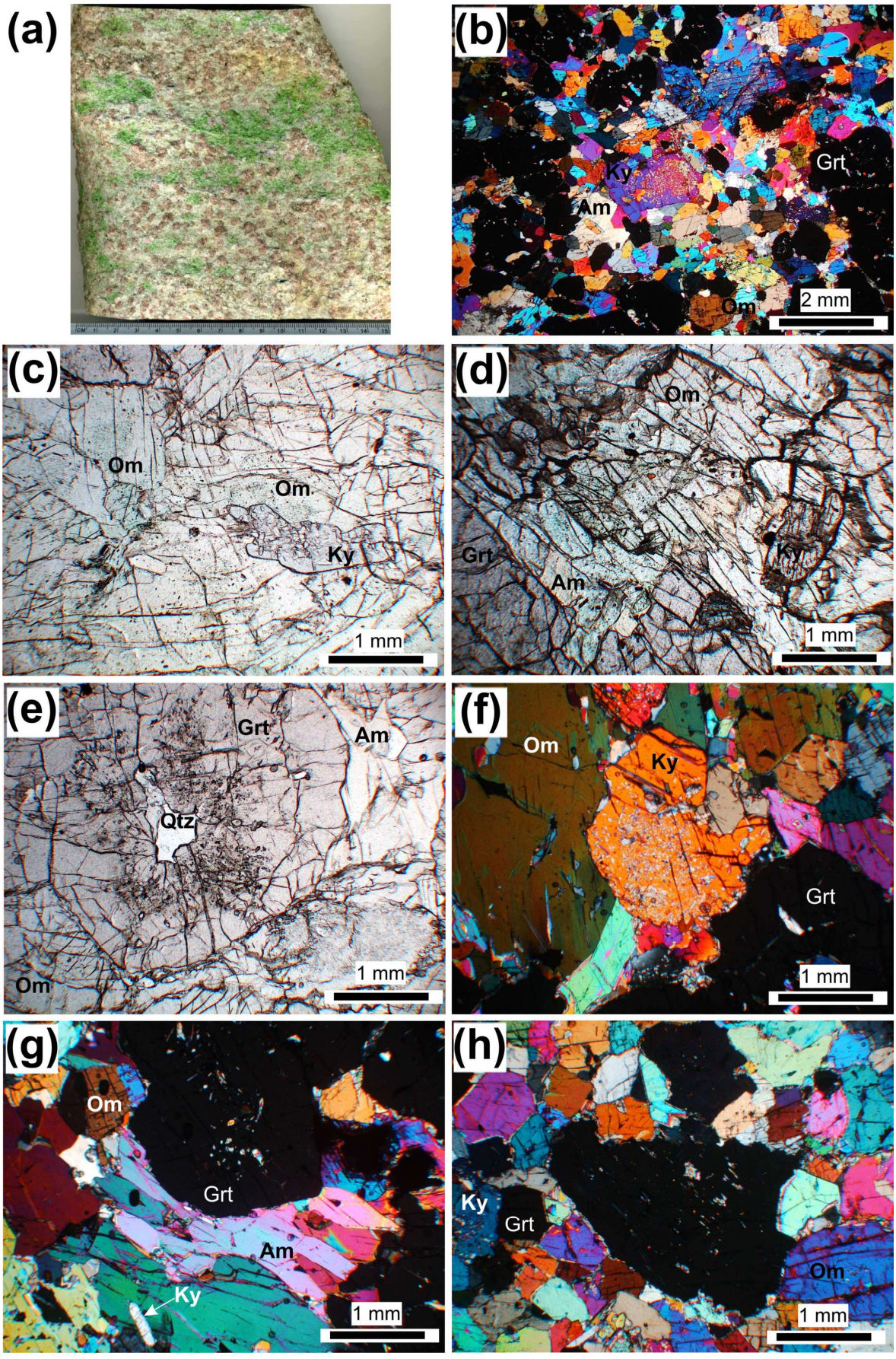
(a)
(b)
Grt
Ky
Am
Om
2 mm
(c)
Om
Om
Ky
1 mm
(d)
Om
Grt
Ky
Am
1 mm
(e)
Grt
Am
Qtz
Om
1 mm
(f)
Om
Ky
Grt
1 mm
(g)
Om
Grt
Am
Ky
1 mm
(h)
Ky
Grt
Om
1 mm

Figure 4.11. Hand specimen and photomicrographs of OAXZ-2 eclogites. All the sections correspond to the XZ structural plane. **(a)** Hand specimen of eclogite. Note the green colour of the elongated polycrystalline aggregates of omphacite. **(b)** Oriented granonematoblastic texture observed in the sample. Crossed nicols. **(c)** and **(d)** Note the occurrence of greenish omphacite and bluish kyanite crystals in contact. The presence of these shades of green and blue is due to the presence of chromium in the crystal lattice. Parallel nicols. **(e)** Large quartz inclusion within garnet. Note the radial fractures in the garnet. Parallel nicols. **(f)** Poikiloblastic kyanite, including the matrix minerals. Crossed nicols. **(g)** Elongated amphibole crystals in equilibrium with the others minerals. Crossed nicols. **(h)** Inclusions of minute rutile within omphacite. Inclusions are parallel to the orientation of the main constituent minerals. Crossed nicols.

b. CO-39

These strongly retrogressed eclogites were first noted by Vogel (1967) and named 'doubtful paragneiss'. The main structural feature of these eclogites is the occurrence of a pervasive penetrative mylonitic foliation (Figure 4.12a-d). The significant reduction of the grain size of all the minerals in the matrix as the result of the deformation accommodated in these rocks, and the occurrence of large centimetric garnet crystals, even larger than 5 cm, can be easily observed at all scales, from the outcrop to the microscope (Figure 4.12a-c). Garnet is present as idiomorphic or rounded crystals enclosing quartz, zoisite, clinopyroxene or amphibole, although kyanite, rutile and apatite may also occur (Figure 4.12b). Kyanite, clinopyroxene, muscovite and amphibole appear both as porphyrocrystals or as small grains making up the matrix of the rock,. Elongated quartz ribbons are also common in those areas sheltered by garnets (Figure 4.12c). The active deformation and retrogression undergone by these rocks led to the amphibolitization and symplectitization of the primary clinopyroxene, kyanite and phengite (Figure 4.12d) and the development of relevant deformational features.

c. Results

Both types of eclogites have been analysed in order to determine their Rb-Sr isotope compositions. The whole rock-amphibole pair was chosen for the sample OAXZ-2 since the presence of mica was not detected, whereas the whole rock-muscovite pair was considered for CO-39, where large muscovite crystals could be easily separated. The results obtained for the Rb-Sr measurements are given in Table 4.4 and are illustrated in Figure 4.13. Although the Rb-Sr data published by Peucat et al. (1990) were not obtained from the eclogites but from the surrounding high-pressure gneisses, they have been recalculated (Table 4.4) using the new ^{87}Rb decay constant of Villa et al. (2015). Those data of Van Calsteren et al. (1979) are assumed to be significant. The ^{87}Rb decay constant in that work was 1.39 x 10^{-11} y^{-1}, close to the value used in the current study. Recalculated data produce ages ca. 5 Ma older than those originally published.

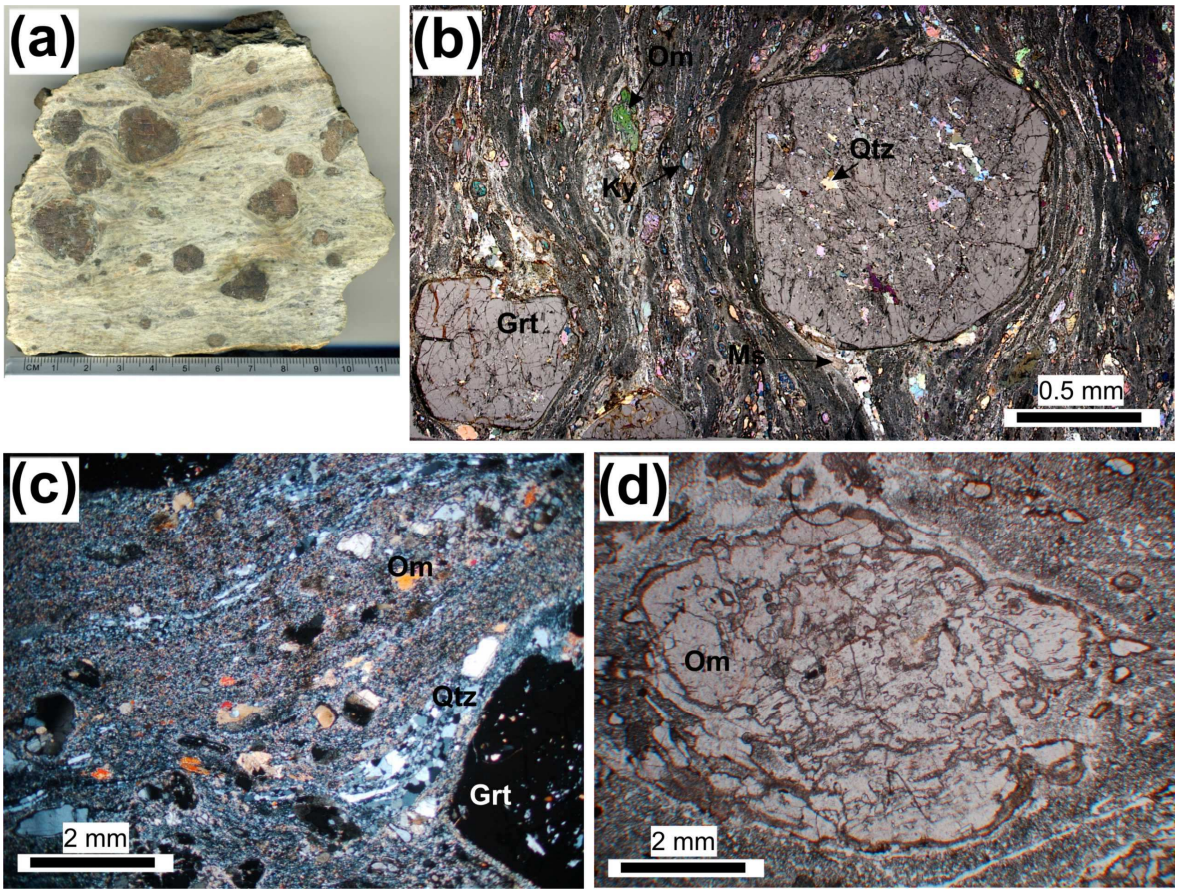

Figure 4.12. Hand specimen, thin-section and photomicrographs of CO-39 eclogites. All the sections correspond to the XZ structural plane. **(a)** Hand specimen. Note the penetrative mylonitic folitation and the centimetric size of garnet. **(b)** Image of a studied thin-section. Note the fine-grained matrix and the kyanite (Ky), omphacite (Om), muscovite (Ms) and garnet (grt) porphyroclasts. Garnet encloses the matrix minerals. **(c)** General photomicrograph of the sample. Garnet (Grt) and omphacite (Om) porphyroclasts wrapped in the matrix. Note the development of quartz ribbons in those areas sheltered by garnets. Parallel nicols. **(d)** Omphacite (Om) porphyroclast surrounded by an amphibolitic corona. Parallel nicols.

As it happened with the sample MT-9619 from the Lower Allochthon, the $^{87}Sr/^{86}Sr$ ratios measured for the amphiboles of the fresh Ky-bearing eclogite (OAXZ-2) are close to the $^{87}Sr/^{86}Sr$ ratio of the sample. This fact, along with the low differentiation of the Rb between Whole-rock and amphibole, leads to a significant error when plotting the results. The three-point isochron for this sample yields an age of 363 ± 43 Ma.

The deformed kyanite-bearing eclogite (CO-39) is richer in Rb, with a concentration value of 16.6 $\mu g.g^{-1}$. That is likely to be the main feature controlling the growth of muscovite in this sample and not in the fresh eclogite. The Rb content in muscovite ranges from 28.7 $\mu g.g^{-1}$ to 110.7 $\mu g.g^{-1}$, and the $^{87}Rb/^{86}Sr$ ratio varies from 1.05 to 2.1. The Rb-Sr age obtained for this sample was calculated using a four-point isochron and gives a value of 368 ± 4 Ma.

Table 4.4. Rb-Sr isotope compositions of the whole rocks and mineral separates.

Label	*Sample wt (mg)*	*Rb ($\mu g.g^{-1}$)*	*Sr ($\mu g.g^{-1}$)*	*$^{87}Rb/^{86}Sr^a$*	*$^{87}Sr/^{86}Sr$*	*2σ error (%)*	*Age (Ma)*	*Initial $^{87Sr}/^{86}Sr$*
CO-39								
Whole-rock	52.3	16.6	130.7	0.3671	0.706360	0.003	368.3 ± 3.8	0.704461 ± 43
Muscovite-1	10.8	28.7	79.3	1.0483	0.709845	0.003		
Muscovite-2	37.1	65.4	112.8	1.6796	0.713082	0.006		
Muscovite-3	24	110.7	153	2.0976	0.715419	0.014		
OAXZ-2								
Whole-rock	58.3	1.20	257.17	0.0135	0.704275	0.003	363 ± 43	0.704209 ± 27
Amphibole-1	40	2.89	131.75	0.0635	0.704527	0.003		
Amphibole-2	50	1.72	113.02	0.0440	0.704456	0.006		
Cariño[b]								
Whole-rock	-	134	229	1.7	0.71923 ± 4			
Muscovite	-	130	256	1.48	0.71802 ± 9			
Biotite	-	237	24.4	28.5	0.85469 ± 4		360.8 ± 7.5	0.71064 ± 26
Chimparra[b]								
Whole-rock	-	72.3	269	0.777	0.71565 ± 3			
Muscovite	-	305	89.3	9.93	0.76394 ± 5		376.6±8.0	0.71155 ± 13
Biotite	-	215	34.2	18.4	0.803088 ±6		354.2±7.2	0.71179 ± 12

a) Uncertainties for $^{87}Rb/^{86}Sr$ for the purpose of regressions and calculations is estimated to be 1 %.
b) Data recalculated after Peucat et al. (1990) with the ^{87}Rb decay constant of Villa et al. (2105). See text for further explanations.

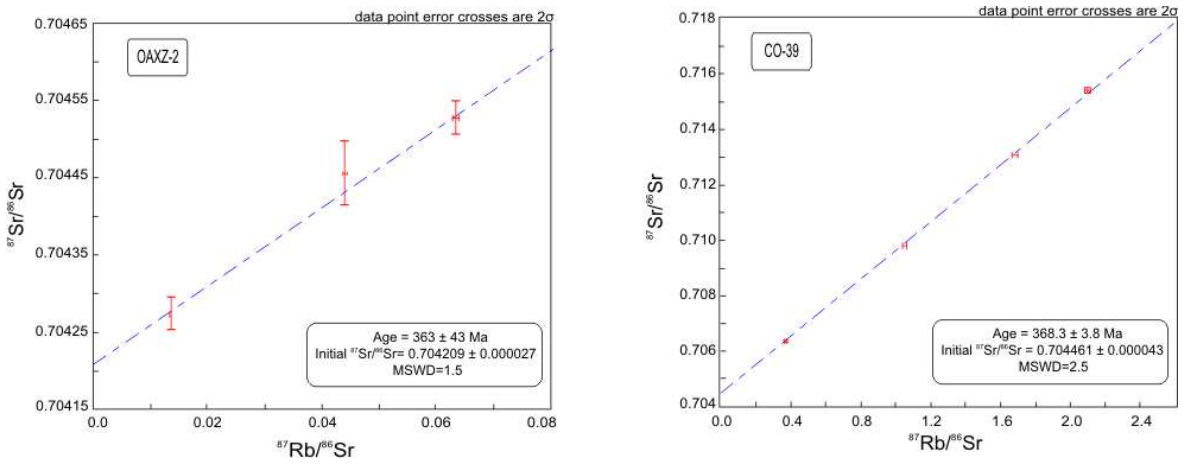

Figure 4.13. Rb-Sr isochrons from the studied eclogites

4.2.b.2. *High-pressure migmatitic gneiss*

The studied outcrops of the migmatitic acid rocks within the high-pressure mafic s.l. granulites of the Bacariza Formation are located between the Herbeira and Limo peridotite massifs (Figure 4.10). These rocks structurally overlie variably retrogressed garnet-plagioclase-clinopyroxene-bearing mafic granulites and are overlain by ultramafic rocks. The high-pressure migmatitic gneiss are easily recognized in the field due to their abundance in garnet and micas, light colour, and evidence of partial melting with development of metatexite structures (Figure 4.14a). The outstanding foliation and lineation are defined by the shape-preferred orientation of the constituent minerals. The abundance of idiomorphic prismatic zircon crystals with oscillatory zoning in the high-pressure migmatitic gneiss, as well as zoisite/clinozoisite with allanite cores, point to essentially acid igneous protoliths or to impure volcanic greywackes with a K-rich granitic (rhyolitic) component. Calculated P-T conditions for these rocks yield values of 800 ^{o}C and 18 kbar (Beranoaguirre, 2010).

Garnet-bearing migmatites show two types of mineral assemblages. On the one hand, some samples, which are less abundant, contain potassium feldspar and antiperthitic plagioclase, together with garnet, muscovite and clinozoisite but no kyanite (Figure 4.14d-e). On the other hand, other samples are formed by quartz, common plagioclase, garnet, biotite, muscovite, clinozoisite and also kyanite (Figure 4.14f-h). Biotite may be a primary matrix mineral forming part of the main mineral assemblage or occur as a reaction product after primary muscovite. The microstructure can be defined as grano-lepidoblastic to oriented porphyroclastic in both cases and is characterized by the occurrence of bands rich in quartz and feldspar alternating with mica-rich bands.

Garnet crystals are elongated parallel to the main foliation and have fractures perpendicular to this direction. They have minute inclusions of quartz and rutile in the core regions and, generally, exhibit inclusion-free rims. Garnet crystals may show optical zoning (Figure 4.14c), and are often replaced by misoriented fine-grained aggregates of biotite, muscovite and plagioclase, suggesting static retrogression (Figure 4.14b, e and g). Plagioclase occurs in the matrix forming either polycrystalline aggregates or larger single crystals with undulose extinction. Patch- and string-like antiperthitic microstructures are common in kyanite-free mineral assemblages (Figure 4.14d). Potassium feldspar (microcline) occurs usually as polycrystalline aggregates.

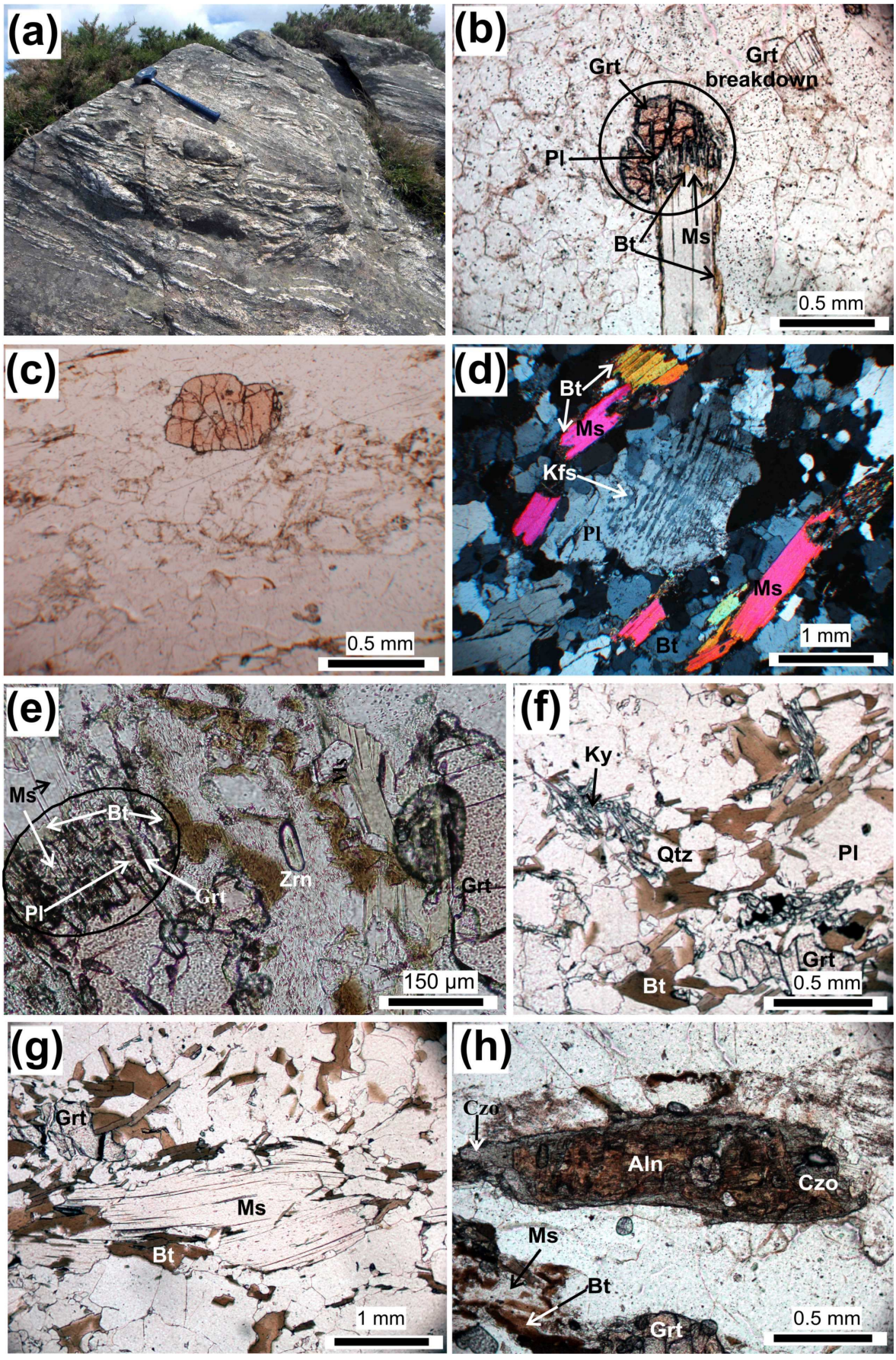
(a)
(b)
Grt
Grt breakdown
Pl
Bt
Ms
0.5 mm
(c)
0.5 mm
(d)
Bt
Ms
Kfs
Pl
Ms
Bt
1 mm
(e)
Ms
Bt
Pl
Grt
Zrn
Ms
Grt
150 µm
(f)
Ky
Qtz
Pl
Grt
Bt
0.5 mm
(g)
Grt
Ms
Bt
1 mm
(h)
Czo
Aln
Czo
Ms
Bt
Grt
0.5 mm

Figure 4.14. Outcrop and photomicrographs of the high-pressure migmatitic gneis of the Bacariza Formation. All the sections correspond to the XZ structural plane. **(a)** Outcrop of high-pressure migmatitic gneiss showing clear evidence of partial melting. **(b)** Replacement of garnet by biotite-muscovite-plagioclase aggregates, and of muscovite by biotite. Parallel nicols. **(c)** Optical zoning in unreacted garnet. Note the quartz feldespathc appeareance of the rock. Parallel nicols. **(d)** Antiperthitic plagioclase and muscovite partially replaced by biotite along the rim. Crossed nicols. **(e)** Muscovite replaced by biotite along the rim, inclusion of subidiomorphic zircon, and garnet replaced by a symplectitic aggregate composed of biotite, muscovite and plagioclase. Parallel nicols. **(f)** Kyanite, garnet, matrix biotite, muscovite and plagioclase ± ilmenite and clinozoiste. Note the development of a biotite rim on muscovite and the presence of resorption textures in garnet. Parallel nicols. **(g)** Mica-fish microstructure of muscovite. Biotite occurs along the rim and in the matrix. Parallel nicols. **(h)** Allanitic core in an elongated crystal of clinozoisite. Note the zircon inclusion in the central part of the image and the partial replacement of muscovite by biotite in the lower left part. Parallel nicols.

Oriented primary muscovite shows abundant evidence of intracrystalline deformation (undulose extinction, boudinage and mica-fish microstructures). It is often replaced by secondary biotite and plagioclase along the rims and cleavage planes (Figure 4.14b, d, e, f and g). Seemingly primary, oriented biotite appears in the matrix of the biotite-rich lithotypes as discrete crystals or irregular polycrystalline aggregates (Figure 4.14f and g). Zoned clinozoisite with shape preferred orientation contains subidiomorphic cores of allanite (Figure 4.14h). Clinozoisite crystals bear inclusions of biotite, quartz and rutile, and may be replaced by micaceous aggregates (white mica). Kyanite occurs in the biotitic types, generally as aggregates of fine-grained crystals (Figure 4.14f). Rutile is included in garnet and does not appear in the matrix. Ilmenite forms part of the matrix assemblage, while magnetite occurs in retrograde aggregates of biotite after muscovite.

One of the most interesting features of these rocks is the abundance of zircons (Figure 4.14e). The zircon crystals in the analysed samples are generally subhedral with a grain size ranging from 25-30 to over 400 µm long. The backscattered scanning electron (BSE) study reveals the presence of two types of zircons: (i) larger zoned grains and (ii) smaller homogenous crystals. The first type shows BSE-bright cores surrounded by BSE-darker overgrown rims (Figure 4.15).

The darkness of the image has been linked to the Hf content of the zircon, where brighter areas correspond to higher Hf contents (Hanchar and Miller, 1993; Corfu et al., 2003a). The occurrence of cores with concentric oscillatory zoning (Figure 4.15a) might be indicative of zircon grains that crystallized in granitic magmas (Hoskin, 2000). However, homogeneous and/or patchy-textures have also been found in these grains where unzoned rims (Figure 4.15b and c) are interpreted as metamorphic overgrowths (Corfu et al., 2003a). Transition between the growth-zoned domains and the homogeneous rims can be gradual or sharp (Figure 4.15b and d). In some cases, the rims crosscut the growth-zoned inner domain (Figure 4.15e). The second type of zircons found in the BSE study is represented by small homogeneous zircon crystals generally less than 40 µm in size (Figure 4.15f).

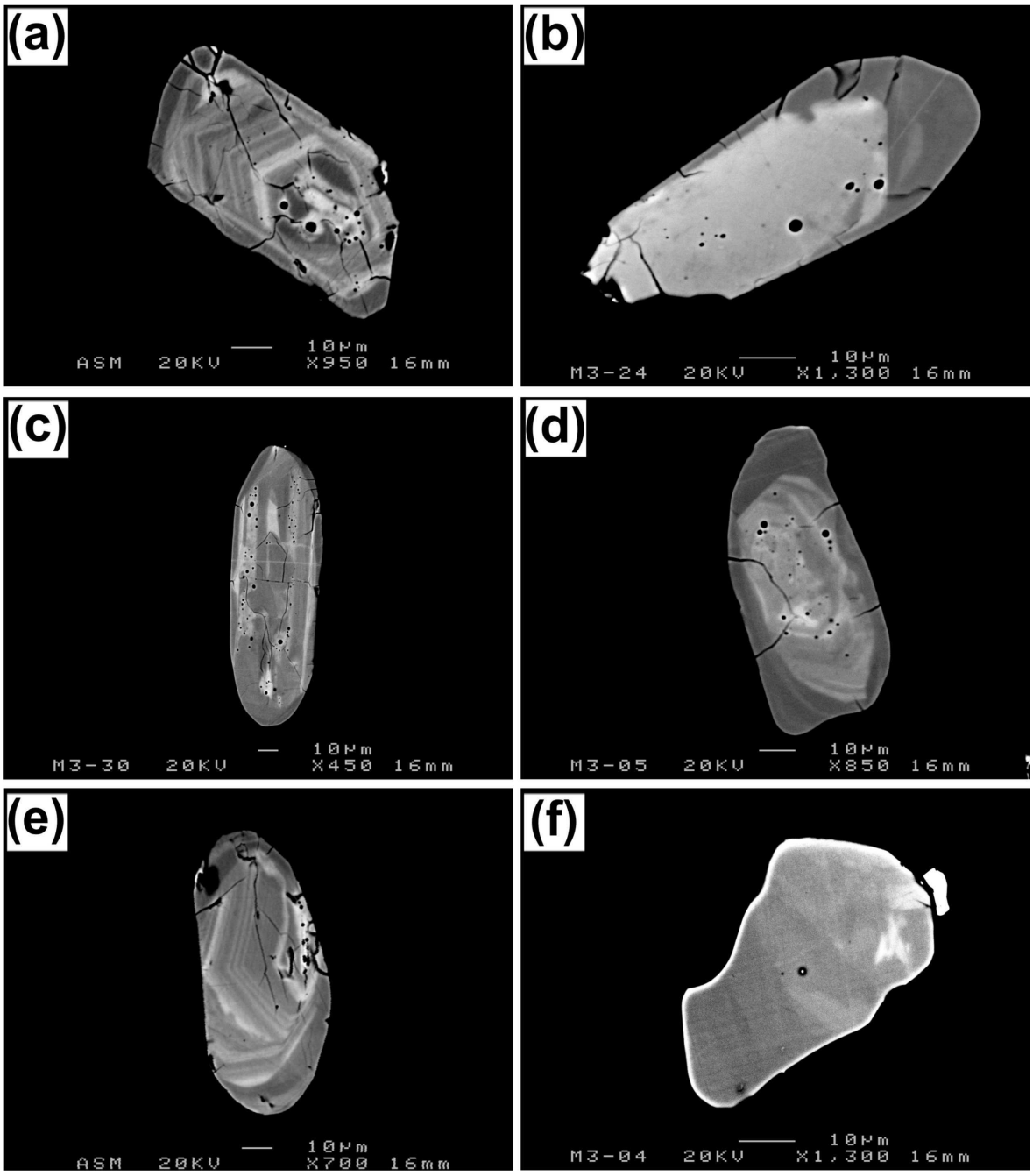

Figure 4.15. BSE images of representative zircons from the high-pressure migmatitic gneiss. **(a)** A growth-zoning pattern can be observed in the core of the zircon. The overgrowth cuts sharply the core. **(b)** Zircon grain showing a homogeneous core and rim. Note the sharp contact between them. **(c)** Zircon core with patchy texture surrounded by a fine rim. **(d)** Zircon grain showing a sharp core-rim contact (upper part of the image). In the lower part of the grain, however, the transition is more continuous. **(e)** Zircon rim crosscutting the inner growth-zoned domain. **(f)** Homogeneous zircon.

a. Results

166 U-Pb analyses performed by LA-ICP-MS on zircons from the high-pressure migmatitic gneisses of the Upper Allochthon of Cabo Ortegal yielded 87 concordant results. The data obtained are listed in Table 4.5 and presented in Figures 4.16 and 4.17.

Thirty concordant analyses correspond to the core areas of the zircons and give a broadly defined relative abundance peak at ca. 485 Ma (Figure 4.16a, n = 7, concordia age of 483.9 ± 3.8 Ma) and a better defined one at ca. 460 Ma (Figure 4.16a, n = 15, concordia age of 460.2 ± 2.4 Ma). These ages are plotted only on histogram and not on a expanded Concordia because is not clear if they represent a long magmatic activity (continued or two pulses) or a Pb loss event. Two of these analyses yielded older Ediacaran ages and they have been interpreted as inherited cores (Figure 4.16b). Thirty two concordant analyses for young zircons provide also two well-defined relative abundance peaks at ca. 390 Ma (n = 19, concordia age of 390.2 ± 2.0 Ma; Figure 4.16c) and 360 Ma (n = 16, concordia age of 357.3 ± 1.9 Ma; Figure 16d). Whereas the age of 390 Ma corresponds to rims of the larger core-bearing crystals, the younger age was obtained essentially on the small homogeneous zircons, with just a few data from 4-5 analyses of the outermost fine rims of the complex zircons which allowed for a few seconds of signal integration.

Among the obtained data, ages around 420-450 Ma are not clearly linked with any particular texture. This group of values is noticeable smaller (n ≈ 11) than the previously described and, in some instances, those ages correspond to analyses performed at the core-rim transition. Therefore, they should be taken with caution and no interpretation is here suggested for this lapse of time.

The Th/U ratio has been classically considered as indicative of the origin of zircons, being low values characteristic of metamorphic zircons (e.g., Rubatto, 2002; Harley et al., 2007). However, this concept has proved to be somewhat ambiguous since low Th/U igneous zircons from granites have also been described (e.g., López Sánchez et al., 2015). At any rate, in the present case the relationship established between the microstructures and the obtained ages is in agreement with the Th/U ratios measured in our samples (Figure 4.17). Thus, Th/U ratios are higher (0.20-0.30) at cores than at rims (ca. 0.10) in the zoned zircons, the latter showing low values of Th/U closer to those of the small homogeneous zircons (<0.05).

Table 4.5. U, Th and Pb LA-ICP-MS data of zircon from high-preeusre migmatitic gneiss (1- Calculated relative to GJ-1 reference zircon; 2- Ratios and errors calculated with Glitter®(Macquarie Research Ltd, 2001; van Achterbergh et al., 2001); 3- Calculated as Meinhold et al. (2010): [(^{206}Pb/2^{38}U age) / (^{207}Pb/^{235}Pb age)]×100)

	U^1	Pb^1		Concordia^2				Age		
Identifier	$\mu g.g^{-1}$	$\mu g.g^{-1}$	*Th/U*	$^{207}Pb/^{235}U$	*2 SE*	$^{206}Pb/^{238}U$	*2 SE*	$^{206}Pb/^{238}U$	*2σ abs*	*% conc*^{3}
35-a-01	342	12	0.01	0.421	0.022	0.057	0.001	356.4	4.2	100
35-a-02	612	31	0.19	0.611	0.024	0.077	0.002	480.2	4.9	99
35-a-04	929	58	0.37	0.709	0.019	0.088	0.002	542.7	4.9	100
35-a-05	1663	77	0.08	0.586	0.015	0.074	0.001	460.3	4.2	98
35-a-08	411	14	0.05	0.416	0.023	0.056	0.001	352.1	4.3	100
35-a-10	579	26	0.08	0.528	0.036	0.069	0.002	429.3	6.0	100
35-a-11	1065	52	0.14	0.584	0.019	0.074	0.001	461.2	4.5	99
35-a-12	416	16	0.01	0.469	0.023	0.063	0.001	392.1	4.4	100
35-a-13	194	7	0.00	0.434	0.040	0.059	0.002	366.7	6.2	100
35-a-14	90	3	0.01	0.426	0.050	0.058	0.002	361.0	7.4	100
35-a-18	591	25	0.05	0.518	0.024	0.067	0.002	417.7	4.7	99
35-a-20	828	31	0.01	0.465	0.024	0.062	0.002	385.8	4.6	100
35-a-23	538	24	0.02	0.579	0.053	0.074	0.003	459.7	8.0	99
35-a-24	216	8	0.01	0.468	0.026	0.062	0.002	386.0	4.7	99
35-a-31	398	15	0.01	0.428	0.029	0.058	0.002	361.8	4.8	100
35-a-33	559	24	0.08	0.475	0.018	0.063	0.001	390.8	3.8	99
35-a-34	605	29	0.21	0.506	0.033	0.067	0.002	416.9	5.4	100
35-b-01	1015	70	0.35	0.788	0.023	0.096	0.002	593.5	5.3	101
35-b-02	1096	40	0.02	0.448	0.019	0.060	0.001	375.1	3.9	100
35-b-03	1026	52	0.25	0.581	0.026	0.074	0.002	462.9	4.9	100
35-b-04	1363	66	0.02	0.621	0.018	0.079	0.001	487.6	4.4	99
35-b-06	1043	43	0.12	0.476	0.016	0.064	0.001	399.9	3.8	101
35-b-07	532	20	0.04	0.455	0.028	0.061	0.002	381.9	4.9	100
35-b-11	217	10	0.01	0.594	0.057	0.075	0.003	466.8	8.3	99
35-b-15	1124	56	0.23	0.584	0.025	0.074	0.002	459.6	4.8	98
55-a-02	1756	69	0.07	0.474	0.021	0.063	0.001	392.2	3.8	100
55-a-05	241	11	0.23	0.567	0.034	0.073	0.002	453.0	5.4	99
55-a-07	1070	47	0.20	0.515	0.026	0.068	0.002	421.5	4.5	100
55-a-09	1023	40	0.09	0.466	0.028	0.062	0.002	388.5	4.6	100
55-a-10	1164	45	0.08	0.472	0.031	0.063	0.002	391.6	4.9	100
55-a-11	1606	62	0.19	0.428	0.021	0.058	0.001	362.3	3.8	100
55-a-12	907	38	0.18	0.475	0.027	0.063	0.001	392.1	4.5	99
55-a-13	152	8	0.23	0.607	0.033	0.078	0.002	483.6	5.4	100
55-a-14	636	34	0.35	0.590	0.025	0.076	0.002	469.7	4.5	100
55-a-17	672	33	0.06	0.587	0.036	0.075	0.002	465.6	5.7	99
55-a-20	1828	76	0.16	0.481	0.033	0.065	0.002	403.9	5.3	101
55-a-23	703	36	0.23	0.609	0.027	0.078	0.002	486.3	4.9	101
55-a-24	824	41	0.34	0.570	0.021	0.074	0.001	457.5	4.2	100
55-a-25	8103	275	0.01	0.424	0.013	0.057	0.001	358.2	3.1	100
55-a-26	1055	50	0.07	0.597	0.026	0.077	0.002	478.8	4.8	101
55-a-27	6611	306	0.05	0.600	0.019	0.077	0.001	475.8	4.1	100
55-a-28	624	24	0.09	0.466	0.044	0.063	0.002	391.7	6.7	101
55-a-29	1218	46	0.07	0.464	0.030	0.062	0.002	385.8	4.9	100
55-a-31	326	14	0.02	0.559	0.035	0.072	0.002	450.7	5.5	100
55-a-32	477	19	0.20	0.472	0.024	0.063	0.001	394.1	4.1	100
55-a-34	1840	87	0.40	0.516	0.019	0.068	0.001	421.5	3.6	100
55-a-39	1410	54	0.33	0.423	0.022	0.057	0.001	356.1	3.8	99
55-a-40	1582	68	0.34	0.467	0.018	0.062	0.001	389.3	3.5	100
55-a-42	1018	36	0.05	0.422	0.017	0.057	0.001	356.4	3.3	100

Identifier	U[1] µg.g^{-1}	Pb[1] µg.g^{-1}	Th/U	Concordia[2] $^{207}Pb/^{235}U$	2 SE	$^{206}Pb/^{238}U$	2 SE	Age $^{206}Pb/^{238}U$	2σ abs	% conc[3]
55-a-43	786	28	0.03	0.422	0.017	0.057	0.001	354.5	3.2	99
55-a-44	782	35	0.16	0.540	0.022	0.069	0.001	433.0	4.0	99
55-a-45	554	26	0.14	0.554	0.035	0.072	0.002	447.4	5.5	100
55-a-46	741	28	0.06	0.451	0.030	0.060	0.002	377.5	4.7	100
55-a-47	795	34	0.37	0.446	0.024	0.060	0.001	376.3	4.0	100
55-a-49	499	20	0.10	0.477	0.026	0.063	0.001	394.4	4.4	100
55-b-01	1472	49	0.06	0.473	0.024	0.063	0.001	391.4	4.2	100
55-b-04	2666	93	0.14	0.463	0.019	0.061	0.001	384.5	3.7	99
55-b-07	1372	59	0.39	0.473	0.024	0.062	0.001	389.5	4.3	99
55-b-11	1264	50	0.17	0.465	0.017	0.062	0.001	385.7	3.6	99
55-b-12	3434	118	0.00	0.429	0.018	0.057	0.001	359.9	3.6	99
55-b-15	626	29	0.15	0.569	0.022	0.074	0.001	459.2	4.4	100
55-b-16	938	42	0.17	0.540	0.022	0.070	0.001	438.5	4.3	100
55-b-18	1242	51	0.24	0.474	0.019	0.063	0.001	394.2	3.8	100
55-b-19	2115	78	0.09	0.426	0.020	0.057	0.001	358.0	3.9	99
55-b-21	442	21	0.25	0.530	0.036	0.069	0.002	432.8	5.9	100
55-b-22	1079	39	0.10	0.422	0.025	0.057	0.001	354.9	4.4	99
55-b-23	2768	95	0.01	0.418	0.017	0.057	0.001	354.6	3.6	100
55-b-24	610	21	0.01	0.427	0.025	0.057	0.001	359.8	4.4	100
55-b-25	306	15	0.01	0.610	0.045	0.078	0.002	483.2	7.0	100
55-b-27	1109	56	0.27	0.570	0.022	0.074	0.001	457.2	4.5	100
55-b-28	613	30	0.18	0.585	0.017	0.075	0.001	467.1	4.1	100
55-b-29	1768	88	0.19	0.582	0.018	0.075	0.001	463.7	4.2	100
55-b-30	1074	51	0.28	0.533	0.031	0.070	0.002	433.2	5.3	100
55-b-31	2322	82	0.04	0.425	0.015	0.057	0.001	357.1	3.4	99
55-b-33	1315	51	0.25	0.420	0.018	0.057	0.001	355.7	3.6	100
55-b-34	500	25	0.27	0.565	0.019	0.074	0.001	457.2	4.3	101
55-b-35	2114	103	0.34	0.538	0.020	0.070	0.001	433.8	4.2	99
55-b-38	464	21	0.18	0.533	0.015	0.069	0.001	432.6	3.8	100
T-4-01	382	35	0.28	0.616	0.018	0.078	0.002	485.1	4.9	100
T-4-05	365	32	0.30	0.583	0.017	0.074	0.002	459.3	4.6	98
T-4-07	370	33	0.26	0.605	0.018	0.076	0.002	472.6	4.7	98
T-4-08	1490	104	0.02	0.478	0.012	0.064	0.001	399.5	3.9	101
T-4-09	1044	75	0.12	0.477	0.012	0.063	0.001	392.3	3.9	99
T-4-20	1964	168	0.28	0.578	0.014	0.073	0.001	456.2	4.5	98
T-4-22	496	43	0.24	0.573	0.016	0.074	0.002	457.2	4.5	99
T-4-23	713	44	0.06	0.420	0.014	0.057	0.001	355.6	3.6	100
T-4-24	105	7	0.02	0.461	0.022	0.061	0.001	381.3	4.1	99

52 valid Hf isotope analyses were obtained from the same zircons. Among them 39 represent core signatures, whereas the other 13 correspond to rim analyses in the larger zoned zircons. Due to spot size limitations, no analysis was performed in the small-sized homogeneous zircons. In T_{DM} or ε_{Hf} studies, it is strongly recommended to perform both the U-Pb and Hf analyses at the same spot or as close as possible. That permits to relate easily the age to a T_{DM} or ε_{Hf}. However, in this work, the U-Pb and Hf isotopes were analysed separately since the study was done directly on the thin section. This procedure, which allows for a good structural control of the

mineral analysed has a drawback, however, and it is that most zircons may be pierced during the ablation process due to the limited thickness in most cases of the target. In the present case, the results obtained for spots close but separated from those analysed for U-Pb are listed in Table 4.6. and represented in Figure 4.18. As it can be observed, two groups of values can be established: (i) $^{176}Hf/^{177}Hf$ ratios of 0.282736 representing cores values, and (2) $^{176}Hf/^{177}Hf$ ratios of 0.282649 that correspond to rim compositions.

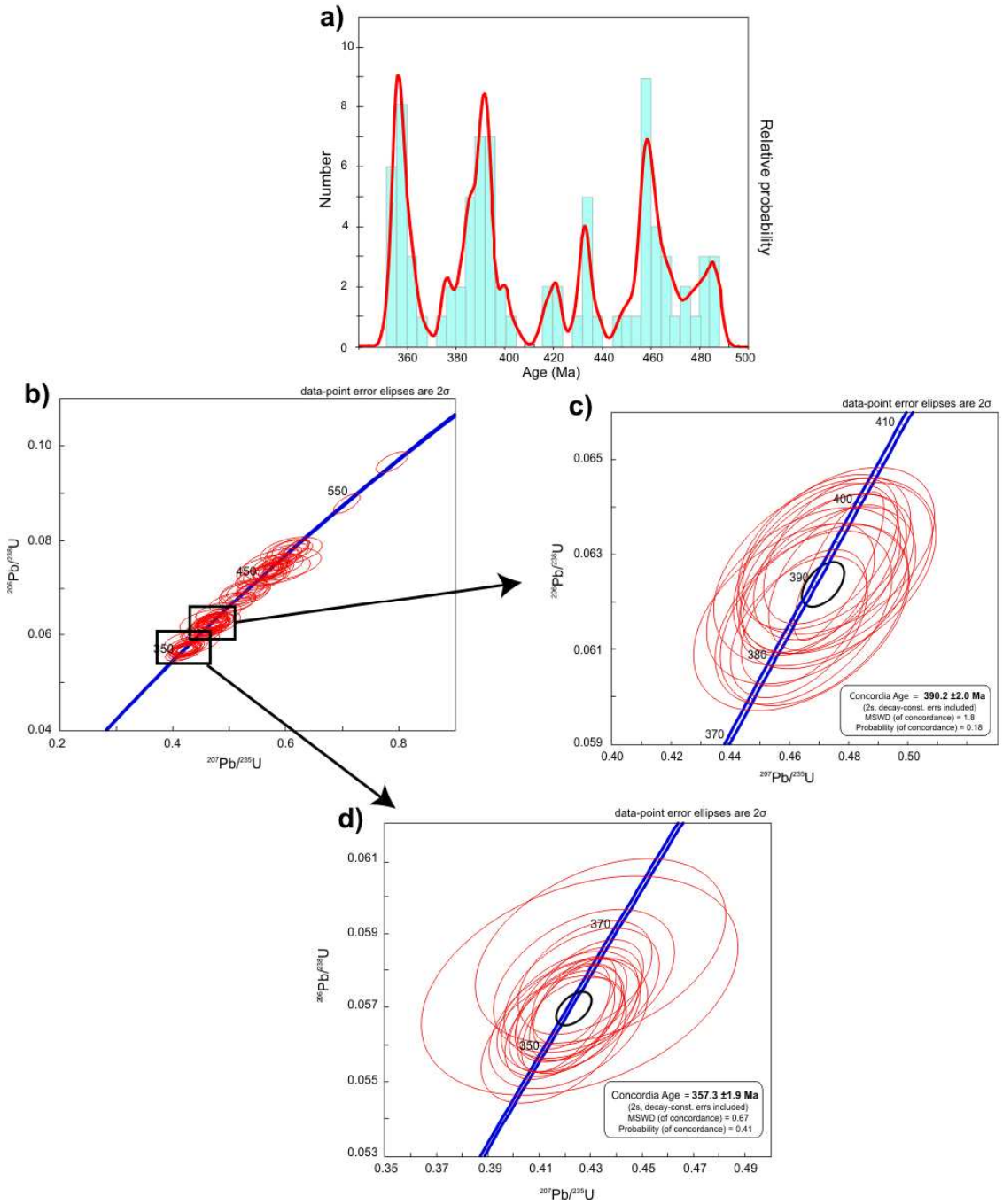

Figure 4.16. **a)** Histogram diagrams of the U-Pb analyses (calculated with Isoplot 2.49, Ludwig, 2001). **b)** U-Pb concordia diagram showing U-Pb zircon analyses of the studied sample. Ellipses represent combined 2σ uncertainties of $^{206}Pb/^{238}U$ and $^{207}Pb/^{235}U$ ratios. **c)** and **d)** U-Pb concordia diagrams expanded from b).

Table 4.6. Lu, Yb and Hf LA-MC-ICP-MS data of zircon from high-pressure migmatitic gneiss [a] ($^{176}Yb/^{177}Hf = (^{173}Yb_{meas} \times (0.7964/(M_{176Yb}/M_{173Yb}))^{\beta(Yb)}/^{177}Hf_{meas} \times (M_{173(Yb)}/M_{177(Hf)})^{\beta(Hf)}$). The $^{176}Lu/^{177}Hf$ was calculated in a similar way using ^{175}Lu, ^{177}Hf, β(Yb) and β(Hf). [b] Uncertainties are calculated with Iolite® (Paton et al. 2011). [c] An approximation to $^{176}Hf/^{177}Hf$ and εHf initial values was done using average ages of 460 Ma and 390 Ma for cores and rims, respectively, and the CHUR parameters: $^{176}Lu/^{177}Hf = 0.0336$, and $^{176}Hf/^{177}Hf = 0.282785$ (Bouvier et al. 2008).

Label	$^{176}Lu/^{177}Hf^{a}$	*2SE*[b]	$^{176}Yb/^{177}Hf^{a}$	*2SE*[b]	*Hf Beam (V)*	$^{178}Hf/^{177}Hf$	*2SE*[b]	$^{176}Hf/^{177}Hf$	*2SE*[b]	$^{176}Hf/^{177}Hf_i^{c}$	$\varepsilon_{Hf(i)}{}^{c}$	*2SE*[b]
X-1	0.00235	42	0.0668	16	7.6	1.46741	12	0.282657	56	0.282601	2.6	2.0
X-2	0.00204	140	0.0572	43	8.4	1.46719	8	0.282644	65	0.282588	2.2	2.3
X-3	0.00202	58	0.0557	16	4.6	1.46732	9	0.282704	56	0.282646	5.7	2.0
X-4	0.00122	60	0.0349	20	5.5	1.46724	8	0.282726	57	0.282674	6.6	2.0
X-5	0.00129	60	0.0353	17	5.5	1.46722	10	0.282723	60	0.282674	6.6	2.1
X-6	0.00133	18	0.0415	7	9.0	1.46728	9	0.282721	46	0.282686	7.1	1.6
X-7	0.00104	67	0.0320	21	9.9	1.46725	6	0.282721	39	0.282692	7.3	1.4
X-8	0.00148	21	0.0436	7	12.1	1.46727	9	0.282769	48	0.282766	9.9	1.7
X-9	0.00142	51	0.0409	14	6.3	1.46728	9	0.282757	46	0.282765	9.9	1.6
X-10	0.00100	16	0.0299	6	10.0	1.46725	6	0.282746	36	0.282759	9.7	1.3
X-11	0.00179	62	0.0557	22	7.5	1.46720	7	0.282793	43	0.282798	11.1	1.5
X-12	0.00169	37	0.0522	10	7.8	1.46724	5	0.282740	49	0.282746	9.2	1.7
X-13	0.00115	42	0.0355	12	8.2	1.46732	8	0.282735	53	0.282743	9.1	1.9
X-14	0.00108	13	0.0332	5	8.8	1.46722	6	0.282715	53	0.282702	7.6	1.9
X-15	0.00066	53	0.0193	16	8.9	1.46726	6	0.282723	33	0.282711	8.0	1.2
X-16	0.00218	46	0.0664	13	7.8	1.46730	7	0.282743	50	0.282745	9.2	1.8
X-17	0.00176	20	0.0541	8	7.8	1.46734	6	0.282760	48	0.282777	10.3	1.7
X-18	0.00132	96	0.0392	30	8.1	1.46723	8	0.282733	60	0.282753	9.5	2.1
X-19	0.00111	28	0.0360	16	7.7	1.46730	7	0.282741	38	0.282745	9.2	1.3
X-20	0.00119	63	0.0348	19	8.5	1.46722	6	0.282708	38	0.282633	5.2	1.4
X-21	0.00119	30	0.0329	11	7.0	1.46722	7	0.282725	53	0.28263	5.1	1.9
X-22	0.00162	89	0.0454	26	10.2	1.46725	5	0.282696	34	0.282610	4.4	1.2
X-23	0.00150	10	0.0457	11	10.9	1.46725	8	0.282699	62	0.282619	4.7	2.2
Y-1	0.00141	50	0.0387	14	11.2	1.46725	6	0.282646	65	0.282623	3.4	2.3
Y-2	0.00200	27	0.0587	13	10.8	1.46719	7	0.282742	54	0.282715	8.1	1.9
Y-3	0.00062	28	0.0177	9	13.6	1.46721	7	0.282756	53	0.282742	9.1	1.9
Y-4	0.00067	5	0.0186	6	16.1	1.46728	7	0.282729	46	0.282715	8.1	1.6
Y-5	0.00159	55	0.0475	17	5.9	1.46726	7	0.282758	56	0.282737	8.9	2.0
Y-6	0.00021	30	0.0061	7	12.7	1.46733	8	0.282667	31	0.282664	4.8	1.1
Y-7	0.00099	110	0.0273	17	14.8	1.46720	12	0.282747	55	0.282737	8.9	1.9
Y-8	0.00069	30	0.0193	6	34.3	1.46728	10	0.282671	56	0.282670	5.0	2.0
Y-9	0.00088	61	0.0260	11	27.3	1.46718	12	0.282654	45	0.282652	4.4	1.6
Y-10	0.00120	210	0.0353	47	21.3	1.46730	13	0.282647	64	0.282642	4.0	2.3
Y-11	0.00102	57	0.0295	18	21.4	1.46719	11	0.282649	58	0.282646	4.2	2.1
Y-12	0.00083	97	0.0247	38	30.2	1.46715	8	0.282656	46	0.282656	4.5	1.7
Y-13	0.00272	33	0.0801	28	21.4	1.46720	15	0.282732	21	0.282718	8.2	0.76
Y-14	0.00186	41	0.0597	66	21.6	1.46728	14	0.282724	30	0.282718	8.2	1.1
Z-1	0.00112	34	0.0312	17	7.9	1.46726	11	0.282653	45	0.282645	4.1	1.6
Z-2	0.00118	95	0.0353	31	10.1	1.46722	7	0.282745	49	0.282734	8.8	1.7
Z-3	0.00112	13	0.0324	16	21.9	1.46717	8	0.282701	44	0.282691	7.3	1.6
Z-4	0.00099	31	0.0263	13	7.8	1.46730	9	0.282604	62	0.282595	2.4	2.2
Z-5	0.00092	61	0.0290	15	8.9	1.46722	10	0.282794	49	0.282785	10.6	1.8
Z-6	0.00255	14	0.0803	11	9.2	1.46726	7	0.282746	51	0.282722	8.4	1.8
Z-7	0.00121	27	0.0363	8	8.6	1.46724	8	0.282733	52	0.282719	8.2	1.8
Z-8	0.00104	35	0.0298	11	13.1	1.46716	5	0.282637	50	0.282621	3.3	1.8
Z-9	0.00127	48	0.0376	14	10.3	1.46727	7	0.282734	36	0.282699	7.5	1.3
Z-10	0.00156	38	0.0443	12	12.3	1.46726	6	0.282735	38	0.282696	7.4	1.3
Z-11	0.00116	45	0.0326	12	12.1	1.46725	9	0.282736	41	0.282700	7.6	1.5
Z-12	0.00125	48	0.0338	13	10.9	1.46722	9	0.282654	52	0.282617	3.1	1.8
Z-13	0.00113	73	0.0338	18	8.3	1.46732	8	0.282748	54	0.282711	8.0	1.9
Z-14	0.00112	56	0.0319	18	12.8	1.46712	8	0.282737	47	0.282700	7.6	1.7
Z-15	0.00167	92	0.0530	50	9.8	1.46728	9	0.282724	48	0.282681	6.9	1.7

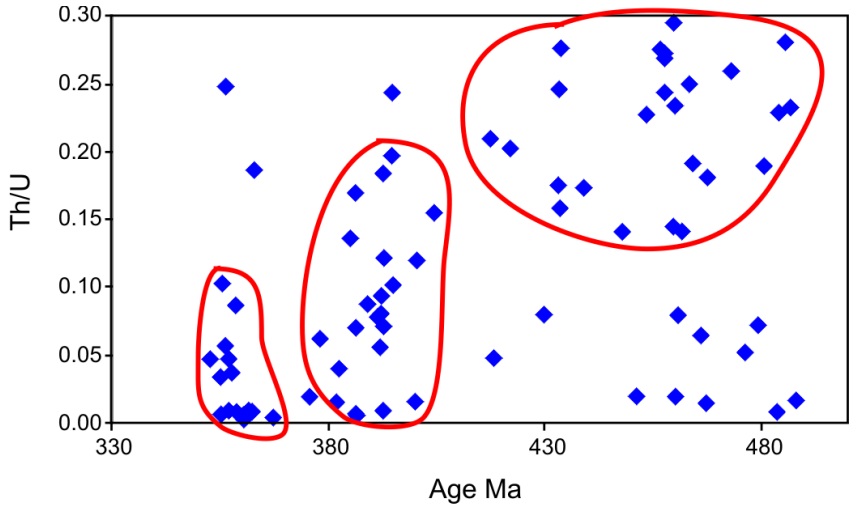

Figure 4.17. Analysed Th/U versus age. The Th/U ratios of the metamorphic (younger) zircon domains are slightly lower than those of the magmatic zircon.

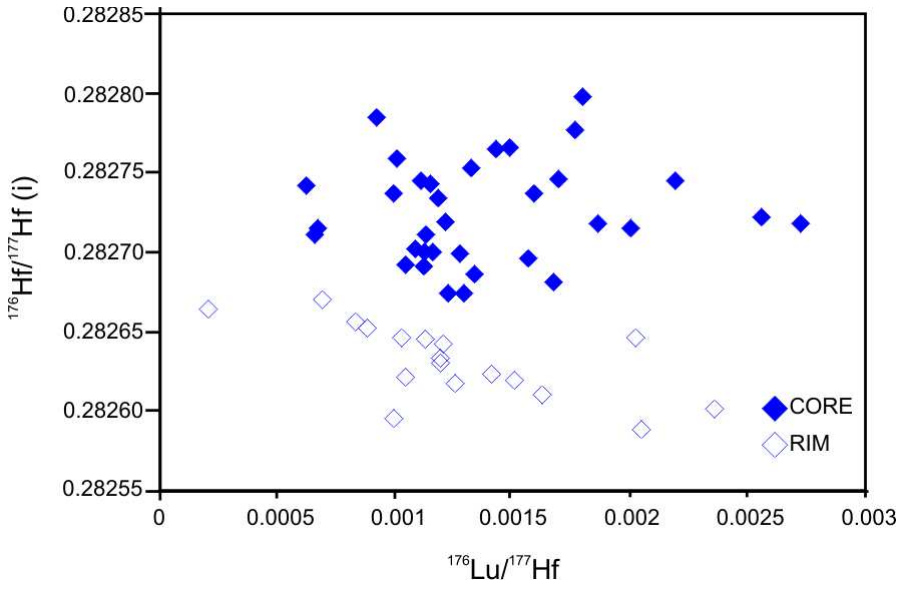

Figure 4.18. Analysed initial $^{176}Hf/^{177}Hf$ versus $^{176}Lu/^{177}Hf$. The $^{176}Hf/^{177}Hf$ ratios of the metamorphic zircon domains are slightly lower than those of the magmatic zircon, whereas the $^{176}Lu/^{177}Hf$ ratio is barely similar. Error bars are not shown, since they complicate the view of Figure.

4.3. Discussion

4.3.a. Lu-Hf and Sm-Nd ages interpretation

When a rock is dated, it is necessary to know the meaning of the calculated age whether it represents the metamorphic peak or cooling age for instance, or if it is meaningless, as it could be the case of a system disturbed during a posterior process.

The closure temperature (T_c) for the Sm-Nd system in garnet is estimated to be ca. 650 ^{o}C or higher (Mezger et al., 1992; Ganguly et al., 1998a; Tirone et al., 2005), although differences between mafic and metapelitic rocks may occur (Thöeni, 2002). Though no experimental diffusion data are available for the Lu-Hf clock, Scherer et al. (2000) concluded that the T_c for Lu-Hf is greater than that for the Sm-Nd system within the same garnet. Anczkiewicz et al. (2007) suggested a minimum T_c for Lu-Hf in garnet of about 900 °C. In this line, estimated metamorphic temperatures for the Malpica-Tui samples reached a maximum value of 610 ^{o}C (Rodríguez, 2005) and therefore, it is unlikely that they have exceeded the closure temperature of both Sm-Nd and Lu-Hf systems.

The petrographic observations and the preservation of the growth zoning patterns observed for the major elements in garnet (Figure 4.19) preclude the recrystallization of this mineral via a dissolution-reprecipitation processes (Kelly et al., 2011). Therefore, the obtained ages should be interpreted as metamorphic ages and they would not represent the closure of the systems upon cooling from high temperature. This interpretation is in accord with the petrographic equilibrium observed between garnet and omphacite.

Published diffusion data suggest that (i) Sm-Nd, Lu-Hf and Fe-Mg are relatively immobile in garnet at temperatures below 600 ^{o}C and (ii) the diffusivity of Mn is faster at medium temperatures, probably more than ten times greater than that of Ca (Mezger et al., 1992; Chernoff and Carlson, 1997; Ganguly et al., 1998a,b; Scherer et al., 2000). The preservation of the Mn growth zoning patterns in garnet (Figure 4.19) suggests that the original distribution of Lu^{3+} and Hf^{4+} has not been disturbed by diffusion. It should be remembered here that 2^{+} ions diffuse significantly faster than 3^{+} (and presumably 4^{+}) ions in garnet (Van Orman et al., 2002).

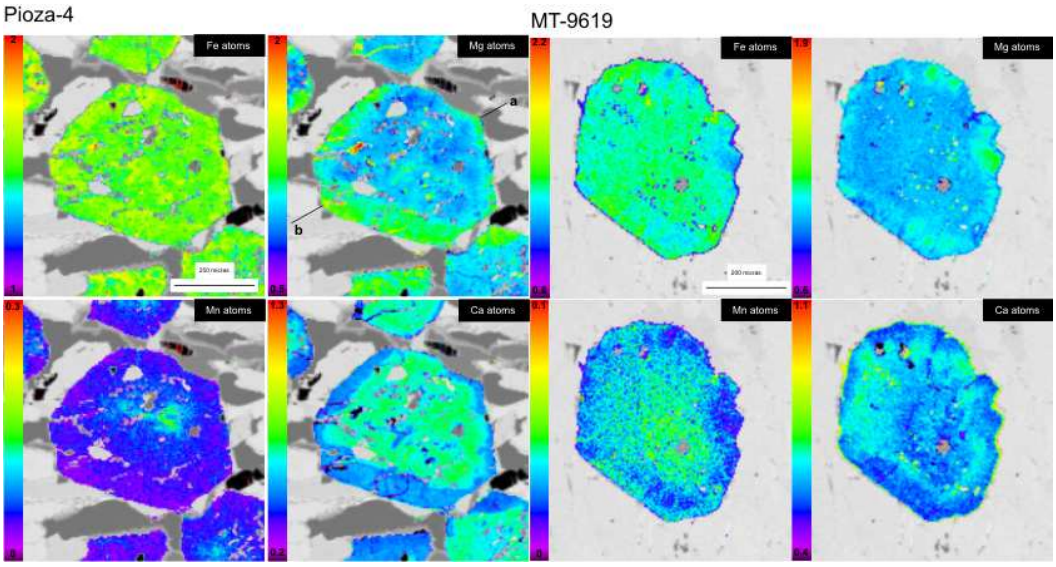

Figure 4.19. Representative major-element maps (Mg, Mn, Fe and Ca) of garnets from the analysed eclogites.

As shown by Lapen et al. (2003), Rayleigh fractionation during garnet growth would preferentially concentrate Lu in the cores of garnet relative to the rims, due to the very high affinity of garnet for Lu, while the distribution of Sm and Nd usually results in flattened profiles or relative enrichments at rims (Cheng et al., 2008). Figure 4.20 illustrates the Sm, Nd and Lu qualitative profiles which have been calculated based on a laser ablation raster and compared to Ti. Those zonation patterns have been interpreted by different authors in terms of age data for the prograde growth of the garnet (e.g., Lapen et al., 2003; Anczkiewicz et al., 2007; Kylander-Clark et al., 2007; Schmidt et al., 2008; Kirchenbaur et al., 2012, among others) assuming that Lu which would concentrate at garnet cores produces a bias toward the early stages of prograde garnet growth.

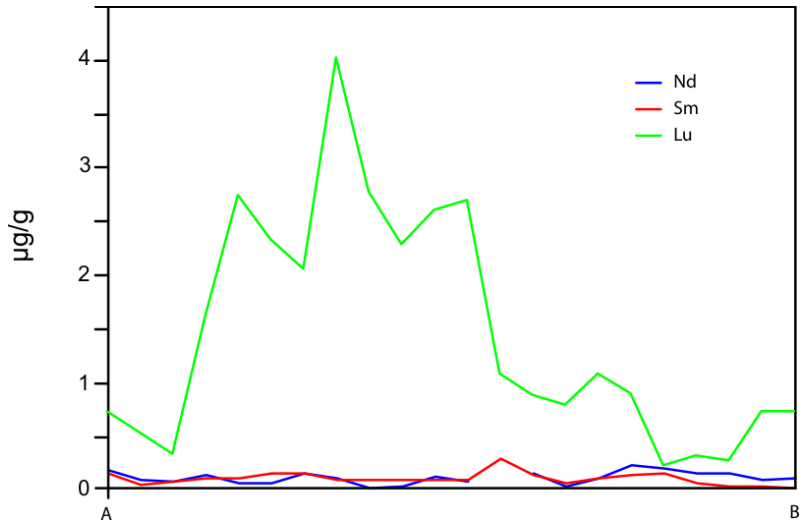

Figure 4.20. Representative Sm-Nd-Lu pattern in a garnet grain from sample Pioza-4. Concentration values are based on raster analysis and normalized to Ti content on the garnet.

Due to the difference between the Lu-Hf and Sm-Nd ages, sample MT-9619 could represent an example of date the growth process in garnet. Although in this sample garnet seems to have grown very fast, crystals grown at similar rates can be also found in the literature (Lagos et al., 2007). However, Skora et al. (2009) showed that although Lu is enriched in early grown cores due to diffusion-limited transport, Lu-Hf ages do not date the onset of garnet growth simply because core concentrations are of minor abundance when weighted over a spherical geometry. The Lu-Hf ages may still be slightly biased towards the onset of growth when garnet grows over a large period of time (even 30 Ma, Skora et al., 2009; Cheng et al., 2011), but must be interpreted cautiously in cases where garnet grew during a short lapse of time.

The Lu-Hf and Sm-Nd ages calculated for MT-9619 and the Lu-Hf age values of Pioza-4 are considered to date the metamorphic peak. Abati et al. (2010) dated eclogites from the same structural position (Malpica-Tui Lower Allochthon) and obtained zircon U-Pb ages of 372 ± 3 Ma, which are in the range of ones obtained here. The U-Pb ages obtained in metamorphic zircons are

suppose to be the age of the eclogitic metamorphism (e.g., Rubatto et al., 1999; Corfu et al., 2003b; Abati et al., 2010), so it can be estimated that the maximum burial of the Malpica-Tui Complex rocks occurred in the Late Devonian, around 375 Ma ago.

Another key feature of the Lu-Hf and Sm-Nd geochronology is the presence of inclusions in the separated mineral fractions. The presence of inclusions and the methods to avoid them have been widely discussed over the last years (e.g, Amato et al., 1999; Baxter et al., 2002; Anczkiewicz and Thirlwall, 2003; Pollington and Baxter, 2011). In the present study, the method of Anczkiewicz and Thirlwall (2003) to chemically remove the possible influence of those inclusions was followed, and the details have been explained in the previous chapter.

Yet, although a great effort was made to separate clean garnet fractions and prevent their influence through chemical leaching, the fact is that not all the microscopic and submicroscopic inclusions can be eliminated by standard mineral separation techniques or leaching techniques. Hence, the cause for the low Sm/Nd ratios in the Pioza-4 garnet fraction could be the presence of Nd-rich inclusions in the mineral separates, the most likely mineral inclusion in those samples being zoisite. A small fraction of a percent of contamination would be sufficient to bring down Nd isotopic ratios to the observed values. Additional contribution from accessory inclusions such as sphene, apatite and zircon, although occurring in much smaller amounts, could also have some influence (Mawby et al., 1999; Prince et al., 2000; Thöeni, 2002; Kylander-Clark et al, 2007). However, it is assumed that its contribution is negligible, since they are considered to be totally removed by the sulfuric acid leaching technique (Anczkiewicz and Thirlwall, 2003). Thus, these younger Sm-Nd ages in Pioza-4 sample suggests that, (i) the separated garnet fraction certainly had undetected inclusions, and (ii) that these inclusions were not in isotopic equilibrium with the garnet. Hence, the Sm-Nd age obtained for Pioza-4 is considered geologically meaningless.

The minerals that lowered the Sm-Nd ratios do not have any perceptible influence on the Lu/Hf system. However the (probable) presence of zircon in the whole-rock fraction results in lower $^{176}Hf/^{177}Hf$ ratios than expected if all the rock-forming minerals were in isotopic equilibrium. For that reason, it has been excluded from the age calculation.

4.3.b. Rb-Sr: dating uplift or something else?

The Rb-Sr system is not widely used in metamorphic terranes due to the (i) possible disequilibria produced by the high mobility of Rb and Sr, or (ii) open system behavior (Gebauer, 1990) that can be linked to deformation or fluid assisted reactions, or to solid-state diffusion recrystallization at the mineral scale (Giletti, 1991; Jenkin et al., 1995; Kühn et al., 2000; Davies and Tommasini, 2000; Glodny et al., 2002, 2008). The closure temperature for the Rb-Sr system in

different minerals is another matter of debate, since it is not well constrained, and it may vary depending on the mineral assemblage, mineral size and shape, intergrowth relations and also on the modal proportion of minerals (Giletti, 1991; Jenkin, 1997). Therefore, the ages obtained with this technique are usually considered problematic because of the possible partial or complete resetting of the system that may lead to incorrect age interpretations. In the few well-constrained Rb/Sr data sets available, these ages are usually discussed only as cooling or recrystallization ages (Santos-Zalduegui, 1995; Amato et al., 1999, among others), and only few authors consider the age of the primary assemblage formation (Glodny et al., 2002).

If one considers that the approximate closure temperature for amphibole (450-500 °C, Harrison and Fitz Gerald, 1986; Li et al., 2000) and muscovite (550 ± 50 °C, Jäger et al., 1967; Blackenburg et al., 1989) have been widely exceeded during the eclogite-facies metamorphism, two hypotheses can be proposed for the ages obtained for OAXZ-2 and CO-39, 363 ± 43 Ma and 368 ± 4 Ma, respectively. Both hypotheses are dependent on the true closure temperature of the U-Pb system in rutile, which is not well defined yet. The U-Pb rutile ages obtained by Valverde-Vaquero and Fernández (1996), Santos Zalduegui (1995) and Roger and Matte (2005) in different rocks from the high-grade regional Upper Allochthon are well constrained at ca. 380-385 Ma. If the closure temperature for U-Pb rutile is considered to be 600-650 °C (Cherniak, 2000, Vry and Baker, 2006), a constant exhumation with or without external inferences could be draw. However, if the assumed closure temperature is 400 °C (Mezger et al., 1989), older Rb-Sr ages would be expected for the studied samples.

In any case, the ductile deformation that affected both rocks (mylonitic to ultramylonitic stages) is very likely to have been operative under fluid-assisted pervasive deformation conditions that might have open the system and cause the isotopic disequilibrium on the samples. Therefore, the obtained ages would represent the age of the fluid-assisted event affecting former shear zones and not a cooling age.

In our view, the ages obtained in the mylonites would indicate that the eclogites reached midcrustal levels ca. 20 Ma after the eclogites-facies metamorphism. Although similar timings have been described in other areas (e.g., the Maksyutov complex in the Urals, Glodny et al., 2002; Hetzel and Romer, 2000; Beane and Conelly, 2000) previous studies in different lithologies from the Upper Allochthon (Mendia, 2000; Ordoñez Casado et al., 2001; Abalos et al. 2003; Puelles et al., 2005) point to a rapid decompression after maximum burial. In that case, the disturbance in the system might be attributed to fluid circulation along ‘weaker’ shear zones.

A similar deliberation could be expected in the case of the high-pressure regional Lower Allocthon of Malpica-Tui. Those ages obtained in the MT-9619 sample could be interpreted as a consequence of the rock, formed at ca. 600 °C, would have gone through the closure temperature

of the Rb-Sr system in amphibole. Although the obtained age should be treated with caution due to the high error, the data is in the range of other previously calculated ages within the same area (Rodriguez et al., 2003) or from equivalent rocks within the European Variscan foldbelt (e.g., Bosse et al., 2000).

On the other hand, taking into account that the peak temperature conditions of the Pioza-4 samples (Rodríguez, 2005) is close the T_c of Rb-Sr in muscovite, the calculated ages, 349 ± 3 Ma, should be expected to be in the range of those obtained by the Lu-Hf technique, 374 ± 4 Ma. However, the analyses yield considerably younger ages, pointing to a younger event that might have disturbed the equilibrium. Abati and Dunning (2002) and Abati et al. (2010) mentioned a fluid circulation event related to partial migmatization in the regional Lower Allochthon. The data obtained by those authors using U-Pb methods on zircon, monazite and rutile, are in agreement with the data presented here, so the fluid circulation event that opened and reset the system appears fairly plausible.

4.3.c. Zircon evolution in high-pressure migmatitic gneisses

Figure 4.16a shows that 3 main ages/events may be disclosed for the migmatitic gneisses within the high-pressure Upper Allochthon of Cabo Ortegal. The older age is not well defined, but it is thought to approach that of the protoliths (e.g., Ordóñez Casado et al., 2001). In any case, the obtained ages are slightly younger than those published before (Table 4.1.), measured generally in basic rocks. The divergency could have different explanations. On one hand, those younger ages could be the result of crystallizing from more evolved melts, a long period (ca. 30 Ma) of crystallization evolution/sequence. It could be explained also as Pb-loss processes produced by a later event. A third option could be linked with various inputs within a volcano-sedimentary arc environment, where while magmatic younger zircons are forming, there is also a contribution of magmatic zircons from rocks formed immediately before. The $^{176}Hf/^{177}Hf$ ratios observed are very homogeneous, which in any case indicate that the zircons come from the same source.

What is clear anyway is that zircons from the protolith have textures that suggest growth from high-T melts (Vavra et al., 1996; Schaltegger et al., 1999; Kelly and Harley, 2005). To refine the hypotheses on the exact origin and geological context of the protolith, a more comprehensive and detailed analysis would be required which is out of the scope of this PhD Thesis.

The age of 390 ± 2 Ma is well defined. This value, along with the lower Th/U and $^{176}Hf/^{177}Hf$ ratios, would indicate the age of the high-pressure and high-temperature metamorphic event within the European Variscan orogen, as described by other authors (Table 4.1).

The $^{176}Hf/^{177}Hf$ ratios obtained for the cores and rims (Figure 4.18) of larger zircons show distinct lower Hf ratios at rims. This feature suggests that the 390 Ma old zircons are crystal overgrowths instead of the result of solid-state recrystallization processes. Note that lead loss may occur during solid-state recrystalization, but it seems that Hf is never 'washed out' from the zircon crystal lattice (e.g., Hoskin and Schaltegger, 2003; Gerdes and Zeh, 2009; Matteini et al., 2010).

The presence of younger zircons with lower $^{176}Hf/^{177}Hf$ ratios also suggests that the overgrowth took place in an open system environment. When a zircon growths, the $^{176}Hf/^{177}Hf$ ratio of it is equal or at least very close to the initial Hf isotopic composition of the whole rock. In a closed system, the Lu present in the rock will produce radiogenic $^{176}Hf^{*}$ and thus, the $^{176}Hf/^{177}Hf$ ratio in the rock will increase over time. As a consequence, any changes in the system would not result in mineral formation with $^{176}Hf/^{177}Hf$ lower than the initial one. The practically equal $^{176}Hf/^{177}Hf$ ratios obtained for the rim analyses points to overgrowth from a single chemically homogeneous fluid phase. Another feature that supports the idea of an external fluid contribution is that the Lu/Hf ratio should decrease in a closed system (because of ^{176}Lu decay), aspect which is not clearly perceptible in the Figure 4.18.

The relatively young 357 ± 2 Ma age of zircons within these gneisses has not been reported before and it could represent a new event within the high-grade regional Upper Allochthon. Although initially it could be possibly attributed to lead loss processes, the fact that the group of small and homogeneous zircons only yielded those ages, without any hint of a previous event, together with the discernible different Th/U ratios (Figure 4.17), suggests that they actually represent newly formed zircons. Unfortunatelly, the small size of those zircons did not allow for Hf isotope analysis which could lend support to this hypothesis.

It may be noted that this younger age is in the range of the Rb-Sr ages calculated above for the OAXZ eclogite, and a bit younger than that for CO-39. Similar Rb-Sr ages have been also reported by Van Calsteren et al. (1979) and Peucat et al. (1990) (recalculated in this PhD Thesis, Table 4.4). All these data suggest that the youngest zircon crystallization could be linked to the release of fluids along the shear zones during the exhumation of the high-grade regional Upper Allochthon.

4.3.d. Implications in regional geology

The petrografic observations, together with the data presented in the precedent sections, suggest that the metamophic rocks from the Allochthonous complexes considered in this study were subjected to a single, mid-latest Devonian subduction-exhumation cycle, as already

suggested by various authors (Ordoñez Casado et al., 2001; Roger and Matte, 2005). Peucat et al. (1990) proposed the existence of another HP metamorphic event, recorded by the mafic-ultramafic units of the Upper Allochthon, that would have taken place 420 Ma ago (mid Silurian). Their proposal was based upon heterogeneous U-Pb zircon radiometric results obtained for high-pressure gneisses from the Cabo Ortegal Complex. It is remarkable that similar age results (or slightly younger) have been published by other authors (Santos Zalduegui et al., 1996; Fernández-Suárez et al., 2007) and interpreted concomitantly. The results obtained in this study after zircons of similar rocks suggest that, by contrast, the reported Silurian age for a previous HP metamorphic event actually might result of mixing different compositional sectors (and thus isotopically heterogeneous) within a given grain, or even of Pb-loss.

The age of the protoliths of the rocks studied from the Basal Units is well constrained as Cambro-Ordovician. In detail, previous works have distinguished an older calc-alcaline suite dated around 495 Ma (Abati et al., 2010), and a younger alkaline magmatism at ca. 470 Ma (Rodríguez et al., 2007). In the case of the Upper Allochthon protoliths, their radiometric ages have been usually considered to be Cambrian to Early Ordovician, too, younger ages being rare. Ordoñez Casado et al. (2001) observed a ca. 25 Ma difference between the protolith ages of magmatic zircons from N-MORB and ky-bearing eclogites from the Cabo Ortegal Complex, which altogether with geochemical data were interpreted as a recording changes in the geodynamic setting of Cambro-Ordovician magmatism. In this study, the Middle to Late Ordovician ages obtained for hugh-pressure migmatitic gneiss from the Cabo Ortegal Upper Allochthon are interpreted as dating deep crustal melts within an arc setting, possibly incorporating material components of continental and mantle sources. In any case, it is suggested that the magmatic activity recorded by Cambro-Ordovician rocks lasted as much in the Allochthonous Complexes as it did in the Basal Units.

The similarity between radiometric ages obtained herein after rock samples from different lithologies and using different techniques (Table 4.1) strongly suggests that a subduction-related high-pressure metamorphic event occurred during the Middle Devonian (ca. 390 Ma) in the Upper Allochthon of the NW Iberian Complexes. It is confirmed as well that the subduction-related high-pressure metamorphic event was radiometrically locked later by the rocks from the Basal Units (at ca. 375-370 Ma), as already noticed by Abati et al. (2010). The explanation for the age difference of ca. 15-20 Ma observed between the high-pressure metamorphism in the Upper Allochthon and the Basal Units requires consideration of how was the consumption of the Rheic Ocean. Among the hypothesis proposed so far, it appears to prevail the idea that this ocean was likely small, as supported by the similar facies and faunas of the Early Ordovician sediments preserved on both sides of the Rheic suture (Robardet et al., 1993).

As regards the exhumation of high-pressure metamorphic rocks, the new zircon data from the Upper Allochthon samples are not conclusive. Radiometric ages obtained after the Rb-Sr system compare to those derived of zircon U-Pb analyses and preclude any confident calculation of cooling or depressurization rates. This concurs with the results obtained by Van Calsteren et al. (1979) and Peucat et al. (1990), both recalculated and presented in the Table 4.4, and contrasts with the proposals previously issued by Ábalos et al. (1996) and Ordóñez-Casado et al. (2001)

Assuming closure temperatures of ca. 550 ^{o}C for muscovite (Jäger et al., 1967; Blackenburg et al., 1989) and of 450-500 °C for amphibole (Harrison and Fitz Gerald, 1986; Li et al., 2000), a depressurization from ca. 2.5 GPa (Mendia, 2000) to 0.6-0.8 GPa would result in an exhumation rate of 1.5 mm/y for eclogites from the Cabo Ortegal Upper Allochthon. These represent low exhumation rates for high-pressure metamorphic rocks, which usually exceed 3 mm/y (e.g.: Dabie-Sulu terrane, Schmidt et al., 2008) and even reach 22 mm/y (e.g.: Dora Maira massif, Gebauer et al., 1997).

The ^{40}Ar/^{39}Ar ages obtained by Dallmeyer et al. (1991) on hornblendes from the structurally underlying ophiolitic unit (Arenas et al., 1986) suggest that the exhumation may occur rapidly after the maximum burial, thus, disagreeing with what stated above. Considering those Ar/Ar ages, together with the U-Pb rutile ages of Valverde-Vaquero et al. (1997), Santos Zalduegui (1996) and Roger and Matte (2005), an exhumation rate of 7-12 mm/y is calculated, value in accord with others calculated for high-pressure terranes (e.g., Kirchembaur et al., 2012). Exhumation rates calculated from the Rb-Sr analyses on amphiboles of this study give exhumations rates for the Malpica-Tui band of ca. 7 mm/y, which would be even higher considering ^{40}Ar/^{39}Ar ages of Rodriguez et al. (2003).

Hence, all these estimations suggest a reset of the Rb-Sr system at 365-355 Ma, coinciding with the growth of new zircons in the high-pressure migmatitic gneiss, probably due to fluid circulation processes. It is likely that release of fluids during the subduction of the Lower Allochthon beneath the Upper Allochthon (and Ophiolite unit) led to an important activity of fluids in the upper units. Infiltration of fluids have described in different lithologies within the Upper Allochthon (Mendia, 2000; Ábalos et al., 2004; Puelles et al., 2005). This fluid circulation would have also affected the Basal units, as it could be inferred from the reset of the Rb-Sr system detected in Pioza muscovites or the formation of new zircon and monazite (Abati and Dunning, 2002; Abati et al., 2010).

Finally, this ensemble of facies, lithologies and units would have been sealed by the closure of the Rheic ocean and the subsequent continental collision, underthrusting of the parautochthon and intrusion of granites during the Carboniferous (see e.g., Stampfli et al., 2013; Schulmann et al., 2014; Díez Fernández and Arenas, 2015) and references therein for

comprehensive reviews of geotectonic models and proposals of evolution of the Iberian allochtonous complexes and their relative autochthon, and of the Gondwana margin and Rheic ocean remnants elsewhere within the European Variscan foldbelt).

Chapter 5: Conclusions

5. Conclusions

Geochronology is an area of vital importance in geosciences. It measures the age of Earth materials and provides the temporal framework in which other geoscience data can be interpreted. The development of Isotope Geochemistry/Geochronology has triggered many technical improvements in the past decades and it has permitted to obtain data with a precision and accuracy levels that were inconceivable years ago. During the elaboration of this PhD Thesis, the implementation of four methods for isotopic measurement has been carried out successfully at the Isotope Geochemistry and Geochronology facility (IBERCRON) of the University of the Basque Country UPV/EHU, solving all the problems that have been encountered for each isotopic system and/or analytical technique. Apart from the main goals presented in the Introduction (Chapter 1), along this process a series of intermediate objectives have been also achieved. They are summarized as follows:

5.1. The Rb-Sr system by ID-MC-ICP-MS

- Concentration and composition of ^{87}Rb and ^{86}Sr tracers have been sucesfully calibrated through reverse isotopic dilution.
- In order to calculate the Sr concentration and isotopic composition of the unknowns, an ^{86}Sr tracer has been used which is economically much more affordable and available than the very expensive ^{84}Sr tracer of high purity and that had never been used before for this purpose. It has been proven to be perfectly valid.
- The appropriateness of the applied corrections, both for fractionation and interferences, in the measurement of Rb and Sr has been verified through the repeated analysis of NIST984 and NIST987 standards.
- The protocol of fussion-dissolution set up for the treatment of geological samples has proven to work fine in all the cases considered and is regarded as fully reliable for geochemical research.
- Isolation of Sr with extraction chromatography material and total separation of Rb from Zr using Dowex cationic resin has been successfully achieved.
- The configuration selected for the Faraday cups in the MC-ICP-MS has enabled the simultaneous measurement of Rb and Zr, and of Sr and Zr, allowing the use of Zr for bias correction.

- The mass bias correction for Rb and Sr in spiked samples was thus successfully achieved by using the $^{91}Zr/^{90}Zr$ ratio.
- The subtraction of the spike contribution has been done externally. The results obtained suggest that it was performed correctly.
- Sample introduction and desolvation using Apex and SIS devices has enabled to measure samples with a wide range of concentrations.
- The results obtained for NIST987 and different CRM geological materials in solution have shown good precision and accuracy for the $^{87}Sr/^{86}Sr$ ratio, comparable with previously published values.
- Calculated concentrations for Rb and Sr in different CRM geological material were also satisfactory, allowing the obtention of precise and accurate $^{87}Rb/^{86}Sr$ data.

Taking into account all the above-mentioned points, it can be stated that the Rb-Sr method by ID-MC-ICP-MS with ^{86}Sr tracer has been successfully implemented. In a near future this work may continue with the development of a new method focused on the measurement of Rb-Sr ages in-situ by laser ablation-MC-ICP-MS.

5.2. The Lu-Hf system by ID-MC-ICP-MS

- Concentration and composition of the mixed ^{179}Hf-^{176}Lu tracer have been sucesfully calibrated through reverse isotopic dilution.
- No problem has been found during the digestion of the sample by alkaline fusion, so it has been considered as the most appropriate for whole rock digestion.
- The protocol of alkaline fussion-dissolution set up for the treatment of whole rock samples yielded good results and is regarded as fully reliable for geochemical research
- As for the mineral separates, digestion by acid attack is considered as the best way to manage Hf-rich inclusions that might invalid the results.
- A procedure for isolation of Hf using Dowex cationic resin and Lu plus Yb with extraction chromatography material has been successfully achieved. The procedure allows for concomitant separation of Sm and Nd and their isotopic analysis using TIMS or MC-ICP-MS.
- The Faraday cups configuration adopted in the MC-ICP-MS has enabled the simultaneous measurement of masses 171, 173, 175, 176, 177, 178 and 179, and therefore, it has been possible to measure all the masses that can interfere both on Lu or Hf, as well as correcting in an adequate manner the mass bias.

- The bias correction for Hf in spiked samples has been done externally through a sequence of mathematical operations. The results obtained suggest that all the functions applied for mass bias and spike subtraction worked properly. In the same way, the ^{176}Lu tracer contribution has also been corrected satisfactorily.
- The appropriateness of the applied corrections, both for fractionation and interferences, has been verified for Hf through the repeated analysis of JMC475 standard.
- The Lu results were tested by means of a Lu Standard for ICP-MS. The values obtained for ^{176}Lu/^{175}Lu indicate that the selected ^{173}Yb/^{171}Yb and ^{173}Yb/^{171}Yb ratios were correct, whereby the fractionation and interferences are properly corrected.
- The results obtained for the dissolution JMC475 and different CRM geological materials have shown good precision and accuracy of the ^{176}Hf/^{177}Hf ratio, comparable with published values of reference.
- Calculated Hf and Lu concentrations in different CRM geological material have also been precise and accurate enough so as to allow precise and accurate ^{176}Lu/^{177}Hf data.

Since it has been possible to find a solution for all the possible uncertainties associated with the measurements of the Lu-Hf system, it can be said that the method has been implemented correctly being now available for the scientific community. Although the sensitivity of the current equipment does not permit in-situ Lu-Hf dating, the author is optimistic about this possibility in the near future given the rapid development of the instrumentation.

5.3. The U-Th-Pb system by LA-Q-ICP-MS

- The modification done in the Super Cell™ type ablation cell has enabled the simultaneous introduction of one thin section and standards.
- It has been established that 20 µm and 25 µm spot sizes using a 213 nm Nd:YG laser source produce enough signal to measure U and Pb in the Q-ICP-MS with confidence.
- Laser parameters have been set by the analysis of the NIST SRM 612 reference glass, which allowed us to optimize the Pb and U signals and minimize the oxides (ThO^+/Th^+ ratio).
- The analytical protocol of measuring the blank and signal on an ongoing basis as well as the sample-standard sequence facilitated the subsequent efficient data processing.
- The residence time for each isotope has been demonstrated to be adequate.
- Data processing carried out with GLITTER® software has yielded ages for standards within the range of previously published values. Yet, the precision and accuracy of the method is

hampered by the intrinsic limitations of the technique whereby they are not comparable to those obtained by TIMS.

The U/Pb ages obtained on different standards under the same conditions as those used for the unknowns demonstrate the validity of the results by the implemented method. The next step to take in the future will be focused on the implementation of the 'Laser Ablation Split Stream' technique (e.g., Yuan et al., 2008, Kylander-Clark et al., 2013) for the simultaneous measurement of U-Pb in a Q-ICP-MS and Hf isotopes in a MC-ICP-MS.

5.4. The Hf isotopes by LA-MC-ICP-MS

- Using the same ablation cell and laser source employed in the LA-Q-ICP-MS experiments, it was established that spot sizes of at least 40 μm are needed for a good precision and accuracy in MC-ICP-MS measurements.
- The Faraday cups configuration adopted in the MC-ICP-MS has enabled the simultaneous monitoring of masses 171, 173, 175, 176, 177, 178 and 179 and, therefore, the measurement at the same time of all the masses that can interfere on Hf, as well as the correctiof of the mass bias.
- The results obtained for the $^{176}Hf/^{177}Hf$ ratios in zircons of reference materials confirm that the selected values of $^{176}Lu/^{175}Lu$, $^{173}Yb/^{171}Yb$ and $^{173}Yb/^{171}Yb$ for interference corrections are correct and, therefore, that these corrections have been properly done.
- The analytical protocol of measuring the blank and signal on an ongoing basis as well as the sample-standard sequence applied has facilitated the efficient off-line processing of the raw data.
- Laser parameters have been optimized by the analysis of the GJ-1 reference zircon crystal, which permits to monitor the N_2 additional gas flow and thus, improves the Hf signals.
- The data processing carried out with Iolite® software resulted in values for the $^{176}Hf/^{177}Hf$ ratio in the measured standards well in the range of the data of reference obtained through analyses done by laser ablation or in solution.

The $^{176}Hf/^{177}Hf$ ratios obtained on different standards under the same conditions as those applied to the unknown samples demonstrate the validity of the results provided by the implemented method. As mentioned above, the next step to take in the future will focus on the implementation of the 'Laser Ablation Split Stream' technique (e.g., Yuan et al., 2008, Kylander-

Clark et al., 2013) for the simultaneous measurement of U-Pb in a Q-ICP-MS and Hf isotopes in a MC-ICP-MS.

5.5. Aplication of the implemented methods

The ultimate goal of the successful set up of these techniques is to apply and develop them through the radiometric dating and geochemical tracing studies of natural samples in order to better interpret geological processes of interest. The same techniques can obviously fully applied whenever necessary in research studies of related disciplines like environmental sciences, archaeology, anthropology, forensic, etc. In this PhD Thesis, these techniques have been used to date and trace high-pressure rocks from the Malpica-Tui and Cabo Ortegal Allochthonous Complexes of the NW Iberian Massif. The main conclusions of such a study are presented below:

- The U-Pb data obtained for the zircons from high-pressure migmatitic gneisses within the regional Upper Allochthon in Ortegal suggest ages of igneous protoliths of ca. 460-485 Ma and a subsequent subduction-related metamorphic event at ca. 390 Ma. A younger set of ages at ca. 360 Ma was obtained for small and homogeneous zircons, the meaning of which is still unclear.
- The Hf isotopic composition of the zircons from those gneisses shows two groups of values, with lower $^{176}Hf/^{177}Hf$ ratios in the presumed metamorphic rims.
- Rb-Sr ages obtained for amphibole and muscovite in eclogites within this regional Upper Allochthon cluster at ca. 365 Ma and attest to relatively late recrystallization processes during exhumation of the complex.
- The Lu-Hf ages obtained for minerals of eclogites from the regional Lower Allochthon in Malpica-Tui suggest a maximum burial of the unit at ca. 375 Ma.
- Rb-Sr ages obtained for minerals in those eclogites are of ca. 360 Ma for amphibole and ca. 350 Ma for muscovite pointing to a faster uprise of this Allochthon.

The Allochthonuos Complexes from northwest Iberia are the westernmost outcrops of the European Variscan Belt and would be formed through a single mid-latest Devonian subduction-exhumation cycle. The subduction of the regional Lower Allocthon took place 15-20 Ma after the subduction of the uppermost high-pressure units units. The lower $^{176}Hf/^{177}Hf$ ratios suggest that the system was partially open during the maximum burial of the Upper Allochton. The Rb-Sr ages of both Allochthons, interpreted as having been reset, along with the zircon growth at 360 Ma, point to an important activity of fluids during the exhumation processes.

References

References

Ábalos, B., Azcárraga, J., Gil Ibarguchi, J.I., Mendia, M.S. and Santos Zalduegui, J.F., 1996. Flow stress, strain rate and effective viscosity evaluation in a high-pressure nappe (Cabo Ortegal, Spain). *J. metamorphic Geol.,* 14, 227-248.

Ábalos, B., Azcárraga, J., Gil Ibarguchi, J.I., Mendia, M.S. and Puelles, P., 2000. Mapa Geológico del Complejo de Cabo Ortegal (NO de España), scale 1:42,750. Inst. Univ. de Xeoloxía Isidro Parga Pondal, La Coruña.

Ábalos, B., Puelles, P. and Gil Ibarguchi, J.I., 2003. Structural assemblage of high-pressure and crustal rocks in a subduction channel (Cabo Ortegal, NW Spain). Tectonics, 22 (2), 1-21.

Ábalos, B., Grassi, K.G., Fountain, D.M. and Gil Ibarguchi, J.I., 2004. Geología estructural, petrofábrica y petrofísica de las eclogitas de Cabo Ortegal (NO de España). Terra Nova 24, 86 p.

Abati, J., Dunning, G.R., Arenas, R., Díaz García, F., González Cuadra, P., Martínez Catalán, J.R. and Andonaegui, P., 1999. Early Ordovician orogenic event in Galicia (NW Spain): evidence from U-Pb ages in the uppermost unit of the Ordenes Complex. *Earth Planet. Sci. Lett.*, 165, 213-228.

Abati, J. and Dunning, G.R., 2002. Edad U-Pb en monacitas y rutilos de los paragneises de la Unidad de Agualada (Complejo de Órdenes, NW del Macizo Ibérico). *Geogaceta*, 32, 95-98.

Abati, J., Castiñeiras, P., Arenas, R., Fernández-Suárez, J., Gómez-Barreiro, J. and Wooden, J., 2007. Using SHRIMP zircon dating to unravel tectonothermal events in arc environments. The early Palaeozoic arc of NW Iberia revisited. *Terra Nova*, 19, 432-439.

Abati, J., Gerdes, A., Fernández-Suárez, J., Arenas, R., Whitehouse, M.J. and Díez Fernández, R., 2010. Magmatism and early-Variscan continental subduction in the northern Gondwana margin recorded in zircons from the basal units of Galicia, NW Spain. *Geological Society of America Bulletin*, 122, 219-235.

Albarède, F., Télouk, P., Blichert-Toft, J., Boyet, M., Agranier, A. and Nelson, B., 2004. Precise and accurate isotopic measurements using multiple-collector ICP-MS. *Geochim Cosmochim Acta,* 68, 2725-2744.

Albert, R., Arenas, R., Gerdes, A., Sánchez Martínez, S., Fernández-Suárez, J., and Fuenlabrada, J. M., 2015a. Provenance of the Variscan Upper Allochthon (Cabo Ortegal Complex, NW Iberian Massif). *Gondwana Research*, 28, 1434-1448.

Albert, R., Arenas, R., Gerdes, A., Sánchez Martínez, S. and Marko, L., 2015b. Provenance of the HP-HT subducted margin in the Variscan belt (Cabo Ortegal Complex, NW Iberian Massif). *J. metamorphic Geol.*, 33, 959-979.

Amato, J.M., Johnson, C.M., Baumgartner, L.P. and Beard, B.L., 1999. Rapid exhumation of the Zermatt-Saas ophiolite deduced from high-precision Sm-Nd and Rb-Sr geochronology. *Earth Planet. Sci. Lett.,* 171, 425-438.

Amelin, Y. and Davis, W.J., 2005. Geochemical test for branching decay of ^{176}Lu. *Geochim. Cosmochim. Acta*, 69, 465-473.

Anczkiewicz, R. and Thirlwall, M.F., 2003. Improving precision of Sm-Nd garnet dating by H_2SO_4 leaching - a simple solution to phosphate inclusions problem. In: D. Vance, W. Mueller, I.M. Villa (eds.). Geochronology: Linking the Isotopic Record with Petrology and Textures, *Spec. Publ.-Geol. Soc. Lond.*, 220, 83-91.

Anczkiewicz, R., Platt, J.P., Thirlwall, M.F. and Wakabayashi, J., 2004. Franciscan subduction off to a slow start: evidence from high-precision Lu-Hf garnet ages on high grade-blocks. *Earth Planet. Sci. Lett.*, 225, 147-161.

Anczkiewicz, R., Szczepanski, J., Mazur, S., Storey, C.D., Crowley, Q., Villa, I.M., Thirlwall, M.F. and Jeffries, T.E., 2007. Lu-Hf geochronology and trace element distribution in garnet: implications for uplift and exhumation of ultra-high pressure granulites in the Sudetes, SW Poland. *Lithos*, 95, 363-380.

Andersen, T., 2002. Correction of common lead in U-Pb analyses that do not report ^{204}Pb. *Chem. Geol*., 192, 59-79.

Andonaegui, P., Castiñeiras, P., González Cuadra, P., Arenas, R., Sánchez Martínez, S., Abati, J., Díaz García, F. and Martínez Catalán, J.R., 2012. The Corredoiras orthogneiss (NW Iberian Massif): Geochemistry and geochronology of the Paleozoic magmatic suite developed in a peri-Gondwanan arc. *Lithos*, 128-131, 84-99.

Anthonioz, P. and Ferragne, A., 1978. Le Precambrien polymétamorphique allochtone du nord−ouest de la Peninsule Ibérique, temoin d'une nappe de charriage caledonienne?. In: Geología de la parte N del Macizo Ibérico. O Castro, La Coruña, 23-41.

Arevalo, R., Bellucci, J. and McDonough, W.F., 2010. GGR Biennial Review: Advances in laser ablation and solution ICP-MS from 2008 to 2009 with particular emphasis on sensitivity enhancements, mitigation of fractionation effects and exploration of new applications. *Geostandards and Geoanalytical Research*, 34, 327-341.

Arenas, R., Gil Ibarguchi, I., González Lodeiro, F., Klein, E., Martínez Catalán, J.R., Ortega Gironés, E., de Pablo Maciá, J.G. and Peinado, M., 1986. Tectonostratigraphic units in the complexes with mafic and related rocks of the NW of the Iberian Massif. *Hercynica*, 2, 87-110.

Arps, C.E.S., 1970. Petrology of a part of the western Galician basement between the Rio Jallas and the Ria de Arosa (NW Spain) with emphasis on zircon investigations. *Leidse Geologische Mededelingen*, 46, 57-116

Arps, C.E.S., 1981. Amphibolites and other metamorphic mafic rocks of the blastomylonitic graben in Western Galicia, NW Spain: field relations and petrography. *Leidse Geologische Mededelingen*, 52, 57-71.

Bard, J.P., Burg, J.P., Matte, Ph. and Ribeiro, A., 1980. La Chaine Hercynienne d'Europe occidentale en termes de Tectonique des Plaques. In: Géologie de l'Europe, du Précambrien aux basins sédimentaires post-Hercyniennes. *Mémoires du B.R.G.M.,* 108, 233-246.

Balcaen, L., De Schrijver, I., Moens, L. and Vanhaecke, F., 2005. Determination of the 87Sr/86Sr isotope ratio in USGS silicate reference materials by multi-collector ICP-mass spectrometry. *International Journal of Mass Spectrometry*, 242, 251-255.

Bastida, F., Marcos, A., Marquínez, J., Martínez-Catalán, J.R., Pérez-Estaun, A. and Pulgar, J.A., 1984. Hoja nº 1 del Mapa Geológico Nacional 1:200.000 (La Coruña) y memoria. *Publicaciones del I.G.M.E*., Madrid, 155 p.

Baxter, E.F., Ague, J.J. and DePaolo, D.J., 2002. Prograde temperature-time evolution in the Barrovian type-locality constrained by Sm/Nd garnet ages from Glen Clova, Scotland. *Journal of the Geological Society*, 159, 71-82.

Bayer, R. and Matte, Ph., 1979. Is the mafic/ultramafic massif of Cabo Ortegal (northern Spain) a nappe emplaced during a Variscan obduction? A new gravity interpretation. *Tectonophysics*, 57, 9-18.

Beane, R. J. and Connelly, J. N., 2000. $^{40}Ar/^{39}Ar$, U-Pb, and Sm-Nd constraints on the timing of metamorphic events in the Maksyutov Complex, southern Ural Mountains. *J. Geol. Soc. London,* 157, 811-822.

Beranoaguirre, A., 2010. Petrology of subduction-related, high-pressure migmatites within granulites of the Cabo Ortegal complex (NW Iberian Massif). MsC thesis, Granada University, 67 p.

Bernard-Griffiths, J., Peucat, J.J., Cornichet, J., Iglesias Ponce de León, M. and Gil Ibarguchi, J.I., 1985. U-Pb, Nd isotope and REE geochemistry in eclogites from the Cabo Ortegal Complex, Galicia, Spain: an example of REE inmobility conserving MORB-like patterns during high-grade metamorphism. *Chem. Geol.*, 52, 217-225.

Black, L.P., Kamo, S., Allen, C.M., Davis, D.W., Aleinikoff, J.N., Valley, J.W., Mundil, R., Campbell, I.H., Korsch, R.J., Williamns, I.S. and Foudoulis, C., 2004. Improved $^{206}Pb/^{238}U$ microprobe geochronology by the monitoring of a trace-element-related matrix effect; SHRIMP, ID-TIMS, ELA-ICP-MS and oxygen isotope documentation for a series of zircon standards. *Chem. Geol.*, 205, 115-140.

Blackenburg, F.V., Villa, I.M, Baur, H., Morteani, G. and Steiger, R.H., 1989. Time calibration of a PT-path from the western Tauern Window, Eastern Alps: the problem of closure temperatures. *Contrib. Mineral. Petrol.*, 101, 1-11.

Bleiner, D. and Günther, D., 2001. Theoretical description and experimental observation of aerosol transport processes in laser ablation inductively coupled plasma mass spectrometry. *Journal Analytical Atomic Spectrometry*, 16:449.

Blichert-Toft, J., 2001. On the Lu-Hf isotope geochemistry of silicate rocks. *Geostandars Newsletter: The Journal of Geostandards and Geoanalysis*, 25, 41-56.

Blichert-Toft, J. and Alvarède, F., 1997. The Lu-Hf isotope geochemistry of chondrites and the evolution of the mantle-crust system. *Earth Planet. Sci. Lett.*, 148, 243-258.

Blichert-Toft, J., Chauvel, C. and Albarède, F., 1997. Separation of Hf and Lu for high-precision isotope analysis of rich samples by magnetic sector-multiple collector ICP-MS. *Contrib. Mineral. Petrol.,* 127, 248-260.

Blichert-Toft, J. and Frei, R., 2001. Complex Sm-Nd and Lu-Hf isotope systematics in metamorphic garnets from the Isua supracrustal belt, West Greenland. *Geochim. Cosmochim. Acta,* 65, 3177-3189.

Boltwood, B., 1907. The Ultimate Disintegration Products of the Radio-active Elements. Part II. The disintegration products of uranium. *American Journal of Science*, 23, 77-88.

Borg, L.E., Gaffney, A.M., Shearer, C.K., DePaolo, D.J., Hutcheon, I.D., Owens, T.L., Ramon, E. and Brennecka, G.A., 2009. Mechanisms for incompatible-element enrichment on the Moon deduced from the lunar basaltic meteorite Northwest Africa 032. *Geochim. Cosmochim. Acta* , 73, 3963-3980.

Bosse, V., Feraud, G., Ruffet, G., Ballèvre, M., Peucat, J.J., and De Jong, K., 2000. Late Devonian subduction and early orogenic exhumation of eclogite-facies rocks from the Champtoceaux Complex (Variscan belt, France). *Geological Journal*, 35, 297-325.

Bowring, S.A., Erwin, D., Parrish, R.R. and Renne, P., 2005. EARTHTIME: a community-based effort towards high-precision calibration of earth history. *Geochim. Cosmochim. Acta,* 69, A316.

Burg. J.P., Iglesias, M., Laurent, Ph., Matte, Ph. and Ribeiro, A., 1981. Variscan intracontinental deformation: the Coimbra-Córdoba Shear Zone (SW Iberian Peninsula). *Tectonophysics*, 78, 15-42.

Burg, J.P., Balé, P., Brun, J.P. and Girardeau, J., 1987. Stretching lineations and transport direction in the Ibero-Armorican Arc during the Siluro-Devonian collision. *Geodinamica Acta*, 1, 71-81.

Cali, J.P., 1970. Certificate of analysis: Standard reference material 984 Rubidium Chloride. http://www.nist.gov/srm/index3column.cfm, NIST.

Carlé, W., 1945. Ergebnisse geologischer Untersuchungen im Grundgebirge von Galicien (Nordspanien). *Geotektonische Forschungen*, 6, 13-36.

Castiñeiras, P., Díaz García, F. and Gómez Barreiro, J., 2010. REE-assisted U-Pb zircon age (SHRIMP) of an anatetic granodiorite: Constraints on the evolution of the A Silva granodiorite, Iberian allochthonous complexes. *Lithos*, 116, 153-166.

Cheng, H., King, R.L., Nakamura, E., Vervoort, J.D. and Zhou, Z., 2008. Coupled Lu-Hf and Sm-Nd geochronology constrains garnet growth in ultra-high-pressure eclogites from the Dabie orogen. *J. metamorphic Geol.*, 26, 741-758.

Cheng, H., Vervoort, J.D., Li, X., Zhang, C., Li, Q. and Zheng, S., 2011. The growth interval of garnet in the UHP eclogites from the Dabie orogen, China. *American Mineralogist*, 96, 1300-1307.

Cheng, H., Zhang, C., Vervoort, J.D., Li, X., Li, Q., Wu, Y. and Zheng, S., 2012. Timing of eclogite facies metamorphism in the North Qinling by U-Pb and Lu-Hf geochronology. *Lithos*, 136-139, 45-59.

Cherniak, D.J., 2000. Pb diffusion in rutile. *Contrib. Mineral. Petrol*., 139, 198-207.

Chernoff, C.B. and Carlson, W. D., 1999. Trace element zoning as a record of chemical disequilibrium during garnet growth. *Geology*, 27, 555-558.

Chu, N.C., Taylor, R., Chavagnac, V., Nesbitt, R., Boella, R., Milton, J., German, C., Bayon, G. and Burton, K., 2002. Hf isotope ratio analysis using multi-collector inductively coupled plasma mass spectrometry: An evaluation of isobaric interference corrections. *J. Anal. At. Spectrom*., 17, 1567-1574.

Claiborne, L.L., Miller, C.F., Flanagan, D.M., Clynne, M.A. and Wooden, J.L., 2010. Zircon reveals protracted magma storage and recycling beneath Mount St. Helens. *Geology*, 38, 1011-1014.

Cocherie, A. and Robert, M., 2008. Laser ablation coupled with ICP-MS applied to U-Pb zircon geochronology: A review of recent advances. *Gondwana Research*, 14, 597-608.

Coke, C. and Ribeiro, A., 2000. Malpica−Lamego shear zone; A major crustal discontinuity in the Iberian Variscan fold belt. Program and Abstracts − *International Conference on Basement Tectonics 15*, 208−210.

Coplen, T.B., 2001. Erratum: ''Atomic Weights of the Elements 1999''. *J Phys Chem,* Ref Data 30:701.

Corfu, F., Hanchar, J.M., Hoskin, P.W.O. and Kinny, P.D., 2003a. Atlas of zircon textures. *Reviews in Mineralogy and Geochemistry*, 53, 469-500.

Corfu, F., Ravna, E.J.K., and Kullerud, K., 2003b. A Late Ordovician U-Pb age for the Tromsø Nappe eclogites, Uppermost allochthon of the Scandinavian caledonides. *Contrib. Mineral. Petrol.*, 145, 502-513.

Crowe, S.A., Fryer, B.J., Samson, I.M., and Gagnon, J.E., 2003. Precise isotope ratio determination of common Pb using quadrupole LA-ICP-MS with optimized laser sampling conditions and a robust mixed-gas plasma. *J. Anal. At. Spectrom.*, 18, 1331-1338.

Dallmeyer, R.D. and Gil Ibarguchi, J.I., 1990. Age of the amphibolitic metamorphism in the Ophiolitic Unit of the Morais allochthon (Portugal): implications for early Hercynian orogenesis in the Iberian massif. *J. Geol. Soc. London*, 147, 873-878.

Dallmeyer, R.D. and Tucker, R.D., 1993. U-Pb zircon age for the Lagoa augen gneiss, Morais Complex, Portugal: tectonic implications. *J. Geol. Soc. London*, 150, 405-410.

Dallmeyer, R.D., Ribeiro, A. and Marques, F., 1991. Polyphase Variscan emplacement of exotic terranes (Morais and Bragança Massifs) onto Iberian successions: evidence from $^{40}Ar/^{39}Ar$ mineral ages. *Lithos*, 27, 133-144.

Dallmeyer, R.D., Martínez Catalán, J.R., Arenas, R., Gil Ibarguchi, J.I., Gutiérrez Alonso, G., Farias, P., Bastida, F., and Aller, J., 1997. Diachronous Variscan tectonothermal activity in the NW Iberian Massif: evidence form $^{40}Ar/^{39}Ar$ dating of regional fabrics. *Tectonophysics*, 277, 307-337.

Dalmasso, J., Barci-Funel, G. and Ardisson, G. J., 1992. Reinvestigation of the decay of the long-lived odd-odd ^{176}Lu nucleus. *International Journal of Radiation Application*, 43, 69-76.

Davies , G.R. and Tommasini, S., 2000. Isotopic disequilibrium during rapid crustal anatexis: implications for petrogenetic studies of magmatic processes. *Chem. Geol*., 162, 169-191.

Davis, D.W., Amelin, Y., Nowell, G.M. and Parrish, R.R., 2005. Hf isotopes in zircon from the western Superior province, Canada: implications for Archean crustal development and evolution of the depleted mantle reservoir. *Precambrian Research*, 140, 132-156.

Deegan, F.M., Troll, V.R., Barker, A.K., Harris, C., Chadwick, J.P., Carracedo, J.C. and Delcamp, A., 2012. Crustal versus source processes recorded in dykes from the Northeast volcanic rift zone of Tenerife, Canary Islands. *Chem. Geol.*, 334, 324-344.

De Laeter, J.R., Bohlke, J.K., De Bievre, P., Hidaka, H., Peiser, H.S., Rosman, K.J.R. and Taylor, P.D.P., 2003. Atomic weights of the elements: Review 2000 - (IUPAC tecnichal report). *Pure Appl. Chem*., 75, 683-800.

Den Tex, E., 1981a. Basement evolution in the northern Hesperian Massif: A preliminary survey of results obtained by the Leiden Research Group. *Leidse Geologische Mededelingen,* 52, 1−21.

Den Tex, E., 1981b. A geological section across the Hesperian Massif in western and central Galicia. *Geologie Mijnbouw,* 60, 33−40.

Den Tex, E. and Floor, P., 1967. A blastomylonitic and polymetamorphic 'graben' in western Galicia (NW Spain). In: 'Etages Tectoniques', La Bacconière, Neuchatel, 169−178.

Díaz García, F., Arenas, R., Martínez Catalán, J.R., González del Tánago, J. and Dunning, G.R., 1999. Tectonic evolution of the Careón Ophiolite (northwest Spain): a remnant of oceanic lithosphere in the Variscan Belt. *Journal of Geology*, 107, 587-605.

Díaz García, F., Sánchez Martínez, S., Castiñeiras, P., Fuenlabrada, J.M. and Arenas, R.. 2010. A peri-Gondwanan arc in NW Iberia. II: Assessment of the intra-arc tectonothermal evolution through U-Pb SHRIMP dating of mafic dykes. *Gondwana Research*, 17, 352-362.

Díez Fernández, R., 2011. Evolución estructural y cinemática de una corteza continental subducida: la Unidad de Malpica-Tui (NO del Macizo Ibérico). *Nova Terra* 40, A Coruña.

Díez Fernández, R. and Martínez Catalán, J. R., 2009. 3D Analysis of an Ordovician igneous ensemble: A complex magmatic structure hidden in a polydeformed allochthonous Variscan unit. *Journal of Structural Geology* 31, 222−236.

Díez Fernández, R. and Arenas, R., 2015. The Late Devonian Variscan suture of the Iberian Massif: A correlation of high-pressure belts in NW and SW Iberia. *Tectonophysics*, 654, 96-100.

Díez Fernández, R., Martínez Catalán, J.R., Arenas, R., Abati, J., Gerdes, A. and Fernández-Suárez, J., 2012. U-Pb detrital zircon analysis of the lower allochthon of NW Iberia: age constraints, provenance and links with the Variscan mobile belt and Gondwana cratons. *Journal of the Geological Society*, 169, 655-665.

Dixon, D., McNair, A. and Curran, S. C., 1954. The natural radioactivity of lutetium. *Philosophical Magazine*, 45, 683-684.

Duchêne, S., Blichert-Toft, J., Luais, B., Télouk, P., Lardeaux, J.M and Albarède. F., 1997. The Lu-Hf dating of garnets and the ages of the Alpine high-pressure metamorphism. *Nature*, 387, 586-588.

Edmunson, J., Borg, L.E., Nyquist, L.E. and Asmeron, Y., 2009. A combined Sm-Nd, Rb-Sr, and U-Pb isotopic study of Mg-suite norite 78238: Further evidence for early differentiation of the Moon. *Geochim. Cosmochim. Acta* , 73, 514-527.

Eggins, S.M, Kinsley, L.P.J. and Shelley, J.M.G., 1998. Deposition and element fractionation processes during atmospheric pressure laser sampling for analysis by ICP-MS. *Appl. Surf. Sci*., 129, 278-286.

Elhlou, S., Belousova, E.A., Griffin, W.L., Pearson, N.J. and O'Reilly, S.Y., 2007. New Standard Reference Material for in-situ U-Pb zircon dating. *Agilent ICP-MS Journal*, 32, 4-5.

Engels, J.P. 1972. The catazonal poly-metamorphic rocks of Cabo Ortegal (NW Spain), a structural and petrographic study. *Leidse Geologische Mededelingen*, 48, 83-133.

Engels, J.P., Hubregtse, J.J.M.W., Floor, P. and Den Tex, E., 1974. Precambrian complexes in the Hercynian orogen of the north-western Iberian Peninsula. P.I.C.G. Précambrien des zones mobiles de l'Europe, Praha. Conference Book, 163-173.

Farias, P., Gallastegui, G., González Lodeiro, F., Marquínez, J., Martín-Parra, L.M., Martínez Catalán, J.R., DE Pablo Maciá, J.G. and Rodríguez-Fernández, L.R., 1987. Aportaciones al conocimiento de la litoestratigrafia y estructura de Galicia Central. Memorias da Faculdade de Ciencias, Museu e Laboratrio Mineralgico e Geolgico, Universidade do Porto 1, 411-431.

Faure, G. and Mensing, T.M., 2005. Isotopes: Principles and Applications. John Wiley & Sons. 897 p.

Fernández-Martínez, F. and Fernández-Pompa, F., 1977. Mapa y memoria explicativa de la Hoja 1:50.000, Nº 1 (Cariño) del Mapa Geológico Nacional (MAGNA). *Instituto Geológico y Minero de España* (IGME), Madrid: 34 p.

Fernández-Pompa, F. and Monteserín, V., 1976. Mapa y memoria explicativa de la Hoja 1:50.000, Nº 7 (Cedeira) del Mapa Geológico Nacional (MAGNA). *Instituto Geológico y Minero de España* (IGME), Madrid: 73 p.

Fernández-Suárez, J., Corfu, F., Arenas, R., Marcos, A., Martínez Catalán, J.R., Díaz García, F., Abati, J. and Fernández, F.J., 2002. U-Pb evidence for a polyorogenic evolution of the HP-HT units of the NW Iberian Massif. *Contrib. Mineral. Petrol.*, 143, 236-253.

Fernández-Suárez, J., Arenas, R., Abati, J., Martínez Catalán, J.R., Whitehouse, M.J. and Jeffries, T.E. 2007. U-Pb chronometry of polymetamorphic high-pressure granulites: An example from the allochthonous terranes of the NW Iberian Variscan belt. In: Hatcher, R.D. Jr., Carlson, M.P., McBride, J.H. and Martínez Catalán, J.R. (Eds.), 4-D Framework of Continental Crust. *Geological Society of America Memoir*, 200, 469-488.

Fritz, J. S. and Dahmer, L. H., 1965. Cation exchange separation of Molybdenum, Tungsten, Niobium, and Tantalum from other metal ions. *Anal. Chem.*, 37, 1272-1274.

Ganguly, J., Tirone, M. and Hervig, R.L., 1998a. Diffusion kinetics of samarium and neodymium in garnet, and a method for determining cooling rates of rocks. *Science*, 281, 805-807

Ganguly, J., Cheng, W. and Chakraborty, S., 1998b. Cation diffusion in aluminosilicate garnets: experimental determination in pyrope-almandine diffusion couples. *Contrib. Mineral. Petrol.*, 131, 171-180.

García Alonso, J.I., 1995. Determination of fission products and actinides by inductively coupled plasma-mass spectrometry using isotope dilution analysis: A study of random and systematic errors. *Anal. Chim. Acta*, 312, 57-78.

García de Madinabeitia, S., 2004. Implementación y aplicación de los análisis isotópicos de Pb al estudio de las mineralizaciones y la geocronología del área Los Pedroches-Alcudia (zona centro-ibérica). Serie tesis doctorales UPV/EHU. 217 p.

García de Madinabeitia, S., Sánchez-Lorda, M.E. and Gil-Ibarguchi, J.I., 2008. Simultaneous determination of major to ultratrace elements in geological samples by fusion-dissolution and inductively coupled plasma mass spectrometry techniques. *Anal. Chim. Acta*, 625, 117-130.

García Garzón, J., de Pablo Maciá, J.G. and Llamas Borrajo, J.F., 1981. Edades absolutas obtenidas mediante el método Rb-Sr de dos cuerpos de ortogneises en Galicia occidental. *Bol. Geol. Minero*, XCII-VI:463-466.

Gebauer, D., 1990. Isotopic systems: Geochronology of eclogites. In: Carswell D.A. (ed.). Eclogite Facies Rocks (ed. D. A. Carswell), 141-159. Blackie, Glasgow, UK.

Gebauer, D., Schertl, H.P., Brix, M. and Schreyer, W., 1997. 35 Ma old ultrahigh-pressure metamorphism and evidence for very rapid exhumation in the Dora Maira Massif, Western Alps. *Litho*s, 41, 5-24.

Gehrels, G.E., Valencia, V.A. and Ruiz, J., 2008. Enhanced precision, accuracy, efficiency, and spatial resolution of U-Pb ages by laser ablation-multicollector-inductively coupled plasma-mass spectrometry. *Geochem. Geophys. Geosyst.*, 9: Q03017.

Gerdes, A. and Zeh, A., 2006. Combined U-Pb and Hf isotope LA-(MC)-ICP-MS analyses of detrital zircons: comparison with SHRIMP and new constraints for the provenance and age of an Armorican metasediment in Central Germany. *Earth Planet. Sci. Lett.*, 249, 47-61.

Gerdes, A. and Zeh, A., 2009. Zircon formation versus zircon alteration - New insights from combined U-Pb and Lu-Hf in-situ LA-ICP-MS analyses, and consequences for the interpretation of Archean zircon from the Central Zone of the Limpopo Belt. *Chem. Geol*., 261, 230-243.

Giletti, B.J., 1991. Rb and Sr diffusion in alkali feldspar, with implications for cooling histories of rocks. *Geochim. Cosmochim. Acta*, 55, 1331-1343.

Gil Ibarguchi, J.I., 1995. Petrology of jadeite-metagranite and associated orthogneiss from the Malpica-Tuy allochthon (Northwest Spain). *European Journal of Mineralogy*, 7, 403-415.

Gil Ibarguchi, J.I. and Ortega Gironés, E., 1985. Petrology, structure and geotectonic implications of glaucophane-bearing eclogites and related rocks from the Malpica-Tuy unit, Galicia, northwest Spain. *Chem. Geol.,* 50, 145-162.

Gil Ibarguchi, J. I., Ábalos, B., Azcárraga, J., Mendia, M.S. and Puelles, P., 2000., A petrological and structural excursion through the high-grade/high-pressure allochthonous units of the Cabo Ortegal

Complex (NW Spain), Basement Tectonics 15, Mid-Conference Field Trip Guide, Int. Basement Tectonics Assoc., La Coruña, Spain.

Glodny, J., Bingen, B., Austrheim, H., Molina, J. F. and Rusin, A., 2002. Precise eclogitization ages deduced from Rb/Sr mineral systematics: the Maksyutov complex, Southern Urals, Russia. *Geochim. Cosmochim. Acta*, 66, 1221-1235.

Glodny, J., Kühn, A. and Austrheim, H., 2008. Diffusion versus recrystallization processes in Rb-Sr geochronology: isotopic relics in eclogite facies rocks, Western Gneiss Region, Norway. *Geochim. Cosmochim. Acta*, 72, 506-525.

Gómez-Barreiro, J., Wijbrans, J.R., Castiñeiras, P., Martínez Catalán, J.R., Arenas, R., Díaz García, F. and Abati, J., 2006. $^{40}Ar/^{39}Ar$ laserprobe dating of mylonitic fabrics in a poly-orogenic terane of NW Iberia. *Journal of the Geological Society*, 163, 61-73.

Gómez Barreiro, J., Martínez Catalán, J.R., Díez Fernández, R., Arenas, R. and Díaz García, F., 2010. Upper crust reworking during gravitational collapse: the Bembibre-Pico Sacro detachment system (NW Iberia). *J. Geol. Soc. London,* 167, 769-784.

Govindaraju, K., 1995. Working values with confidence limits for twenty-six CRPG, ANRT and IWG-GIT. Geostandars Newsletter: *The Journal of Geostandards and Geoanalysis*, 19 , 1-32.

Guillong, M. and Gunther, D., 2002. Effect of particle size distribution on ICP-induced elemental fractionation in laser ablation-inductively coupled plasma-mass spectrometry, *J. Anal. At. Spectrom.*, 17, 831-837.

Guillong, M., Horn, I. and Günther, D., 2003. A comparison of 266 nm, 213 nm and 193 nm produced from a single solid state Nd:YAG laser for laser ablation ICP-MS. *J. Anal. At. Spectrom*., 18, 1224-1230.

Guillong, M. and Heinrich, C.A., 2007. Sensitivity enhancement in laser ablation ICP-MS using small amounts of hydrogen in the carrier gas. *J. Anal. At. Spectrom*., 22, 1488-1494.

Günther, D., Frischknecht, R., Heinrich, C.A. and Kahlert, H.J., 1997. Capabilities of an argon fluoride 193 nm excimer laser for laser ablation inductively coupled plasma mass spectometry microanalysis of geological materials*. J. Anal. At. Spectrom.*, 12, 939-944.

Günther, D. and Heinrich, C.A., 1999a. Comparison of the ablation behaviour of 266 nm Nd:YAG and 193 nm ArF excimer lasers for LA-ICP-MS analysis. *J. Anal. At. Spectrom*., 14, 1369-1374.

Günther, D. and Heinrich, C. A., 1999b. Enhanced sensitivity in laser ablation-ICP mass spectrometry using helium-argon mixtures as aerosol carrier. Plenary Lecture. *J. Anal. At.Spectrom*., 14, 1363-1368.

Hanchar, J.M. and Miller, C.F., 1993. Zircon zonation patterns and interpretation of crustal histories. *Chem. Geol.*, 110, 1-13.

Hahn, O., Stramann, H., Mattauch, J. and Ewald, H., 1943. Geologische Altersbestimmungen nach der Strontiummethode. *Chem.-Ztg.,* 67, 55-56.

Halliday, A. N., Lee, D.C., Christensen, J.N., Walder, A.J., Freedman, P.A., Jones, C.E., Hall, C.M., Yi,W. and Teagle, D., 1995. Recent development in inductively coupled plasma magnetic sector multiple collector mass spectrometry. International Journal of Mass Spectrometry and Ion Processes, 146/147, 21-33.

Harley, S., Kelly, N.M. and Möller, A., 2007. Zircon behaviour and the thermal histories of mountain chains. *Elements*, 3, 25-30.

Harrison, T.M. and Fitz Gerald, J.D., 1986. Exsolution in hornblende and its consequences for $^{40}Ar/^{39}Ar$ age spectra and closure temperature. *Geochim. Cosmochim. Acta*, 50, 247-253.

Hawkesworth, C.J. and Kemp, A.I.S., 2006. Evolution of the continental crust. *Nature*, 443, 811-817.

Henderson., W. and Scott McIndoe, J., 2005. Mass Spectrometry of Inorganic, Coordination and Organometallic Compounds: Tools - Techniques - Tips. Wiley, 292 p.

Hergenroder, R., 2006. Hydrodynamic sputtering as a possible source for fractionation in LA-ICP-MS. *J. Anal. At. Spectrom.*, 21, 517-524.

Herwartz, D., Münker, C., Scherer, E.E., Nagel, T.J., Pleuger, J. and Froitzheim, N., 2008. Lu-Hf garnet geochronology of eclogites from the Balma Unit (Pennine Alps): implications for Alpine paleotectonic reconstructions. *Swiss J Geosci*, 101, 173-189.

Hetzel, R. and Romer, R. L., 2000. A moderate exhumation rate for the high-pressure Maksyutov complex, southern Urals, Russia. *Geolog. J.*, 35, 327-344.

Hinthorne, J.R., Andersen, C.A., Conrad, R.L. and Lovering, J.F., 1979. Single-grain $^{207}Pb/^{206}Pb$ and U/Pb age determinations with a 10-µm spatial resolution using the ion microprobe mass analyzer (IMMA). *Chem. Geol.*, 25, 271-303.

Hoffmann, E. and Stroobant, V., 2007. Mass Spectrometry: Principles and Applications, 3rd Edition, Wiley, 502 p

Horn, I., Rudnick, R.L. and McDonough, W.F., 2000. Precise elemental and isotope ratio determination by simultaneous solution nebulization and laser ablation-ICP-MS: Application to U-Pb geochronology. *Chem. Geol.,* 164, 281-301.

Horn, I. and Günther, D., 2003. The influence of ablation carrier gasses Ar, He and Ne on the particle size distribution and transport efficiencies of laser ablation-induced aerosols: Implications for LA-ICP-MS. *Applied Surface Science*, 207, 144-57.

Horstwood, M.S.A., Foster, G.L., Parrish, R.R., Noble, S.R. and Nowell, G.M., 2003. Common-Pb corrected in situ U-Pb accessory mineral geochronology by LA-MC-ICP-MS. *J. Anal. At. Spectrom.,* 18, 837-846.

Hoskin, P.W.O., 2000. Patterns of chaos: Fractal statistics and the oscillatory chemistry of zircon: *Geochim. Cosmochim. Acta*, 64, 1905-1923.

Hoskin, P.W.O. and Ireland, T.R., 2000. Rare earth element chemistry of zircon and its use as a provenance indicator. *Geology*, 28, 627-630.

Hoskin, P. W. O. and Schaltegger, U., 2003. The Composition of Zircon and Igneous and Metamorphic Petrogenesis. *Reviews in Mineralogy and Geochemistry,* 53, 27-62.

Houk, R.S., Fassel, V.A., Flesch, G.D., Svec, H.J., Gray, A.L. and Taylor, C.E., 1980. Inductively Coupled Argon Plasma as an Ion Source for Mass Spectrometric Determination of Trace Elements. *Anal. Chem.*, 52, 2283-2289.

Hu, Z., Gao, S., Liu, Y., Hu, S., Chen, H. and Yuan, H., 2008. Signal enhancement in laser ablation ICP-MS by addition of nitrogen in the central channel gas. *J. Anal. At. Spectrom*., 23, 1093.

Huang, X.L., Niu, Y., Xu, Y.G., Ma, J.L., Qiu, H.N. and Zhong, J.W., 2013. Geochronology and geochemistry of Cenozoic basalts from eastern Guangdong, SE China: constraints on the lithosphere evolution beneath the northern margin of the South China Sea. *Contrib. Mineral. Petrol.*, 165, 437-455.

Ickert, R.B., Hiess, J., Williams, I.S., Holden, P., Ireland, T.R., Lanc, P., Schram, N., Foster, J.J. and Clement, S.W., 2008. Determining high precision, in situ, oxygen isotope ratios with a SHRIMP II: Analyses of MPI-DING silicate-glass reference materials and zircon from contrasting granites. *Chem. Geol.*, 257, 114-128.

Inza, A., 2010. Estudio de series temporales y composición química de material particulado atmosférico en distintas áreas del País Vasco. Serie tesis doctorales UPV/EHU. 286 p.

Iglesias, M., Ribeiro, M.L. and Ribeiro, A., 1983. La interpretación aloctonista de la estructura del Noroeste Peninsular. In: Comba J.A. (ed). Geología de España (Libro Jubilar J.M.Rios), Tomo I, *Instituto Geológico y Minero de España* (IGME), Madrid, 459-467.

Jackson, S.E., Pearson, N.J., Griffin, W.L. and Belousova, E.A., 2004. The application of laser ablation-inductively coupled plasma-mass spectrometry to in situ U-Pb zircon geochronology. *Chem. Geol.* 211, 47-69.

Jäger, E., Niggli, E. and Wenk, E., 1967. Rb-Sr Altersbestimmungen an Glimmern der Zentralalpen. *Beiträge zur Geologischen Karte Schweiz*, 134, 67.

Jenkin, G. R. T., 1997. Do cooling paths derived from mica Rb/Sr data reflect true cooling paths? *Geology* 25, 907-910.

Jenkin, G.R.T., Rogers, G., Fallick, A.E. and Farrow, C.M., 1995. Rb - Sr closure temperatures in bi-mineralic rocks: a mode effect and test for different diffusion models. *Chem. Geol.*, 122, 227-240.

Jochum, K.P. and Nehring, F., 2006. GeoReM preferred values (11/2006). GeoReM. http://georem.mpch-mainz.gwdg.de

Julivert, M., Fonboté, J.M., Ribeiro, A. y Conde, L.A., 1972. Mapa Tectónico de la Península Ibérica y Baleares a escala 1:1.000.000 y memoria explicativa. *Publicaciones del I.G.M.E.*, 113 p.

Keasberry, E., 1979. An interpretation model of semi-circular Bouguer anomalies found over the peripheral belt of the Ordenes Complex (NW Spain). *Geologie in Mijnbouw*, 58, 65-70.

Kelly, E.D., Carlson, W.D. and Connelly, J.N., 2011. Implications of garnet resorption for the Lu-Hf garnet geochronometer: an example from the contact aureole of the Makhavinekh Lake Pluton, Labrador. *J. metamorphic Geol.*, 29, 901-916.

Kelly, N. and Harley, S., 2005. An integrated microtextural and chemical approach to zircon geochronology: refining the Archaean history of the Napier Complex, east Antarctica. *Contrib. Mineral. Petrol.*, 149, 57-84.

Kemp, A., Foster, G., Schersten, A., Whitehouse, M., Darling, J. and Storey, C., 2009. Concurrent Pb-Hf isotope analysis of zircon by laser ablation multi-collector ICP-MS, with implications for the crustal evolution of Greenland and the Himalayas. *Chem. Geol.*, 261, 244-260.

Kirchenbaur, M., Pleuger, J., Jahn-Awe, S., Nagel, T.J., Froitzheim, N., Fonseca, R.O.C. and Münker, C., 2012. Timing of high-pressure metamorphic events in the Bulgarian Rhodopes from Lu-Hf garnet geochronology. *Contrib. Mineral. Petrol.*, 163, 897-921.

Koch, J. and Günther, D., 2011. Review of the state-of-the-art of laser ablation inductively coupled plasma mass spectrometry. *Appl. Spectrosc.,* 65, 155-162.

Košler, J. and Sylvester, P.J., 2003. Present trends and the future of zircon in geochronology: Laser ablation ICP-MS. In: Hanchar, J.M. and Hoskin, P.W.O. (eds.). Zircon. *Reviews in Mineralogy and Geochemistry*, 53, 243-275.

Košler, J., Wiedenbeck, M., Wirth, R., Hovorka, J., Sylvester, P. and Mikova, J. 2005. Chemical and phase composition of particles produced by laser ablation of silicate glass and zircon-Implications for elemental fractionation during ICP-MS analysis. *J. Anal. At. Spectrom*., 20, 402-409.

Košler, J., Sláma, J., Belousova, E., Corfu, F., Gehrels, G.E., Gerdes, A., Horstwood, M.S.A., Sircombe, K.N., Sylvester, P.J., Tiepolo, M., Whitehouse, M.J. and Woodhead, J.D., 2013. U-Pb detrital zircon analysis - results of an inter-laboratory comparison. *Geostand. Geoanal. Res*., 37, 243-259.

Kossert K., 2003. Half-life measurements of ^{87}Rb by liquid scintillation counting. *Appl. Radiat. Isot*., 59, 377-382.

Kostitsyn, Y. S. and Zhuravlev, A. Z., 1987. Analysis of errors in and methods of optimizing the method ofisotope dilution. *Geokhimia*, 7, 1024-1036.

Kretz, R., 1983. Symbols for rock-forming minerals*. American Mineralogist*, 68, 277-279.

Kuijper, R.P., 1979. U-Pb systematics and the petrogenetic evolution of infracrustal rocks in the Paleozoic basement of Western Galicia, NW Spain. Berh. *ZWO Laboratorium voor Isotopen, Geologie*, 5, 1-101.

Kuijper, R.P., Priem, H.N.A. and Den Tex, E., 1982. Late Archean - Early Proterozoic source ages of zircons in rocks from the Paleozoic Orogen of Western Galicia, NW Spain. *Precambrian Research*, 19, 1-29.

Kühn, A., Glodny, J., Iden, K. and Austrheim, A., 2000. Retention of Precambrian Rb/Sr phlogopite ages through Caledonian eclogite facies metamorphism, Bergen Arc Complex, W-Norway. *Lithos*, 51, 305-330.

Kylander-Clark, A. R.C., Hacker, B. R., Johnson, C. M., Beard, B. L., Mahlen, N. J. and Lapen, T. J., 2007. Coupled Lu-Hf and Sm-Nd geochronology constrains prograde and exhumation histories of high- and ultrahigh-pressure eclogites from western Norway. *Chem. Geol*., 242, 137-154.

Kylander-Clark, A. R.C., Hacker, B. R. and Cottle, J.M., 2013. Laser-ablation split-stream ICP petrochronology. *Chem. Geol*., 345, 99-112.

Lagos, M., Scherer, E.E., Tomaschek, F., Münker, C., Keiter, M., Berndt, J. and Ballhaus, C., 2007. High precision Lu-Hf geochronology of Eocene eclogite-facies rocks from Syros, Cyclades, Greece. *Chem. Geol.,* 243, 16- 35.

Lapen, T.J., Johnson, C.M., Baumgartner, L.P., Mahlen, N.J., Beard, B.L. and Amato, J.M., 2003. Burial rates during prograde metamorphism of an ultra-high-pressure terrane: an example from Lago di Cignana, western Alps, Italy. *Earth Planet. Sci. Lett.,* 215, 57-72.

Lapen, T. J., Mahlen, N. J., Johnson, C. M. and Beard, B. L., 2004. High precision Lu and Hf isotope analyses of both spiked and unspiked samples: A new approach*, Geochem. Geophys. Geosyst*., 5, Q01010

Le Fèvre, B., 2002. Developpements chimiques et instrumentaux en geochimie, en vue des analyses isotopiques Lu-Hf et Sm-Nd. applications a la geochronologie des roches metamorphiques de haut degre. PhD Thesis, Universite Blaise Pascal, Clermont-Ferrand. 253 p.

Le Fèvre, B. and Pin, C., 2001. An Extraction Chromatography Method for Hf Separation Prior to Isotopic Analysis Using Multiple Collection ICP-Mass Spectrometry. *Anal. Chem*., 73, 2453-2460.

Le Fèvre, B. and Pin, C., 2002. Determination of Zr, Hf, Th, and U by Isotope Dilution and ICP-Quadrupole Mass Spectrometry after concomitant separation using Extraction Chromatography. *Geostandars Newsletter: The Journal of Geostandards and Geoanalysis*, 26, 161-170.

Le Fèvre, B. and Pin, C., 2005. A straightforward separation scheme for concomitant Lu-Hf and Sm-Nd isotope ratio and isotope dilution analysis. *Anal. Chim. Acta*, 543, 209-221.

Lefort, J.P., 1989. Basement Correlations across the North Atlantic. Springer-Verlag, Berlin-Heidelberg, Germany: 148 p.

Lefort, J.P. and Ribeiro, A., 1980. La faille Porto-Badajoz-Cordoue a-t-elle controlé l'évolution de l'océan paléozoique sud-armoricain? *Bulletin de la Societé Géologique de France*, 22: 455-462.

Li, S., Jagoutz, E., Chen, Y and Li, Q., 2000. Sm-Nd and Rb-Sr isotopic chronology and cooling history of ultrahigh pressure metamorphic rocks and their country rocks at Shuanghe in the Dabie Mountains, Central China. *Geochim. Cosmochim. Acta*, 64, 1077-1093.

Llana-Fúnez, S., 2001. La estructura de la unidad de Malpica-Tui (Cordillera varisca en Iberia). Serie de Tesis Doctorales 1. Madrid, Instituto Geológico y Minero de España (IGME).

Llana-Fúnez, S. and Marcos, A., 2002. Structural record during exhumation and emplacement of high-pressure-low-to intermediate-temperature rocks in the Malpica-Tui unit (Variscan Belt of Iberia). In: Martínez Catalán J.R., Hatcher Jr, R.D., Arenas, R and Díaz García, F. (eds). Variscan-Appalachian dynamics: The building of the late Paleozoic bassamen. *Geological Society of America, Special Paper* 125-142.

López-Carmona, A., 2015. Blueschist-facies rocks from the Malpica-Tui Complex (NW Iberian Massif). *Nova Terra* 47, 299 p.

López-Carmona, A., Abati, J., Pitra, P. and Lee, J.K.W., 2014. Retrogressed lawsonite blueschists from the NW Iberian Massif: P-T constraints from numerical modelling and $^{40}Ar/^{39}Ar$ geochronology. *Contrib. Mineral. Petrol.*, 167, 1-20.

López-Sánchez, M.A., Aleinikoff, J.N., Marcos, A., Martínez, F.J. and Llana-Fúnez, S., 2015. An example of low-Th/U zircon overgrowths of magmatic origin in a late orogenic Variscan intrusion: the San Ciprián massif (NW Spain). *Journal of the Geological Society*, *In press.*

Lotze, F., 1945. Zur gliederung der varisziden der Iberischen Meseta. *Geotektonische Forschungen*, 4, 78-92.

Ludwig, K.R., 2001. Isoplot/Ex version 2.49, Geochronological toolkit for microsoft excel. Berkeley Geochronology Center Spec. Pub. 1a.

Maaskaant, P., 1970. Chemical petrology of polymetamorphic ultramafic rocks from Galicia, NW Spain. *Leidse Geologische Mededelingen*, 45, 237-325.

Mana, S., Furman, T., Carr, M.J., Mollel, G.F., Mortlock, R.A., Feigenson, M.D., Turrie, B.D. and Swisher, C.C. III, 2012. Geochronology and geochemistry of the Essimingor volcano: Melting of metasomatized lithospheric mantle beneath the North Tanzanian Divergence zone (East African Rift). *Lithos*, 155, 310-325.

McCoy-West, A.J., Baker, J.A., Faure, K. and Wysoczanski, R., 2010. Petrogenesis and Origins of Mid-Cretaceous Continental Intraplate Volcanism in Marlborough, New Zealand: Implications for the Long-lived HIMU Magmatic Mega-province of the SW Pacific. *J. Petrology*, 51, 2003-2045.

McLean, N.M., Condon, D.J., Schoene, B. and Bowring, S.A., 2015. Evaluating uncertainties in the calibration of isotopic reference materials and multi-element isotopic tracers (EARTHTIME tracer calibration part II). *Geochim. Cosmochim. Acta*, 164, 481-501.

MacPherson, J., 1881. Apuntes petrográficos de Galicia. *Anales de la Real Sociedad Española de Historia Natural*, 10, 49-87.

MacPherson, J., 1883. Sucesión estratigráfica de los terrenos arcaicos de España. *Anales de la Real Sociedad Española de Historia Natural*, 12, 3-40.

Maréchal, C.L., Télouk, P. and Albarède, F., 1999. Precise analysis of copper and zinc isotopic compositions by plasma-source mass spectrometry. *Chem. Geol.*, 156, 251-273.

Martin, L.A.J., Rubatto, D., Créspisson, C., Hermann, J., Putlitz, B. and Vitale-Brovarone, A., 2014. Garnet oxygen analysis by SHRIMP-SI: Matrix corrections and application to high-pressure metasomatic rocks from Alpine Corsica. *Chem. Geol.*, 374-375, 25-36.

Martínez-Catalán, J.R., 1990. A non-cylindrical model for the northwest Iberian allochthonous terranes and their equivalents in the Hercynian belt of Western Europe. *Tectonophysics,* 179, 253-272

Martínez-Catalán, J.R., Arenas, R., Díaz-García, F. and Abati, J., 1997. Variscan accretionary complex of northwest Iberia: terrane correlation and succession of tectonothermal events. *Geology*, 25, 1103-1106.

Martínez-Catalán, J.R., Arenas, R., Díaz-García, F., González Cuadra, P., Gómez-Barreiro, J., Abati, J., Castiñeiras, P., Fernández-Suárez, J., Sánchez Martínez, S., Andonaegui, P., González Clavijo, E., Díez Montes, A., Rubio Pascual, F.J. and Aguado, B.V., 2007. Space and time in the tectonic evolution of the northwestern Iberian Massif: Implications for the Variscan belt. *Geological Society of America Memoirs,* 200, 403-423.

Martínez Catalán, J.R., Arenas, R., Abati, J., Sánchez Martínez, S., Díaz García, F., Fernández-Suárez, J., González Cuadra, P., Castiñeiras, P., Gómez-Barreiro, J., Díez Montes, A., González Clavijo, E., Rubio Pascual, F.J., Andonaegui, P., Jeffries, T. E., Alcock, J. Díez Fernández, R. and López-Carmona, A., 2009. A rootless suture and the loss of the roots of a mountain chain: The Variscan belt of NW Iberia. *Comptes Rendus Geosciences,* 341, 114-126.

Marques, F.O., Ribeiro, A. and Munhá, J., 1996. Geodynamic evolution of the Continental Allochthonous Terrane (CAT) of the Bragança Nappe Complex, NE Portugal. *Tectonics*, 15, 747-762.

Marques, F.G., Ribeiro, A. and Pereira, E., 1992. Tectonic evolution of the deep crust: Variscan reactivation by extension and thrusting of Precambrian basement in the Bragança and Morais Massifs (Tras-os-Montes, NE Portugal). *Geodinamica Acta*, 5, 135-151.

Marquínez García, J.L., 1984. La geología del área esquistosa de Galicia Central (Cordillera Herciniana, NW de España). *Memorias del Instituto Geológico y Minero de España* (IGME) 100, 231 p.

Matteini, M., Dantas, E.L., Pimentel, M.M. and Bühn, B., 2010. Combined U-Pb and Lu-Hf isotope analyses by laser ablation MC-ICP-MS: methodology and applications. *Anais da Academia Brasileira de Ciências*, 82, 479-491.

Mattison, J.M., 1972. Preparation of hydrofluoric, hydrochloric and nitric at ultralow lead levels. *Analytical Chemistry,* 44, 1715-1716.

Mattinson, J.M., 2005. Zircon U-Pb chemical-abrasion ('CA-TIMS') method: Combined annealing and multi-step dissolution analysis for improved precision and accuracy of zircon ages. *Chem. Geol.,* 220, 47-56.

Matte, Ph., 1991. Accretionary history and crustal evolution of the Variscan belt in Western Europe. In: R.D. Hatcher, Jr. and L. Zonenshain (eds.). Accretionary Tectonics and Composite Continents. *Tectonophysics*, 196, 309-337.

Matte, P. and Ribeiro, A., 1967. Les rapports tectoniques entre le Précambrienn ancien et le Paléozoïque dans le Nord-Ouest de la Péninsule Ibérique: grandes nappes ou extrusions? *Comptes Rendus de la Académie des Sciences de Paris*, 264, 2268-2271.

Mawby, J., Hand, M. and Foden, J., 1999. Sm-Nd evidence for high-grade Ordovician metamorphism in the Arunta Block, Central Australia, *J. Metamorph. Geol*., 17, 653-668.

Meinhold, G., Kostopoulos, D., Frei, D., Himmerkus, F. and Reischmann, T., 2010. U-Pb LA-SF-ICP-MS zircon geochronology of the Serbo-Macedonian Massif, Greece: palaeotectonic constraints for Gondwana-derived terranes in the Eastern Mediterranean. *Int J Earth Sci*., 99, 813-832.

Mendia, M. 2000. Petrología de la Unidad Eclogítica del Complejo de Cabo Ortegal (NW de España). *Nova Terra* 16, 424 p.

Menéndez Martínez, M., 2001. Petrogénesis del macizo de Guitiriz (NO de la Península Ibérica). Implicaciones en la génesis de granitoides y en procesos de hibridación mantélico-corticales. *Nova Terra* 19,367 p.

Mezger, K., Hanson, G.N. and Bohlen, S.R., 1989. High-precision U-Pb ages of metamorphic rutile - application to the cooling history of high grade terranes. *Earth Planet. Sci. Lett.,* 96, 106-118.

Mezger, K., Essene, E.J. and Halliday, A.N., 1992. Closure temperatures of the Sm-Nd system in metamorphic garnets. *Earth Planet. Sci. Lett*., 113, 397-409.

Minster, J.F. and Ricard, L.P., 1981. The isotopic composition of zirconium. *Int. J. Mass Spectrom. Ion Phys.,* 37, 259-272.

Montero, P., 1993. Geoquímica y petrogénesis del complejo peralcalino de la Sierra del Galiñeiro (Pontevedra, España). Unpublished PhD thesis, Universidad de Oviedo, 318 p.

Montero, P. and Bea, F., 1998. Accurate determination of $^{87}Rb/^{86}Sr$ and $^{147}Sm/^{144}Nd$ ratios by inductively-coupled-plasma mass spectrometry in isotope geoscience: an alternative to isotope dilution analysis. *Anal. Chim. Act*a, 358, 227-233.

Montero, P., Floor, P. and Corretgé, G., 1998. The accumulation of rare-earth and high-field-strength elements in peralcaline granitic rocks: The Galiñeiro orthogneissic complex, northwestern Spain. *Can. Mineral*., 36, 683-700.

Montero, P., Bea, F., Corretgé, L.G., Floor, P. and Whitehouse, M.J., 2009. U-Pb ion microprobe dating and Sr and Nd isotope geology of the Galiñeiro Igneous Complex. A model for the peraluminous/peralkaline duality of the Cambro-Ordovician magmatism of Iberia. *Lithos,* 107, 227-238.

Morel, M.L.A., Nebel, O., Nebel-Jacobsen, Y.J., Miller, J.S. and Vroon, P.Z., 2008. Hafnium isotope characterization of the GJ-1 zircon reference material by solution and laser-ablation MC-ICP-MS. *Chem. Geol*., 255, 231-235.

Nebel, O., Mezger, K., Scherer, E.E. and Münker, C., 2005. High precision determinations of $^{87}Rb/^{85}Rb$ in geologic materials by MC-ICP-MS. *International Journal of Mass Spectrometry*, 246, 10-18.

Nebel, O., Nebel-Jacobsen, Y., Mezger, K. and Berndt, J.. 2007. Initial Hf isotope compositions in magmatic zircon from early Proterozoic rocks from the Gawler Craton, Australia: A test for zircon model ages. *Chem. Geol*., 241, 23-37.

Nebel, O., Scherer, E. E. and Mezger K., 2011. Evaluation of the ^{87}Rb decay constant by age comparison against the U-Pb system. *Earth Planet. Sci. Lett.,* 301, 1-8.

Nir-El, Y. and Lavi, N., 1998. Measurement of the half-life of ^{176}Lu. *Applied Radiation and Isotopes*, 49, 1653-1655.

Nocete, F., Sáez, R., Bayona, M.R., Nieto, J.M., Peramo, A., López, P., Gil-Ibarguchi, I., Inácio, N., García, S. and Rodríguez, J., 2014. Gold in the Southwest of the Iberian Peninsula during the 3rd Millennium BC. *Journal of Archaelogical Science*, 41, 691-704.

Ordóñez Casado, B., Gebauer, D., Schäfer, H.J., Gil Ibarguchi, J.I. and Peucat, J.J. 2001. A single Devonian subduction event for the HP/HT metamorphism of the Cabo Ortegal complex within the Iberian Massif. *Tectonophysics* 332, 359-385.

Ortega Cuesta, L.A., 1994. Caracterización geoquímica y petrogénesis del granito de La Espenuca (La Coruña). *Nova Terra* 14, 572 p.

Ortega Gironés, E. and Gil Ibarguchi, J.I., 1983. La Unidad de Malpica-Tuy ('Complejo Antiguo'-'Fosa Blastomilonítica'). In: Comba J.A. (ed). Geología de España (Libro Jubilar J.M.Rios), Tomo I, *Instituto Geológico y Minero de España* (IGME), Madrid, 430-440.

Parga Pondal, I., 1953a. Mapa geológico de España. Explicación de la hoja 43 (Lage). *Instituto Geológico y Minero de España* (IGME), Madrid.

Parga Pondal, I., 1953b. Mapa geológico de España. Explicación de la hoja 44 (Carballo). *Instituto Geológico y Minero de España* (IGME), Madrid.

Parga Pondal, I., 1953c. Mapa geológico de España. Explicación de la hoja 261 (Tuy-Valença). *Instituto Geológico y Minero de España* (IGME), Madrid.

Parga Pondal, I., 1956. Nota explicativa del mapa geológico de la parte NO de la provincia de La Coruña. *Leidse Geologische Mededelingen*, 21, 468-484.

Patchett, P. J. and Tatsumoto, M., 1980. A routine high-precision method for Lu-Hf isotope geochemistry and chronology. *Contrib. Mineral. Petrol.*, 75, 263-267.

Paton, C., Woodhead, J.D., Hellstrom, J.C., Hergt, J.M., Greig, A. and Maas, R., 2010. Improved laser ablation U–Pb zircon geochronology through robust downhole fractionation correction. *Geochem. Geophys. Geosyst.,* 11, Q0AA06.

Paton, C., Hellstrom, J., Paul, B., Woodhead, J. and Hergt, J., 2011. Iolite: freeware for the visualisation and processing of mass spectrometric data. *J. Anal. At. Spectrom*., 26, 2508-2518.

Peucat, J.J., Bernard-Griffiths, J., Gil Ibarguchi, J.I., Dallmeyer, R.D., Menot, R.P., Cornichet, J. and Iglesias Ponce de León, M., 1990. Geochemical and geochronological cross section of the deep variscan crust: the Cabo Ortegal high-pressure nappe (NW Spain). In: Ph. Matte (ed.): Terranes in the Variscan Belt of Europe and Circum-Atlantic Paleozoic Orogens. *Tectonophysics*, 177, 263-292.

Pin, C. and Santos Zalduegui, J.F., 1997. Sequential separation of light rare-earth elements, thorium and uranium by miniaturized extraction chromatography: Application to isotopic analyses of silicate rocks. *Anal. Chim. Acta*, 339, 79-89.

Pin, C., Ortega Cuesta, L. A. and Gil Ibarguchi, J.I., 1992. Mantle-derived, early Paleozoic A-type metagranitoids from the NW Iberian massif: Nd isotope and trace-element constraints. *Bulletin de la Societe Geologique de France,* 163, 483-494.

Pin, C., Le Fèvre, B. and Joannon, S., 2000. Dilution isotopique et spectrométrie de masse à source plasma: une combinaison optimale pour l'analyse de haute précision des elements en traces. Canadian *Journal of Analytical Sciences and Spectroscopy*, 45, 13-27.

Pin, C. and Joannon, S., 2002. Combined cation-exchange and extraction chromatography for the concomitant separation of Zr, Hf, Th, and the Lanthanides from geological materials. *Talanta*, 57, 393-403.

Pin, C., Joannon, S., Bosq, C., Le Fèvre, B. and Gauthier, P.J., 2003. Precise determination of Rb, Sr, Ba, and Pb in geological materials by isotope dilution and ICP-quadrupole mass spectrometry following selective separation of the analytes. *J. Anal. At. Spectrom.*, 18, 135-141.

Pollington, A.D. and Baxter, E.F., 2011. High precision microsampling and preparation of zoned garnet porphyroblasts for Sm-Nd geochronology. *Chem. Geol.*, 281, 270-282.

Pourmand, A, and Dauphas, N., 2010. Distribution coefficients of 60 elements on TODGA resin: Application to Ca, Lu, Hf, U and Th isotope geochemistry. *Talanta*, 81, 741-753.

Priem, H.N.A., Boelrijk, N.A.I.M., Verschure, R.H., Hebeda, E.H. and Verdurmen, E.A.Th., 1970. Dating events of acid plutonism through the Paleozoic of the Western Iberian Peninsula. *Eclogæ Geol. Helv*. 63/1, 255-274.

Prince, C.I., Košler, J., Vance, D. and Gunther, D., 2000. Comparison of laser ablation ICP-MS and isotope dilution REE analyses-implications for Sm-Nd garnet geochronology. *Chem. Geol*., 168, 255-274.

Prohaska, T., Irrgeher, J., Zitek, A. and Jakubowski, N., 2014. Sector field mass spectrometry for elemental and isotopic analysis. *Royal Society of Chemistry*, 664 p.

Puelles, P., 2004. Deformación, metamorfismo y exhumación de las granulitas de alta presión de la Bacariza (Complejo de Cabo Ortegal, NO de España). *Nova terra* 23, 411 p.

Puelles, P., Ábalos, B. and Gil Ibarguchi, J.I., 2005. Metamorphic evolution and thermobaric structure of the subduction-related Bacariza high-pressure granulite formation (Cabo Ortegal Complex, NW Spain). *Lithos*, 84, 125-149.

Quesada, C., 1990. Geological constraints on the Paleozoic tectonic evolution of tectonostratigraphic terranes in the Iberian Massif. *Tectonophysics*, 185, 225-245.

Raczek, I., Stoll, B., Hofmann, A.W. and Jochum, K.P., 2001. High-Precision Trace Element Data for the USGS Reference Materials BCR-1, BCR-2, BHVO-1, BHVO-2, AGV-1, AGV-2, DTS-1, DTS-2, GSP-1 and GSP-2 by ID-TIMS and MIC-SSMS. *Geostandars Newsletter: The Journal of Geostandards and Geoanalysis*, 25, 77-86.

Ribeiro, A., Andriessen, P.A.M., Beetsma, J.J., Ferreira, N. and Oen, I.S., 1993. Precambrian Sm-Nd age of UATC of Morais Massif (NE Portugal). *Terra abstracts. Terra Nova* vol 5.

Ries, A. and Shackleton, R.M., 1971. Catazonal complexes of north-western Spain and north Portugal; remmants of a hercynian thrust plate. *Natural and Physical Science*, 234, 65-69.

Robardet, M., Blaise, J., Bouyx, E., Gouvernnec, R, Lardeux, H, Leherisse, A., Lemenn, J., Melou, M., Paris, F., Plusquellec, Y, Poncet, J., Regnault, S, Rioult, M. and Weyant, M., 1993. Palèogéographie del'Europe occidentale de l'Ordovicien au Dévonien. *Bulletin de la Societe Geologique de France*, 164, 683-696.

Robinson, P., Townsend, A.T., Yu, Z. and Münker, C., 1998. Determination of Scandium, Ytrium and Rare Earth Elements in Rocks by High Resolution inductively Coupled Plasma-Mass Spectrometry. *Geostandars Newsletter: The Journal of Geostandards and Geoanalysis*, 23, 31-46.

Rodríguez, J., 2005. Recristalización y deformación de litologías supracorticales sometidas a metamorfismo de alta presión (Complejo de Malpica-Tui, NO del Macizo Ibérico). *Nova Terra* 29, 572 p.

Rodríguez, J., Cosca, M.A., Gil Ibarguchi, J.I. and Dallmeyer, R.D., 2003. Strain partitioning and preservation of $^{40}Ar/^{39}Ar$ ages during Variscan exhumation of a subducted crust (Malpica-Tui complex, NW Spain). *Lithos*, 70, 111-139.

Roger, F. and Matte, Ph., 2005. Early Variscan HP metamorphism in the western Iberian Allochthon—A 390 Ma U-Pb age for the Bragança eclogite (NW Portugal). *Int J Earth Sci (Geol Rundsch)*, 94, 173-179.

Rotenberg E., Davis D. W., Amelin Y., Ghosh S. and Bergquist, B.A., 2012. Determination of the decay-constant of ^{87}Rb by laboratory accumulation of ^{87}Sr. *Geochim. Cosmochim. Acta*, 85, 41-57.

Rubatto, D., 2002. Zircon trace element geochemistry: Partitioning with garnet and the link between U-Pb ages and metamorphism. *Chem. Geol.*, 184, 123-138.

Rubatto, D., Gebauer, D., and Compagnoni, R., 1999. Dating of eclogite facies zircons: The age of Alpine metamorphism in the Sesia-Lanzo Zone (western Alps). *Earth Planet. Sci. Lett.*, 167, 141-158.

Rubatto, D. and Hermann, J., 2007. Experimental zircon/melt and zircon/garnet trace element partitioning and implications for the geochronology of crustal rocks. *Chem. Geol*., 241, 38-61.

Russell, W.A., Papanastassiou, D.A. and Tombrello, T.A., 1978. Ca isotope fractionation on the Earth and other solar system materials. *Geochim. Cosmochim. Acta*, 42, 1075-90.

Russo, R.E., Mao, X., Gonzalez, J.J., Zorba, V. and Yoo, J., 2013. Laser ablation in analytical chemistry. *Anal. Chem.*, 85, 6162-6177.

Rutherford, E. and Soddy, F., 1902. The radioactivity of thorium compounds II. The cause and nature of radioactivity. *J. Chem. Soc. Lond*., 81, 837-860.

Sahoo, S.K. and Masuda, A., 1997. Precise measurement of zirconium isotopes by thermal ionization mass spectrometry. *Chem. Geol*., 141, 117-126.

Sánchez-Lorda, M.E., 2013. Avances en espectrometría de masas con fuente de plasma: análisis simultáneo de elementos mayores y trazas mediante Q-ICP-MS y análisis de isótopos de Sm-Nd mediante HR-MC-ICP-MS. Aplicación en estudios geoquímicos. PhD Thesis, Universidad del País Vasco/Euskal Herriko Unibertsitatea. 243 p.

Sánchez-Lorda, M.E., García de Madinabeitia, S., Pin, C. and Gil Ibarguchi, J.I., 2013. Concomitant measurement of ^{143}Nd/^{144}Nd and ^{147}Sm/^{144}Nd ratios without isotope dilution in geological samples: an assessment of MC-ICP-MS capabilities*. International Journal of Mass Spectrometry*, 333, 34-43.

Sánchez Martínez, S., 2009. Geoquímica y geocronología de las Ofiolitas de Galicia. *Nova Terra* 37, 351 p.

Sánchez Martínez, S., Arenas, R., Gerdes, A., Castiñeiras, P., Potrel, A. and Fernández-Suárez, J., 2011. Isotope geochemistry and revised geochronology of the Purrido Ophiolite (Cabo Ortegal Complex, NW Iberian Massif): Devonian magmatism with mixed sources and involved Mesoproterozoic basement*. Journal of the Geological Society*, 168, 733-750.

Sanloup, C., Blichert-Toft, J., Telouk, P., Gillet, P. and Alberede, F., 2000. Zr isotope anomalies in chondrites and the presence of ^{92}Nb in the early solar system. *Earth Planet. Sci. Lett.*, 184, 75-81.

Santos, J.F., Marques, F.O., Munhá, J. and Tassinari, C., 1995. A new isotopic tale for Bragança eclogites. *Terra Nova*, 7, Abstracts Supplement 1, 108.

Santos, J.F., Marques, F.O., Munhá, J., Ribeiro, A. and Tassinari, C., 1997. First dating of a Precambrian (1.0 to 1.1 Ga) HP/HT metamorphic event in the uppermost allochthonous unit of the Bragança Massif (Iberian variscan chain, northern Portugal). *Terra Nova*, 9, Abstracts Supplement 1, 497.

Santos Zalduegui, J.F., 1995. Geocronología y geoquímica isotópica de diferentes unidades de los Complejos Alóctonos de Cabo Ortegal y Malpica-Tuy (NO de España). *Nova Terra* 11, 177 p.

Santos Zalduegui, J.F., Schärer, U., Gil Ibarguchi, J.I. and Girardeau, J.J., 1996. Origin and evolution of the Paleozoic Cabo Ortegal ultramafic-mafic complex (NW Spain): U-Pb, Rb-Sr and Pb-Pb isotope data. *Chem. Geol.*, 129, 281-304.

Santos Zalduegui, F.J., García de Madinabeitia, S., Gil Ibarguchi, J.I. and Palero, F. 2004. A lead isotope database: the Los Pedroches - Alcudia area (Spain); implications for archaeometallurgical connections across southwestern and southeastern Iberia. *Archaeometry*, 46, 625-634

Schäfer, H.J., Gebauer, D., Gil Ibarguchi, J.I. and Peucat, J.J., 1993. Ion-microprobe U-Pb dating on the HP/HT Cabo Ortegal complex (Galicia, NW Spain): preliminary results. *Terra Nova*, Abstract Suplement, 4, 22.

Schaltegger, U., Fanning, C. M., Günther, D., Maurin, J. C., Schulmann, K. and Gebauer, D., 1999. Growth, annealing and recrystallization of zircon and preservation of monazite in high-grade metamorphism: conventional and in-situ U-Pb isotope, cathodoluminescence and microchemical evidence. *Contrib. Mineral. Petrol*., 134, 186-201.

Schaltegger, U., Schmitt, A.K. and Horstwood, M.S.A., 2015. U-Th-Pb zircon geochronology by ID-TIMS, SIMS, and laser ablation ICP-MS: Recipes, interpretations, and opportunities. *Chem. Geol.*, 402, 89-110.

Scherer, E. E., Cameron, K. L. and Blichert-Toft, J., 2000. Lu-Hf garnet geochronology: closure temperature relative to the Sm-Nd system and the effects of trace mineral inclusions. *Geochim. Cosmochim. Acta*, 64, 3413-3432.

Scherer, E.E., Münker, C. and Mezger, K., 2001. Calibration of the Lutetium-Hafnium clock. *Science,* 293, 683-687.

Schmadicke, E., 1991. Quartz pseudomorphs after coesite in eclogites from the Saxonian Erzgebirge. *European Journal of Mineralogy*, 3, 231-238.

Schmidt, A., Mezger, K. and O'Brien, P.J., 2011. The time of eclogite formation in the ultrahigh pressure rocks of the Sulu terrane. Constraints from Lu-Hf garnet geochronology. *Lithos*, 125, 743-756.

Schoene, B., 2014. U-Th-Pb geochronology. The Crust Vol. 4, 2nd ed. Elsevier Ltd. 341-378 p.

Schoene, B., Schaltegger, U., Brack, P., Latkoczy, C., Stracke, A. and Günther, D., 2012. Rates of magma differentiation and emplacement in a ballooning pluton recorded by U-Pb TIMS-TEA, Adamello batholith, Italy. *Earth Planet. Sci. Lett*., 355-356, 162-173.

Schulmann, K., Martínez Catalán, J.R., Lardeaux, J.M., Janoušek, V. and Oggiano, G., 2014. The Variscan orogeny: extent, timescale and the formation of the European crust. *Geological Society, London, Special Publications*, 405 p.

Schulz, G., 1835. Descripción geognóstica del Reyno de Galicia. *Gráficas Reunidas, S.A*., Madrid, 176 p.

Schwieters, J.B., Bouman, C., Deerberg, M., Wills, J.D. and Gerdes, A., 2009. Simultaneous in situ Analysis of U-Pb Age and Hf Isotopes of Zircon by Laser Ablation Sector-Field (MC-) ICP-MS. *Thermo Application Note*: 30170.

Segal, I., Halicz, L. and Platzner, I.T., 2003. Accurate isotope ratio measurements of ytterbium by multiple collection inductively coupled plasma mass spectrometry applying erbium and hafnium in an improved double external normalization procedure. *J. Anal. At. Spectrom*., 18, 1217-1223

Seth, B, Jung, S. and Gruner, B., 2008. Deciphering polymetamorphic episodes in high-grade metamorphic orogens: Constraints from PbSL, Sm/Nd and Lu/Hf garnet dating of low- to high-grade metasedimentary rocks from the Kaoko belt (Namibia). *Lithos*, 104, 131-146.

Shellnutt, J.G. and Zhou, M.F., 2007. Permian peralkaline, peraluminous and metaluminous A-type granites in the Panxi district, SW China: Their relationship to the Emeishan mantle plume. *Chem. Geol*., 243, 286-316.

Simonetti, A., Heaman, L.M., Hartlaub, R.P., Creaser, R.A., MacHattie, T.G. and Bohm, C., 2005. U-Pb zircon dating by laser ablation-MC-ICP-MS using a new multiple ion counting Faraday collector array. *J. Anal. At. Spectrom.*, 20, 677-686.

Skora, S., Lapen, T.J., Baumgartner, L.P., Johnson, C.M., Hellebrand,E. and Mahlen, N.J., 2009. The duration of prograde garnet crystallization in the UHP eclogites at Lago di Cignana, Italy. *Earth Planet. Sci. Lett.*, 287, 402-411.

Sláma, J., Košler, J., Condon, D.J., Crowley, J.L., Gerdes, A., Hanchar, J.M., Horstwood, M.S.A., Morris, G.A., Nasdala, L., Norberg, N., Schaltegger, U., Schoene, B., Tubrett, M.N. and Whitehouse, M.J., 2008. Plešovice zircon - A new natural reference material for U-Pb and Hf isotopic microanalysis. *Chem. Geol.*, 249, 1-35.

Söderlund, U., Patchett, P.J., Vervoort, J.D. and Isachsen, C.E., 2004. The ^{176}Lu decay constant determined by Lu-Hf and U-Pb isotope systematics of Precambrian mafic intrusions. *Earth Planet. Sci. Lett.*, 219, 311-324.

Stampfli, G.M., Hochard, C., Vérard, C., Wilhem, C., and von Raumer, J., 2013. The geodynamics of Pangea formation. *Tectonophysics*, 593, 1-19.

Steiger, R. H. and Jäger, E., 1977. Subcommission on geochronology: convention on the use of decay constants in geo- and cosmochronology. *Earth Planet. Sci. Lett*., 36, 359-362.

Sulcek, Z. and Povondra, P., 1989. Methods of Decomposition in Inorganic Analysis, CRC Press, Boca Raton. FL, 325 pp.

Sylvester, P.J., 2008. LA-(MC)-ICP-MS trends in 2006 and 2007 with particular emphasis on measurement uncertainties. *Geostandards and Geoanalytical Research*, 32, 469-488.

Taylor, P.D.P., De Bievre, P., Walder, A.J. and Entwistle, A., 1995. Validation of the analytical linearity and mass discrimination correction model exhibited by a multiple collector inductively coupled plasma mass spectrometer by means of a set of synthetic uranium isotope mixtures. *Journal of Analytical Atomic Spectrometry*, 10, 395-398.

Taylor, H.E., 2001. Inductively Coupled Plasma-Mass Spectrometry: Practices and Techniques. Academic Press, 308 p.

Thirlwall, M.F. and Walder, A.J.,1995. In-situ hafnium isotope ratio analysis of zircon by inductively coupled plasma multiple collector mass spectrometry. *Chem. Geol*., 122, 241-247.

Thöeni, M., 2002. Sm-Nd isotope systematic in garnets from different lithologies (Eastern Alps): age results and an evaluation of potential problems for garnet Sm-Nd chronometry, *Chem. Geol*., 185, 255-281.

Tirone, M., Ganguly, J., Dohmen, R., Langenhorst, F., Hervig, R. and Becker, H.W., 2005. Rare earth diffusion kinetics in garnet: experimental studies and applications. *Geochim. Cosmochim. Acta*, 69, 2385-2398.

Todd, E., Gill, J.B., Wysoczanski, R.J., Handler, M.R., Wright, I.C. and Gamble, J.A., 2010. Sources of constructional cross-chain volcanism in the southern Havre Trough: New insights from HFSE and REE concentration and isotope systematic. *Geochem. Geophys. Geosyst*., 11, Q04009.

Tunheng, A. and Hirata, T., 2004. Development of signal smoothing device for precise elemental analysis using laser ablation-ICP-mass spectorometry. *J. Anal. At. Spectrom.*, 19, 932-934.

Valverde-Vaquero, P. and Fernández, F.J., 1996. Edad de enfriamiento U-Pb en rutilos del Gneiss de Chímparra (Cabo Ortegal, NO de España). *Geogaceta*, 20, 475-478.

Van Achterbergh, E., Ryan, C.G., Jackson, S.E. and Griffin, W.L., 2001. Data reduction software for LA-ICP-MS: appendix. In: Sylvester, P.J. (Ed.), Laser Ablation-ICP-Mass Spectrometry in the Earth Sciences: Principles and Applications, Mineralog. Assoc. Canada (MAC) Short Course Series, Ottawa, Ontario, Canada, 29, 239- 243.

Van Calsteren, P.W.C., 1977. Geochronological, geochemical and geophysical investigations in the Hercynian basement of Galicia (NW Spain). *Leidse Geologische Mededelingen*, 51, 57-61.

Van Calsteren, P.W.C., 1978. Geochemistry of the polymetamorphic mafic-ultramafic complex at Cabo Ortegal (NW Spain). *Lithos*, 11, 61-72.

Van Calsteren, P.W.C. and Den Tex, E., 1978. A mantle-plume interpretation for the Variscan basement of Galicia (NW Spain). *Memorie di Scienze Geologiche,* 33, 243-246.

Van Calsteren, P.W.C., Boelrijk, N.A.I.M., Hebeda, E.H., Priem, H.N.A., Den Tex, E., Verdurmen, E.A.T. and Verschure, R.H., 1979. Isotopic dating of older elements (including the Cabo Ortegal mafic-ultramafic complex) in the hercynian orogen of NW Spain: manifestations of a presumed early Palaeozoic mantle-plume. *Chem. Geol.*, 24, 35-56.

Van der Wegen, G., 1978. Garnet-bearing metabasites from the Blastomylonitic Graben, Western Galicia, Spain. *Scripta Geologica*, 45, 1-95.

Vanhaecke, F., De Wannemacker, G., Moens, L. and Van den haute, P., 2001. The use of sector field ICP–mass spectrometry for Rb-Sr geochronological dating. *Fresenius J. Anal. Chem.*, 371, 915-920.

Vanhaecke, F. and Degryse, P., 2012. Isotopic analysis: fundamentals and applications using ICP-MS. Wiley, 550 p.

Van Orman, J.A., Grove, T.L., Shimizu,N. and Layne,G.D., 2002. Rare earth element diffusion in a natural pyrope single crystal at 2.8 GPa. *Contrib. Mineral. Petrol*., 142, 416-424.

Van Overmeeren, R.A., 1975. A gravity investigation of the catazonal rock complex at Cabo Ortegal (NW Spain). *Tectonophysics*, 26, 293-307.

Vavra, G., Gebauer, D., Schmid, R. and Compston, W., 1996. Multiple zircon growth and recrystallization during polyphase Late Carboniferous to Triassic metamorphism in granulites of the Ivrea Zone (Southern Alps): an ion microprobe (SHRIMP) study. *Contrib. Mineral. Petrol*., 122, 337-358.

Vervoort, J.D., Patchett, P.J, Söderlund, U. and Baker, M., 2004. Isotopic composition of Yb and the determination of Lu concentrations and Lu/Hf ratios by isotope dilution using MC-ICP-MS. *Geochem. Geophys. Geosyst.*, 5, Q11002.

Villa, I.M., De Bièvre, P., Holden, N.E. and Renne, P.R., 2015. IUPAC-IUGS recommendation on the half life of ^{87}Rb. *Geochim. Cosmochim. Acta*, 164, 382-385.

Vry, J.K., Baker, J., Maas, R., Little, T.A., Grapes, R. and Dixon, M., 2004. Zoned (Cretaceous and Cenozoic) garnet and the timing of high grade metamorphism, Southern Alps, New Zealand. *J. metamorphic Geol.*, 22, 137-157.

Vogel, D.E., 1967. Petrology of eclogite- and pirigarnite-bearing polymetamorphic rock complex at Cabo Ortegal, NW Spain. *Leidse Geologische Mededelingen*, 40, 121-213.

Vogel, D.E., 1984. Cabo Ortegal, mantle plume or double klippe. *Geologie in Mijnbouw*, 63, 131-140.

Vogel, D.E. and Abdel Monem, A.A., 1971. Radiometric evidence for a Precambrian metamorphic event in NW Spain. *Geologie in Minjbouw*, 50, 749-750.

Von Raumer, J.F. and Stampfli, G.M., 2008. The birth of the Rheic Ocean-Early Palaeozoic subsidence patterns and subsequent tectonic plate scenarios. *Tectonophysics,* 46, 9-20.

Vry, J.K. and Baker, J.A., 2006. LA-MC-ICP-MS Pb-Pb dating of rutile from slowly cooled granulites: confirmation of the high closure temperature for Pb diffusion in rutile. *Geochim. Cosmochim. Acta*, 70, 1807-1820.

Waight, T., Baker, J. and Willigers, B., 2002. Rb isotope dilution analyses by MC-ICP-MS using Zr to correct for mass fractionation: towards improved Rb-Sr geochronology? *Chem. Geol.,* 186, 99-116.

Webster, R. K., 1960. Mass spectrometric isotope dilution analysis. In: Smales, A.A. and Wager, L. R., (eds.). Methods in geochemistry. *Intersciences Publishers Inc*. 202-246.

Weis, D., Kieffer, B., Hanano, D., Nobre Silva, I., Barling, J., Pretorius, W., Maerschalk, C. and Mattielli, N., 2007. Hf isotope compositions of U.S. Geological Survey reference materials. *Geochem. Geophys. Geosyst*., 8, Q06006.

Wetherill, G.W., 1956. Discordant uranium-lead ages. *Transactions of the American Geophysical Union*, 37, 320-326.

Whalen, J.B., Currie, K.L. and Chappell, B.W., 1987. A-type granites: geochemical characteristics, discrimination and petrogenesis. *Contrib. Mineral. Petrol.,* 95, 407-419.

Wiedenbeck, M., Allé, P., Corfu, F., Griffin, W.L., Meier, M., Oberli, F., Quadt, A. V., Roddick, J.C. and SpiegeL, W., 1995. Three natural zircon standards for U-Th-Pb, Lu-Hf, trace element and REE analyses. *Geostandars Newsletter: The Journal of Geostandards and Geoanalysis*, 19, 1-23

Wieser, M.E. and Schwieters, J.B., 2005. The development of multiple collector mass spectrometry for isotope ratio measurements. International Journal of Mass Spectrometry. 242,97-115

Willbold, M. and Jochum, K.P., 2005. Multi-Element Isotope Dilution Sector Field ICP-MS: A Precise Technique for the Analysis of Geological Materials and its Application to Geological Reference Materials. *Geostandars Newsletter: The Journal of Geostandards and Geoanalysis*, 29, 63-82.

Williams, I.S., 1998. U-Th-Pb geochronology by ion microprobe. In: McKibben, M.A, Shanks, W.C. and Ridley, W.I. (eds.). Applications of Microanalytical Techniques to Understanding Mineralizing Porcesses. Reviews in Economic Geology, 7, Society of Economic Geologists, 1-35.

Willigers, B.J.A., Mezger, K. and Baker, J., 2004. Development of high precision Rb-Sr phlogopite and biotite geochronology; an alternative to $^{40}Ar/^{39}Ar$ tri-octahedral mica dating. *Chem. Geol*., 213, 339-358.

Woodhead, J., Hergt, J., Shelley, M., Eggins, S. and Kemp, R., 2004. Zircon Hf-isotope analysis with an excimer laser, depth profiling, ablation of complex geometries and concomitant age estimation. *Chem. Geol*., 209, 121-135.

Woodhead, J.D. and Hergt, J.M., 2005. A preliminary appraisal of seven natural zircon reference materials for in situ Hf isotope determination. *Geostandards and Geoanalytical Research*, 29, 183-195.

Wombacher, F., Rehkämper, M., Mezger, K. and Münker, C. 2003. Stable isotope compositions of cadmium in geological materials and meteorites determined by multiple-collector ICP-MS. *Geochim. Cosmochim. Acta*, 67, 4639-4654.

Yang, l., Peter, C., Panne, U. and Sturgeon, R.E., 2008. Use of Zr for mass bias correction in strontium isotope ratio determinations using MC-ICP-MS. *J. Anal. At. Spectrom*., 23, 1269-1274.

Yang, Y.H., Wu, F.Y., Wilde, S.A., Liu, X.M., Zhang, Y.B., Xie, L.W. and Yang J.H., 2009. In situ perovskite Sr-Nd isotopic constraints on the petrogenesis of the Ordovician Mengyin kimberlites in the North China Craton. *Chem. Geol*., 264, 24-42.

Yang, Y.H., Zhang, H.F., Chu, Z.Y., Xie, L.W. and Wu, F.Y., 2010. Combined chemical separation of Lu, Hf, Rb, Sr, Sm and Nd from a single rock digest and precise and accurate isotope determinations of Lu-Hf, Rb-Sr and Sm-Nd isotope systems using Multi-Collector ICP-MS and TIMS. *International Journal of Mass Spectrometry*, 290, 120-126.

Yang, W. and Li, S., 2008. Geochronology and geochemistry of the Mesozoic volcanic rocks in Western Liaoning: Implications for lithospheric thinning of the North China Craton. *Lithos*, 102, 88-117.

Yu, Z., Robinson, P. and McGoldrick, P., 2001. An Evaluation of Methods for the Chemical Decomposition of Geological Materials for Trace Element Determination using ICP-MS. *Geostandars Newsletter: The Journal of Geostandards and Geoanalysis*, 25, 199-217.

Yuan, H.L., Gao, S., Dai., M.N., Günther, D., Fontaine, G.H., Liu, X.M. and Diwu, C.R., 2008. Simultaneous determinations of U/Pb age, Hf isotopes and trace element compositions of zircon by excimer laser ablation quadrupole and multiple collector ICP-MS. *Chem. Geol*., 247, 100-118.

Zhang, W., Hu, Z., Liu, Y., Chen, L., Chen, H., Li, M., Zhao, L., Hu, S. and Gao, S., 2012. Reassessment of HF/HNO_3 decomposition capability in the high-pressure digestion of felsic rocks for multi-element determination by ICP-MS. *Geostandards and Geoanalytical Research*, 36, 271-289.

Appendix 1: Additional information related to the high-pressure migmatitic gneisses of the Cabo Ortegal Complex

Appendix 1. Additional information related to the high-pressure migmatitic gneisses of the Cabo Ortegal Complex.

A brief description of the high-pressure muscovite-bearing migmatitic gneisses from Cabo Ortegal was already given in the Chapter 4.2.b.2. of the present memoir. The scope of that part of the study was mainly the application of the implemented methods for U-Pb and Hf analysis in zircons. Within the same outcrop, other lithologies less rich in zircon are found which are also described here. Additionally, we present here complementary information on the mineral chemistry and P-T conditions determined for all these rock types.

A.1. Field aspects of the high-pressure migmatites

The studied outcrops of the migmatitic acid rocks within the high-pressure mafic s.l. granulites of the Bacariza Formation are located between the Herbeira and Limo peridotite massifs (Figure a.1). These rocks structurally overlay variably retrogressed garnet-plagioclase ± clinopyroxene-bearing granulites and are overlain by ultramafic rocks. The high-pressure migmatitic gneiss are easily recognized in the field due to their abundance in garnet and micas, light colour, and evidences for partial melting and development of metatexite structures. A foliation and associated lineation are defined by the preferred and shape orientation of the constituent minerals. The foliation is nearly horizontal, whereas the lineation trends NNE.

Different lithologies of high-pressure migmatitic gneiss have been identified (Figure a.1): 1) Muscovite-bearing migmatites contain either muscovite +/- biotite, whereas 2) biotite migmatites lack muscovite. The abundance of these rock types is barely similar and altogether account for more than 80 % of the outcrops. The transition from one type to the other is gradual and may occur in the same outcrop. The abundance of idiomorphic prismatic zircon crystals with oscillatory zoning in the high-pressure migmatitic gneiss, particularly in the muscovite-bearing rocks (see below), as well as of zoisite/clinozoisite with allanite cores, point to essentially acid igneous protoliths or to impure volcanic greywackes with K-rich granitic (rhyolitic) component. These rock types show clear evidence of migmatization (Figure a.1a-c) and are rich in garnet. The lithologic varieties of the unit also include 3) felsic gneisses and 4) mafic to intermediate tectonites that occur as boudins or at the contacts with the ultramafic massifs. The former are distinctly light-coloured and are rich in quartz and plagioclase, with minor garnet, zoisite and clinopyroxene. These gneissic felsic rocks, commonly referred to as leptynites in the literature, lack evidence of partial melting. They form bands up to 20 cm thick and exhibit sharp contacts

with the neighbouring mica-bearing lithotypes (Figure a.1d). Felsic gneisses constitute less than 10 % of the acid migmatitic unit (Figure a.1d). The latter are variably retrogressed, mafic blastomylonites, similar to the mafic granulites outcropping elsewhere in the Bacariza Formation, occurring as metre-size boudins within the mica-bearing migmatitic rocks (Figure a.1c). These ductilely deformed rocks also crop out as a band parallel to the eastern boundary of the migmatitic unit and are metamorphic tectonites with a porphyroclastic microstructure resembling those studied by Puelles et al. (2007).

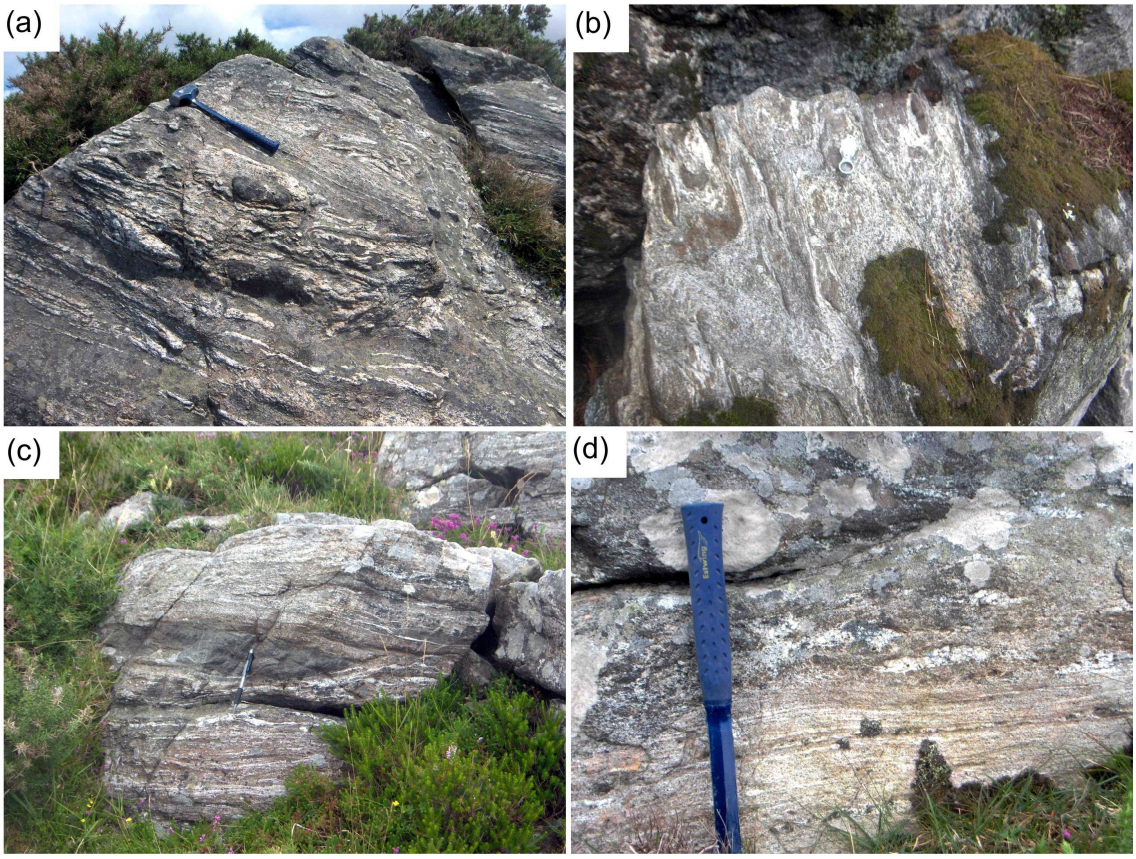

Figure a.1. Outcrop views of the high-pressure migmatitic gneiss within the Bacariza Formation of the Cabo Ortegal Complex; **(a)** and **(c)**, metatexites including boudins of mafic granulite; **(b)** migmatite with an advanced stage of partial melting; **(d)** common migmatite on top and felsic gneiss.

A.2. Analytical techniques

Mineral analyses and X-ray maps were obtained using a Cameca SX-100 electron microprobe equipped with a Energy Dispersive (EDS) and five Wavelength Dispersive (WDS) spectrometers at the Centro de Instrumentación Científica (CIC) of the University of Granada. The operating parameters used in the analysis were: 15 kV accelerating voltage, 15 nA beam current, 5 µm beam diameter and 10 to 30 s counting time (peak) depending on the element abundance.

The X-ray maps were acquired using 15 kV accelerating voltage, 100 nA beam current, 5µm beam diameter and 30 µs counting time per pixel. The images were processed with Imager software (Torres-Roldán and García-Casco, unpublished) to obtain quantitative element images and profiles (Figures a.5 and a.6; see procedure in García-Casco, 2007 and García-Casco et al., 2009).

Whole-rock analyses of major elements were carried out at the CIC in the University of Granada. Major element compositions were determined in PHILIPS Magix Pro (PW-2440) X-ray fluorescence (XRF) equipment using a glass beads, made of 0.6g of powdered sample diluted in 6g of $Li_2B_4O_7$.

Amphibole compositions were normalized following Leake et al. (1997) and Fe^{3+} was calculated after the method of Schumacher (Leake et al., 1997). Garnet composition was normalized to 8 cations and 12 oxygens, and Fe^{3+} was estimated by stoichiometry. Clinopyroxene was normalized to 4 cations and 6 oxygens, and Fe^{3+} was estimated by stoichiometry. Epidote and feldspars were normalized to 12.5 and 8 oxygens, respectively, and assuming $Fe_{total} = Fe^{3+}$. Muscovite, biotite and chlorite were normalized to 22, 22 and 28 oxygens, respectively, considering $Fe_{total} = Fe^{2+}$. Rutile, ilmenite, kyanite, magnetite and apatite were normalized to 2, 3, 5, 4 and 5 oxygens respectively. Mineral and end-member abbreviations are after Kretz (1983), except for amphibole (Amp). Atoms per formula unit is abbreviated apfu.

A.3. Petrography

A.3.a. Muscovite-bearing migmatitic gneiss

Those rocks are essentially described in the Chapter 4.2.b.2. of the PhD Thesis.

A.3.b. Biotite migmatitic gneiss

The mineral assemblage in this type of rock comprises quartz, plagioclase, garnet and biotite, with accessory rutile, ilmenite, epidote and amphibole (Figure a.2a-f). The microtexture can be defined as grano-lepidoblastic and is characterized by alternate bands rich in quartz-plagioclase and garnet-biotite.

Garnet occurs as subidiomorphic crystals with abundant inclusions of biotite, quartz, rutile and opaque minerals (Figure a.2b and c). Locally, the inclusions are obliquely oriented relative to the garnet shape preferred orientation (Figure a.2b). The zonation of garnet, in particular in the largest crystals, is remarkable, displaying darker cores and lighter rims in plane polarized light

(Figure a.2a and c). Garnet grains are usually fractured and replaced by biotite (+plagioclase) along their rims (Figure a.2d), though textural equilibrium between garnet and biotite (+rutile) is also common.

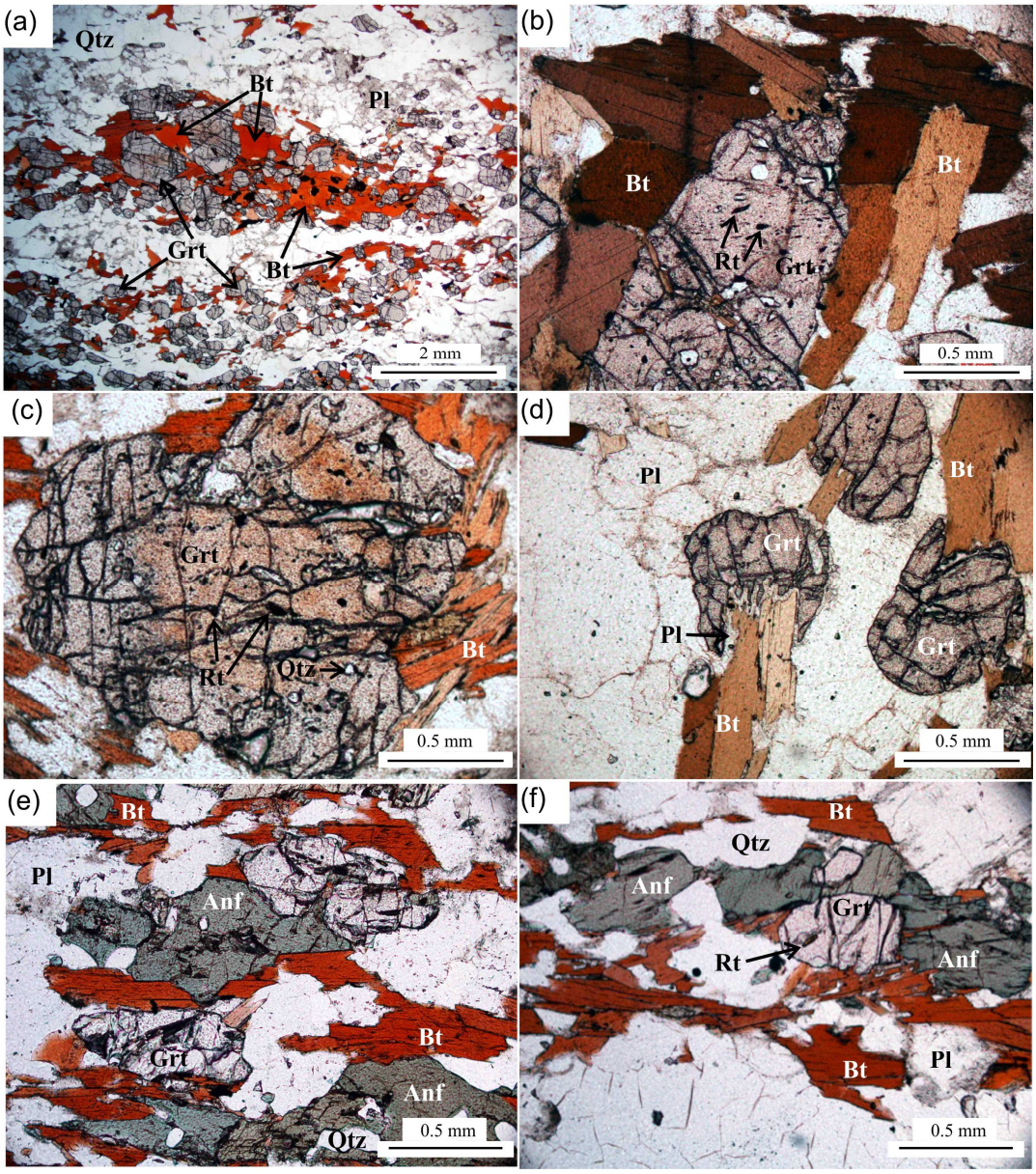

Figure a.2. Photomicrographs of the garnet-biotite ± amphibole-bearing migmatites. All sections correspond to the XZ structural plane. **(a)** Elongated polycrystalline aggregates of biotite and garnet defining the main foliation. Parallel nicols. **(b)** Oriented inclusions of rutile and quartz in subidiomorphic garnet defining a relict foliation. Parallel nicols. **(c)** Optically zoned garnet with inclusions of quartz and rutile. Parallel nicols. **(d)** Partial resorption of garnet to biotite ± muscovite and plagioclase. Parallel nicols. **(e)** and **(f)** Bands containing elongated garnet, biotite and amphibole. Parallel nicols.

Polycrystalline aggregates of biotite, locally associated with garnet (Figure a.2a), define the foliation of the rocks. These aggregates contain quartz, rutile, monazite and zircon. In retrogressed samples, biotite is replaced by chlorite. Plagioclase is abundant, occurring as single crystals variably replaced by micaceous aggregates (sericite). Green-brown-yellowish amphibole

crystals occur in specific areas of some samples, as a result of chemical heterogeneities in the protoliths,. Amphibole crystals are subidiomorphic, less than 1 mm in size, appear in equilibrium with biotite and other matrix minerals (Figure a.2e and f), and their shape fabric also defines the rock foliation.

A.3.c. Felsic gneisses

The mineral assemblage of this type of rock comprises quartz, plagioclase, garnet and zoisite with minor amounts of one or more of the following minerals: rutile, pyroxene, amphibole and biotite (Figure a.3a-f). These rocks exhibit an oriented granoblastic microstructure with deformation focused in quartz- and plagioclase-rich narrow bands that appear to have formed late in the recrystallization sequence of events and where the crystal size is minimized. Minute biotite crystals often occur in these bands (Figure a.3e).

Garnet crystals are 0.2-1 mm in size, idiomorphic, and with sub-rounded rims. Locally, they are elongated subparallel to the foliation defining a stretching direction (Figure a.3b and f). Stretching likely caused the fractures perpendicular to the long axis of the largest grains. Some garnet grains show quartz-, zoisite- and rutile- inclusion-rich cores and inclusion-free rims. Garnet rims are locally retrogressed to micaceous aggregates.

Zoisite crystals are usually the largest crystals in these rocks, forming prisms up to more than 4 mm in length and 1 mm in width, which may contain allanite cores. Zoisite appears usually in association with garnet, either showing inclusion relationships of each other mineral or as zoisite associated with garnet rims (Figure a.3f). It also displays the same type of fractures observed in garnet and may appear stretched and boudinaged (Figure a.3c). Some crystals show greyish zoisite cores overgrown by (bluish, under crossed polars, e.g.: Figure a.3d) clinozoisite rims or apical overgrowths.

Plagioclase is abundant and forms xenomorphic crystals ranging in size from 3 mm in the granoblastic matrix up to a few microns in the strongly deformed areas. Yet, all the crystals show similar characteristics, including polysynthetic and deformation twinning, undulose extinction and subgrain boundaries. It may bear small inclusions of zircon.

Biotite is concentrated in areas of intense deformation. Clinopyroxene occurs in samples with relatively low plagioclase content (Figure a.3a). It forms narrow bands made of crystals elongated parallel to the foliation, bears inclusions of plagioclase, quartz, rutile and garnet, and is locally retrogressed to amphibole (Figure a.3a and b). Amphibole may appear also as discrete crystals unrelated to retrogressed pyroxene (Figure a.3a). Abundant rutile is present either in the

matrix or as inclusions in clinopyroxene and amphibole. Ilmenite and apatite also occur as variably abundant accessories.

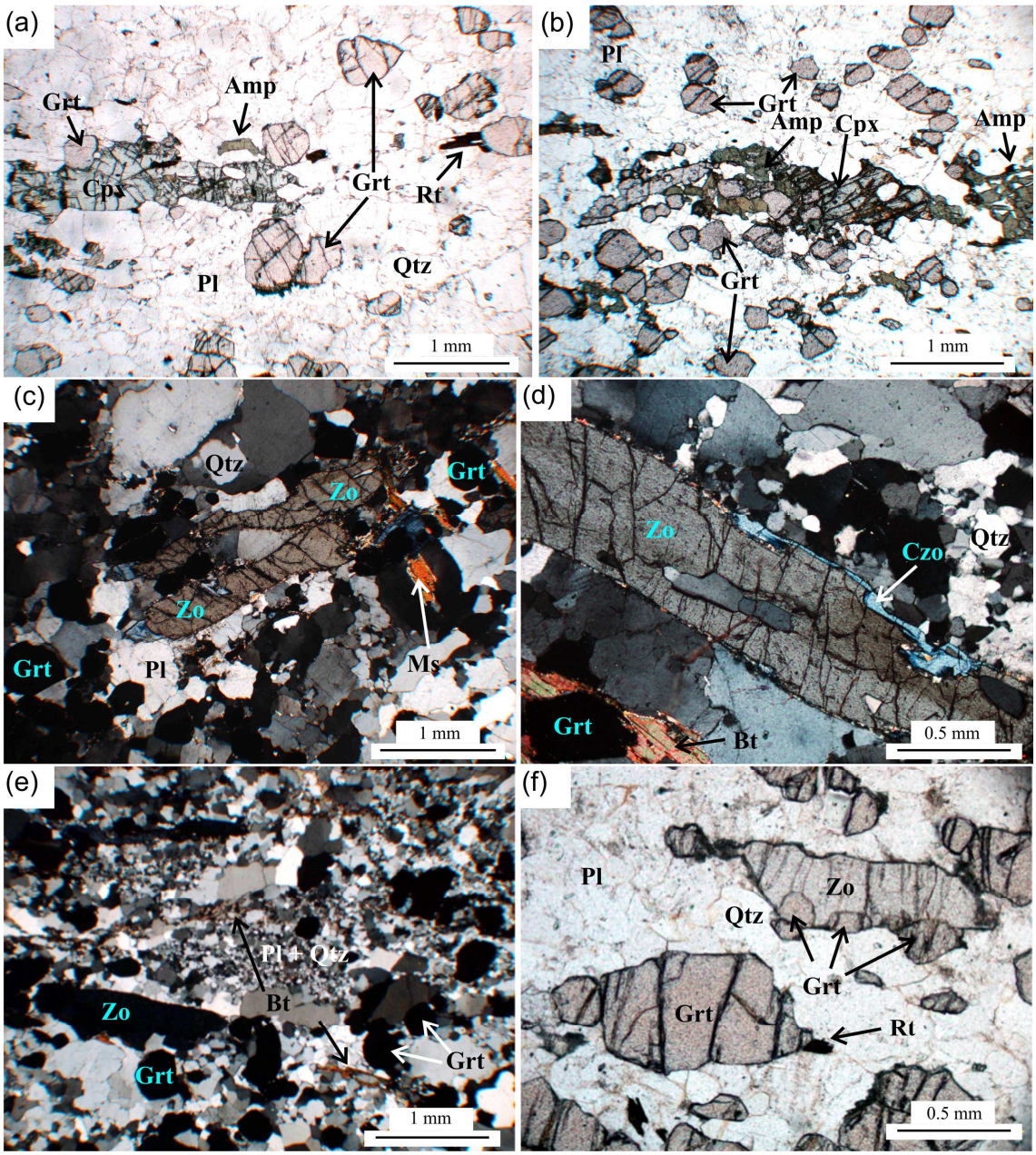

Figure a.3. Photomicrographs of the felsic gneisses. All sections correspond to the XZ structural plane. **(a)** and **(b)** Bands containing minor amounts of elongated clinopyroxene, amphibole and zoisite; note the fractures oblique to the foliation in the garnets. Parallel nicols. **(c)** and **(d)** Elongated crystals of zoisite with rims and overgrowths of clinozoisite; note also the fractures of zoisite in (c) oblique to the foliation. Crossed nicols. **(e)** Zone of extreme grain size reduction with minute crystals of biotite. Crossed nicols. **(f)** Large elongated garnets and small equidimensional garnets around elongated zoisite. Parallel nicols.

A.3.d. Mafic tectonites

Although these are neither acid rocks nor migmatites, they are included in the present study because they occur as boudins within other lithologies and also crop out along the east boundary between the acid lithotypes described above and the Herbeira peridotites. These rocks can provide additional information for a better reconstruction of the metamorphic evolution of the high-pressure acid migmatitic unit. They are blastomylonites with porphyroclastic microstructure and will not be considered in detail from the otherwise relevant structural and rheological points of view, since they are out of scope of the present study (see Puelles et al., 2009, and references therein, for further details). The deformation of these rocks was heterogeneous and resulted in different petrographic types. Porphyroclasts of amphibole, zoisite with allanite cores and garnet 3-4 mm in grain size are embedded by a finer grained matrix made of 0.5 mm to millimetre size crystals of amphibole (Figure a.4a-c). The matrix is composed of amphibole, garnet, plagioclase and biotite, with minor amounts of quartz and epidote. Its microtexture may be defined as oriented, grano- to nemato-lepidoblastic.

Garnets appear strongly fractured and usually elongated in various directions. Garnets contain abundant inclusions of biotite, amphibole, rutile, quartz and plagioclase. They can also occur as inclusion in amphibole.

Abundant subidiomorphic to subrounded amphiboles exhibit a shape-preferred orientation and may bear inclusions of biotite, garnet and plagioclase. These features are similar to those of amphiboles in shear zones elsewhere within the Bacariza granulites (Puelles et al., 2006, 2007). Yet, in the present case intracrystalline deformation in the amphiboles are not so widespread.

Biotite occurs either as inclusion in garnet and amphibole or as oriented microliths in the matrix. Nearly all the biotite was transformed into chlorite (Figure a.4d). Abundant rutile and ilmenite is related to these microlithic areas. Xenomorphic plagioclase with weak undulose extinction and oblique grain boundaries is also present (Figure a.4b). Epidote crystals usually contain allanite cores, epidote outer areas and clinozoisite rims. Abundant magnetite occurs scattered in the fine grained matrix.

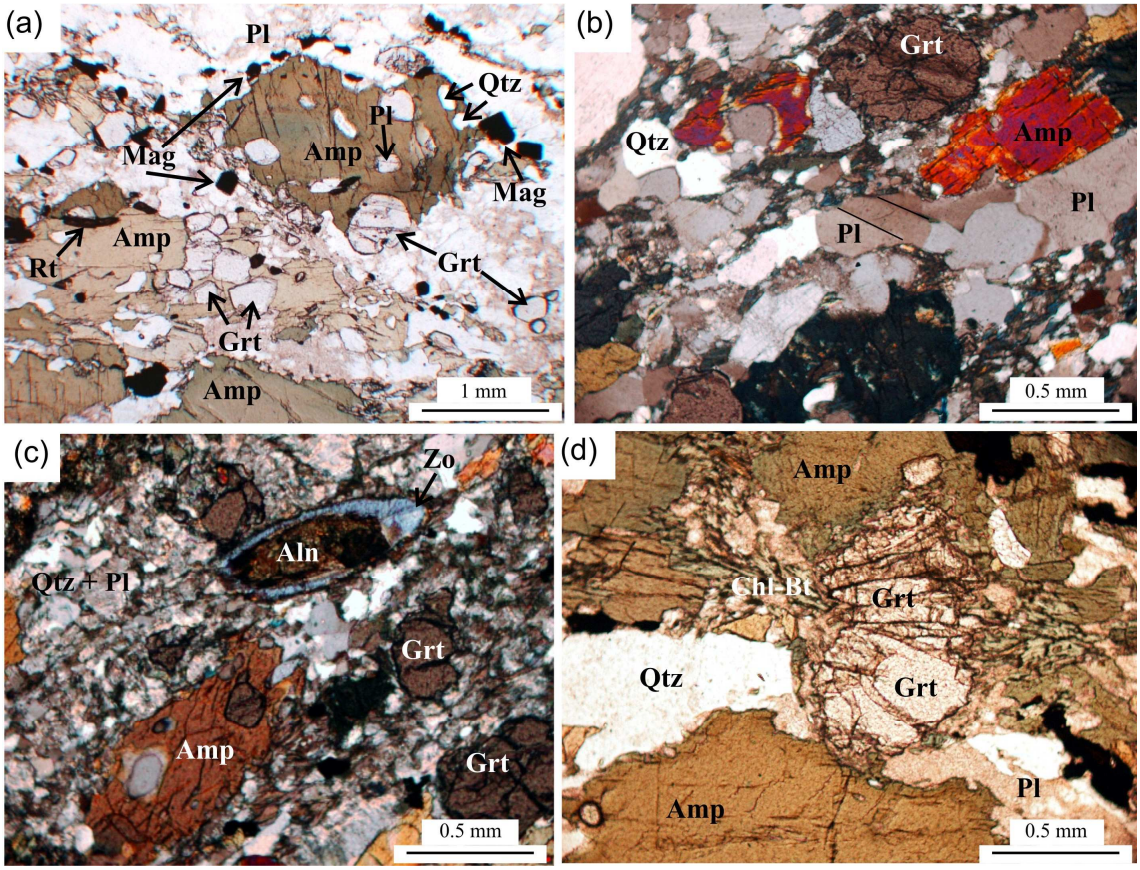

Figure a.4. Photomicrographs of the retrogressed mafic granulite tectonites. All sections correspond to the XZ structural plane. **(a)** and **(b)** Typical aspect of the mafic granulite in the shear band with zoned amphibole and garnet porphyroclasts in a matrix containing bands of extreme grain size reduction made of quartz, amphibole and plagioclase. Parallel nicols. **(c)** Same as (a) and (b) under partially crossed nicols showing the fine grained matrix, with amphibole porphyroclast containing inclusions of quartz and garnet, and zoisite porphyroclast with allanite core. **(d)** Garnet breakdown in the retrogressed mafic granulite of the shear band. Parallel nicols.

A.4. Mineral chemistry

A.4.a. Garnet

Representative garnet compositions are given in Table a.1, and X-ray maps and profiles are presented in Figures a.5 and a.6. Garnet from muscovite-bearing migmatitic gneiss is richer in Fe and Ca and poorer in Mg than garnet from the biotite migmatitic gneiss. Yet, both show similar zoning patterns with homogeneous cores and thin rims (Figures a.5, a.6, a.7b and a.7c). The compositional variations involve a decrease in pyrope and grossular contents and an increase in almandine and spessartine near the rims (Figures a.7b and c). These variations are more pronounced in the muscovite-bearing gneisses. The Mg/Mg+Fe ratio generally slightly decreases towards the rims.

Garnet from the felsic gneisses is fairly homogeneous with compositions of ca. $Alm_{44-48}Grs_{25-32}Prp_{18-24}And_{1-3}Sps_{1}$. A weak asymmetric retrograde zoning involves a slight decrease in grossular content and an increase in the Mg/Mg+Fe ratio from core to rim (Figure a.7a), without noticeable variation in almandine and pyrope contents. This zoning pattern is unrelated to the type of mineral in contact with the garnet rim.

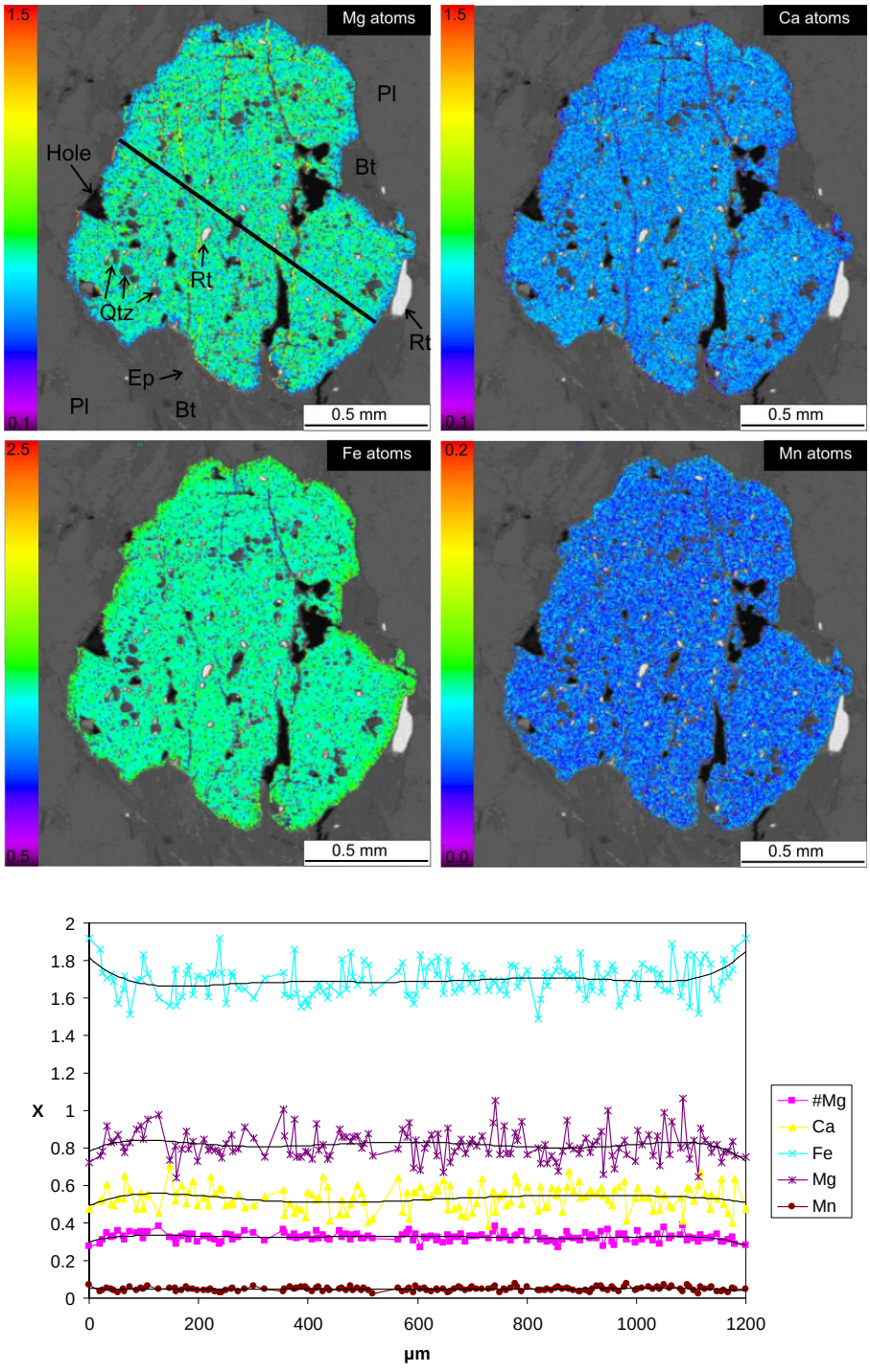

Figure a.5. Quantified X-ray maps (cations per 12 oxygens, colour code) and compositional profile of a typical garnet from the biotite migmatitic gneisses. The garnet images are laid on top of a gray-scale BSE image of the scanned area.

Garnet from the mylonites is also rather homogeneous ($Alm_{44-50}Grs_{23-28}Prp_{16-24}$ $And_{0-2}Sps_{2-7}$) with barely perceptible decrease in pyrope and Mg/Mg+Fe ratio, and increase in almandine and spessartine contents towards the rims (Figure a.7d).

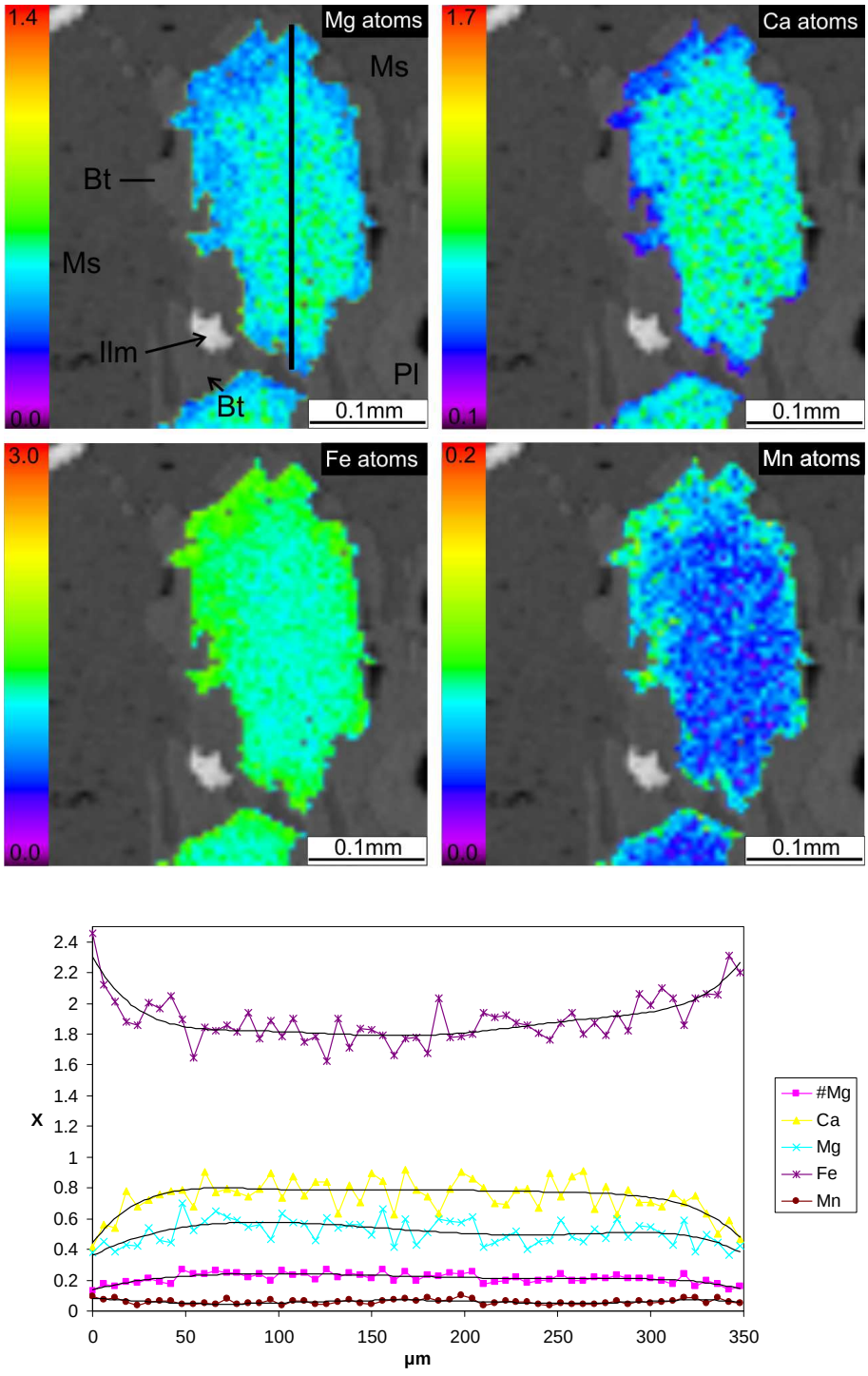

Figure a.6. Quantified X-ray maps (cations per 12 oxygens, colour code) and compositional profile (see line in a) of a typical garnet from the muscovite-bearing migmatitic gneisses. The garnet images are laid on top of a gray-scale BSE image of the scanned area.

Overall, the observed garnet zoning was produced by diffusional homogenization (cores) as a result of high temperatures during peak metamorphism, and further diffusional adjustments (rims) during retrograde resorption and cation exchange with the matrix assemblages upon cooling. The complementary zoning of plagioclase in contact with garnet (see below and Figure a.8) suggests a pressure decrease during retrogression.

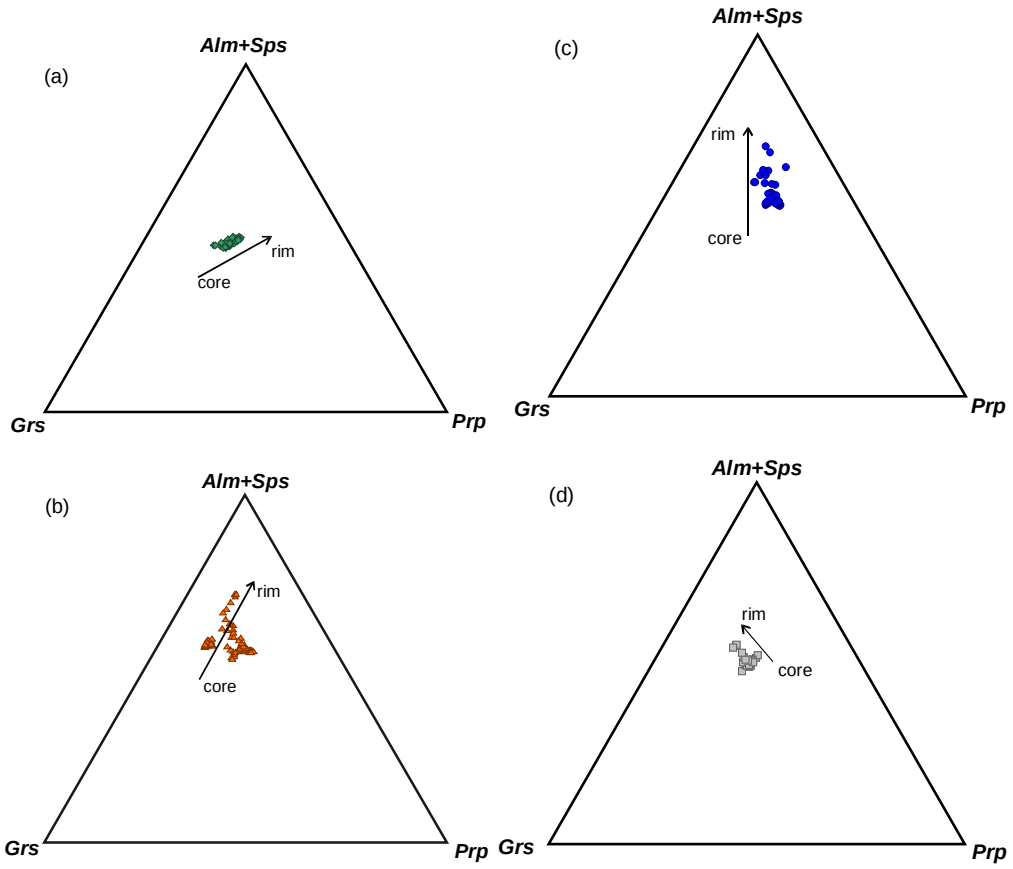

Figure a.7. Alm+Sps-Grs-Prp triangular plot showing the compositional trend of garnet from **(a)** felsic gneisses, **(b)** muscovite migmatites, **(c)** biotite migmatites and **(d)** mylonites.

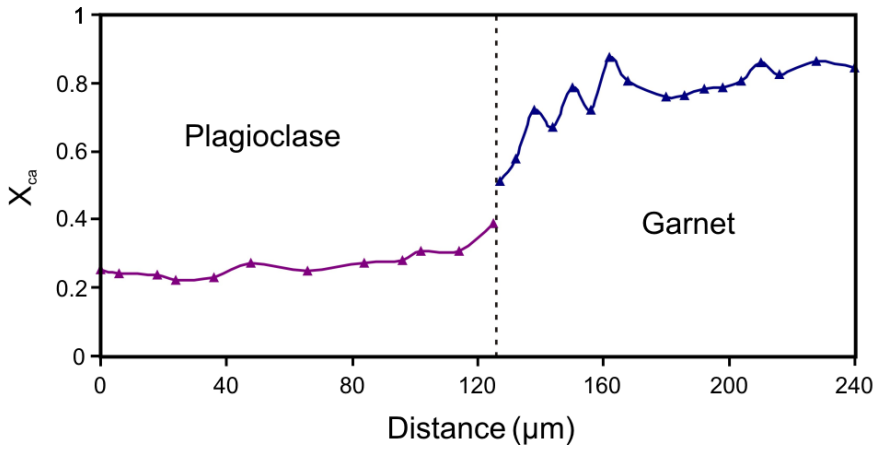

Figure a.8. Antithetic variation of Ca atoms in garnet (12 O) and adjacent plagioclase (8 O) from sample CO35 (muscovite-bearing migmatitic gneiss).

A.4.b. Feldspar

Plagioclase from muscovite-bearing migmatitic gneisses lacking primary biotite is homogeneous in composition (andesine, $An_{21-42,}$ Figure a.9). Antiperthitic K-feldspar has a composition of Ab_8Or_{92}. In the muscovite-bearing migmatitic gneisses bearing (minor amounts of) primary biotite, plagioclase shows an increase in An content from oligoclase cores to andesine rims (Figure a.9). This feature is appreciated in all grains analysed, but it is more clearly developed in areas of plagioclase in contact with biotite. This zoning pattern is opposite to the Ca zoning of coexisting garnet, and reflects the incorporation of Ca to plagioclase through the breakdown of the grossular component of garnet (Figure a.8).

Plagioclase from the biotite migmatitic gneisses and felsic gneisses are of oligoclase composition ($An_{17-21,}$ Figure a.9), the latter with a continuous slight increase in An content from core to rim irrespective of the mineral in contact with plagioclase. Plagioclase from the mylonitic mafic rocks is also of oligoclase composition (Figure a.9), but slightly richer in An (An_{23-26}).

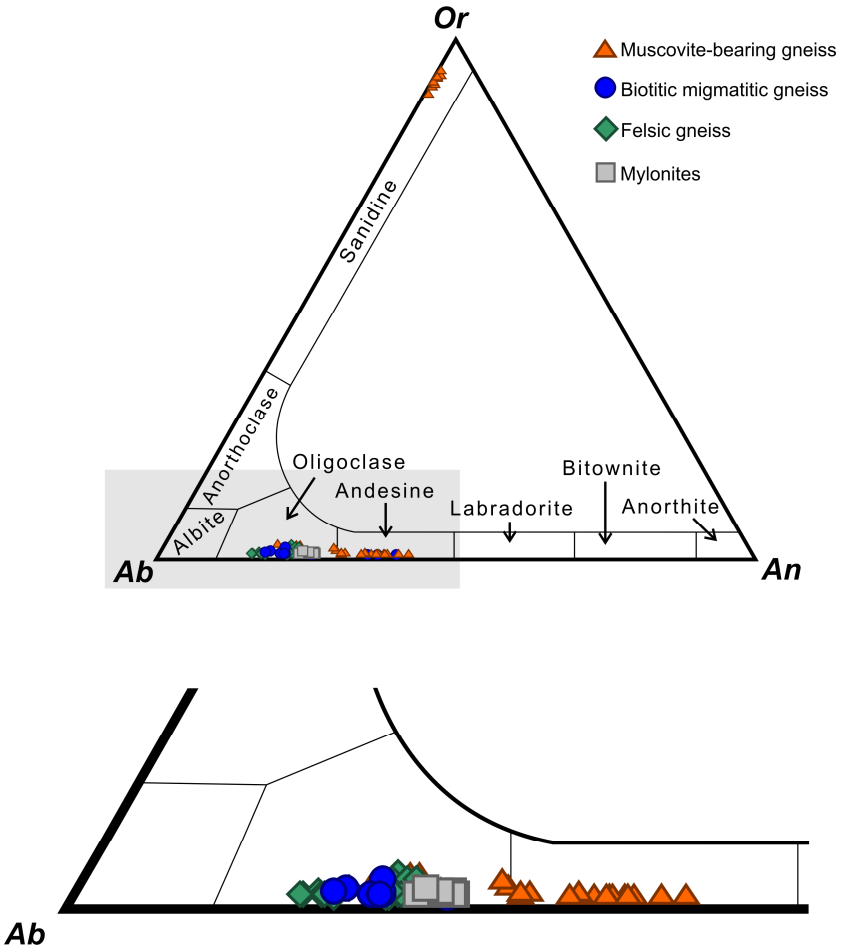

Figure a.9. Composition of plagioclase from the different types of rocks studied.

A.4.c. Clinopyroxene

The cores of clinopyroxenes from the felsic gneisses are relatively homogeneous with an average composition of $Aug_{0.79}Jd_{0.20}Ac_{0.01}$, while the rims show a marked Al and Na decrease and Mg and Ca increase. This trend towards Na-poorer augite from core to rim (Figure a.10) is related to partial re-equilibration during retrogression, and suggests significant decompression after peak metamorphic conditions.

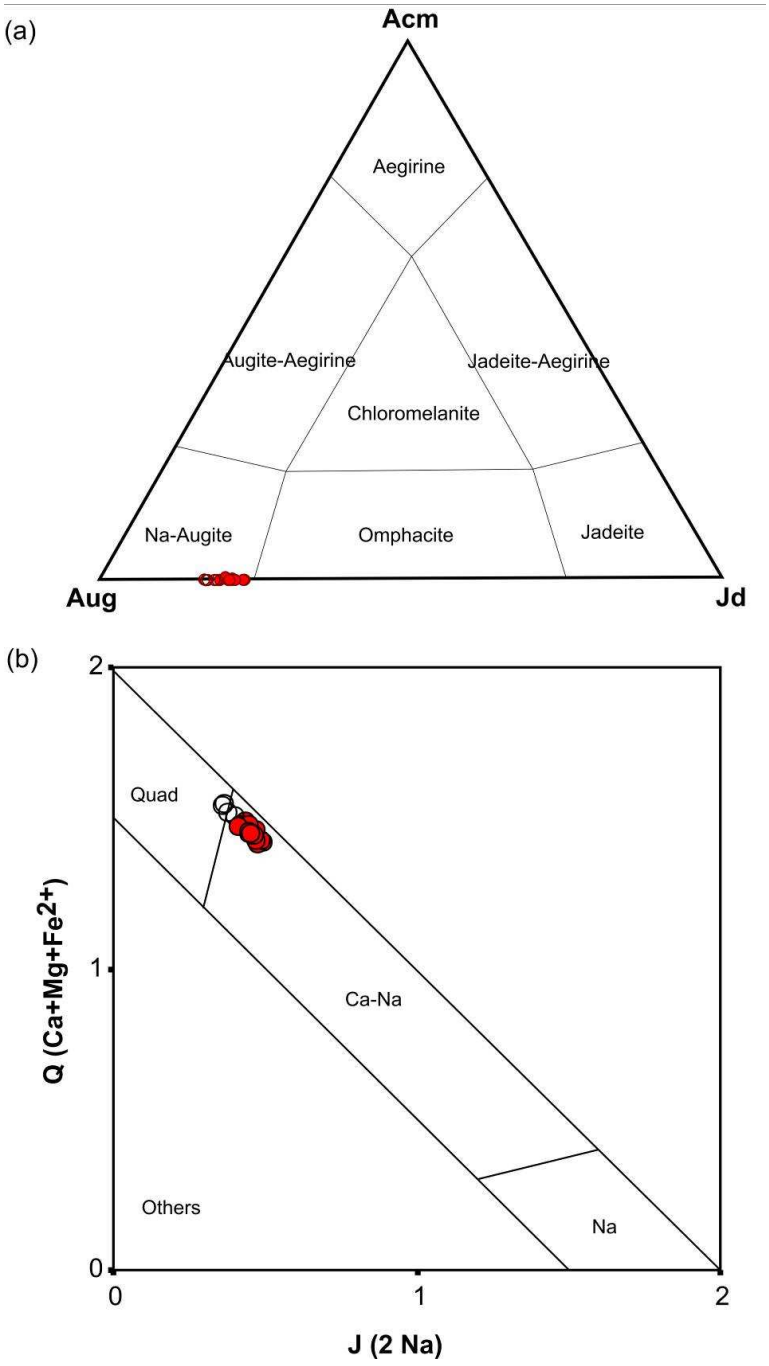

Figure a.10. **(a)** Acmite-Augite-Jadeite plot (Essene and Fyfe, 1967) and **(b**) J-Q plot (Morimoto et al., 1988) for clinopyroxene from the felsic gneisses. Filled circles represent cores compositions, while the empty circles represent the rims.

A.4.d. Amphibole

Amphibole occurs sparsely in the felsic gneisses and biotite migmatitic gneisses, and is an major constituent of the mafic mylonites. All amphiboles are calcic in composition and fairly homogeneous. Amphiboles from the felsic gneiss, which are related to retrogression of primary clinopyroxene (see above) are of pargasite composition (according to Leake et al., 1997, Figure 16) with an average composition of $(Na_{0.4}K_{0.3})(Na_{0.1}Ca_{1.8}Fe^{2+}_{0.1})$ $(Fe^{2+}_{1.5}Mg_{2.5}Fe^{3+}_{0.2}Ti_{0.2}Al_{0.6})(Al_{1.7}Si_{6.3})O_{22}(OH)_2$. Mg/(Mg+Fe) ratios range from 0.60 to 0.64 and Si contents ranges from 6.2 to 6.5 apfu. In the mafic mylonites amphibole porphyroclasts are also pargasite (Figure a.11) with an average compositions of $(Na_{0.3}K_{0.2})(Na_{0.2}Ca_{1.7}Fe^{2+}_{0.1})(Fe^{2+}_{1.4}Mg_{2.4}Fe^{3+}_{0.3}Ti_{0.1}Al_{0.8})(Al_{1.7}Si_{6.3})O_{22}(OH)_2$. Their composition is slightly poorer in Si (6.2-6.3 apfu), Fe and Ca and richer in Al than amphibole from the felsic gneisses, with slightly more variable Mg/(Mg+Fe) ratios (0.58-0.70). Amphibole from the biotite migmatitic gneisses have a lower occupancy in the A-site (< 0.5 apfu) site being classified as tschermakite with average composition $(Na_{0.2}K_{0.2})(Na_{0.2}Ca_{1.7}Fe^{2+}_{0.1})$ $(Fe^{2+}_{1.3}Mg_{2.3}\ Fe^{3+}_{0.5}\ Ti_{0.1}\ Al_{0.9})(Al_{1.8}Si_{6.2})O_{22}(OH)_2$ (Figure a.11). The Si (6.0-6.2 apfu) and Na contents are low, while total Al content is high relative to amphiboles from other types of rock. Relatively high Ti contents of amphibole from the mafic mylonites and felsic gneisses (0.10-0.18 apfu) are compatible high-grade conditions. Ti contents of the biotite migmatitic gneiss are slightly lower (0.08-0.11 apfu).

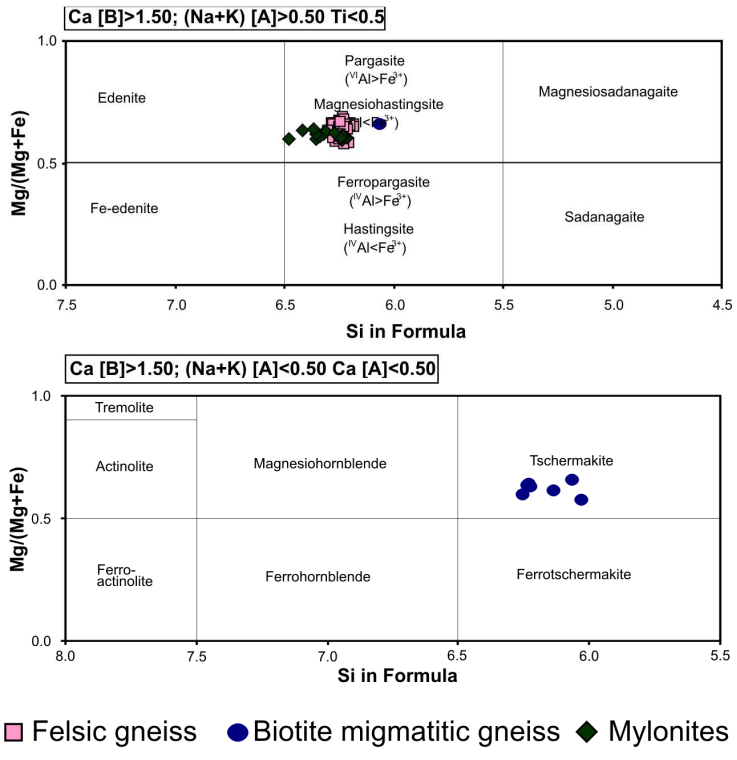

Figure a.11. Summary of amphibole compositions of felsic gneisses, biotite migmatitic gneisses and mylonites plotted according the classification of Leake et al. (1997).

A.4.e. Biotite

The average composition of biotite replacing muscovite in the K-feldspar bearing rocks is $K_{0.94}Na_{0.02}(Mg_{1.57}Fe_{0.89}Al_{0.27}Ti_{0.17})(Al_{1.28}Si_{2.72})O_{10}(OH)_2$, while primary matrix biotite from muscovite migmatites lacking K-feldspar has a composition richer in MgO and $^{[VI]}Al$, averaging $K_{0.94}Na_{0.04}(Mg_{0.88}Fe_{1.49}Al_{0.48}Ti_{0.14})(Al_{1.22}Si_{2.78})O_{10}(OH)_2$ (Figure a.12).

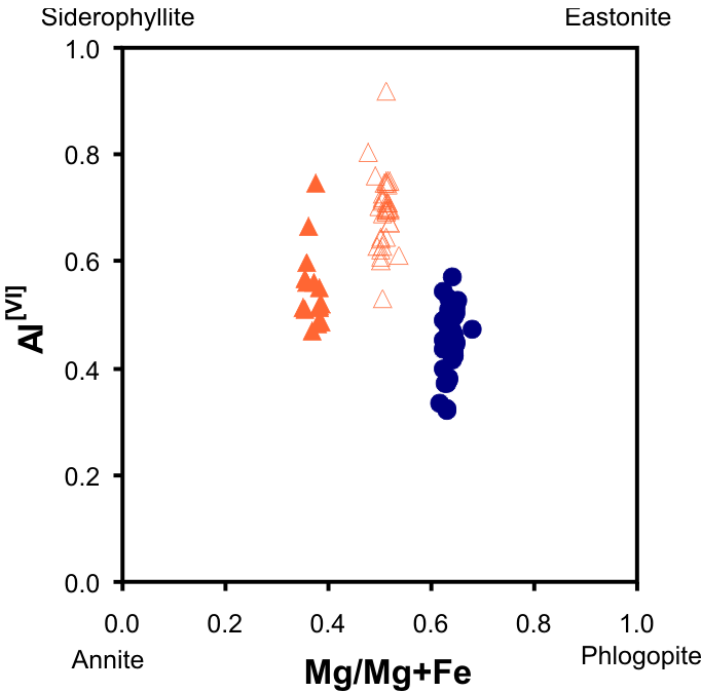

Figure a.12. Chemical compositions of biotite. Circles: biotite from biotite migmatitic gneisses, filled triangles: biotite replacing muscovite from the muscovite-bearing gneiss, empty triangles: matrix biotite from muscovite-bearing gneiss.

In the biotite migmatitic gneisses, biotite has homogeneous compositions averaging $K_{0.86}Na_{0.05}(Mg_{1.57}Fe_{0.89}Al_{0.22}Ti_{0.16})(Al_{1.22}Si_{2.78})O_{10}(OH)_2$, with higher Mg/Mg+Fe ratios and less $^{[VI]}Al$ than in the muscovite-bearing gneiss (Figure a.12).

Biotite of all types of rock is rich in Ti (0.25-0.45 apfu) contents, suggesting high crystallization temperature. Biotite crystals in contact with garnet show a slight increase in Mg/Mg+Fe towards the garnet-biotite interface, indicating retrograde diffusional reequilibration through exchange of Fe-Mg between both phases.

A.4.f. Muscovite

Muscovite partially replaced by biotite from the K-feldspar and antiperthite-bearing rocks has an average compositions of $K_{0.95}Na_{0.04}(Al_{1.57}Fe_{0.26}Mg_{0.14}\ Ti_{0.07})(Al_{0.82}Si_{3.18})O_{10}(OH)_2$, while those in equilibrium with matrix biotite in the Ky-bearing K-feldspar-lacking rocks are poorer in FeO with an average compositions of $K_{0.89}Na_{0.09}(Al_{1.65}Fe_{0.17}Mg_{0.14}Ti_{0.07})\ (Al_{0.85}Si_{3.15})O_{10}(OH)_2$. In all types of

rock muscovite is poor in celadonite component, the paragonite component is almost absent (Figure a.13a and b), and are rich in TiO_2 (0.05-0.20 apfu), indicating high temperature of formation.

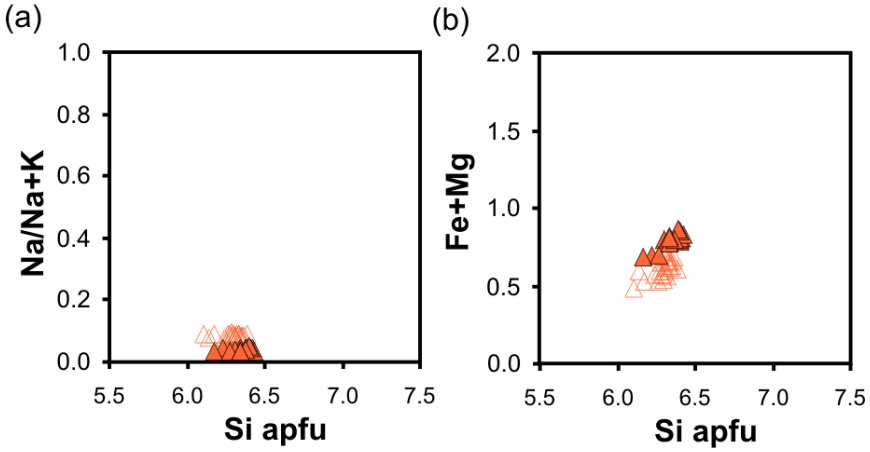

Figure a.13. Compositions of muscovite. **(a)** Si versus Na/Na+K and **(b)** Si versus Fe+Mg. Filled triangles: biotite-lacking rocks; empty triangles: biotite-bearing rocks.

A.4.g. Fe-Ti oxides

Rutile is almost pure TiO_2 = 98.7-99.9 wt%, while ilmenite compositions are variable in terms of FeO and TiO_2 (38-46 wt% FeO and 46-57 wt% TiO_2). Magnetite, only locally present, is almost pure in composition (99 wt% FeO_{total}).

A.4.h. Kyanite

Kyanite from the muscovite and biotite migmatitic gneisses has minor amounts of Fe_2O_3 (0.70-0.95 wt%).

A.4.i. Epidote group minerals

Epidote group minerals occur in all types of rock studied and exhibit chemical differences that reflect the timing of their crystallization. Primary zoisite from the felsic gneisses is homogeneous ferric zoisite (Fe_2O_3 > 1.6 wt%) with ca. 16 mol % pistacite contents in inner regions while the rims and overgrowths are slightly poorer in Fe with ca. 12 mol % pistacite. Secondary epidote after garnet in the same rock type has up to 28 mol % pistacite content. Zoisite overgrowths around allanite cores in the mafic tectonites are also homogeneous, with 10-14 mol % pistacite. In the biotite migmatitic gneisses, epidote is often related to biotite and shows heterogeneous compositions from 15 to 35 mol % pistacite content, but regular zoning has not

been observed. Finally, epidotes from the muscovite-bearing gneiss have allanite cores and present a slight zoning from ca 20 mol % pistacite contents in inner regions to 14 % at the rims.

A.5. P-T conditions and paths

Variably deformed and retrogressed garnet-biotite migmatitic rocks similar to those described here occur elsewhere in the Cabo Ortegal Complex (forming decametre-scale bodies in the Bacariza Formation, most of the Chimparra gneiss unit and equivalent rocks in the Carreiro zone of tectonic movement). Using conventional thermobarometry, minimum peak P-T conditions for these rocks have been estimated at ca. 800 °C and 1.7 GPa, while P-T estimates for the muscovite-bearing gneiss of the Bacariza formation yielded ca. 795 °C, 1.8 GPa (Fernández Rodríguez, 1997; Puelles et al., 2005a).

In this study, we have refined peak P-T conditions using selected compositions of the following matrix mineral assemblages: (1) Grt+Bt+Ms+Ep+Pl+Ky+Qtz and Grt+Ms+Ep+Pl+Kfs+Mt+Qtz in the muscovite-bearing gneiss (samples CO35 and T4, respectively); (2) Grt+Cpx+Pargasitic Amp+Pl+Ep+Qtz in the felsic gneisses (sample CO49), and (3) Grt+Bt+Ep+Pl+Pargasitic Amp+Qtz in the biotite migmatitic gneisses (sample CO5b). The assemblages used for P-T calculations are shown in the AKF, AFN and ACF phase diagrams of Figure a.14, calculated using the CSpace software (Torres-Roldán et al., 2000). These diagrams are projected from coexisting phases and appropriate exchange vectors, which allow condensation of the composition space. Mica-rich samples are plotted in the AKF diagram (Figure a.14a, a.14b and a.14c, for samples CO5b, CO35 and T4 respectively), whereas samples CO07 and CO49 are plotted in the AFN and ACF diagrams respectively (Figure a.14d and e). The ACF projection for the felsic gneiss CO49 shows that clinopyroxene is paragenetic with peak amphibole + garnet + epidote, indicating eclogite to high-pressure granulite facies, while the presence of muscovite in the projections for samples T4 and CO35 would indicate eclogite-facies conditions.

Retrograde conditions in the migmatitic rocks were calculated using the composition of secondary phases for the following assemblages: Grt+Bt+Ms+Pl+Qtz and Grt+Ms+Bt+Ep+Pl+Kfs+Ilm+Qtz (muscovite migmatite samples CO35 and T4, respectively), and Amp+Grt+Bi+Pl+Qtz (biotite migmatite sample CO5b). Initial retrogression under high grade conditions in the mafic granulites is represented by the assemblage Grt+Amp+Ep+Pl+Qtz of porphyroclasts in the mafic tectonites of the eastern shear band, while subsequent dynamic retrogression is represented by the fine grained matrix assemblage Grt+Amp+Pl+Ep+Qtz.

A.5.a. Average P-T calculations

P-T conditions were calculated using the average P-T method (Powell and Holland, 1994) and software THERMOCALC, version 3.33 with the dataset 5.5 (Holland and Powell, 1998). The calculations were performed for the lower variance mineral assemblages containing garnet, because these produce a larger number of linearly independent reactions. An H_2O-fluid was included in all assemblages. The activities and activity uncertainties of each end-member included in the calculations were obtained with the program AX (Holland and Powell, unpublished). In order to reduce the error, phase components with low activities (e.g.: spss in garnet, gl in amphibole, cel or fcel in muscovite, etc; end-member abbreviations after Holland and Powell, 1998) were occasionally excluded from the calculations (cf. Powell and Holland, 1994). The results of calculations are given below and in Figure a.15 including the correlations (referred to corr in the following paragraphs), sigfit values (sigfit), and uncertainty ellipses (calculated following Powell and Holland, 1994).

The calculated peak conditions are 774 ± 49 °C , 16.9 ± 1.5 GPa (corr: 0.89, sigfit: 1.19) and 770 ± 50 °C , 17.4 ± 1.9 GPa (corr: 0.82, sigfit: 1.41) in the muscovite-bearing gneiss (CO35) and felsic gneiss (CO49), respectively; and 814 ± 54 °C , 13.5 ± 1.5 GPa (corr: 0.91, sigfit: 1.09) in the biotitic samples (CO5b). It was not possible to calculate the peak conditions using this method for the antiperthite- and muscovite-bearing migmatites T4, probably due to equilibrium problems. However, the peak conditions for this sample were estimated using a pseudosection approach (see below).

These results suggest that all the rocks underwent similar peak P-T conditions ranging from ca. 760 to 810 °C and 1.5 to 1.8 GPa. The lower peak pressure conditions for sample CO5b reflect adjustments during initial stages of an essentially adiabatic decompression of the rock. These conditions are above the wet-saturated solidus of granite composition and would account for wet partial melting processes experienced by these rocks during subduction.

Conditions for initial retrogression of the mafic granulites in the bounding shear zone (sample CO07) are estimated at 816 ± 49 °C , 16.2 ± 1.5 GPa (corr: 0.85, sigfit: 0.82), while the calculated conditions for the shear zone are 760 ± 49 °C, 14.5 ± 1.5 GPa (corr: 0.85, sigfit: 0.69), suggesting that uplift processes began shortly after reaching the maximum depth. The calculated retrograde conditions are 661 ± 47 °C , 7.6 ± 1.3 GPa (corr: 0.67, sigfit: 0.96) in the biotite migmatite sample CO5b and of 666 ± 32 °C , 8.7 ± 1.0 GPa (corr: 0.79, sigfit: 0.58) and 656 ± 25 °C , 9.2 ± 0.7 GPa (corr: 0.74, sigfit: 0.93) in the muscovite migmatite samples CO35 and T4, respectively. These P-T conditions reflect a considerable drop in pressure, whereas the temperature decreased to a lesser extent. Peak conditions are within the eclogite-facies or

eclogite-high-pressure granulite transition, and retrogression occurred within the amphibolite-facies (Figure a.15). These trajectories are characteristic of a rapid uplift (Puelles et al., 2005a, Ábalos et al., 2003).

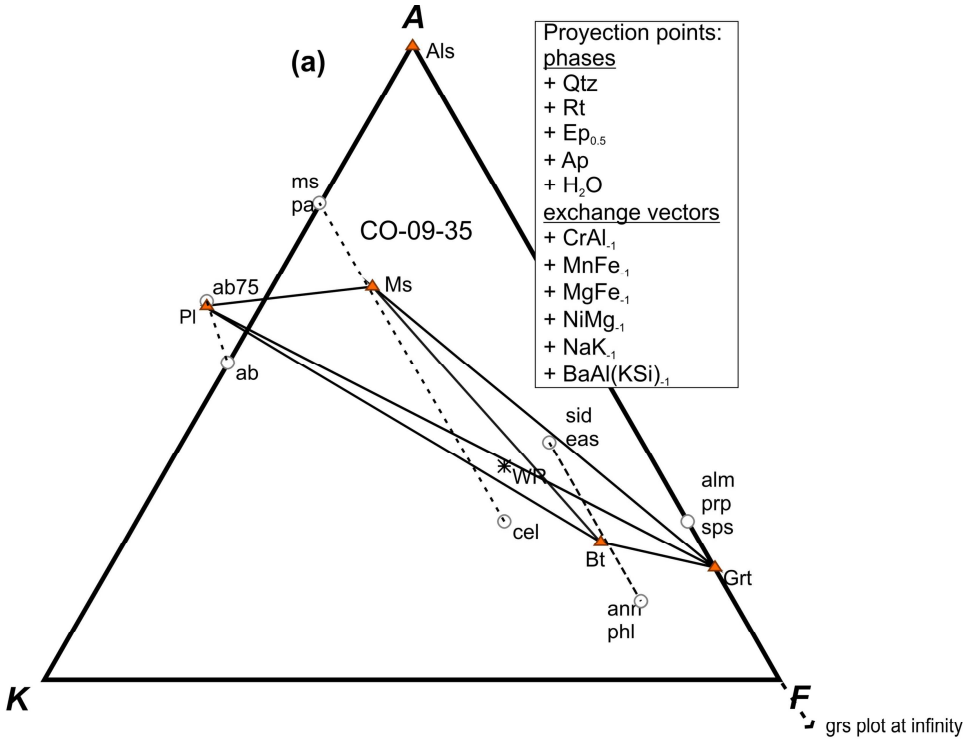

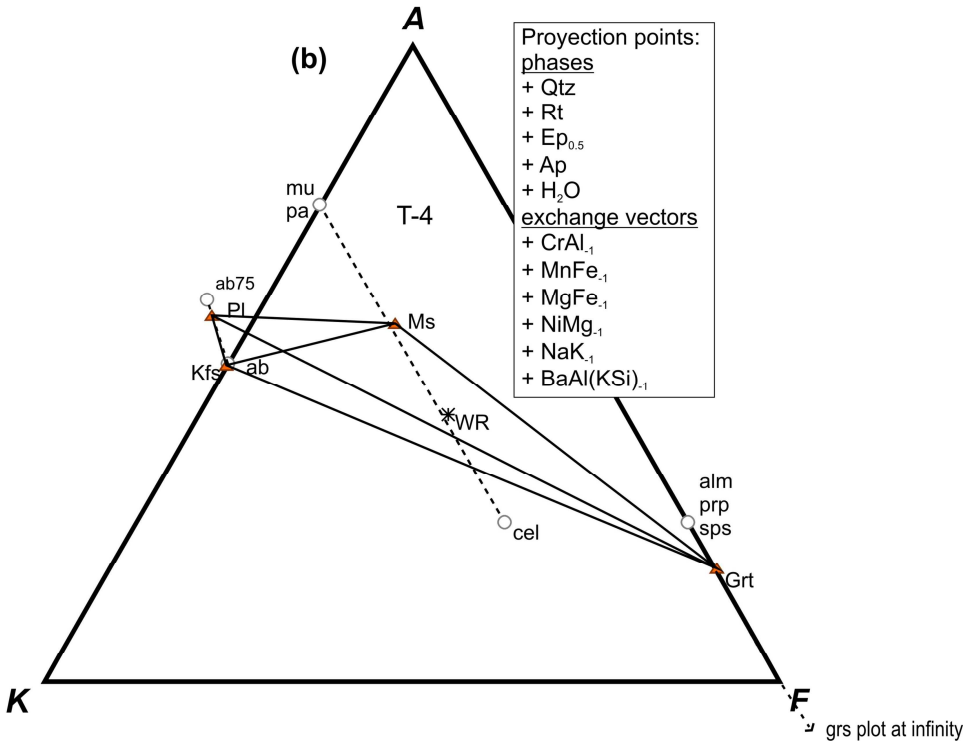

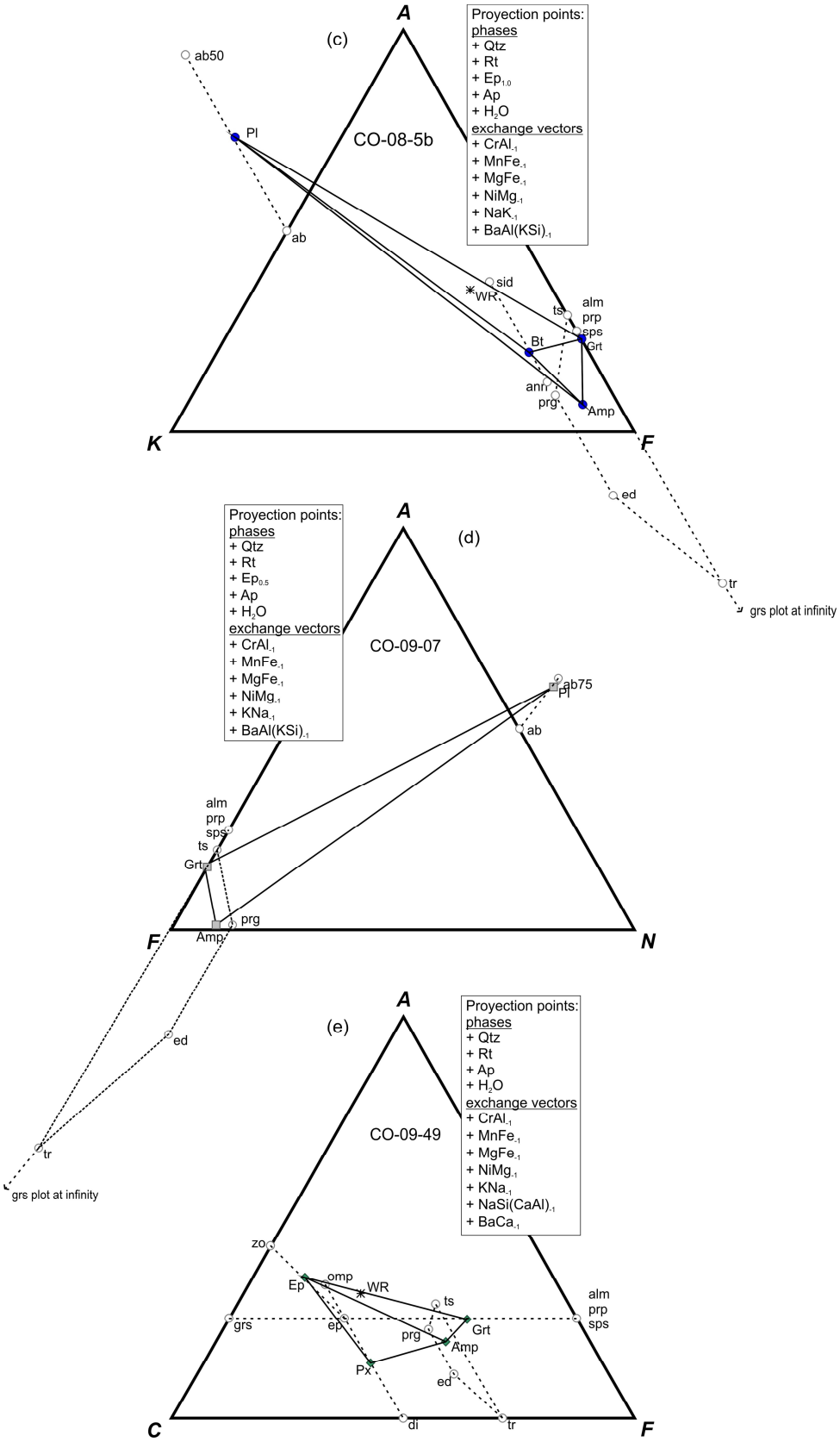

Figure a.14. (a), (b) and **(c)** AKF, **(d)** AFN and **(e)** ACF phase diagrams showing peak assemblages of representative samples of the different studied rocks, and for mylonitic (post-peak) assemblage of sample CO07 (d). End-members of the solid solutions on interest are indicated by empty circles joined by dashed lines. Diagrams calculated using CSpace software (Torres-Roldán et al., 2000).

A.5.b. Isochemical P-T projections

Two isochemical P-T projections (pseudosections) were calculated in the NCKFMASHTO system using THERMOCALC 3.33 software and 5.5 dataset (Holland and Powell, 1998). A fluid phase, assumed to be pure H_2O, is assumed to be in excess. The MnO component is neglected due to its very low concentration in the rocks studied. The solution models used for garnet, silicate melt and biotite are from White et al. (2007), for epidote from Holland and Powell (1998), for plagioclase and potassium feldspar from Holland and Powell (2003), for muscovite from Coggon and Holland, (2002) and for ilmenite from White et al. (2000).

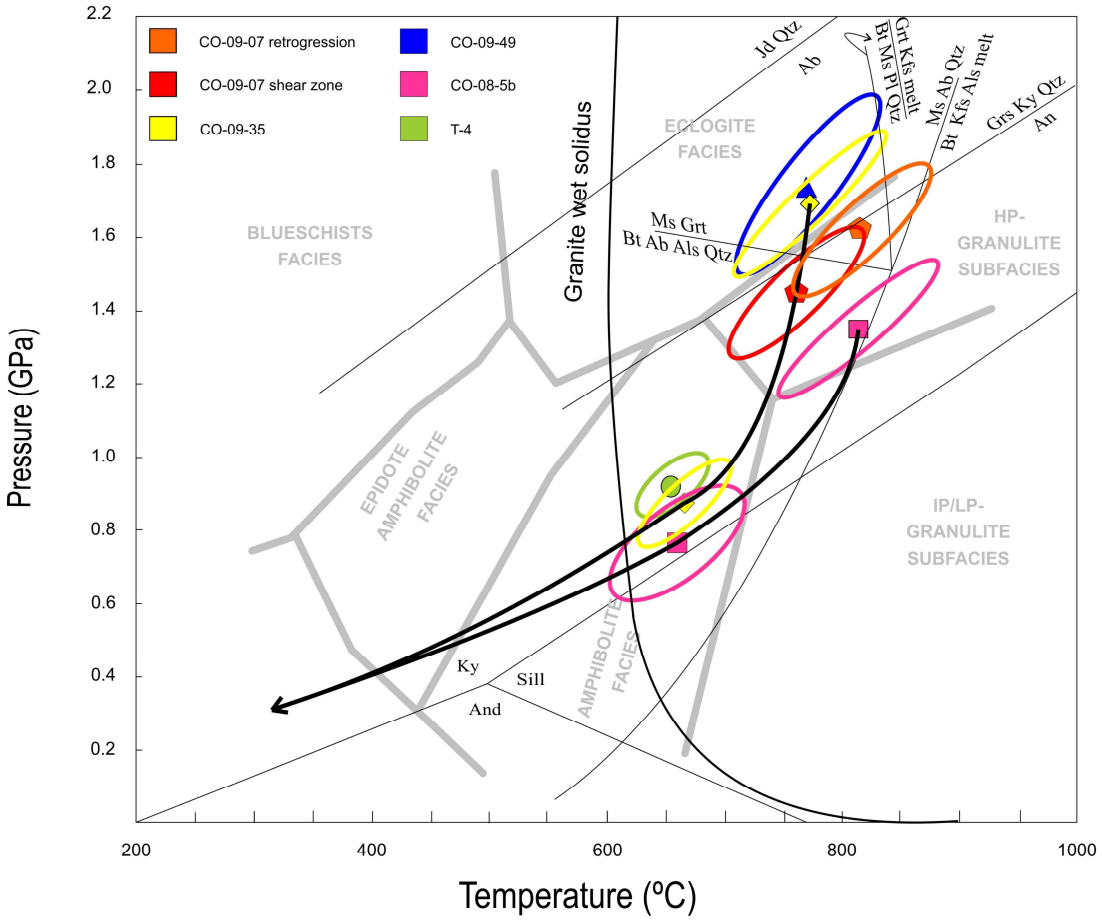

Figure a.15. P-T diagram showing paths for studied samples calculated with THERMOCALC (average P-T method). Metamorphic facies are from Oh and Liou (1998). Aluminosilicate stability fields are from Holdaway (1971). Ab-out and An-out reactions are from Berman (1988). Reactions involving muscovite are after Thompson (1982), Grant (1985), and Vielzeuf and Holloway (1988). The wet granite solidus is after Thompson (1992).

Isochemical P-T projections were calculated for muscovite-bearing gneiss samples T4 and CO35 (Figure a.16a and b). This approach allows investigating the stability of muscovite at high temperature in these rocks. The results are consistent with the observed mineral assemblages and with the peak conditions calculated by the average P-T method (see above). Also, and has been indicated by a number of authors (e.g., Thompson, 1982; Vielzeuf and Holloway, 1988),

biotite disappears at lower T than muscovite, in agreement with a high-pressure gradient metamorphic evolution. This feature is particularly obvious in the muscovite-bearing gneiss lacking peak biotite (T4), even at moderate temperatures (600 °C , Figure a.16a). In the muscovite-bearing gneiss bearing matrix biotite (CO35), the biotite-free area formed at pressures above 1.7 GPa and 750 °C (Figure a.16b). The lack of biotite in these areas is due to different bulk rock composition (richer in Al_2O_3, FeO and MgO and poorer in SiO_2).

A pseudosection for the K-feldspar-bearing muscovite migmatite sample T4 (Figure a.16a), for which it was not possible to infer P-T values using the average P-T method (see above), was constructed in order to calculate peak metamorphic conditions. Isopleths of grossular component in garnet and paragonite component in muscovite have been drawn in order to establish the peak conditions, resulting in 790 °C and 1.8 GPa (black dot in Figure a.17c). These conditions are in agreement with estimations for other samples.

Isopleths of mineral composition and abundance are presented in Figure a.17. The melting process is predicted to proceed together with consumption of plagioclase within a very restricted area around 600-650 °C and 1.2-1.5 GPa (Figure a.17b). Moreover, melt mode isopleths show rapid increase in melt during beginning of melting and at higher temperature during consumption of muscovite along the prograde path. At peak conditions the rocks suffer approximately 30% of partial melting. The molar abundance of garnet (Figure 17a) shows growth during the prograde path, in parallel to melt production. The predicted Ca decrease in garnet during the retrogression is in agreement with the observed lower grossular content at the rim of the garnet grains analysed (Figures a.5, a.6 and a.7).

(a) **NCKFMASHTO (+ H_2O)**

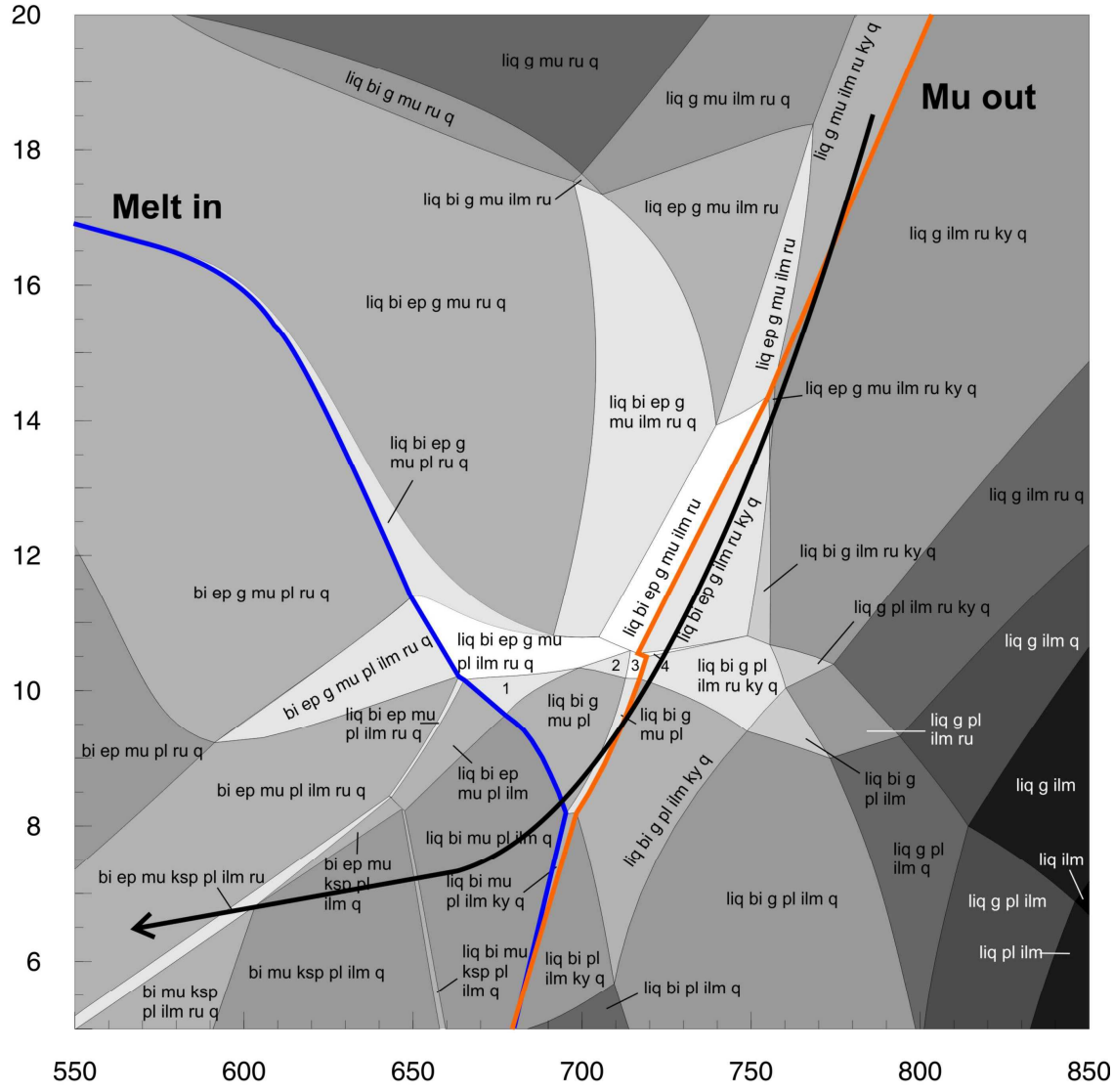

1 liq bi ep g mu pl ilm q
2 liq bi g mu pl ilm ru q
3 liq bi g mu pl ilm ru ky q
4 liq bi ep g pl ilm ru ky q

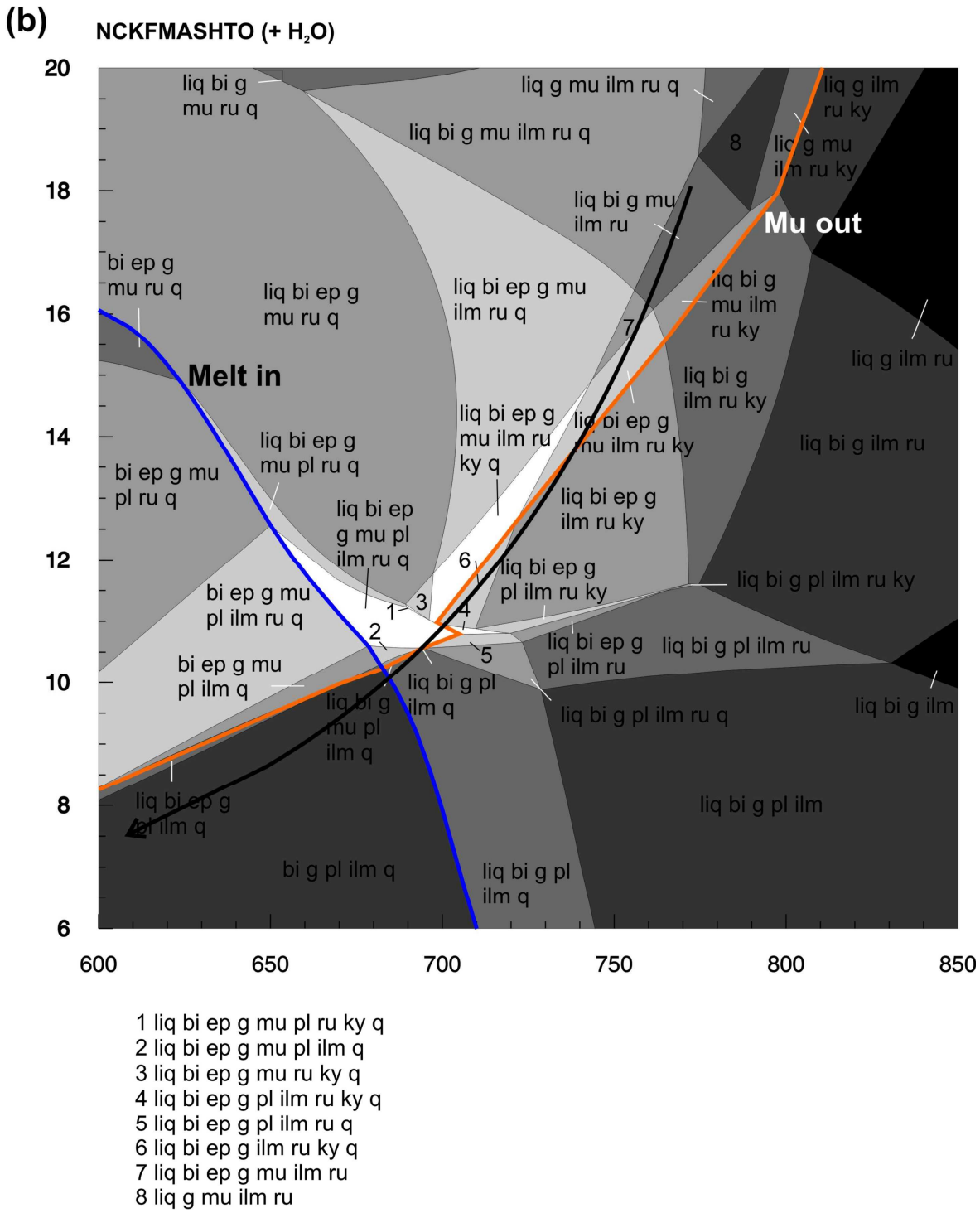

1 liq bi ep g mu pl ru ky q
2 liq bi ep g mu pl ilm q
3 liq bi ep g mu ru ky q
4 liq bi ep g pl ilm ru ky q
5 liq bi ep g pl ilm ru q
6 liq bi ep g ilm ru ky q
7 liq bi ep g mu ilm ru
8 liq g mu ilm ru

Figure a.16. Isochemical P-T equilibrium phase diagram for samples **(a)** T4 (muscovite migmatite lacking matrix biotite) and **(b)** CO35 (biotite-bearing muscovite migmatite) calculated with THERMOCALC in the system NCKFMASHTO. Mineral codes are liq (melt), bi (biotite), ep (epidote), g (garnet), mu (muscovite), pl (plagioclase), ru (rutile), ky (kyanite), q (quartz), ilm (ilmenite) and ksp (potassium feldspar). Whole rock compositions are: SiO_2=78.33, TiO_2=0.39, Al_2O_3=8.43, FeO=4.20, MgO=1.79, CaO=3.00, Na_2O=2.10, K_2O=1.75, O=0.25 and SiO_2=62.73, TiO_2=0.86, Al_2O_3=12.28, FeO=8.17, MgO=5.13, CaO=5.34, Na_2O=3.29, K_2O=2.21, O=0.49; (percent molar units) for samples T4 and CO35, respectively. Colour code: white 2-variant, with increasing darker shades of grey as variance increases.

(a)

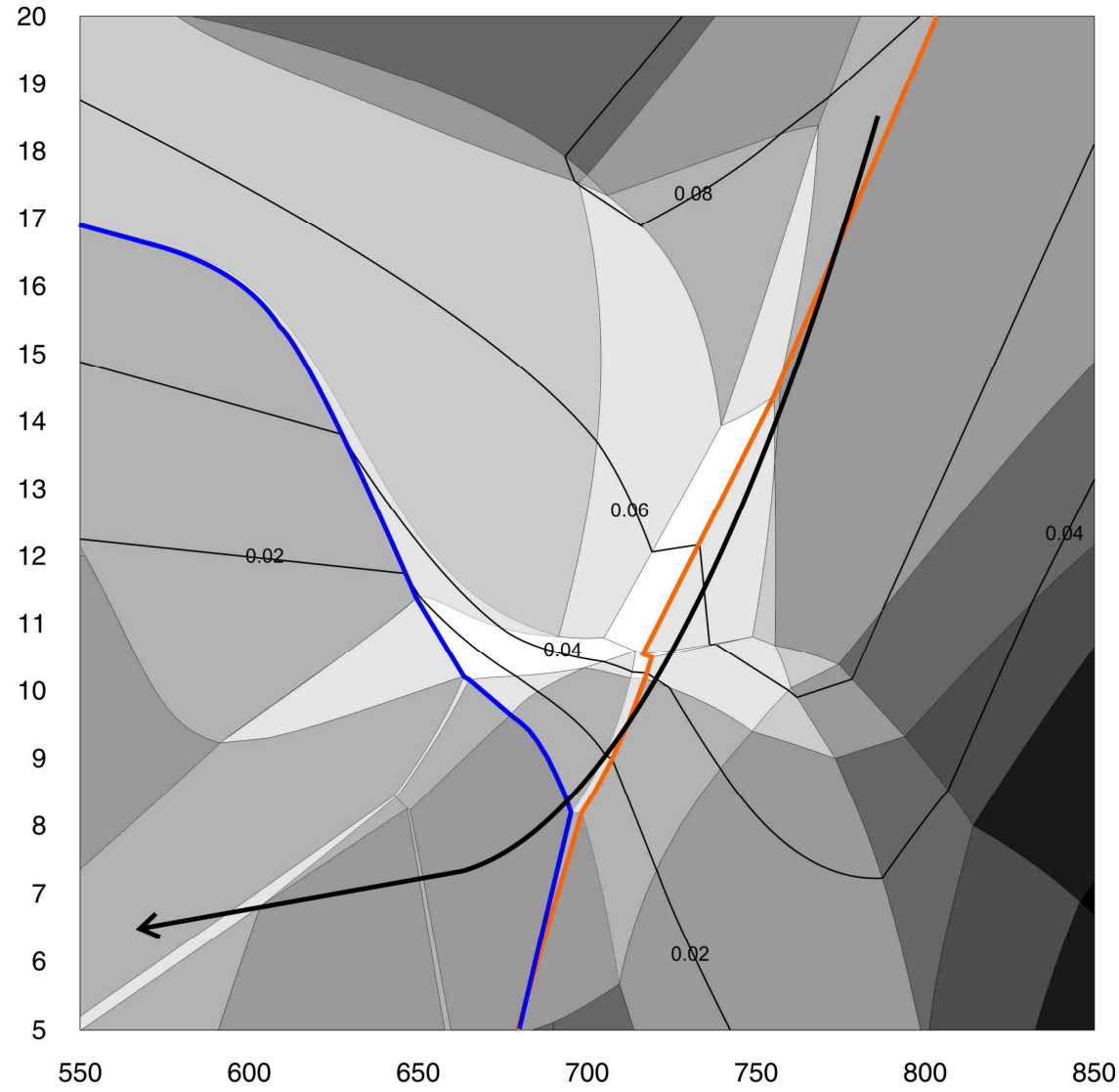
20
19
18
17
16
15
14
13
12
11
10
9
8
7
6
5
550
600
650
700
750
800
850
0.08
0.06
0.04
0.02
0.04
0.02

(b)

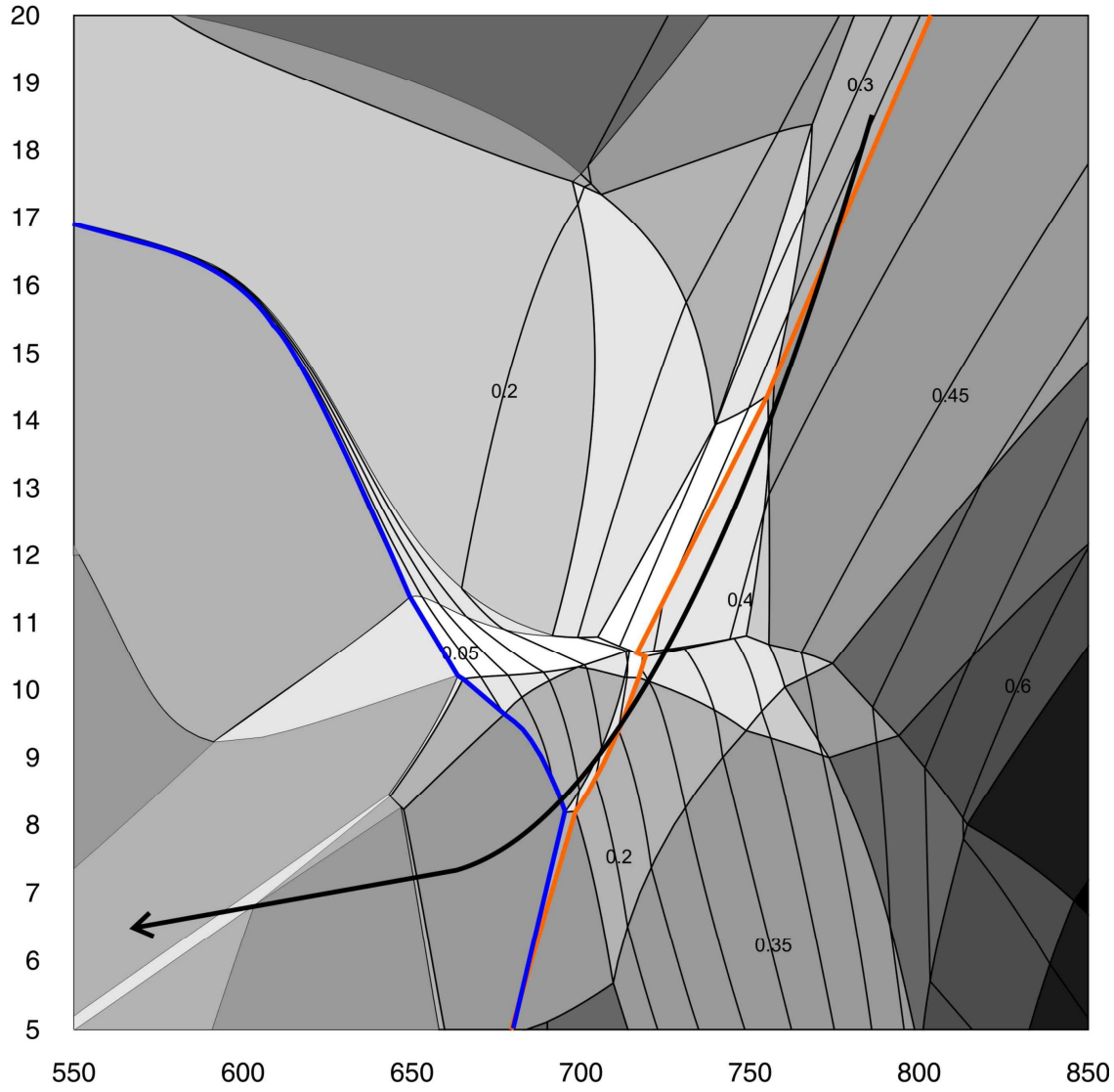
20
19
18
17
16
15
14
13
12
11
10
9
8
7
6
5
550
600
650
700
750
800
850
0.3
0.2
0.45
0.4
0.05
0.6
0.2
0.35

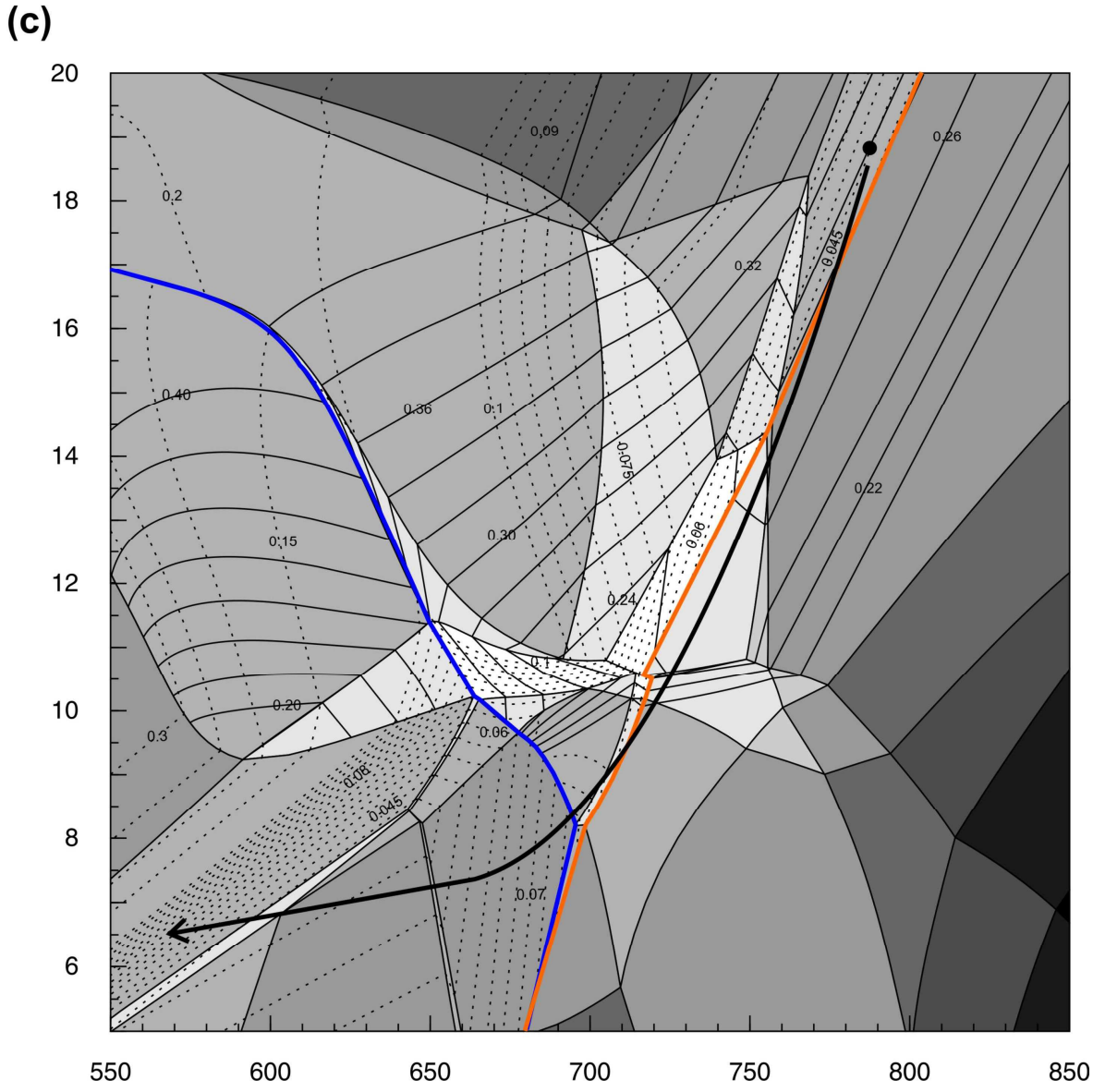

Figure a.17. Mineral abundance and composition isopleths for sample T4 calculated with THERMOCALC (see Figure 21 for mineral assemblages and colour codes). **(a)** Molar proportion of garnet. **(b)** Molar proportion of melt. **(c)** Mole fraction of grossular in garnet (continuous line), and of paragonite in white mica (dashed line). The dot in (c) shows the peak conditions for sample T4.

A.6. Discussion

A.6.a. On the breakdown of muscovite and garnet

The absence of primary muscovite in Qtz-bearing rocks is a critical parameter in the current definition of granulites according to the proposals by the IUGS (Coutinho et al., 2007). The presence of this mineral at the peak of the metamorphism of the studied muscovite-bearing migmatites is however in agreement with the calculated P-T conditions of 800 °C and 1.8 GPa

typical of high-T eclogite-facies conditions. During subsequent decompression-dominated retrogression, muscovite breakdown to biotite took place. These observations are in accordance with experimental evidence (e.g., Vielzeuf and Holloway, 1988, NCK(FM)ASH system; Figure a.15). In fact, according to Vielzeuf and Holloway's experiments, the breakdown of muscovite would have started shortly after the peak conditions were reached. These inferences are confirmed by the pseudosections calculated for the two muscovite-bearing samples, although in the case of the antiperthite- and K-feldspar-bearing sample T4 the muscovite breakdown would have taken place at lower pressure conditions (0.7 GPa at 600-650 °C).

On the other hand, garnet breakdown, which is also observed in the muscovite-bearing samples, in particular in T4 , attests to temperatures of formation higher than those inferred for the muscovite-bearing rocks, which is in agreement with experimental evidence by Vielzeuf and Holloway (1988) for lithologies not very different from those here studied (semipelitic Cariño gneisses of the Cabo Ortegal Complex). The studied rocks would thus have crossed the garnet decomposition reaction located at higher temperatures in the P-T space during their retrogressive evolution after reaching the thermal, and perhaps also the isobaric, peak. Yet, it is not possible to calculate these thermal peak conditions because almost all of the original garnet reacted to form the muscovite-biotite-plagioclase aggregates.

A.6.b. On the tectonic model

The elevated pressures recorded by the studied rocks indicate depths of about 60-70 km in a subduction tectonic setting. The stable peak associations would have formed at these depths, where the syn-metamorphic principal foliation and lineation would have formed.

The near-isothermal PT decompression path observed reflects active tectonic exhumation mechanisms precluding heating during depressurization. Once the high-pressure migmatites reached the maximum depth, they were amalgamated in a subduction conduit, underplating the ultramafic massifs and being subsequently underplated by other units of the complex through discrete shear zones (Figure a.18). During the underthrusting processes, the eclogites were emplaced below the high-pressure granulite unit. The dehydration of the subducted materials produces the free water that could saturate the slab interface. It is also likely that the eclogites released water during eclogitization. These fluid fluxes thereby contributed to the retrograde breakdown reactions of muscovite and garnet.

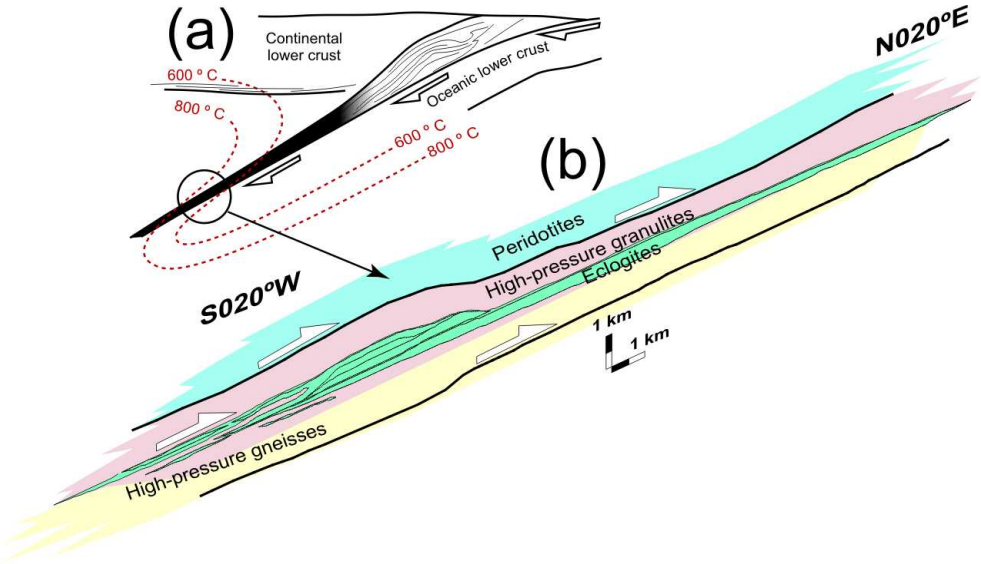

Figure a.18. (a) Model of a moderately dipping subduction zone including the traces of the 600 °C and 800 °C isotherms and of shear surfaces in the subduction channel (shaded) after Gerya et al. (2008). **(b)** Reconstructed section of the upper allochthon of Cabo Ortegal along a projection plane parallel to the regional high-pressure lineation and normal to the foliation. Modified after Puelles et al. (2009).

The observations described above, as well as the pressure and temperature conditions calculated for the evolution of HP acid migmatite unit are in agreement with the interpretations proposed by Ábalos et al. (2003) and Puelles et al. (2005) about amalgamation and subsequent exhumation of metamorphic nappes in a "subduction channel" setting (Figure a.18).

A.7. Conclusions

Thermobarometric calculations, mineral chemistry and petrological data of the high-pressure migmatitic gneiss of the Bacariza Formation granulites of the Cabo Ortegal complex (north-west Iberian Massif) evidence an important decompression path during the exhumation. The breakdown of garnet and muscovite confirm the decompression evolution for these units. According to the mineralogical assemblages the migmatitic gneiss can be divided in three groups of rocks (muscovite-bearing migmatites, biotite migmatitic gneisses and felsic gneisses). The peak conditions for these rocks determined using the average P-T method were attained at ca. 1.8 GPa (i.e. 60 km) and 790 °C while retrogression occurred at ca. 0.8 GPa and 650 °C. Isochemical P-T projections for muscovite-bearing migmatites confirm the decompression path determined with the average P-T calculations and allow concluding that the rocks underwent a partial melting event (i.e. 30 % of molar proportion).

The migmatitic gneiss were accreted to the mantle wedge and exhumed during the active tectonic simultaneously with the other units. These results, as well as the pressure and

temperature conditions calculated for the evolution of HP acid migmatite unit are in agreement with previous pretrologic-tectonic interpretations for the Cabo Ortegal complex.

A. References

Ábalos, B., Azcárraga, J., Gil Ibarguchi, J.I., Mendia, M.S. and Santos Zalduegui, J.F., 1996. Flow stress, strain rate and effective viscosity evaluation in a high-pressure nappe (Cabo Ortegal, Spain). *J. metamorphic Geol.,* 14, 227-248.

Ábalos, B., Puelles, P. and Gil Ibarguchi, J.I., 2003. Structural assemblage of high-pressure and crustal rocks in a subduction channel (Cabo Ortegal, NW Spain). Tectonics, 22 (2), 1-21.

Ashwall, L.D., Morgan, P. and Hoisch, T.D., 1992. Tectonics and heat sources for granulite metamorphism of supracrustal-bearing terranes. *Precambrian Research*, 55, 525-538.

Berman, R.G., 1988. Internally-consistent thermodynamic data for minerals in the system K_2O-Na_2O-CaO-MgO-FeO-Fe_2O_3-$Al2O_3$-SiO_2-TiO_2-H_2O-CO_2. *Journal of Petrology*, 29, 445-522.

Bohlen, S.R., 1991. On the formation of granulites. *J. metamorphic Geol.*, 9, 223- 229.

Chemenda, A.I., Mattauer, M., Malavieille, J.and Bokun, A.N., 1995. A mechanism for syn-collisional rock exhumation and associated normal faulting: results from physical modelling. *Earth Planet. Sci. Lett.*, 132, 225-232.

Chemenda, A.I., Mattauer M. and Bokun, A.N., 1996. Continental subduction and a mechanism for exhumation of high-pressure metamorphic rocks: New modelling and field data from Oman. *Earth and Planet. Sci. Letters*, 143, 173-182.

Chemenda, A.I., Burg, J.P. and Mattauer, M., 2000. Evolutionary model of the Himalaya-Tibet system: geopoem based on new modelling, geological and geophysical data. *Earth Planet. Sci. Lett.*, 174, 397-409.

Coggon, R. and Holland, T.J.B., 2002. Mixing properties of phengitic micas and revised garnet-phengite thermobarometers. *J. metamorphic Geol.*, 20, 683-696.

Coutinho, J., Kräutner, H., Sassi, F., Schmid, R. and Sen, S. 2007. Amphibolite and granulite. In: Fettes, D. and Desmons, J. (eds.). Metamorphic Rocks - A Classification and Glossary of Terms. *Cambridge University Press*, 51-57.

Dallmeyer, R.D., Martínez Catalán, J.R., Arenas, R., Gil Ibarguchi, J.I., Gutiérrez Alonso, G., Farias, P., Bastida, F., and Aller, J., 1997. Diachronous Variscan tectonothermal activity in the NW Iberian Massif: evidence form $^{40}Ar/^{39}Ar$ dating of regional fabrics. *Tectonophysics*, 277, 307-337.

de Paoli, M. C., Clarke, G. L., Klepeis, K. A., Allibone, A. H. and Turnbull, I. M., 2009. The Eclogite-Granulite Transition: Mafic and Intermediate Assemblages at Breaksea Sound, New Zealand. *Journal of Petrology*, 50, 2307-2343.

Drury, S.A., 1980. The geochemistry of the high-pressure gneisses from Cabo Ortegal (NW Spain): residues of deep anatexis. *Geologie on Mijnbouw*, 59, 61-64.

Ellis, D.J., 1987. Origin and evolution of granulites in normal and thickened crust. *Geology*, 15, 167-170.

Essene, E.J. and Fyfe, W.S., 1967. Omphacite in Californian metamorphic rocks. *Contrib. Mineral. Petrol.,* 15, 1-23.

Fernández Rodríguez, F.J. 1997. Estructuras desarrolladas en gneises bajo condiciones de alta P y T (gneises de Chímparra, Cabo Ortegal). *Nova Terra* 13, 249 p.

Fernández-Suárez, J., Arenas, R., Abati, J., Martínez Catalán, J.R., Whitehouse, M.J. and Jeffries, T.E. 2007. U-Pb chronometry of polymetamorphic high-pressure granulites: An example from the

allochthonous terranes of the NW Iberian Variscan belt. In: Hatcher, R.D. Jr., Carlson, M.P., McBride, J.H. and Martínez Catalán, J.R. (Eds.), 4-D Framework of Continental Crust. *Geological Society of America Memoir*, 200, 469-488.

Galán, G. and Marcos, A., 1997. Geochemical evolution of the high-pressure mafic granulites from the Bacariza formation (Cabo Ortegal complex, NW Spain): an example of a heterogeneous lower crust. *Geologisches Rundschau*, 86, 539-555.

Galán, G. and Marcos, A., 2000. The metamorphic evolution of the high-pressure mafic granulites of the Bacariza Formation (Cabo Ortegal Complex, Hercynian belt, NW Spain). *Lithos*, 54, 139-171.

García-Casco, A., 2007. Magmatic paragonite in trondhjemites from the Sierra del Convento mélange, Cuba. *American Mineralogist,* 92, 1232-1237.

García-Casco, A., Rodriguez Vega, A., Cárdenas Párraga, J., Iturralde-Vinent, M., Lázaro, C., Blanco-Quintero, I., Rojas-Agramonte, Y., Kröner, A., Nuñez Cambra, K., Millán, G., Torres-Roldán, R. and Carrasquilla, S., 2009. A new jadeitite jade locality (Sierra del Convento, Cuba): First report and some petrological and archaeological implications. *Contrib. Mineral. Petrol.*, 158, 1-26.

Gerya, T.V., Perchuk, L.L. and Burg J. P., 2008. Transient hot channels: Perpetrating and regurgitating ultrahigh-pressure, high-temperature crust-mantle associations in collision belts. In: T.V. Gerya, J.A.D. Connolly and L.L. Perchuk (eds.). "Rocks Generated under Extreme Pressure and Temperature Conditions: Mechanisms, Concepts, Models". *Lithos*, 103, 236-256.

Gerya, T.V., Stöckhert, B. and Perchuk, A.L., 2002. Exhumation of high-pressure metamorphic rocks in a subduction channel: a numerical simulation. *Tectonics*, 21(6), 1056.

Gil Ibarguchi, J.I., Mendía, M., Girardeau, J. and Peucat, J.J., 1990. Petrology of eclogites and clinopyroxene-garnet metabasites from the Cabo Ortegal Complex (northwestern Spain). *Lithos*, 25, 133-162.

Gil Ibarguchi, J. I., Ábalos, B., Azcárraga, J., Mendia, M.S. and Puelles, P., 2000., A petrological and structural excursion through the high-grade/high-pressure allochthonous units of the Cabo Ortegal Complex (NW Spain), Basement Tectonics 15, Mid-Conference Field Trip Guide, Int. Basement Tectonics Assoc., La Coruña, Spain.

Girardeau, J., Gil Ibarguchi, J.I. and Ben Jamaa, N. 1989. Evidence for a heterogeneous upper mantle in the Cabo Ortegal Complex, Spain. *Science*, 245, 1231-1233.

Grant, J.A., 1985. Phase equilibria in partial melting of pelitic rocks. In: Ashworth, J.R. (ed.). Migmatites. *Blackie, Glasgow*, 96-144.

Gravestock, P.J., 1992. The chemical causes of uppermost mantle heterogeneities. *Ph.D. Thesis, The Open University (UK)*, 299 p.

Harley, S.L., 1989. The origins of granulites: a metamorphic perspective. *Geological Magazine*, 126, 215-247.

Holdaway, M.J., 1971. Stability of andalusite and the aluminium silicate phase diagram. *American Journal of Science*, 271, 97-131.

Holland, T.J.B., and Powell, R., 1998. An internally consistent thermodynamic data set for phases of petrological interest. *J. metamorphic Geol.*, 16, 309-343.

Holland, T.J.B and Powell, R., 2003. Activity-composition relations for phases in petrological calculations: an asymmetric multicomponent formulation. *Contrib. Mineral. Petrol.*, 145, 492-501.

Kretz, R., 1983. Symbols for rock-forming minerals. *American Mineralogist*, 68, 277-279.

Leake, B.E., Woolley, A.R., Arps, C.E.S., Birch, W.D., Gilbert, M.C., Grice, J.D., Hawthorne, F.C., Kato, A., Kisch, H.J., Krivovichev, V.G., Linthout, K., Laird, J., Mandarino, J.A., Maresch, W.V., Nickel, E.H., Rock, N.M.S., Schumacher, J.C., Smith, D.C., Stephenson, N.C.N., Ungaretti, L., Whittaker, E.J.W. and Touzhi, G., 1997. Nomenclature of amphiboles: Report of the Subcommittee on Amphiboles of the International Mineralogical Association, Commission on New Minerals and Mineral Names. *American Mineralogist,* 82, 1019-1037.

Martínez-Catalán, J.R., Arenas, R., Díaz-García, F. and Abati, J., 1997. Variscan accretionary complex of northwest Iberia: terrane correlation and succession of tectonothermal events. *Geology*, 25, 1103-1106.

Matte, Ph., 1986. Tectonics and plate tectonics model for the Variscan Belt of Europe. *Tectonophysics*, 126, 329-374.

Matte, Ph., 1998. Continental subduction and exhumation of HP rocks in Paleozoic orogenic belts: Uralides and Variscides. *GFF*, 120, 209-222.

Matte, Ph., 2002. Variscides between the Appalachians and the Urals: similarities and differences between Paleozoic subduction and collision belts. In: Martínez Catalán, J.R., Hatcher, R.D.Jr., Arenas, R., and Díaz García, F. (eds.). Variscan-Appalachian dynamics: the building of the Late Paleozoic basement. *Geological Society of America*, Special Paper 364, 239-251.

Matte, Ph., and Burg, J.P., 1981. Sutures, thrusts and nappes in the Variscan Arc of western Europe: Plate tectonic implications. In: K. R. McKlay and N. J. Price (eds.).Thrust and Nappe Tectonics. *Spec. Publ. Geol. Soc. London*, 9, 353 -358.

Morimoto, N., Fabries, J., Ferguson, A.K., Ginzburg, I.V., Ross, M., Seifeit, F.A., Zussman, J., Aoki, K. and Gottardi, G., 1988. Nomenclature of pyroxenes. *American Mineralogist,* 73, 1123-1133

O'Brien, P.J., 1993. Partially retrograded eclogites of the Manchberg Massif, Germany: records of a multi-stage variscan uplift history in the Bohemian Massif. *J. metamorphic Geol.*, 11, 241-260.

O'Brien, P.J., 1997. Garnet zoning and reaction textures in overprinted eclogites, Bohemian Massif, European Variscides: a record of their thermal history during exhumation. *Lithos*, 41, 119-133.

O'Brien, P.J., 2001a. Subduction followed by collision: Alpine and Himalayan examples. *Physics of the Earth and Planetary Interiors*, 127, 277-291.

O'Brien, P.J., 2001b. High Pressure Granulites: Formation, Survival of HP-(U)HT Relics and Implications for Tectonics. *Geological Association of Canada-Mineralogical Association of Canada 2001 Joint Annual Meeting. Technical programme.*

O'Brien, P.J. and Rötzler, J., 2003. High-pressure granulites: formation, recovery of peak conditions and implications for tectonics. *Journal of Metamorphic Petrology*, 21, 3-20.

Oh, C.W. and Liou, J.G., 1998. A petrogenetic grid for eclogite and related facies under high-pressure metamorphism. *Island arc*, 7, 36-51.

Ordóñez Casado, B., Gebauer, D., Schäfer, H.J., Gil Ibarguchi, J.I. and Peucat, J.J. 2001. A single Devonian subduction event for the HP/HT metamorphism of the Cabo Ortegal complex within the Iberian Massif. *Tectonophysics* 332, 359-385.

Peucat, J.J., Bernard-Griffiths, J., Gil Ibarguchi, J.I., Dallmeyer, R.D., Menot, R.P., Cornichet, J. and Iglesias Ponce de León, M., 1990. Geochemical and geochronological cross section of the deep variscan

crust: the Cabo Ortegal high-pressure nappe (NW Spain). In: Ph. Matte (ed.): Terranes in the Variscan Belt of Europe and Circum-Atlantic Paleozoic Orogens. *Tectonophysics*, 177, 263-292.

Powell, R., and Holland, T.J.B., 1994. Optimal geothermometry and geobarometry: *American Mineralogist*, 79, 120-133.

Puelles, P., 2004. Deformación, metamorfismo y exhumación de las granulitas de alta presión de la Bacariza (Complejo de Cabo Ortegal, NO de España). *Nova terra* 23, 411 p.

Puelles, P., Ábalos, B. and Gil Ibarguchi, J.I., 2005a. Metamorphic evolution and thermobaric structure of the subduction-related Bacariza high-pressure granulite formation (Cabo Ortegal Complex, NW Spain). *Lithos*, 84, 125-149.

Puelles, P., Mulchrone, K., Ábalos, B. and Gil Ibarguchi, J.I., 2005b. Structural analysis of high-pressure shear zones (Bacariza Formation, Cabo Ortegal, NW Spain). *Journal of Structural Geology*, 27, 1046-1060.

Puelles, P., Ábalos, B. and Gil Ibarguchi, J.I., 2006. Ultramilonitas de apariencia fluidal, pseudotaquilitas o algo intermedio? (Formación Bacariza, Cabo Ortegal). *Geogaceta*, 40, 111-114.

Puelles, P., Ábalos, B. and Gil Ibarguchi, J.I., 2007. Microstructural evidence for thermal runaway and deep paleoseismic activity (Cabo Ortegal, NW Spain). *Terra Nova,* 19, 219-224.

Puelles, P., Ábalos, B. and Gil Ibarguchi, J.I., 2009. Transposed high-pressure granulite fabrics (Cabo Ortegal, NW Spain): implications on the scales of deformation localization. *Journal of Structural Geology,* 31, 776-790.

Ries, A. and Shackleton, R.M., 1971. Catazonal complexes of north-western Spain and north Portugal; remmants of a hercynian thrust plate. *Natural and Physical Science*, 234, 65-69.

Santos Zalduegui, J.F., Schärer, U. and Gil Ibarguchi, J.I., 1996. Isotope constraints on the age and origin of magmatism and metamorphism in the Malpica-Tuy Allochthon. *Chem. Geol.*, 121, 91-103.

Santos Zalduegui, J.F., Schärer, U., Gil Ibarguchi, J.I. and Girardeau, J., 2002. Genesis of pyroxenite-rich peridotite at Cabo Ortegal (NW Spain): geochemical and Pb-Sr-Nd isotope data. *Journal of Petrology*, 43, 17-43.

Thompson, A.B., 1982. Dehydratation melting of pelitic rocks and generation of H_2O-undersaturated granitic liquids. *American Journal of Science*, 282, 1567-1595

Thompson, A.B., 1983. Fluid-absent metamorphism. *J.Geol. Soc. London*, 140, 533-547.

Thompson, A.B., 1992. Metamorphism and fluids. In: Brown, G. C. (ed). Understanding the Earth: A new Synthesis, 222-248.

Torres-Roldán, R.L., García-Casco, A., and García-Sánchez, P.A., 2000, CSpace: An integrated workplace for the graphical and algebraic analysis of phase assemblages on 32-bit Wintel platforms: *Computers and Geosciences*, 26, 779-793.

Valverde-Vaquero, P. and Fernández, F.J., 1996. Edad de enfriamiento U-Pb en rutilos del Gneiss de Chímparra (Cabo Ortegal, NO de España). *Geogaceta*, 20, 475-478.

Vielzeuf, D. and Holloway, J.R., 1988. Experimental determination of the fluid-absent melting reaction in the pelitic system. *Contrib. Mineral. Petrol.,* 98, 257-276.

Vogel, D.E., 1967. Petrology of eclogite- and pirigarnite-bearing polymetamorphic rock complex at Cabo Ortegal, NW Spain. *Leidse Geologische Mededelingen*, 40, 121-213.

White, R.W., Powell, R., Holland, T.J.B. and Worley, B.A, 2000. The effect of TiO_2 and Fe_2O_3 on metapelitic assemblages at greenschist and amphibolite facies conditions: mineral equilibria calculations in the system K_2O-FeO-MgO-Al_2O_3-SiO_2-H_2O-TiO_2-Fe_2O_3. *J. metamorphic Geol.*, 18, 497-511.

White, R.W., Powell, R. and Holland, T.J.B., 2007. Progress relating to calculation of partial melting equilibria for metapelites. *J. metamorphic Geol.*, 25, 511-527.

A. Tables

Table a.1. Representative analyses of garnet (normalized to 12 O and 8 cations).

Rock	Muscovite Gneiss				Biotite Gneiss		Felsic Gneiss	Mylonite	
Sample	CO35		T4		CO5b		CO49	CO07	
Type	Peak	Retro	Peak	Retro	Peak	Retro	Peak	Static-retro	Shear-zone
SiO_2	37.87	37.03	38.16	38.29	39.49	38.49	38.86	38.26	38.21
TiO_2	0.06	0.04	0.04	0.02	0.01	0.00	0.07	0.05	0.01
Al_2O_3	21.18	20.76	21.50	21.45	22.09	21.40	21.34	21.50	21.47
FeO_{total}	24.51	30.23	25.85	26.78	24.99	30.18	22.51	21.87	23.77
MnO	0.62	3.27	0.71	0.72	0.77	1.65	0.53	1.73	2.09
MgO	5.36	2.78	3.29	3.21	6.65	4.85	5.49	5.81	5.05
NiO	0.00	0.00	0.00	0.00	0.00	0.00	0.00	0.00	0.00
CaO	9.90	5.70	10.99	10.53	7.81	4.63	11.87	10.55	9.53
Total	99.51	99.80	100.54	101.00	101.81	101.20	100.66	99.77	100.13
Si	2.95	2.96	2.98	2.98	3.00	3.00	2.98	2.96	2.97
Ti	0.00	0.00	0.00	0.00	0.00	0.00	0.00	0.00	0.00
Al	1.95	1.96	1.98	1.97	1.98	1.97	1.93	1.96	1.97
Fe^{3+}	0.14	0.11	0.06	0.06	0.03	0.03	0.11	0.12	0.10
Fe^{2+}	1.45	1.91	1.63	1.69	1.56	1.94	1.33	1.30	1.44
Mn	0.04	0.22	0.05	0.05	0.05	0.11	0.03	0.11	0.14
Mg	0.62	0.33	0.38	0.37	0.75	0.56	0.63	0.67	0.58
Ca	0.83	0.49	0.92	0.88	0.64	0.39	0.98	0.87	0.79
Mg#	0.30	0.15	0.19	0.18	0.33	0.23	0.32	0.34	0.29

Table a.2. Representative analyses of plagioclase (normalized to 8 O).

Rock	Muscovite Gneiss				Biotite Gneiss		Felsic Gneiss	Mylonite	
Sample	CO35		T4		CO5b		CO49	CO07	
Type	Peak	Retro	Peak	Retro	Peak	Retro	Peak	Static-retro	Shear-zone
SiO_2	61.87	57.69	63.97	61.77	61.40	58.89	63.49	62.05	62.13
TiO_2	0.00	0.01	0.00	0.00	0.00	0.01	0.02	0.01	0.00
Al_2O_3	23.61	26.40	22.68	24.45	25.79	26.37	23.00	23.19	23.51
FeO_{total}	0.00	0.12	0.08	0.05	0.04	0.10	0.03	0.15	0.08
MnO	0.00	0.00	0.00	0.00	0.03	0.00	0.05	0.00	0.01
MgO	0.00	0.01	0.00	0.01	0.00	0.02	0.00	0.00	0.00
NiO	0.00	0.01	0.00	0.00	0.00	0.00	0.00	0.03	0.03
CaO	5.26	8.63	4.13	6.06	7.23	8.29	4.26	4.88	5.03
BaO	0.00	0.00	0.00	0.00	0.03	0.00	0.00	0.00	0.04
Na_2O	8.76	6.61	9.18	8.08	7.51	6.94	9.45	8.76	8.69
K_2O	0.12	0.09	0.21	0.23	0.09	0.09	0.12	0.22	0.13
Total	99.63	99.56	100.25	100.65	102.12	100.71	100.42	99.29	99.66
Si	2.75	2.59	2.82	2.73	2.68	2.62	2.80	2.77	2.76
Ti	0.00	0.00	0.00	0.00	0.00	0.00	0.00	0.00	0.00
Al	1.24	1.40	1.18	1.27	1.33	1.38	1.19	1.22	1.23
Fe^{3+}	0.00	0.00	0.00	0.00	0.00	0.00	0.00	0.01	0.00
Mn	0.00	0.00	0.00	0.00	0.00	0.00	0.00	0.00	0.00
Ca	0.25	0.42	0.20	0.29	0.34	0.39	0.20	0.23	0.24
Ba	0.00	0.00	0.00	0.00	0.00	0.00	0.00	0.00	0.00
Na	0.76	0.58	0.78	0.69	0.63	0.60	0.81	0.76	0.75
K	0.01	0.01	0.01	0.01	0.01	0.01	0.01	0.01	0.01
X_{ab}	0.75	0.58	0.79	0.70	0.65	0.60	0.79	0.76	0.75

Table a.3. Representative analyses of amphibole (normalized to 22 O and 2 OH).

Rock	Biotite Gneiss		Felsic Gneiss	Mylonite	
Sample	CO5b		CO49	CO07	
Type	Peak	Retro	Peak	Static-retro	Shear-zone
SiO_2	40.63	42.62	41.51	41.32	41.84
TiO_2	0.86	0.75	1.59	1.19	1.13
Al_2O_3	17.02	15.39	13.95	14.96	14.64
FeO_{total}	15.79	15.62	14.22	12.81	13.06
MnO	0.13	0.11	0.03	0.18	0.25
MgO	9.24	10.01	10.83	11.26	11.07
NiO	0.00	0.01	0.03	0.04	0.00
CaO	10.64	10.83	11.39	10.72	10.92
BaO	0.05	0.04	0.04	0.04	0.04
Na_2O	1.52	1.44	1.72	1.80	1.63
K_2O	1.2	0.68	1.62	1.35	1.27
Total	97.98	97.50	96.94	95.67	95.84
Si	6.03	6.25	6.21	6.18	6.25
Ti	0.10	0.08	0.18	0.13	0.13
Al	2.98	2.66	2.46	2.64	2.58
Fe^{3+}	0.45	0.45	0.18	0.32	0.29
Fe^{2+}	1.51	1.47	1.60	1.28	1.34
Mn	0.02	0.01	0.00	0.02	0.03
Mg	2.04	2.19	2.42	2.51	2.46
Ca	1.69	1.70	1.83	1.72	1.75
Na	0.44	0.41	0.50	0.52	0.47
K	0.23	0.13	0.31	0.26	0.24
Mg#	0.58	0.60	0.60	0.66	0.65

Table a.4. Representative analyses of biotite (normalized to 20 O and 4 OH).

Rock	Muscovite Gneiss			Biotite Gneiss	
Sample	CO35		T4	CO5b	
Type	Peak	Retro	Retro	Peak	Retro
SiO_2	35.07	34.95	36.3	37.35	37.6
TiO_2	2.82	1.99	2.75	3.26	2.3
Al_2O_3	17.24	18.38	16.84	16.45	16.99
FeO_{total}	17.94	17.68	22.47	14.81	13.92
MnO	0.04	0.05	0.12	0.05	0.02
MgO	10.15	10.55	7.14	13.77	14.65
CaO	0.07	0.11	0.05	0.03	0.02
BaO	0.35	0.32	0.35	0.31	0.25
Na_2O	0.26	0.26	0.19	0.34	0.42
K_2O	9.32	9.17	9.55	9.19	9.14
Total	93.25	93.47	95.76	95.56	95.31
Si	5.45	5.40	5.60	5.55	5.56
Ti	0.33	0.23	0.32	0.36	0.26
Al	3.16	3.35	3.06	2.88	2.96
Fe^{2+}	2.33	2.29	2.90	1.84	1.72
Mn	0.00	0.01	0.02	0.01	0.00
Mg	2.35	2.43	1.64	3.05	3.23
Ca	0.01	0.02	0.01	0.00	0.00
Ba	0.02	0.02	0.02	0.02	0.01
Na	0.08	0.08	0.06	0.10	0.12
K	1.85	1.81	1.88	1.74	1.73
Mg#	0.50	0.52	0.36	0.62	0.65

Table a.5. Representative analyses of muscovite (normalized to 20 O and 4 OH).

Rock	Muscovite Gneiss			
Sample	CO35		T4	
Type	Peak	Retro	Peak	Retro
SiO_2	46.32	44.61	46.65	45.99
TiO_2	1.29	0.97	1.81	0.59
Al_2O_3	31.22	32.22	28.94	31.45
FeO_{total}	2.72	2.80	4.53	4.40
MnO	0.00	0.01	0.03	0.02
MgO	1.23	0.98	1.41	0.98
NiO	0.00	0.01	0.00	0.05
CaO	0.01	0.04	0.00	0.02
BaO	0.41	0.47	0.38	0.45
Na_2O	0.67	0.66	0.34	0.26
K_2O	10.20	10.26	10.96	11.04
Total	94.06	93.04	95.05	95.25
Si	6.32	6.17	6.39	6.28
Ti	0.13	0.10	0.19	0.06
Al	5.02	5.26	4.67	5.06
Fe^{2+}	0.31	0.32	0.52	0.50
Mn	0.00	0.00	0.00	0.00
Mg	0.25	0.20	0.29	0.20
Ca	0.00	0.01	0.00	0.00
Ba	0.02	0.03	0.02	0.02
Na	0.18	0.18	0.09	0.07
K	1.78	1.81	1.92	1.92
Mg#	0.45	0.39	0.36	0.28
Na/(Na+K)	0.09	0.09	0.05	0.03

Table a.6. Representative analyses of epidote (normalized to 12 O and 1 OH).

Rock	Muscovite Gneiss		Biotite Gneiss	Felsic Gneiss	Mylonite	
Sample	CO35	T4	CO5b	CO49	CO07	
Type	Peak	Peak	Peak	Peak	Static-retro	Shear-zone
SiO_2	37.98	37.29	35.44	38.23	37.74	37.43
TiO_2	0.23	0.2	1.01	0.11	0.21	0.05
Al_2O_3	27.31	25.66	21.84	28.09	26.64	24.60
FeOtotal	6.78	8.34	10.93	6.09	6.50	4.08
MnO	0.06	0.01	0.13	0.00	0.05	0.10
MgO	0.24	0.24	0.46	0.19	0.33	2.77
NiO	0.00	0.01	0.00	0.04	0.00	0.00
CaO	23.34	21.82	21.22	23.66	22.41	22.86
BaO	0.00	0.00	0.02	0.00	0.00	0.00
Na_2O	0.00	0.02	0.03	0.02	0.02	0.04
K_2O	0.02	0.02	0.03	0.01	0.02	0.02
Total	95.96	93.61	91.11	96.42	93.91	91.95
Si	2.99	3.02	2.99	2.99	3.03	3.07
Ti	0.01	0.01	0.06	0.01	0.01	0.00
Al	2.54	2.45	2.17	2.59	2.52	2.38
Fe^{3+}	0.45	0.56	0.77	0.40	0.44	0.28
Mn	0.00	0.00	0.01	0.00	0.00	0.01
Mg	0.03	0.03	0.06	0.02	0.04	0.34
Ca	1.97	1.89	1.92	1.99	1.93	2.01
Ba	0.00	0.00	0.00	0.00	0.00	0.00
Na	0.00	0.00	0.00	0.00	0.00	0.00
K	0.00	0.00	0.00	0.00	0.00	0.00
X_{ps}	0.15	0.19	0.26	0.13	0.15	0.11

Table a.7. Representative analyses of potassium feldspar and clinopyroxene (normalized to 8 O and 6 O respectively).

	Kfs			Cpx
Rock	Muscovite Gneiss		Rock	Felsic Gneiss
Sample	T4		Sample	CO49
Type	Peak	Retro	Type	Peak
SiO_2	64.42	64.96	SiO_2	51.77
TiO_2	0.00	0.00	TiO_2	0.39
Al_2O_3	18.36	18.47	Al_2O_3	8.12
FeO_{total}	0.01	0.01	FeO	7.79
MnO	0.00	0.01	MnO	0.03
MgO	0.00	0.00	MgO	9.65
NiO	0.01	0.00	NiO	0.02
CaO	0.02	0.05	CaO	18.60
BaO	0.90	0.60	BaO	0.02
Na_2O	0.95	0.89	Na_2O	3.21
K_2O	15.27	15.52	K_2O	0.02
Total	99.94	100.51	Total	99.64
Si	2.99	2.99	Si	1.90
Ti	0.00	0.00	Ti	0.01
Al	1.00	1.00	Al	0.35
Fe^{3+}	0.00	0.00	Fe^{3+}	0.05
Fe^{2+}			Fe^{2+}	0.19
Mn	0.00	0.00	Mn	0.00
Ca	0.00	0.00	Mg	0.53
Ba	0.02	0.01	Ca	0.73
Na	0.09	0.08	Na	0.23
K	0.90	0.91	K	0.00
X_{or}	0.91	0.92	Mg#	0.73

Appendix 2: Mantle wedge deformation recorded by high-temperature peridotite fabric superposition and hydrous retrogression (Limo massif, Cabo Ortegal, NW Spain)

Int J Earth Sci (Geol Rundsch)
DOI 10.1007/s00531-012-0761-8

ORIGINAL PAPER

Mantle wedge deformation recorded by high-temperature peridotite fabric superposition and hydrous retrogression (Limo massif, Cabo Ortegal, NW Spain)

P. Puelles · J. I. Gil Ibarguchi · A. Beranoaguirre · B. Ábalos

Received: 22 June 2011 / Accepted: 29 January 2012

Abstract The Limo harzburgites constitute a hm-thick tectonic stack where extremely elongated meter-scale sheath folds occur, bearing axes parallel to the macroscopic lineation recognized across the whole complex. They can be identified as close to L-type tectonites, with a weak foliation, a well-developed stretching, and a mineral lineation defined by the mineral assemblage in equilibrium. The linear fabric is recognizable at every scale, from aerial photos to the crystallographic orientation of the harzburgite-forming minerals measured by means of the electron back-scatter diffraction technique. These rocks registered initial deformation under high-temperature and low water fugacity conditions at low stress levels in an anhydrous mantle wedge context, as it is inferred from the activity of the [100](010) slip system in olivine. Then, the ongoing eo-Variscan subduction incorporated fluid/melts from the subducting plate into the suprasubduction mantle wedge zone. The variation in the ambient physicochemical conditions led to the operation of the [001](010) slip system in olivine, indicative of lower temperature and higher water fugacity and stress levels. These changes are recorded, too, by synkinematic recrystallization of oriented chlorite. The L-type fabric of clinopyroxene points to constriction conditions during deformation. The active deformational processes continued along the subduction conduit with the thrust of the peridotites onto the high-pressure granulites of the Bacariza Formation. Posteriorly, the whole ensemble would have shared a common deformational history related to exhumation and initial amphibolitization. Subsequent deformation processes under greenschist facies conditions took place until effective continental collision during the Early Carboniferous gave rise to the Variscan orogen.

Keywords Peridotite · Petrofabric · Mantle wedge · Subduction · Cabo Ortegal · Spain

P. Puelles (✉) · B. Ábalos
Departamento de Geodinámica, Universidad del País Vasco UPV/EHU, PO Box 644, 48080 Bilbao, Spain
e-mail: pablo.puelles@ehu.es

J. I. Gil Ibarguchi · A. Beranoaguirre
Departamento de Mineralogía y Petrología, Universidad del País Vasco UPV/EHU, PO Box 644, 48080 Bilbao, Spain

Introduction

Complex interactions between petrological and deformation processes take place in the mantle wedge above the subducting slab. Among others, dehydration of subducting materials, fluid migration, partial melting in the mantle wedge, and magma transport during deformation of the mantle materials are considered as important factors that may be able to promote changes in the rheology of the suprasubduction mantle and, therefore, play a key role in the dynamics of subduction zones (e.g., Mackwell et al. 1985; Karato et al. 1986; Hirth and Kohlstedt 1995; Zimmerman and Kohlstedt 2004; Soustelle et al. 2010). To gain insight into the geodynamics of the suprasubduction zone mantle, it is essential to carefully analyse those rocks that have experienced deformations in these domains. However, the scarcity of direct samples from the mantle wedge brought up to the surface is a handicap that has not helped identify clearly the processes operative in this domain.

The study of the preferred crystallographic orientation of the main constituent minerals in the upper mantle may be crucial in this regard. Mantle rocks are stronger than crustal rocks (e.g., Nicolas 1986) and therefore, although they may undergo some metamorphic variations and deformation during their ascent to the Earth's surface, the

Published online: 19 February 2012

mantle-related deformational fabrics will be preserved. Thus, they may provide valuable information on the structure and kinematics of mantle flow.

Among the minerals making up the mineral assemblage of these rocks, olivine is very likely to be the most abundant and most deformable under a wide range of conditions (e.g., Kohlstedt and Goetze 1974; Karato and Wu 1993). In almost all cases, the development of a crystallographic preferred orientation has been interpreted in terms of propagation of dislocations and dynamic recrystallization, although other mechanisms such as diffusion creep have also been invoked. For this reason, in order to ascertain the control that this phase may exert on the rheology of the upper mantle, detailed studies have been carried out on olivine from different perspectives, including melt segregation (Holtzman et al. 2003), hydrostatic pressure (Mainprice et al. 2005; Jung et al. 2009) and dynamic recrystallization (Lee et al. 2002). In light of recent investigations, greater emphasis must be laid on the influence of the incorporation of water on the active slip systems in olivine (Jung and Karato 2001; Jung et al. 2006). According to these works, the presence of trace amounts of water would promote a change of the slip system and, consequently, modify the lattice-preferred orientation (LPO) pattern register in this mineral. Therefore, eventual changes of the LPO patterns registered in this phase may reflect changes in the strength of upper mantle rocks with direct implications for the kinematics of mantle flow.

This work deals with an exceptional outcrop of mantle wedge rocks that have registered deformation in a suprasubduction context. The new set of field, petrographic, thermobarometric, microstructural, geochemical and crystallographic data collected for the Limo peridotite massif (Cabo Ortegal Complex, NW Spain) reveals high-temperature deformation, percolation of melts/fluids coming from a subducting slab in a suprasubduction mantle wedge, and deformations in a subduction channel before the final exhumation. Thus, although the Limo massif has been described so far as a homogeneous (Ben Jamaa 1988; Girardeau and Gil Ibarguchi 1991; García Izquierdo 2005) and structurally simple harzburgitic body (e.g., Girardeau and Gil Ibarguchi 1991; Ábalos et al. 2003), the data presented in this paper highlight the great relevance of this massif as an exceptional study case to gain insight into the dynamics of the mantle wedge in a suprasubduction context.

Geological setting

The NW sector of the Iberian Massif (Variscan orogenic belt, Fig. 1a) contains five Allochthonous Complexes preserved as structural synforms or megaklippen: the Cabo Ortegal, Malpica-Tui and Órdenes complexes in Spain, and the Bragança and Morais complexes in Portugal. The complexes consist of a pile of Proterozoic to lower Palaeozoic metasedimentary and metaigneous units that preserve evidence of both Variscan and pre-Variscan deformation and metamorphism. Various nappe units that might represent dismembered and duplicated terrane relics have been identified in the complexes. Currently, they are categorized into three main structural elements that can be correlated at a regional scale among the complexes. These are (1) the Basal Unit or Lower Allochthon, (2) an intermediate Ophiolitic Unit, and (3) the Upper Allochthon. At Cabo Ortegal (Fig. 1b), the latter allochthon contains high-pressure granulite, N-MORB eclogite, metagabbro, metaserpentinite, metaperidotite, and ortho- and paragneisses that were obducted onto the Gondwana edge during the Variscan orogeny (cf. Vogel 1967; Martínez Catalán et al. 1997; Arenas et al. 2000; Gil Ibarguchi et al. 2000; Marcos et al. 2002, among others).

High-pressure and high-temperature tectonic processes of middle Devonian age (Ordóñez Casado et al. 2001) are responsible for the primary structure of the Cabo Ortegal Complex. The ultramafic sheet defined by the major outcrops of peridotites appears on top of the high-pressure granulite facies rocks of the Bacariza Formation which, in turn, rest on the underlying eclogites. The entire ensemble overlies the high-pressure gneisses (Fig. 1c). All these units are separated by ductile thrust contacts (Ábalos et al. 1996, 2003) and exhibit deformational features that might be related to accretion in deep tectonic realms of an oblique subduction/collision orogenic channel active between ca. 395 and 365 Ma (Ordóñez Casado et al. 2001; Santos Zalduegui et al. 1996, 2002). Retrogression was estimated at ca. 380 Ma or slightly younger (Van Calsteren et al. 1979; Peucat et al. 1990; Santos Zalduegui et al. 1996), whereas greenschist-facies retrogradation was dated between ca. 360 and 350 Ma (Peucat et al. 1990; Dallmeyer et al. 1997).

The ultramafic sheet in the Upper Allochthon of the Cabo Ortegal Complex

Ultramafic rocks in the Upper Allochthon of the Cabo Ortegal Complex define three major massifs (Limo, Herbeira and Uzal from N to S) and a number of much smaller (dam- to hm-across) klippen structures (Fig. 1b). These rocks are amphibole-bearing harzburgite, chromian spinel- and PGE-bearing dunite, and garnet-bearing massive pyroxenite. Other mafic rocks, such as garnet-rich pyroxenites and late pyroxenite veins and granitic intrusives, occur to a lesser extent. Girardeau and Gil Ibarguchi (1991), Moreno et al. (2001) and Santos Zalduegui et al. (2002), among others, provided comprehensive petrographic and mineralogical

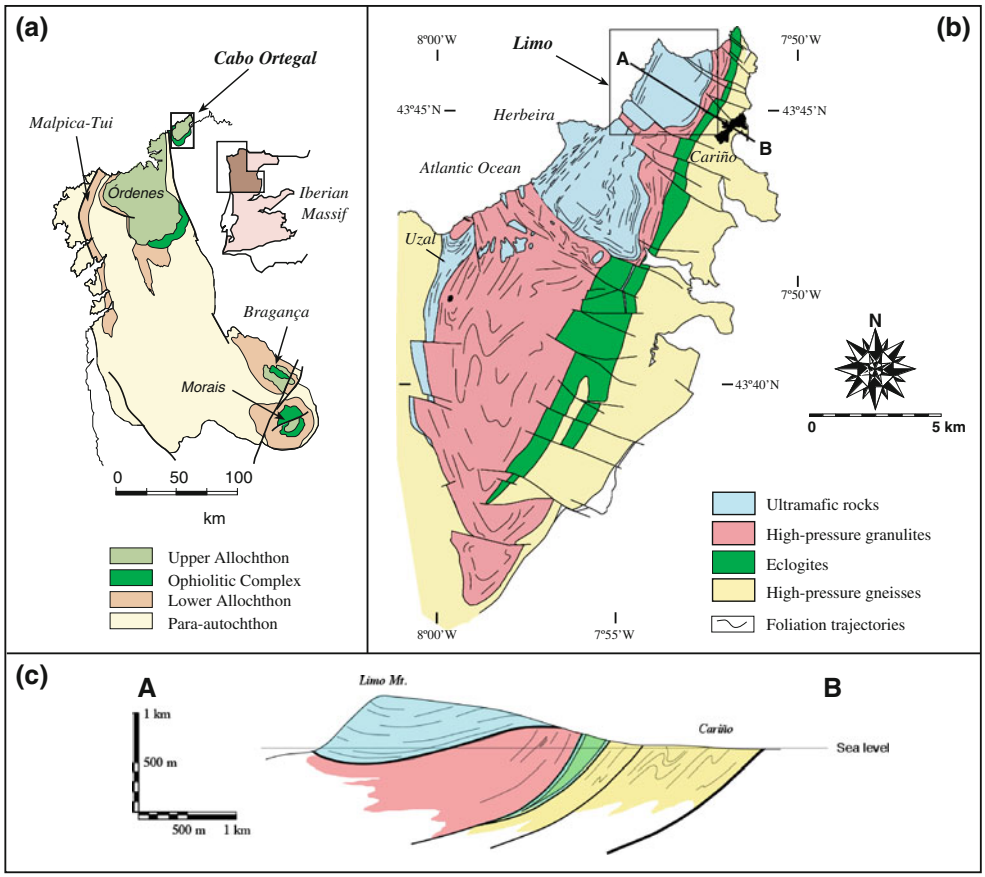

Fig. 1 **a** Geological sketch of NW Iberia showing the units that constitute the Allochthonous Complexes and their para-autochthon. **b** Simplified geological map of the high-pressure rocks of Cabo Ortegal Complex. Note the location of the Limo massif. **c** Geological cross-section of the Limo massif showing the structural relationship between ultramafic rocks, high-pressure granulites, eclogites and high-pressure gneisses. The cross-section corresponds to a plane perpendicular to the high-pressure mineral lineation

description on these rocks. However, harzburgite is the most common rock type throughout the ultramafic sheet. Harzburgites show strong serpentinization and may contain a variable amount of amphibole, chlorite and spinel. In fact, two main lithotypes might be differentiated: (1) spinel-bearing harzburgite without or with little amphibole or chlorite and (2) spinel-bearing harzburgites with a high content in amphibole (>30%) and less so in chlorite.

Major and trace element bulk rock and mineral compositions of harzburgite have residual characteristics comparable to those of peridotites from arc settings. A fractionation trend from dunite to pyroxenite suggests that the latter crystallized from primitive arc-related magmas but with components that attest to isotopic disequilibrium and contamination (Van Calsteren et al. 1979; Peucat et al. 1990; Gravestock 1992; Laribi-Halimi 1992; Santos Zalduegui et al. 2002; García Izquierdo 2005). In this line, the authors cited as well as Moreno et al. (2001) have proposed a suprasubduction arc-root setting for the peridotite-pyroxenite ensemble, variably modified by fluid/melt infiltration derived from subducted oceanic lithosphere. These rocks might have originated for their most part ca. 500 Ma ago (Van Calsteren et al. 1979; Santos Zalduegui et al. 2002) with some younger garnet pyroxenites around 392 Ma (Peucat et al. 1990).

The recrystallization conditions suggested by the microstructural and petrofabric data obtained for the Herbeira massif (Ben Jamaa 1988; García Izquierdo 2005) attest to a high-temperature stage (>1,000°C) followed by a complex tectonothermal history involving a late, synkinematic development of garnet after spinel in pyroxenites at 800°C, 1.65 GPa (Girardeau and Gil Ibarguchi 1991). Precise U–Pb ages of ca. 383–395 Ma and less precise internal Sm–Nd isochrons of ca. 390 Ma were obtained for this event (Ordóñez Casado et al. 2001; Santos Zalduegui et al. 1996, 2002), postdated by a granitic pegmatite intrusive dated at ca. 387 Ma (Santos Zalduegui et al. 1996). This reports a short magmatic event coeval with high-pressure/high-temperature metamorphism and deformation.

The Limo massif

The Limo ultramafic massif, located in the northern part of the Cabo Ortegal Complex, occupies an extension of 6.6 km^2. This has been described so far as a rather homogeneous harzburgitic massif, from both petrological and structural points of view (e.g., Ben Jamaa 1988; Girardeau and Gil Ibarguchi 1991; García Izquierdo 2005). However, our latest field observations, orientation measurements, and microstructural data presented in this study have allowed us to interpret this massif in a totally different manner.

Amphibole- and spinel-bearing harzburgite is the most common rock type in the Limo massif. Apart from the exposures located along the cliffs to the North and East of the massif, the quality of the rest of the outcrops is not very good. Harzburgites are strongly serpentinized, appear often as decameter to hectometer in size isolated blocks, and show a characteristic brownish to yellowish color due to weathering. When chlorite is present, the harzburgites exhibit a greyish color. In most inland outcrops, it is rather difficult to recognize any type of structure but, when the exposures are good enough, as it is the case on top of the massif near and along the cliffs, it is possible to observe a very weak subhorizontal foliation (Fig. 2a) containing N010-030°E trending mineral and stretching lineations (Fig. 2b). The foliation is defined by the preferred orientation of minerals forming the equilibrium assemblage (olivine, pyroxene and spinel) and, when visible, it runs parallel to the compositional banding determined by the concentration of these minerals in mm-thick domains (Fig. 3a). The well-developed mineral and stretching lineation is defined by the preferred orientation of orthopyroxene and spinel. This linear fabric is present at all scales, from the hand specimen to the aerial photo scales, making it possible to classify these rocks as close to L-type tectonites (Fig. 3b).

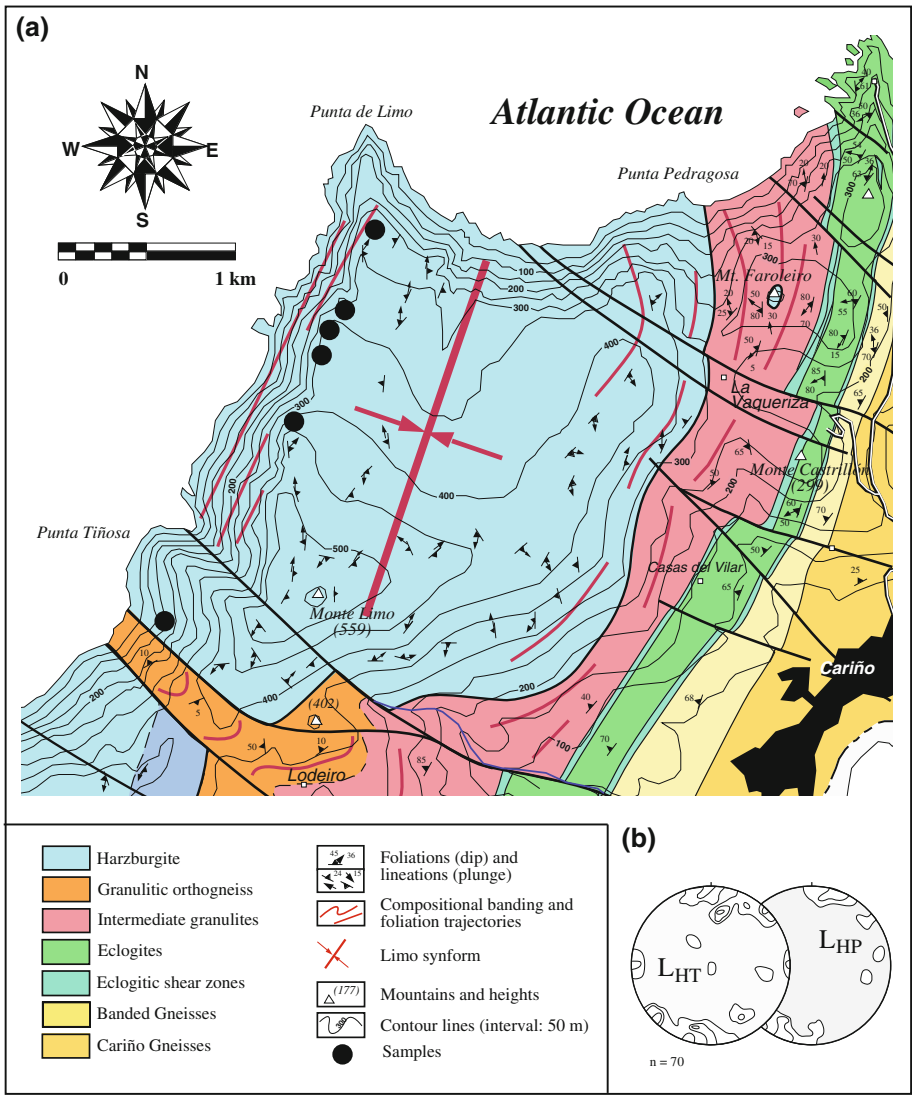

Fig. 2 **a** Geological and structural map of the Limo massif. **b** Equal area projection showing the principal orientations of the mineral/stretching lineation across the massif

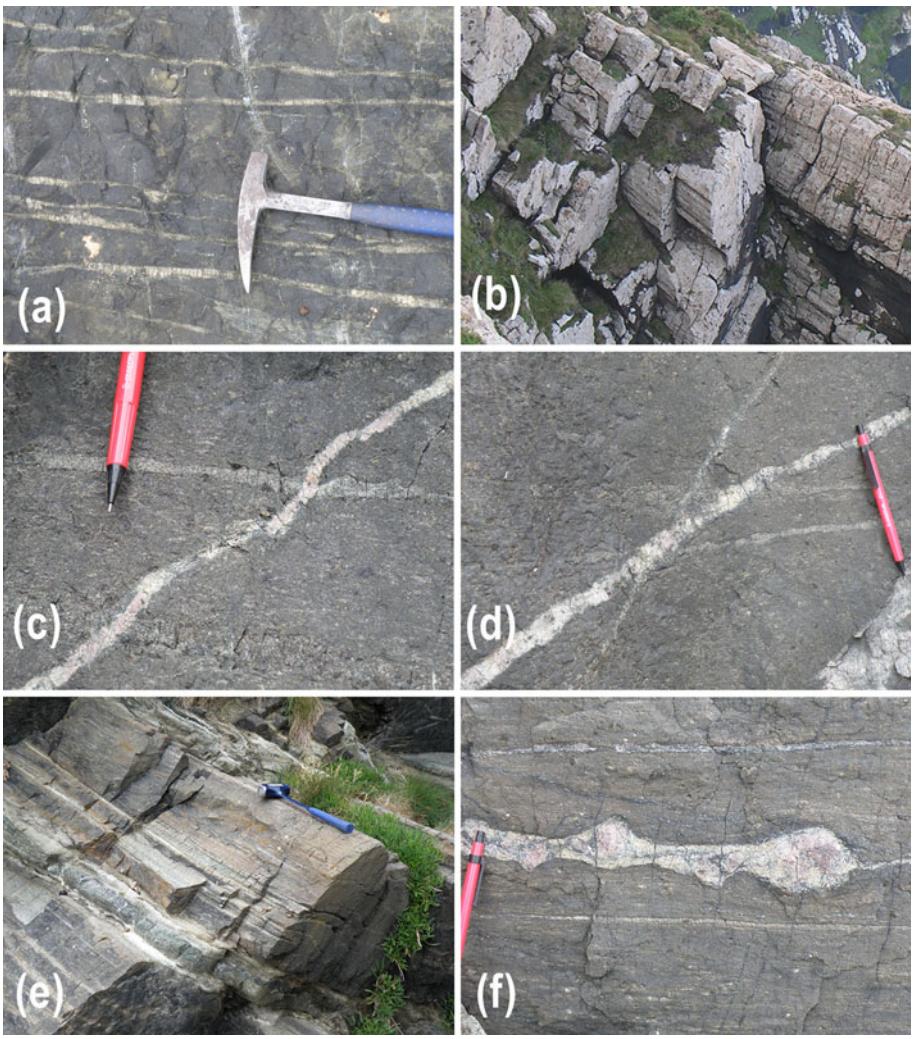

Fig. 3 **a** Millimeter-thick pyroxenite layers parallel to the weak foliation developed. **b** Linear fabric shown by the Limo harzburgites. Note the presence of tubular structures parallel to the mineral/stretching lineation recognized at the outcrop scale. **c** Later garnet (Grt)-, pyroxene (Px)- and spinel (Spl)-bearing bands crosscutting previous pyroxenite layers. **d** Conjugate mm-thick pyroxenite layers crosscut by the previously mentioned Grt-, Px- and Spl-bearing bands. **e** Mylonitic fabric depicted by the Limo harzburgites close to the contact with the underlying high-pressure granulites. **f** Porpyhroclastic asymmetric aggregates indicating relative tectonic displacement of the hanging wall blocks to the NE

The rare pyroxenite layers run parallel to the tectonic foliation, whereas later garnet-, pyroxene-, and spinel-bearing bands crosscut them (Fig. 3c). In some cases, it has been recognized the presence of conjugate systems (Fig. 3d). Close to the boundaries with the underlying granulites, it is also possible to define a planolinear mylonitic fabric related to the thrust of the ultramafic sheet onto the high-pressure migmatitic gneisses of the granulite unit (Fig. 3e). Amphibole-rich bands occur in these areas, as a consequence of the strong amphibolitization and replacement of primary clinopyroxenite layers. The shear sense criteria point there to a top-to-the-NE tectonic displacement of the hanging wall blocks (Fig. 3f).

Structural observations made in the Limo peridotite massif, mainly along the cliffs to the NW and NE, have revealed that the whole massif is in fact a hm-thick stack composed of extremely elongated sheath folds. These folds exhibit tubular geometries and have their long axes parallel to the macroscopic mineral/stretching lineation present throughout the complex. These structures can be traced on aerial photos too (Fig. 4a). The shape ratios of fold geometries (measures between fold profile inflection points) are >15 in XZ structural sections and around 1.5 in sections perpendicular to the lineation (Fig. 4b). At the outcrop scale it is also possible to observe the presence of intrafoliar folds with the same axial orientation. These folds show extremely thickened hinges and thinned fold limbs (Fig. 4c) and, in some cases, they correspond to XZ sections of sheath folds with eye-like morphologies in structural sections perpendicular to the lineation (Fig. 5a, b). These structures appear associated with low-angle shear zones that indicate a top-to-the-NE tectonic displacement of the hanging wall blocks. The shear sense criteria are in agreement with those associated with the sigmoidal shape of peridotite foliation trajectories recognized in the XZ structural sections along the western cliffs of the Limo massif (Fig. 5c).

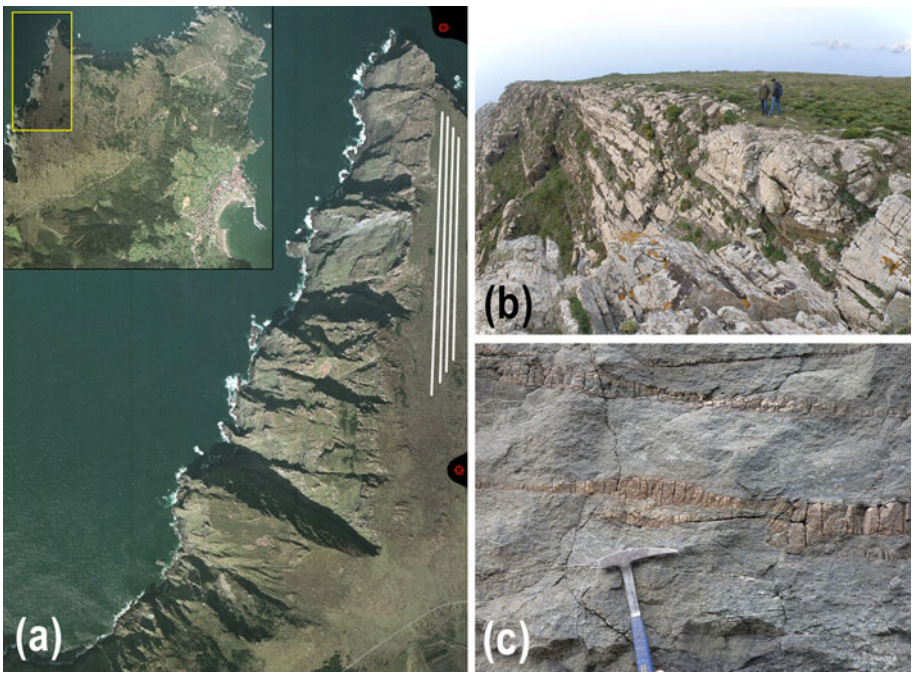

Fig. 4 **a** Traces of the tubular structures shown in **b** on the aerial photos of the area. *White lines* are parallel to the traces. **b** Pileup of sheath folds in the upper part of the Limo massif. Note the extremely elongated morphologies and the tubular structures developed. **c** Intrafoliar folds within the Limo harzburgites. Note the thickened hinges and thinned limbs

Methods

Standard oriented thin sections were used for conventional petrographic microscopy. The sections were cut parallel to the XZ structural plane (XY: microscopic foliation plane orientation; X: mineral and stretching lineation orientation).

Minerals from representative samples of the Limo harzburgite were analyzed on standard polished thin sections with a SX100 microprobe at the University of Clermont-Ferrand. Operating conditions were: 10 s counting time (peak), ca. 10 nA beam current and 15 kV accelerating voltage. Calibration was against BRGM (French Geological Survey) standard minerals, and the ZAF correction procedure was used. The average detection limit is 0.1% at 2σ confidence limit. Table 1 presents a selection of mineral analyses with details on structural formulas. Fe^{3+}/Fe^{2+} was estimated by charge balance criteria (cf. Droop 1987; Dale et al. 2000) assuming: 4 cations and 6 O (pyroxene), 23 O (amphibole); 3 cations and 4 O (olivine and spinel). Whole-rock major element analysis of one harzburgite sample was made at the SGIker facility of the University of the Basque Country using ICP-MS techniques following sample decomposition with lithium metaborate (see García de Madinabeitia et al. 2008 for additional details).

The electron back-scattered diffraction (EBSD) study was performed on selected rock sections. These were previously ultra-polished with a colloidal silica suspension for around 3 h to remove surface damage. Samples were covered with an Au–Pa layer before polishing completion to avoid electric charging induced by holes and grain loss after lapping. Finally, they were carbon coated in an attempt to prevent them from charging.

Crystallographic preferred orientation measurements were performed at the University of the Basque Country (Electron Microscopy Facility-SGIker) with an automated electron back-scattered diffraction system (Channel5, HKL) attached to a JEOL JSM-7000F Field Emission Scanning Electronic Microscope (FE-SEM). Samples were mounted in this apparatus on a stage tilted 70°, with the rock lineation (structural X reference direction) parallel to the SEM *X*-axis. The beam working distance was 15 mm (Prior et al. 1999). A low acceleration voltage of 10 kV, a beam current of ca. 14 nA and a copper tape attached to the sample surface surrounding the measurement area were used to reduce charging affects. Crystallographic orientation solutions with mean angular deviation (MAD) values over 1.2 (between detected and simulated patterns) were rejected to assure EBSD measurement reliability.

Crystallographic orientations and orientation maps were obtained using the Channel5 software package after automated EBSD analysis on predefined sampling grid steps of around 20 μm. These steps are sometimes significantly smaller than the average grain size of some mineral aggregates, so that all the grains are analyzed at least in one point. Although the interpretation of EBSD data is typically based on one-point-per-grain orientations, the collection of data from highly altered and serpentinized peridotites makes it very difficult to reconstruct grain boundaries and extrapolate all the analyzed points in a grain to a single orientation. However, although it might create artifacts in the pole figure contours, recent studies have shown that the

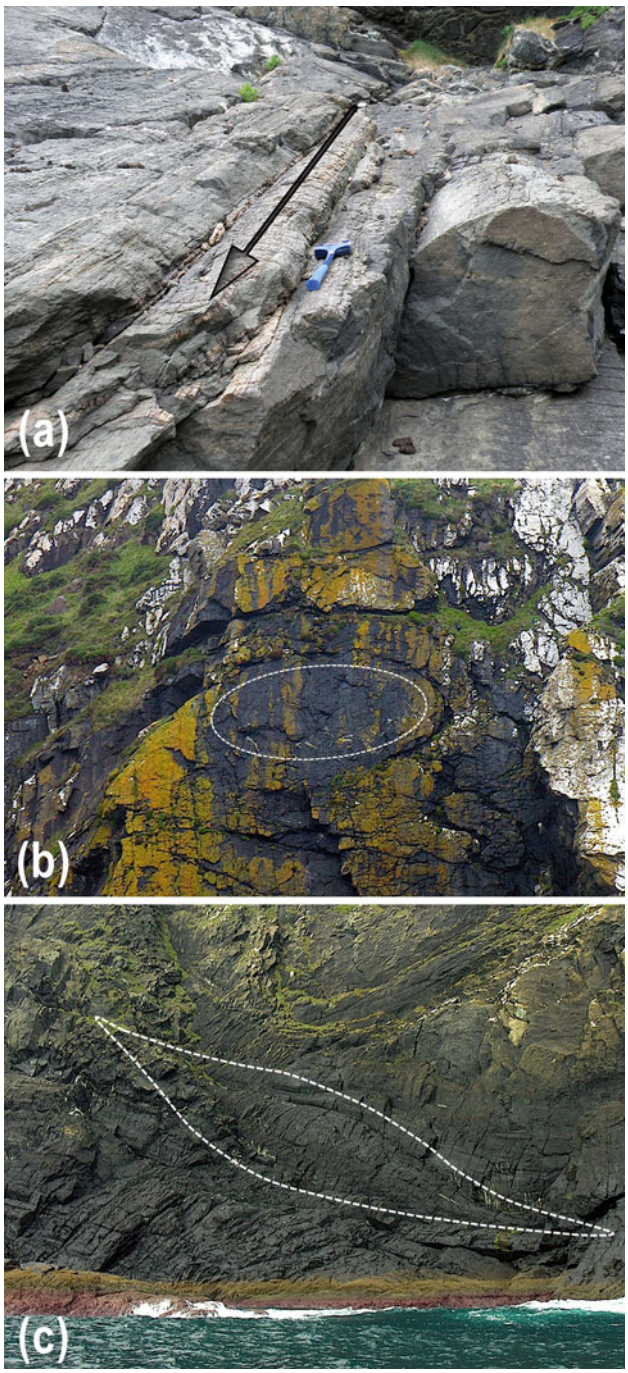

Fig. 5 **a** Sheath folds at the foot of the Limo cliffs. Note the elongated tubular structures developed and the close geometries in sections perpendicular to the lineation. The *black arrow* illustrates the shallow plunge of the pronounced and prominent lineation recognized in the area. **b** *Eye-shaped* morphologies corresponding to sheath folds observed in XZ structural sections. **c** *Sigmoidal shape* of peridotite foliation trajectories found in the western cliffs of the Limo massif. XZ structural section

"raw" EBSD LPO data are comparable to one-point-per-grain LPO data in both strength and orientation (Achenbach et al. 2011). The data are presented in lower hemisphere, equal area stereographic diagrams. The projection plane always corresponds to structural XZ sections and the macroscopic foliation is represented there as the equatorial diameter (E–W). The lineation is horizontal within the same plane. The strength of the fabric was expressed by the texture index J, calculated as the mean square value of the orientation distribution function (ODF).

Results

Petrography, geochemistry, and lattice-preferred orientations

The Limo harzburgite samples were collected in the northern and central part of the massif (Fig. 2a), far from its basal tectonic contact. These samples, therefore, are supposed to have registered deformation phases previous to those responsible for the thrusting of the ultramafic massifs onto the granulites (Fig. 1c). They show mineral assemblages in equilibrium composed of primary olivine, orthopyroxene, clinopyroxene, and spinel, with variable amounts of amphibole and chlorite, and serpentine and carbonate as secondary minerals. Minor amounts of opaque minerals and phlogopite are also present. The modal composition of the preserved primary phases ranges between 40 and 81% for olivine, 3–11% for orthopyroxene, and 1–5% for clinopyroxene, while amphibole accounts for up to 11–43% and chlorite is rarely more abundant than 10%. The serpentinization process affected pervasively these rocks, reaching in some cases up to 70% of the rock volume. Chrysotile is the main phase associated with the serpentinization processes, while talc is exceedingly rare in these peridotites (cf. Vogel 1967).

The microstructures recognized in these samples vary from granoblastic and porphyroclastic in the structural uppermost parts of the massif to mylonitic along the contacts with the bounding granulites (Fig. 3e). In the first case, the tectonic foliation is very weak although, as it has been stated above, pyroxene and spinel contribute to the development of the macroscopic lineation. In the second case, at the microscopic scale, it can be seen that relic olivine porphyroclasts are surrounded by fine-grained olivine neoblasts of similar composition. In principle, this observation excludes an origin through dehydration of secondary serpentine. The newly formed olivine crystals make up the matrix of the rock, although in most cases they have been completely replaced by serpentine.

Olivine

The average composition of olivine is $Forsterite_{90}$. Representative compositions are reported in Table 1. This phase

Table 1 Representative analyses and structural formulae of olivine (Ol), orthopyroxene (Opx), clinopyroxene (Cpx), spinel (Spl), amphibole (Am) and chlorite (Chl)

Sample Mineral	200b Ol	200ii Ol	272 Ol	200b Opx	200ii Opx	272 Opx	200b Cpx	272 Cpx	200b Spl	200ii Spl	272 Spl	200 Am	275 Am	200b Chl	200ii Chl
SiO_2	39.86	40.86	40.36	53.50	53.91	54.18	54.46	53.34	0.02	0.01	0.03	46.12	47.43	29.96	30.01
TiO_2	b.d.l.	b.d.l.	b.d.l.	0.06	0.11	0.05	0.11	0.18	0.07	0.08	0.07	0.29	0.36	0.05	0.04
Al_2O_3	b.d.l.	b.d.l.	b.d.l.	4.53	5.29	4.70	0.94	2.20	53.18	36.91	53.00	18.63	18.88	19.90	19.31
Cr_2O_3	b.d.l.	b.d.l.	b.d.l.	0.51	0.55	0.59	0.04	0.49	10.70	24.55	12.04	0.93	0.63	0.66	1.03
FeO	10.29	9.63	9.83	7.34	6.18	6.73	1.98	2.01	17.99	25.08	16.92	4.16	3.72	3.61	3.36
MnO	0.13	0.18	0.10	0.11	0.13	0.14	0.09	0.11	0.11	0.22	0.09	0.02	0.05	0.00	0.02
MgO	49.29	50.39	48.67	33.15	32.24	33.10	17.86	17.10	17.00	12.10	17.00	11.88	11.69	31.44	31.78
NiO	0.39	0.43	0.31	0.12	0.12	0.10	0.02	0.03	0.43	0.23	0.35	0.07	0.06	0.09	0.32
CaO	0.00	0.01	0.00	0.58	1.98	0.27	24.36	23.79	0.00	0.02	0.00	12.74	12.47	0.10	0.00
Na_2O	b.d.l.	b.d.l.	b.d.l.	0.00	0.05	0.02	0.07	0.11	0.01	0.00	0.00	1.72	1.65	0.01	0.01
K_2O	0.00	0.00	0.00	0.01	0.00	0.00	0.02	0.00	0.01	0.01	0.00	0.75	0.56	0.01	0.02
Total	99.96	101.51	99.29	99.89	100.55	99.88	99.95	99.36	99.50	99.20	99.51	97.31	97.5	85.84	85.89
O	4	4	4	6	6	6	6	6	4	4	4	23	23	14	14
Si	0.98	0.99	1.00	1.85	1.85	1.87	1.98	1.95	0.00	0.00	<0.01	6.48	6.59	2.87	2.88
Al	_	_	_	0.18	0.22	0.19	0.04	0.10	1.68	1.28	1.68	3.09	3.09	2.25	2.18
Ti	_	_	_	<0.01	<0.01	<0.01	<0.01	0.01	<0.01	<0.01	<0.01	0.03	0.04	<0.01	<0.01
Cr	_	_	_	0.01	0.02	0.02	<0.01	0.01	0.23	0.57	0.26	0.10	0.07	0.05	0.08
Fe^{3+}	_	_	_	0.1	0.06	0.05	0.01	0.00	0.09	0.15	0.07	–	–	–	–
Fe^{2+}	0.21	0.20	0.20	0.12	0.12	0.15	0.05	0.06	0.31	0.46	0.31	0.49	0.43	0.29	0.27
Mn	<0.01	<0.01	<0.01	<0.01	<0.01	<0.01	<0.01	<0.01	<0.01	<0.01	<0.01	<0.01	<0.01	0.00	<0.01
Mg	1.81	1.82	1.79	1.71	1.65	1.71	0.97	0.93	0.68	0.53	0.68	2.49	2.42	4.49	4.54
Ni	<0.01	<0.01	<0.01	<0.01	<0.01	<0.01	0.00	<0.01	<0.01	<0.01	<0.01	<0.01	<0.01	<0.01	0.03
Ca	0.00	0.00	0.00	0.02	0.07	0.01	0.95	0.93	0.00	0.00	0.00	1.92	1.86	0.01	0.00
Na	_	_	_	<0.01	<0.01	<0.01	0.01	0.01	0.00	0.00	0.00	0.47	0.45	<0.01	<0.01
K	0.00	0.00	0.00	0.00	0.00	0.00	<0.01	0.00	0.00	0.00	0.00	0.13	<0.01	<0.01	<0.01

b.d.l. below detection limits (see text for further explanations)

exhibits subrounded and anhedral morphologies with a grain size of 0.5–1 mm. The olivine grains appear concentrated in irregular dunitic bands intercalated between pyroxene-, spinel- and amphibole-rich layers (Fig. 6a). They are altered to secondary serpentine minerals with pseudomorphic texture (mesh microstructures; Fig. 6b). In some cases, it can be observed that serpentine minerals outline almost perfectly the shape of previous olivine crystals, enabling recognition of sigmoidal olivine porphyroclast geometries and identification of top-to-the-NE tectonic displacement of the hanging wall blocks (Fig. 6c).

Olivine LPOs determined after indexing the obtained EBSD patterns are presented in Fig. 7. Due to the orthorhombic symmetry of this phase, poles to the {010}, {001} and {100} plane families represent the [010], [001] and [100] crystallographic directions, respectively. The analyzed minerals show their [001] axes oriented close to the lineation and define a point-maximum along the X structural direction. [100] axis orientations show higher dispersion, although the presence of a submaximum parallel to the lineation is still recognizable. [010] orientations, in turn, scatter and define incomplete girdles perpendicular to X. Two submaxima can be identified, one close to Y and the other around the pole to the foliation. The J texture index yields values between 1.5 and 2.1. Asymmetry of the pole distributions with respect to the external reference frame provided by the foliation and lineation is also remarkable.

Orthopyroxene

Orthopyroxene can be identified compositionally as enstatite (Morimoto 1989), with average values of $Enstatite_{88}$ $Ferrosilite_{10}$ $Wollastonite_{02}$ (Table 1). This phase occurs as aggregates due to the disintegration of previous thicker bands, or as subspheric porphyroclasts with a large grain size (>1 mm; Fig. 6d). It contains clinopyroxene and spinel inclusions and exhibits crystal-plastic deformational features, such as undulatory extinction. Clinopyroxene exsolutions, presently altered to secondary amphibole, are visible (Fig. 6d).

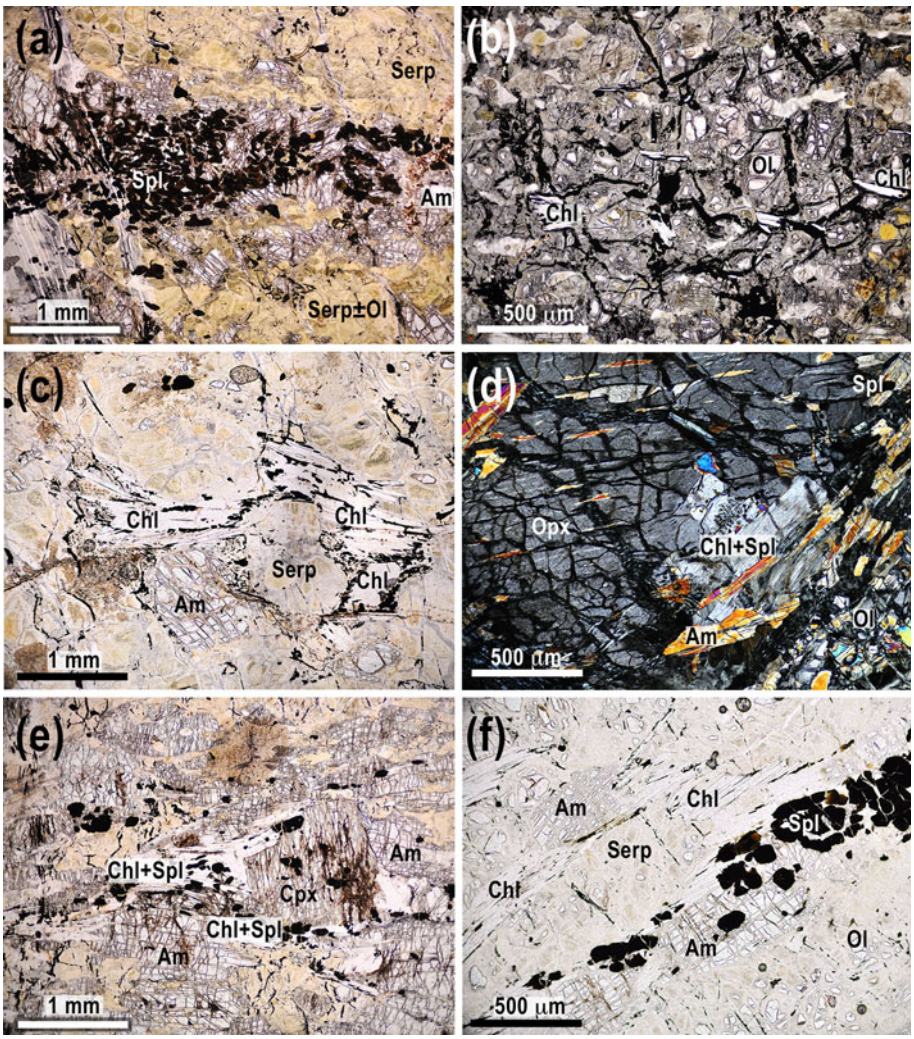

Fig. 6 Photomicrographs of Limo harzburgites. **a** Compositional banding showing serpentinized (*Serp*) olivine (*Ol*)-rich domains alternating with bands composed mainly of amphibole (*Am*) and spinel (*Spl*). Plane-polarized light. **b** Mesh texture in serpentinized olivine. Note the shape-preferred orientation of chlorite. Plane-polarized light. **c** Pseudomorph of olivine completely serpentized (*Serp*). Note the sigmoidal geometry of the aggregate and the presence of oriented chlorite. Plane-polarized light. **d** Opx porphyroclast showing Cpx lamella altered to Am. Note the presence of the central Chl crystal and the small Spl aggregate associated. Cross-polarized light. **e** Cpx porphyroclast with inclusions of Spl. Note the asymmetry of the porphyroclastic system and the development of synkinematic chlorite and spinel. Plane-polarized light. **f** Shape-preferred orientation of Am and Spl aggregates. Note how secondary chlorite shows exactly the same orientation as that defined by the primary phases. Plane-polarized light

Orthopyroxene LPO patterns (Fig. 8a) are relatively weak, with *J* values around 1.21. They show poles to the {001} planes (corresponding to [001] axes due to the symmetry of the crystals) oriented close to the macroscopic rock lineation. [100] axes tend to be aligned close to the pole to the foliation, whereas poles to the {010} planes are distributed around the Y structural direction. LPOs are oblique with respect to the XYZ reference system too.

Clinopyroxene

Clinopyroxene is not very abundant, contains spinel inclusions, and appears as isolated crystals or making up discontinuous mm-thick layers (Fig. 6e). Compositionally it can be classified as diopside with average values of $Enstatite_{49}$ $Ferrosilite_{03}$ $Wollastonite_{48}$ (Table 1).

Clinopyroxene LPOs (Fig. 8b, c) are strong and their *J* texture indexes show values up to 2.5. These distribution patterns are characterized by poles to the {001} planes oriented around the X structural direction, forming a well-defined point-maximum parallel to the rock lineation. Poles to the {010} planes draw an almost continuous girdle perpendicular to both foliation and lineation. Two diffuse submaxima can be identified within the girdle, one of them close to the pole to the foliation (Z structural direction) and the other around Y. Poles to the {100} planes are also distributed along a more discontinuous girdle perpendicular to the lineation. No systematic submaxima can be defined. These LPO patterns also present a clear obliquity with respect to the external structural reference system. This feature indicates the existence of components of rotational strain.

Spinel

The Al-rich spinel ($X_{Al} > 0.83$) is brown to green in color. It shows a grain size <2 mm and appears as minute crystals or discontinuous aggregates running parallel to the weak foliation developed in these rocks (Fig. 6a, f).

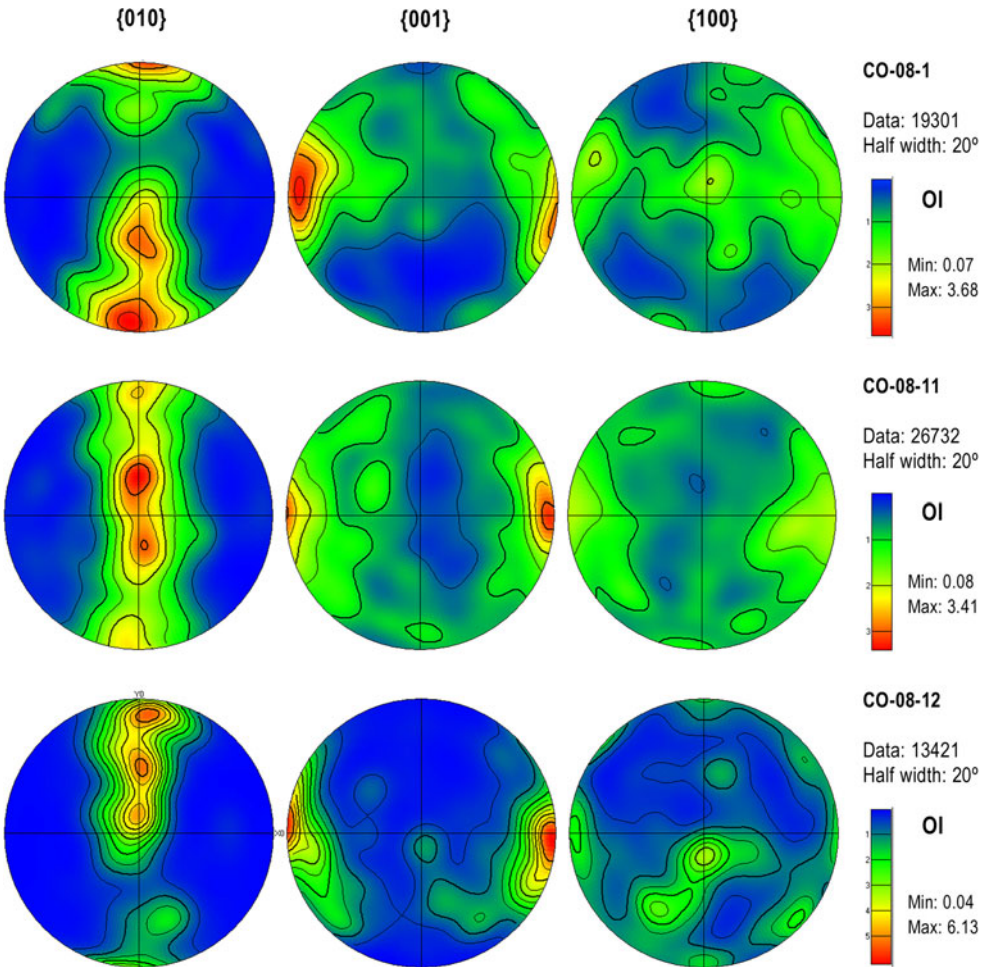

Fig. 7 Orientations of the poles to olivine {010}, {001} and {100} planes. Stereoplot color patterns represent multiples of mean uniform density. Lower hemisphere, equal area stereographic projections of XZ structural sections (foliation is the equatorial diameter E–W and the lineation is horizontal within that plane)

Spinel shows no preferred orientation, but the obtained EBSD pole figures present elliptical maxima defined by the crystallographic axes [100], [110], and [111], which suggests plastic distortion of the crystal lattice (Fig. 8d).

Chlorite

This Mg-rich chlorite ($X_{Mg} = 0.94$) is sometimes seen replacing spinel or as a discrete mineral in mm size bands. It shows a shape-preferred orientation in accord with that marked by pyroxene, spinel, and amphibole (Fig. 6c, e, f). In some cases, it is possible to find evidence of its synkinematic origin (Fig. 6c, e).

Chlorite LPO patterns (Fig. 9a) have strong texture values ($J = 2.05$). Poles to the {001} planes concentrate in a point-maximum around the Z structural direction, indicating that basal planes are disposed parallel to the foliation. Poles to the {010} and {100} planes, in turn, scatter along a discontinuous girdle parallel to the foliation plane. In the first case, a diffuse maximum can be found close to Y, whereas in the second one, the weak submaximum seems to be close to the orientation of the lineation of the rock (X structural direction).

Amphibole

Amphibole is compositionally Mg-rich edenitic hornblende ($X_{Mg} > 0.9$; Table 1). It is slightly pleochroic, subidiomorphic and shows a grain size of about 0.5 mm. It occurs as isolated grains or as polycrystalline aggregates leading to the formation of thin layers parallel to the weak foliation developed in these rocks. It seems to replace previous primary clinopyroxene affected by retrograde metamorphism under amphibolite facies conditions (Vogel 1967; Maaskant 1970; Girardeau and Gil Ibarguchi 1991).

Amphibole LPO patterns (Fig. 9b–d) show J values up to 4.0. Poles to the {100} planes scatter very close to the Z structural direction, whereas axes normal to the {001} planes are oriented close to the lineation and define a well-developed point-maximum. Poles to the {010} planes, in turn, form weak girdles normal to the lineation, although a submaximum close to the Y axis can also be recognized.

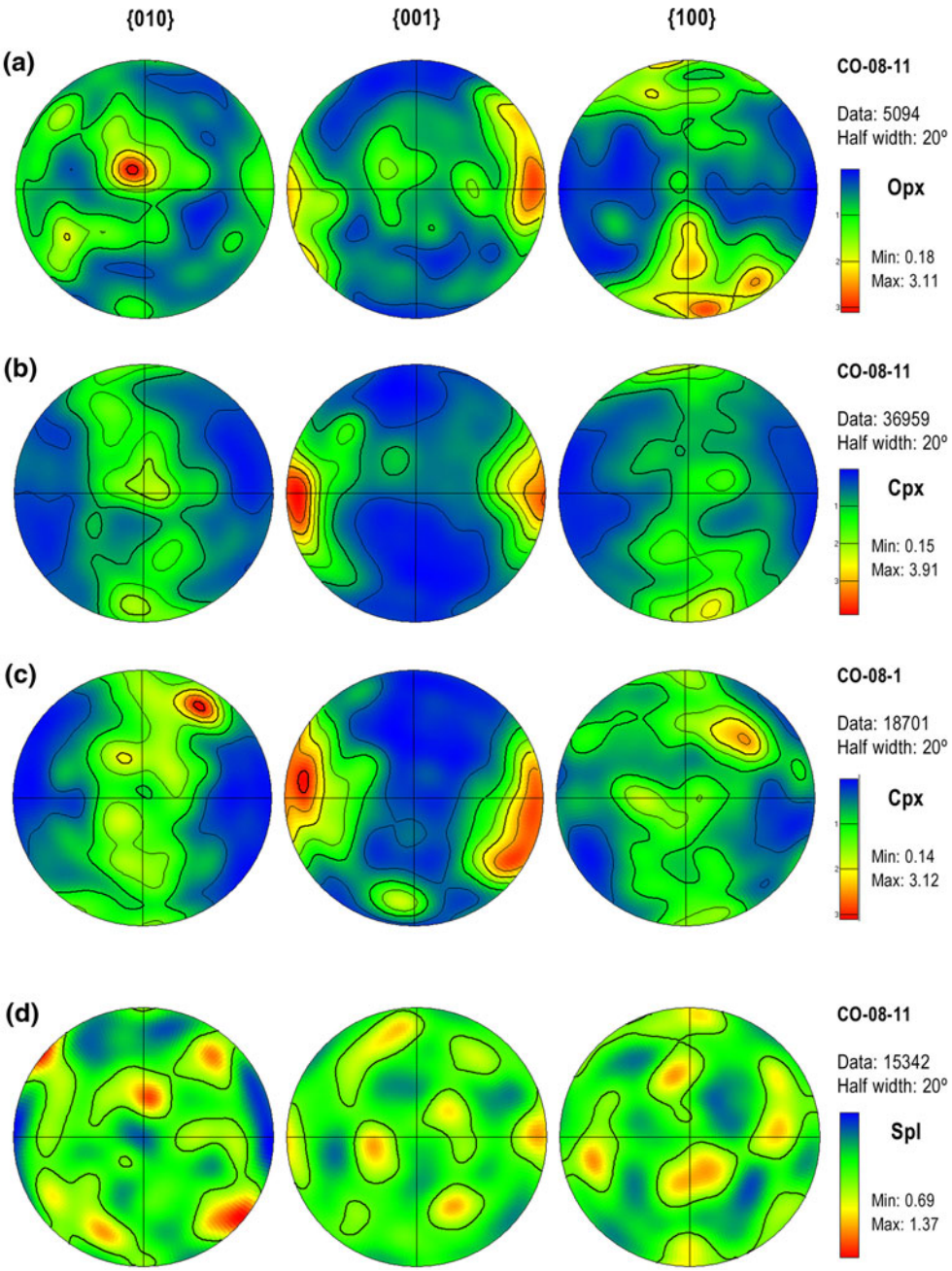

Fig. 8 Orientations of the poles to orthopyroxene (**a**) and clinopyroxene (**b** and **c** {010}, {001} and {100} planes. **d** Orientations of the poles to spinel {100}, {110} and {111} planes. In all the stereograms stereoplot color patterns represent multiples of mean uniform density. Lower hemisphere, equal area stereographic projections of XZ structural sections (foliation is the equatorial diameter E–W and the lineation is horizontal within that plane)

P–T evolution

In an attempt to model the stability of the primary mineral assemblage and the reactions of formation of subsequent mineral assemblages, a pseudosection for a representative bulk rock composition of harzburgite and its constituent minerals was calculated (Fig. 10) using Perple_X software (Connolly 2005). The bulk rock composition of the harzburgite studied is SiO_2:Al_2O_3:FeO:MgO:CaO 40.29:2.44:7.46:37.21:1.57. Thermodynamic data were taken from the internally consistent database of Holland and Powell (1998), whereas the solid solutions used for the calculations are from Holland and Powell (1998) for olivine and spinel, from Holland and Powell (1996) for orthopyroxene and clinopyroxene, and from Holland et al. (1998) for chlorite. Amphibole models are not still well developed, at least for high pressures and temperatures. The model that best fits those of high-grade rocks is the ideal binary Mg–Fe solid solution model. Also, since amphibole is replacing the clinopyroxene and is the only Ca-bearing phase, all amphibole models are based on this solid solution for the calculus. Talc and antigorite (the Atg model is the only existing one) were treated as ideal binary Fe–Mg solid solutions. The fluid phase, assumed as pure

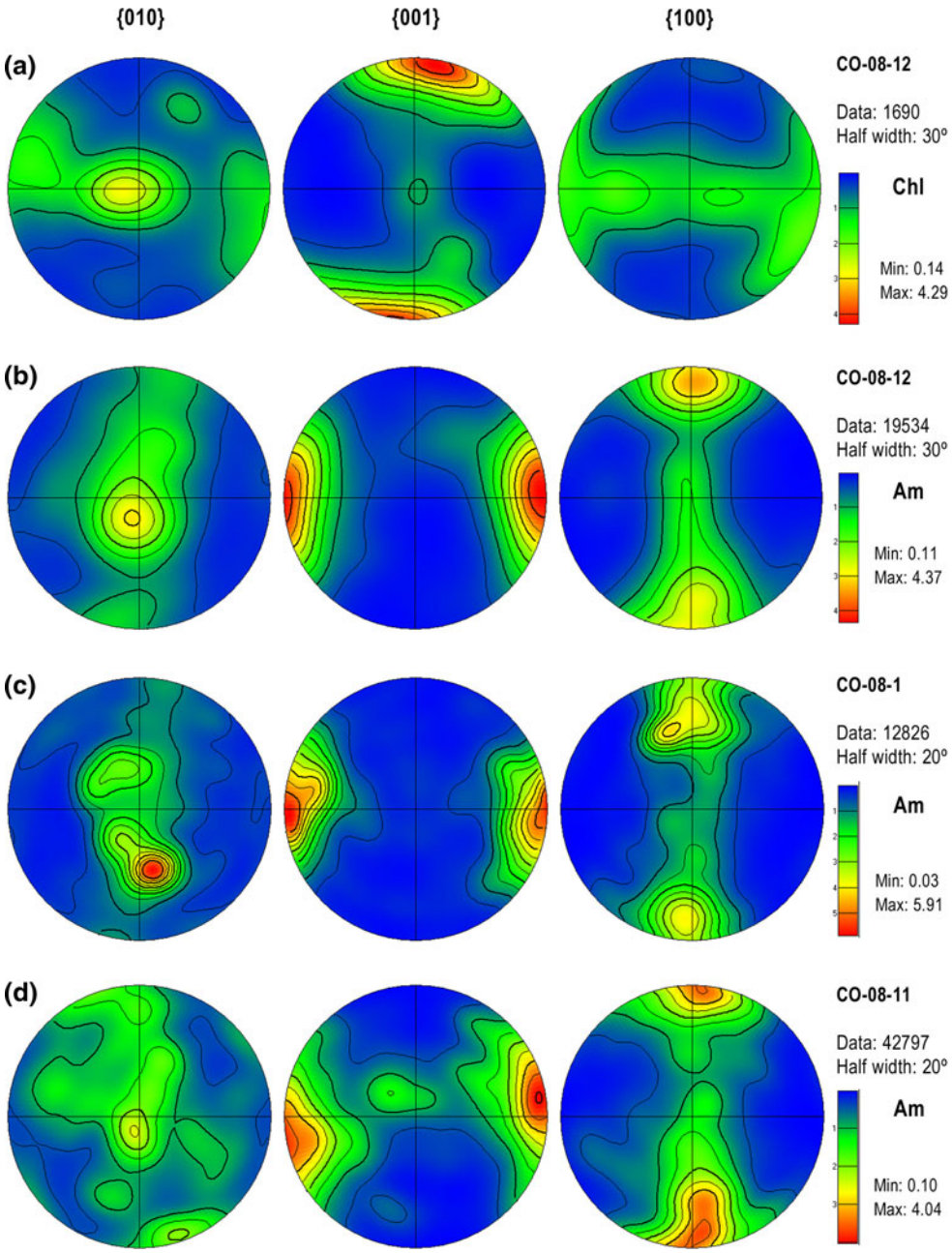

Fig. 9 Orientations of the poles to chlorite (**a**) and amphibole (**b–d**) {010}, {001} and {100} planes. Stereoplot color patterns represent multiples of mean uniform density. Lower hemisphere, equal area stereographic projections of XZ structural sections (foliation is the equatorial diameter E–W and the lineation is horizontal within that plane)

H_2O, is considered to be in excess. The rock was modeled in the CFMASH system. The dotted line in Fig. 10 represents the high-temperature stage of recrystallization at >800°C and 1.6 GPa calculated by Girardeau and Gil Ibarguchi (1991) for the garnet pyroxenites (including olivine-websterites) within peridotites of the Herbeira massif using conventional thermobarometry. The solid line path represents the exhumation history of the Complex as inferred from retrograde assemblages in high-pressure granulites and eclogites associated with the ultramafic rocks (Mendia et al. 2001; Puelles et al. 2005).

Discussion

The data available so far have permitted to probe that the fold nappes making up the Upper Allochthon in the Cabo Ortegal Complex represent a complex train of kilometer-scale sheath folds (Azcárraga et al. 2002) depicting the structural style characteristic of rocks deforming in a deep subduction setting (Ábalos et al. 2003). So far, these large folds had been recognized in all the units that conform the structural assemblage, except for the Herbeira and Limo peridotite massifs. Identification of mesoscale sheath folds

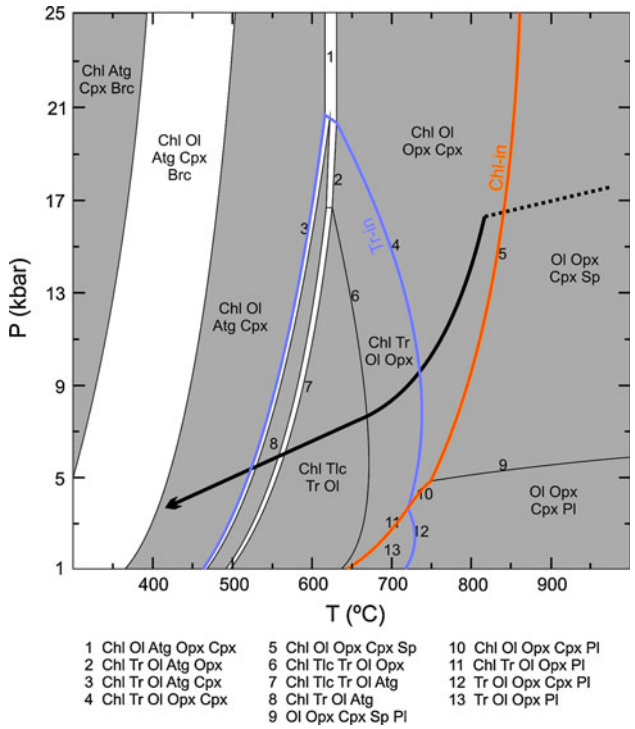

Fig. 10 Phase diagram section for the Limo Harzburgite calculated with Perple_X. *Blue* and *orange lines* represent the stability fields of tremolite (*Tr*) and chlorite (*Chl*), respectively. *Dotted line* for peak metamorphic conditions after Girardeau et al. (1989) and Girardeau and Gil Ibarguchi (1991); retrogression path after Mendia et al. (2001) and Puelles et al. (2005)

in these massifs has been precluded by the homogeneous and altered character of the harzburgitic outcrops, on one hand, and to the inaccessibility of the area, on the other hand. However, the new field data presented in this study for the Limo peridotite massif have revealed that what was supposed to be an exception is in fact a conspicuous structural feature. The observations made along the cliffs on the seashore have made possible to establish that the entire massif is actually a pileup of meter-scale sheath folds with the same orientation as that recognized in folds from other lithostratigraphic units of the Upper Allochthon. Its large-scale geometry corresponds to an asymmetric synform (Fig. 1c) with the western limb thicker than the eastern one. The maximum thickness measured along the normal to the subhorizontal foliation is 750 m. All the described and recognized sheath folds exhibit tubular 3D geometries, with isoclinal morphologies and extreme limb elongations in outcrop surfaces parallel to the XZ structural sections. Characteristic eye-shaped closed geometries have been found in sections perpendicular to the macroscopic lineation. All the structures show a clear monoclinic symmetry, pointing to the existence of non-coaxial components of the deformation related to a top-to-the-NE tectonic displacement of the hanging wall blocks. A renewed structural inspection in the course of the present study of the Uzal peridotite outcrops along the Cartés section and of the megaboudin-like structures and isoclinal folds described by Girardeau and Gil Ibarguchi (1991) from the peridotite-pyroxenite Herbeira massif points to the occurrence of abundant sheath folds there arranged in trains decameter to hectometer in size across the foliation, as in the Limo peridotite massif.

The study of the crystallographic preferred orientation distributions obtained for the primary minerals in equilibrium has permitted to obtain very valuable information on the evolution of the Limo harzburgite. On the one hand, the LPO patterns obtained for olivine show a weak submaximum of [100] axes around the lineation in almost all the samples, along with a strong maximum for [010] axes close to the pole to the foliation. This fabric corresponds to the A-type of Jung and Karato (2001) and was explained in terms of dislocation creep on (010) planes along the [100] direction (Durham et al. 1977; Darot and Gueguen 1981; Karato et al. 1986; Hirth and Kohlstedt 1995). This slip system would be operative under high-temperature conditions and low water fugacity at low stress levels (Jung et al. 2006; Zhang and Karato 1995), as it has been reported for olivine in naturally deformed peridotites from depleted lithosphere (e.g., Jung 2009; Machek et al. 2009). On the other hand, the strongest olivine fabrics denote a systematic presence of [001] and [010] axes around the X and Z structural directions, respectively. The parallelism between the crystallographic elements and the shear plane and shear direction would indicate that the activity of the [001](010) slip system in olivine was also responsible for the accommodation of part of the deformation registered in these rocks. This LPO pattern corresponds to the B-type of Jung and Karato (2001). Experimental studies have shown that the activity of olivine slip systems can be affected by variations in pressure (Mainprice et al. 2005; Jung et al. 2009) and water content (Chopra and Paterson 1984; Mackwell et al. 1985). Accordingly, modification in the water content and stress has been invoked to explain the change from the [100] to [001] Burger vector (Jung and Karato 2001; Katayama et al. 2004; Jung et al. 2006). Thus, the B-type fabric would point to lower temperatures and higher water fugacity and stress levels, as it has been mostly proposed for deformations in the mantle wedge above a subducted plate (Kneller et al. 2007). B-type LPOs have been reported in natural rocks, such as deformed peridotites in the Yushigou peridotite of China (Song and Su 1998), the Almklovdalen massif of southern Norway (Cordellier et al. 1981), the Sanbagawa metamorphic belt of Japan (Mizukami et al. 2004), the Cima di Gagnone area of Switzerland (Skemer et al. 2006), and the Val Malenco of Italy (Jung 2009). This work reports a new occurrence of the olivine B-type LPO in harzburgites from the Cabo Ortegal Complex (Spain).

The change from the A-type to the B-type LPO in olivine may have interesting implications for unraveling the evolution of the mantle wedge zone in the particular case of the Cabo Ortegal Complex. While the rest of the lithotypes that presently make up the Upper Allochthon were affected by subduction processes (Ábalos et al. 2003; Puelles 2004), the Limo harzburgite represented a different scenario where a "hot" and initially dry mantle was experiencing low stress deformations preserved by A-type olivine LPOs. The subsequent incorporation of the fluids released by dehydration of hydrous minerals within the subducting slab led to a change in the rheology of the mantle wedge rocks, as it has already been suggested in a number of works (e.g., Peacock 1993; Hirth and Kohlstedt 2003). This was the case for the Limo and Herbeira massifs, where the presence of H_2O-rich fluids is clearly attested by the abundance of chlorite and amphibole formed after preexistent anhydrous minerals. A related effect of the fluids would promote lowering of the solidus T in portions of the mantle wedge and whereby the production of melts. These melts, through segregation and deformation of the products, account for the conspicuous occurrence of dunite-harzburgite-pyroxenite compositional banding in some sections of the Ortegal ultramafic massifs, particularly in Herbeira. This banding is now seen parallel to the weak tectonic foliation originated in the tectonites. As these rocks became directly involved in the subduction, the ambient conditions changed dramatically and induced a change in operative olivine intracrystalline slip systems. B-type olivine LPO patterns recorded deformations under lower temperature conditions and higher water fugacity and stress levels. Meanwhile, the rest of the units conforming the Upper Allochthon (peridotites, eclogites and high-pressure gneisses) were experiencing increasing temperature and pressure in the active subduction zone (Puelles 2004). It was during the subsequent process of accretion (Fig. 11) when the Limo harzburgite developed the deformational features related to deformation in deep tectonic realms of an oblique subduction/collision orogenic channel described by Ábalos et al. (2003).

The CPO displayed by the other minerals of the peridotite equilibrium assemblage can also provide some information on the deformational processes operative in these rocks. Clinopyroxene has been traditionally used to characterize the strain geometry and kinematics (Helmstaedt et al. 1972; Avé Lallemant 1978; Buatier et al. 1991; Boundy et al. 1992; Godard and Van Roermund 1995), being the most common slip systems ½ < 110 > {110}, [001]{110} and [001](100) (e.g., Godard and van Roermund 1995; Mauler et al. 2001; Bascou et al. 2002). The LPO patterns found in the clinopyroxenes of the Limo harzburgite belong to the "L-type" of Helmstaedt et al. (1972), interpreted as an indicators of constriction conditions during deformation. This strain geometry might have also controlled the crystal growth, as a predominance of crystals with [010] axes oriented normal to the lineation and [001] axes parallel to it is favoured by the higher elastic modulus of [001] crystallographic directions (Bass 1995). The fabrics depicted by orthopyroxene crystals, in turn, correspond to the AC-type LPO patterns of Jung et al. (2010), which are interpreted as indicating dominant dislocation glide on (100) crystallographic planes along the [001] direction. These patterns are similar to those obtained for naturally deformed rocks where [001] axes tend to orientate parallel to the stretching lineation and (100) or (010) planes parallel the foliation (e.g., Etheridge 1975; Ross and Nielsen 1978; Sawaguchi and Ishii 2003). The orthopyroxene LPOs show coincidence between their (100) planes and the (010) planes in olivine.

The orientation of [001] crystallographic axes in olivine, clinopyroxene and orthopyroxene is fairly constant (Figs. 7, 8). It can be observed that slip directions run parallel to the macroscopic stretching and mineral lineations recognized both at the outcrop and microscopic scales, thus representing the shear direction. The asymmetry of the obtained LPO patterns with respect to the external structural reference system provided by the foliation and lineation is in agreement with the constant shear sense criteria observed at the outcrop scale. In all cases, they point to a top-to-the-NE tectonic displacement of the hanging wall blocks.

The calculated pseudosection is consistent with the petrographic evidence found in the peridotites under study. They show a primary olivine-clinopyroxene-orthopyroxene-spinel mineral assemblage and formation of oriented chlorite after spinel at the beginning of the exhumation-related shear deformation events that affected the ultramafic massifs. This reaction occurs in a narrow near-isothermal area around 800°C (solid line labeled Chl-in, Fig. 10). This early deformational stage would be responsible for the LPO patterns observed in chlorite and its shape-preferred orientation in accord with that of the phases that make up the primary mineral assemblage in equilibrium. As it has been previously described for other phyllosilicates, the deformation of chlorite would be dominated by the very easy slip along (001) planes and the ability to form subgrain boundaries subparallel to (001) by dislocation climb and the activation of hard slip systems (Bons 1988).

During the ascent to the surface, these rocks would have reached the amphibole stability field (solid line labeled Tr-in, Fig. 10), which develops after clinopyroxene at slightly lower temperatures than 700°C. This stage is likewise extensively recorded in the mafic rocks of the Cabo Ortegal Complex. Thus, amphibole LPOs provide information on the later retrogression active processes during the

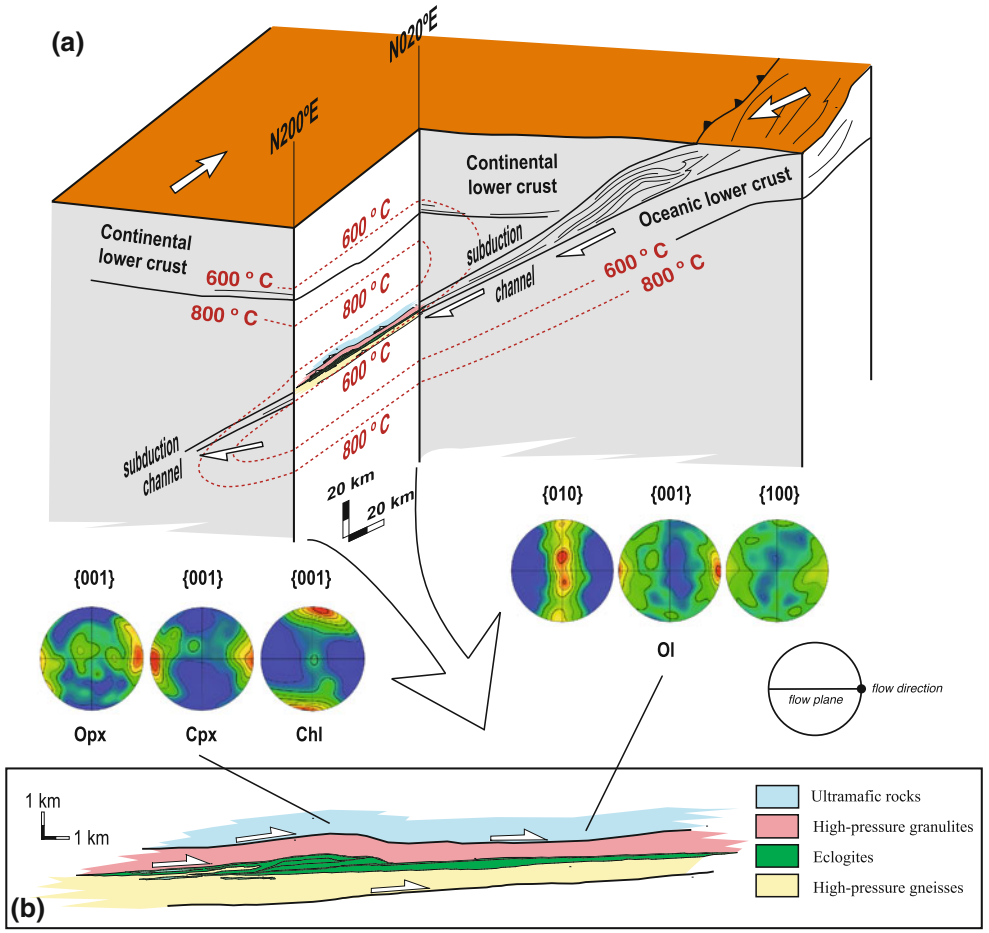

Fig. 11 **a** Tectonic model established for the Upper Allochthon of the Cabo Ortegal Complex, including the traces of the 600 and 800°C isotherms. **b** Reconstructed section of these units in a projection plane perpendicular to the foliation and parallel to the high-pressure lineation. Note the LPO patterns obtained for the high-pressure mineral assemblage

subsequent exhumation of these rocks. These patterns mimic those of clinopyroxene, though they are stronger, suggesting that its orientation resulted from epitaxial growth after static replacement of the primary clinopyroxene. The point-maximum defined by the orientation of the poles to the {001} planes parallel to the lineation, as well as that revealed by the orientation of the poles to {100} close to the Z structural direction, have been described in previous studies of amphibole LPO (e.g., Gapais and Brun 1981; Siegesmund et al. 1989, 1994; Kruhl and Huntemann 1991; Ji et al. 1993; Barruol and Kern 1996; Ivankina et al. 2005; Díaz Azpiroz et al. 2007; Tatham et al. 2008). This pattern is often interpreted in terms of the operation of <001> slip on (100) crystallographic planes. This intracrystalline slip system has been already detected in naturally deformed amphiboles at medium- to high-temperature conditions (over 650°C) (Rooney et al. 1975; Biermann and van Roermund 1983; Cumbest et al. 1989; Reynard et al. 1989; Hacker and Christie 1990; Skrotzki 1990, 1992, Kenkmann and Dresen 2002; Baratoux et al. 2005). These temperatures are in agreement with those depicted by the phase diagram elaborated for these rocks (Fig. 10), where amphibolite facies conditions were reached for $T > 700$°C.

As the temperature decreased, other mechanisms such as twinning, solution mass transfer, and dissolution-precipitation creep became more important (e.g., Dollinger and Blacic 1975; Biermann 1981; Imon et al. 2002). At temperatures ranging from >700°C to the lower epidote amphibolite facies, rigid-body rotation (e.g., Shelley 1994; Berger and Stünitz 1996; Díaz Azpiroz et al. 2007) has also been considered to play an important role in textural and shape-preferred orientation development. In fact, at even lower pressures and temperatures than those of amphibole formation, other reactions of hydration were responsible for the appearance of secondary minerals such as talc or serpentine (Atg in Fig. 10) in the ultramafic lithotypes. Subsequent deformation processes under greenschist-facies conditions took place before continental collision and plate blocking in the Early Carboniferous (Puelles 2004).

Conclusions

The Limo harzburgite massif has undergone a complex deformation history, as it can be inferred from the study of phase diagram sections and LPO patterns of equilibrium mineral assemblages. Thus, olivine A-type LPO patterns would indicate the activity of deformation mechanisms such as dislocation creep, mainly on (010) crystallographic planes along the [100] direction, under high-temperature conditions at low stress levels in a "hot" suprasubduction mantle. The change to B-type LPO patterns, coherent with the onset of the [001](010) slip system, would reflect a drastic change in the rheology of these materials at lower temperatures and higher stress levels, accompanied by the presence of fluids and melts derived from the subducting plate. These changes would correspond to the incorporation of these rocks to the active subduction channel under constriction conditions, as suggested by the clinopyroxene L-type fabrics. At this stage, the peridotite massifs acquired deformational structures such as the described hectometer-scale pileup of sheath folds and the outstanding linear fabrics. Meanwhile, the rest of the units of the Upper Allochthon at Cabo Ortegal (eclogites, high-pressure granulites and high-pressure gneisses) suffered pressurization and increasingly higher temperatures in this subduction realm (Ábalos et al. 2003; Puelles 2004). The high-pressure deformation event occurring in the subduction conduit continued with the stack of the different units of the Upper Allochthon of the Cabo Ortegal.

After the stacking of the different units, the entire ensemble shared a common metamorphic and tectonic history during exhumation. At an initial stage of the exhumation process undergone by these rocks, chlorite formed after spinel and deformed plastically, mainly due to slip on (001) planes accompanied by dislocation climb and activation of hard slip systems. During the subsequent stages, the retrogressive amphibolitization process proceeded to such an extent that some layers of primary clinopyroxene were completely replaced by secondary amphibole. Amphibole LPOs mimic those of clinopyroxene, though they are stronger. We interpret that its preferred orientation resulted from epitaxial growth after static replacement of the primary clinopyroxene, though components of intracrystalline [001] slip on (100) crystallographic planes at temperatures over 650°C, assisted by dynamic recrystallization, cannot be excluded.

Acknowledgments Financial support was provided by the Spanish Ministerio de Ciencia e Innovación (Grupo Consolidado, project CGL2008-01130/BTE) and the Universidad del País Vasco (project GIU09/61). The authors also want to express their appreciations to F. Deschamps and an anonymous reviewer for critically reading the manuscript and making several useful remarks.

References

Ábalos B, Azcárraga J, Gil Ibarguchi JI, Mendia MS, Santos Zalduegui JF (1996) Flow stress, strain rate and effective viscosity evaluation in a high-pressure nappe (Cabo Ortegal, Spain). J Metamorph Geol 14:227–248

Ábalos B, Puelles P, Gil Ibarguchi JI (2003) Structural assemblage of high-pressure mantle and crustal rocks in a subduction channel (Cabo Ortegal, NW Spain). Tectonics. doi:10.1029/2002TC001405

Achenbach K, Cheadle M, Faul U, Kelemen P, Swapp S (2011) Lattice-preferred orientation and microstructure of peridotites from ODP Hole 1274A (15°39′N), Mid-Atlantic Ridge: testing models of mantle upwelling and tectonic exhumation. Earth Planet Sci Lett 301:199–212

Arenas R, Díaz García F, Martínez Catalán JR, Abati J, González Cuadra P, Andoanegui P, González del Tánago J, Rubio Pascual F, Castiñeiras P, Gómez Barreiro J (2000) Structure and evolution of the Ordenes Complex. Basement Tectonics 15, Pre-conference field trip. La Coruña, p 160

Avé Lallemant HG (1978) Experimental deformation of diopside and websterite. Tectonophysics 48:1–27

Azcárraga J, Ábalos B, Gil Ibarguchi JI (2002) On the relationship between km-scale sheath folds, ductile thrusts and minor structures in the basal high-pressure units of the Cabo Ortegal complex (NW Spain). J Struct Geol 24:1971–1989

Baratoux L, Schulmann K, Ulrich S, Lexa O (2005) Contrasting microstructures and deformation mechanisms in metagabbro mylonites contemporaneously deformed under different temperatures (c. 650°C and c. 750°C). In: Gapais D, Brun JP, Cobbold PR (eds) Deformation mechanisms, rheology and tectonics: from minerals to the lithosphere. J Geol Soc London Spec Publ 243: 97–125

Barruol G, Kern H (1996) Seismic anisotropy and shear-wave splitting in lower-crustal and upper-mantle rocks from the Ivrea Zone-experimental and calculated data. Phys Earth Planet In 95:175–194

Bascou J, Tommasi A, Mainprice D (2002) Plastic deformation and development of clinopyroxene lattice-preferred orientation in eclogites. J Struct Geol 24:1357–1368

Bass JD (1995) Elasticity of minerals, glasses and melts. In: Ahrens TJ (ed) Handbook of physical constants: mineral physics and crystallography. AGU, Washington, pp 45–63

Ben Jamaa N (1988) Les peridotites de Bay of Islands (Terre Neuve) et de Cap Ortegal (Espagne): approche petro-structurale. Dissertation, Université Paris

Berger A, Stünitz H (1996) Deformation mechanisms and reaction of hornblende: examples from the Bergell tonalite (Central Alps). Tectonophysics 257:149–174

Biermann C (1981) (100) deformation twins in naturallydeformed amphiboles. Nature 292:821–823

Biermann C, van Roermund HLM (1983) Defect structures in naturally deformed clinoamphibole—a TEM study. Tectonophysics 95:267–278

Bons J (1988) Deformation of chlorite in naturally deformed low-grade rocks. Tectonophysics 154:149–165

Boundy TM, Fountain DM, Austrheim H (1992) Structural development and petrofabrics of eclogite facies shear zones, Bergen Arcs, western Norway: implications for deep crustal deformational processes. J Metamorph Geol 10:127–146

Buatier M, van Roermund HLM, Drury MR, Lardeaux JM (1991) Deformation and recrystallization mechanisms in naturally deformed omphacites from the Sesia-Lanzo zone: geophysical consequences. Tectonophysics 195:11–27

Chopra PN, Paterson MS (1984) The role of water in the deformation of dunite. J Geophys Res 89:7861–7876

Connolly JAD (2005) Computation of phase equilibria by linear programming: a tool for geodynamic modeling and its application to subduction zone decarbonation. Earth Planet Sci Lett 236:524–541

Cordellier F, Boudier F, Boullier AM (1981) Structural study of the Almklovdalen peridotite massif (Southern Norway). Tectonophysics 77:257–281

Cumbest R, van Roermund HLM, Drury MR, Simpson C (1989) Burgers vector determination in clinoamphibole by computer simulation. Am Miner 74:586–592

Dale J, Holland T, Powell R (2000) Hornblende-garnet-plagioclase thermobarometry: a natural assemblage calibration of the thermodynamics of hornblende. Contrib Miner Petrol 140:353–362

Dallmeyer RD, Martínez Catalán JR, Arenas R, Gil Ibarguchi JI, Gutiérrez Alonso G, Farias P, Bastida F, Aller J (1997) Diachronous variscan tectonothermal activity in the NW Iberian Massif: evidence from 40Ar/39Ar dating of regional fabrics. Tectonophysics 277:307–337

Darot M, Gueguen Y (1981) High-temperature creep of forsterite single crystals. J Geophys Res 86(B7):6219–6234

Díaz Azpiroz M, Lloyd GE, Fernández C (2007) Development of lattice preferred orientation in clinoamphiboles deformed under low-pressure metamorphic conditions—a SEM/EBSD study of metabasites from the Aracena metamorphic belt, SW Spain. J Struct Geol 29:629–645

Dollinger G, Blacic JD (1975) Deformation mechanisms in experimentally and naturally deformed amphiboles. Earth Planet Sci Lett 26:409–416

Droop GTR (1987) A general equation for estimating Fe3+ concentrations in ferromagnesian silicates and oxides from microprobe analyses, using stoichiometric criteria. Miner Mag 51:431–435

Durham WB, Goetze C, Blake B (1977) Plastic flow of oriented single crystals of olivine: observations and interpretations of dislocation structures. J Geophys Res 82(36):5755–5770

Etheridge MA (1975) Deformation and recrystallization of orthopyroxene from Giles Complex, Central Australia. Tectonophysics 25:87–114

Gapais D, Brun JP (1981) A comparison of mineral grain fabrics and finite strain in amphibolites from eastern Finland. Can J Earth Sci 18:995–1003

García de Madinabeitia S, Sánchez Lorda ME, Gil Ibarguchi JI (2008) Simultaneous determination of major to ultratrace elements in geological samples by fusion-dissolution and inductively coupled plasma mass spectrometry techniques. Anal Chim Acta 625(2):117–130

García Izquierdo B (2005) Evolución geodinámica y procesos mantélicos en el Macizo de Herbeira, complejo de Cabo Ortegal (NO de la Península Ibérica). Dissertation, Universidad Complutense de Madrid

Gil Ibarguchi JI, Ábalos B, Azcárraga J, Mendia M, Puelles P (2000) A petrological and structural excursion through the high-grade/high-pressure allochthonous units of the Cabo Ortegal Complex (NW Spain). In: Basement Tectonics 15, Mid-conference field trip. La Coruña, pp 1–59

Girardeau J, Gil Ibarguchi JI (1991) Pyroxenite-rich peridotites of the Cabo Ortegal Complex (Northwestern Spain): evidence for large-scale upper-mantle heterogeneity. J Petrol Special Lherzolites Issue, pp 135–154

Girardeau J, Gil Ibarguchi JI, Ben Jamaa N (1989) Evidence for a heterogeneous upper mantle in the Cabo Ortegal Complex, Spain. Science 245:1231–1233

Godard G, van Roermund L (1995) Deformation-induced clinopyroxenes fabrics from eclogites. J Struct Geol 17(10):1425–1443

Gravestock PJ (1992) The chemical causes of uppermost mantle heterogeneities. Dissertation, Open University

Hacker BR, Christie JM (1990) Brittle/ductile and plastic/cataclastic transition in experimentally deformed and metamorphosed amphibolite. In: Duba AG, Durham WB, Handin JW, Wang HF (eds) The brittle-ductile transition in rocks. AGU, Geophysical Monograph, pp 127–148

Helmstaedt H, Anderson OL, Gavasci AT (1972) Petrofabric studies of eclogite, spinel-websterite, and spinel-lherzolite xenoliths from kimberlite-bearing breccia pipes in southeastern Utah and northeastern Arizona. J Geophys Res 77:4350–4365

Hirth G, Kohlstedt DL (1995) Experimental constraints on the dynamics of the partially molten upper mantle: deformation in the diffusion creep regime. J Geophys Res 100:1981–2001

Hirth G, Kohlstedt D (2003) Rheology of the upper mantle and the mantle wedge: a view from the experimentalists. In: Eiler J (ed) Inside the subduction factory. AGU, Geophysical Monograph: 138. Washington, pp 88–105

Holland TJB, Powell R (1996) Thermodynamics of order–disorder in minerals. Symmetric formalism applied to solid solutions. Am Miner 81:1425–1437

Holland TJB, Powell R (1998) An internally consistent thermodynamic data set for phases of petrological interest. J Metamorph Geol 16:309–343

Holland TJB, Baker J, Powell R (1998) Mixing properties and activity-composition relationships of chlorites in the system MgO–FeO–Al2O3–SiO2–H2O. Eur J Mineral 10:395–406

Holtzman BK, Kohlstedt DL, Zimmerman ME, Heidelbach F, Hiraga T, Hustoft J (2003) Melt segregation and strain partitioning: implications for seismic anisotropy and mantle flow. Science 301:1227–1230

Imon R, Okudaira T, Fujimoto A (2002) Dissolution and precipitation processes in the deformed amphibolites: an example from the ductile shear zone of the Ryoke metamorphic belt, SW Japan. J Metamorph Geol 20:297–308

Ivankina TI, Kern HM, Nikitin AN (2005) Directional dependence of P- and S-wave propagation and polarization in foliated rocks from the Kola superdeep well: evidence from laboratory measurements and calculations based on TOF neutron diffraction. Tectonophysics 407:25–42

Ji S, Salisbury MH, Hammer S (1993) Petrofabric, P-wave anisotropy and seismic reflectivity of high-grade tectonites. Tectonophysics 222:195–226

Jung H (2009) Deformation fabrics of olivine in Val Malenco peridotite found in Italy and implications for the seismic anisotropy in the upper mantle. Lithos 109:341–349

Jung H, Karato S (2001) Water-induced fabric transitions in olivine. Science 293:1460–1463

Jung H, Katayama I, Jiang Z, Hiraga T, Karato S (2006) Effect of water and stress on the lattice-preferred orientation of olivine. Tectonophysics 421:1–22

Jung H, Mo W, Green HW (2009) Upper mantle seismic anisotropy resulting from pressure-induced slip transition in olivine. Nat Geosci 2:73–77

Jung H, Park M, Jung S, Lee J (2010) Lattice preferred orientation, water content, and seismic anisotropy of orthopyroxene. J Earth Sci 21:555–568

Karato S, Wu P (1993) Rheology of the upper mantle: a synthesis. Science 260:771–778

Karato S, Paterson M, Fitzgerald JD (1986) Rheology of synthetic olivine aggregates: influence of grain size and water. J Geophys Res 91:8151–8176

Katayama I, Jung H, Karato S (2004) New type of olivine fabric from deformation experiments at modest water content and low stress. Geology 32:1045–1048

Kenkmann T, Dresen G (2002) Dislocation microstructure and phase distribution in a lower crustal shear zone: an example from the Ivrea Zone, Italy. Int J Earth Sci 91:445–458

Kneller EA, van Keken PE, Katayama I, Karato S (2007) Stress, strain, and B-type olivine fabric in the fore-arc mantle: sensitivity tests using high-resolution steady-state subduction zone models. J Geophys Res Solid Earth 112:B004406

Kohlstedt DL, Goetze C (1974) Low-stress high-temperature creep in olivine single crystals. J Geophys Res 79(14):2045–2051

Kruhl JH, Huntemann T (1991) The structural state of the former lower continental crust in Calabria (S. Italy). Geol Rundsch 81:289–302

Laribi-Halimi A (1992) Relations géochimiques dans les péridotites et pyroxénites du Cabo Ortegal (Espagne): Application de l'analyse par activation neutronique. Dissertation, Université de Paris VI-IPGP

Lee KH, Jiang Z, Karato S (2002) A scanning electron microscope study of the effects of dynamic recrystallization on lattice preferred orientation in olivine. Tectonophysics 351:331–341

Maaskant P (1970) Chemical petrology of polymetamorphic ultramafic rocks from Galicia, NW Spain. Leidse Geol Meded 45:237–255

Machek M, Ulrich S, Janousek V (2009) Strain coupling between upper mantle and lower crust: natural example from the Bestvina granulite body, Bohemian Massif. J Metamorph Geol 27:721–737

Mackwell SJ, Kohlstedt DL, Paterson MS (1985) The role of water in the deformation of olivine single-crystals. J Geophys Res Solid Earth 90:1319–1333

Mainprice D, Tommasi A, Couvy H, Cordier P, Frost DJ (2005) Pressure sensitivity of olivine slip systems and seismic anisotropy of Earth's upper mantle. Nature 433:731–733

Marcos A, Farias P, Galán G, Fernández FJ, Llana Fúnez S (2002) Tectonic framework of the Cabo Ortegal Complex: a slab of lower crust exhumed in the Variscan orogen (northwestern Iberian Peninsula). Geol Soc Am Special Pap 364:143–162

Martínez Catalán JR, Arenas R, Díaz García F, Abati J (1997) Variscan accretionary complex of northwest Iberia: terrane correlation and succession of tectonothermal events. Geology 25:1103–1106

Mauler A, Godard G, Kunze K (2001) Crystallographic fabrics of omphacite, rutile and quartz in Vendeé eclogites (Armorican Massif, France). Consequences for deformation mechanisms and regimes. Tectonophysics 342:81–112

Mendia M, Gil Ibarguchi JI, Ábalos B (2001) Evolución metamórfica P-T-d-t y significado geodinámico de la unidad eclogítica del complejo de Cabo Ortegal (NO España). Cuad Labo Xeol Laxe 26:155–178

Mizukami T, Wallis SR, Yamamoto J (2004) Natural examples of olivine lattice preferred orientation patterns with a flow normal a-axis maximum. Nature 427:432–436

Moreno T, Gibbons W, Prichard HM, Lunar R (2001) Platiniferous chromitite and the tectonic settings of ultramafic rocks in Cabo Ortegal, NW Spain. J Geol Soc Lond 158:601–614

Morimoto N (1989) Nomenclature of pyroxenes. Can Miner 27:143–156

Nicolas A (1986) A melt extraction model based on structural studies in peridotites. J Petrol 27:999–1022

Ordóñez Casado B, Gebauer D, Schäfer HJ, Gil Ibarguchi JI, Peucat JJ (2001) A single Devonian subduction event for the HP/HT metamorphism of the Cabo Ortegal complex within the Iberian Massif. Tectonophysics 332:359–385

Peacock SM (1993) Large-scale hydration of the lithosphere above subducting slabs. Chem Geol 108:49–59

Peucat JJ, Bernard-Griffiths J, Gil Ibarguchi JI, Dallmeyer RD, Menot RP, Cornichet J, Iglesias Ponce de León M (1990) Geochemical and geochronological cross section of the deep variscan crust: the Cabo Ortegal high-pressure nappe (NW Spain). In: Matte Ph (ed) Terranes in the Variscan Belt of Europe and Circum-Atlantic Paleozoic Orogens. Tectonophysics 177:263–292

Prior DJ, Boyle AP, Brenker F, Cheadle MC, Day A, Lopez G, Potts GJ, Reddy S, Spiess R, Timms N, Trimby P, Wheeler J, Zetterstrom L (1999) The application of electron backscatter diffraction and orientation contrast imaging in the SEM to textural problems in rocks. Am Miner 84:1741–1759

Puelles P (2004) Deformación, metamorfismo y exhumación de las granulitas de alta presión de la Bacariza (Complejo de Cabo Ortegal, NO España). Nova Terra 23, Ediciós do Castro, Spain

Puelles P, Ábalos B, Gil Ibarguchi JI (2005) Metamorphic evolution and thermobaric structure of the subduction-related Bacariza high-pressure granulite formation (Cabo Ortegal Complex, NW Spain). Lithos 84:125–149

Reynard B, Gillet P, Williame C (1989) Deformation mechanisms in naturally deformed glaucophanes: a TEM and HREM study. Eur J Miner 1:611–624

Rooney TP, Riecker RE, Gavasci AT (1975) Hornblende deformation features. Geology 3:364–366

Ross JV, Nielsen KC (1978) High-temperature flow of wet polycrystalline enstatite. Tectonophysics 44:233–261

Santos Zalduegui JF, Schäfer U, Gil Ibarguchi JI, Girardeau J (1996) Origin and evolution of the Paleozoic Cabo Ortegal ultramafic-mafic complex (NW Spain): U-Pb, Rb-Sr and Pb–Pb data. Chem Geol 129:281–306

Santos Zalduegui JF, Schäfer U, GilI barguchi JI, Girardeau J (2002) Genesis of pyroxenite-rich peridotite at Cabo Ortegal (NW Spain): geochemical and Pb-Sr-Nd isotope data. J Petrol 43:17–43

Sawaguchi T, Ishii K (2003) Three-dimensional numerical modeling of lattice- and shape-preferred orientation of orthopyroxene porphyroclasts in peridotites. J Struct Geol 25:1425–1444

Shelley D (1994) Spider texture and amphibole preferred orientation. J Struct Geol 16:709–717

Siegesmund S, Takeshita T, Kern H (1989) Anisotropy of Vp and Vs in an amphibolite of the deeper crust and its relationship to the mineralogical microstructural and textural characteristics of the rock. Tectonophysics 157:25–38

Siegesmund S, Helmig K, Kruse R (1994) Complete texture analysis of a deformed amphibolite: comparison between neutron diffraction and U-stage data. J Struct Geol 16:131–142

Skemer P, Katayama I, Karato S (2006) Deformation fabrics of the Cima di Gagnone peridotite massif, Central Alps, Switzerland: evidence of deformation at low temperatures in the presence of water. Contrib Miner Petrol 152:43–51

Skrotzki W (1990) Microstructure in hornblende of a mylonitic amphibolite. In: Knipe RJ, Rutter EH (eds) Deformation mechanisms, rheology and tectonics. J Geol Soc Lond Spec Publ 54:321–325

Skrotzki W (1992) Defect structures and deformation mechanisms in naturally deformed hornblende. Phys Status Solidi 131:605–624

Song S, Su L (1998) Rheological properties of mantle peridotites at Yushigou in the North Qilian Mountains and their implications for plate dynamics. Acta Geol Sin (English Edition) 72:131–141

Soustelle V, Tommasi A, Demouchy S, Ionov A (2010) Deformation and fluid-rock interaction in the supra-subduction mantle: microstructures and water contents in peridotite xenoliths from the Avacha volcano, Kamchatka. J Petrol 51:363–394

Tatham D, Lloyd G, Butler R, Casey M (2008) Amphibole and lower crustal seismic properties. Earth Planet Sci Lett 267:118–128

Van Calsteren PWC, Boelrijk NAIM, Hebeda EH, Priem HNA, Den Tex E, Verdurmen EAT, Verschure RH (1979) Isotopic dating of older elements (including the Cabo Ortegal mafic-ultramafic complex) in the Hercynian orogen of NW Spain: manifestations

of a presumed early Palaeozoic mantle-plume. Chem Geol 24:35–56

Vogel DE (1967) Petrology of eclogite- and pyrigarnite-bearing polymetamorphic rock complex at Cabo Ortegal, NW Spain. Leidse Geol Meded 40:121–213

Zhang SQ, Karato S (1995) Lattice preferred orientation of olivine aggregates deformed in simple shear. Nature 375:774–777

Zimmerman ME, Kohlstedt DL (2004) Rheological properties of partially molten lherzolite. J Petrol 45(2):275–298

Chapter 2: Instrumentation

2. Instrumentation

The work carried out during this PhD Thesis has been mainly focussed on mass spectrometry analysis. To this purpose, two mass spectrometers have been used: (i) a high resolution multicollector inductively coupled plasma mass spectrometer (MC-ICP-MS, Neptune, Thermo Fisher Scientific, Figure 2.1; upgraded through the use of a large dry interface pump and specific cones, the so-called Jet interface), and (ii) a quadrupole inductively coupled plasma mass spectrometer (Q-ICP-MS, XSeries 2, Thermo Fisher Scientific, Figure 2.2; also with enhanced sensitivity through a dual pumping system). Whereas in the MC-ICP-MS, solid and liquid samples have been introduced, depending on the particular requirements of the analysis, in the Q-ICP-MS only solid samples have been analysed. For the solid samples analysis a Nd: YAG solid-state laser ablation system has been used (UP213, New Wave Research).

The above mentioned equipment is available at the Isotope Geochemistry and Geochronology facility (IBERCRON) of the University of the Basque Country UPV/EHU.

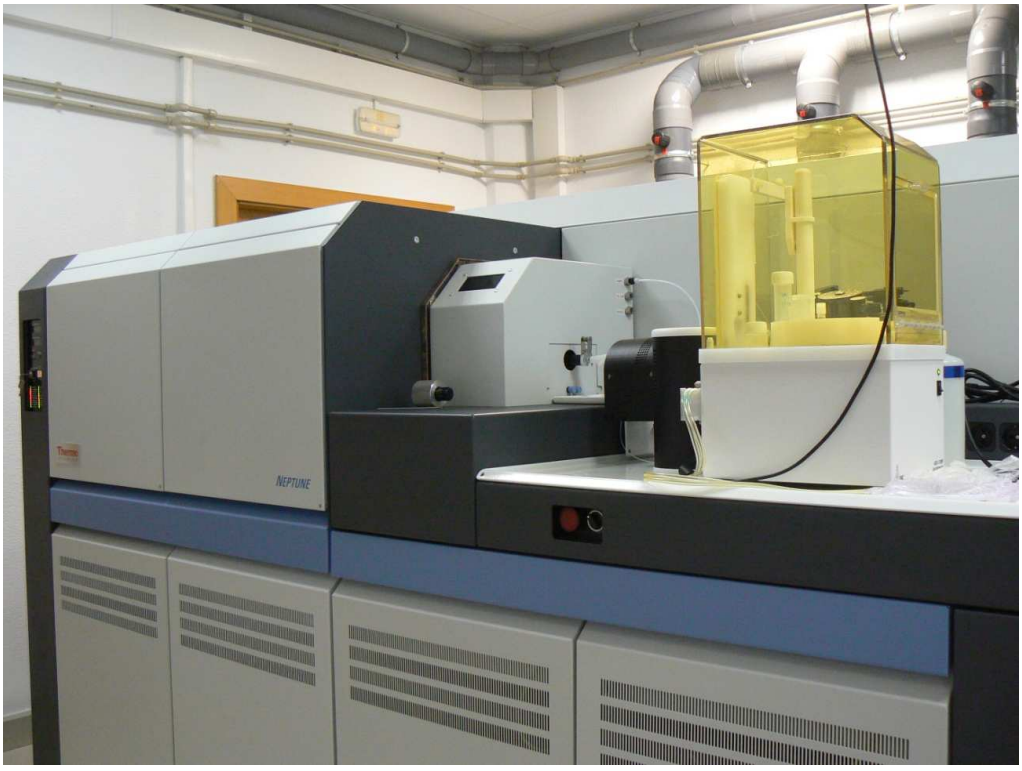

Figure 2.1. The Neptune MC-ICP-MS spectrometer used in this PhD Thesis.

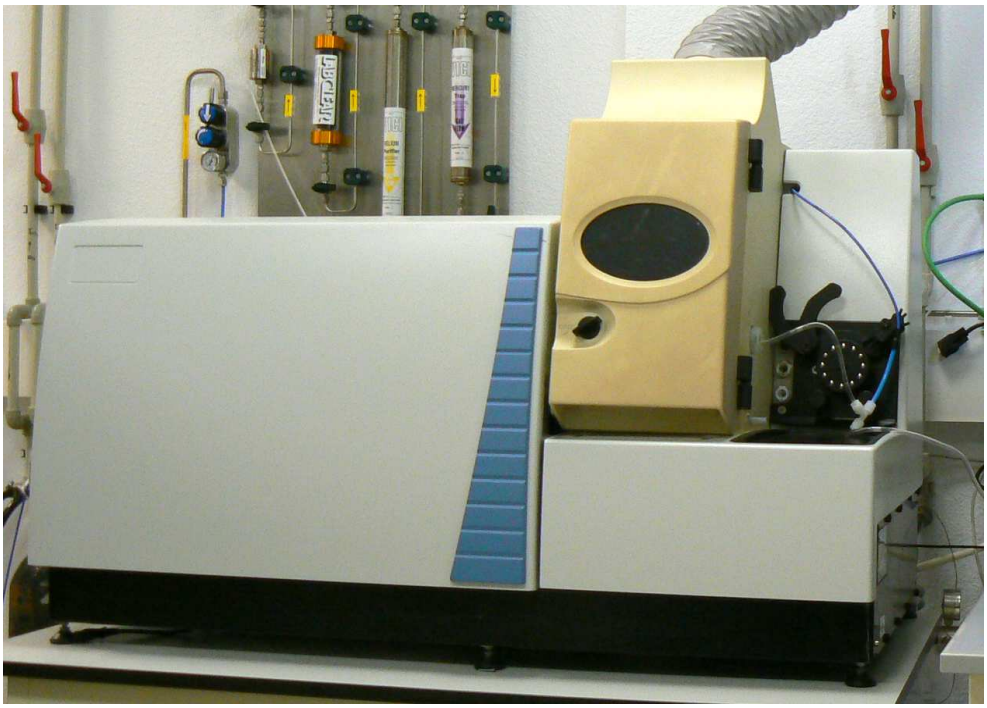

Figure 2.2. The XSeries2 Q-ICP-MS spectrometer used in this work.

Both spectrometers, as well as the laser ablation system, are installed in a laboratory with air conditioning and over-pressure filtered air (HEPA filter terminals and pre-filters). An uninterruptible power supply (UPS) unit ensures constant electric power supply to the spectrometers.

The basis of the mass spectrometry technique and the main features of the equipment employed, with a focus on specific requisites of the analyses carried out in our study, will be briefly described in the following sections. For extended descriptions of the instruments capabilities and other aspects related to plasma source mass spectrometry the reader is referred to a number of publications available in the literature, from classic ones to very recent monographies and manufacturer application notes (e.g., Taylor, 2001; Wieser and Schwieters, 2005; Hoffmann and Stroobant, 2007; Vanhaecke and Degryse, 2012; Prohaska et al., 2014; etc.).

2.1. Mass spectrometry

The mass spectrometry is a technique capable of analysing with great accuracy the composition of different chemical compounds and atomic isotopes, separating ions according to their mass-to-charge ratio(m/z). It may be used to identify different chemical elements forming a compound or to determine the isotopic content of different elements within the same compound.

The analysis via mass spectrometry has a simple basis, although the instrumentation used for it is extremely complex. In a simplified way, a spectrometer comprises the following parts: a sample introduction system, an ion generator, a mass analyser and a detector (Figure 2.3).

1.- The sample introduction system aims to introduce a small amount of sample in the apparatus. Usually the sample introduction system includes the vaporizing of it, either from the liquid or solid state. There are different introduction systems (Section 2.3).

2.- The aim of the ionization source is to ionize the elements or molecules that reach the mass spectrometer. Ionization can be achieved through different techniques, as for example, electron or molecules bombardment, or by using electrical or thermal energy. Indeed, there is a wide variety of ionization systems, being this a determining factor for the possible applications of the mass spectrometer. The energy applied during the ionization drastically affects the type of ions formed (polyatomic ions, isolated isotopes, complex molecules, etc.) and, thereby, the analytical possibilities of the equipment.

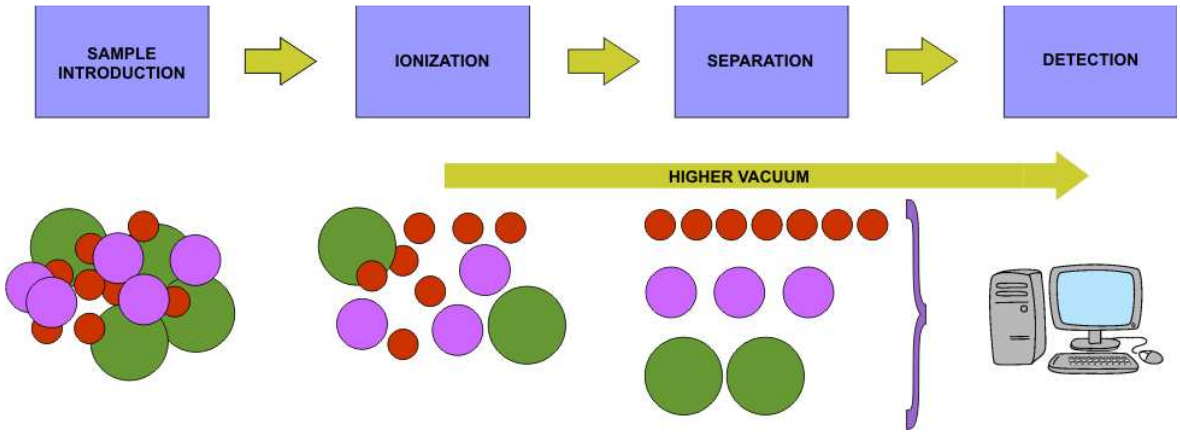

Figure 2.3. Basic scheme of a mass spectrometer.

3.- The mass analyser is the device responsible for the separation of the ions formed according to their mass/charge ratio (m/z). The most commonly used analysers are quadrupole, magnetic sector, time-of-flight and ion trap.

4.- The detector converts the ion beam into an electrical signal that can be processed and stored. The most commonly used detector is the secondary electrons multiplier (SEM), although there are others, generally less sensitive.

The combination of different sources with different separation systems allows a wide variety of spectrometer configurations, with different capabilities and applications. Therefore, the techniques employed usually combine various acronyms which refer to the ion source, the analyser and, in some cases, the detection system (GC-MS, Q-ICP-MS, TIMS, SIMS, SF-ICP-MS, VPD-ICP-MS, HPLC-ICP-MS, UHR-SEC-HPLC-ICP-MS, etc.).

2.1.a. Ionization source: ICP

The ionization source used in this work is the Inductively Coupled Plasma (ICP), the most common one in non-organic mass spectrometry. The most interesting feature of this source is the high temperature of the plasma (7,000-10,000 K) capable of breaking all the bonds within the samples, allowing elemental and isotopic analysis.

In order to create the plasma, argon gas is passed through a quartz torch and placed in an induction coil. It is here where a radio frequency energy between 750 and 1,700 W is applied, causing an intense electromagnetic field in its area of influence (Figure 2.4).

If a spark is applied to the argon (Ar) flowing through the torch, some electrons will be separated from the Ar atoms. These electrons are then trapped in the magnetic field and are accelerated in closed circular paths. This process is known as 'inductive coupling' and that is why the formed plasma is called inductively coupled plasma (ICP). The fast-moving electrons collide with neutral argon atoms, separating more electrons from atoms and thus, establishing a chain reaction. This collision process generates the high-temperature plasma, formed by neutral Ar atoms, positively charged Ar ions and electrons. The plasma will persist while the radio frequency is applied to the induction coil. The function of the plasma is to transform the sample, both solid and liquid, into ions. Thus, the sample, introduced as an aerosol, is immediately desolvated, atomized and vaporized, and finally, partially ionized.

The torch consists of three concentric quartz tubes through which Ar gas is passed with different flows. The sample is introduced through the innermost tube or injector. Argon flowing through the outer tube is the 'cooling gas' that will be converted into plasma. This gas, with a relatively high flow of ca. 15 l/min, is introduced tangentially into the torch to generate a circular flow. Thus, the plasma is separated from the quartz torch and prevents it from melting. The Ar introduced through the intermediate tube is called 'auxiliary gas' and the typical flow rate ranges from 0.45 l/min for the MC-ICP-MS to 0.7 l/min for the Q-ICP-MS. Its main function is to push away the plasma from the innermost tube, avoiding the melting of the injector. The torch is usually covered up with a cylindrical silver cover called 'torch screen' or 'guard electrode', which helps to increase the signal of the instrument (Figures 2.5). Finally, the torch is surrounded by 3 loops of a copper induction coil, through which water is passed in order to cool the coil and maintain a stable functioning (Figure 2.6). The induction coil is connected to a radio frequency source, creating a magnetic field inside the coil and at the end of the torch.

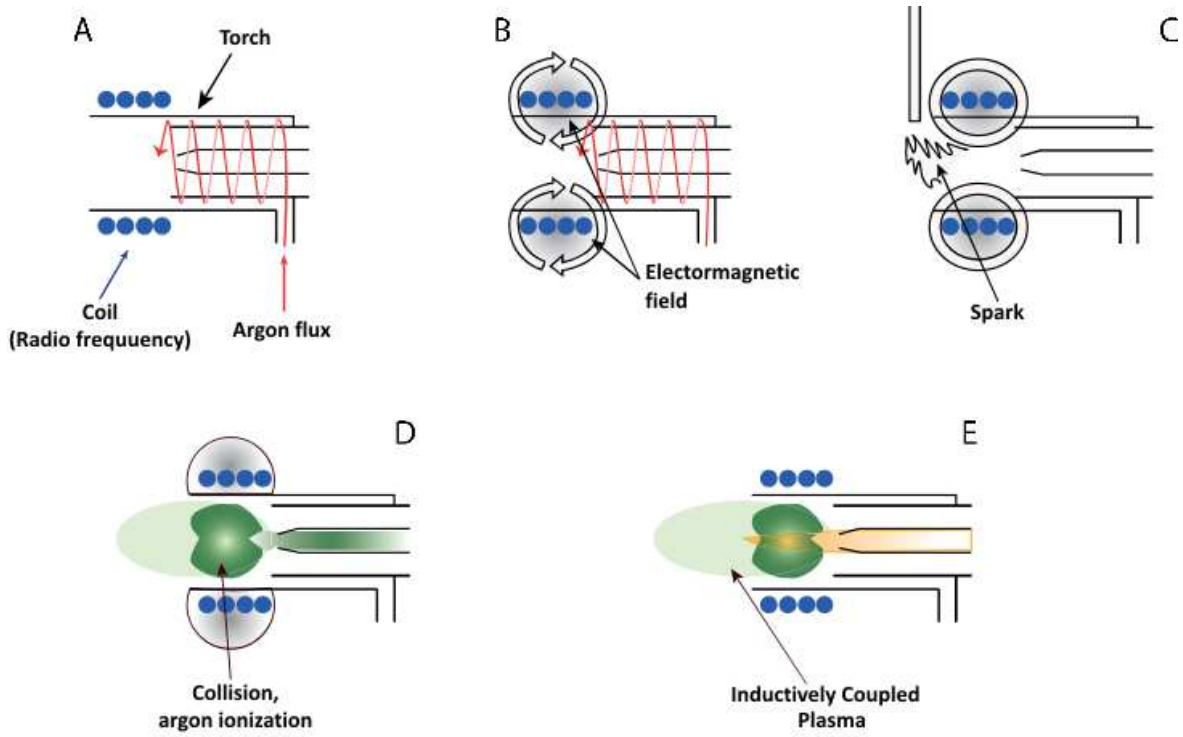

Figure 2.4. Scheme of the plasma generation process.

The most important difference between the torches used in the mass spectrometers for study lies in their geometry. Whereas the Q-ICP-MS torch consists of a single piece of quartz, that of the MC-ICP-MS is removable and has a sapphire injector. There is no difference in the plasma generation process.

2.1.b. Interface

The main function of the interface is to guide those ions produced in the plasma source to the mass analyser maintaining the vacuum conditions. This is crucial, since the ion source is at atmospheric pressure whereas the mass analyser works under high-vacuum conditions.

The interface is composed of two metal cones with a very small hole in the centre, the so-called ‘sampler cone’ and ‘skimmer cone’ (Figure 2.7). To achieve the required vacuum conditions in the area between the two cones, vacuum pumps are used and set up every day before the plasma ignition. In addition, there is a separatingvalve, called ‘slide valve’ or ‘skimmer valve’ that keeps the needed vacuum conditions in the mass analyser and that is opened only when suitable vacuum conditions are reached in the interface.

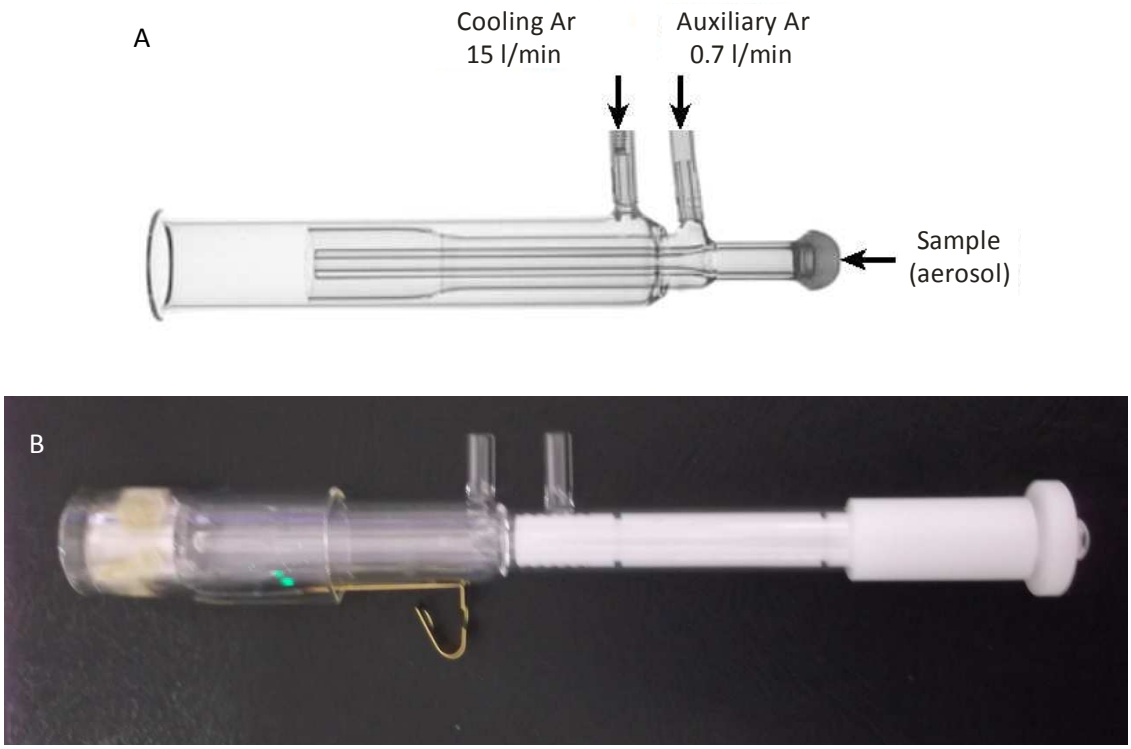

Figure 2.5. Torches used in this PhD Thesis. A: Q-ICP-MS. B: MC-ICP-MS.

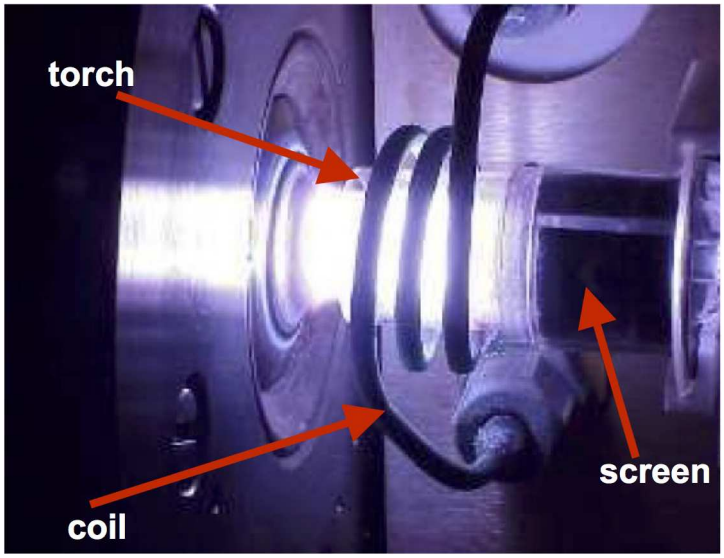

Figure 2.6. Image of the torch, ignition coil and 'torch screen'.

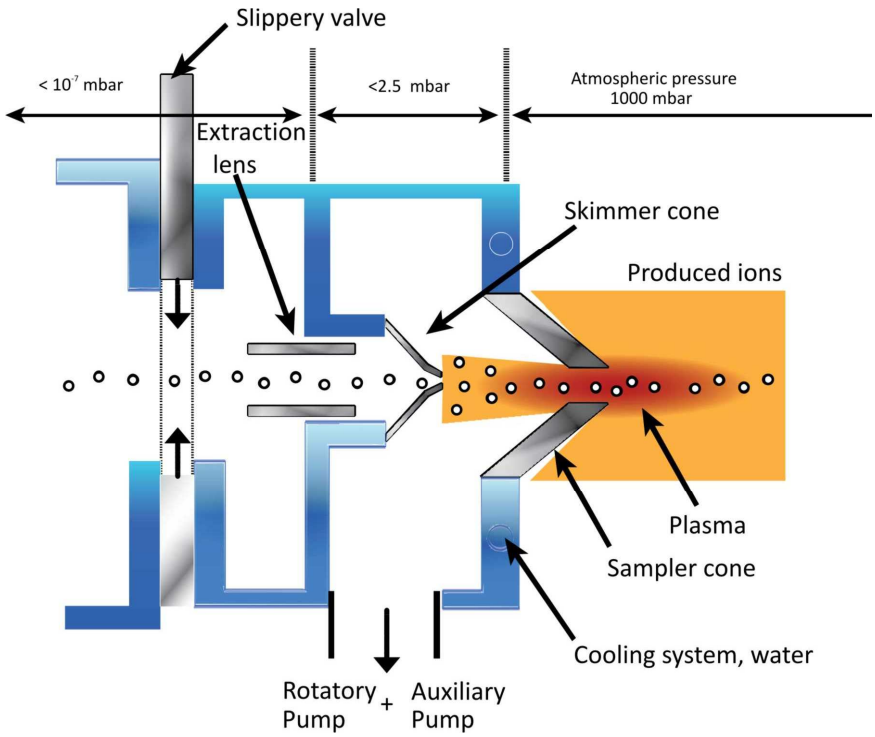

Figure 2.7. Scheme of a common ICP-MS interface area (skimmer cone, sampler cone, cooling system)

The cones used in ICP-MS instruments are different depending on the sample introduction system. In the case of the Q-ICP-MS XSeries 2, an interface designed for greater matrix tolerance, the 'Xt' interface, with nickel cones is used (Figure 2.8).

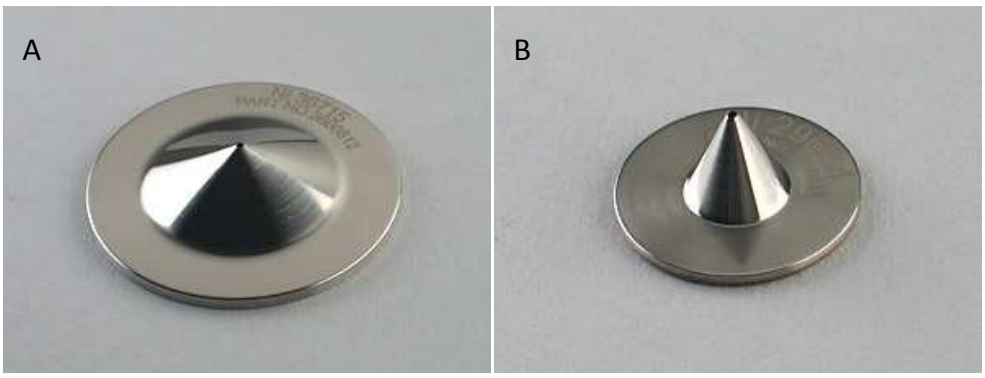

Figure 2.8. Cones used in the interface of the XSeries 2 instrument. A: Sampler cone. B: Skimmer cone.

As for the Neptune MC-ICP-MS, it requires different standard nickel cones for liquid (Figures 2.9A and C) and solid samples (Figure 2.9B). In the latter case the sampler cone has a more pronounced peak to increase the signal.

Figure 2.9. Interface cones. A: Skimmer cone (useful in both dry and wet plasmas). B: Sampler cone (Jet cone) for dry plasma. C: Sampler cone used with wet plasma.

The vacuum conditions in the interface are directly linked to the sensitivity of the spectrometer. Due to this fact, both the multicollector and quadrupole instruments used in this study have been enhanced through the use of Pfeiffer OnTool Booster and Edwards E2M28 pumps, respectively.

2.1.c. Ion focus system

The ion focus system is a part of special importance within the ICP-MS, since the ion beam that will reach the mass analyser is guided in this area. Its function is to maximize the amount of ions that are brought to the analyser, excluding at the same time the majority of the components of the matrix.

In the case of the ICP Thermo instruments at the UPV/EHU facility, the systems are composed of a series of metal ionic lenses, to which a voltage is applied to change the trajectory of ions. That is, those lenses carry electrostatically the analytes from the interface to the mass analyser system. This part also holds the extraction lens, responsible for separating the positive ions from the non-ionic species, such as particles, neutral species (atoms and molecules) and photons, preventing the latter from reaching the mass analyzer and detector. Ionic lenses are located in a low-pressure area, since the vacuum conditions increase towards the detector.

The ion focus system and vacuum conditions are very different in the Q-ICP-MS and MC-ICP-MS. The quadrupole is equipped with a simple ionic lens system, which works between 10^{-7}-10^{-6} mbar. The case of the MC-ICP-MS is much more complex (Figure 2.10), since in the area between the interface and the analyser, ions are not only guided but also separated. For that purpose, the ion focus system of the Neptune includes several ionic lenses composed of the following parts: (i) Electrostatic Sector Analiser (ESA), (ii) quadrupole, and (iii) entrance slit for changing the resolution, all operating under high-vacuum conditions (ca. 10^{-7} mbar). The electrostatic analyser consists of two curved plates. When a direct current is applied to them the internal plates with negative polarity attract the positive ions, whereas the positively charged

outer plates deviate them. In such a way, the ion-beam is focussed while passing between both plates, creating a tilted angle of 40°. That is, the plates act as an efficient energy filter and only ions with a certain kinetic energy will be able to go through the ESA.

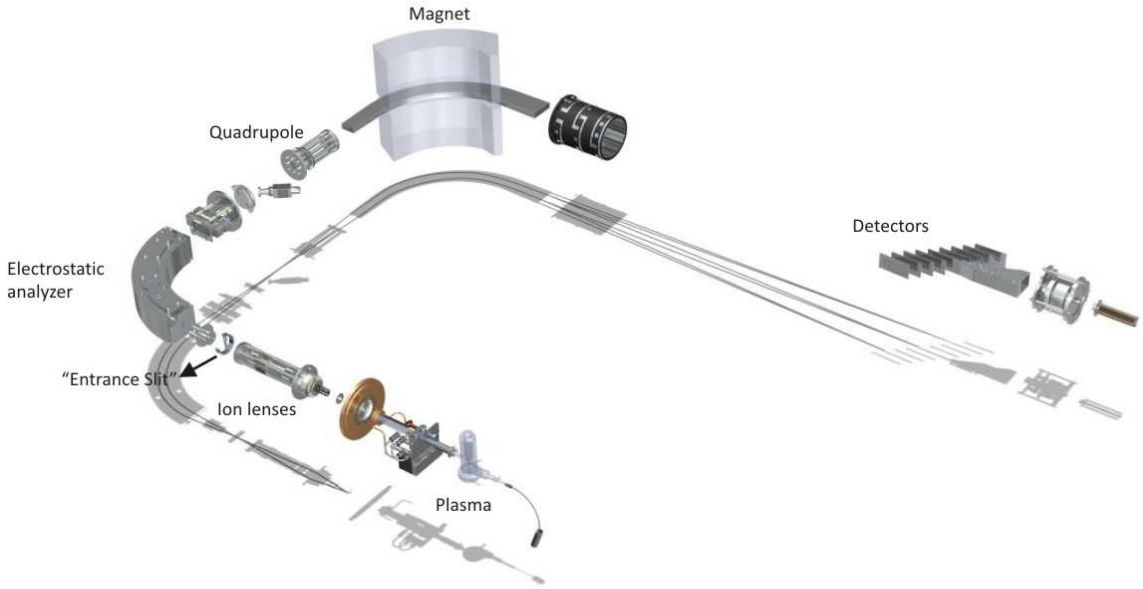

Figure 2.10. Ion focus system in the MC-ICP-MS. Other parts of the equipment, such as the mass analyser and detector, are described below.

2.1.d. Mass analyser

The mass analyser is located between the ion focus system and the detector. After going through the ion lens system, an ion discrimination is done in the mass analyser or filter according to their mass/charge ratio. Once in the analyser, the inert gas is separated from the positively charged ions and it is pumped away with a turbomolecular pump. The major difference between the two ICPs used in this work is the mass analyser itself.

2.1.d.1. *Q-ICP-MS*

The Thermo XSeries2 is equipped with a quadrupolar mass filter. This apparatus consists of four cylindrical rods of molybdenum, set parallel to each other and equidistant from a central axis (Figure 2.11). Applying an opposite current and radio frequency voltage in an opposing rod pair a positive direct current will be obtained, obtaining a negative current for the other pair.

Radio frequency voltages in each pair are offset by 180°, that is, they are of opposite sign, with different amplitude.

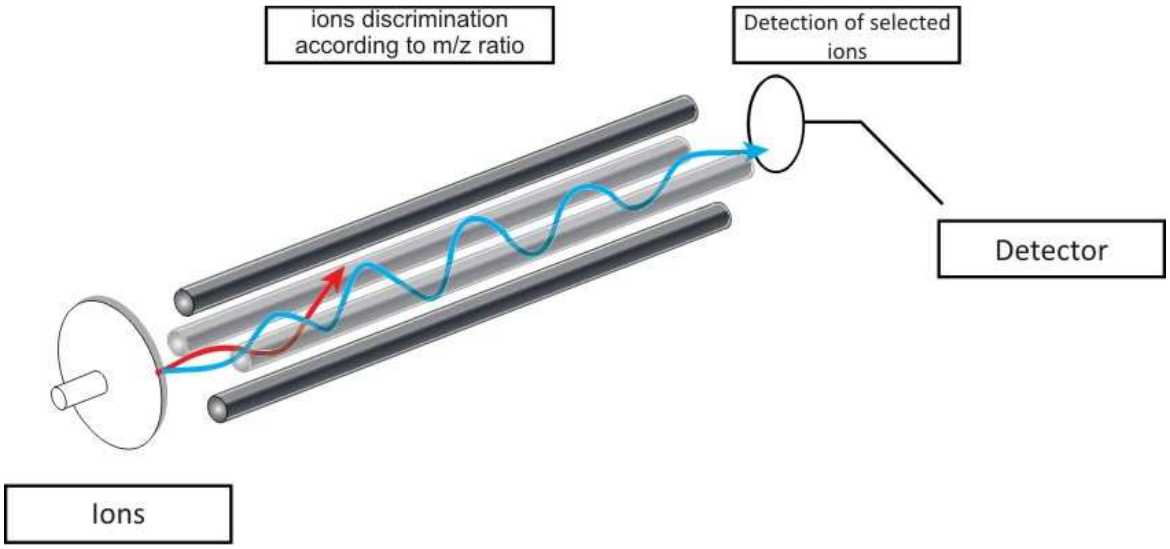

Figure 2.11. Scheme of the quadrupolar mass analyser.

Ions entering the quadrupole undergo oscillatory trajectories due to the radio frequency voltage. If proper values of the radio frequency and current voltage are set, only those ions with a specific mass/charge ratio will traverse the entire length of the quadrupole and reach the opposite end. The rest of the ions will follow very large oscillatory trajectories and collide with the bars, being neutralized before reaching the detector (Figure 2.11).

2.1.d.2. *MC-ICP-MS*

This type of mass spectrometer separates ions in a circular route induced by the electromagnet (Figure 2.12).

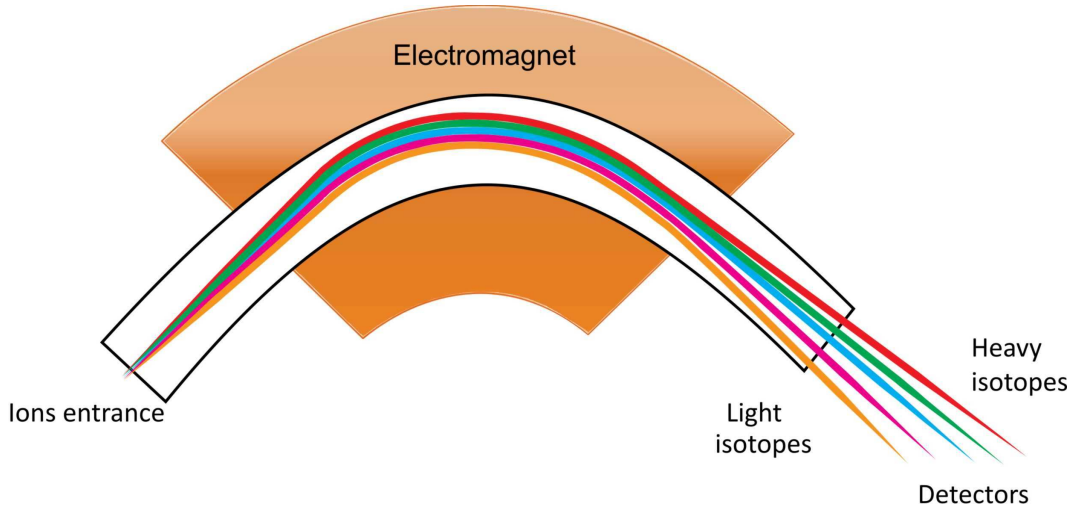

Figure 2.12. Scheme of the analyser in a magnetic sector spectrometer.

Once the ions are in the electromagnet influence field, they are separated according to their mass-to-charge ratio. Ions with different mass follow different circular paths (Figure 2.12) and consequently, changes in the configuration of the magnetic field will permit to select ions with a particular mass/charge ratio.

2.1.e. Detector system

Once the different ions have been separated according to their respective mass/charge ratio, they reach the detector under high-vacuum conditions. Different detector systems have been designed and they will be described in the following section.

2.1.e.1. *Q-ICP-MS*

The detector used in the Q-ICP-MS is a Secondary Electron Multiplier (SEM, Figure 2.13), which can measure simultaneously both analog signals and pulses counting with a linear dynamic range of over eight orders of magnitude. Therefore, it allows a simultaneous measurement of elements in major, minor and trace concentrations in a single analysis.

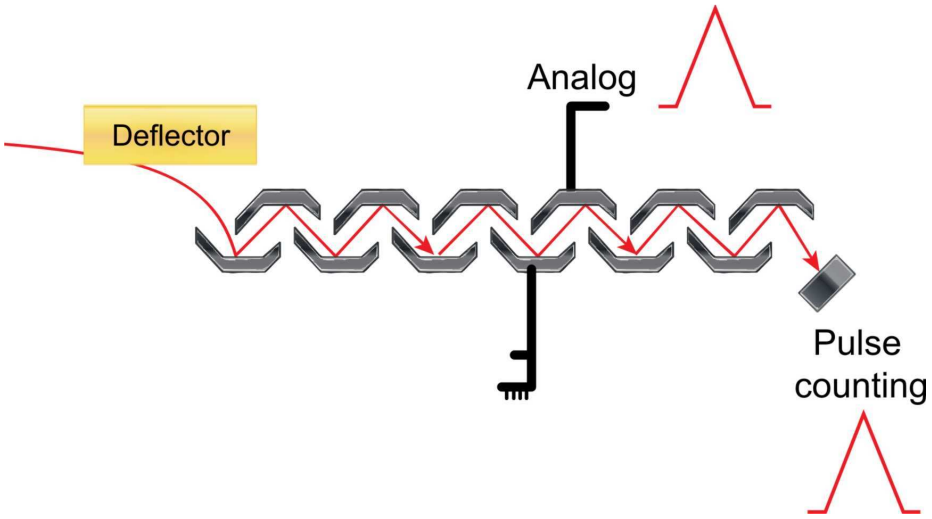

Figure 2.13. Scheme of a Secondary Electron Multiplier detector.

The electron multiplier type detectors have a very high sensitivity for plasma source spectrometers. In the daily use, they are operated for signals above 10^7 counts per second (cps).

2.1.e.2. *MC-ICP-MS*

The MC-ICP-MS is a multi-detector instrument comprising 3 different types of detectors:

- Faraday cups: ions that reach those detectors are amplified and counted. The most important benefit of the Faraday cups is the stability and lack of deviation in the masses, allowing accurate measurements of isotopic ratios. These detectors are used when there are high signals.
- SEM: the same as explained for the quadrupole.
- MIC (Multi Ion Counting): it works similarly to the SEM and it is used with low signals (< 10^6 cps).

The Fisher Scientific Neptune spectrometer used in this PhD Thesis has a special configuration that includes nine Faraday cups, eight ion counters and one secondary electron multiplier. This configuration permits the measurement of a large number of isotopic ratios (Figure 2.14) and has been specifically designed to overcome the routinary problems encountered during the analytical procedure established in the laboratories of the University of the Basque Country UPV/EHU.

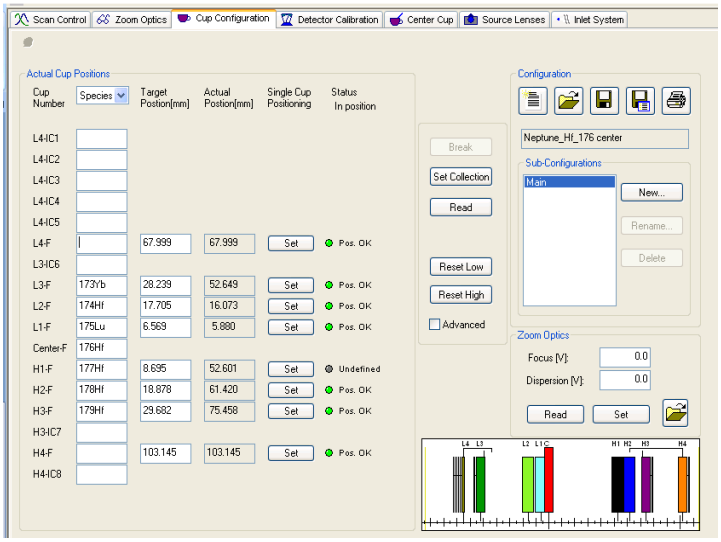

Figure 2.14. Example of a detector configuration, measuring simultaneously mass/charge ratios between 173 and 179.

2.1.f. Problems associated with the ICP

Although the most common problems associated with the ICP-MS are generated by the interference of different elements (spectral and non-spectral) and the isotopic fractionation, other problems may occur.

Spectral interferences occur when the mass of the analyte coincide with an interferent of the same mass. This type of interference may be isobaric or molecular, that is, produced by different elements or by the molecules generated by the plasma. The latter may be due to the argon in the plasma and/or reagents used in the preparation of the sample. They may also be the

consequence of the creation of hydroxides and oxides or the occurrence of double charged species (mass/charge ratios are measured). There are several options to avoid these problems. One of them is the elimination of interferents. This may be done by (i) breaking up the molecules, (ii) early detection of their presence by chromatographic techniques or (iii) selection of the best analytical conditions for the equipment.

Non-spectral or matrix interferences tend to reduce the signal and therefore, different strategies should be considered. The following are the most common ones: (i) use of dilution factors and internal standards to make corrections, (ii) isotopic dilution, (iii) changes in the sample absorption system, or (iv) separation chromatography.

The use of a plasma source requires the solution of the inherent problems associated with the technique, most of them related to the sample introduction system, e.g., if the sample is introduced as a solution or if it comes from a laser ablation system. In the first case, several problems may occur, such as obstruction in the nebulizer, matrix problems, etc. Most of them can be overcome by using appropriate materials and elements, and by using different strategies for the analysis. Matrix problems may also occur in the sample introduction system. In order to avoid them, it is advisable to use standards with a similar matrix as the unknowns. Another problem can come for the wrong synchronization between the software controlling the spectrometer and that of the laser system. Though they work at the same time they are different and therefore, timing problems can occur. Finally it also should be remarked that the laser ablation system uses both helium and argon, and, sometimes, nitrogen too, so it is essential to control the gases to achieve a stable signal.

Besides the above-mentioned instrumentation and interference problems, one of the main complications of the multi-detector instruments is the distinction between masses. In this process, differential measurements are generated related to the masses of the isotopes, that is, small variations in the measured abundance of the mass. The variations are related to the so-called ‘isotopic fractionation’ processes. Although isotopes of an element have the same chemical properties, they have different physical properties, due to the difference in mass between them. That is why the isotopic fractionation happens. Molecules with the heaviest isotope of a particular element, will have different weight, volume, speed of reaction, etc. compared to those with lighter isotopes. This will lead to an isotopic enrichment or impoverishment of the sample as a result of natural processes such as evaporation or precipitation.

Apart from this, in mass spectrometry-based isotope ratio analysis, light isotopes enter faster into the aerosol than heavy ones during the ionization process of the sample. Over time, the proportion of heavy and light isotopes changes, which creates a difference between the isotopic ratio measured in the spectrometer and that of the real sample. In some isotopic

systems, such as Sr or Hf, there is one stable isotopic ratio that permits to establish an internal correction. However, in other cases, known isotopic standards or materials are needed to monitor and correct this fractionation.

2.1.g. Sample introduction system

The aim of the introduction system is to put a small quantity of sample in the spectrometer. Since the sample must be in gas state within the mass spectrometer it must be first converted into aerosol, from both liquid and solid states. There are several options for introducing the sample into the mass spectrometer. The ones used in this work are described below.

2.1.g.1. ***Liquid***

As mentioned above, to introduce a liquid sample into the spectrometer it is necessary to create a fine aerosol and filter the large droplets that might have been generated, so that they do not enter the plasma. The aerosol is produced by the nebulizer and the filtration process takes place in the spray chamber.

In this work, two different systems have been used for the analysis of liquid samples. Although the main purpose is the same, there are some differences and it is advisable to adapt the system for each case.

a. Standard Introduction System: SIS

The Standard Introduction System (SIS) has been used for the analysis of high concentration samples (Figure 2.15). In this system the nebulizer is made of PFA and works with a flow rate of 100 µl/min. Due to the influence of the gas flow the liquid is divided into drops of various sizes. It is in the spray chamber where an air stream produced by a peristaltic pump is used to separate the large droplets and block their access to the mass spectrometer.

b. Desolvatation system: Apex

This system has been used for the analysis of low concentration samples and with the aim of increasing sensitivity. However, it should be noted that with increasing sensitivity, the impact of pollution is also higher, and thus, cleaning protocols take a great importance.

The high sensitivity sample introduction system Apex (Elemental Scientific, USA, Figure 2.16A) has been the desolvation system used in this PhD Thesis. It is composed of the following elements: (1) spray chamber made of quartz, (ii) PFA concentric nebulizer with a flow rate of 50 µl/min flow (Figure 2.16B), (iii) Peltier cooled condenser and (iv) and additional quartz chamber for mixing that permits measurements requiring high precision and stability. This system reduces or eliminates the water content of the samples, and thus, the sensitivity can be improved and the interferences of polyatomic particles or oxides are prevented.

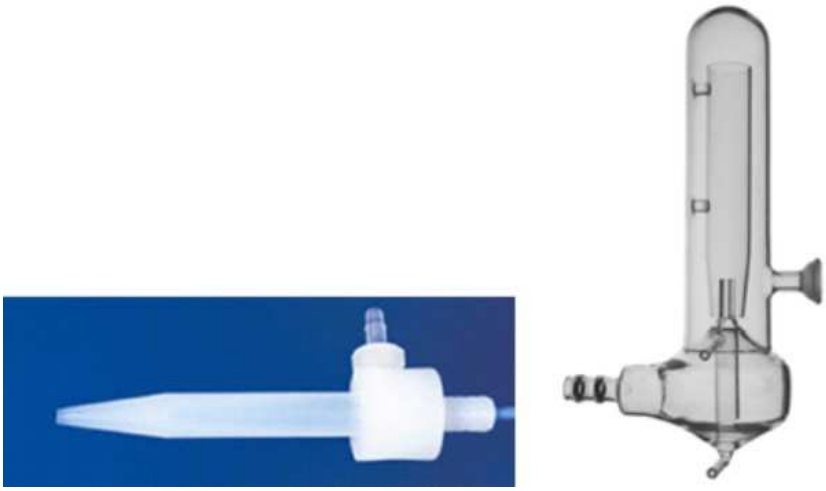

Figure 2.15. Images of the nebulizer (left) and spray chamber (right) used in this work.

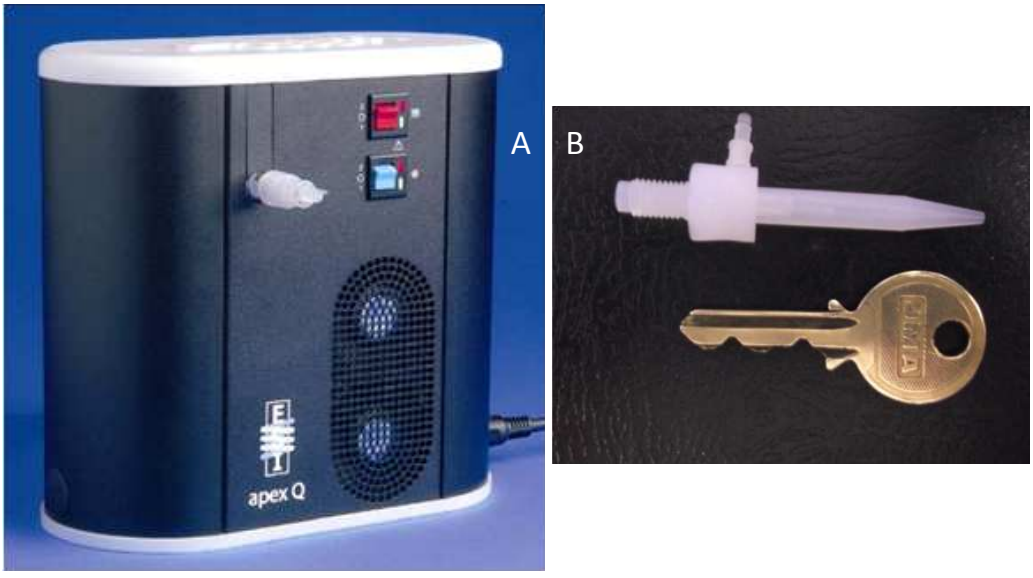

Figure 2.16. A: Image of the Apex desolvation system. B: Image of the concentric nebulizer.

If it becomes necessary to increase the sensitivity and completely destroy the oxides and polyatomic interferences, the accessory device Spiro (Elemental Scientific) may be coupled to the Apex. The Spiro is a macroporous membrane made by Teflon® PTFE material.

2.1.g.2. *Solid-state: Laser ablation system*

***L**ight **A**mplification by **S**timulated **E**mission of **R**adiation (Laser)* is the technique used for in situ analysis of solid samples. The photons from the laser system are focused to interact with the sample as a large blow of energy. As a consequence of this interaction, an aerosol is formed in the surface of the sample with ions, atoms and small particles released from the sample (Figure 2.17). Currently available laser systems permit to work with both high (<5 microns) and small spatial resolution (> 100 microns). The aerosol produced by the laser beam contains a very small quantity of sample, and thus, systems with a high analytical sensitivity are needed, especially for the analysis of trace and ultra-trace elements.

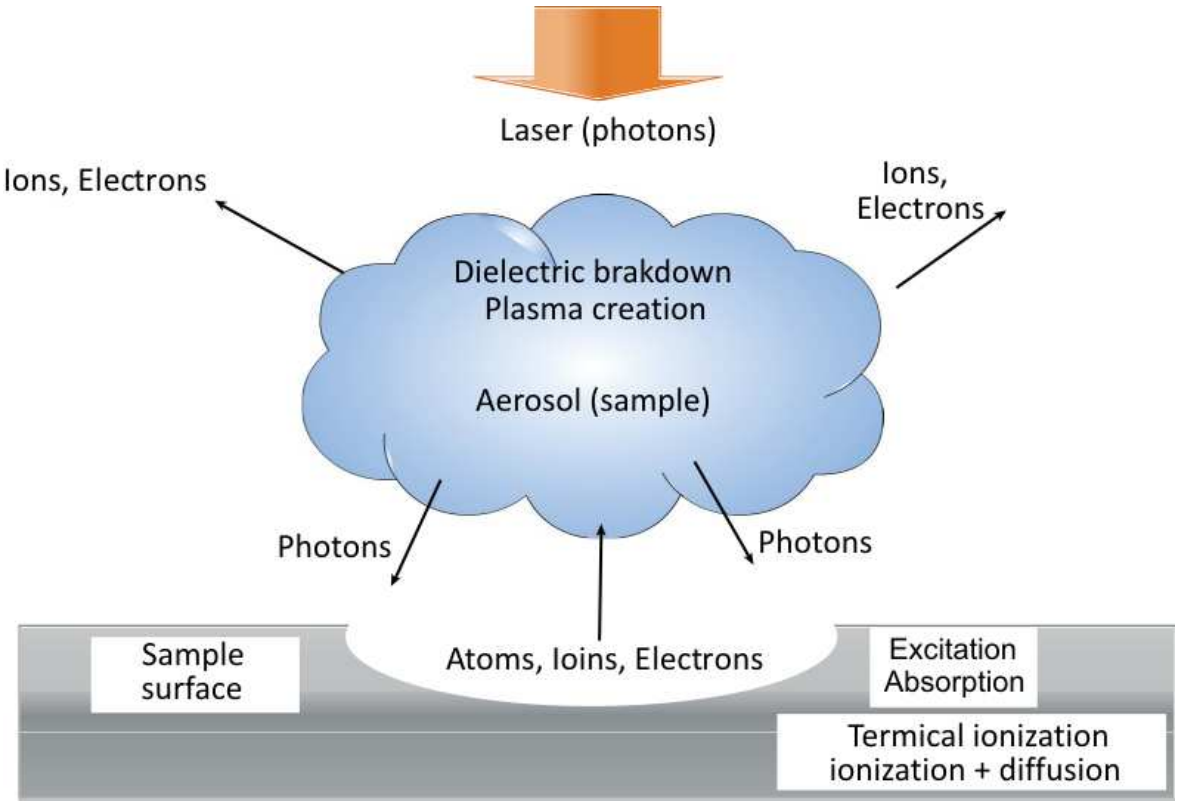

Figure 2.17. The sample ablation process.

Broadly, the laser ablation system is composed of the following sections: a photon generator system, an ablation cell where the sample is located, and a software-based control and vision system, which controls the entire system and allows the selection of the points to be analysed.

The laser ablation system available at the Isotope Geochronology and Geochemistry facility (IBERCRON) of the University of the Basque Country (UPV/EHU) is a UP213 model of New Wave Research (Figure 2.18). It is a solid-state laser where the laser source is a solid matrix, usually composed of a crystal doped with small amounts of trivalent metal ions such as Cr^{3+} or Nd^{3+}.

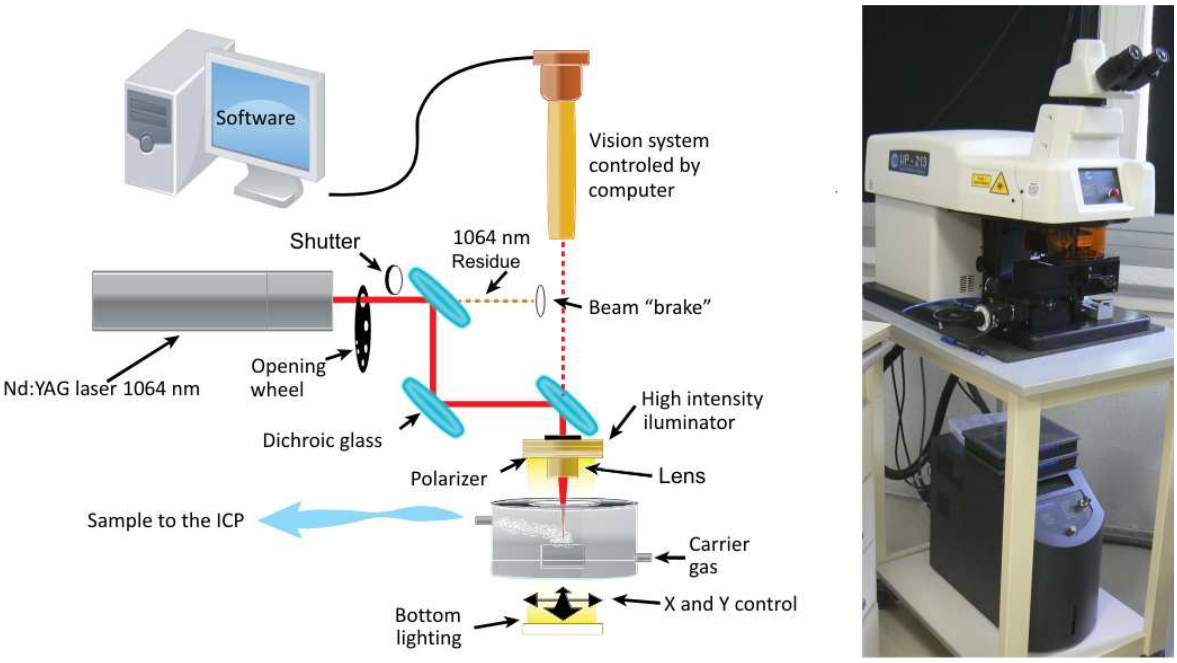

Figure 2.18. Scheme of a Nd:YAG laser system and the UP213 laser used in this PhD Thesis.

The UP213 is a Nd:YAG type laser, composed of yttrium-bearing garnet doped with neodymium, Nd-$Y_3Al_5O_{15}$ (Figure 2.18). These systems are four-level lasers (Figure 2.19). In order to create the laser beam, the Nd ions are excited to a major energy level (pumping level), from where they fall rapidly to a metastable level (laser level). Between these metastable upper and lower laser levels, there is a population inversion, a crucial step for generating a laser beam. The interval between the upper and lower levels will condition the laser beam wavelength. The most powerful wavelength is 1064 nm. With the help of dichroic mirrors, the wavelength of 213 nm is obtained.

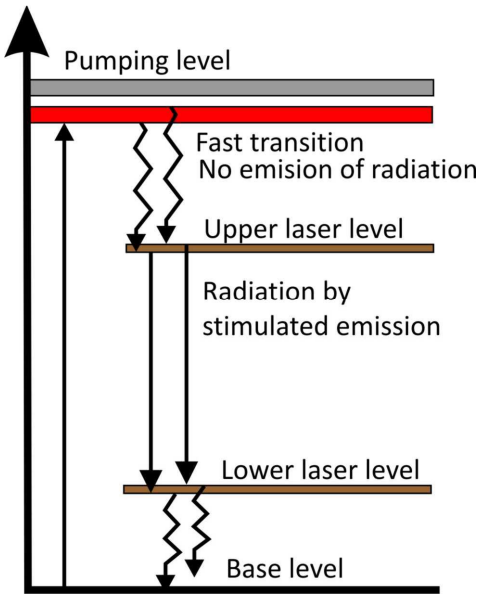

Figure 2.19. Creation of the laser beam in a Nd:YAG solid-state laser-system.

Different gas mixtures have been proposed for the aerosol transport. These might change the signal strength and noise level, and therefore they play a key role in the analytical process (Günther and Heinrich, 1999b). Among them, argon is the most common one. Its main advantage is that it may pass directly from the ablation cell to the ICP torch without adding any other gas, and therefore, without any effect on the plasma conditions.

If nitrogen (N_2) is added to the transport gas the intensity for high mass elements may increase but, at the same time, it is more possible to form polyatomic ions ($^{14}N^{14}N^{1}H$ or $^{14}N^{14}N^{14}N$) that could cause interferences.

The signal/background ratio could also increase if helium is used as carrier gas inside the ablation cell and if it is mixed with argon once it is out of cell (Eggins et al., 1998; Günther and Heinrich, 1999b). There are several explanations for this phenomenon, but it is obvious that the use of helium reduces the accumulation of particles around the ablation point. Both gases have different characteristics in terms of thermal conductivity and thus, the laser induced microplasmas on the surface of the sample are different (Figure 2.19).

The ablation cell is composed of the following parts: (i) a gas entry and exit, (ii) a window transparent to the laser, (iii) a place to put the sample and (iv) optical lighting devices for lightening the sample, either by transmitted or reflected light. The sample can be seen by means of a digital video camera coupled to a microscope.

The ablation cell volume and geometry, closely related to the carrier gas and flow, are important features that condition the signal reaching the mass spectrometer. As long as the mass of interest is still measurable, any improvement during the transportation might permit to reduce the size of the laser spot, and therefore, increase the spatial resolution. Therefore, depending on the size or physico-chemical characteristics of the sample to be analysed, certain changes should be accomplished in the ablation cell.

In this PhD Thesis, a Super Cell^{TM} type ablation cell has been used (Figure 2.20). This cell permits a laminar flow inside that increases the transport efficiency and decreases the cleaning time. To achieve this, the orientation of the gas input and output has been modified and a gas dispersion system has been added. As a consequence of these changes in design, the cleaning time is less than 2 seconds for a volume of 33 cm^3, 4 times less than the 8 seconds needed in the standard cell.

Although the ablation cell design optimizes the washing time, it only allows the introduction of a single sample. In the UPV/EHU laboratories, this design has been modified to allow the introduction of samples and standards simultaneously (Figure 2.20).

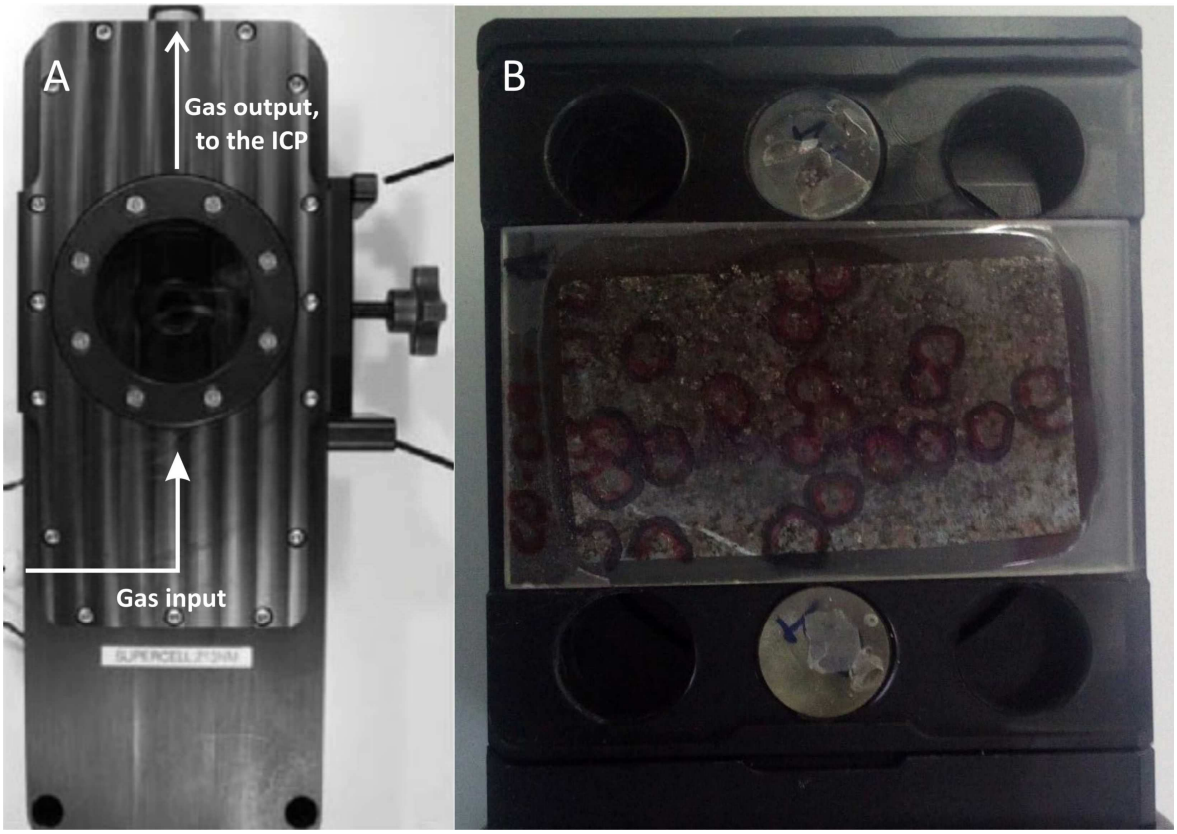

Figure 2.20. Modified Supercell^{TM} type ablation cell. A: Upper view. B: Modified device, which allows the simultaneous introduction of samples and standards.

2.1.h. From the laser to the ICP

There are different ways for carrying the sample from the laser ablation system to the ICP, depending on the objective of the analysis. The laser ablation system and the mass spectrometer are two independent instruments, so a proper coupling must be done for the correct functioning. Those used in this work are listed below.

2.1.h.1. *Q-ICP-MS*

As noted above, the ablation cell has an entrance for the carrier gas and an exit that allows the mixture of sample aerosol and gas to reach the ICP torch. During the ablation process helium is used and once the aerosol is formed, it passes through a device where argon is added before entering the ICP (Figure 2.21). After a number of tests using different mixing and particle filtering devices (e.g., Günther and Heinrich, 1999b; Bleitner and Günther, 2001; Guillong and Günther, 2002), the one used in our study was a baffled-type stabilizer based on that described by Tunheng and Hirata (2004).

Apart from the specific ablation parameters, which are controlled by the laser-system software, it is necessary to control the He flow in the ablation cell. The gas-flow controller installed in the mass spectrometer is used for this purpose. Thus, the He used during the ablation passes through the ICP, and the gas flow is controlled by the spectrometer software.

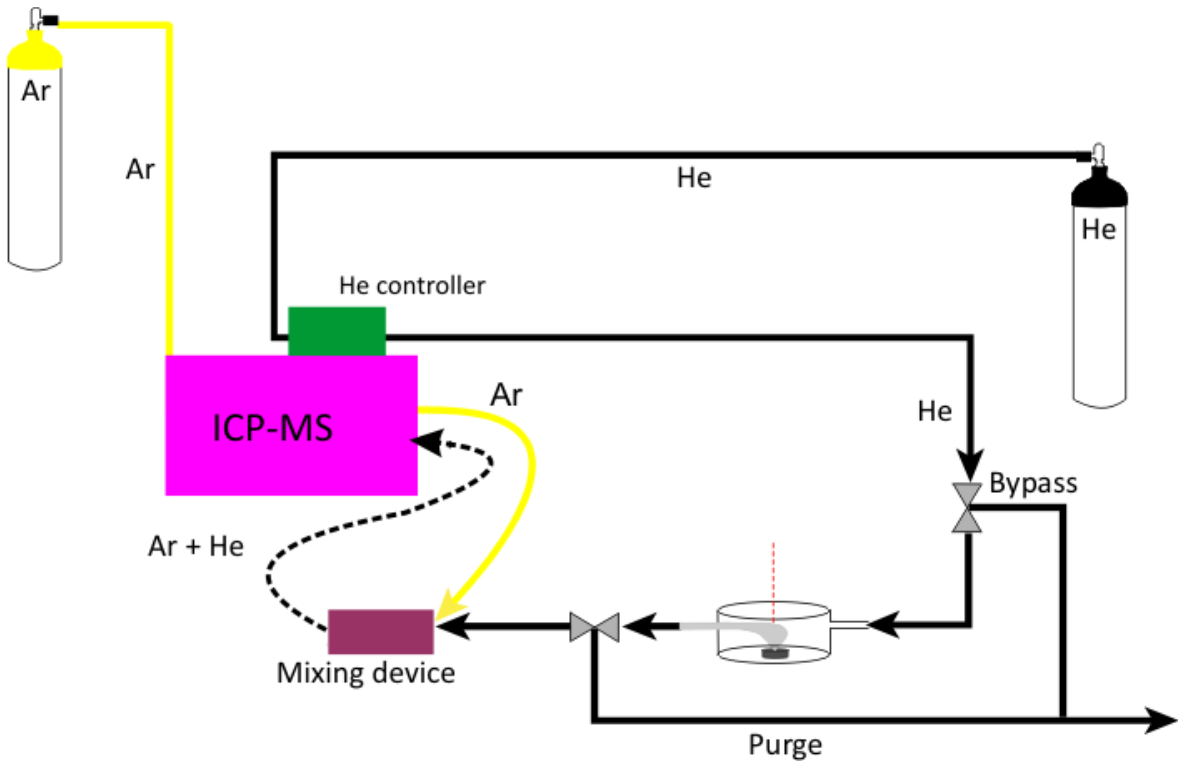

Figure 2.21. Scheme of the coupling between a laser ablation system and a Q-ICP-MS, showing the distribution of the gases.

2.1.h.2. *MC-ICP-MS*

Samples introduced in the MC-ICP-MS have many similarities with the system described for the Q-ICP-MS. As commented before, the addition of nitrogen to the carrier gas increases the signal intensity (Crowe et al., 2003; Hu et al., 2008) and, due to the nature of the analytes measured in this PhD Thesis, this step has been included during the analytical protocol. Thus, nitrogen is added to the mixture coming from the ablation cell (He + sample), and then, just before getting to the torch, argon is injected. The nitrogen to be introduced in the ICP passes also through a gas-flow controller (Figure 2.22). The most common flow is about 10 ml/min.

Figure 2.22. Gas-flow controller used for adding nitrogen.

2.2. Reagents and materials

When doing trace or ultra-trace elements analysis, it is extremely important to use high purity materials and reagents. This is the best way to minimize the pollution problems (see below) that could influence the quantification of low concentration elements (e.g., Robinson et al., 1998).

2.2.a. Reagents

The H_2O used in all the processes is ultrapure and has a resistivity higher than 18 MΩ.cm^{-1}. To obtain this reagent the tap water is firstly deionizated using an Elix (Milipore) device, and then it is purified by reverse osmosis using an Easypure II (Barnstead) equipment.

a. Nitric acid, HNO_3 (% 69.8) and hydrochloric acid, HCl (% 37) are of Pro Analysi (Merck) quality. HNO_3 and HCl are purified by subboiling distillation in Berghof sub-boiling acid purification system.

b. Fluorhydric acid, HF (% 50.2) is also of Pro Analysi (Merck) quality and is purified by subboiling distillation (Matison, 1972) in a Savillex® PFA jar assemblies (Menéndez, 2001; García de Madinabeitia, 2004).

c. Perchloric acid, $HClO_4$ (% 70-72), with Pro Analysi (Merck) quality, is used without further purification.

d. The $LiBO_2$ used as a flux is of high purity (Corporation Scientifique Claisse, For Analysis Grade Pure). The solution used as non-stick is a dilution to 50 % of LiBr (Merck Suprapur) with ultrapure H_2O (18 MΩ.cm^{-1}).

2.2.b. Materials

The laboratory material is an important source of pollution. To avoid or at least minimize that problem, Teflon® PFA containers of 15 ml (Savillex®) are used during the chemical treatment of the samples. They are cleaned using warm 'aqua regia' and rinsed with warm ultrapure H_2O. This cycle is repeated twice.

Whenever possible, disposable materials have been used, such as 1 ml and 5 ml polypropylene micropipettes (Eppendorf), polypropylene containers (Gosselin), etc. Before using them, they have been kept in dilute HNO_3 for 24 hours and then rinsed with ultrapure H_2O. This cycle is repeated twice.

The materials used for isolating the elements of interest are the following: Extraction chromatography (EXC) materials (Sr-Spec and Ln-Spec, both with 50-100 µm particle size) manufactured by Eichrom Industries (Darien Il, USA) and purchased from Triskem International (France), while the conventional cation-exchange resin AG50Wx8, 200–400 mesh size, was obtained from Fluka Analytical and Sigma Aldrich (Buchs, Switzerland and Madrid, Spain, respectively). Sr-Spec and Ln-Spec are washed directly in the columns with concentrate and dilute HNO_3 and HCl, respectively. Dowex cation-exchange resin is washed in a polypropylene container, first with HCl and then with H_2O miliQ. The washing cycle is repeated several times. This cleaning is only done before the resin is used for the first time. From the first chromatography on, the columns are cleaned by several rinses of concentrated HNO_3 and HCl and ultrapure H_2O.

2.2.c. Standards and isotopic tracers

To set up a new analytical method in a laboratory, it is necessary to validate the method by multiple measurements of known materials, Certified Reference Materials (CRM) or international standards. They can be bought in well-known institutions such as the French 'Centre de Recherches et Géochimiques Pétrographiques' (CNRS) or the Geological Services of Japan or United States (GSJ and USGS, respectively). The standards used in this PhD Thesis are the following: (i) AC-E, AGV-2, BHVO-2, FK-N, G-2 and W-2 for solution measurements and (ii) 91500, GJ-1, Plêsovice and Temora zircons for Laser Ablation analyses. References of all those material are given in the Discussion section of Chapter 3.

Similarly, to check that the equipment works properly and there is no instrumental drift over time, known comercial solutions have been measured for a long period before setting up the methods. The solutions used for this purpose are the following: SRM984 for Rb (National Institute for Standards and Technology, NIST, USA), SRM987 for Sr (NIST), JMC 475 Johnson Matthey

(provided by Professor P. Jonathan Patchett) for Hf and Standard for ICP Solution (Fluka Analytical) for Lu.

The Isotope Dilution technique has been followed for measurements made in solution mode (see introduction of the Chapter 3). All the isotopically-enriched tracers used in this work (specifically, ^{176}Lu: 44.23 %, ^{179}Hf: 89.87 %, ^{87}Rb: 98 %, ^{86}Sr: 97.02 %) were provided by Dr. Brieuc Le Fèvre and Dr. Christian Pin, and they were prepared from Oak Ridge National Laboratory (USA) products. These isotopic tracers solutions were calibrated by reverse isotope dilution against two mixed gravimetric normal solutions. The single element solutions used in our analyses are the following: 'Standard for ICP Solution' (Fluka Analytical) with 997 ± 5 mg/l concentration in nitric acid medium for Lu, 'CertiPUR ICP Standard 170322' (Merck) solution with 1000 mg/l concentration in hydrochloric + hydrofluoric acids medium for Hf, 'Rubidium Plasma Standard Specpure 13872' (Alpha Aesar) with 1000 ± 2 mg/l concentration in nitric acid medium for Rb and 'Strontium standard for ICP 75267' (Fluka Analytical) with 1000 ± 2 mg/l concentration in nitric acid medium for Sr. For Lu and Rb-Sr measurements 'Ytterbium ICP Standard 601902A' and 'Zirconium dichloride oxide hydrate, Puratrornic, 99.9985% (metal basis) 11135' are used, respectively.

2.3. Other instrumentation

In order to avoid contamination of samples and standards, the chemical treatment (dissolution, evaporation, chromatography, etc.) has been done in protected areas under laminar flow conditions and inside total exhaust resistant-to-acid workstations made of polypropylene (LFE-1500BT, Salare Inc.). The cabins are located in a room with over pressure filtered air (1: 10,000 class clean room).

Handy H51 Sartorius weighing scales with a 30 ± 0.0001 g capacity have been used to measure the weight of the samples, tracers or flux.

A Katanax K1 (Canada) fluxer has been used to melt electrically (Joule effect) the samples (Figure 2.23). This instrument is controlled by a micro-processer which regulates the temperature and enables an in situ dissolution of the molten sample in the crucible. The crucibles are made of platinum, and they are cleaned in dilute HNO_3 in an ultrasonic bath.

Figure 2.23. Image of the Katanax K1 fluxer used in this work.

2.4. Mineral separation

Some of the samples introduced into the mass spectrometer in liquid state correspond to concentrates of a particular mineral. The equipment used for this purpose belongs to the Department of Mineralogy and Petrology of the University of the Basque Country UPV/EHU.

In order to obtain the mineral concentrations, the rock to be analysed is first reduced to fragments of ca. 5 cm with the aid of a geologist's hammer, and then crushed into ca. 1 cm-sized pieces with a jaw crusher (Retsch bb200 Wolframcarbid). When necessary, the obtained sample is divided into two fractions: the first one is used for mineral separation and the second one for bulk rock analysis.

The fraction used for bulk rock analysis is grinded using a Retsch RS1 type ring-mill with widia rings for major elements analysis and with agate rings for trace or rare earth elements. The fraction for mineral separation is passed through a Reuland disk-mill to obtain the needed grain size, which depends on the desired mineral. If necessary, sieving is done at this step. Since the rock crushing method generates a lot of dust. All this process is done in a laboratory equipped with air extractors.

Once the magnetic minerals and metal chips are removed with a powerful magnet, the separation process continues with a Frantz magnetic isodynamic separator (Frantz Company, Inc., Model 13). Changes in the magnetic field and magnet inclination of the Frantz enable a selective mineral separation. Although the obtained mineral concentrations are relatively clean, a magnifying binoculars glass (Olympus in our protocol) is normally used to discard non-desired elements.

2.5. Contamination

Before setting up a new analytical method in isotope geochemistry it must be considered what level of contamination might be acceptable and where this contamination may come from. The main contamination sources are the following:

Contamination associated with the crushing and grinding of the rock. To avoid cross-contamination between samples, it is essential to clean all the materials before and after using them. This is of particular importance in the mills and sieves, where left-overs or isolated minerals might pass from one sample to another.

Direct atmospheric contamination. This could be reduced by using a room with over-pressure filtered air (white room).

Contamination introduced by the scientist. Particles attached to the body, hair, etc. might be transferred to the samples. Proper work habits and clothing are crucial at this point.

Contamination of laboratory materials and reagents. The reagents used during the sample preparation may contain trace elements (Sr, Pb, ...). In order to eliminate or minimize them these reagents can be treated through destilation in quartz or Tefflon distillers under sub-boiling conditions (Mattison, 1972). In some cases, the contamination can be originated in the reagent container itself due to (i) 'wash' of the container wall and/or (ii) 'memory effect' of the vessels used for the sample dissolution if they are not cleaned properly after use. That is why the U-Pb system requires necessarily a continuous cleaning of materials and reagents.

Contamination within the spectrometers. A large number of sample ions can be deposited in different parts of the spectrometer. These deposits can cause a secondary emission over time, creating interferences in the analysis. To avoid them, it is essential a periodic cleaning of the nebulizer, torch inyectors and cones by soaking in diluted nitric acid (0.05 %).

Chapter 3: Geochronology-Geochemistry – Methods

3. Geochronology – Geochemistry – Methods

During this PhD thesis, analytical methods for three of the most commonly used geochronological systems have been set up in the laboratories of the SGIker facility of the University of the Basque Country UPV/EHU. Rb-Sr and Lu-Hf systems have been analysed as solutions in a MC-ICP-MS, whereas the U-Th-Pb have been analysed with a laser ablation (LA) device connected to a Q-ICP-MS. However, before deeply entering in these questions, a brief review of some basic aspects will be done.

3.1. Introduction

3.1.a. Decay/growth of radiogenic isotopes

In the nature, there are almost 300 naturally occurring isotopes (Henderson and Scott McIndoe, 2005). Some of them are stable and some not. For the purpose of dating minerals and rocks, radioactive or unstable isotopes are used.

The decay rate of a radioactive parent nuclide to a stable daughter product is proportional to the number of atoms, *n*, present at any time *t* (Rutherford and Soddy, 1902):

$$-\frac{dn}{dt} = \lambda n \quad [1]$$

where λ is the constant of proportionality, which is characteristic of the radionuclide in question and is called the decay constant (expressed in units of reciprocal time). The decay constant states the probability that a given atom of the radionuclide will decay within a stated time. The term $\frac{dn}{dt}$ is the rate of change of the number of parent atoms, and is negative because this rate decreases with time. On rearranging equation [1], we obtain:

$$\frac{dn}{dt} = -\lambda n \quad [2]$$

This expression is integrated from *t = 0* to *t*, given that the number of atoms present at time *t = 0* is n_0:

$$\int_{n_0}^{n} \frac{dn}{n} = -\lambda \int_{t=0}^{t} dt \quad [3]$$

Hence,

$$\ln\left(\frac{n}{n_0}\right) = -\lambda t \quad [4]$$

which can also be written as

$$n = n_0 e^{-\lambda t} \quad [5]$$

Equation [5] gives the number of radioactive parent atoms (*n*) that remain at any time (*t*) of an original number of atoms (n_0) that were present when *t=0*. It is the basic equation describing all radioactive decay processes.

The number of radiogenic daughter atoms formed, D^*, is equal to the number of parent atoms consumed:

$$D^* = n_0 - n \quad [6]$$

but n_0=neλt (from [5]); so substituting for n_0 in [6] yields

$$D^* = ne^{\lambda t} - n \quad [7]$$

i.e.,

$$D^* = n\left(e^{\lambda t} - 1\right) \quad [8]$$

If the number of daughter atoms at time *t = 0* is D_0, then the total number of daughter atoms after time *t* is given as

$$D = D_0 + n\left(e^{\lambda t} - 1\right) \quad [9]$$

This equation is the fundamental basis of most geochronological dating tools. Both *D* and *n* in equation [9] can be measured with adequate instrumentation, and the equation can then be solved for time *t*:

$$t = \frac{1}{\lambda} ln\left(\frac{D - D_0}{n} + 1\right) \quad [10]$$

The numerical value of *t* obtained from equation [10] is a date in the past. The interpretation of this date depends on certain assumptions about the geological history of the rock or mineral being dated and about the numerical values of D_0 and λ being used in the calculation. The assumptions are as follows:

1.- The rock or mineral sample being dated has not gained or lost parent or daughter atoms, except by decay of the parent to stable daughter.

2.- The decay constant of the parent nuclide is independent of time, is not affected by the physical conditions to which the nuclide may have been subjected and its value is known accurately.

3.- An appropriate value of D_0 is used in the calculation based on either knowledge of the chemical properties of the daughter element or its isotope composition in the terrestrial reservoir from which the rock or mineral originated.

4.- The measured values of *D* and *n* are accurate and representative of the rock or minerals being dated.

3.1.b. Isotope dilution (ID)

For the isotopic systems measured as solutions in this PhD Thesis, isotope dilution techniques have been used in order to achieved a precise and accurate measurement.

Isotope dilution is generally agreed to be the best analytical method for very accurate concentration determinations. Faure and Mensing (1986) listed the benefits of using this technique, as well as difficulties of its use. In this technique, a sample containing an element of natural isotopic composition is mixed with a tracer or 'spike' solution, which contains a known concentration of the element, artificially enriched in one of its isotopes. When known quantities of the two solutions are mixed, the resulting isotopic composition (measured by mass spectrometry) can be used to calculate the concentration of the element in the sample solution, as follows:

Let R_m be the ratio of two isotopes *A* and *B* and let *A* and *B* be expressed in numbers of atoms, while the suffixes *m*, *t* and *s* refer respectively to the mixture, the tracer and the sample analysed. Then,

$$R_m = \left(\frac{A}{B}\right)_m = \frac{A_t + A_s}{B_t + B_s} \quad [11]$$

By dividing the numerator and denominator of the right-hand side by B_t to show the known $\frac{A_t}{B_t}$ ratio (i.e., the ratio of the reference tracer, R_t), the following is obtained:

$$R_m = \frac{R_t + \frac{A_s}{B_t}}{1 + \frac{B_s}{B_t}} \quad [12]$$

where $\frac{B_s}{B_t}$ is the unknown to be determined.

Indeed, knowing the amount of tracer added and its isotopic composition, B_t can be deduced, and therefore, B_s can be calculated.

By re-arranging [12] as follows:

$$R_m = \frac{R_t + \frac{A_s B_s}{B_s B_t}}{1 + \frac{B_s}{B_t}} \quad [13]$$

so,

$$R_m \left[1 + \frac{B_s}{B_t}\right] = R_t + R_s \frac{B_s}{B_t} \quad [14]$$

and,

$$R_m + R_m \frac{B_s}{B_t} = R_t + R_s \frac{B_s}{B_t} \quad [15]$$

by grouping the terms in $\frac{B_s}{B_t}$,

$$\frac{B_s}{B_t}(R_m - R_s) = R_t - R_m \quad [16]$$

which finally,

$\frac{B_s}{B_t} = \left(\frac{R_t - R_m}{R_m - R_s}\right)$ [17]

Therefore: $B_s = \frac{R_t B_t - R_m B_t}{R_m - R_s}$ [18]

As $A_t = [A]_t M(t)$, where *M(t)* represents the mass (g) of tracer added to the sample, and $[A]_t$ the concentration of the tracer isotope *A* (in µmol.g^{-1}), $B_s = \frac{\left[1 - R_m\left(\frac{B}{A}\right)_t\right][A]_t M(t)}{R_m - R_s}$ is expressed as number of atoms (µmol).

Having chosen the isotope B as the reference isotope to express the isotopic composition of the element in the form of abundance ratios $\frac{K}{B}$, it then only remains to multiply B_s by each abundance ratio (constant or variable in nature), and then by the atomic weight *P(K)* of the corresponding isotope to obtain the mass k_s of each isotopes present in the sample analysed:

$k_s = \left(\frac{K}{B}\right)_s B_s\ (\mu\text{mol})\ \text{P(K)}\ (\text{g.mol}^{-1})$ [19]

The sum of the weight of different isotopes corresponds to the mass of the element considered, that must be divided by the mass of sample analysed (g) to obtain the concentration (µg.g^{-1}):

$$content\ (\mu g.g^{-1}) = \sum_{k=1}^{k=n} k\ (\mu g)\frac{1}{M_s(g)} \quad [20]$$

3.1.b.1. *Error propagation in the isotopic dilution*

The total error on the content determined by isotope dilution mass spectrometry (ID-MS) depends, on one hand, on the random errors of the measurement itself. When the ID is on stable isotopes of the elements, the propagated error is proportional to the error on R_m. When the isotopic composition of the measured element varies considerably, as well as its molecular weight, the random error is increased by the errors of different measures of isotopic compositions and those on the recalculated molar masses (see García Alonso, 1995; for a detailed treatment of calculated errors in that case).

On the other hand, the error depends also of other systematic factors, which are the uncertainties on the mass bias correction, correction of dead time of the detector and the tracer concentration and the presence of more or less significant isobaric interferences. The latter source of error can be minimized by different means like chemical separation, desolvation, changing plasma conditions, etc. Finally, weighings done during the preparation of the sample may also be a source of error but their accuracy is usually such that the error due to weighing is negligible compared to other sources of error.

Detailed explanations of the error formulas are provided elsewhere (Pin et al., 2000), so, this will not be discussed here. The total error propagated in k_s can be writted as follows:

$$\left(\frac{\sigma\,[\mathrm{k_s}]}{[\mathrm{k_s}]}\right)^2 = \left(\frac{\sigma\,[A]_t}{[A]_t}\right)^2 + \left(\frac{\sigma(R_{corr})}{(R_{corr})}\right)^2 M \quad [21]$$

where *M* is the amplification factor of the error defined by Webster (1960) as:

$$M = (R_t - R_s)\left[\frac{R_m}{(R_m - R_s)(R_t - R_{m)}}\right] \quad [22]$$

3.2. The Rb-Sr system by ID-MC-ICP-MS

3.2.a. Introduction

The couple Rb-Sr can be used both as a tracer in isotope geochemical processes as well as a geochronometer by virtue of the radioactive decay of ^{87}Rb into ^{87}Sr, through the emission of a β particle and an anti-neutrino ($^{-}\nu$);

$^{87}Rb \rightarrow {}^{87}Sr + \beta^{-} + {}^{-}\nu + Q$

where Q is the decay energy.

Rubidium, an alkali metal belonging to group IA, has an ionic radius (1.48 Å) which is sufficiently similar to that of K^+ (1.33 Å) to allow it to substitute for K^+ in K-bearing minerals, such as micas, K-feldspar, certain clay minerals and evaporite minerals. Meanwhile, the ionic radius of Sr^{2+} (1.13 Å), member of the alkaline earths of group II, is slightly larger than that of Ca^{2+} (0.99 Å), which it can replace in many minerals. These contrasting features are responsible for the fractionation of both elements in different minerals and rocks, allowing a range of Rb/Sr ratios to be observed, and radiometric dates to be calculated by using the isochron method.

The first parameter of a system for radiometric dating is of course to establish the decay constant of the isotope father. However, the half-life of ^{87}Rb is difficult to determine because of the low decay energy of the particles it emits (0.275 MeV) and because of the slow rate of decay. During the last fifty years, values of the decay constant used in geological age calculations have varied between 1.47×10^{-11} (physically measured) and 1.39×10^{-11} y^{-1} (geologically deduced) corresponding to $t_{1/2}$ = 46.8-50.0 Ga. The most commonly used value of 1.42×10^{-11} y^{-1} ($t_{1/2}$ = 48.8 Ga) was adopted by the International Union of Geological Sciences, IUGS, after discussion in Steiger and Jäger (1977). The values published in the lasts years, based on age comparison with U-Pb system, are closer to 1.395×10^{-11} y^{-1} (Kossert, 2003; Nebel et al., 2011; Rotenburg et al., 2012; Villa et al., 2015).

Isotopic compositions and atomic weights of the elements involved in the spectroscopy of Rb and Sr are presented in the tables below (Tables 3.1; 3.2 and 3.3).

Table 3.1. Abundance of the Rb and Sr isotopes (in %) together with the potentially interfering ^{83}Kr, ^{84}Kr and ^{86}Kr isotopes and the ^{90}Zr and ^{91}Zr isotopes used for correcting the instrumental mass bias inherent to ICP-MS instruments. Values recommended by the IUPAC (International Union of Pure and Applied Chemistry; De Laeter et al., 2003).

	83	84	85	86	87	88	90	91
Kr	11.50	57.00		17.27				
Rb			72.17		27.83			
Sr		0.56		9.87	7.04	82.53		
Zr							51.45	11.22

Table 3.2. Atomic masses of rubidium, according to the IUPAC (International Union of Pure and Applied Chemistry; De Laeter et al., 2003).

Isotope	85	87
Mass	84.9117924	86.9091858

Table 3.3. Atomic masses of strontium, according to the IUPAC (International Union of Pure and Applied Chemistry; De Laeter et al., 2003).

Isotope	84	86	87	88
Mass	83.913426	85.9092647	86.9088816	87.9056167

3.2.b. Sample dissolution, isotope dilution, and chemical separation

Prior to isotope ratio measurements, it is necessary to isolate the elements of interest from the matrix elements. Although ICP-MS is generally less demanding than TIMS in terms of analyte purity, the reverse is true in the case of the Rb-Sr system, because, in contrast with TIMS, it is not possible to selectively ionize Rb or Sr based on their different boiling temperatures and ionization potentials. Indeed, the highly energetic inductively coupled plasma source achieves extremely high temperatures at which both Rb and Sr are completely ionized. As a result, the isobaric interference of Rb and Sr at m/z=87 is a major source of concern, which necessitates a high degree of mutual separation of both elements. The following section describes the process of the sample treatment developed in our study for the Rb-Sr system, this is the result of repeated essays for the optimization of the method and is mostly based on procedures presented in Pin and Santos Zalduegui (1997).

1.- The appropriate amounts of the sample powder (ca. 100 mg) are weighed in a 15 ml container made of PFA Teflon (Savillex®).

2.- In a first acid attack, 1 ml of HNO_3 14 mol/l and 2 ml of HF 29 mol/l are added and the beaker is closed and slightly heated (approx. 70 ° C) to dissolve the sample. This step takes at least 12 hours (one night).

3.- The resulting solution is gently evaporated at temperatures ca. 100 °C in order to volatilize the excess of silicon fluorides. Before complete evaporation, 0.1 ml of $HClO_4$ 11 mol/l is added, to prevent formation of acid insoluble fluorides that may 'mask' some elements (Sulcek and Povondra, 1989). To evaporate the perchloric acid, higher temperatures are required, so the sample is taken to dryness with the heat generated by a silica glass infra-red heater, together with the hotplate at 100 °C.

4.- Once that all of the acids (HF, HNO_3 and $HClO_4$) have been evaporated, the sample is taken up in 5 ml of HCl 6 mol/l for another night at moderate temperature (approx. 70 °C) thus converting all nitrates into chlorides. Then, the sample is brought to dryness again.

5.- The residue is dissolved in 1 ml of HNO_3 14 mol/l, overnight at ca. 70 °C on the hotplate, in order to destroy some fluorides that may still remain. Acid is evaporated until its complete elimination.

6.- The salts of the sample are taken up in 2 ml of HCl 1.25 mol/l, and leaved them at moderate temperature (ca. 50 °C) for 2-3 hours.

In the case of spiking the samples with highly enriched ^{84}Sr ('double pass') the addition of the tracers would be done during the attack, due to the possibility of simultaneous measurement of $^{84}Sr/^{86}Sr$ (for isotope dilution) and $^{87}Sr/^{86}Sr$ (making correction, since the ^{84}Sr is not 100 % pure, and the $^{87}Sr/^{86}Sr$ and $^{88}Sr/^{86}Sr$ ratios -for normalization- are modified by adding the tracer). However, when the added tracer is enriched in ^{86}Sr, there is no possibility of simultaneous measurements, and the sample solution must be split in two aliquots, one to measure spiked $^{88}Sr/^{86}Sr$ and the other to measure the sample $^{87}Sr/^{86}Sr$. The Rb tracer does not represent any concern as to when to add it, because only the isotope dilution run is required in this case.

The tracers used in this thesis are ^{86}Sr (enriched to 97.02 %, Oak Ridge National Laboratory, USA) and ^{87}Rb (enriched to 98 %, Oak Ridge National Laboratory, USA). Individual solutions were prepared, and their concentration was calibrated by reverse isotope dilution against normal solutions. These were prepared by accurate gravimetric dilution of 1000 ± 2 mg/l single element solutions purchased from Sigma-Aldrich for the Sr and Alfa Aesar for the Rb. The isotopic compositions of the enriched tracers used in isotope dilution calculations were measured by MC-ICP-MS. The characteristic of the tracers are given in the Table 3.4.

Due to the use of the ^{86}Sr tracer, it is necessary to made two aliquots of the sample solution, as mentioned above. The aliquoting step was made on a weight basis. First, appropriate quantities (depending on the expected analyte concentrations) of single element tracers were

weighed sequentially in a 15 ml container of Teflon PFA (Savillex®) and evaporated to dryness. Then, the sample aliquot (from the 6th step of the dissolution), typically one fifth of the bulk solution, corresponding to about 15-20 mg of the solid sample, was added to the Teflon PFA (Savillex®) and evaporated to dryness. In order to promote isotopic equilibration between the sample and the isotopic tracers, the dry salts were dissolved again in 1 ml of 6 mol/l HCl, followed by evaporation to dryness. This dissolution-evaporation step was repeated with 1 ml of 7 mol/l HNO_3. At this stage, the sample was ready for separation chemistry.

Table 3.4. Characteristics of the tracers ^{87}Rb and ^{86}Sr

Trace isotope	Abundance of tracer isotope	Elemental concentration ($\mu g.g^{-1}$)	Concentration in tracer isotope ($\mu mol.g^{-1}$)
^{87}Rb	98.00 %	0.978 ± 0.008 (2σ)	$1.13.10^{-2}$ ± 0.05 % (RSD)
^{86}Sr	89.87 %	1.210 ± 0.014 (2σ)	$1.41.10^{-2}$ ± 0.05 % (RSD)

3.2.c. Chemical separation

As ^{87}Sr and ^{87}Rb have the same mass, it is necessary to chemically separate Sr and Rb prior to the measurements with MC-ICP-MS. In addition, both fractions need to be free of Zr, because Zr (Alfa Aesar) is added in order to correct for the instrumental mass bias in the measurements (Waight et al., 2002; Nebel et al., 2005; Yang et al., 2008, see below). To carry out this, the samples must undergo two separation processes with different resins based on extraction and ion exchange chromatography.

3.2.c.1. *First column: Separation of Sr*

For this purpose, Sr-Spec (Eichrom Europe, Paris, France) extraction chromatography material (50-100 µm particle size) has been used. The procedure for separation of Sr has been adapted from Pin et al. (2003), adjusting the columns and acids employed by successive column calibrations. During the adjustment method, the columns were calibrated with reference solutions of geological materials, collecting all fractions of reagents used to check where the Sr fraction was eluted.

The protocol is as follows (Figure 3.1):

Sr-Spec resin is weighed (ca. 83 mg), then slurried in 0.05 mol/l HNO_3 and transferred to a 0.5 mm (i.d.) quartz glass column to give a ca. 0.25 ml bed. Prior to use, the column is thoroughly cleaned with 1 ml 6 mol/l HCl then 1 ml 0.05 mol/l HNO_3, and then preconditioned with 2 ml of 2 mol/l HNO_3. The sample, left as a nitrate residue, is dissolved with 1.5 ml 2 mol/l HNO_3 and loaded onto the column as 0.5 ml portions. Ba and Sr (also Pb) are extracted by the Sr Spec resin. All the

other elements, including Rb, passed through the column to another column located beneath, where the Rb fraction will be purified (see below). The column is rinsed with 1 ml of 2 mol/l HNO_3 which included the Rb fraction. A Ba fraction is eluted from the Sr Spec column with 2 ml of 7 mol/l HNO_3 followed by 1 ml of 2 mol/l HNO_3. Finally, the Sr fraction is back-extracted using 2 ml 0.05 mol/l HNO_3.

3.2.c.2. *Second column: Cleaning of the Rb fraction*

In the next step, a perfect separation of the Rb and Zr is required. The purification is achieved with the Dowex AG50-W8 (200-400 mesh) cationic resin, loading 2 ml of it onto a 0.7 mm i.d. quartz glass column. Total separation of both elements is easily achieved by passing 2 mol/l HNO_3 (in 0.5 ml steps) through the column. The Zr is eluted (as a negatively charged fluoride ion) in the first steps (2 ml), while the Rb fractions is collected after in 2 ml (Figure 3.1). The Dowex resin also cleans part of the major elements. In fact, semi-quantitative analisys by Q-ICP-MS shows that the Rb cut also contains part of the major elements, above all, K, Na, Mg and Ca. Yet, the plasma ionizes all the elements and, as shown by Nebel et al. (2005) for instance, the presence of such matrix elements does not represent any analytical problem.

The analyte recovery achieved with this protocol is at least 95 %. Total procedures blanks, including the sample dissolution and the chemical separation process are less than 1 ng for Rb and ca. 4 ng for Sr.

3.2.d. Rb spectrometry

Isotopic analysis of Rb have been performed with a multicollection inductively coupled plasma mass spectrometer Fisher Scientific Neptune at the SGIker facility (UPV/EHU). See chapter 2 for more information about the equipment. The analysis are done in static mode employing Faraday cups positioned as shown in Table 3.5.

Table 3.5. Configuration of the collectors for Rb analysis.

L3	L2	L1	Center	H1	H2	H3	H4
83	84	85	86	87	88	90	91
Kr	Sr/Kr	Rb	Sr/Kr	Rb/Sr	Sr	Zr	Zr

The masses used for Rb measurements are 85 (Rb) and 87 (Rb/Sr). The only isobaric interference on a Rb isotope is ^{87}Sr. This interference can be reduced by the chemical separation of Rb from Sr prior to ICP-MS measurements as described above. Any interference from remaining Sr can be corrected by monitoring ^{88}Sr. In natural samples, the $^{87}Sr/^{88}Sr$ is variable due to the decay of ^{87}Rb. As pointed out by Waight et al. (2002), a 'common' $^{87}Sr/^{88}Sr$ composition for

interference correction can, in theory, only serve as a first approximation. For a robust correction, the true $^{87}Sr/^{88}Sr$ must be determined by separate Sr isotope measurements. In practice, these corrections are minor, because the use of Sr-Spec resin leads to nearly complete removal of sample Sr from the Rb cut. Thus, a Sr isotope composition of $^{87}Sr/^{88}Sr$ of 0.085 (corresponding to a $^{87}Sr/^{86}Sr$ of ~ 0.71) can be used for the interference correction.

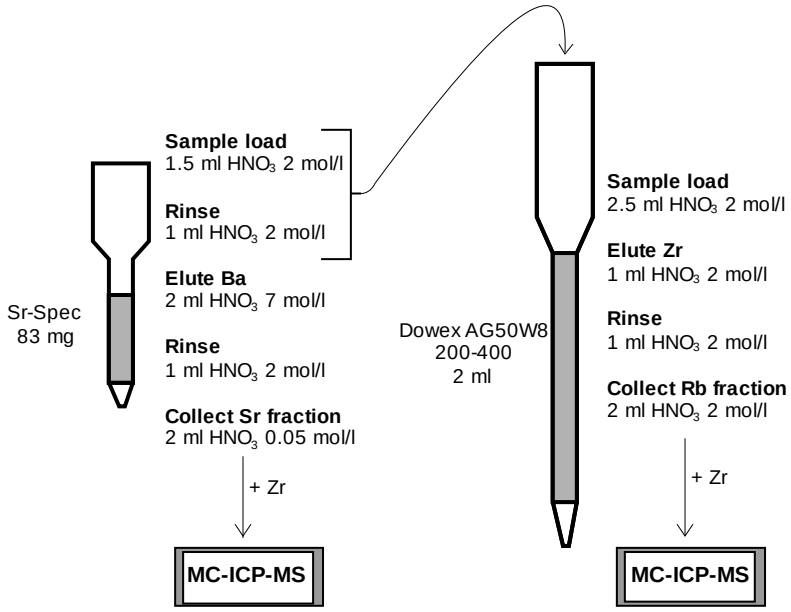

Figure 3.1. Diagram of the chemistry procedure for the separation of the analytes of interest, by using the Sr-Spec resin for Sr and the AG50Wx8 cation-exchange resin for Rb. See the text for further explanations.

The instrumental mass bias for Rb isotopes is corrected online to the Zr isotope composition of an admixed Zr Alpha-Aesar® standard solution (Waight et al., 2002). The isotopic composition of the Zr was firstly measured and mass bias corrected by $^{88}Sr/^{86}Sr$. The value obtained for the $^{90}Zr/^{91}Zr$ ratio was 4.5880, within the range of those presented by Sahoo and Masuda (1997) ($^{90}Zr/^{91}Zr$ = 4.5874 ± 74; 2 s.d.) and in good agreement with those of Minster and Ricard (1981) and Sanloup et al. (2000).

The $^{87}Rb/^{85}Rb$ ratio (corrected for isobaric ^{87}Sr) is then corrected for fractionation using the following exponential expression:

$$\left(\frac{^{87}Rb}{^{85}Rb}\right)_{true} = \left(\frac{^{87}Rb}{^{85}Rb}\right)_{meas} / \left(\frac{^{90}Zr/^{91}Zr}{4.5880}\right)^{\frac{\ln(mass^{87}Rb/mass^{85}Rb)}{\ln(mass^{90}Zr/mass^{91}Zr)}} \quad [23]$$

Calibration of the measurements is done by reference to a standard of Rb (SRM 984, Figure 3.2), which is then measured between samples regularly to ensure absence of any drift of the apparatus over time. The obtained value for $^{85}Rb/^{87}Rb$ ratio is 2.5905 ± 0.0005 (2 s.d, Figure 3.2), lower than those values obtained by TIMS (2.5976 by Edmunson et al., 2009; 2.612 by Borg et al., 2009), but within error. However, the value certified by the National Institute of Standards

and Technology (NIST) is 2.593 ± 0.002 (95 % CL; Cali, 1970), which is closer to the value obtained in our study. Nebel et al. (2005) obtanied a value of 2.5937 ($^{87}Rb/^{85}Rb$ = 0.38554 ± 30, 2 s.d.) using MC-ICP-MS methods, higher than that obtained here. The difference between theirs and our result would arise from the mass bias correction since Nebel et al. (2005) corrected by using the $^{92}Zr/^{90}Zr$ ratio whereas we have corrected by using the $^{90}Zr/^{91}Zr$. According to Nebel et al. (2005) rubidium ratios corrected with $^{90}Zr/^{91}Zr$ appear to be systematically higher than those corrected with $^{92}Zr/^{90}Zr$ (although both corrections would overlap within errors).

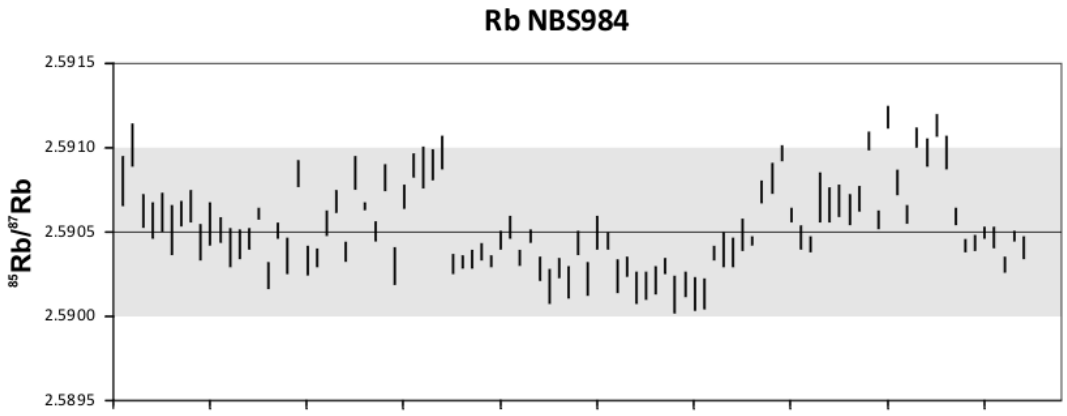

Figure 3.2. Analysis of NBS984 performed during this PhD Thesis.

3.2.e. Sr spectrometry

Isotopic analysis of Sr were also performed with the Neptune MC-ICP-MS at the SGIker facility (UPV/EHU). See chapter 2 for more information about the equipment. The analysis were done in static mode with Faraday cups positioned as shown in Table 3.6.

Table 3.6. Configuration of the collectors for Sr analysis.

L3	L2	L1	Center	H1	H2	H3	H4
83	84	85	86	87	88	90	91
Kr	Sr/Kr	Rb	Sr/Kr	Rb/Sr	Sr	Zr	Zr

The masses used for Sr measurements are 86 (Sr/Kr), 87 (Rb/Sr) and 88 (Sr). Minor isobaric interferences from ^{86}Kr on ^{86}Sr, and ^{87}Rb on ^{87}Sr are automatically corrected for based on the intensities simultaneously measured on the ^{83}Kr and ^{85}Rb cups (IUPAC values for $^{83}Kr/^{86}Kr$ and $^{85}Rb/^{87}Rb$ were assumed).

As mentioned previously, two aliquots, one of them spiked, are necessary to measure both isotopic composition and concentration of the Sr. The aliquot with no tracer is directly measured to obtain the $^{87}Sr/^{86}Sr$ composition. The ratio is internally corrected for mass fractionation by exponential law using a constant value of 0.1194 for $^{88}Sr/^{86}Sr$. The spiked aliquot, used to calculate the concentration of the sample, is dopped with Zr in the same way as the Rb

cut is. The instrumental mass bias for Sr isotopes is corrected online to the Zr isotope composition of an admixed Zr Alpha-Aesar® standard solution (Yang et al. 2008). The common practice of using a fixed value for $^{86}Sr/^{88}Sr$ ratio to implement internal standardization for mass bias correction is not possible to apply in these measurements due to the addition of the tracer, and therefore the unknown $^{86}Sr/^{88}Sr$ ratio. The mass bias correction is done as follows:

$$\left(\frac{^{86}Sr}{^{88}Sr}\right)_{true} = \left(\frac{^{86}Sr}{^{88}Sr}\right)_{meas} / \left(\frac{^{90}Zr/^{91}Zr}{4.5880}\right)^{\frac{\ln(mass^{86}Sr/mass^{88}Sr)}{\ln(mass^{90}Zr/mass^{91}Zr)}} \qquad [24]$$

Calibration of the measurements was made by reference to a standard of Sr (SRM 987, Figure 3.3), which is then measured between samples regularly to ensure absence of any drift of the apparatus over time. There are more than 100 reference values for the SRM 987 $^{87}Sr/^{86}Sr$ ratio measured with a MC-ICP-MS (http://georem.mpch-mainz.gwdg.de/). The values range from 0.7101 to 0.71065, being most of them around 0.71025. The value obtained in our measurements of 0.710251 ± 0.000026 (2 s.d.) closely agrees to this reference value.

3.2.f. Measurements parameters

The operating parameters are summarized in Table 3.7. Before starting the measuring sequence, it's worth to wait until plasma and Apex desolvation device are stabilized, around 45 minutes. After this time, optimization and adjustment of ion lens for maximum sensitivity and good peak shape for ^{86}Sr is performed in each session. For this purpose the Neptune Multi Element Standard Solution (8 element) sold by Thermo is used (Tune-Up Solution, ref. 1149340). The solution has 200 $ng.g^{-1}$ of Sr, and in case of using the Apex, it is diluted until 25 $ng.g^{-1}$ of Sr before analysis. The signal intensity of the isotope ^{86}Sr in this standard solution is about 3 V. This optimization, by monitoring the Sr, is also done before Rb analyses.

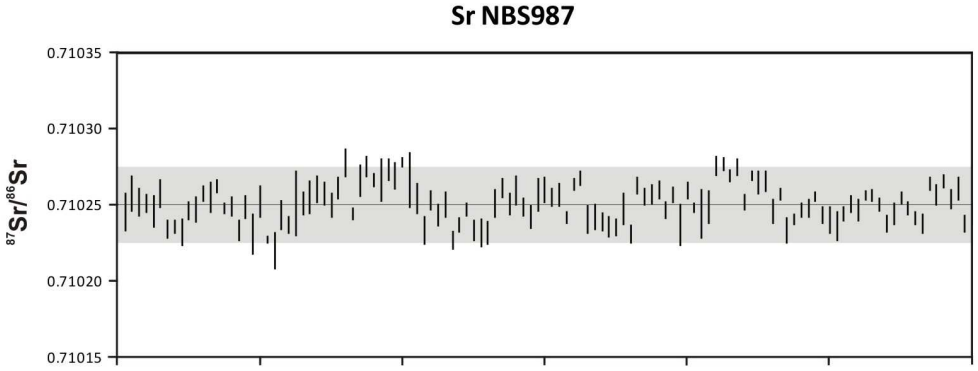

Figure 3.3. Analysis of NBS987 performed during this PhD Thesis and reference value ($^{87}Sr/^{86}Sr$ = 0.71025).

Once the parameters are adjusted, the analytical experiment is planned. The data acquisition is performed in static mode, 7 blocks of 10 measurement cycles are done, resulting in a 6 minutes data.

When samples are analysed by MC-ICP-MS, instrumental drift is a parameter that must be controlled. For that purpose, NBS987 and NBS984, are interspersed with the unknowns for Sr and Rb, respectively. Although the signal intensity will vary during long experiments, even up to ca. 10 %, no systematic shift of $^{87}Sr/^{86}Sr$ or $^{85}Rb/^{87}Rb$ have been found during analytical sessions. Acoordingly, no external correction (of the standard bracketing type for instance) has been applied to the unknowns.

3.2.g. Method validation on international standards

In order to validate the method, the results obtained by this method and the recommended values (both concentration and isotopic ratios) have been compared for 6 Certified Reference Materials (CRM) international standards. The standards have been selected to cover a wide range of compositions. Whenever possible, recommended values were selected from measurements with plasma based instruments. If ICP values were not found, values obtained by ID-TIMS have been taken into account.

The results are shown in Table 3.8. It should be noted that each value is the mean of two measurements of the same solution.

Table 3.7. MC-ICP-MS parameters for isotopic Sr and Rb measurements.

ICP Conditions	
RF power	1200 W
Sample gas flow	0.75-0.8 l/min
Coolant gas flow	15 l/min
Auxiliary gas flow	0.45 l/min
Aditional gas flow (N_2)	0.28-0.35 l/min
Sample uptake	60 sec
Washing time	60 sec
Uptake time (wash)	120 sec
Sampling time	ca. 6 min (7 blocks of 10 cycles each)
Integration time	4.194 sec/cycle
Idle time	3 sec
Apex	
T Apex 1	140 ^{o}C
T Apex 2	2 ^{o}C

Measured ratios for $^{87}Sr/^{86}Sr$ after sample preparation and subsequent separation by the method described above are within the margin of error of the expected value, except for the third analysis of each sample (sample C in each case). The measurements also appear moderately

dispersed showing that the whole analytical method leads to reproducible results. The measurements are sufficiently accurate and precise to enable the methods to be used in geochemical reasearch. Isotope ratios for samples AC-E and FK-N are not available in the literature. A higher inaccuracy in the $^{87}Sr/^{86}Sr$ ratio measurements of these two Rb-rich materials is observed but not accounted for at the moment. Given the correctness of the Rb separation and absence of Rb in the Sr fraction we can only speculate on a possible heterogeneity of the sample but this has to be demonstrated yet.

As previously stated, no consistent values have been obtained for the third repetition of each standard. During the sample separation, aliquot without tracer are always separate first, and after cleaning the resin, the spiked aliquots are loaded into the column. After both separations the resin is replaced. In the samples called 'C' the protocol was done in the other way around, loading first the spiked aliquot and then the clean one. After measuring the samples, it has been observed that all the samples are contaminated by spiked aliquot, so, this order of separation should not be follow.

The data obtained for concentrations of Rb and Sr are also reproducible, except for the analysis of AGV-2 D, which yielded significantly higher values for both elements. Moreover, the concentrations found are relatively close to the expected values. Since the Rb and Sr aliquots are set apart in two different containers after separation, we assume that the problem with sample AGV-2 D was related to sample preparation. Thus, since the $^{87}Rb/^{86}Sr$ for this sample is in the same range of the other AGV-2 repetitions, the error is attributed probably to a mistake when writing down the weighed quantity.

Sr concentration in AGV-2 A is higher than in other samples, which, together with similar Rb concentrations and lower values of $^{87}Rb/^{86}Sr$ ratios, suggest a small contamination in the Sr container in the time lapse between separation and measurement. It should be noted that AGV-2 aliquots, with the highest Sr concentration, needed to be strongly diluted before measuring, so a small contamination at this stage could be possible. At any rate, AGV-2 A value is within error compared to the other AGV-2 repetitions. The 5 repetitions were measured the same day, so analytical inaccuracies are not considered.

Rb concentrations are systematically lower than recommended values, although they are within error. It could be argued here that the difference between those measurement and the recommended values is due to a tracer inaccuracy during reverse isotopic dilution, or a loss during the attack. However, ID-TIMS values obtained for AGV-2 and BHVO-2 (Raczek et al., 2001; Willbold and Jochum, 2005) are in a better agreement with the data presented here. The difference could in this case be explained simply by the fact that the instruments and analytical methodologies used are themselves very different. On one hand, single detector ICP-MS with

external adjustment (standard bracketing correction) and according to a linear law of mass bias from a natural isotopic composition and, on the other hand, ID-MC-ICP-MS with internal correction according to an exponential law of mass bias (see above).

Table 3.8. Results obtained for international standards by the isotopic composition-isotope dilution method described in the text. Comparison with the recommended values. (a) Yang et al. (2012); (b) Balcaen et al. (2006); (c) Yang et al. (2010); (d) Zhang et al. (2012); (e) Georem Preferred Value (Jochum and Nehring, 2006); (f) Yu et al. (2001); (g) Govindaraju (1995).

Standard	$^{87}Sr/^{86}Sr$			Sr concentration			Rb concentration			$^{87}Rb/^{86}Sr$	± 2σ
	Reference	Measured	± 2 S.E.	Reference	Measured	± 2σ	Reference	Measured	± 2σ		
AGV-2-A	0.703994 ± 15 (2σ) (a)	0.703974	2E-05	654 ± 3 (1σ) (d)	675	8	67.7 ± 0.7 (1σ) (d)	65.3	0.5	0.2802	0.0014
AGV-2-B		0.703993	1E-05		649	7		65.2	0.5	0.2910	0.0015
AGV-2-C					664	8		66.2	0.5	0.2888	0.0014
AGV-2-D		0.704004	2E-05		723	8		72.8	0.6	0.2912	0.0015
AGV-2-E		0.703994	1E-05		664	8		66.2	0.5	0.2886	0.0014
BHVO-2-A	0.703479 ± 20 (2σ) (a)	0.703477	2E-05	396 ± 1 (1σ) (e)	397	5	9.11 ± 0.04 (1σ) (e)	8.84	0.07	0.0645	0.0003
BHVO-2-B		0.703476	3E-05		399	5		8.92	0.07	0.0648	0.0003
BHVO-2-C					396	5		8.83	0.07	0.0645	0.0003
BHVO-2-D		0.703509	2E-05		397	5		8.83	0.07	0.0644	0.0003
BHVO-2-E		0.703485	2E-05		397	5		8.91	0.07	0.0650	0.0003
G-2-A	0.70977 ± 16 (2σ) (TIMS) (b)	0.709774	2E-05	483 ± 2 (1σ) (d)	483	6	166 ± 4 (1σ) (d)	164	1	0.9816	0.005
G-2-B		0.709744	2E-05		485	6		164	1	0.9774	0.005
G-2-C					485	6		164	1	0.9782	0.005
G-2-D		0.709729	2E-05		481	5		164	1	0.9895	0.005
G-2-E		0.709766	3E-05		481	5		164	1	0.9897	0.005
W-2-A	0.706966 ± 31 (2σ) (TIMS) (c)	0.706983	2E-05	202 ± 3 (1σ) (d)	195	2	19.5 ± 0.1 (1σ) (d)	19.24	0.15	0.2861	0.0014
W-2-B		0.706973	2E-05		195	2		19.39	0.16	0.2875	0.0014
W-2-C					198	2		19.29	0.15	0.2823	0.0014
W-2-D		0.706999	2E-05		196	2		19.14	0.15	0.2825	0.0014
W-2-E		0.706995	2E-05		198	2		19.33	0.15	0.2835	0.0014
AC-E-A		0.86623	1E-04	2.6 ± 8.14 RSD(%) (f)	No tracer added		148 ± 5 RSD(%) (f)	145	1		
AC-E-B		0.85935	5E-05					145	1		
AC-E-C					2.61	0.03		144	1	162.24	0.81
AC-E-D		0.85342	7E-05		2.60	0.03		145	1	163.23	0.82
AC-E-E		0.86356	7E-05		2.60	0.03		145	1	163.35	0.82
FK-N-A		1.2080	3E-05	39 (g)	No tracer added		860 (g)	849	7		
FK-N-B		1.2063	1E-04					856	7		
FK-N-C					38.7	0.4		850	7	66.701	0.33
FK-N-D		1.2075	2E-05		38.4	0.4		853	7	67.446	0.34
FK-N-E		1.2080	4E-05		38.4	0.4		853	7	67.524	0.34

As far as we know, $^{87}Rb/^{86}Sr$ ratios in international standards are currently non-existent in the literature. It is worth mentioning that the ratios determined after analysis by the method explained here are perfectly reproducible. External reproducibility is identical to the internal precision for all samples, and systematically lower than 3 % RSD.

The results obtained for six international standars, both for $^{87}Sr/^{86}Sr$ ratios and Rb and Sr concentrations, allow us to infer that the protocol set up is valid for the application of it to the Rb-Sr systematics in geochronology.

3.3. The Lu-Hf system by ID-MC-ICP-MS

3.3.a. Introduction

The Lu-Hf couple is another system used for isotope tracing and dating of geological events. ^{176}Lu displays a branched isobaric decay, by β-emission to ^{176}Hf and by electron capture to ^{176}Yb. However, the latter makes up only a few percent at most of the total activity and can be neglected (Dixon et al., 1954).

$$^{176}Lu \rightarrow {}^{176}Hf + \beta^{-} + Q$$

Lutetium lies at the end of the lanthanide series as the 'heaviest' of the Rare Earth Elements (REE), whereas the Hf is an element of the High Field Strength Element (HFSE) group. Therefore, many geochemical processes strongly decouple this two elements, which allows the individualization of reservoirs having contrasting degree of radiogenic character within the same geological assemblage. Specifically, the Lu can easily enter the crystal lattice of the garnet (also apatite or lawsonite), while Hf is only compatible with a limited number of accessory minerals (zircon, rutile, baddeleyite).

For ^{176}Lu, there is no consensus about the value of the decay constant (Scherer et al., 2000; Blichert-Toft, 2001). A great deal of values have been published over the past, both by direct counting (Dalmasso et al., 1992; Nir-El et Lavi, 1998) or by inter-comparison with the U-Pb system (Scherer et al., 2001). In this study, lutetium-hafnium ages are calculated using the ^{176}Lu decay constant of $1.867\times10^{-11}y^{-1}$ (Scherer et al., 2001; Söderlund et al., 2004), which is the most widely used value in the recent publications (Anczkiewicz et al., 2007, Kylander-Clark et al., 2007, Schmidt et al., 2008, Kirchenbaur et al., 2012).

Isotopic compositions and atomic weights of the elements involved in the spectrometry of Lu and Hf are presented in the tables below (Tables 3.9; 3.10; 3.11 and 3.12).

Table 3.9. Abundance of Yb, Lu and Hf isotopes (in %), according to the IUPAC (International Union of Pure and Applied Chemistry; De Laeter et al., 2003).

	168	170	171	172	173	174	175	176	177	178	179	180
Yb	0.13	3.04	14.28	21.83	16.13	31.83		12.76				
Lu							97.41	2.59				
Hf						0.16		5.26	18.60	27.28	13.62	35.08

Table 3.10. Atomic masses of yttterbium, according to IUPAC (International Union of Pure and Applied Chemistry; De Laeter et al., 2003).

Isotope	168	170	171	172	173	174	176
Mass	167.933895	169.934759	170.936322	171.936378	172.938207	173.938858	175.94256

Table 3.11. Atomic masses of lutetium, according to the IUPAC (International Union of Pure and Applied Chemistry; De Laeter et al., 2003).

Isotope	175	176
Mass	174.940768	175.942682

Table 3.12. Atomic masses of hafnium, according to the IUPAC (International Union of Pure and Applied Chemistry; De Laeter et al., 2003).

Isotope	174	176	177	178	179	180
Mass	173.940042	175.941403	176.9432204	177.9436981	178.9458154	179.9465488

3.3.b. Spike addition and sample digestion

Sample digestion will vary depending on the aim of the measurement. Accessory minerals such as zircon or rutile are major hosts for Hf, and whether they are brought into solution or not, the significance of the final results will have different meaning, sometimes being useless. Another problem associated to these minerals is their refractory character, making them difficult to dissolve. In our case, attack by alkaline fusion is done when we have interest in dissolving the refractory minerals, thus guaranteeing that all the Hf in the sample will be found inside the dissolution. If our interest is to measure the Hf of a specific part of the rock (i.e. separate of minerals), attack by acids is considered more appropriate, because it may allow us to leave the highly refractory zircons (by far the most important repository of Hf in silicic rocks) essentially undissolved.

The tracers used in this thesis are ^{176}Lu (enriched to 44.23 %, Oak Ridge National Laboratory, USA) and ^{179}Hf (enriched to 89.87 %, Oak Ridge National Laboratory, USA). Their concentration was calibrated by reverse isotope dilution against normal solutions. These were prepared by accurate dilution, by weight, of ca. 1000 ± 2 mg/l single element solutions purchased from Fluka Analytica for the Lu and Merck for the Hf. The isotopic compositions of the enriched tracers used in isotope dilution calculations were measured by MC-ICP-MS, with correction for instrumental mass bias by standard bracketing. A mixture made from a pure fraction of both ^{176}Lu

and ^{179}Hf allows to obtain a mixed tracer of Lu-Hf concentrated enough to allow the addition of a small amount prior to the attack by fusion. The Lu/Hf ratio in the tracer is high enough (about 6) to be used on a wide range of samples, ranging from subchondritic rock ratios (Lu/Hf ≈ 0.23) to garnet samples (Lu/Hf up to 30).

Considering the usual contents of rocks and garnets (our 'target' minerals for Lu-Hf geochronology, see Chapter 4) and given the interest of adding small tracer volumes (typically 100 µl of tracer to 100 mg of sample), the optimum concentration of Hf in the tracer has been calculated in the range of 0.25 µg.g^{-1}. The content of Lu is therefore adjusted to about 6 times the content of Hf, approximately 1.5 µg.g^{-1}.

These concentrations have important benefits. The Hf is the most sensitive element in the tracer/sample ratio, as we need to measure the ^{176}Hf/^{177}Hf ratio of the sample. Therefore, ^{176}Hf/^{177}Hf should be preserved as much as possible after adding the tracer (minimizing the magnitude of the required correction). Besides, this allows a ^{179}Hf/^{177}Hf ratio of about 1 to be measured, thereby keeping the error magnification of isotopic dilution calculations (Webster, 1960) to a minimum.

The characteristics of the mixed tracer ^{176}Lu-^{179}Hf are given in Table 3.13.

Table 3.13. Characteristics of the mixed tracer ^{176}Lu-^{179}Hf

Trace isotope	Abundance of tracer isotope	Elemental concentration (µg.g^{-1})	Concentration in tracer isotope (µmol.g^{-1})
^{176}Lu	44.23 %	1.629 ± 0.024 (2σ)	$9.29.10^{-3}$ ± 0.05 % (RSD)
^{179}Hf	97.02 %	0.2132 ± 0.0016 (2σ)	$1.191.10^{-3}$ ± 0.05 % (RSD)

3.3.b.1. *Method of attack by alkaline fusion*

An electrical Joule-effect automatic fusion machine (Katanax, K1 Prime Fluxer) is used for sample decomposition by fusion following a procedure after Le Fèvre and Pin (2002). Parts of the furnace that can get into contact with the sample are cleaned before each sample.

In order to add optimal quantities of the isotopic tracers, it is useful to know approximately the concentrations of the analytes in the samples to be analysed. A preliminary semi-quantitative Q-ICP-MS analysis is therefore done if needed to provide an estimate of Lu and Hf content.

Sample powder (50-100 mg) is weighed into a platinum crucible with flat bottom. The weighted quantity depends on the Hf concentration of the sample, and is chosen in order to permit the extraction of at least 40 ng of Hf (usually there is no problem with bulk rock analysis). The flux ($LiBO_2$) is added to the sample, until a final flux to sample ratio of 5:1 is reached. This flux/sample ratio is a bit high, but the characteristics of the fusion machine and crucible obliged

us to work with such a large amount of flux, otherwise the melt does not drop out to the beaker. The blank level and the values obtained for international standards were acceptable (see below), enabling us to conclude that using a flux to sample ratio as high as five does not cause major problems.

The mixed isotopic tracer is then added in a liquid form and weighed. After addition of the isotopically enriched tracers, the beaker is manually agitated, until sample powder/flux and spikes are well mixed, and dried locating the crucible next to the furnace for a while. After thorough homogenization, the sample-flux blend is placed during 10 minutes in the furnace, at a temperature of 1200 °C (this is the actual temperature in the crucible according to the manufacturer).

The resulting melt is poured and quenched in disposable 30 ml polystyrene beakers containing 10 ml of 2 mol/l HCl + 0.15 % H_2O_2 continuously stirred with a magnetic bar. Hydrogen peroxide is added in order to prevent, or at least slow down the hydrolysis of the HFSE (Dahmer and Fritz, 1965). Complete dissolution and cooling are achieved within 10-15 minutes.

3.3.b.2. *Method of attack by acid digestion*

As explained before, for some samples it is preferable to use an acid attack. The choice of this method is subject to a specific need, especially, avoiding to decompose any inclusions of zircon or rutile in garnet, which are enriched in Hf and thus, could contaminate the sample.

During the chemical separation of Lu, other REE of interest (Sm and Nd) could be easily extracted and measured either by TIMS or MC-ICP-MS. The presence of REE-rich mineral inclusions (phosphates as apatite and monazite) will be a source of problems in the Sm-Nd system. To circumvent this problems, a sulfuric acid (H_2SO_4) partial dissolution technique was used, following the procedure of Anczkiewicz and Thirlwall (2004, see below).

During this PhD Thesis, Sm and Nd are collected during the Lu purification step, but only for the real samples (Chapter 4). Since the protocol for separation and measuring these elements was validated in our lab long time ago (Menéndez, 2001 or Sanchez-Lorda et al., 2013), so it has been considered suitable for measurements.

Another difficulty is that Hf is very sensitive to hydrolysis and it is difficult to keep stable solutions for a long time without the use of a suitable complexing agent like HF. However, fluoride complexes are not retained by the material used for the separation of Hf (Dowex AG50-W8). In order to reduce fluorine to a sufficiently low level, we chose to treat the solutions to strong fumes of perchloric acid ($HClO_4$), as described by Pin and Joannon (2003). To prevent hydrolytic problems, hydrogen peroxide was used, and the solutions were handled promptly.

The protocol of the acid attack is as follows:

An appropriate amount of the sample (aiming to separate about 40 ng Hf at least) is crushed in an agate mortar and cleaned with acetone and H_2O. After drying the sample, the powder is transferred to a container of Teflon PFA (Savillex®). As described by Anczkiewicz and Thirlwall (2004), 0.5 ml to 1 ml of sulfuric acid is added (depending on the sample size) and the vial is heated at 180 °C for 24 hours (sulfuric acid leaching, aiming to dissolve phosphate accessory minerals). The leachate is discarded and the sample is rinsed several times with H_2O in order to remove all the sulfuric acid, since sulfuric acid cannot be evaporated below the melting point of Teflon. Careful rinsing at this step is crucial. Additional difficulty is caused by the high viscosity of H_2SO_4. Smaller grains remain suspended longer in the acid and might be removed during cleaning, having a severe sample loss. Repetitive rinses with H_2O reduces acid concentration (and viscosity), thereby helping to avoid sample loss.

Once cleaned, the sample is transferred in a drop of water into a new vial, dried and weighed. The evaporation should be done slowly and at low temperature, otherwise samples will tend to 'jump' out from the beaker due to electrostatic forces. Slow evaporation will also help in the total evaporation of the H_2O, which otherwise could lead to an overestimation of the sample weight. Before the acid attack of the sample, both Lu-Hf and Sm-Nd tracers are added, by weight.

The acid attack protocol starts with the addition of 2 ml of 14 mol/l HNO_3, 1 ml of 29 mol/l HF and 0.5 ml of 11.8 mol/l $HClO_4$. The beaker is closed and slightly heated overnight (about 75 °C) to dissolve the sample. After opening the vial, the excess of hydrofluoric and nitric acids are evaporated, together with volatile SiF_4. During evaporation, 4 ml of 11.8 mol/l $HClO_4$ are added and the solution is brought to strong fumes of perchloric acid under an infra-red heater, taking care not to 'overcook' the mixture, which must remain in the liquid state. The condensates that form on the walls of the beaker are regularly rinsed with H_2O. The fuming step is stopped well before evaporation goes to completion, leaving about 0.5-1 ml of liquid. 5 ml of 6 mol/l HCl are added and transferred to a centrifuge tube to isolate undissolved minerals (mainly zircon and rutile). The supernatant, clear solution is placed in the container of attack, and again evaporated until about 1ml is left.

Just prior to column work, the approximately 1 ml sample solution is diluted with 9 ml of 1.5 mol/l HCl-0.15 % H_2O_2. The sample is therefore in a medium and a volume identical to those prepared by fusion (10 ml of 2 mol/l HCl - 0.15 % H_2O_2), which allows the use of a single separation scheme for the two methods of attack.

3.3.c. Chemical separation

As ^{176}Yb, ^{176}Lu and ^{176}Hf obviously interfere with each other, it is necessary to chemically separate Yb and Lu from Hf prior to the measurements with MC-ICP-MS. To carry out this, the samples, must undergo two separation processes with different resins based on ion exchange chromatography and extraction chromatography, respectively (Figure 3.4).

3.3.c.1. ***First column: Separation of Hf + REE by cation exchange***

The separation of the Hf from the matrix elements is achieved with the Dowex AG50-W8 (200-400 mesh) cationic resin, loading 8 ml of it onto a 1 cm i.d. quartz glass column. Prior to use (the day before), the column is thoroughly cleaned with several rinses of 6 mol/l HCl and 5 mol/l HNO_3 - 0.1 mol/l HF. Finally, H_2O is allowed to flow through the column during the night. Our reservoir allows us to leave 100 ml of H_2O passing overnight. Prior to sample loading, the column is preconditioned with 10 ml 2 mol/l HCl. The sample is then loaded onto the column. During the procedure applied, other elements are separated, and although not of interest in the present case, they will be mentioned.

In the first step, the column is rinsed with 20 ml of 2 mol/l HCl. After this, 20 ml of 2 mol/l HNO_3 are loaded onto the column. This fraction contains U and Rb, and can be collected if required. With a further 30 ml of the same acid, Sr can be collected. Another 25 ml of this nitric acid are added to elute Ba, and discarded. Then, 40 ml of 0.5 mol/l H_2SO_4 allows most of the Zr to be eluted. At this step, we go back to nitric acid, but 3.5 mol/l in that case. 15 ml of that acid are first discarded; then, the REE (Sm, Nd, Lu for our purpose) are collected in the next 20 ml. Other 15 ml are eluted. For separation of the Hf, a mixture of 5 mol/l HNO_3 - 0.1 mol/l HF is needed. First of all, 4 ml of this mixture are eluted and, finally, adding another 3 ml onto the column, the Hf is collected. This fraction is ready for Hf isotopic analyses by MC-ICP-MS. We usually stop at this step, but if one is interested in collecting Th, this element can be eluted with an additional volume of 13 ml of 5 mol/l HNO_3 - 0.1 mol/l HF.

3.3.c.2. ***Second column: Concomitant separation of the REE by Extraction Chromatography***

The separation of the Sm, Nd and Lu is achieved following the method described by Le Fèvre and Pin (2005) which uses the Ln-Spec extraction chromatography material, loading 0.6 ml of it onto a 0.5 mm i.d. quartz glass column. Before loading the sample, the column is cleaned with 6 mol/l HCl and the conditioning is done with 0.05 mol/l HNO_3.

The 20 ml of 3.5 mol/l HNO_3 containing the REE, separated on the first column, are evaporated to dryness overnight. The residue is taken up with 1 ml of 0.05 mol/l HNO_3 and loaded onto the column. The Ln-Spec material allows the separation of all the REE, and the sequence used in our case consists of 8 ml of 0.25 mol/l HCl (La-Ce-Pr pro parte), 2 ml of 0.25 mol/l HCl (Nd plus Pr pro parte), elution of 1.5 ml of 0.75 mol/l HCl, another 1.5 ml of 0.75 mol/l HCl (Sm plus <5% Eu), followed by 15 ml of 3 mol/l HNO_3 (Gd-Tb-Dy-Ho-Er-Tm), 7 ml of 5 mol/l HNO_3 (ca. 90 % of Yb). Finally, the Lu (plus ~10 % of Yb) is collected with 8 ml of 5 mol/l HNO_3. The reason for collecting ca. 10 % of Yb within the Lu cut will be explained in the part of Lu spectrometry (see below).

If the Nd and Sm fractions are going to be measured, each of them is collected in single-use, polystyrene pots and evaporated to dryness before isotopic analyses by either TIMS or MC-ICP-MS. Specific protocols for this purpose have been presented elsewhere (Menéndez, 2001 or Sanchez-Lorda et al., 2013).

The recoveries achieved with this protocol are 95 % or more. Total procedural blanks, including the sample dissolution and the chemical separation are ca. 35 pg for Hf and 20 pg for Lu.

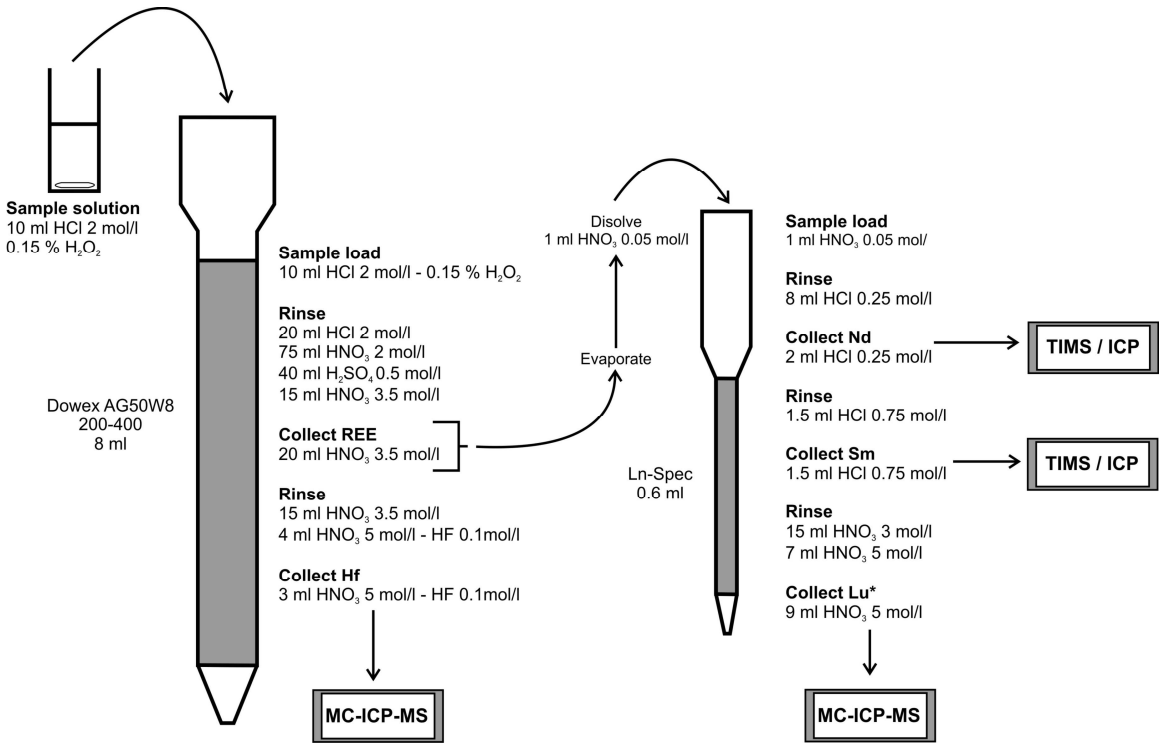

Figure 3.4. Diagram of the chemistry procedure for the separation of the analytes of interest using the AG50Wx8 cation-exchange resin for Hf, and the Ln-Spec material for Sm, Nd and Lu*. Lu*: this cut contains part of Yb. See the text for further explanations.

3.3.d. Lu spectrometry

Isotopic analysis of Lu is performed with a multicollection inductively coupled plasma mass spectrometer Thermo Fisher Scientific Neptune at the SGIker facility of the University of the Basque Country UPV/EHU. See chapter 2 for more information about the equipment. The analysis is done in the static mode, with the cup configuration shown in Table 3.14.

The masses used for Lu measurements are 175 (Lu) and 176 (Yb, Lu, Hf). Lu has only two isotopes, so it is not possible to standardize the measurements to a constant ratio. To correct for the instrumental mass bias, a neighboring element with similar mass and chemical properties is used: Yb, although this element directly interferes with Lu at m/z 176. This is why ca. 10 % of the Yb of the sample is collected together with the Lu fraction. The ratio $^{171}Yb/^{173}Yb = 0.88296$ (Amelin and Davis, 2005) is used to correct the Lu, assuming that the mass bias is comparable. The interference of ^{176}Yb on ^{176}Lu is corrected based on the ratio $^{176}Yb/^{173}Yb = 0.7964$ (Amelin and Davis, 2005), constant in nature, and taking into account the mass bias of the spectrometer. The absence of Hf in the measured fraction is monitored at m/z = 178 (or 177 or 179). The Hf signal, however, is usually close to the background level, and the interference is therefore not significant.

Table 3.14. Configuration of the collectors for Lu analysis.

L4	L3	L2	L1	Center	H1	H2
171	173	175	176	177	178	179
Yb	Yb	Lu	Lu/Yb/Hf	Hf	Hf	Hf

Calibration of the measurements is made by reference to the single element standard solution purchased in our laboratory (the same used for reverse isotope dilution), which is measured between samples regularly to ensure absence of any significant drift of the instrument. The value obtained for the natural $^{176}Lu/^{175}Lu$ ratio is 0.02656 ± 0.00001 (2 s.d., Figure 3.5), similar to the values obtained by other authors for this ratio (Patchett and Tatsumoto, 1980; Blichert-Toft and Albarède, 1997; Scherer et al., 2001; Vervoort et al., 2004). For these determinations, the correction for mass bias was done by the addition of Yb from a single element standard solution.

3.3.d.1. *Correction of the participation of Yb on the mass 176*

Collect Yb within the Lu cut creates the problem that there is a strong interference of the Yb in Lu on the mass 176. This interference must be corrected in advance, according to the method described below.

Measurement of the ratio $\left(\frac{176}{175}\right)_{meas} = \frac{^{176}Lu + ^{176}Yb}{^{175}Lu}$, from this we calculate the ratio $\frac{^{176}Lu}{^{175}Lu}$.

Now, we can write:

$$\frac{^{176}Lu}{^{175}Lu} = \frac{^{176}Lu + ^{176}Yb}{^{175}Lu} \cdot \frac{^{176}Lu}{^{176}Lu + ^{176}Yb} = \left(\frac{176}{175}\right)_{meas} \cdot \frac{^{176}Lu}{^{176}Lu + ^{176}Yb} \quad [25]$$

Where ^{176}total = ^{176}Yb + ^{176}Lu, so:

$$\frac{^{176}Lu}{^{176}Lu + ^{176}Yb} = 1 - \frac{^{176}Yb}{^{176}Lu + ^{176}Yb} \quad [26]$$

We can now multiply the second part of the Eq. [26] by $\frac{^{173}Yb}{^{173}Yb}$, to find the measured or known values:

$$1 - \frac{^{176}Yb}{^{173}Yb} \cdot \frac{^{173}Yb}{^{176}Lu + ^{176}Yb} = 1 - \left(\frac{\left(\frac{176}{173}\right)\text{Yb}}{\left(\frac{176}{173}\right)_{meas}}\right) \quad [27]$$

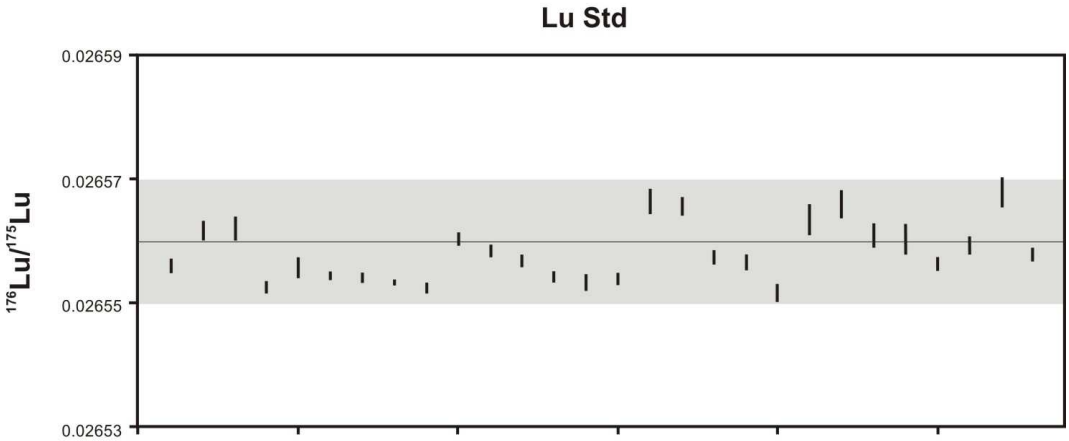

Figure 3.5. ^{176}Lu/^{175}Lu ratios for analyses of the lutetium standard (Fluka Analytica) performed during this PhD Thesis.

Replacing in the Eq. 25, we get:

$$\frac{^{176}Lu}{^{175}Lu} = \left(\frac{176}{175}\right)_{meas} - \left[1 - \left(\frac{\left(\frac{173}{176}\right)\text{Yb}}{\left(\frac{176}{173}\right)_{meas}}\right)\right] \quad [28]$$

In this case, the instrumental mass bias affecting the ^{176}Yb/^{173}Yb ratio must be assigned, being assumed to be comparable to the measured ratio $\left(\frac{^{176}Lu + ^{176}Yb}{^{173}Yb}\right)_{meas}$. This assigned mass bias is calculated on the basis of the natural and constant ratio ^{176}Yb/^{173}Yb, and reversing the used fractionation law. This is done by using an exponential law, which is of the form:

$$\left(\frac{I_1}{I_2}\right)_{true} = \left(\frac{I_1}{I_2}\right)_{meas} \cdot \left(\frac{MM\,(I_1)}{MM\,(I_2)}\right)^f \quad [29]$$

where I_1 and I_2 are two isotopes of the element measured, expressed in numbers of atoms, *MM* is the molar mass of the isotope indicated between the parentheses, and *f* is the correction factor of bias. The exponential law is chosen because, empirically, it seems to be the most appropriate to describe the mass bias of plasma source devices (Taylor et al., 1995; Halliday et al., 1995).

This law is easily reversed to give the 'measured' ratio according to the natural ratio (or true):

$$\left(\frac{I_1}{I_2}\right)_{meas} = \left(\frac{I_1}{I_2}\right)_{true} \cdot \left(\frac{MM\,(I_1)}{MM\,(I_2)}\right)^{-f} \quad [30]$$

In the case of the Yb, with masses analyzed in our measurements, the unique possibility to calculate the *f* factor is from the interference free isotopes of Yb (171 and 173).

We calculate (from Eq. [29] and Eq. [30]):

$$f_{173} = \frac{\ln\left(\frac{\left(\frac{171}{173}\right)_{nat}}{\left(\frac{171}{173}\right)_{meas}}\right)}{\ln\left(\frac{MM(171)}{MM(173)}\right)}, \quad [31] \qquad \text{then,}$$

$$\left(\frac{^{176}Yb}{^{173}Yb}\right)_{meas} = \left(\frac{^{176}Yb}{^{173}Yb}\right)_{nat} \cdot \left(\frac{MM\,(176)}{MM\,(175)}\right)^{-f_{173}} \quad [32]$$

From the Eq. [28], we can calculate the ^{176}Lu/^{175}Lu ratios. These ratios are not corrected for the mass bias at this stage and need to be corrected according to the exponential law, taking as the value of *f* the value used to calculate the corresponding ^{176}Yb/^{173}Yb ratio.

3.3.d.2. *Calculation of the concentration*

The calculation of the concentration of Lu uses the equation of the isotope dilution, detailed in the introduction of this chapter. Just to remember, the final equation used is as follows:

$$^{175}Lu_s = \frac{\left(\frac{^{176}Lu}{^{175}Lu}\right)_m \left(\frac{^{175}Lu}{^{176}Lu}\right)_t - 1}{\left(\frac{^{176}Lu}{^{175}Lu}\right)_s - \left(\frac{^{176}Lu}{^{175}Lu}\right)_m} \cdot \left[^{176}Lu\right]_t \cdot Pds(t) \quad [33]$$

3.3.d.3. *Error propagation and final uncertainty*

For detailed calculations of propagation of errors on the concentration of Lu, the reader will be referred again to the theory of the isotope dilution method at the beginning of the chapter. Here we remind the expression of this uncertainty, which is equal to:

$$\left(\frac{\sigma\,[Lu]}{[Lu]}\right)^2 = \left(\frac{\sigma\left[^{176}Lu\right]_t}{\left[^{176}Lu\right]_t}\right)^2 + \left(\frac{\sigma\left(\frac{^{176}Lu}{^{175}Lu}\right)_m}{\left(\frac{^{176}Lu}{^{175}Lu}\right)_m}\right)^2 M \quad [34]$$

where the values in brackets indicate concentration (mass for the Lu, and molar to 176_t), and where *M* is the amplification factor of the error (Webster, 1960).

3.3.e. Hf spectrometry

Isotopic analyses of Hf were performed with an multicollection inductively coupled plasma mass spectrometer Thermo Fisher Scientific Neptune at SGIKER (UPV/EHU). See Chapter 2 for more information about the equipment. The analyses were done in static multi-collection mode with the cups positioned as shown in Table 3.15.

Table 3.15. Configuration of the collectors for Hf analysis.

L4	L3	L2	L1	Center	H1	H2
171	173	175	176	177	178	179
Yb	Yb	Lu	Lu/Yb/Hf	Hf	Hf	Hf

During hafnium isotope analysis, any ^{176}Yb and ^{176}Lu isobaric interferences on ^{176}Hf are monitored by measuring masses 173 and 175, respectively, and corrected for, if required. The values for constant isotope ratios used for correction of isobaric interferences are: ^{176}Yb/^{173}Yb = 0.7964 (Amelin and David, 2004), and ^{176}Lu/^{175}Lu= 0.02656 (Patchett and Tatsumoto, 1980; this study), respectively. However, the ^{176}Lu/^{175}Lu ratio is different from the natural value when a mixed Lu-Hf spike is used. To avoid any bias in 176 due to unnatural Lu compositions, it would be possible to correct for the interference by using the ^{176}Lu/^{175}Lu ratio previously measured during the Lu isotope dilution run. However, Lapen et al. (2004) noted that this approach produces significant discrepancy between the ^{176}Hf/^{177}Hf ratios measured on spiked and unspiked samples. Following the suggestion of these authors, we have decided to use the isotope ratio of natural Lu to correct for isobaric interferences because it is likely that the sample to blank (natural Lu) ratio of Lu in the Hf cut is very low.

Calibration of the measurements is made externally by reference to a standard of Hf (JMC 475 Johnson Matthey) which is then regularly measured between samples in order to ensure absence of any drift of the instrument over time. The value obtained in our instrument for the ^{176}Hf/^{177}Hf ratio is 0.282151 ± 6 (2 s.d., Figure 3.6), close to other measurements done in other laboratories with the same model of MC-ICP-MS (e.g., Schmidt et al., 2011; Cheng et al., 2012; 0.282152).

The instrumental mass bias is corrected by using an exponential law, and a reference value for ^{179}Hf/^{177}Hf = 0.7325 (Patchett and Tatsumoto, 1980), and all the ratios are in reference to the mass 177. Measurements of Hf isotopic composition and associated errors presented in this work are those calculated online during the acquisition.

Isotopic composition-isotopic dilution simultaneous measurements on totally spiked samples are made by using the same procedure, but the 'raw' measurements, corrected only for any significant interference on the mass 176, are processed offline for mass bias correction and tracer contribution, because the natural values for reference isotope ratios cannot be used any

longer, due to the addition of the 179-tracer, which is not 100 %-enriched. The calculation method is described in the following pages.

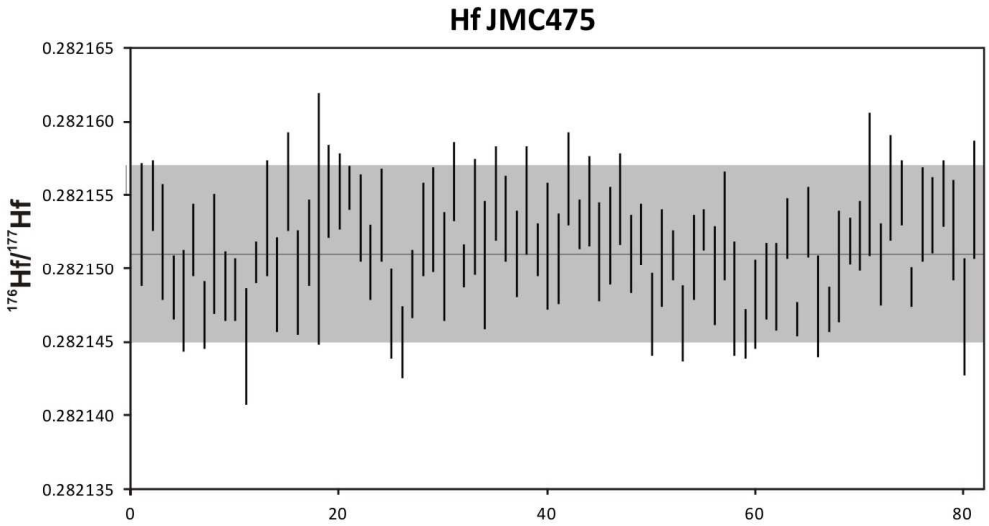

Figure 3.6. Results of $^{176}Hf/^{177}Hf$ ratio for analysis of JMC475 performed during this PhD Thesis.

3.3.e.1. *Mass bias correction*

Several approaches to this problem have been proposed, differing in general by combinations made from the constant terms, for example: Kostitsyn and Zhuravlev (1987). The method used in this work is based on that used by Brieuc LeFèvre (2002) in his PhD Thesis, using a procedure set up and updated by Jean Louis Birck (IPG Paris, personal communication).

The calculation is based on three isotopes *A*, *B* and *C* of the same element, forming two independent ratios $\frac{A}{B}$ and $\frac{C}{B}$. *A* is the tracer isotope, *B* is the reference isotope and *C* is the normalization isotope. The equation of the isotope dilution (see introduction of the chapter) allows us to write two expressions of the mixture (*m*) between the tracer (*t*) and sample (*s*):

$$\frac{B_s}{B_t} = \frac{\left(\frac{A}{B}\right)_m - \left(\frac{A}{B}\right)_t}{\left(\frac{A}{B}\right)_S - \left(\frac{A}{B}\right)_m} \text{ and } \frac{B_s}{B_t} = \frac{\left(\frac{C}{B}\right)_m - \left(\frac{C}{B}\right)_t}{\left(\frac{C}{B}\right)_s - \left(\frac{C}{B}\right)_m} \quad [35]$$

after rearranging;

$$\overbrace{\left(\frac{A}{B}\right)_t\left(\frac{C}{B}\right)_s - \left(\frac{A}{B}\right)_s\left(\frac{C}{B}\right)_t}^{\alpha} = \left(\frac{A}{B}\right)_m \cdot \overbrace{\left(\left(\frac{C}{B}\right)_s - \left(\frac{C}{B}\right)_t\right)}^{\beta} + \left(\frac{C}{B}\right)_m \cdot \overbrace{\left(\left(\frac{A}{B}\right)_s - \left(\frac{A}{B}\right)_t\right)}^{\gamma} \quad [36]$$

and finally,

$$\left(\frac{C}{B}\right)_m = \frac{\alpha - \left(\frac{A}{B}\right)_m \cdot \beta}{\gamma} \quad [37]$$

Remembering the exponential law for correction of the mass bias,

$$\left(\frac{I_1}{I_2}\right)_{true} = \left(\frac{I_1}{I_2}\right)_{meas} \cdot \left(\frac{MM\,(I_1)}{MM\,(I_2)}\right)^f \quad [38]$$

the suffixes true and meas refer to mass bias corrected and measured ratios, respectively.

So:

$$\left(\frac{C}{B}\right)_m = \left(\frac{C}{B}\right)_{meas} \cdot \left(\frac{MM(C)}{MM(B)}\right)^f = \frac{\alpha - \left(\frac{A}{B}\right)_m \cdot \beta}{\gamma} \quad [39]$$

As it is known that $a^b = e^{b \ln a}$, it is possible to write:

$$\left(\frac{C}{B}\right)_{meas} \cdot e^{f \ln\left(\frac{MM(C)}{MM(B)}\right)} = \frac{\alpha - \left(\frac{A}{B}\right)_m \cdot \beta}{\gamma} \quad [40]$$

After rearranging the previous equation:

$$f = \ln\left(\frac{\alpha - \left(\frac{A}{B}\right)_m \cdot \beta}{\gamma \cdot \left(\frac{C}{B}\right)_{meas}}\right) \cdot \frac{1}{\ln\left(\frac{MM(C)}{MM(B)}\right)} \quad [41]$$

And finally:

$$f = \ln\left(\frac{\alpha - \left(\frac{A}{B}\right)_{meas}\left(\frac{MM(A)}{MM(B)}\right)^f \cdot \beta}{\gamma \cdot \left(\frac{C}{B}\right)_{meas}}\right) \cdot \frac{1}{\ln\left(\frac{MM(C)}{MM(B)}\right)} \quad [42]$$

This equation has no an analytical solution for *f*, and an iterative approach is needed, in which a value f_0 is introduced into the following iterative relationship, until convergence:

$$f_{n+1} = \ln\left(\frac{\alpha - \left(\frac{A}{B}\right)_{meas}\left(\frac{MM(A)}{MM(B)}\right)^{f_n} \cdot \beta}{\gamma \cdot \left(\frac{C}{B}\right)_{meas}}\right) \cdot \frac{1}{\ln\left(\frac{MM(C)}{MM(B)}\right)} \quad [43]$$

In the particular case of the Hf, this general equation is used as follows.

Hf has six isotopes (174, 176, 177, 178, 179 and 180), three of which are not interfered with by isotopes of other elements (177, 178 and 179). Moreover, the ratio of normalization used in the IC measurements with the Neptune is $^{179}Hf/^{177}Hf$ and all listed 'raw' ratios are referenced over ^{177}Hf, since we used the same procedure for IC and IC-ID analysis. The normalization ratio is $^{178}Hf/^{177}Hf$ for which a reference value of 1.46711 (consistent with $^{179}Hf/^{177}Hf$ = 0.7325) is used. Finally, our tracer is enriched in ^{179}Hf. That is why we made the following choices for the application of the general calculation described above to the case of Hf:

A (tracer isotope):^{179}Hf

B (reference isotope):^{177}Hf

C (isotope of normalization): ^{178}Hf

This choice allows us to calculate the *f* factor from two ratios that do not suffer isobaric interference, thereby alleviating the need for interference correction. The iteration described above is initiated with f_0 = -2, value which generally is not far from the real value of the bias factor. Convergence is quickly obtained, with $| f_4 - f_3 | < 10^{-5}$.

3.3.e.2. *Calculation of the $^{176}Hf/^{177}Hf$ ratio of the sample*

We can now correct the mass bias of the measured ratios, since *f* is determined. This will allow us to calculate the $^{176}Hf/^{177}Hf$ ratio in the sample, ratio which is variable in nature due to the radioactive decay of ^{176}Lu to ^{176}Hf. After rearranging equations for the ratios $^{176}Hf/^{177}Hf$ and $^{179}Hf/^{177}Hf$ we can finally write:

$$\left(\frac{^{176}Hf}{^{177}Hf}\right)_s = \frac{\left(\frac{^{176}Hf}{^{177}Hf}\right)_m \cdot \left(\left(\frac{^{179}Hf}{^{177}Hf}\right)_s - \left(\frac{^{179}Hf}{^{177}Hf}\right)_t\right) + \left(\frac{^{176}Hf}{^{177}Hf}\right)_t \cdot \left(\left(\frac{^{179}Hf}{^{177}Hf}\right)_m - \left(\frac{^{179}Hf}{^{177}Hf}\right)_s\right)}{\left(\frac{^{179}Hf}{^{177}Hf}\right)_m - \left(\frac{^{179}Hf}{^{177}Hf}\right)_t} \quad [44]$$

3.3.e.3. *Calculation of the Hf concentration*

The calculation of the concentration of Hf is made by the equation of the isotope dilution as described elsewhere (see beginning of this chapter), and simply repeated here:

$$^{177}Hf_s = \frac{\left(\frac{^{179}Hf}{^{177}Hf}\right)_m \left(\frac{^{177}Hf}{^{179}Hf}\right)_t - 1}{\left(\frac{^{179}Hf}{^{177}Hf}\right)_s - \left(\frac{^{179}Hf}{^{177}Hf}\right)_m} \cdot \left[^{179}Hf\right]_t \cdot Pds(t) \quad [45]$$

3.3.e.4. *Calculation of the uncertainties and error propagation*

The development of formulas used for the correction of errors are long and complex, and will not be discussed here. For detailed explanations of the calculation of the uncertainties and errors, the reader is referred to Le Fèvre (2002). In this thesis only the final formulae for the several errors and uncertainties are given.

3.3.e.5. *Uncertainty on f*

We have seen (Eq. [41]) that *f* depends on the tracer ratio of the ID mixture ($^{179}Hf/^{177}Hf$ in our case) and the normalization ratio ($^{178}Hf/^{177}Hf$). The final equation of this uncertainty is:

$$\left(\frac{\sigma f}{f}\right)^2 \approx \left(\frac{-\beta}{\left(\alpha - \left(\frac{^{179}Hf}{^{177}Hf}\right)_m \cdot \beta\right) \cdot ln\left(\frac{MM(^{178}Hf)}{MM(^{177}Hf)}\right)}\right)^2 \cdot \left(\frac{\sigma\left(\frac{^{179}Hf}{^{177}Hf}\right)_{meas}}{\left(\frac{^{179}Hf}{^{177}Hf}\right)_{meas}}\right)^2 + \left(\frac{-1}{\left(\frac{^{178}Hf}{^{177}Hf}\right)_{meas} \cdot ln\left(\frac{MM(^{178}Hf)}{MM(^{177}Hf)}\right)}\right)^2 \cdot \left(\frac{\sigma\left(\frac{^{178}Hf}{^{177}Hf}\right)_{meas}}{\left(\frac{^{178}Hf}{^{177}Hf}\right)_{meas}}\right)^2 \quad [46]$$

3.3.e.6. *Uncertainty propagated by the ratios corrected for mass bias*

All the measured ratios are corrected following an exponential law (Eq. [14]). Let $R = \left(\frac{I_1}{I_2}\right)$ be the ratio of two isotopes in the tracer-sample mixture, the law of propagation of errors leads us to:

$$\left(\frac{\sigma R_m}{R_m}\right)^2 = \left(\frac{MM(I_1)}{MM(I_2)}\right)^{2f} \cdot \left(\frac{\sigma R_{meas}}{R_{meas}}\right)^2 + \left(\ln\left(\frac{MM(I_1)}{MM(I_2)}\right) \cdot R_{meas} \cdot e^{f \ln\left(\frac{MM(I_1)}{MM(I_2)}\right)}\right)^2 \cdot \left(\frac{\sigma f}{f}\right)^2 \quad [47]$$

3.3.e.7. *Uncertainty propagated in the $^{176}Hf/^{177}Hf$ ratio*

The expression of this ratio, given in the Eq. [37], shows that the specific variables subjected to uncertainties are $\left(\frac{^{176}Hf}{^{177}Hf}\right)_m$ and $\left(\frac{^{179}Hf}{^{177}Hf}\right)_m$.

After applying Eq. [40], the final equation is obtained:

$$\left(\frac{\sigma\left(\frac{^{176}Hf}{^{177}Hf}\right)_s}{\left(\frac{^{176}Hf}{^{177}Hf}\right)_s}\right)^2$$

$$= \left(\frac{\left(\frac{^{179}Hf}{^{177}Hf}\right)_s - \left(\frac{^{179}Hf}{^{177}Hf}\right)_t}{\left(\frac{^{179}Hf}{^{177}Hf}\right)_m - \left(\frac{^{179}Hf}{^{177}Hf}\right)_t}\right)^2 \cdot \left(\frac{\sigma\left(\frac{^{176}Hf}{^{177}Hf}\right)_m}{\left(\frac{^{176}Hf}{^{177}Hf}\right)_m}\right)^2$$

$$+ \left(\frac{\left(\frac{^{176}Hf}{^{177}Hf}\right)_m \cdot \left(\left(\frac{^{179}Hf}{^{177}Hf}\right)_t - \left(\frac{^{179}Hf}{^{177}Hf}\right)_s\right) + \left(\frac{^{176}Hf}{^{177}Hf}\right)_t \cdot \left(\left(\frac{^{179}Hf}{^{177}Hf}\right)_s - \left(\frac{^{179}Hf}{^{177}Hf}\right)_t\right)}{\left(\frac{^{179}Hf}{^{177}Hf}\right)_m - \left(\frac{^{179}Hf}{^{177}Hf}\right)_t}\right) \cdot \left(\frac{\sigma\left(\frac{^{176}Hf}{^{177}Hf}\right)_m}{\left(\frac{^{176}Hf}{^{177}Hf}\right)_m}\right)^2 \quad [48]$$

3.3.e.8. *Uncertainty in the Hf concentration*

For detailed calculations of propagation of errors on the concentration of Lu, the reader is referred again to the theory of ID at the beginning of the chapter. Briefly, this uncertainty is given by:

$$\left(\frac{\sigma\,[Hf]}{[Hf]}\right)^2 = \left(\frac{\sigma\left[^{179}Hf\right]_t}{\left[^{179}Hf\right]_t}\right)^2 + \left(\frac{\sigma\left(\frac{^{179}Hf}{^{177}Hf}\right)_m}{\left(\frac{^{179}Hf}{^{177}Hf}\right)_m}\right)^2 M \quad [49]$$

where the values in brackets indicate concentration (mass for the Hf, and molar to $^{179}Hf_t$), and where *M* is the amplification factor of the error (Webster, 1960).

In practice, the measurements made with the Neptune MC-ICP-MS are sufficiently precise that only the uncertainty of the tracer concentration is significant, so the relative uncertainty in the concentration of Hf is equal to the relative uncertainty on the tracer concentration.

3.3.f. Measurements parameters

The operating parameters are summarized in Table 3.7. Before starting the measuring sequence, it's worth to wait until plasma and Apex are stabilized, around 45 minutes. After this time, optimization and adjustment of ion lens for maximum sensitivity and good peak shape for ^{176}Hf is performed in each session. For this purpose the Multi Element Standard Solution (8 element) sold by Thermo Fisher Scientific (Tune-Up Solution, ref. 1149340) is used. The solution has 200 $ng.g^{-1}$ of Hf, and before analysis, it is diluted until 25 $ng.g^{-1}$ of Hf. The signal intensity of

the isotope ^{176}Hf in this standard solution is about 1.5 V. These optimization monitoring the Hf is also done before Lu analyses.

Once the parameters are adjusted, the analytical experiment is planned. The data acquisition is performed in static mode, 8 blocks of 10 measurement cycles are recorded, resulting in a 7 minutes data.

When samples are analyzed by MC-ICP-MS, instrumental drift is a parameter that must be controlled. For that purpose, JMC475 and Lu Standard Solution, are interspersed with the unknowns, for Hf and Lu respectively. Although the signal intensity will vary during long experiments, even ca. 10 %, no systematic shift of $^{176}Hf/^{177}Hf$ or $^{176}Lu/^{175}Lu$ have been found during analytical sessions. Accordingly, no correction has been applied to either the unknowns or the standards of known composition.

3.3.g. Method validation on international standards

In order to validate the method, the results obtained by this method and the recommended values (both content and isotopic ratios) have been compared for 4 international standards. The standards have been selected to cover a wide range of compositions. Whenever possible, recommended values were selected from measurements with MC-ICP-MS. If MC-ICP-MS values were not available, values obtained by ID-TIMS have been taken into account.

The results are shown in Table 3.16. It should be noted that each pair of values (A-B, C-D and E-F) are two measurements of the same solution.

Measured ratios for $^{176}Hf/^{177}Hf$ after sample preparation and subsequent separation by the method described above are within the margin of error of the expected value. The measurements also appear just moderately dispersed, showing that all of the analytical methodology leads to reproducible results. Ratios obtained for BHVO-2 standard are relatively lower than recommended value (mean of different data). However, similar values have been obtained by TIMS (Yang et al., 2009) or MC-ICP-MS analyses (Todd et al., 2010; McCoy-West et a., 2010).

The data obtained for concentrations of Hf and Lu are also reproducible, except for AGV-2 A and AGV-2 B analysis. Also, the concentrations found are fairly close to the expected values. AGV-2 A and AGV-2 B analysis yielded significantly lower values for both elements. As explained before, calculation of $^{176}Hf/^{177}Hf$ and Hf concentrations are done from the same analysis. Thus, although an accidentally and isolated small contamination could happen in both aliquots, since the ratios obtained are a little bit higher than the other 4 repetitions, the most probable error

input would be referred to the concentration calculation, surely a mistake during sample weighing.

Table 3.16. Results obtained for international standards by the CI-DI method set up in this study. Comparison with the recommended values. (a) Pourmand and Dauphas (2010); (b) Georem Preferred Value (Jochum and Nehring, 2006); (c) Weis et al. (2007); (d) Le Fèvre and Pin (2001); (e) Zhang et al. (2012).

Standard	$^{176}Hf/^{177}Hf$			Hf concentration			Lu concentration			$^{176}Lu/^{177}Hf$	± 2σ
	Reference	Measured	± 2 S.E.	Reference	Measured	± 2σ	Reference	Measured	± 2σ		
AGV-2-A	0 .282981 ± 9 (2σ) (a)	0 .282996	4E-06	5 .23 ± 0 .1 (1σ) (e)	4 .95	0 .04	0 .25 ± 0 .01 (1σ) (e)	0 .225	0 .001	0 .00646	0.001
AGV-2-B		0 .283000	8E-06		4 .95	0 .04		0 .225	0 .001	0 .00646	0.001
AGV-2-C		0 .282987	1E-05		5 .20	0 .04		0 .262	0 .002	0.00715	0.001
AGV-2-D		0 .282973	1E-05		5 .22	0 .04		0 .263	0 .002	0.00715	0.001
AGV-2-E		0 .282977	1E-05		5 .19	0 .04		0 .266	0 .002	0.00728	0.001
AGV-2-F		0 .282972	5E-06		5 .19	0 .04		0 .266	0 .002	0.00728	0.001
BHVO-2-A	0 .283104 ± 12 (2σ) (b)	0 .283095	4E-06	4 .36 ± 0 .1 (1σ) (b)	4 .32	0 .03	0.274 ± 0 .1 (1σ) (b)	0 .294	0 .002	0 .00965	0.002
BHVO-2-B		0 .283094	7E-06		4 .32	0 .03		0 .294	0 .002	0 .00965	0.002
BHVO-2-C		0 .283093	9E-06		4 .33	0 .03		0 .287	0 .002	0 .00947	0.002
BHVO-2-D		0 .283085	7E-06		4 .33	0 .03		0 .291	0 .002	0 .00954	0.002
BHVO-2-E		0 .283099	9E-06		4 .34	0 .03		0 .289	0 .002	0 .00947	0.002
BHVO-2-F		0 .283097	8E-06		4 .33	0 .03		0 .290	0 .002	0 .00953	0.002
G-2-A	0 .282529 ± 26 (2σ) (c)	0 .282527	4E-06	7 .88 ± 0 .26 (1σ) (e)	7 .75	0 .06	0 .11 ± 0 .01 (1σ) (e)	0 .110	0 .001	0 .00202	0.0004
G-2-B		0 .282533	4E-06		7 .75	0 .06		0 .110	0 .001	0 .00202	0.0004
G-2-C		0 .282528	1E-05		7 .68	0 .06		0 .107	0 .001	0 .00197	0.0004
G-2-D		0 .282518	9E-06		7 .68	0 .06		0 .107	0 .001	0 .00199	0.0004
G-2-E		0 .282515	1E-05		7 .78	0 .06		0 .108	0 .001	0 .00198	0.0004
G-2-F		0 .282527	1E-05		7 .78	0 .06		0 .108	0 .001	0 .00198	0.0004
W-2-A	0 .282715 ± 30 (2σ) (d)	0 .282711	9E-06	2 .45 ± 0 .18 (1σ) (b)	2 .48	0 .02	0 .31 ± 0 .01 (1σ) (b)	0 .314	0 .002	0 .01799	0.004
W-2-B		0 .282724	9E-06		2 .48	0 .02		0 .314	0 .002	0 .01799	0.004
W-2-C		0 .282732	8E-06		2 .47	0 .02		0 .318	0 .002	0 .01809	0.004
W-2-D		0 .282728	9E-06		2 .47	0 .02		0 .318	0 .002	0 .01804	0.004
W-2-E		0 .282722	1E-05		2 .46	0 .02		0 .313	0 .002	0 .01809	0.004
W-2-F		0 .282702	1E-05		2 .46	0 .02		0 .313	0 .002	0 .01809	0.004

Hf concentration range in G-2 is wider than for the other standards, and although is within error, it is the one that is furthest from the recommended value. G-2 is a granitic rock, so it is rich in zircons, which in turn, are rich in Hf. Although rock standards are homogeneous by definition, G-2 will be considered to have a kind of heterogeneity in what refers to Hf. Published data for Hf in G-2 varies from 1.9 $\mu g.g^{-1}$ (laser ablation analysis of an area without zircon) to 8.7 $\mu g.g^{-1}$ (Mana et al., 2012 and Shellnutt and Zhou, 2007, respectively). Actually, the values obtained in our study are consistent with those reported by Garcia de Madinabeitia et al. (2008) by ICP-MS and fusion-

dissolution treatment of the sample in the same SGIker laboratory, i.e. for the same G-2 container. Since the Lu is not retained in zircon crystal lattice, there is no such a wide range of results for Lu of the same standard.

The contents of Lu are reproducible, and close to the recommended values for G-2 and W-2, but a bit higher for AGV-2 and BHVO-2. Various hypothesis could be invoked to explain why the measurements of these standards resulted in higher Lu concentration values, e.g. instrumental differences between, TIMS, ICP-MS and ID-MC-ICP-MS, problems related to tracer, melting process, contamination, etc. In our opinion, there is nothing unusual or specific to say about this shift in the results. The BHVO-2 values obtained here are higher for instance than those reported by Raczek et al. (2001) using ID-TIMS, but fairly similar to many other values in the literature (e.g. Garcia de Madinabeitia et al., 2008 - in the same SGIker laboratory - or Deegan et al. 2013), so it can be assumed that the method is good enough. The case of AGV-2, also with values higher than the recommended one, is similar but there are less data with similar results to ours (e.g. Yang and Li, 2008; Huang et al., 2013).

As far as we know, $^{176}Lu/^{177}Hf$ ratios in CRMs are almost non-existent in the literature. Le Fèvre (2002) calculated the $^{176}Lu/^{177}Hf$ ratio in BHVO-2, being ca. 0.0108, higher than that obtained during this research. However, both $^{176}Hf/^{177}Hf$ ratio and Hf and Lu concentrations were far from the recommended value. Also, the ratios determined by the method developed in our study are fully reproducible. External reproducibility is identical to the internal precision for all samples, and systematically lower than 3 % RSD.

In conclusion, the results obtained on four CRMs for $^{176}Lu/^{177}Hf$ ratios and Lu and Hf concentrations are regarded as adequate and allow us to consider that the protocols set up during this PhD Thesis are valid for their application in Lu-Hf isotope studies.

3.4. The U-Th-Pb system by LA-Q-ICP-MS

3.4.a. Introduction

The U-Th-Pb is probably the most used geochronometer in the geological sciences, above all for zircon dating. Three are the decay sets involved, decay of two U isotopes to Pb, and decay of Th to Pb (values are from Steiger and Jäger, 1977):

$^{238}U \rightarrow {}^{206}Pb$ ($\lambda = 1.55125 \times 10^{-10}$ y^{-1} or 4.468 Ga half-life)

$^{235}U \rightarrow {}^{205}Pb$ ($\lambda = 9.8485 \times 10^{-10}$ y^{-1} or 0.704 Ga half-life)

$^{232}U \rightarrow {}^{206}Pb$ ($\lambda = 4.9475 \times 10^{-11}$ y^{-1} or 14.01 Ga half-life)

Uranium and thorium are two HFSE (High Field Strengh Elements) with similar chemical properties. They are highly incompatible elements and, because of that, they tend to concentrate in accessory minerals such as zircon or monazite, among others. Lead meanwhile, belongs to the LILE (Large Ion Litophile Elements) group, with totally different chemical properties. Its strong chalcophile affinity causes that Pb usually appears associated to sulfides, particularly forming galena (PbS ≈ 85 % of Pb). These contrasting features are responsible for the fractionation of both elements in different minerals and rocks, allowing a range of U/Pb and Th/Pb ratios to be observed, and radiometric dates to be calculated.

The U-Pb isotopic results can be graphically represented in the Concordia diagram (Figure 3.7; Wetherill, 1956), because the $^{238}U/^{235}U$ is constant in crustal rocks (137.88; Steiger and Jäger, 1977). It is a binary diagram ($^{207}Pb/^{235}U$ vs. $^{206}Pb/^{238}U$), in which the Concordia curve links all the points where the $^{207}Pb/^{235}U$ age is equal to the $^{206}Pb/^{238}U$ age. Because $^{238}U/^{235}U$ is constant in the nature, it is also possible to determine an age just by measuring $^{206}Pb^*$ and $^{207}Pb^*$, which is the slope of the line from the origin to the point on the Concordia. The age is calculated (iteratively solving for t) as follows:

$$^{206}Pb/^{207}Pb = 137.88\left[\left(e^{\lambda_1 t}-1\right)/\left(e^{\lambda_2 t}-1\right)\right] \quad [50]$$

This type of graphic is helpful to know if the system has been closed, i.e. the analyses are concondant and are projected on the Concordia curve, or if the system has been open during the rock evolution, i.e. the analyses are discordant and are placed above or below the Concordia line. The interpretation of the results is however not always easy.

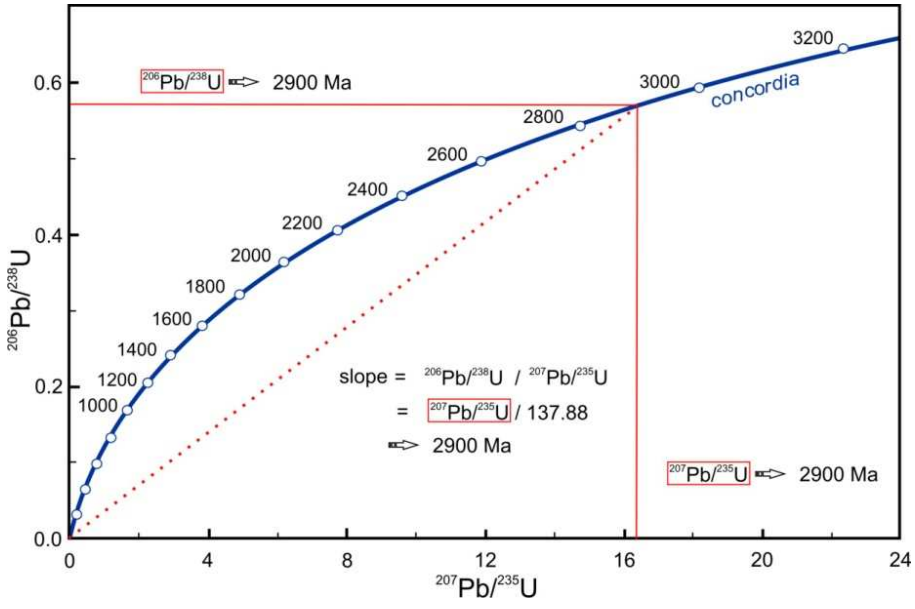

Figure 3.7. Concordia diagram showing the $^{207}Pb/^{235}U$, $^{206}Pb/^{238}U$ and $^{206}Pb/^{207}Pb$ ages for a concordant analysis.

Isotopic compositions and atomic weights of the elements involved in the spectroscopy of U, Th and Pb are presented in the tables below (Tables 3.17; 3.18; 3.19 and 3.20).

Table 3.17. Abundance of the U, Th and Pb isotopes (in %). Values recommended by the IUPAC (International Union of Pure and Applied Chemistry; De Laeter et al., 2003).

	204	206	207	208	232	234	235	238
Pb	1.4	24.1	22.1	52.4				
Th					100			
U						0.005	0.72	99.27

Table 3.18. Atomic masses of lead, according to the IUPAC (International Union of Pure and Applied Chemistry; De Laeter et al., 2003).

Isotope	204	206	207	208
Mass	203.973028	205.974449	206.975880	207.976636

Table 3.19. Atomic masses of thorium, according to IUPAC (International Union of Pure and Applied Chemistry; De Laeter et al., 2003).

Isotope	232
Mass	232.0380495

Table 3.20. Atomic masses of uranium, according to the IUPAC (International Union of Pure and Applied Chemistry; De Laeter et al., 2003).

Isotope	234	235	238
Mass	234.0409447	235.0439222	238.0507835

3.4.b. Sample preparation

As mentioned before, the modification in the *SuperCell*^{TM} ablation cell allows us to introduce both standards and samples (Figure 2.20, Chapter 2) for the analytical session. The sample is introduced in the center of the cell as a 'thick' petrographic section, i.e. a common polished thin section but somewhat thicker than usual (ca. 50-80 µm). The standards are mounted in 10 mm diameter epoxy plugs and introduced on both sides of the thin section. As a routine, one of the mounts contains crystals of GJ-1 and 91500 zircon standards, while the other has NIST SRM 612 glass that is used to tune the instrument parameters before starting the analysis.

Laser ablation analysis do not require a thorough polishing of the sample, although for easy identification of the grains of interest in the laser ablation system, which has lower lighting possibilities and image quality than an optical microscope, it is strongly recommended to polish the surface until the edges of the different minerals are recognizable.

Before the in situ analysis, we should obtain as much information as possible about the structure of the zircon, such as zoning composition, growth pattern or presence of inherited core and inclusions. This should prevent to analyse portions of the zircon with different Pb isotopic compositions that would generate misleading results. The best methods to obtain images of the

internal structure of zircon on (sub) polished surfaces are the Cathodoluminescence (CL) and the Back Scattered Electrons (BSE) techniques. During this research, BSE was the chosen technique. The microphotographs were taken in the Scanning Electronic Microscopy (SEM) facility of the SGIker (Euskal Herriko Unibertsitatea UPV/EHU) with a JEOL JSM-6400 instrument.

3.4.c. Data acquisition and reduction

Isotopic analyses of U-Pb were performed with a Nd:YAG 213 nm New Wave laser ablation system connected to a cuadrupole inductively coupled plasma mass spectrometer XSeries 2 at the Geochronology and Isotope Geochemistry facility of SGIker (UPV/EHU). See chapter 2 for more information about the equipment.

The alignment of the instrument and mass calibration was performed before every analytical session using the NIST SRM 612 reference glass by inspecting the signal of ^{238}U (at least 400,000 cps for ^{238}U) and by minimizing the ThO^+/Th^+ ratio (<< 1 %). The usual instrument parameters are summarized in Table 3.21.

Once the instrument is in optimal conditions, and after a minimum time of 30 minutes for plasma stabilization, the analytical sequence is ready to start. The first 4 analysis are performed on the GJ-1 standard zircon, then followed by 10 sample analyses and another 2 of the standard, in order to check any signal drift during the sequence. This sequence of 10 samples - 2 standards is repeated as many times as necessary until the number of desired analysis. For ending the experiment, another 4 analysis of the GJ-1 are performed. Analysis of the 91500 zircon standard are interspersed between samples to confirm that all corrections are done reliably and the final ages are accurate. Data acquisition for each analysis is performed for 90 seconds, the first 30 for the blank signal of the used gases, and the next 60 for the ablation. The acquisition involves the continuous sweep of the isotopes of interest with 10 ms residence time for ^{202}Hg, ^{204}Pb, ^{206}Pb, ^{208}Pb, ^{232}Th, ^{238}U and 20 ms for ^{207}Pb isotopes. The occurrence of common Pb in the sample can be monitored by the evolution of the ^{204}(Pb+Hg) signal intensity, but no common Pb correction was applied owing to the large isobaric interference from Hg. The ^{235}U signal is calculated from ^{238}U on the basis of the ratio $^{238}U/^{235}U$= 137.88.

The raw data collected from each analysis, that is, the time resolved signal of single isotopes and isotope ratios was monitored and carefully inspected to verify the presence of perturbations related to inclusions, fractures, mixing of different age domains or common Pb. In general, the signal is considered homogeneous when the respective lines of the analyzed masses are parallel, interpreting that relations between all elements analyzed are constant over time. During this research, data reduction was carried out with the software package GLITTER®

(Macquarie Research Ltd, 2001; van Achterbergh et al., 2001; Jackson et al., 2004). Analyses of GJ-1 are used for correcting the fractionation and instrumental drift. Analyses with a discordance higher than 10 % (calculated as [($^{206}Pb/^{238}U$ age)/($^{207}Pb/^{206}Pb$ age)]x100, Meinhold et al., 2011) were not taken into account. The analyses with reduced integration intervals or variable signal were also discarded.

Calculated ratios were exported and Concordia ages and diagrams were generated using the Isoplot/Ex v.2.49 software package by Ludwig (2001). The concentrations in U-Th-Pb were calibrated relative to the certified contents of GJ-1 zircon standard (Jackson et al., 2004).

Table 3.21. Operating parameters for U-Th-Pb isotopic measurements.

Laboratory Information	
Laboratory name	SGIker, Euskal Herriko Unibertsitatea UPV/EHU
Sample preparation	'Thick' petrographic section for samples, 10 mm diameter resin mount for standards
Imaging	BSE, JEOL JSM-6400
Laser ablation system	
Make, Model & type	New Wave Research, UP213, Nd:YAG
Ablation cell & volume	Modified SuperCell™, volume c.33 cm^3
Laser wavelength	213 nm
Pulse width	3-5 ns
Fluence	5 $J.cm^{-2}$
Repetition rate	10 Hz
Ablation duration	90 secs (30 secs for blank and 60 secs for sample)
Spot size	25-30 µm
ThO^+/Th^+	< 0.05 %
Carrier gas	100% He in the cell, Ar make-up gas combined using a Y-piece along the sample transport line to the torch.
Cell carrier gas flow	0.9-1 l/min
ICP-MS Instrument	
Make, Model & type	Thermo Fisher Scientific, X-Series 2, Q-ICP-MS
Sample introduction	Ablation aerosol
RF power	1350 W
Make-up gas flow	ca. 0.90 l/min (optimized daily)
Plasma gas flow	14.9 l/min
Auxiliary gas flow	0.9 l/min
Scanning mode	Peak jumping, 1 point per peak
Detector mode	Pulse counting, dead time correction applied, and analog mode when signal intensity > 1 million CPS.
Masses measured	202, 204, 206, 207, 208, 232, 238
Integration time per peak/dwell times	10 ms for each isotope, except 20 ms for 207

Error propagation is a subject of great debate within the scientific community, and is out of scope of this PhD thesis. However, the programs designed for data reduction of LA-ICP-MS analysis usually considers those corrections and uncertainties as follows:

a. Counting statistics while measuring each peak

b. Beam instability/drift

c. Elemental fractionation (between U and Pb), during ablation and ionization

d. Mass fractionation (between isotopes of the same element), during ablation/ionization

e. Matrix-induced bias

f. Detector calibration (linearity and relative gain)

g. Spatial variability, in the cell and on the mount

h. Hg correction (magnitude of correction and Hg IC, or isotopic composition)

i. Common Pb correction (both magnitude and IC)

j. Background correction, for gas blank and tracer blank

k. Ratio determinations for the primary standard

l. Standard age uncertainty

m. Decay constant uncertainties

3.4.d. Method validation on international standards

Zircon analysis in thin section using LA-Q-ICP-MS involves the adaptation of the classic analytical routine (plug with minerals separated through Wilfley table, heavy liquids, etc.) due to the characteristics of the sample holder. Thus, factors such as lack of thickness of the desired mineral and the characteristics of the underlying mineral, if any, must be taken into account. Other factors are common to the traditional technique, as the degree of fixation of the zircon or its homogeneity in depth. Laser ablation parameters must be adapted and controlled so that the sensitivity be enough for instrumental quantification.

In this respect, a crucial factor for determining the parameters of the ablation is the spot diameter. As it has been explained before, the GJ-1 zircon has been used as calibration standard, so it was conscientiously analyzed several times with different parameters in order to check the best analytical conditions. After testing different diameters of spot, it was considered that diameters of 25 to 30 µm were appropriate for solving geological problems, whereby all the other parameters, such as frequency or laser energy, were adapted accordingly.

The analyses of GJ-1 standard zircon, plotted in the Figure 3.8, were performed using these conditions, and the obtained U-Pb ages are comparable to those of reference in the literature (e.g. Jackson et al., 2004). The results for other zircons used as secondaries/validation

are also in good agreement with published data (91500: Wiedenbeck et al., 1995 and Plesovice: Sláma et al., 2008; Figure 3.8). Results for the older 91500 zircon standard yield an age of 1059.9 ± 4.2 Ma while the younger Plesovice zircon gave an age of 338.0 ± 1.9 Ma. The higher error in 91500 reflects the limitations of the technique for zircons with low U, Th and Pb contents.

The determination of isotopic $^{232}Th/^{208}Pb$ ratios and ages in analyzed zircons under these measurement conditions has not been possible due to the low concentration of Th (11 $\mu g.g^{-1}$) and the consequent low value of ^{208}Pb in the GJ -1 (Elhlou et al., 2007).

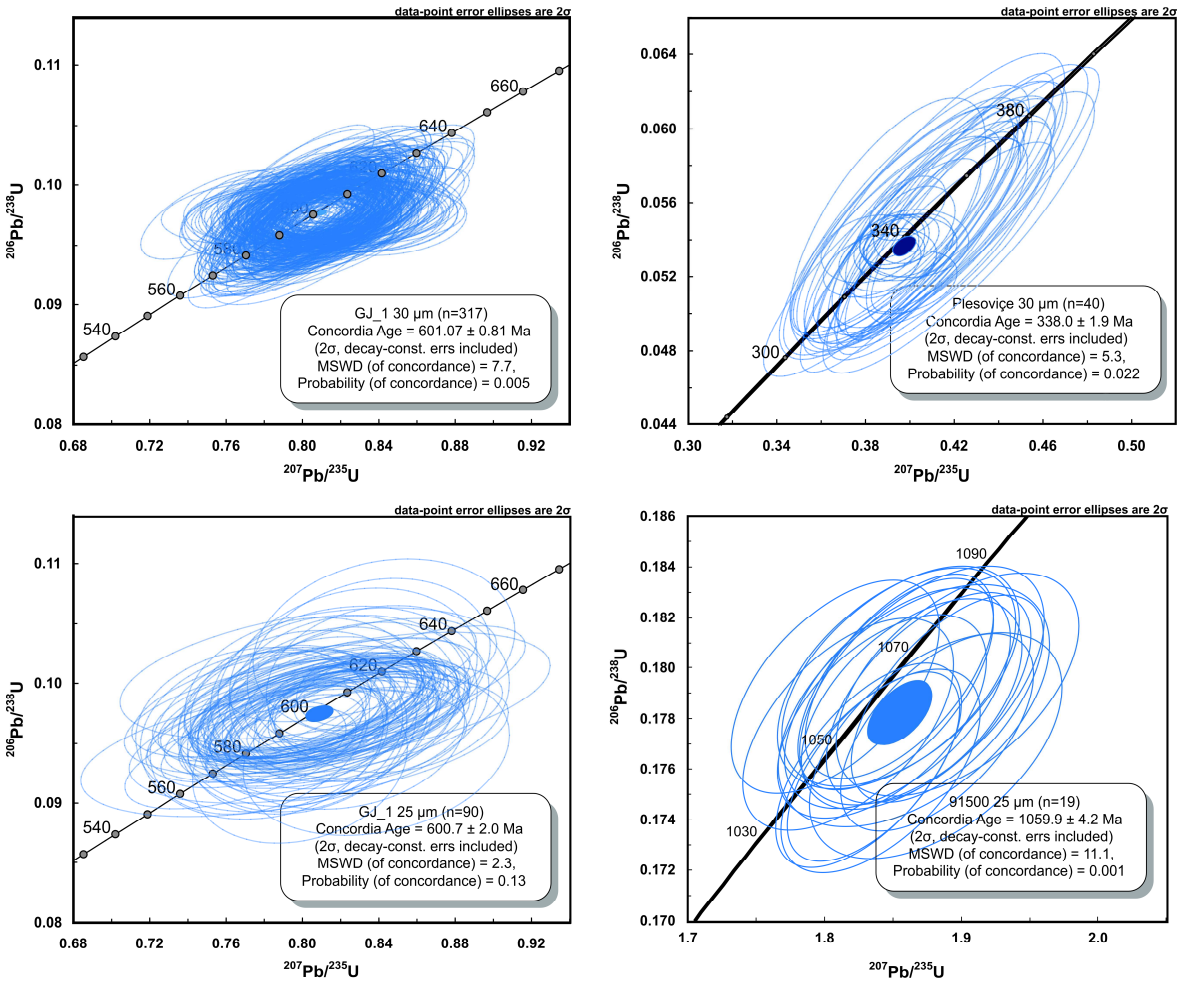

Figure 3.8. Concordia diagrams for U-Pb system analyses in standard zircons.

3.5. The Hf isotopes by LA-MC-ICP-MS

3.5.a. Introduction

The Lu-Hf systematics allows the Hf isotope composition to be used as an isotopic tracer for some minerals, being zircon the most important of them (others are rutile, baddeleyite, wadeite, …). Having a geochemical behavior very similar to zirconium, Hf is much more

compatible in zircon than the Rare Earth Elements (REE), especially Lu. Thus, Hf may reach a higher concentration (up to 3 %) and is retained more easily than Lu in the zircon lattice. For this reason, zircons are characterized by very low $^{176}Lu/^{177}Hf$ ratios (< 0.001) and, consequently, the isotopic variations of Hf due to the radiogenic ^{176}Hf are practically negligible. The main corollary of this is that zircons preserve initial $^{176}Hf/^{177}Hf$ isotopic ratios inherited from the magma where they crystallized. This characteristic, together with the high content of Hf and its very low diffusivity in zircon, permits to preserve, in a single crystal, different Hf isotopic compositions, generated during crystal growth under the variable P, T and compositional conditions.

3.5.a.1. *Hf evolution in the Earth's crust and mantle*

The Lu-Hf isotope system is utilized to study the history of differentiation of the Bulk Silicate Earth (BSE) that led to the formation of the crust-mantle system. Lu and Hf are a Heavy Rare Earth Element (HREE) and a HFSE, respectively. This implies a very different behavior for Lu and Hf during the evolution of the crust-mantle system. Hf is more incompatible than Lu during the partial melting processes in the mantle; so, during the first events of juvenile crust generation in the Archean time, the crust has been enriched in Hf and depleted in Lu, leaving a mantle enriched in Lu and depleted in Hf. Thus, starting from a unique primordial mantle with chondritic Lu and Hf isotopic composition, which is referred to as CHUR (Chondritic Uniform Reservoir) composition, two reservoirs with different Lu/Hf ratio were generated: the crust with $Lu/Hf_{crust} < Lu/Hf_{CHUR}$ and the depleted mantle with $Lu/Hf_{mantle} > Lu/Hf_{CHUR}$.

As for other isotope systems, the deviation of the $^{176}Hf/^{177}Hf$ from the chondritic (CHUR) values for a sample is indicated by the Epsilon (ε) notation:

$$\varepsilon_{Hf} = \left[\frac{\left(^{176}Hf/^{177}Hf\right)_{Sample}}{\left(^{176}Hf/^{177}Hf\right)_{CHUR}} - 1\right].10^4 \quad [51]$$

while the model age is calculated in reference to the Depleted Mantle by the following formula:

$$\text{Hf } T_{DM} = \frac{1}{\lambda} \ln\left\{\frac{\left(^{176}Hf/^{177}Hf\right)_{CHUR} - \left(^{176}Hf/^{177}Hf\right)_{DM}}{\left(^{176}Lu/^{177}Hf\right)_{CHUR} - \left(^{176}Lu/^{177}Hf\right)_{DM}} + 1\right\} \quad [52]$$

Whereas a single stage T_{DM} age is commonly calculated for whole rock analyses, for zircon studies a two stage T_{DM} age is needed (Nebel et al., 2007).

The T_{DM} age in zircon is calculated from the initial Hf isotopic composition of the zircon, using an average crustal Lu/Hf ratio. The initial Hf composition of zircon represents the $^{176}Hf/^{177}Hf$ value calculated at the time the zircon crystallized, namely the U-Pb age previously obtained on

the same crystal. Such model ages indicate the crustal residence time for the rocks that hosted the zircon.

3.5.b. Sample preparation

The samples are prepared in the same way as for U-Pb analysis. However, it is interesting to mention that for the Hf isotope geochemistry in zircon, the BSE imagery is preferable rather than the cathodoluminescence because the brightness of the image is atomic mass dependent and, therefore, it is possible to easily discriminate regions with different Hf content in the same zircon crystal. Higher brightness in the image corresponds to higher Hf contents in the zircon (e.g. Hanchar and Miller, 1993; Corfu et al. 2003).

3.5.c. Hf spectrometry

Isotopic analyses of Hafnium were performed with a Nd:YAG 213 nm New Wave laser ablation system connected to a multicollection inductively coupled plasma mass spectrometer Thermo Fisher Scientific Neptune at SGIKER (UPV/EHU). See chapter 2 for more information about the equipment. The analyses were done in the static multi-collection mode with the cups positioned as shown in Table 3.15.

3.5.d. Interferences and fractionations correction

Unlike measurements in solution, where species are chemically separated, with laser ablation mode, all the matrix goes into the plasma. Accurate determination of $^{176}Hf/^{177}Hf$ is challenging because of the fractionation of Hf, Yb and Lu isotopes during ionization, and because Yb and Lu also have isotopes at mass 176. The later corrections are specially critical given that ^{176}Yb and ^{176}Lu generally constitute 10 %-30 % (rarely > 70 %) of the ^{176}Hf present.

Isotope fractionation of Hf is determined and corrected by the measurement of $^{179}Hf/^{177}Hf$, both of which are free of interferences. $^{179}Hf/^{177}Hf$ is constant in nature and is known to be 0.7325 (Patchett and Tatsumoto, 1980). The mass bias, β_{Hf}, is calculated from the following law (Russell et al., 1978):

$$\beta = \frac{\ln\left(\frac{\left(^{179}Hf/^{177}Hf\right)_{meas}}{\left(^{179}Hf/^{177}Hf\right)_{true}}\right)}{\ln\left(\frac{m_{179}}{m_{177}}\right)} \quad [53]$$

Isotope fractionation of Yb is not exactly the same as for Hf (Chu et al., 2002; Woodhead et al., 2004), so β_{Yb} must be determined from the measurement of $^{173}Yb/^{171}Yb$ (both are

interference free). $^{173}Yb/^{171}Yb$ is also constant in nature, and its value is 1.13255 (Amelin and Davis, 2005).

Given the presence of only two isotopes, ^{176}Lu and ^{175}Lu, it is not possible to determine the mass bias for Lu directly. Accordingly, it is assumed that Lu and Yb behave similarly, and β_{Yb} is used for β_{Lu}. The impact of this assumption is negligible because there is generally much less ^{176}Lu than ^{176}Yb or ^{176}Hf.

Correction for interference of ^{176}Yb is determined by monitoring ^{173}Yb and assuming a $^{176}Yb/^{173}Yb$ ratio of 0.7964 (Amelin and Davis, 2005). As noted above, measurement of $^{173}Yb/^{171}Yb$ is used to determine β. Correction for the interference of ^{176}Lu is determined by monitoring ^{175}Lu and using β_{Yb} and $^{176}Lu/^{175}Lu=0.02656$ (Patchett and Tatsumoto, 1980).

It has been noted before that the Yb interference correction is crucial for precise and accurate $^{176}Hf/^{177}Hf$ ratios obtained by laser ablation analysis (e.g., Woodhead et al., 2004; Hawkesworth and Kemp, 2006). A range of Yb isotope ratios are reported in the literature (e.g., Chu et al., 2002; Segal et al., 2003; Vervoort et al., 2004; Amelin and Davis, 2005). At moderate Yb/Hf ratios of 0.06 these different Yb isotope compositions propagate into shifts in $^{176}Hf/^{177}Hf$ similar to the analytical uncertainty (Gerdes and Zeh, 2009; Kemp et al., 2009). However, for higher Yb/Hf ratios the different compositions can result in considerable over- or undercorrection. The most appropriate composition for interference correction might vary for different instrumentations.

It should be noted, however, that the accuracy of the measured $^{176}Hf/^{177}Hf$ is sensitive to the Yb isotope composition used. Using only a slightly different composition (Segal et al., 2003), would led to a 0.03 % lower $^{176}Hf/^{177}Hf$ of ca. 0.282110.

Because the interference corrections described above need to be robust and yield reliable $^{176}Hf/^{177}Hf$ ratios, all the ratios used for corrections and assumptions must be checked carefully. This has been done by measuring the JMC475 Hf standard doped with Yb and Lu. Once the instrument parameters are set (see the Table 7), JMC475 solutions containing varying amounts of Yb and Lu are measured to ensure that the correction for $^{176}Hf/^{177}Hf$ is still right.

Figure 3.9 shows the results of solution analyses. The observation is that there is no correlation between $^{176}Hf/^{177}Hf$ and the concentration of Yb and Lu, which demonstrates that the interference corrections are robust.

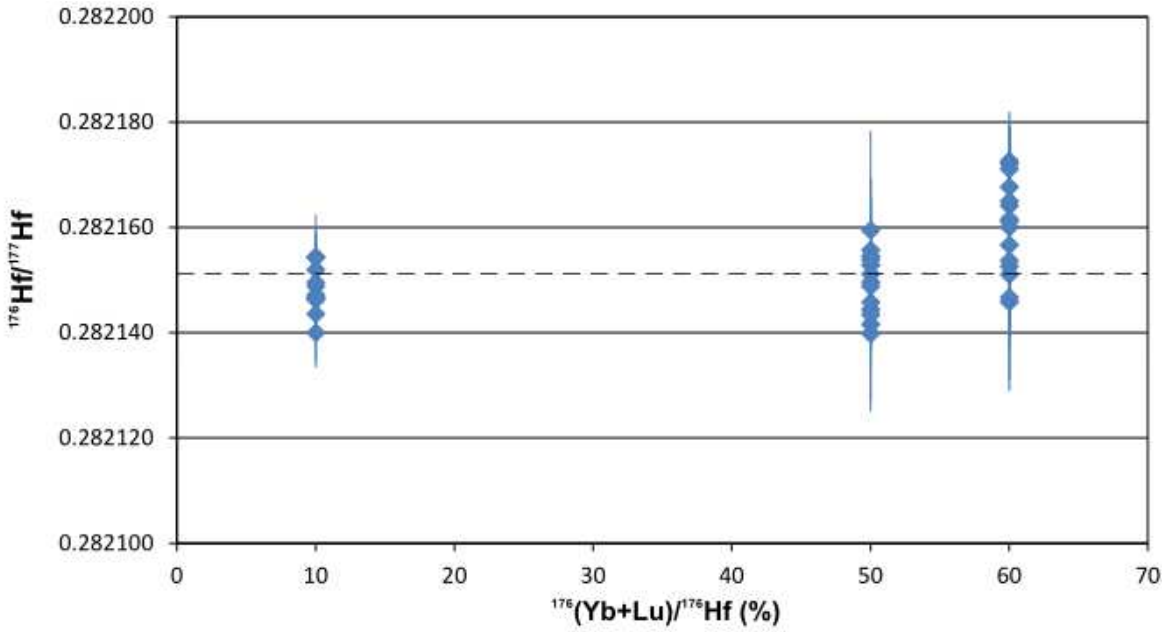

Figure 3.9. $^{176}Hf/^{177}Hf$ plotted against relative proportion of $^{176}(Yb+Lu)/^{176}Hf$ (shown as percentage), for all solution analyses performed. The dashed line is the known $^{176}Hf/^{177}Hf$ of JMC475 solution (0.282151, see in the previous chapter).

3.5.e. Data adquisition

Once solution analyses have confirmed that fractionation and interference corrections are robust, zircon standards are analyzed by LA-MC-ICP-MS. These standards are mounted as explained before for U-Th-Pb system analyses.

In situ Hf isotope data is acquired using a 40 µm diameter spot size (see below), and the other analytical parameters used during the measurements are resumed in the Table 3.22. It is worth to mention that nitrogen (N_2) is introduced as make up gas flow together with Ar. This allowed to suppress oxide formation in the plasma and enhanced the signal sensitivity by about 30 %.

The adquisition protocol is similar to the explained for U-Th-Pb analyses. Zircon standards are analyzed at the start of a session, at the end of a session and between every 10 unknown analyses. In that case, GJ-1 standard (Jackson et al., 2004) is only measure to check that there's no instrumental drift. The data reduction was carried out with Iolite® software (Paton et al. 2011).

3.5.f. Spot size

When laser ablation analysis is performed, the scientist is looking forward to optimize the analysis of small volumes of material so that it will be possible to take advantage of the spatial resolution of LA-ICP-MS while still generating isotope ratios reasonably precise and accurate.

One of the major challenging features of Hf isotope analysis by laser ablation is the size of the sampling point, usually much higher than that needed for the U-Pb analysis. The optimization of the method allows to reduce the size of the analysis point, but always with the need to maintain an acceptable signal.

Table 3.22. Operating parameters for Hf isotopic measurements by LA-MC-ICP-MS.

Laboratory Information	
Laboratory name	SGIker, Euskal Herriko Unibertsitatea UPV/EHU
Sample preparation	'Thick' petrographic section for samples, 10 mm diameter resin mount for standards
Imaging	BSE, JEOL JSM-6400
Laser ablation system	
Make, Model & type	New Wave Research, UP213, Nd:YAG
Ablation cell & volume	Modified SuperCell™, volume c.33 cm^3
Laser wavelength	213 nm
Pulse width	3-5 ns
Fluence	5 $J.cm^{-2}$
Repetition rate	10 Hz
Ablation duration	90 secs (30 secs for blank and 60 secs for sample)
Spot size	40 µm
Carrier gas	100% He in the cell, N_2 (first) and Ar (after) make-up gases combined using two Y-piece along the sample transport line to the torch.
Cell carrier gas flow	ca. 0.35 l/min
ICP-MS Instrument	
Make, Model & type	Thermo Finnigan Neptune, MC-ICP-MS
Sample introduction	Ablation aerosol
RF power	1300 W
Make-up gas flow (N_2)	ca. 10 ml/min
Make-up gas flow (Ar)	ca. 0.75 l/min (optimized daily)
Plasma gas flow	15.0 l/min
Coolant gas flow	0.45 l/min
Scanning mode	Static
Detector mode	Faraday cups
Masses measured	171, 173, 175, 176, 177, 178, 179

During the setting up of the Hf-Hf method in the SGIker facility, analysis with 15 µm, 25 µm, 30 µm and 40 µm have been done, the last diameter, with 5 Hz and 10 Hz repetition rate. Figure 3.10 shows the different results obtained with the different spot sizes. As can be seen, the spots of 15 µm and 25 µm are totally imprecise and inaccurate. The values for the 30 µm spot size are not bad at all, giving ratios close to the reference material, but errors are significantly high. Analyses with 40 µm spot size, both at 5 Hz and 10 Hz, give acceptable results and errors. The errors are better (less error) with 10 Hz repetition rate, because the generated aerosol contains more sample particles and, therefore, higher signal is reaching the detector.

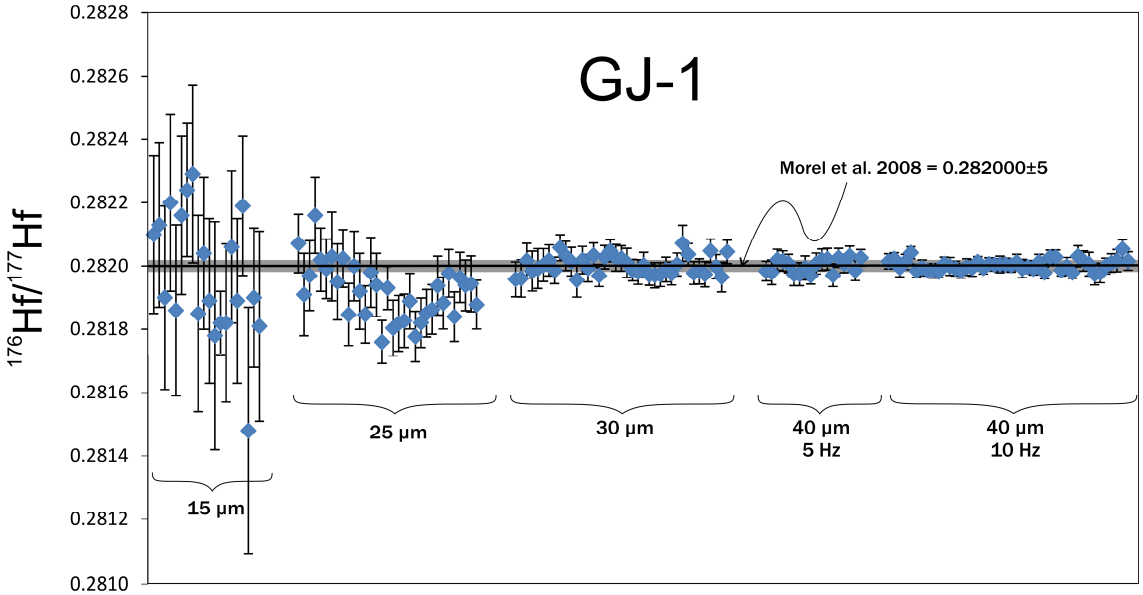

Figure 3.10. Graphic showing the analysis performed with various spot sizes and frequencies.

3.5.g. Validation of the method

For optimization and method validation four of the most commonly used zircon standards have been systematically analyzed: GJ-1, 91500, Mudtank and Plešovice (Figure 3). These zircons cover a wide range of $^{176}Hf/^{177}Hf$ ratios and Yb concentrations, the last in order to check that the values used for corrections are working properly.

Figure 3.11 and Table 3.23 show the results obtained for these zircons during the setting up of the method, together with the reference values. It should be remembered that the analyses performed in solution always have lower errors due to the stability of the signal and the absence of matrix.

The analyses of the reference materials yield values identical, within error, and only about 2-3 times less precise than the solution mode MC-ICP-MS data of the Lu and Yb free Hf fraction. For a typical session, each of the standards yields an average $^{176}Hf/^{177}Hf$ that is within one epsilon unit of the known value, i.e. analyses are accurate to within approximately one epsilon unit.

Table 3.23. Reference values, both for solution and laser ablation analysis, and results obtained for the standards zircons. Errors are 2σ. 1: Morel et al. (2008); 2: Woodhead and Hergt (2005); 3: Slama et al. (2008); 4: Schwieters et al. (2009).

	Solution	Laser Ablation[4]	This PhD Thesis	n
GJ-1	0.282000±5[1]	0.282015±29	0.282003±17	44
91500	0.282306±8[2]	0.282299±26	0.282288±15	10
Mudtank	0.282507±6[2]	0.282522±19	0.282508±13	20
Plesovice	0.282484±8[3]	0.282486±28	0.282472±12	20

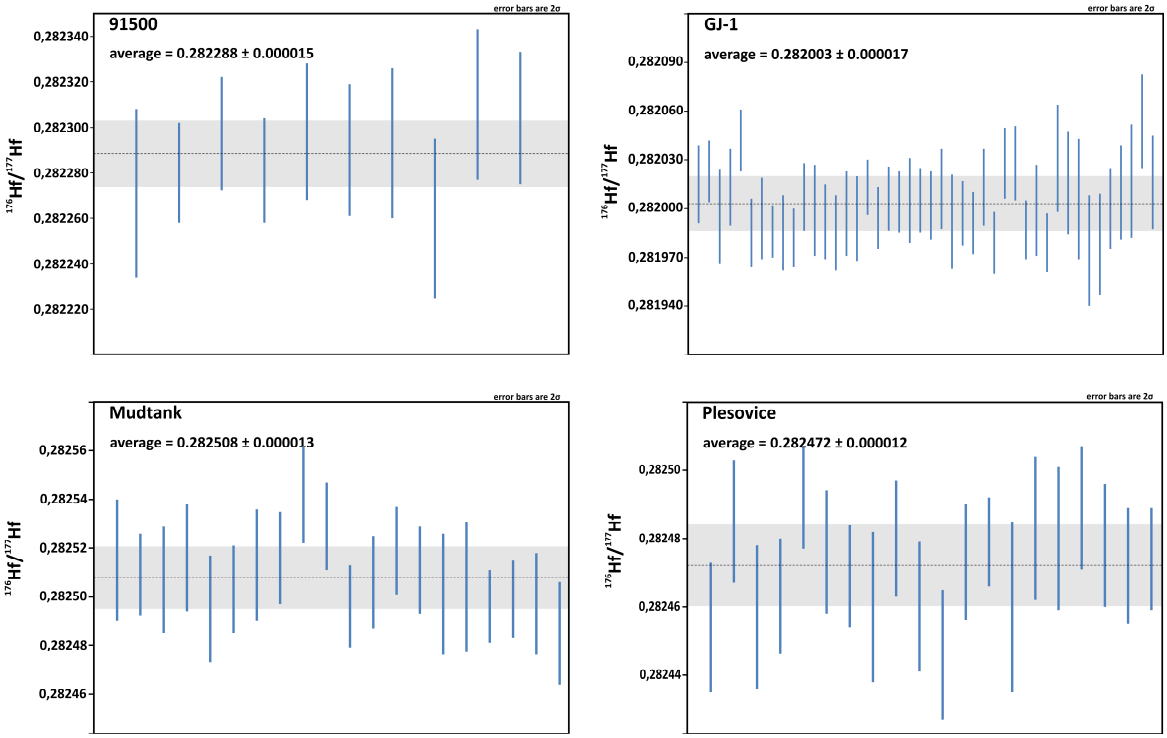

Figure 3.11. Results for Hf isotope analyses in standard zircons by LA-MC-ICP-MS.

eman ta zabal zazu

Universidad del País Vasco
Euskal Herriko Unibertsitatea

NAZIOARTEKO BIKAINTASUN CAMPUSA
CAMPUS OF INTERNATIONAL EXCELLENCE